Surface Chemistry Guidance In Controllable Neural Stem Cell Differentiation To Direct Stem Cell Fate.

Future Applications In Building Artificial Neural Networks.

HALA SHAKIB DHOWRE

Thesis submitted to The University of Nottingham for the degree of Doctor of Philosophy

FEBRUARY 2018

DECLARATION

All sentences or passages quoted in this thesis from other people's work have been specifically acknowledged by clear cross-referencing authors, works and page(s). Any illustrations which are not the work of the author of this thesis have been used in explicit permission of the originator (where possible) and are specifically acknowledged. I have used some sections of my published review paper, Hala et al. 2015, in the scientific background chapter.

I understand that failure to do this amounts to plagiarism and will be considered grounds for failure in this thesis and the degree examination as a whole.

Name: **HALA SHAKIB DHOWRE**

Signature:

Date: **14th February 2018**

DEDICATION

First and foremost, Glory be to the Most High and The Most Wise for making this journey feasible.

Allah I profoundly thank you.

To my dearest and beloved, Hooyo Macaan & Aabo Macaan, know that you are the epitome of unconditional love.

I cherish you.

Know that I carried your endless words of advice and encouragement with me throughout this journey.

I appreciate you.

Last but not least my siblings, Hana, Hibatullah & Abdirahman, the greatest gifts in my life. You shared my happiness and sorrow by listening when I talked, laughed when I laughed, and held my hand well before I realized that I needed it.

As the Somali proverb goes 'Either be a mountain or lean on one' and through this journey you were my mountain.

I am grateful to you.

♥ I dedicate this thesis to you, My Family ♥

ABSTRACT

Cell instructive biointerfaces are versatile tools to mimic a natural cellular environment and control cell fate *in vitro*. The particular interest lies in combining information gained from surface and interface analysis tools with biological analysis to explore and understand fundamental processes such as neuronal stem cell differentiation at the biointerface. A major challenge in biointerface design is to mimic and study the complex interactions of the natural processes in the extracellular matrix (ECM) with artificially designed surfaces and interfaces. In the past, peptide surfaces have been used as ECM mimics, however, more research is required in this field to tune the properties of peptide surface to modulate the outcome of stem cell fate.

The present work aims to address this challenge by designing new synthetic peptide surfaces with well controlled composition and functionality able to impart have control over the differentiation of neuronal stem cells with the ultimate goal to relate surface properties and stem cell response to understand and control how neuronal networks function.

Compositionally well-defined surfaces of two short laminin peptide sequences, Arg-Gly-Asp (RGD) and Ile-Lys-Val-Ala-Val (IKVAV) were prepared of various ratios via the "grafting from" stepwise approach. The surface modification was confirmed with surface analysis techniques to indicate successful peptide functionalization. The neural progenitor stem cells (NPSCs) were set up from embryonic rat hippocampi (E18). Immunocytochemistry (ICC) observed cell viability and differentiation to specific NPSCs lineages for βIII-Tubulin and GFAP. The surface characterizing techniques of WCA, AFM, ToF-SIMS, and XPS validated the successful orthogonal functionalization of controllable peptides composition surfaces with the increase of RGD composition a relative decrease in the IKVAV composition was observed. The increase in the normalized total ion fragments of RGD in the ToF-SIMS measurements can be related linearly to the % area coverage of neurons versus astrocytes observed on the controllable peptide composition surfaces.

Well-defined peptide surfaces were designed and successfully demonstrated that the amount of RGD peptide composition present on the surface influences cell adhesion, proliferation and differentiation to a desirable cell fate or controllable cell population (i.e. neurons and astrocytes).

Recent technological developments demonstrate a shift from two-dimensional (2D) surfaces to three-dimensional (3D) surfaces, so we used the designed versatile 2D surfaces as the template to design comparable 3D surfaces to examine the biological response of NPSCs to both microenvironments.

This study proposes the design of novel 3D nanoparticles (NPs) made of gold and surface-conjugated with differentiation-inducing peptides. The NPs-peptides will guide stem cell differentiation to neurons that self-aggregate around the NPs by cell-cell contacts to form neurospheres. The neural stem cells will establish 3D structures biomimicking the cytoarchitecture of the brain. Successively, they could be used as an alternative 3D *in vitro* model for neurotoxicity testing of drugs and chemicals. Size-controllable NPs will be surface-conjugated with RGDC and IKVAVC(19) peptides via the SPPS "grafting to" approach. Two different sizes of NPs were characterized as AuNPs and SiO_2@AuNPs characterization and validated by TEM, DLS, ζ-potential, EDX; and the surface functionalization on NPs was successfully confirmed by UV/vis spectroscopy and ζ-potential. The NPSCs were set up from E18 rat hippocampi and cell viability and differentiation to specific NSPCs lineages was stained for βIII-Tubulin and GFAP. AuNPs and SiO_2@AuNPs peptide immobilized surfaces supported cell adhesion, proliferation, and survival. The confocal light scanning microscope (CLSM) images indicate that the RGDC functionalized AuNPs and SiO_2@AuNPs surfaces induced a preferential differentiation towards a neurons cell fate and the IKVAVC(19) functionalized surfaces of AuNPs and SiO_2@AuNPs favored an astrocytes cell. The cellular uptake of functionalized AuNPs by the cells in the neurospheres was observed via TEM micrographs, whilst the micrographs of functionalized SiO_2@AuNPs surfaces suggest that they were not taken-up into the cells. Hence, indicating that there is a difference in the cellular uptake mechanism for the functionalized AuNPs and SiO_2@AuNPs, which might be due to the agglomeration of the nanoparticles than the individual size of the nanoparticles.

In conclusion, the relation between the 2D and 3D surfaces may provide new insight in understanding how surface properties affect the regulation of physiological relevance in directing neural cell differentiation, which will be essential to understand how neural networks function.

ACKNOWLEDMENTS

Foremost, I would like to thank my supervisors Dr Mischa Zelzer and Dr Noah Russell for giving me the opportunity to work in this fascinating field of cell responsive materials. I value their support, scientific guidance and all the times that they have challenged me to think outside the box.

I also would like to thank my colleagues in the Biointerface and Neurophotonics Laboratory Research groups for the pleasant working atmosphere, help and stimulating discussions over the academic years. I am very thankful to Christopher Towlson for training me in the cell culture procedures and for always being there when I needed scientific guidance, which has continued even after completing his Postdoctoral position; David Scurr for training me on the ToF-SIMS; Emily Smith for acquiring the XPS measurements; Alessandro La Torre for acquiring the nanoparticles TEM measurements; Denise McLean for being amazing and training me on how to prepare biological samples for TEM imaging and acquiring the TEM micrographs; Tim Shelf and Seema Rajani for the assistance in acquiring the CLSM images.; and Ruggero Foralosso for not given up on the hard work and long hours we put into the peptide synthesis and analysis of the RGD and RGDC peptides.

Houda Sahaf, Zahra Abada, and Solomon Idinyang for being there for me through the great and difficult times we experienced together, for providing me with scientific guidance and challenges, as well as transferring skills across our interdisciplinary fields of biology, physics, chemistry and engineering.

I would also like to acknowledge the researchers in this field whose papers I have referenced, without their work this report would not have been possible to complete. Last but not least, I would like to express gratitude to my family for supporting and encouraging me through this challenging period in my life writing this thesis.

CONTENTS

DECLARATION ii

DEDICATION iii

ABSTRACT iii

ACKNOWLEDMENTS vi

CONTENTS vii

LIST OF FIGURES xv

LIST OF SCHEMATIC DIAGRAMS xxii

LIST OF TABLES xxv

LIST OF EQUATIONS xxvii

ABBREVIATIONS xxviii

1 INTRODUCTION 1

1.1 SCIENTIFIC BACKGROUND 1

1.2 AIM OF THESIS 2

1.2.1 OVERVIEW OF THE CHAPTERS 4

2 SCIENTIFIC BACKGROUND 7

2.1 INTRODUCTION 7

2.2 CELLS AND THEIR NATURAL ENVIRONMENT 7

2.2.1 NEURAL PROGENITOR STEM CELLS (NPSCs) 9

2.2.1.1 NEURONS 10

2.2.1.2 GLIA 12

2.2.1.2.1 ASTROCYTES 12

2.2.2 EXTRACELLULAR MATRIX (ECM) 13

2.2.2.1 CELL ADHESION MOLECULES (CAMs) 16

2.2.2.1.1 INTEGRINS 16

2.2.2.1.2 CELL ADHESION FRAGMENTS OF LAMININ 19

2.3 BIOMATERIALS AND THEIR PROPERTIES 21
2.3.1 SURFACE PROPERTIES 22
2.3.1.1 SURFACE CHEMISTRY 22
2.3.1.2 SURFACE TOPOGRAPHY 22
2.3.1.3 SURFACE ELASTICITY/ STIFFNESS 24
2.3.2 SURFACE MODIFICATION 24
2.3.2.1 TYPES OF BIOMATERIALS 24
2.3.2.2 PATTERNING SURFACE CUES VIA LITHOGRAPHY 26
2.3.2.3 FUNCTIONALIZATION VIA PHYSICAL AND CHEMICAL ADSORPTION 27
2.3.3 CELL RESPONSE TOWARDS THE BIOMATERIALS 31
2.3.3.1 CELL RESPONSE TO SINGLE PEPTIDE COMPOSITION SURFACES 33
2.3.3.1.1 RGD FUNCTIONALIZED SURFACES 33
2.3.3.1.2 IKVAV FUNCTIONALIZED SURFACES 37
2.3.3.2 CELL RESPONSE TO MIXED PEPTIDE COMPOSITION SURFACES 38
2.3.3.3 CELL RESPONSE TO 2D AND 3D SURFACES 43
2.4 SURFACE ANALYSIS TECHNIQUES 49
2.4.1 SENSILLE DROP WATER CONTACT ANGLE (WCA) 50
2.4.2 FLUORESCENCE SPECTROSCOPY 51
2.4.3 UV/ VISIBLE SPECTROSCOPY 51
2.4.4 ATOMIC FORCE MICROSCOPY (AFM) 52
2.4.5 TIME OF FLIGHT – SECONDARY ION MASS SPECTROSCOPY (ToF-SIMS) 53
2.4.6 X-RAY PHOTOELECTRON SPECTROSCOPY 55
2.4.7 DYNAMIC LIGHT SCATTERING (DLS) AND ζ-POTENTIAL 56
2.4.8 TRANSMISSION ELECTRON MICROSCOPY (TEM) 59
2.4.9 OPTICAL MICROSCOPY 63
2.4.9.1 FLUORESCENCE MICROSCOPY 63
2.4.9.2 CONFOCAL LASER SCANNING MICROSCOPY (CLSM) 64
2.4.10 OTHER TECHNIQUES 66

3 METHODOLOGY 67

3.1 SURFACE PREPARATION AND CHARACTERIZATION 67

3.1.1 CLEANING OF GLASS SURFACES 67

3.1.2 SILANISATION OF GLASS SURFACES 67

3.1.3 PEG_{18}-DIAMINE COUPLING TO SILANISED GLASS SURFACES 67

3.1.4 PEPTIDE COUPLING TO PEG_{18}-DIAMINE 68

3.1.4.1 SURFACES WITH SINGLE PEPTIDE COMPOSITION 68

3.1.4.2 OPTIMISATION OF SURFACES WITH MIXED PEPTIDE COMPOSITION 69

3.1.4.2.1 BIOFUNCTIONALITY OF $-NH_2$ and -OH SURFACES 69

3.1.4.2.2 BIOFUNCTIONALITY OF $-NH_2$ and -Cl SURFACES 69

3.1.4.2.3 BIOFUNCTIONALITY OF -Fmoc and $-OCH_3$ SURFACES 69

3.1.5 PEPTIDE COUPLED TO GOLD EVAPORATED ON GLASS SURFACES 70

3.1.5.1 GOLD EVAPORATED ON GLASS SURFACES 70

(i) AUT ON Au SURFACES 71

(ii) Benzene-1,4-dithiol/ AuNPs/ AUT 71

3.1.5.2 PEPTIDE COUPLED TO AUT ON Au SURFACES 71

3.1.6 SYNTHESING PEPTIDE IN REACTION VESSEL 72

3.1.6.1 RESIN SWELLING 72

3.1.6.2 STANDARD WASHING PROCEDURE 72

3.1.6.3 STANDARD COUPLING PROCEDURE 72

3.1.7 CONJUGATING PEPTIDE TO GOLD NANOPARTICLES 73

3.1.7.1 PREPARATION OF AuNPs 73

3.1.7.2 PREPARATION OF GOLD-COATED SiO_2 NANOPARTICLES 74

3.1.7.2.1 SYNTHESIS OF SiO_2NPs 74

3.1.7.2.2 SiO_2-Core Au-Shell NANOPARTICLES (SiO_2@AuNPs) 74

3.1.7.3 CONJUGATING PEPTIDE TO Au NANOPARTICLES 75

3.1.7.3.1 GRAFTING PEPTIDES TO NANOPARTICLES 75

3.2 CELL CULTURE AND CHARACTERIZATION 75

3.2.1 ETHICS 75

3.2.2 COATING OF CONTROL SURFACES FOR CELL CULTURE 76
3.2.3 ISOLATION OF HIPPOCAMPI FROM E18 BRAIN 76
3.2.3.1 ANIMAL DISSECTION 76
3.2.3.2 HIPPOCAMPAL DISSECTION 77
3.2.3.3 NEURAL PROGENITOR STEM CELLS (NPSCs) CULTURE 78
3.2.3.3.1 NPSCs TWO-DIMENSIONAL CULTURE (2D) 79
3.2.3.3.2 NPSCs THREE-DIMENSIONAL CULTURE (3D) 79
3.2.3.4 CELL ADHESION AND PROLIFERATION 79
3.2.3.5 CELL DIFFERENTIATION – IMMUNOCYTOCHEMISTRY (ICC) 80
3.2.3.6 PROCESSING CELLS FOR TRANSMISSION ELECTRON MICROSCOPY (TEM) 81
3.3 ANALYTICAL TECHNIQUES 81
3.3.1 WATER CONTACT ANGLE (WCA) 81
3.3.2 FLUORESCENCE SPECTROPHOTOMETERY 82
3.3.3 ATOMIC FORMCE MICROSCOPE (AFM) 82
3.3.4 TIME OF FLIGHT – SECONDARY IONISATION MASS SPECTROSCOPY (TOF-SIMS) 83
3.3.5 X-RAY PHOTOELECTRON SPECTROSCOPY (XPS) 83
3.3.6 HIGH-PRESSURE LIQUID CHROMATOGRAPHY (HPLC) 83
3.3.7 ELECTROSPRAY IONISATION MASS SPECTROSCOPY (ESI-MS) 84
3.3.8 NUCLEAR MAGNETIC RESONANCE (NMR) 84
3.3.9 UV/ VISIBLE SPECTROSCOPY 84
3.3.10 ZETASIZER 84
3.3.11 TRANSMISSION ELECTRON MICROSCOPY (TEM) 84
3.3.12 OPTICAL MICROSCOPY 85
3.3.13 CONFOCAL FLUORESCENCE MICROSCOPY 85
3.3.14 STATISTICAL ANALYSIS 85
3.3.15 MILLIQ-GRADE WATER 85
3.4 CHEMICALS, SOFTWARE AND TECHNIQUES 86

4 IMMOBILIZING PEPTIDES ON GLASS SURFACES 92

4.1 INTRODUCTION 92

4.2 BACKGROUND 92

4.2.1 ORGANOSILANES 92

4.2.2 POLY(ETHYLENE)GLYCOL LINKERS 94

4.2.3 PEPTIDES 95

4.3 SURFACE PREPARATION, CHARACTERIZATION AND VALIDATION 98

4.3.1 SURFACE WETTABILITY AND FLUORESCENCE SURFACES WITH SINGLE PEPTIDE COMPOSITION 98

4.3.2 SURFACE TOPOGRAPHY OF SURFACES WITH SINGLE PEPTIDE COMPOSITION 103

4.3.3 TOF-SIMS STUDIES OF MODIFIED GLASS SURFACES 107

4.3.4 XPS STUDIES OF MODIFIED GLASS SURFACES 114

4.3.4.1 WIDE SURVEY O 1s, C 1s, Si $2p_{3/2}$ and N 1s spectra 114

4.3.4.2 HIGH-RESOLUTION O 1s, C 1s, Si $2p_{3/2}$ AND N 1s SPECTRA 117

4.4 CELL RESPONSE TOWARDS THE IMMOBILIZED PEPTIDE SURFACES 122

4.4.1 CELL SURVIVAL 122

4.4.2 CELL DIFFERENTIATION 128

4.5 SUMMARY 132

5 IMMOBILIZING CONTROLLED PEPTIDE COMPOSITIONS ON GLASS SURFACES 135

5.1 INTRODUCTION 135

5.2 BACKGROUND 135

5.2.1 PRESENTING ORTHOGONALITY 136

5.2.1.1 Boc AND Fmoc PROTECTING GROUPS 138

5.2.1.2 SAFETY-CATCH LINKER 138

5.3 SURFACE PREPARATION, CHARACTERIZATION AND VALIDATION 140

5.3.1 DESIGN AND OPTIMISING ORTHOGONAL FUNCTIONAL SURFACES . 140

5.3.1.1 OPTIMISING SURFACE WETTABILITY 141
5.3.1.1.1 ORTHOGONAL -OH AND -NH_2 SURFACES 141
5.3.1.1.2 ORTHOGONAL -Cl AND -NH_2 SURFACES 143
5.3.1.1.3 ORTHOGONAL FMOC-GABA-OH AND MONOMETHYL GLUTARATE SURFACES 143
5.3.1.2 OPTMISING SURFACE HOMGENEITY ON THE ORTHOGONAL Fmoc GABA-OH AND MONOMETHYL GLUTARATE SURFACES 145
5.3.2 SURFACE WETTABILITY OF SURFACES WITH MIXED PEPTIDE COMPOSITION 149
5.3.3 SURFACE TOPOGRAPHY OF SURFACES WITH MIXED PEPTIDE COMPOSITION 152
5.3.4 SURFACE HOMOGEINITY OF SURFACES WITH MIXED PEPTIDE COMPOSITION 155
5.3.4.1 REGION OF INTEREST 161
5.4 CELL RESPONSE TO CONTROLLABLE COMPOSITION OF PEPTIDES 162
5.4.1 CELL SURVIVAL 163
5.4.2 CELL DIFFERENTIATION 170
5.5 SUMMARY 177

6 IMMOBILIZING PEPTIDES TO DESIGN 2D AND 3D MICROENVIRONMENTS 180

6.1 INTRODUCTION 180
6.2 BACKGROUND 181
6.2.1 THREE-DIMENSIONAL (3D) MODEL MICROENVIRONMENTS 181
6.2.1.1 NEUROSPHERES 184
6.2.1.2 NANOPARTICLES 187
6.2.2 SELF-ASSEMBLED MONOLAYERS (SAMs) OF THIOLS 188
6.3 SURFACE PREPARATION, CHARACTERIZATION AND VALIDATION 191
6.3.1 NANOPARTICLE SYNTHESIS AND CHARACTERIZATION 191
6.3.1.1 MORPHOLOGY OF NANOPARTICLES 191

6.3.1.2 SIZE OF NANOPARTICLES 192
6.3.1.3 SURFACE CHARGE OF NANOPARTICLES 194
6.3.1.4 SURFACE CHEMISTRY OF NANOPARTICLES 195
6.3.2 SURFACE FUNCTIONALIZATION OF AuNPs AND SiO_2@AuNPs 196
6.3.2.1 DIRECT PEPTIDE CONJUGATION APPROACH ON 2D GOLD SURFACES 198
6.3.2.1.1 SURFACE WETTABILITY OF Au PEPTIDE SURFACES 198
6.3.2.1.2 SURFACE TOPOGRAPHY OF Au PEPTIDE SURFACES 199
6.3.2.1.3 SURFACE HOMOGENEITY OF Au PEPTIDE SURFACES 201
6.3.2.2 DIRECT PEPTIDE CONJUGATION APPROACH ON 3D GOLD SURFACES 208
6.3.3 SURFACES FUNCTIONALIZATION OF 2D GOLD SURFACES 211
6.3.3.1 SURFACE WETTABILITY OF Au FLAT AND Au NPs SURFACES 211
6.3.3.2 SURFACE TOPOGRAPHY OF Au FLAT AND Au NPs SURFACES 213
6.3.3.2.1 Au FLAT SURFACES 213
6.3.3.2.2 Au NPs SURFACES 215
6.3.3.2.3 COMPARING Au FLAT VS Au NPs VS Au PEPTIDES SURFACES 217
6.3.3.3 SURFACE HOMOGEINITY OF Au FLAT AND Au NPs SURFACES 217
6.3.3.3.1 Au FLAT SURFACES 218
6.3.3.3.2 SURFACE HOMOGEINITY OF Au NPs SURFACES 224
6.4 CELL RESPONSE TO 2D AND 3D SURFACES 231
6.4.1 CELL SURVIVAL ON 2D SURFACES 231
6.4.1.1 ADHESION AND PROLIFERATION ON Au FLAT AND Au NPs SURFACES 231
6.4.1.1.1 FUNCTIONALIZED Au FLAT SURFACES 235
6.4.1.1.2 FUNCTIONALIZED Au NPs SURFACES 235
6.4.1.1.3 FUNCTIONALIZED CONTROL SURFACES 236
6.4.2 CELL DIFFERENTIATION ON FUNCTIONALIZED 2D SURFACES 239
6.4.2.1 FUNCTIONALIZED Au FLAT SURFACES 239
6.4.2.2 FUNCTIONALIZED Au NPs SURFACES 239
6.4.2.3 FUNCTIONALIZED CONTROL SURFACES 240

6.4.3 CELL SURVIVAL ON 3D SURFACES 246
6.4.3.1 ADHESION AND PROLIFERATION ON AuNPs AND SiO_2@AuNPs SURFACES 246
6.4.3.1.1 ADHESION AND PROLIFERATION ON FUNCTIONALIZED Au PEPTIDES SURFACES 246
6.4.3.1.2 CELL DIFFERENTIATION ON FUNCTIONALIZED Au PEPTIDES SURFACES 249
6.4.3.2 CELL ADHESION AND PROLIFERATION ON FUNCTIONALIZED AuNPs AND SiO_2@AuNPs SURFACES 252
6.4.3.2.1 FUNCTIONALIZED AuNPs 252
6.4.3.2.2 FUNCTIONALIZED SiO_2@AuNPs 253
6.4.3.2.3 PEPTIDES AS A SOLUBLE FACTOR 257
6.4.4 CELL DIFFERENTIATION ON 3D SURFACES 260
6.4.4.1 FUNCTIONALIZED AuNPs 260
6.4.4.2 FUNCTIONALIZED SiO_2@AuNPs 264
6.4.5 CELLULAR UPTAKE OF 3D SURFACES 268
6.4.6 COMPARING 2D VS 3D SURFACES 271
6.5 SUMMARY 272

7 CONCLUSION & OUTLOOK 276
7.1 CONCLUSION 276
7.2 FUTURE WORK 278
7.2.1 WORK TO BE CONTINUED 278
7.2.2 OUTLOOK 281
7.3 YESTERDAY, TODAY, & TOMORROW 282

APPENDICES 283
BIBLIOGRAPHY 289

LIST OF FIGURES

Figure 2.1 Tissue engineering triad of cells influenced by the environment. 31

Figure 2.2 Confocal immunofluorescent expression of Tuj1.. 33

Figure 2.3 (A) Importance of chemical adsorptions when using small molecules is illustrated by culturing cryopreserved rat cortical neurons on surfaces that have circular regions of physisorbed and chemisorbed cyclo(RGDFK-PEG). 35

Figure 2.4 Schematic representation of IPN synthesis (not to scale). (A) Sequential polymerization steps create an IPN that is swollen in aqueous media and conjugated with bioactive peptides. 40

Figure 2.5 Fluorescent microscopy images of hMSCs on different polymer surfaces. 41

Figure 2.6 Characterization of HA hydrogels and differentiation of mDA neurons. (A) Schematic of the 3D HA-RGD-hep. 42

Figure 2.7 Human embryonic palatal mesenchyme (HEPM) cells, mesenchymal stem cells (MSCs), and adipose derived stem cells (ADSCs) cultured on flat hydrogels of 0.5% alginate-RGD, 2% alginate-RGD, and 2% unmodified alginate on day 7. 46

Figure 2.8 Process flow showing cryogel synthesis, pyrolysis, NSCs culture, fixing, and MRI. 48

Figure 2.9 MRI of NSCs cultured on a glassy carbon scaffold. 48

Figure 2.10 Fluorophore chart aligning emission and excitation fluorescence spectra to guide the correct selection of fluorophore. 64

Figure 4.1 The change in the WCA through the cleaning process respectively; (A) as-received, (B) organic solvent cleaned, and (C) piranha cleaned glass coverslips. 98

Figure 4.2 Water contact angle measurements through the modification steps to achieve (A) RGD and (B) IKVAV peptide surfaces. 100

Figure 4.3 Intrinsic fluorescence intensity of the Fmoc-protecting group signal in the present (green) and absence (red and blue) is detected to confirm the build-up of the amino acids to achieve the RGD or IKVAV peptide sequence functionality. 102

Figure 4.4 The AFM topography images observe the change in surface roughness (nm) through the two-step cleaning process respectively to the peptide functionalized surfaces. (A) As-received, (B) organic solvent cleaned, (C) piranha cleaned, (D) GOPTS, (E) PEG_{18}-diamine, (F) RGD, (G) IKVAV, and (H) PLO.Laminin functionalized glass coverslips. 105

Figure 4.5 (A) Z-range and (B) RMS measurements of the functionalized surfaces obtained from the corresponding AFM Height images, n = 3. 106

Figure 4.6 ToF-SIMS overall spectrum of the functionalized surfaces annotated with the selected positive ion peaks and normalized to the total ion count. 110

Figure 4.7 ToF-SIMS characterization of marker ion fragments of amino acids distinguishable for surface modification and normalized to the total ion count..... 111

Figure 4.8 ToF-SIMS analysis of the marker ion fragments as raster images to illustrate the homogenous surfaces and normalized to the total ion count, scale is 500 μm x 500 μm. 112

Figure 4.9 ToF-SIMS analysis of the marker ion fragments as raster images to illustrate the homogenous surfaces and normalized to the total ion count, scale is 3 mm x 3 mm. 113

Figure 4.10 XPS anlysis of (A) chemical structures, (B) the wide survey spectra, and (C) high resolution spectra curve fits of the C 1s, N 1s and Si $2p_{3/2}$ core levels of the surfaces. 115

Figure 4.11 The relative atomic concentration (%) of the main elements (A) carbon, oxygen and silicon, and (B) nitrogen on functionalized surface. 116

Figure 4.12 The concentration (%) of the chemical environments in C 1s core levels through the surface functionalization. 119

Figure 4.13 The concentration (%) of the chemical environments in N 1s core levels through the surface functionalization. 120

Figure 4.14 Phase contrast images of E18 NPSCs incubated on positive control PLO.Laminin surfaces after (A) 6 hrs and (B) 24 hrs. 123

Figure 4.15 Phase contrast images of E18 NPSCs incubated on control PEG_{18}-diamine at (A) 2DIV and (B) 7DIV. 123

Figure 4.16 Phase contrast images of E18 NPSCs cell cultures on PLO.Laminin, RGD and IKVAV surfaces that are low surface coverage to high surface coverage, n = 3. 124

Figure 4.17 % Area coverage of E18 NPSCs on RGD and IKVAV surfaces in comparison to the control PLO.Laminin surface. 127

Figure 4.18 Fluorescent microscopy images of differentiated E18 NPSCs on PLO.Laminin, RGD and IKVAV surfaces. 129

Figure 4.19 Quantification of E18 NPSCs differentiation into neurons (βIII-Tubulin positive, green) and astrocytes (GFAP positive, red) as relative area coverage by each cell type the RGD, IKVAV, and PLO.Laminin surfaces. 131

Figure 5.1 ToF-SIMS analysis of the marker ion fragments to illustrate the composition of the surfaces with mixed chemical functionalities.. 147

Figure 5.2 ToF-SIMS analysis of the raster images of the marker ion fragments to illustrate the composition and homogeneity of the surfaces with mixed chemical functionalities. 148

Figure 5.3 Water contact angle measurements through the modification steps to achieve mixed peptide composition in a 1:1 of RGD and IKVAV peptide surfaces. 151

Figure 5.4 WCA measurements for mixed peptide compositions as a percentage of (A) Fmoc(NH_2) functionality and (B) RGD functionality for the final orthogonal functionalized surfaces. 152

Figure 5.5 (A) Z-range and (B) RMS measurements of the functionalized surfaces obtained from the corresponding AFM Height images, n =3 153

Figure 5.6 The AFM topography images observe the change in surface roughness (nm) through the orthogonal chemistry functionalization to the well controlled composition peptide surfaces 154

Figure 5.7 ToF-SIMS overall spectrum of the functionalized surfaces annotated with the selected positive ion peaks and normalized to the total ion count. 157

Figure 5.8 ToF-SIMS characterization of marker ion fragments of amino acids distinguishable for surface modification and normalized to the total ion count 158

Figure 5.9 ToF-SIMS analysis of the marker ion fragments as raster images to illustrate the homogenous surfaces and normalized to the total ion count 159

Figure 5.10 The summary of region of interest (ROI) of the of the mixed peptide composition of marker ion fragments of IKVAV in relation to those of RGD on the orthogonal functionalized surfaces. 160

Figure 5.11 The summary of the mixed peptide composition of IKVAV in relation to RGD on the orthogonal functionalized surfaces. 161

Figure 5.12 Phase contrast images of E18 NPSCs cell cultures on 0% RGD – 50% RGD surfaces that are low surface coverage to high surface coverage, n = 3. 164

Figure 5.13 Phase contrast images of E18 NPSCs cell cultures on 75% RGD – 100% RGD surfaces that are low surface coverage to high surface coverage, n = 3. 165

Figure 5.14 Phase contrast images of E18 NPSCs cell cultures on PLO.Laminin, RGD and IKVAV surfaces that are low surface coverage to high surface coverage, n = 3 166

Figure 5.15 % Area coverage of E18 NPSCs on 0% RGD – 100% RGD surfaces with PLO.Laminin, RGD and IKVAV surfaces as controls 168

Figure 5.16 Fluorescent microscopy images of differentiated E18 NPSCs on 0% RGD – 100% RGD surfaces. 171

Figure 5.17 Quantification of E18 NPSCs differentiation into neurons (βIII-Tubulin positive) and astrocytes (GFAP positive) as relative area coverage by each cell type on 0% RGD – 100% RGD surfaces and the control surfaces of PLO.Laminin, RGD and IKVAV. 173

Figure 5.18 Quantification of E18 NPSCs differentiation as a change in the relative composition of the cell population expressed as ratio of % area coverage of neurons (βIII-Tubulin positive) and astrocytes (GFAP positive) on 0% RGD – 100% RGD surfaces and the control surfaces of PLO.Lamin, RGD and IKVAV. 175

Figure 5.19 The quantification of E18 NPSCs differentiation into neurons (βIII-Tubulin positive) in relation to the increase in % RGD peptides ion fragments on the surfaces. 176

Figure 6.1 Colours of nanoparticles. (A) AuNPs is wine coloured, (B) SiO_2NPs is white in colour and a colour change is observed to lilac when the gold is adsorbed on the silica core to form SiO_2@AuNPs. 191

Figure 6.2 TEM micrographs of (A) AuNPs, (B) SiO_2NPs, and (C) SiO_2@AuNPs seeded on copper grips to determine nanoparticles size. 193

Figure 6.3 EDX spectra to illustrate the elemental mapping of (A) AuNPs and (B) SiO_2@AuNPs in correspondence to the TEM micrograph region of the nanoparticles. 195

Figure 6.4 WCA measurements following the surface functionalization of XYZ surfaces with RGDC and IKVAVC(19) peptides, n = 3. 198

Figure 6.5 (A) Z-range and (B) RMS measurements of the functionalized Au Peptide surfaces obtained from the corresponding AFM Height images, n =3. 199

Figure 6.6 The AFM topography images observe the change in surface roughness (nm) through the oxygen plasma activation respectively to the Au Peptide functionalized surfaces. 200

Figure 6.7 ToF-SIMS overall spectrum of the Au Peptide functionalized surfaces annotated with the selected negative ion peaks and normalized to the total ion count. 203

Figure 6.8 ToF-SIMS overall spectrum of the Au Peptide functionalized surfaces annotated with the selected positive ion peaks and normalized to the total ion count. 204

Figure 6.9 ToF-SIMS characterization of marker ion fragments of amino acids distinguishable for Au Peptide surface modification and normalized to the total ion count. 205

Figure 6.10 ToF-SIMS analysis of the marker ion fragments as raster images to illustrate the Au Peptide homogenous surfaces and normalized to the total ion count, scale is 3 mm x 3 mm. 206

Figure 6.11 UV/ visible spectra of (A) AuNPs and (B) SiO_2@AuNPs at 400-800 nm of the peptide conjugation on the gold surfaces. 208

Figure 6.12 WCA measurements following the surface functionalization of RGD and IKVAV peptides on (A) Au Flat and (B) Au NPs surfaces, n = 3. 212

Figure 6.13 (A) Z-range and (B) RMS measurements of the functionalized Au Flat surfaces obtained from the corresponding AFM Height images, n = 3. 213

Figure 6.14 The AFM topography images observe the change in surface roughness (nm) through the oxygen plasma activation respectively to the Au Flat peptide functionalized surfaces. 214

Figure 6.15 (A) Z-range and (B) RMS measurements of the functionalized Au NPs surfaces obtained from the corresponding AFM Height images, n =3. 215

Figure 6.16 The AFM topography images observe the change in surface roughness (nm) through the oxygen plasma activation respectively to the Au NPs peptide functionalized surfaces. 216

Figure 6.17 ToF-SIMS overall spectrum of the Au Flat functionalized surfaces annotated with the selected negative ion peaks and normalized to the total ion count. 220

Figure 6.18 ToF-SIMS overall spectrum of the Au Flat functionalized surfaces annotated with the selected positive ion peaks and normalized to the total ion count. 221

Figure 6.19 ToF-SIMS characterization of marker ion fragments of amino acids distinguishable for Au Flat surface modification and normalized to the total ion count. 222

Figure 6.20 ToF-SIMS analysis of the marker ion fragments as raster images to illustrate the Au Flat homogenous surfaces and normalized to the total ion count, scale is 3 mm x 3 mm. 223

Figure 6.21 ToF-SIMS overall spectrum of the Au NPs functionalized surfaces annotated with the selected negative ion peaks and normalized to the total ion count. 227

Figure 6.22 ToF-SIMS overall spectrum of the Au NPs functionalized surfaces annotated with the selected positive ion peaks and normalized to the total ion count. 228

Figure 6.23 ToF-SIMS characterization of marker ion fragments of amino acids distinguishable for Au NPs surface modification and normalized to the total ion count..... 229

Figure 6.24 ToF-SIMS analysis of the marker ion fragments as raster images to illustrate the Au NPs homogenous surfaces and normalized to the total ion count, scale is 3 mm x 3 mm. 230

Figure 6.25 Phase contrast images of E18 NPSCs cell cultures on Au Flat surfaces functionalized with RGD or IKVAV surfaces that are low surface coverage to high surface coverage, n = 3. 232

Figure 6.26 Phase contrast images of E18 NPSCs cell cultures on Au NPs surfaces functionalized with RGD or IKVAV surfaces that are low surface coverage to high surface coverage, n = 3. 233

Figure 6.27 Phase contrast images of E18 NPSCs cell cultures on control surfaces respectively, (i) PLO.Laminin (glass), (ii) Au Flat-AUT, and (iii) Au NPs-AUT surfaces that are low surface coverage to high surface coverage, n = 3. 234

Figure 6.28 % Area coverage of E18 NPSCs on Au Flat, Au NPs surfaces and the PLO.Laminin surface as comparison control surface. 238

Figure 6.29 Fluorescent microscopy images of differentiated E18 NPSCs on Au Flat surfaces functionalized with RGD and IKVAV 242

Figure 6.30 Fluorescent microscopy images of differentiated E18 NPSCs on Au NPs surfaces functionalized with RGD and IKVAV. 243

Figure 6.31 Fluorescent microscopy images of differentiated E18 NPSCs on control surfaces respectively, (i) PLO.Laminin (glass), (ii) Au Flat-AUT, and (iii) Au NPs-AUT surfaces functionalized with RGD and IKVAV. 244

Figure 6.32 Quantification of E18 NPSCs differentiation into neurons (βIII-Tubulin positive) and astrocytes (GFAP positive) as relative area coverage by each cell type on Au Flat, Au NPs surfaces functionalized with RGD, IKVAV and the control surface of PLO.Laminin... 245

Figure 6.33 Phase contrast images of E18 NPSCs cell cultures on Au-RGDC and Au-IKVAVC(19) surfaces that are low surface coverage to high surface coverage, n = 3. 247

Figure 6.34 Adhesion of NPSCs on functionalized Au Peptides surfaces and the PLO.Laminin surface as comparison control surface. 248

Figure 6.35 Fluorescent microscopy images of differentiated E18 NPSCs on Au Peptides surfaces functionalized with RGDC and IKVAV(19) 250

Figure 6.36 Quantification of E18 NPSCs differentiation into neurons (βIII-Tubulin positive) and astrocytes (GFAP positive) as relative area coverage by each cell type on Au Peptides surfaces functionalized with RGDC, IKVAVC(19) and the control surface of PLO.Laminin. 251

Figure 6.37 Phase contrast images of E18 NPSCs aggregates forming neurospheres with bare AuNPs, AuNPs-RGDC and AuNPs-IKVAVC(19), n = 3. 254

Figure 6.38 Phase contrast images of E18 NPSCs aggregates forming neurospheres with bare SiO_2@AuNPs, SiO_2@AuNPs-RGDC and SiO_2@AuNPs-IKVAVC(19), n = 3 255

Figure 6.39 Quantification of the neurospheres diameter due to aggregated e18 NPSCs on functionalized AuNPs and SiO_2@AuNPs surfaces and the bare AuNPs and SiO_2@AuNPs surfaces as the comparison control surfaces. 256

Figure 6.40 Phase contrast images of E18 NPSCs aggregates forming neurospheres in serum-free media with (i) no peptides, (ii) RGD, and (iii) IKVAVC(19) at 30 days of *in vitro*, n = 3. 257

Figure 6.41 Fluorescent microscopy images of differentiated E18 NPSCs aggregates forming neurospheres in serum-free media with (i) no peptides (control), (ii) RGD, and (iii) IKVAVC(19). 259

Figure 6.42 Confocal microscopy images of E18 NPSCs aggregates forming AuNPs-Control neurospheres (i) stack of the maximum intensity projection, (ii) orthogonal sectioning in xyz axis, and (iii) 3D reconstruction of the AuNPs-Control neurosphere. 261

Figure 6.43 Confocal microscopy images of E18 NPSCs aggregates forming AuNPs-RGDC neurospheres (i) stack of the maximum intensity projection, (ii) orthogonal sectioning in xyz axis, and (iii) 3D reconstruction of the AuNPs-RGDC neurosphere. 262

Figure 6.44 Confocal microscopy images of e18 NPSCs aggregates forming AuNPs-IKVAVC(19) neurospheres (i) stack of the maximum intensity projection, (ii) orthogonal sectioning in xyz axis, and (iii) 3D reconstruction of the AuNPs-IKVAVC(19) neurosphere. 263

Figure 6.45 Confocal microscopy images of E18 NPSCs aggregates forming SiO_2@AuNPs-Control neurospheres (i) stack of the maximum intensity projection, (ii) orthogonal sectioning in xyz axis, and (iii) 3D reconstruction of the SiO_2@AuNPs-Control neurosphere. 265

Figure 6.46 Confocal microscopy images of E18 NPSCs aggregates forming SiO_2@AuNPs-RGDC neurospheres (i) stack of the maximum intensity projection, (ii) orthogonal sectioning in xyz axis, and (iii) 3D reconstruction of the SiO_2@AuNPs-RGDC neurosphere. 266

Figure 6.47 Confocal microscopy images of E18 NPSCs aggregates forming SiO_2@AuNPs-IKVAVC(19) neurospheres (i) stack of the maximum intensity projection, (ii) orthogonal sectioning in xyz axis, and (iii) 3D reconstruction of the SiO_2@AuNPs-IKVAVC(19) neurosphere. 267

Figure 6.48 Representative TEM micrographs of ultrathin sections of the functionalized AuNPs and SiO_2@AuNPs neurospheres. 270

LIST OF SCHEMATIC DIAGRAMS

Schematic 1.1 Illustrates the SLAB model for analysing learning mechanisms in neuronal circuits by reducing the complexity of the brain to three elements, (i) stimuli, (ii) response, and (iii) reinforcement. 4

Schematic 1.2 Illustrates the immobilization of (A) single peptide surfaces in Chapter 4 and (B) mixed peptide surfaces in Chapter 5. 5

Schematic 1.3 Illustrates the immobilization of peptides on two-dimensional (2D) gold surfaces in Chapter 6 (A) Au Flat surfaces, (B) Au NPs surfaces, and (C) Au Peptide surfaces. 6

Schematic 1.4 Illustrates the immobilization of peptides on three-dimensional (3D) gold surfaces in Chapter 6 (A) Silica core-gold shell nanoparticles/ SiO_2@AuNPs surfaces and (B) gold nanoparticles/ AuNPs surfaces. 7

Schematic 2.1 Illustrating the NPSCs line established from dissociated embryonic hippocampi. 8

Schematic 2.2 Illustration of the neural lineage markers as a set of unique transcription factors, enzymes, cytoskeletal proteins and receptors. 11

Schematic 2.3 Illustration of a cell membrane showing the connection between actin filaments of the cytoskeleton and the extracellular matrix through integrins. 14

Schematic 2.4 Structural features of integrin receptors. 18

Schematic 2.5 Comparison of the sequences of the 'linker' regions of the mouse laminin α-chains. 19

Schematic 2.6 Illustration of the surface modification techniques. 25

Schematic 2.7 The water contact angle formed by sessile liquid drops on a smooth homogeneous solid surface. 50

Schematic 2.8 The water contact angle of the sensille droplet under (A) Young-Laplace, (B) Wenzel, and (C) Cassie-Baxter conditions. 51

Schematic 2.9 The schematic components of the AFM. 53

Schematic 2.10 The schematic illustration of generating secondary ions with a primary ion beam. 54

Schematic 2.11 X-ray adsorption by an atom in a core level leads to the emission of a photoelectron. 56

Schematic 2.12 Illustration of the distribution of charge around a negatively charged particle, which is counterbalanced by the positively charged ions from the surrounding solution and forms a diffuse layer. 58

Schematic 2.13 Illustrates the concept of forming TEM images in two stages. 62

Schematic 2.14 Illustration of the simplified optical principle in the CLSM. 65

Schematic 4.1 Illustrates the chemical adsorption of GOPTS on borosilicate coverslips. 93

Schematic 4.2 The dissection of a peptide structure whilst taking into consideration potential anchoring sites. 96

Schematic 4.3 The mechanism of peptide coupling. 97

Schematic 4.4 The SPPS approach by which the glass coverslips are functionalized to achieve the RGD or IKVAV peptide sequence functionality. 99

Schematic 5.1 Highlights the different 'click chemistry' approaches to generate complex biomaterials as two-dimensional, three-dimensional surfaces and biological systems. 137

Schematic 5.2 The mechanism of the base hydrolysis of esters. 139

Schematic 5.3 Concept diagram on designing orthogonally functionalized surfaces of mixed peptide ratios. 140

Schematic 5.4 Strategies for the formation of orthogonally functionalized surfaces by carbodiimide chemistry 142

Schematic 5.5 Optimising orthogonally functionalized surfaces by carbodiimide chemistry of two linker functional groups. 144

Schematic 5.6 Concept diagram of the orthogonal surface functionalization of mixed peptide ratios of RGD and IKVAV. 149

Schematic 5.7 The orthogonal innovative method by which the glass coverslips are functionalized with mixed peptide compositions of RGD and IKVAV to achieve peptide functionality. 150

Schematic 6.1 Concept diagram of the traditional two-dimensional (2D) monolayer cell culture (A) and three typical three-dimensional (3D) cell culture systems: cell spheroids/ aggregates grown on matrix (B), cells embedded within matrix (C), or scaffold-free cell spheroids in suspension (D). 182

Schematic 6.2 The typical zones of cell proliferation in a 3D spheroid, with the models of oxygenation, nutrition, and CO2 removal. 183

Schematic 6.3 Illustrates the approaches used for the 3D culturing of stem cells. 185

Schematic 6.4 Illustrates the edge of a neurosphere as a niche model. 186

Schematic 6.5 Typical synthetic methods of NPs for the bottom-up and top-down approaches. Taken and adapted from Khan et al., 2017. 187

Schematic 6.6 Illustrates the chemical adsorption of (A) AUT on gold coated borosilicate coverslips and (B) the thiolated amino acid (i.e. cysteine) on nanoparticles. 189

Schematic 6.7 Illustrates the process by which a gold shell is grafted around silica nanoparticle cores. 190

Schematic 6.8 Illustration of the direct peptide conjugation approach via the thiol-gold chemistry as 1.7 nmol peptide per 1 mL of (A) AuNPs and (B) SiO_2@AuNPs in PBS. 207

Schematic 6.9 The peptide functionalization of Au Flat and Au NPs surfaces via the 'grafting from' approach. 210

LIST OF TABLES

Table 2.1 Comparison of the properties of neuroepithelial and radial glial cells. 9

Table 2.2 Differences between physical adsorption and chemical adsorption. 27

Table 2.3 Compatibility of weak and strong anchors to different surface materials. 29

Table 2.4 The dynamic chemical properties incorporated in responsive materials. 30

Table 2.5 Key differences in cellular characteristics and processes in two-dimensional and three-dimensional culture systems. 45

Table 2.6 Secondary antibody labelling with a fluorophore. 64

Table 4.1 Z-range and RMS measurements of the functionalized surfaces obtained from the corresponding AFM Height images, n = 3. 106

Table 4.2 Positive ion peaks selected for the ToF-SIMS analysis to construct as raster images to illustrate the homogenous surfaces. 109

Table 4.3 XPS chemical shifts (in eV) analysis of the functional groups composition of the surface functionalization. 116

Table 4.4 Ratios of C/O and N/C were recorded to observe the change throughout the surface functionalization. 121

Table 5.1 Z-range and RMS measurements of the functionalized surfaces obtained from the corresponding AFM Height images, n = 3. 153

Table 5.2 Positive ion peaks selected for the ToF-SIMS analysis to construct as raster images to illustrate the homogenous surfaces. 156

Table 6.1 The nanoparticles average radius (r_n), hydrodynamic radii (R_H), and ζ-potential was characterized via TEM, DLS and electrophoretic mobility measurements. 192

Table 6.2 Z-range and RMS measurements of the functionalized Au Peptide surfaces obtained from the corresponding AFM Height images, n = 3. 199

Table 6.3 Negative and positive ion peaks selected for the ToF-SIMS analysis to construct raster images to illustrate the homogenous Au Peptide surfaces. 202

Table 6.4 The ζ-potential surface charge of the nanoparticles without and with peptide conjugation in PBS. 209

Table 6.5 Z-range and RMS measurements of the functionalized Au Flat surfaces obtained from the corresponding AFM Height images, n = 3. 213

Table 6.6 Z-range and RMS measurements of the functionalized Au NPs surfaces obtained from the corresponding AFM Height images, n = 3. 215

Table 6.7 Negative and positive ion peaks selected for the ToF-SIMS analysis to construct as raster images to illustrate the homogenous Au Flat surfaces. 219

Table 6.8 Negative and positive ion peaks selected for the ToF-SIMS analysis to construct as raster images to illustrate the homogenous Au NPs surfaces. 226

LIST OF EQUATIONS

Equation 2.1 50

Equation 2.2 54

Equation 2.3 55

Equation 2.4 57

Equation 2.5 59

Equation 2.6 59

Equation 2.7 59

Equation 6.1 192

ABBREVIATIONS

0% RGD	Controlled peptide composition of IKVAV surface
25% RGD	Controlled peptide composition of RGD:IKVAV surface (1:3)
50% RGD	Controlled peptide composition of RGD:IKVAV surface (1:1)
75% RGD	Controlled peptide composition of RGD:IKVAV surface (3:1)
100% RGD	Controlled peptide composition of RGD surface
2D	Two-dimensional
3D	Three-dimensional
3Rs	Repair, regenerate, replace
AFM	Atomic Force Microscopy
APTES	(3-Aminopropyl)triethoxysilane
APTMS	(3-Aminopropyl)trimethoxysilane
Au	Gold
Au Flat surface	Gold surface without any features, 'grafted from'(i.e. flat)
Au NPs surface	Gold surfaces with features, gold nanoparticles functionalized on the surface 'grafted from'
Au Peptides surface	Gold surfaces 'grafted to' with peptides
AuNPs	Gold nanoparticles ~ 16 nm
AUT	11-amino-1-undecanethiol
BF	Bright field
bFGF	Basic fibroblast growth factor
Boc	Tert-butyloxycarbonyl
BSA	Bovine serum albumin
CLSM	Confocal Laser Scanning Microscopy
DAPI	4',6-diamidino-2-phenylindole
DCC	*N'*,*N'*-Dicyclohexylcarbodiimide
DCM	Dichloromethane
DIC	*N'*,*N'*-Diispropylcarbodiimide
DIPEA	N,N'-Diisopropylethylamine
DIV	Days *in vitro*
DMAP	4-(Dimethylamino)pyridine
DMF	*N'*,*N'*-Dimethylformamide
DLS	Dynamic light scattering
ECM	Extracellular matrix
EDS/ EDX	Energy dispersive spectroscopy
EELS	Electron energy loss spectroscopy
EGF	Epidermal growth factor

EHICA	Ethyl(hydroimino)cyanoacetate
EM	Electron microscopy
ESCs	Embryonic stem cells
ESI-MS	Electrospray ionisation mass spectroscopy
E18	Embryonic rat brain tissue, day 18
Fmoc	Fluorenylmethoxycarbonyl
Fmoc(NH_2)	Fmoc-GABA-OH
FWHM	Full width at high maximum
GFAP	Anti-glial fibrillary acidic protein antibody
GOPTS	(3-Glycidyloxypropyl)trimethoxysilane
HPLC	High-pressure liquid chromatography
ICC	Immunocytochemistry
IKVAV	Iso-Lys-Val-Ala-Val
IKVAVC(19)	Cys – Laminin A Chain (Cys – Ser – Arg – Ala – Arg – Lys – Gln – Ala – Ala – Ser – Ile – Lys – Val – Ala – Val – Ser – Ala – Asp – Arg)
LMIG	Liquid metal ion gun
MTBE	Methyl tert-butyl ether
NMR	Nuclear magnetic resonance
NPs	Nanoparticles
NPSCs	Neuroprogenitor stem cells
OCH_3	Monomethyl Glutarate
PBS	Phosphate buffer solution
PDI	Poly dispersity index
PDMS	Polydimethylsiloxane
PEG	Polyethylene glycol
PLO.Laminin	Poly-L-ornithine and Laminin coated surfaces
PZT	Piezoelectronic transduces
RGD	Arg-Gly-Asp
RGDC	Arg-Gly-Asp-Cys
RM	Regenerative medicine
RMS	Root mean square
ROI	Region of interest
SAMs	Self-assembling monolayers
SiO_2NPs	Silica-core nanoparticles
SiO_2@AuNPs	Silica-core with gold-shell nanoparticles
SPPS	Solid phase peptide synthesis
SPR	Surface plasmon resonance
TCEP	Tris (2-carboxyethyl)phosphine hydrochloride
TEM	Transmission Electron Microscopy
TEOS	Tetraethyl orthosilicate

TFA	Trifluoroacetic acid
THF	Tetrahydrofuran
Ti	Titanium
TIS	Triispropylsilane
TNBS	2,4,6-Trinitrobenzenesulfonic acid solution
ToF-SIMS	Time of Flight - Secondary Ion Mass Spectroscopy
UV/ Vis	Ultra Violet/ Visible light spectroscopy
WCA	Water contact angle
XPS	X-ray photoelectron spectroscopy
X-Y-Z dimensions	Height, width, and depth dimensions

1 INTRODUCTION

1.1 SCIENTIFIC BACKGROUND

Humans have been trying to understand and imitate the complex network of the biological system since the first scientists (i.e. history of classical antiquity). The Greek physician Claudius Galen is one of those first scientists that contributed to the medical field with his remarkable observations and novel concepts that influenced the evolution of modern medicine (i.e. scientific disciplines such as anatomy, pharmacology, neurology and many more) in Europe and the Middle East throughout the Middle Ages and Renaissance [1]. The novel frontier field of regenerative medicine (RM) is a major advancement in the current technological developments of modern medicine. RM is a translation field within tissue engineering and molecular biology, where the principles of stem cell technology along with the interdisciplinary knowledge from the basic sciences (i.e. engineering, math, physics, chemistry, and psychology) are bridged to develop state-of-the-art technologies [2]. Currently, one of the most devastating and costly problems in the medical field which we are still facing lies in the surgical transplantation and reconstruction of patients with tissue and organ failures due to, (i) shortage of donors, (ii) unwanted side effects (i.e. tumor development, infection, donor morbidity), (iii) expensive therapies (i.e. recipients must follow lifelong immunosuppression regimes), and (iv) artificial organs and medical devices present limitations in functionality of the implants (i.e. durability, infection, thromboembolism) [3-5]. Consequently, in response RM presents the platform to create solutions for clinical procedures to restore structural and functional properties through repair, regenerate (i.e. engineering the cells), and replace (3Rs) the cells in previously untreatable injuries and diseases (i.e. lost due to age, disease, damage, or congenital defects) to establish normal function; as well as bring the cost down from a national healthcare prospective (i.e. better prevention, detection, and treatment) [6, 7].

An interdisciplinary approach in mimicking the extremely dynamic and complex cellular microenvironment of cells has been taken by designing biomaterials that have the ability to augment, support and replicate the properties (i.e. chemical and physical) to match those of the tissue that they are replacing [8-10]. The successful application of the biomaterials

depends on the ability of the surface properties (i.e. surface chemistry, surface topography) to elicit the appropriate cellular response by directing cell adhesion, proliferation, and maintaining cells in an undifferentiated state (i.e. cell therapy) or differentiation to a specific type (i.e. tissue engineering) [11, 12]. Moreover, in considering the interactions that cells have with their physical, mechanical and biological microenvironments significant efforts have been made to modify the surface of medical devices to establish enhanced biocompatibility by developing and integrating surface modification techniques [13]. Two-dimensional (2D) and three-dimensional (3D) model microenvironments provide an *in vitro* and *in vivo* insight into the development and disease characteristics of the biological functions of cells, with the later model providing more complexity in the biological and anatomical relevance in the study to that of the natural niche of the cells.

The brain is one of the most interesting systems to study for cognitive and behavioral processes, as well as in disease, damage and degeneration (i.e. glioblastoma, neurological disorders, stroke, trauma and senescence). Therefore, in order to understand the underlying problem of these conditions, a less complex model needs to be studied. This model need to be able to provide the environmental components and maintains the intrinsic functions of the brain at a cellular system level [14]. Here, we present a novel and versatile approach in surface modification to tune surface properties (i.e. wettability, topography, surface chemistry) in order to guide controllable neural stem cell differentiation and influence specific stem cell fate.

1.2 AIM OF THESIS

The scope of this thesis is part of the 'Building a Simple Living Artificial Brain' (SLAB) system that the Neurophotonics Laboratory (NPL) at the University of Nottingham is developing. SLAB presents the "brain in a dish" system that enables a small network of cultured neural progenitor stem cells (NPSCs) to differentiate into mature neurons and glia cells to interact with an artificial environment, which then permits for the environment input and network response to be correlated in real-time.

The overall aim of this thesis is to develop a suitable method to engineer versatile biointerfaces that direct stem cells to preferentially differentiate to a specific composition of

neurons and glia to permit for the integration into the fully-controlled and monitored SLAB system. Thus, enabling the interfacing of the cultured neural cells in an environment that is a feedback paradigm that emulates brain activity and interaction with an environment to gain the essential knowledge for producing 3D brain-like models, Schematic 1.1.

The strategy that we took to achieve the aim of developing these versatile biointerfaces was to use surface chemistry to control NPSCs to a specific stem cells by synthesizing peptides as a physiochemical parameter critical for long-term neuronal survival, proliferation and differentiation to a specific cell linages. In addition, these biointerfaces have future applications as a tool in building artificial neural networks in biological studies (i.e. neurodegenerative diseases).

The material chosen as the basic starting point in developing biointerfaces in the SLAB system are glass coverslips coated with/without gold deposition, which enables the integration of the various projects such as (i) molecular biology (i.e. optogenetics), (ii) microfluidics (i.e. media supply, drug delivery, neuromodulation, nanoparticles), (iii) neuroelectronics (i.e. multi-electrode arrays (MEA), surface plasmon resonance imaging (SPR)), and (iv) optical engineering (i.e. lab-on-chip, custom CMOS sensor). Thus, facilitating the assimilation of the cultured neuronal network with the virtual environment formulized through the input of computer science and mathematics computations.

Consequently, the surface chemistry functionalization on a solid surface approach was taken throughout this thesis where the 2D were glass coverslips coated with/without gold deposition and the 3D surfaces were gold nanoparticles with/without a silica-core. The designed 2D and 3D microenvironments were cultured in freshly isolated hippocampi (i.e. neuroprogenitor stem cells, NPSCs) from embryonic rat brain tissue at day 18 (E18) as they demonstrate a high degree of similarity to human brain cells.

Each chapter has been divided into sections to investigate and confirm (i) the method by which the surfaces are prepared, (ii) the surface characterizing techniques employed to validate the successful immobilization of the peptides, and (iii) the desired cell response of the NPSCs on the designed surfaces. The summary in each chapter will discuss the overall

outcome of the results and the implications they have in the following chapter and any future work.

1.2.1 OVERVIEW OF THE CHAPTERS

Chapter 1 and 2 introduce the purpose for conducting this Ph.D thesis and the scientific background of the Ph.D question that will be tackled in this thesis and is divided as, (i) biological response, (ii) surface properties and materials, and (iii) surface characterizations techniques, respectively.

Chapter 3 provides a detailed insight into the experimental procedures in (i) surface preparation, (ii) cell culture, and (iii) surface characterization techniques.

Whilst the experimental chapters will discuss the surface design, characterization, and validation before subjecting the immobilized peptide surfaces for *in vitro* evaluation to determine the ability of the surfaces to influence the desired biological response in the stem cells.

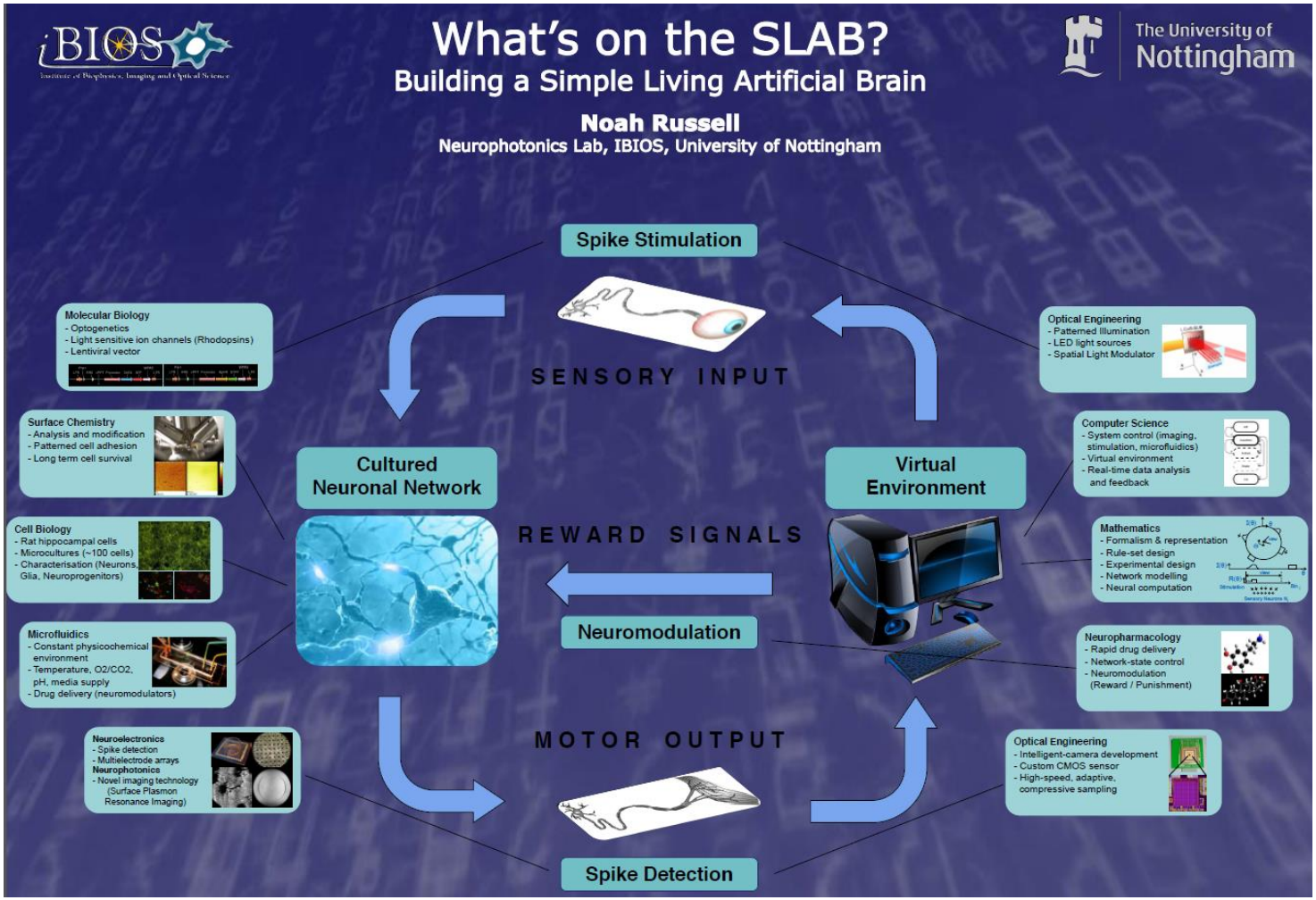
Chapter 4 focuses on implementing a single immobilized peptide biomimetic surfaces that imitate the *in vivo* extracellular matrix (ECM) composition (i.e. biochemical and mechanical properties) with the emphasis on two specific peptide sequences (i.e. RGD and IKVAV) present in the fibrous protein laminin that interact and instruct signaling events in the NPSCs to influence the stem cell fate, Schematic 1.2A.

Chapter 5 investigates the hypothesis that by controlling the peptide composition of more than one peptide on the same surface we would be able to control the preferential differentiation of the NPSCs and influence a controlled microenvironment of neurons and astrocytes to mimic more closely the akin characteristics of the ECM. This due to the fact that peptides sequences are present concurrently within the dynamic and complex natural niche (i.e. laminin), Schematic 1.2B.

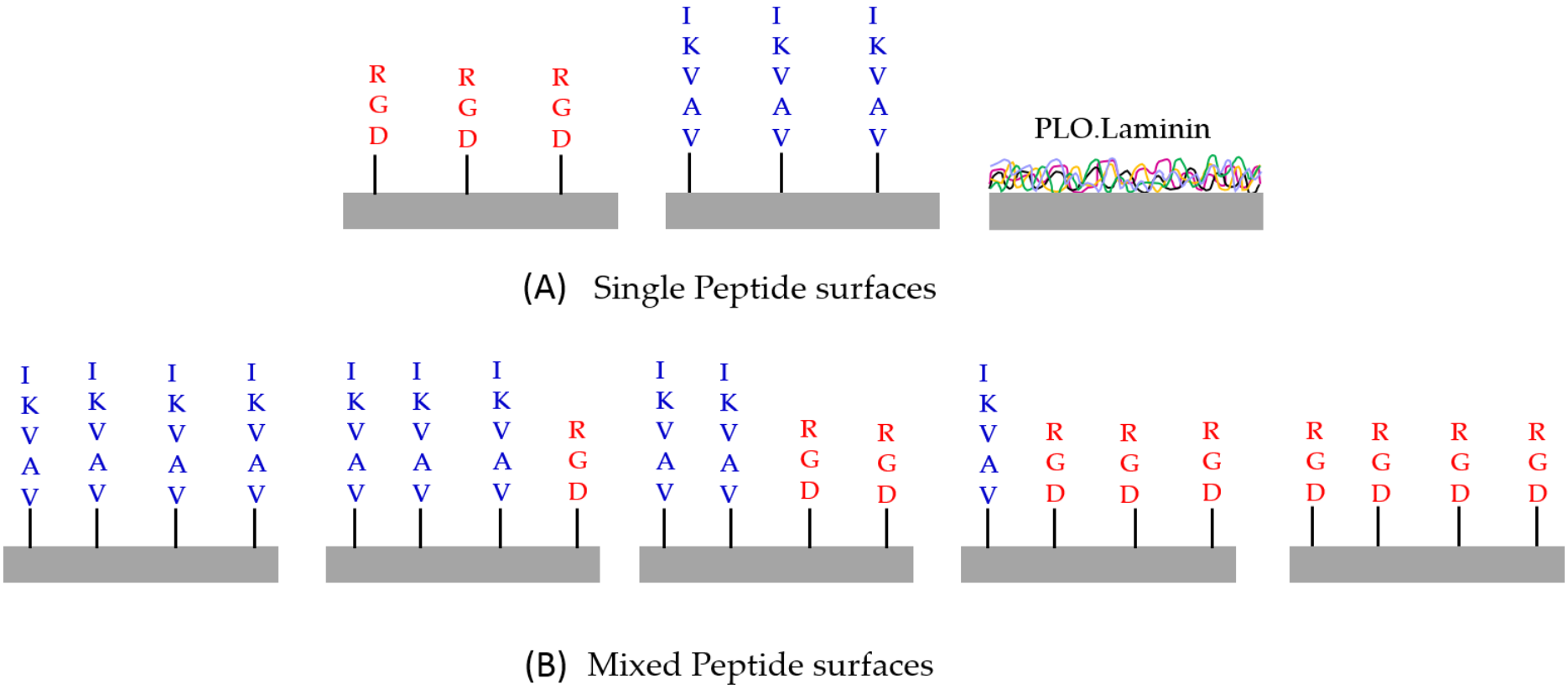
Chapter 6 presents the immobilization of peptides on comparable 2D and 3D surfaces to examine the biological response of the NPSCs to both microenvironment in order to add to the understanding how the cells behave to the spatial integrity that the 2D culturing system is lacking and the 3D environment provides (i.e. neurospheres). Thus, contributing to the state-of-art research in bridging the transition of engineering versatile biointerfaces from

culturing NPSCs on 2D to 3D surfaces. In order to establish a miniature 3D *in vitro* model that is a step closer to the natural niche of the brain, Schematic 1.3 and Schematic 1.4.

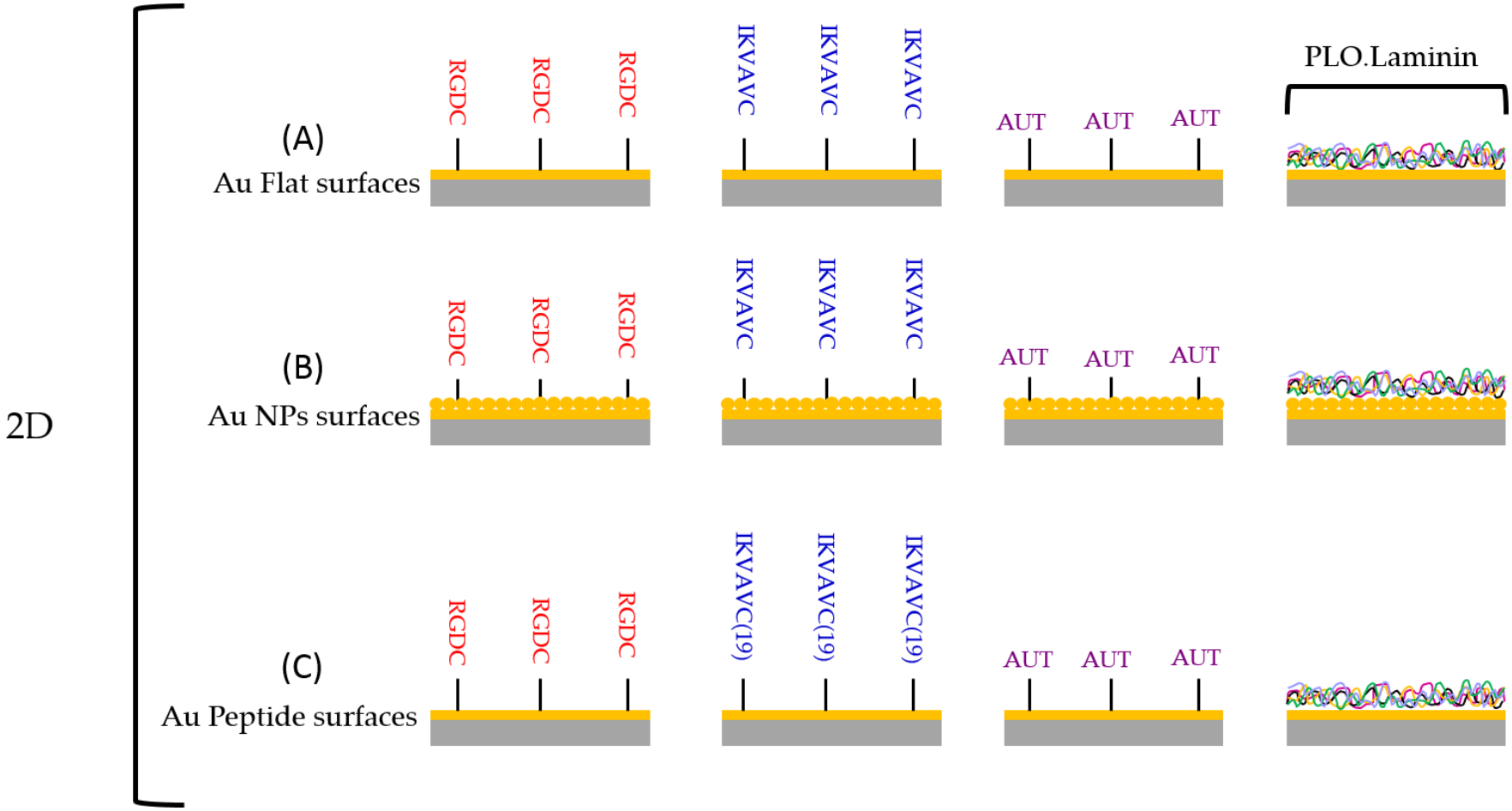
Chapter 7 concludes the scientific findings presented in this Ph.D thesis, and discusses the progress made in the field of regenerative medicine and future works.



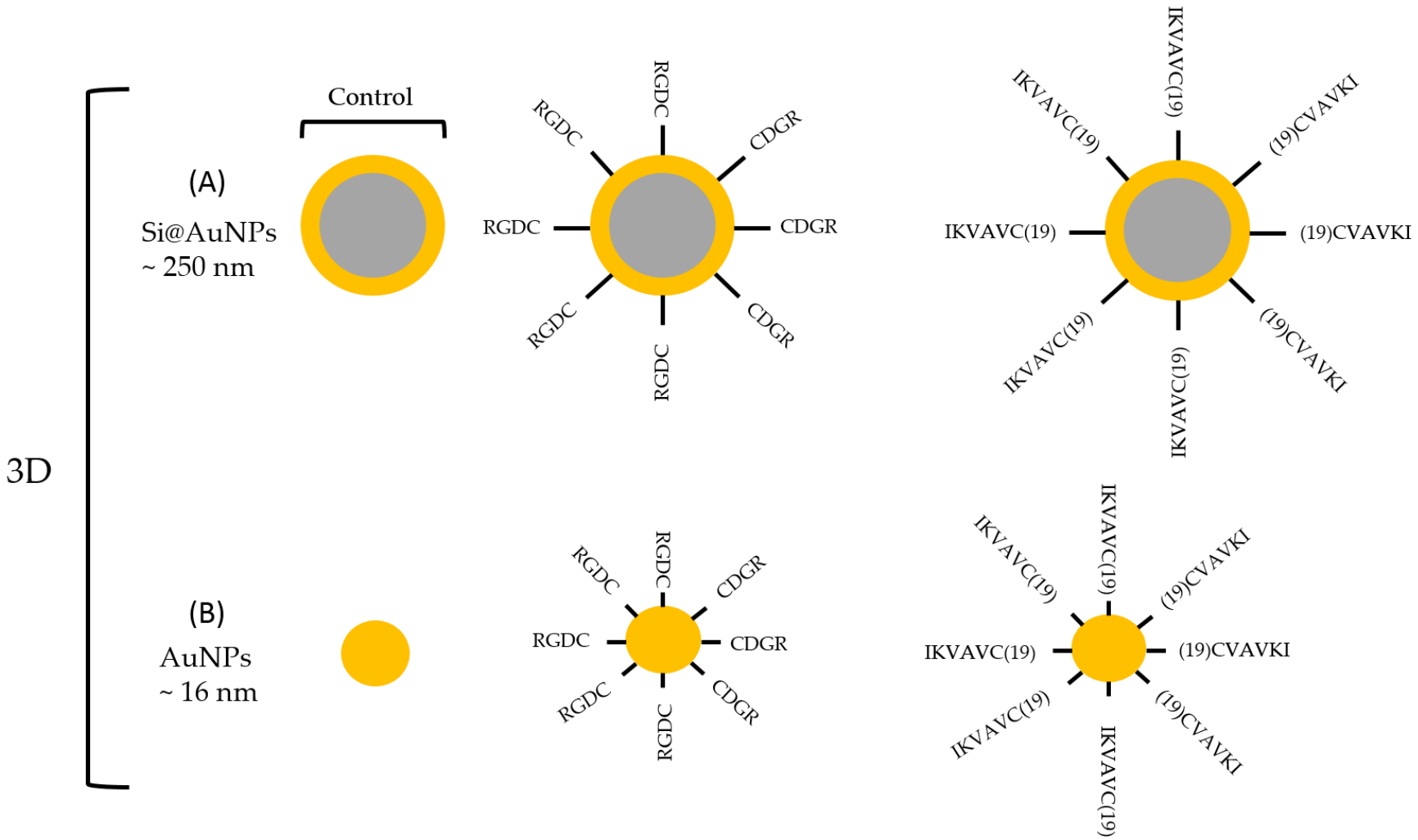
Schematic 1.1 Illustrates the SLAB model for analyzing learning mechanisms in neuronal circuits by reducing the complexity of the brain to three elements, (i) stimuli, (ii) response, and (iii) reinforcement.



Schematic 1.2 Illustrates the immobilization of (A) single peptide surfaces in Chapter 4 and (B) mixed peptide surfaces in Chapter 5.



Schematic 1.3 Illustrates the immobilization of peptides on two-dimensional (2D) gold surfaces in Chapter 6 (A) Au Flat surfaces, (B) Au NPs surfaces, and (C) Au Peptide surfaces.



Schematic 1.4 Illustrates the immobilization of peptides on three-dimensional (3D) gold surfaces in Chapter 6 (A) Silica core-gold shell nanoparticles/ SiO_2@AuNPs surfaces and (B) gold nanoparticles/ AuNPs surfaces.

2 SCIENTIFIC BACKGROUND

2.1 INTRODUCTION

The development and innovation in the biomaterials field over the last 30 years has progressed our understanding from determining interaction between material and the biological system to influencing the desired biological processes (i.e. proliferation, migration, and differentiation) and minimizing the damaging effects [15].

Consequently, the purpose of this scientific background is to illustrate the basic principles that are representative to the scope of the thesis and therefore we do not present an exhaustive review. This chapter is divided into four main parts; (i) cells and their natural environment, (ii) biomimetic materials and their properties, (iii) cell response towards the biomimetic materials, and (iv) surface analysis techniques.

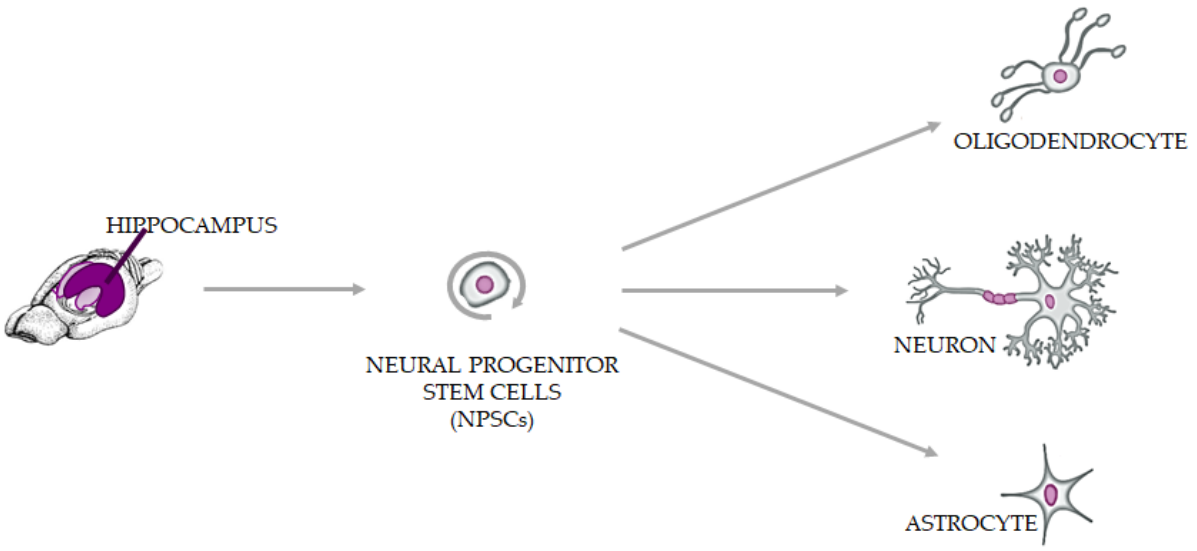
2.2 CELLS AND THEIR NATURAL ENVIRONMENT

Biological systems are dynamic and complex, this enables us to study them at different levels (i.e. organismal, tissue, cellular and molecular levels) to gain understanding of their structural, functional and biological interactions within the system. The most basic and smallest unit of a biological system is the cell (i.e. 'building block of life') and at a developmental stage these are recognized as stem cells.

Stem cells are undifferentiated cells that do not present any phenotypical characteristics of cells, thus, they have the ability to develop and generate any other type of cell through differentiation (i.e. muscle, epithelial, immune, and neural cells) [16-18]. Stem cells are categorized into three types, (i) physiological stem cells such as embryonic (i.e. early stage of life) and adult, (ii) induced pluripotent stem cells (i.e. engineered), and (iii) pathological cell with stem cell properties (i.e. cancer). Regardless of their category stem cells exhibit pluripotency, are undifferentiated, and are capable of generating differentiated cells [19, 20].

Embryonic stem cells (ESCs) are the most studied type of stem cells and with an original studies associated with the bizarre tumors of teratocarcinomas, which demonstrated that ESCs had the ability to generate all constituent cell types of the tumor and remained

pluripotent [21, 22]. The first isolation and *in vitro* culture of ESCs were of mouse embryos a technique established by Evans & Kaufman (1981), with embryonic biology research advancing ESCs culture and cell-line research in 1990s (i.e. human embryonic stem cells) to recent developments (i.e. stem cell therapy) [23]. ESCs research is at the forefront of understanding developmental biology (i.e. healthy and/or diseased cells), and ESCs application in tissue engineering and regenerative medicine [24, 25]. Due to spontaneous differentiation occurring in the ESCs *in vitro*, these cells must be inducted (i.e. instructive factors) to promote them to a specific lineage (i.e. neural stem cells) and not several lineages (i.e. mesenchymal stem cells and hematopoietic stem cells) [26] . The natural niche of the ESCs plays the role of induction in *in vivo* during processes such as development, regeneration, replacement and repair. The ESCs can be induced to differentiate into the two neural cell types of neurons and glia, which the later compromise of astrocytes and oligodendrocytes, 1 [27] .



Schematic 2.1 Illustrating the NPSCs line established from dissociated embryonic hippocampi.
Adapted from Abcam.com/neuralmarkers (Copyright © 2016 Abcam. All rights reserved).
Retrieved September 9th, 2017, from https://docs.abcam.com/pdf/neuroscience/neural-lineage-markers-web.pdf.

2.2.1 NEURAL PROGENITOR STEM CELLS (NPSCs)

NPSCs are the intermediate stage when ESCs are induced to differentiate into the neural cell types. The NPSCs reside in the hippocampal dentate gyrus in the embryonic and early postnatal murine brain, a zone where the NPSCs are retained after embryonic development for the production of new cells of the nervous system (i.e. NPSCs niche) [17, 28]. Hence, supporting neurogenesis and gliogenesis to generate neurons and glia (i.e. astrocytes and oligodendrocytes) [17].

Table 2.1 Comparison of the properties of neuroepithelial and radial glial cells. Adapted from Magdalena Götz and Wieland B. Huttner, 2005.

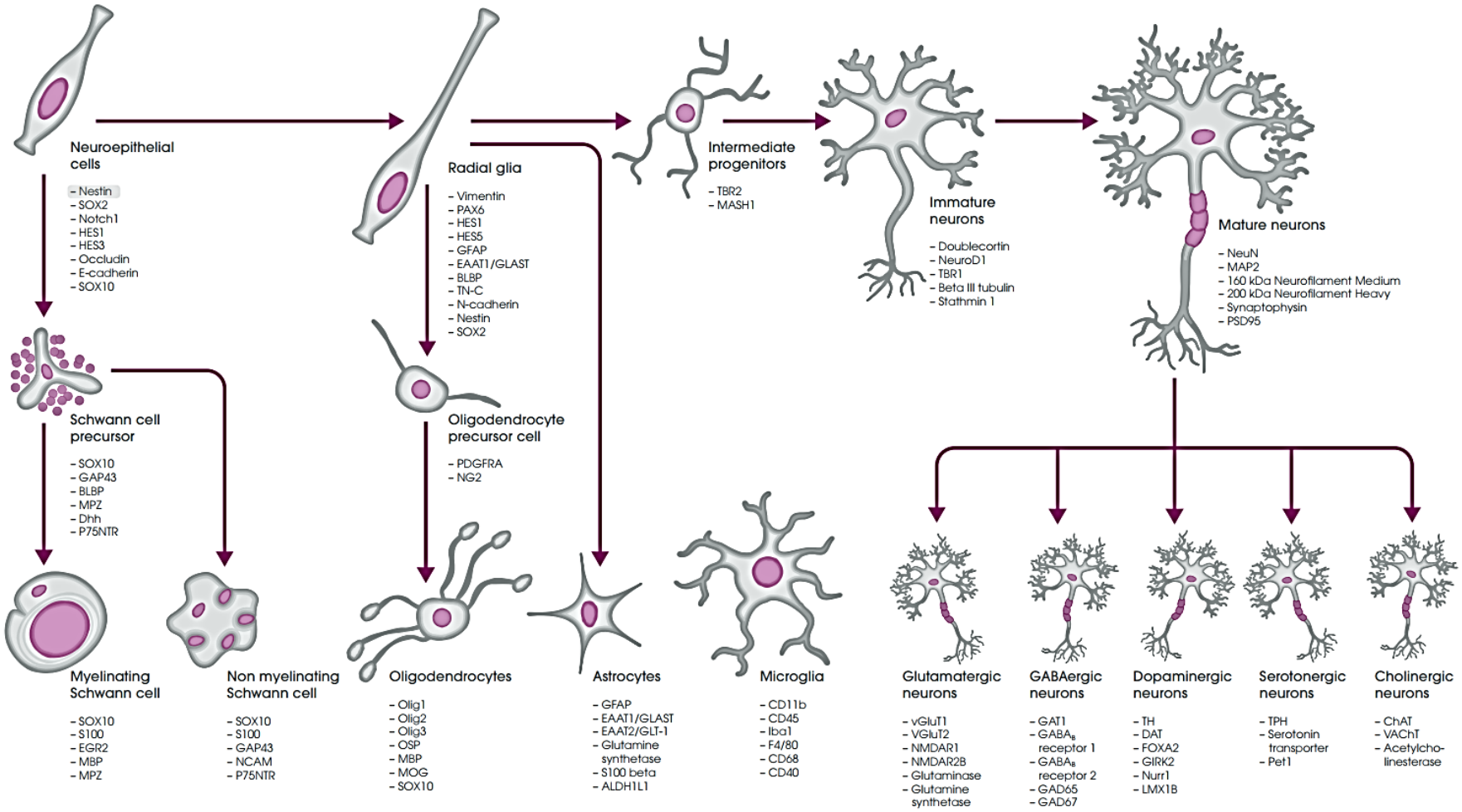
Property	**Neuroepithelial Cells**	**Radial Glial cells**
Interkinetic Nuclear Migration	Apical-Basal	Apical-Basal to the boundary of the ventricular or subventricular zone (SVZ)
Apical Surface	Present	Present
Apical-Basal Polarity	Present	Present, but downregulated
Tight Junctions	Present (early stages)	Absent
Basal Lamina Contact	Present	Present
Nestin Expresion	Present	Present
HES1 Expression	Present	Present
SOX2 Expression	Present	Present
Neural Markers (i.e. E-cadherin, NeuN, Notch1, MAP2, βIII-Tubulin)	Present	Absent
Glial Markers (i.e. N-cadherin, Vimentin, CD45, SOX10, GFAP)	Absent	Present
Tis21 Expression*	Confined to the neurogenic subpopulation	Present in the neurogenic subpopulation
Neurogenesis	First phase	Subsequent phases

*The antiproliferative gene Tis21 is a molecular marker that is selectively expressed in virtually all neuroepithelial cell that are about to undergo a neurogenic division, but not proliferating neuroepithelial cells.

A stem cell niche in general is comprised of two key components that are reliant on each other, (i) the microenvironment and (ii) the stem cell, and influenced by environmental cues that can be intrinsic (i.e. originate from the cells such as Cdc42, Lis-1, ArpC1) or extrinsic (i.e. originate from the ECM such as JAK-STAT, BMP, IL1β) [29, 30]. The primary components in the stem cell niche such as stromal cells (i.e. secrete soluble factors that signal stem cells), ECM proteins (i.e. provide a scaffold for stem cell attachment), blood vessels (i.e. provide nutrition and transport of cells around the body), and neural input (i.e. propagate and integrate signals from different organ systems) allow for a dynamic relation between the stem cells and their niches (i.e. enabling stem cell proliferation, retention, or mobilization) [31]. To balance stem cell quiescence the ECM of the NPSCs niche provides the appropriate intrinsic and extrinsic microenvironmental cues and cell-cell interactions to support proliferation and direct neurogenesis (i.e. neuroepithelial cells) versus gliogenesis (i.e. radial glial cells) lineage cell fate, Table 2.1 and Schematic 2.2 [17, 32].

2.2.1.1 NEURONS

Neurogenesis occurs from early embryonic development until early postnatal stages to generate the recognized basic unit of the nervous system the neurons (i.e. ≈ 100 billion in humans, numbers vary between species). The process produces a variety of classes of neurons (i.e. sparse neurogliaform cell, bipolar cell, Deep Martinotti cell, Basket cell, and Thick-tufted cell), with morphologies that differ in some aspects such as differing functions. However, all neurons contain the four distinct regions in their morphology, (i) soma, (ii) dendrites, (iii) axon, and (iv) axon terminals [33]. The soma (i.e. cell body) is the central part of the neuron (i.e. spherical, ≈ 20 μm in diameter) that contains all the important organelles (i.e. nucleus, rough-endoplasmic reticulum, smooth-endoplasmic reticulum, Golgi apparatus, and mitochondria) required for the synthesis of the components needed in the renewal of the axon and nerve termini (i.e. anterograde transport). The axon is highly specialized only to neurons and are involved in the transfer of information over distances (i.e. away from the soma to the axon terminals) that extend from less than a millimeter to over a meter long in the nervous system by conducting action potentials (i.e. electric impulses). Action potentials (i.e. speeds up to 100 ms^{-1}) occur across the plasma membrane (i.e. ~ 8-10 nm), which acts as a leaky capacitor during sudden changes in the voltage.



Schematic 2.2 Illustration of the neural lineage markers as a set of unique transcription factors, enzymes, cytoskeletal proteins and receptors. Taken from Abcam.com/neuralmarkers (Copyright © 2016 Abcam. All rights reserved). Retrieved November 15th, 2017, from https://docs.abcam.com/pdf/neuroscience/neural-lineage-markers-web.pdf.

The axon terminals form synapses (i.e. connections) with dendrites of other neuron cells, which receive the action potential as chemical signals (i.e. neurotransmitters) and transmit them as converted small electrical impulses towards the cell body. The neurons are organized into networks and form signaling circuits to (i) stimulate or inhibit activities, (ii) receive and process signals, and (iii) signal out a response.

2.2.1.2 GLIA

Gliogenesis starts during late embryogenesis and continues in postnatal stages, producing microglia, astrocytes, oligodendrocytes, and NG2-glia (i.e. their progenitors) [34, 35]. The glia constitute between 33%-66% of the total brain mass (i.e. varies between species) and provide insulation, support and nourish neighboring neurons. The morphology of the glia population lack the long processes that connect sensory and effector organs. Initially scientists considered the glia to play a simple supportive roles for neurons. However, recent advances in the research of astrocytes have demonstrated that these cells play an active role as information processors in the function of the brain.

2.2.1.2.1 ASTROCYTES

Glia cells introduce complexity to the neuron-glia networks as the number of cells involved are increased, possible connectivity and signaling processes in comparison to that of the neuron-neuron networks. Astrocytes are the most abundant glia cell type and exhibit a star-shaped morphology as their name indicates; stars and cells in Greek is respectively, *astra* and *cyte* (i.e. derived from *kytos,* "meaning" hollow, as a cell or container) [36]. However, not all astrocytes are star-shaped (i.e. protoplasmic in gray matter and fibrous in white matter) as some have an elongated (i.e. Müller cell spanning the retina and Bergmann glia in the molecular layer of the cerebellum) morphology like an ornamental bushy shrub [36, 37]. Astrocytes are highly dynamic subcellular elements that shape the extracellular space structurally and functionally, thus, controlling the extracellular homeostasis in the brain (i.e. mobility, retraction and extension). Astrocytes are responsible for providing neurons with energy (i.e. adenosine triphosphate/ATP) and substrates for neurotransmission (i.e. neurotransmitters such as glutamate), as well as acting as a physical barrier for neighboring neurons preventing synaptic connections between neighboring neurons. Moreover,

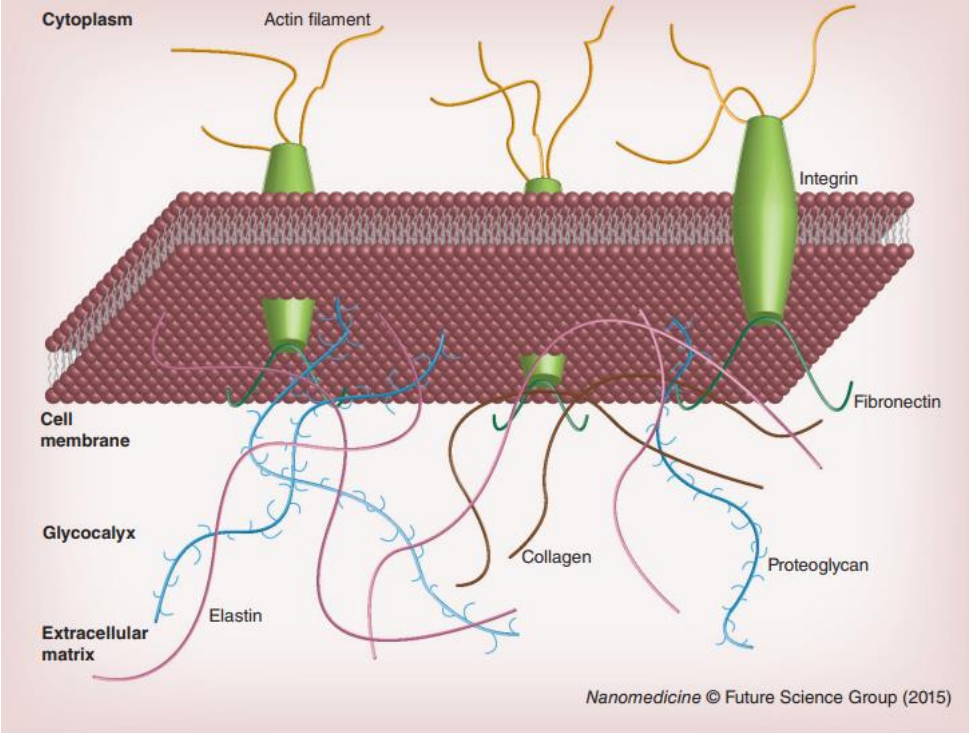
astrocytes enable discrete and precise encoding of synaptic signals and transmission by removing excess neurotransmitter molecules from the extracellular space. They communicate with neurons through dynamic bidirectional communication in synapse formation, as the astrocytes have the ability to sense and integrate neuronal information through ionic channels, neurotransmitter receptors and transporters, and intracellular signaling pathways (i.e. modulating synaptic function such as stability, trafficking) [38-42]. The dynamic bidirectional communication is performed through the mechanism of uptake and release of (i) neuroactive factors (i.e. neurotransmitters and ATP) and (ii) morphological plasticity. Astrocytes are able to influence the termination action of neurotransmitters secreted by neurons through the glutamate-glycamine cycle by recycling them back into the neurons, as well as being responsible for changing the extracellular space volume through a plastic physical coverage of neurons [40, 42]. Furthermore, literature has demonstrated that astrocytes influence neuronal survival through the regulation of the processes of glutamate excitotoxicity, oxidative stress and acidosis (i.e. primary mediators of neuronal death), as well secreting neurotrophic factors crucial in the regeneration of vascular and neuronal cells after stroke [43]. Astrocytes use the change in cytoplasmic Ca^{2+} concentrations (i.e. stored in the endoplasmic reticulum), as they are electrically non-excitable cells (i.e. no action potential), as the cellular signal to propagates between astrocytes and other cells. Moreover, these cellular signals can be triggered by neuronal and synaptic activity through the activation of neurotransmitter receptors expressed by the astrocytes and in turn stimulate the release of neuroactive substances required to regulate neuronal excitability and synaptic transmission. Consequently, astrocytes are an integral part of the neuron-glia networks as they have demonstrated the ability to integrate and process synaptic information, as well as control synaptic transmission and plasticity [41, 44, 45].

2.2.2 EXTRACELLULAR MATRIX (ECM)

In nature, cells are in continuous communication with their microenvironment of characterizing cellular neighbors, signaling molecules (i.e. soluble), and environmental factors presented by the ECM [46]. The ECM is the non-cellular component present within all tissues and organs and is involved in regulating the fundamental processes such as cell

adhesion, survival, proliferation, migration, differentiation, apoptosis, and tissue morphogenesis [47-53]. The ECM is composed of water, proteins and polysaccharide and its composition and topology is unique to the type of cells in their microenvironment (i.e. blood, bone, nerve, muscle, and cancer cells).

The ECM can be categorized into two types, (i) the interstitial connective tissue matrix and (ii) the basement membrane. The interstitial connective tissue matrix that is mostly comprised of collagen I and fibronectin, and its function is to surround the cells to provide a structural scaffold for the tissues. Whilst the basement membrane is a more compact specialized form of the ECM that separates the epithelium from the surrounding stroma, as well as facilitate controlled cell organization and differentiation through the interactions with cell surface receptors and ECM proteins [54]. Hence, making the ECM distinctly complex heterogeneous protein-based hydrogel of which most of its macromolecules participate in supramolecular assemblies (i.e. forming networks) where their biological properties are modified by the molecules with which they interact, Schematic 2.3 [55].



Schematic 2.3 Illustration of a cell membrane showing the connection between actin filaments of the cytoskeleton and the extracellular matrix through integrins. Taken from Hala S. Dhowre, 2015 [55].

The two main classes of macromolecules that comprise the ECM are the fibrous proteins (i.e. collagen, elastins, fibronectins, and laminin) and the proteoglycans (i.e. small leucine-rich proteoglycans, modular proteoglycans, and cell-surface proteoglycans) [56].

The majority of the extracellular interstitial space within the tissue is filled by the proteoglycans (i.e. as a hydrated gel), which demonstrate hydrating, binding and force-resistance properties [56].

Collagen is identified as the most abundant fibrous protein (i.e. 28 types of collagen) with a total protein mass constituent of 30% and is involved in (i)provides tensile strength, (ii) regulate cell adhesion, (iii) support chemotaxis and migration, and (iv) direct tissue development [56]. The recoil properties are introduced into the tissues that undergo repeated stretch by the ECM fiber elastin, which closely associates with collagen (i.e. provides tensile strength, but crucially limits the stretch) [56]. Fibronectin is a fibrous protein that is involved in mediating cell attachment (i.e. anchoring cells to collagen or proteoglycan substrates), directing the organization of the interstitial ECM (i.e. extracellular mechano-regulator), and function (i.e. tissue repair, blood clotting, embryogenesis, cell migration and adhesion) [56].

The ECM illustrates functional diversity and yet allows for highly specialized function. This is very evident in formation of the BMs, which are highly specialized extracellular matrices that form thin acellular layers that underlie, separate and connect cell to their interstitial matrix. The BMs are comprised (i.e. self-assembly) of diverse individual components (i.e. laminins, perlecan, collagen IV, nidogen-1, and nidogen-2) that regulate different biological activities (i.e. proliferation, differentiation, migration) and control cellular function (i.e. binding and modulating concentrations of growth factors and cytokines). Thus, making the BMs a prerequisite for normal tissue development and function, with the laminins being the major constituent and provide structural support as well as organizing the complex interactions of the BMs [57-60]. The BMs laminins are also the first detectable glycoproteins in the embryo [61].

One of complexities of the ECM lies in that the structure is highly dynamic and is constantly being remodeled (i.e. enzymatically, or non-enzymatically), which means that the molecular components are subjected to countless modifications. This enables the ECM to generate specific biochemical and mechanical properties specific to each organ (i.e. tensile/

compressive strength, elasticity, protection by buffering action to maintain extracellular homeostasis, and water retention) [56, 62].

Moreover, cells secrete locally extracellular molecules composed of a variety of proteins (i.e. collagen, fibronectin, elastin, and laminin) and polysaccharides (i.e. GAGs) that assemble and organize in close association with the surface of the cell to provide structural, binding site and biochemical support.

The ECM instructs signaling events in the cell through cell surface factors receptors and adhesion molecules (i.e. cell adhesion molecules) such as integrins and proteoglycans [53].

2.2.2.1 CELL ADHESION MOLECULES (CAMs)

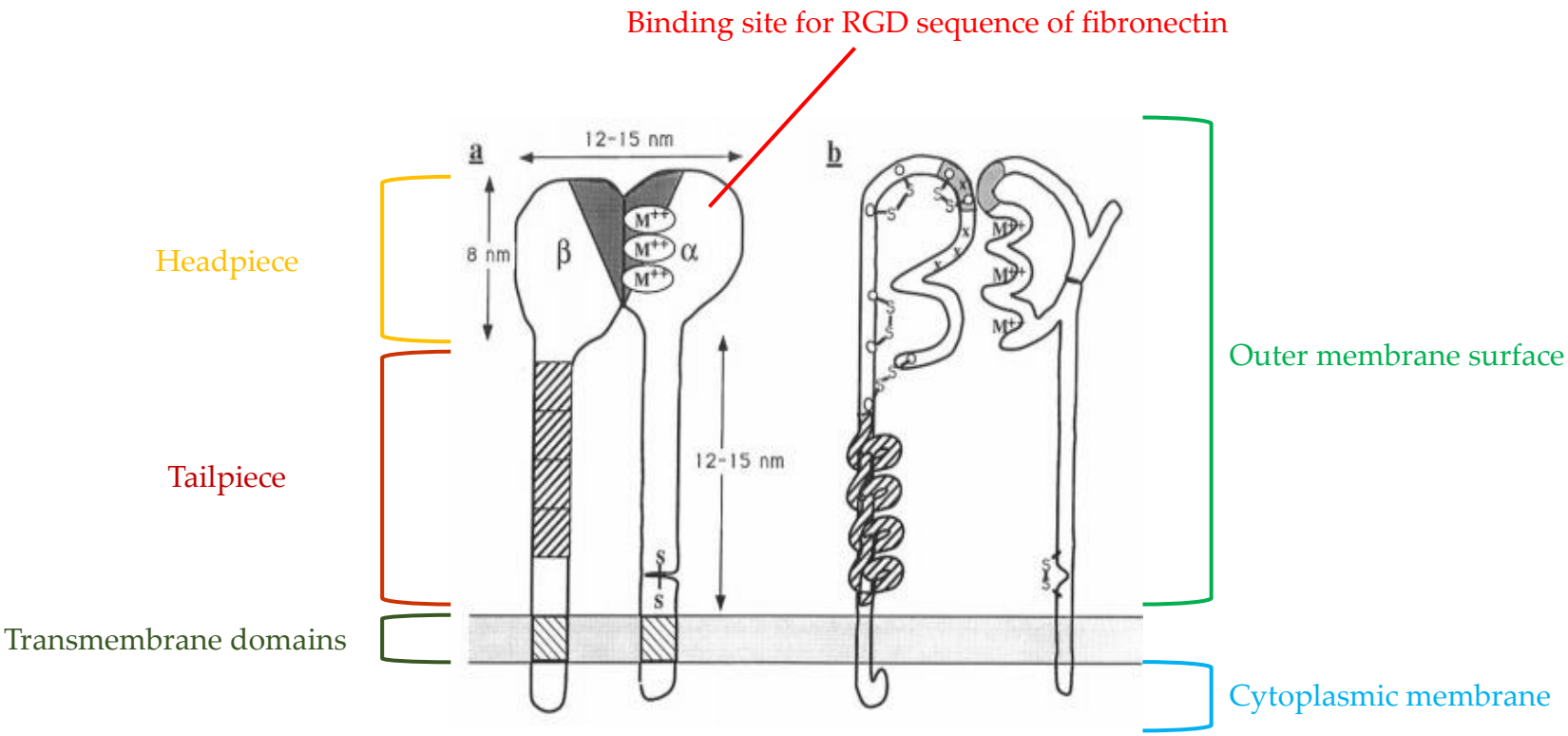
Cells have specialized protein molecules that are attached or integrated into their cell membrane that govern the critical information passing from outside to inside the cell, thus, receiving, processing and sending signals (i.e. specific ligands such as hormones and neurotransmitters) [63-65]. Cell adhesion molecules (CAMs) are such proteins located on the cell surface that facilitate the binding (i.e. cell adhesion process) with other cells and the ECM. The CAMs have a structure composed of (i) an intracellular domain that interacts with the cytoskeleton, (ii) a transmembrane domain, and (iii) an extracellular domain [66].

CAMs can be categorized into four major super families, (i) the immunoglobulin super family of cell adhesion molecules (IgCAMs), (ii) cadherins, (iii) integrins, and (iv) the superfamily of C-type of lectin-like domains proteins (CTLDs) [66]. The interaction of cells with the ECM is mediated by the widely expressed family of integrins receptors alongside the other receptors (i.e. cadherins, IgCAMs, selectins, syndecans) and the actin cytoskeleton [67, 68].

2.2.2.1.1 INTEGRINS

The integrin receptors are formed through non-covalent association of two type I transmembrane glycoproteins, the α- (i.e. 700 amino acids) and the β- (i.e. 1000 amino acids) subunits, that can assemble into 24 different receptors with different binding properties and different tissue distribution [69-71]. The integrin subfamilies are categorized into four subgroups as (i) the RGD-binding integrins, (ii) laminin-binding integrins, (iii) leukocyte integrins, and (iv) collagen integrins [72]. The ligand binding of integrin is complex due to

their evolutionary selection of common acidic peptide motifs in ECM proteins, thus, given them their ability to bind a wide variety of ligands and being ambiguous in their specificity [73, 74]. Integrins interact primarily with ECM proteins such as laminins, collagens, and fibronectin by integrating mechanical and chemical signals, and directly associating with the cytoskeleton through ligand motifs [53]. One of the most studied ECM ligands is the tri-peptide RGD active site, firstly identified in fibronectin by Pierschbacher & Ruoslahti (1984)), serves as a recognition motif in multiple ligands for several different integrins (i.e. vitronectin, fibrinogen, collagen, laminin, and many others) [71, 75, 76]. The binding site of the RGD peptides is at an interface between the α- and β-subunits (i.e. on $\alpha 5\beta 1$, $\alpha IIb\beta 3$, and all or most $\alpha v\beta$) with the basic residue fitting in the α-subunit, and the acidic residue in the β-I-domain, Schematic 2.4 [69]. The binding of integrins to extracellular ligands is specific and can be categorized into four group of integrin-ligand binding combinations, (i) the RGD-binding integrins recognizes the RGD tripeptide active site on a ligand, (ii) the LDV-binding integrins bind to an acidic amino acid motif referred to as LDV (i.e. functionally related to RGD), (iii) the A-domain $\beta 1$ integrins that contain an α-subunit with an inserted αl domain that pairs with $\beta 1$ integrins to form a specific subfamily of laminin/collagen-binding integrins, and (iv) the non-αA-domain-containing laminin binding integrins that lack the α-subunit with an inserted αl domain that pairs with $\beta 1$ integrins to form specific laminin receptors [73]. While RGD is possibly the most well-known integrin-binding motif, other integrin-binding peptides (i.e. specific integrin-recognition cell-binding sites) have been reported, among them RGD, YIGSR, YKVAV, LGTIPG, PDGSR, LRE, LRGDN and IKLL from laminin, RGD and DGEA from collagen, and RGD, KQAGDV, PHSRN, REDV and LDV from fibronectin [77-84]. A number of integrins (i.e. $\alpha IIb\beta 3$, $\alpha V\beta 3$, $\alpha V\beta 6$, $\alpha V\beta 1$, $\alpha 5\beta 1$, and $\alpha 8\beta 1$) are able to engage fibronectin for instance through the RGD motif (i.e. promote several cell responses, cell adhesion). Moreover, neighboring peptide sequences can inhibit or suppress each other due to conformational restrictions that shield integrin binding. This effect is observed when the $\alpha 5\beta 1$ integrin binds to fibronectin as the interaction requires both the peptide sequences of RGD and PHSRN (i.e. the synergy site) to drive which integrins cells use to bind fibronectin (i.e. affinity and selectivity).

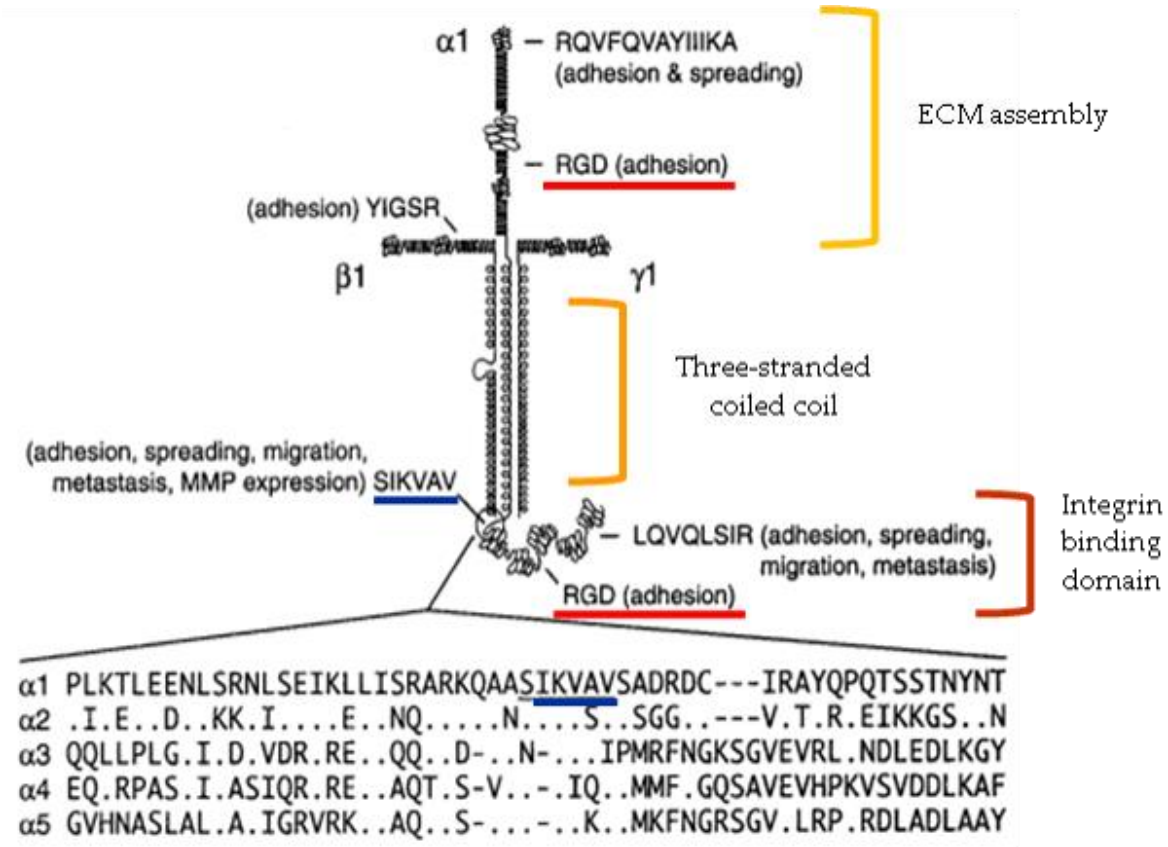


Schematic 2.4 Structural features of integrin receptors. (A) Illustrates the overall shape, as deduced from electron microscopy and (B) schematizes the arrangement of the polypeptide chains. The shaded area represents the RGD ligand-binding region that is known to be made up from both subunits based on cross-linking and binding data. Image adapted from Richard O. Hynes, 1992 [69].

Therefore, different integrin-binding peptides can control different aspects of cell behavior (i.e. proliferation, differentiation, adhesion, migration) [83, 85].

2.2.2.1.2 CELL ADHESION FRAGMENTS OF LAMININ

Laminin is a heterotrimeric glycoprotein (i.e. α-, β-, and γ-polypeptide chains) that has diverse biological functions such as promoting cell adhesion, migration, differentiation, proliferation, neurite outgrowth and tumor growth [86]. Laminins are approximately 400-900 kDa in size, have a T-shape with short arms composing parts of one chain and the long arm is formed by parts of the three chains, Schematic 2.5 [88]. Thus, enabling laminin to bind to proteoglycans, other ECM proteins, as well as other laminins [87].



Schematic 2.5 Comparison of the sequences of the 'linker' regions of the mouse laminin α-chains. A diagrammatic representation of the Ln-1 active sites is illustrated. The amino acid sequences of the 'linker' region between the coiled-coil and the globular domains of the mouse laminin α-chains that are identical to α1 chain. Image partly adapted from Robert M. Senior, 2003 [88].

During embryogenesis laminin-111 and laminin-511 are amongst the first ECM proteins expressed, whereas laminin (Ln)-1 is the best characterized laminin [89, 90]. Ln-1 is composed of the polypeptide α1, β1, and γ1 chains, which contain a number of cell adhesion active peptide sites (i.e. RGD, IKVAV and YIGSR), of which the IKVAV is the most potent active site [91]. Integrins α1β1 and α3β1 interact with RGD and IKVAV, respectively, based on their location in Ln-1 as these peptides can exhibit different affinity and selectivity due to the flanking residues, confirmation and accessibility towards the integrins [63]. Therefore, indicating that high affinity ligands would require a lower density of peptide vs low affinity ligands with high density of peptides to achieve the same effect on cellular behavior [92].

The C-terminus of the laminin α chain consists of five laminin G-like (LG) domains of which the α2 LG4-LG5 domain pair (i.e. binding sites for heparin and the cell surface receptor α-dystroglycan) is disulfide bonded to an extended N-terminus segment to the LG5 to stabiles the domain pair. The stabilization is facilitated by the flanking residues Leu2755 and Phe2931 in the LG4-LG5 domain pair to form two main chain hydrogen bonds in an antiparallel β-sheet-like fashion [73, 93]. Consequently, certain flanking amino acid residues play a significant role in influencing the most active confirmation of the RGD in the loop structure, which might explain why so many different RGD sequences are found in natural integrin ligands [94, 95].

Adhesion peptides such as RGD and IKVAV facilitating cell adhesion, which is a crucial basis for many biological processes such guiding cells into their appropriate locations in the body, providing cell anchorage, and controlling cell proliferation, differentiation, and apoptosis [96, 97]. These adhesion peptides bind to integrins to promote cell adhesion when immobilized (i.e. mimicking the ECM) on a surface and when in solution the peptides competitively inhibit the binding to the cell surface receptor [98]. Consequently, adhesion peptides are being tethered to surfaces to improve the biocompatibility of biomaterials, whereas in the soluble form these adhesion peptides are being investigated for application in targeted drug delivery [99-102].

2.3 BIOMATERIALS AND THEIR PROPERTIES

Scientist and engineers are taking an interdisciplinary approach in mimicking the extremely dynamic and complex cellular microenvironment of cells by designing biomaterials that have the ability to augment, support and replicate the properties (i.e. chemical and physical) to match those of the ECM that they are replacing [8-10]. The introduction of biomaterials (i.e. man-made) in a living biological environment either *in vitro* (i.e. cell culture) or *in vivo* (i.e. biomedical implants) have demonstrated to alter the cellular environment and consequently affect the cellular function and processes.

The surface of the material is the first plane of contact between the material and the cells (i.e. interface), thus, biocompatibility is crucial for the surface properties to elicit the appropriate cellular response (i.e. cell adhesion). The cell response to a surface strongly depends on the properties (e.g. type, concentration, distribution, and motility) of the surface adsorbed proteins (i.e. secreted by the cells or functionalized on the surface), modification of the biomaterials' surface properties affects the nature of the protein layer and provides control over the response of cells to the biomaterials [103-107].

Biomaterials that provide two-dimensional (2D) and three-dimensional microenvironments (3D) for cells have been designed to mimic the cellular microenvironment, which is 3D organization that provides directional cues (i.e. spatial and temporal). The 3D materials would represent the ideal platform for cell-cell and cell-surface interaction, however, there are certain problems that come with this model (i) the system is complex, (ii) difficulties in getting the nutrients in the media to all of the cells which can lead to apoptosis, and (iii) imaging difficulties in observing the cells development due to the 3D scaffold size, material transparency, and microscope depth. Consequently, the 2D biomaterials remain the norm as the 3D culture introduces many unmet needs and drawbacks that include performance, sensitivity and compatibility with high-throughput screening instruments [108, 109]. Currently, these difficulties are still significant in designing 3D environments which need to be fine-tuned to tackle the challenges presented in applications such as (i) research, (ii) toxicity testing, and (iii) safety screening.

2.3.1 SURFACE PROPERTIES

Three surface properties have been identified as main determinants of cell behavior and cell fate, (i) surface chemistry, (ii) surface topography, and (iii) surface elasticity or stiffness [110].

2.3.1.1 SURFACE CHEMISTRY

Variations in the chemical composition of material surfaces has been shown to affect a broad range of cell properties, including adhesion, spreading, migration, proliferation, and differentiation. Cell responses have been related to both specific (i.e. specific molecules or molecular structures) and nonspecific (e.g. hydrophilicity/hydrophobicity and charge) surface chemical properties [111-119].

Nonspecific chemical properties such as charge and wettability have been shown to affect cell adhesion or phenotype and functionality of mesenchymal stem cells. As the surface of cells is typically negatively charged, the presence of positive surface charges often promotes cell adhesion [120]. Similarly, moderately hydrophilic molecules also tend to promote cell adhesion to a surface [121]. In particular, cell adhesion on surfaces containing amine group functionalities has been shown to be increased when compared with other functional groups such as carboxyl (negatively charged), methyl (hydrophobic) and hydroxyl (neutral and hydrophilic) groups [122]. Biomolecules can be immobilized on a surface to exploit the specific interaction of cell-surface ligands with the ECM. Immobilized proteins (i.e. laminin), peptide sequences (i.e. RGD) and carbohydrates (i.e. galactose) have been used to control cell behavior [113, 123]. The RGD peptide sequence was originally discovered in fibronectin and received particular attention to promote integrin-mediated cell adhesion to artificial surfaces; as well as being the most important recognition site (i.e. fibronectin, collagen, laminin) for the majority of all known integrins [124, 125].

2.3.1.2 SURFACE TOPOGRAPHY

Physical properties such as surface topography, roughness, pattern dimensions and order play a large part in directing cellular responses at the cell-material interface [84, 126, 127]. The dimensions of topographical features are crucial as they affect the cell's ability to detect

and respond to them [128]. Micron-sized features that match the dimensions of whole cells may not be recognized by cell-surface receptors, whereas nanoscale features that are similar in size to cell receptors have been shown to have a major impact on the response of cells to a surface [126]. For example, topographical features with several tens of nanometers in depth can affect cell adhesion and differentiation [129, 130, 131]. In 2007, Khang et al., presented their work on the role of nanometer and sub-micron surface features on vascular and bone cell adhesion in comparison to a flat titanium surface. The results in comparison to the flat titanium surfaces demonstrated a 27% increase in surface energy and promoted endothelial cell adhesion density by 200% on the sub-micron surface features and a 10% increase in surface energy and a 50% increase in endothelial cell adhesion density on the nanometer surface features. Although, the results indicated that the sub-micron features presented the highest cytocompatibility properties, however, the nanometer surface features presented more efficient surface features compared to the altered width of surface features. This was due to the smaller changes in surface area and surface roughness with respect to increase in both surface energy (i.e. important factor that controls cell adhesion) and adhesion density [132]. Papageorgiou et al., published in 2014 their research on the capacity of dural epithelial cells to take up nanometer sized particles (i.e. readily penetrating the cells), whilst the study suggested that there was some barrier to the penetration of micron-sized particles [133]. It is not only the feature size that affects cell response; the way nanoscale features are organized on a surface equally impacts cell fate. In 2016, Anderson et al., reviewed highly ordered patterns and highly controlled-disorder patterns and results demonstrated that the disordered arrangements of circular pits (100 nm deep, 120 nm diameter) caused increased osteoblastic differentiation of mesenchymal stem cells compared with ordered patterns (square or hexagonal alignments) of pits with the same dimension [127]. It was postulated by the Spatz Group suggested that the disordered nature facilitated the adhesive points to group closer together (i.e. within the critical 70 nm range described by Cavalcanti-Adam) enabling the gathering of the integrins and the formation of super mature adhesions (> 5 μm long) [134].

2.3.1.3 SURFACE ELASTICITY/ STIFFNESS

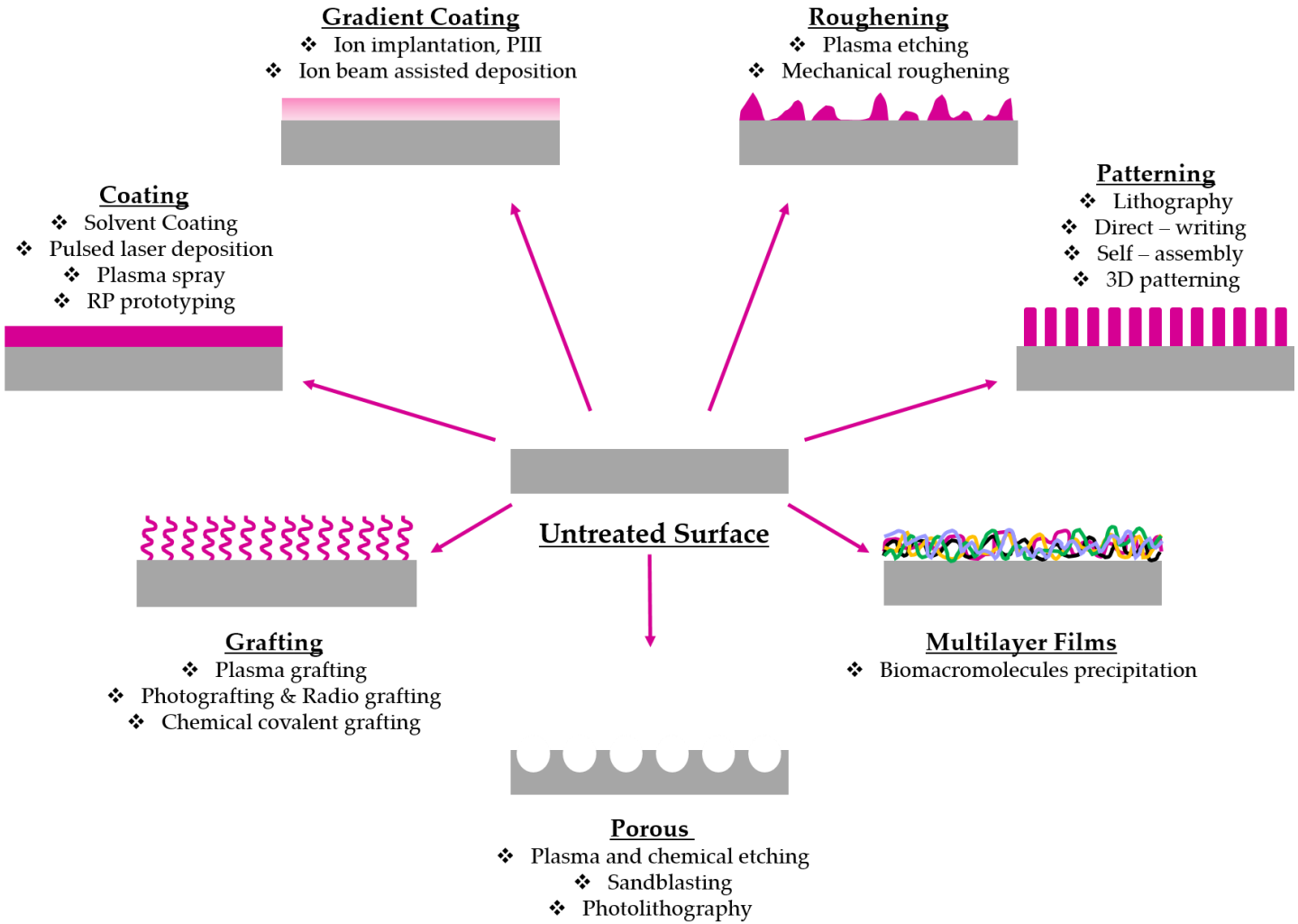
Besides surface topography, matrix elasticity (or stiffness) of a material has been recognized as another physical property that directs stem cell fate [135]. The lineage of mesenchymal stem cells was shown to correlate with variations in the stiffness of the material. The differentiated cell type obtained on a material with a particular stiffness corresponded to the natural stiffness of the relevant tissue.

2.3.2 SURFACE MODIFICATION

Surface modification techniques are employed to retain the favorable bulk properties, whilst catering to the specific needs of the cells to enhance biocompatibility and control specific cell processes [108, 136, 137]. The design of these materials are fabricated through means of micro- and nanotechnology by using physical and chemical micron and sub-micron scale features, Schematic 2.6 [145, 146].

2.3.2.1 TYPES OF BIOMATERIALS

The surface properties and choice of surface modification strategy will be influenced by the selected material, which should tailor to the application requirements of the biomaterial. Virtually all available types of materials have been tested for use and those many different types of materials are mainly classified as (i) metals and alloys, (ii) ceramics, (iii) polymer (i.e. natural and synthetic), and (iv) composite biomaterials [138, 139]. All metal biomaterials (i.e. stainless steel, titanium, cobalt based alloys and platinum) are metal oxides and are used when there is an anticipated high mechanical load to be exerted on the implant (i.e. cells will interface with metal oxide coated metals). Thus, the metals and alloys will provide electrical and thermal conductivity (i.e. pacemaker), are mechanical strength (i.e. external prosthesis), easily sterilized (i.e. surgical instruments) and have relatively good wear resistance (i.e. dental implants, bone and joint replacement) [140]. Bioceramic biomaterials (i.e. aluminum oxide, calcium phosphates, calcium aluminates, titanium oxide, carbon, and Bioglass®) provide high biocompatible (i.e. heart valves), compression strength (i.e. knee implants), corrosion resistance (i.e. dental implants), and low thermal and electrical conductivity (i.e. cochlear implant) [141].



Schematic 2.6 Illustration of the surface modification techniques. Adapted from Qie et al. 2014 and Shandas et al. 2014 [145, 146].

The polymer biomaterials can be natural (i.e. protein, nucleic acids, and polysaccharides) and/or synthetic (i.e. polyolefins, PTFE, polyesters, polyamides, and methacrylates) and provide structural and mechanical property when complex forms or high flexibility is needed for instance, agarose and PMMA, respectively. Polymers are widely used in the medical field as suture material, drug delivery systems, coating of stents, and hemodialysis membranes are amongst a few [142-144] .

2.3.2.2 PATTERNING SURFACE CUES VIA LITHOGRAPHY

The lithography techniques are able to fabricate precise and complicated 2D and 3D structures at a micro- and nano- topological scale (i.e. printing). The lithography method was initially used for designing semi-conductors, integrated circuits and electronic components in the field of electronics. The advances in the lithography techniques of photolithography, electron beam lithography and focused ion beam lithography enabled the development of the soft lithography, nanoimprint lithography and dip-pen lithography techniques [147-152]. Moreover, this became the driving force for the techniques to expand into the biomedical field as cost, complexity of operation and accessibility of the techniques became available to scientists [153, 154].

Consequently, such recent developments of lithography in the biomedical field are the use of drawing lithography and holographic lithography [155-161]. Drawing lithography has been used for the fabrication of three kinds of microneedles, (i) an ultrahigh-aspect ratio (UHAR) hollow microneedle, (ii) a dissolving microneedle, and (iii) a hybrid electro-microneedle (HEM) as an innovative drug and gene delivery system [162]. Whereas the holographic lithography techniques has been implemented in the fabrication of pillars on PEG-DA scaffolds to investigate their potential to be interconnection channel networks to facilitate cell-cell interactions, enable the delivery of nutrients and removal of metabolic waste, as well as vascular capillary ingrowth. The results demonstrated a promising development in the successful fabrication of micro-structuring 3D scaffold from biodegradable hydrogels [163].

2.3.2.3 FUNCTIONALIZATION VIA PHYSICAL AND CHEMICAL ADSORPTION

Adsorption is the accumulation of gas or liquid solute (i.e. adsorptive) on a surface of a solid or liquid (i.e. adsorbent) to form either a molecular, ionic or atomic film [164]. The adsorption processes are classified into two broad classes, physical adsorption and chemical adsorption, Table 2.2 [164].

Table 2.2 Differences between physical adsorption and chemical adsorption. Adapted from Milan Králik, 2014 [164].

Property	**Physical Adsorption**	**Chemical Adsorption**
Type of bonding forces	Van der Waals (i.e. non-covalent)	Chemical bond formation (i.e. ionic or covalent)
Enthalpy of adsorption	Low, 10-40 $kJmol^{-1}$	High, 20-400 $kJmol^{-1}$
Enthalpy (heat) of ΔH	Exothermic	Endothermic or exothermic
Chemical change of adsorptive	None	Formation of a surface compound
Reversibility	Fully reversible, desorption of adsorbate occurs by decreasing the activity of the adsorptive in the fluid surrounding the surface	The processes is irreversible, as the desorbed compounds are different from the adsorbed ones
Activation energy	Very low, close to zero	High
Electron transfer	None, although polarization of absorptive may occur	Yes, bond formation between adsorptive and surface
Effect of temperature	Reactions occur at low temperature, and adsorption decreases with increase in temperature	At first adsorption increases with increase in temperature
Specificity of adsorbate - absorbent interactions	Low degree of specificity	High degree of specificity (i.e. 20-400 $kJmol^{-1}$) depends on the number of active sites
Surface area	Adsorption increases with the increase in surface area of the absorbent	Adsorption increases with the increase in surface area of the absorbent
Formation of multilayers	Multilayer adsorption. In gas phase adsorption usually accompanied by liquefaction in micro- and mesopores	Monolayer adsorption, they will usually occupy certain adsorption sites on the surface and only one layer of chemically adsorbed molecules is formed

Surfaces can be functionalized with different types of adsorptive, natural and synthetic, biomolecules to achieve biocompatibility and both classes have their advantages and disadvantages [165]. Functionalizing surfaces with the natural (i.e. biologically extracted) components of the ECM enables surfaces to be bioactive, biocompatible and of similar mechanical properties as native tissue. However, along with the advantages there are certainly some disadvantages such as (i) limited control over physiochemical properties, (ii) difficulties in sterilization and purification, (iii) isolation can cause contamination (i.e. pathogen/viral issues), and (iv) high production cost [166, 167].

In contrast, synthetic materials can be tailored to mimic the components of the cellular microenvironment (i.e. biomolecules) to exhibit (i) suitable mechanical properties, (ii) highly reproducible chemical and physical properties (ii) low immune response, and (iv) low production costs [165].

As a result, short sequenced biomolecules are favored as they are more stable, reproducible and can be mass-produced in the laboratory in comparison to those of whole proteins. Consequently, the adsorption process selected for the most effective surface modification will entirely depend on the application of the surface material. The aim is to design biomaterials that have the highest sensitivity, specificity and selectivity of the role they will play *in vivo*, Table 2.3 [168]. Moreover, surfaces can be engineered to have responsive interfaces where by a stimuli (i.e. chemical and/or physical) can be provided externally by a device or internally by the cells to elicit various cell responses such as adhesion, migration and differentiation, Table 2.4 [55].

Table 2.3 Compatibility of weak and strong anchors to different surface materials. Adapted from Eril Reimhult and Fredrik Hook 2015 [168].

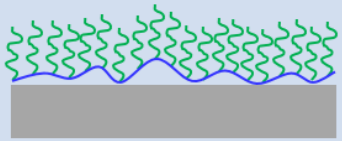
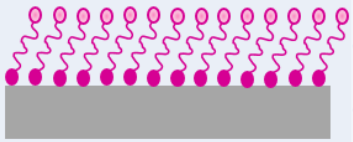
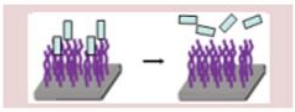
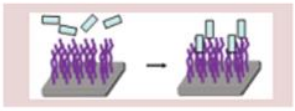
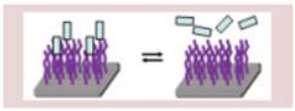
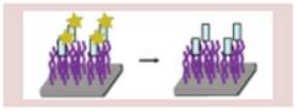
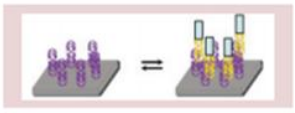
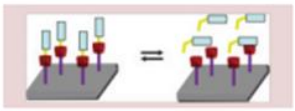
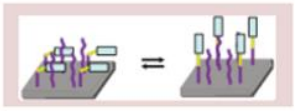
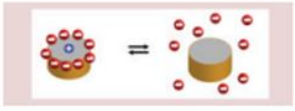
Type of Anchor	Schematic	Anchors	Properties of functionalised surface	References
Weak anchors (physical adsorption)		❖ Amino acids, proteins ❖ Polyelectrolytes ❖ Hydrophobic chains ❖ Hydrophilic lipid head groups	❖ Flexible but non-specific ❖ Metal oxides, charged surfaces ❖ Hydrophobic surfaces ❖ Hydrophilic surfaces	[169, 170] [171, 172] [173, 174] [173, 175]
Strong anchors (chemical adsorption)		Silanes	SiO_2 (metal and non-metal oxides/ hydroxides)	[176, 177]
		Thiols	Au, Ag, Cu, Pt, ITO	[178, 179]
		Phosp(on)ates	TiO_2, Al_2O_3, TiO_2 and many other transition metal oxides	[180, 181]
		Catechols	TiO_2, Fe_3O_4 (metal oxides)	[182, 183]

Table 2.4 The dynamic chemical properties incorporated in responsive materials [55].

Chemical surface change	Schematic representation	Ref.
Wettability		[184-187]
Detachment of peptide sequence		[188-191]
Attachment of peptide sequence		[192, 193]
Reversible binding of peptide sequence		[194]
Unblocking of peptide sequence		[195]
Reversible display of peptide sequence through self assembly – leucine zipper domains		[196, 197]
Reversible display of peptide sequence through self assembly – cyclodextrins		[198, 199]
Reversible display of peptide sequence through conformational changes		[200-205]
Polymer-bound electrodes – regulation of glutamate		[206]
Reversible availabiity of enzymes through surface porosity regulated by stress		[207]
Accessible enzyme: ; Blocker: ; Cyclodextrin: ; Electrode: ; Inaccesible enzyme: ; Leucine zipper: ; Molecular Ion: ; Peptide: Sequence: ; Responsive unit: ; Surface: ; Tether: ; Water droplet:		

2.3.3 CELL RESPONSE TOWARDS THE BIOMATERIALS

The integration of cells and the biomaterial occurs at the interface for therapeutic purposes in engineering new tissue for repair, replacement or regeneration of the diseased and/or damaged cells, Figure 2.1 [208]. Accordingly, *in vitro* most animal cells can only grow when they are attached to surfaces through the ECM [53].

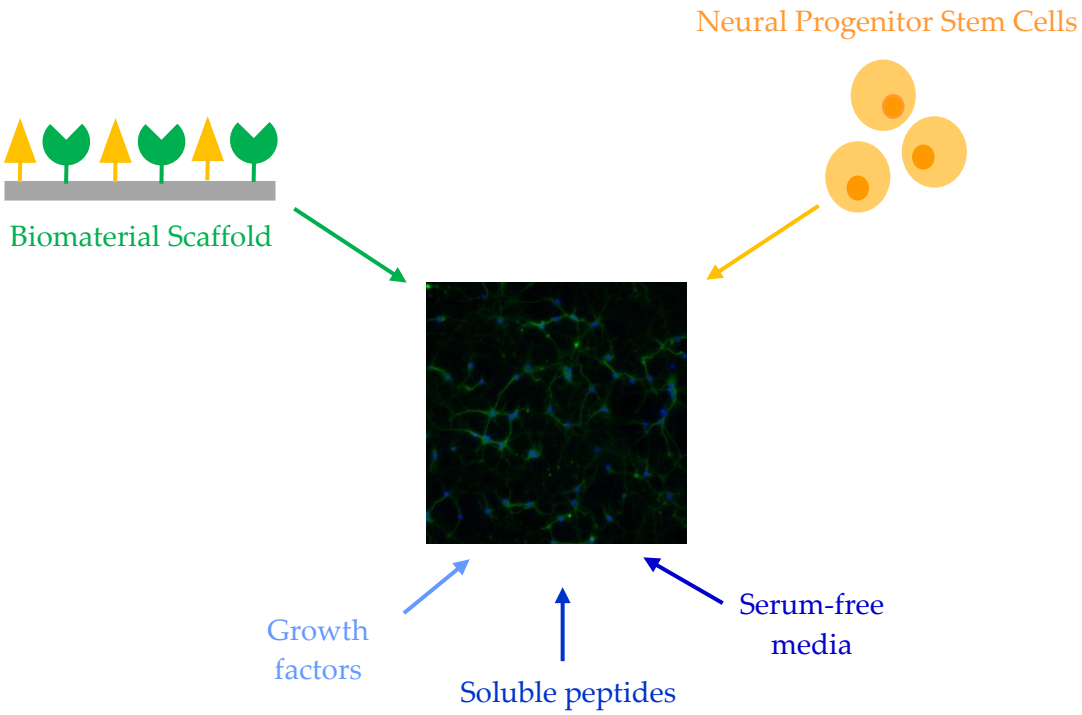


Figure 2.1 Tissue engineering triad of cells influenced by the environment. Signals provided chemically by growth factors and soluble peptides in the media, or chemically and physically by the scaffold which acts as a template for tissue formation by allowing cells, to adhere, proliferate, migrate, differentiate, and produce tissue. Parts of image of adapted from Fergal J. O'Brien, 2011 [208].

To mimic a natural cellular environment and control cell fate has been a major challenge in the biomaterials field as it has been quite difficult to determine the precise intracellular and/or extracellular conditions (i.e. parameters) alike to that of the ECM. As a result scientist have been studying the biological architecture and mimicking specific components of the ECM to design their biomaterials [8]. Peptide motifs are one of those components in the ECM that are associated with biological function and have a pivotal role in the dynamics of protein-protein interactions [209, 210]. Consequently, new synthetic peptide surfaces with

well controlled composition and functionality can be designed with the ability to control stem cell adhesion, proliferation, survival and differentiation [98].

In this thesis we present the functionalization of the two peptide sequences, RGD and IKVAV, to control neural stem cell differentiation to a specific cell lineage with the intention to integrate these surfaces in the SLAB system. The strategy is to initially establish the method by which the peptides will be immobilized on the surfaces and the cell differentiation response to the peptides, Chapter 4. Secondly, the ECM environment is not compromised of singular peptides, but a dynamic composition of various peptides that work together to create the complexity of the natural niche that the NPSCs find themselves in. Thus, in Chapter 5 we optimize the established method in Chapter 4 to design surfaces that more closely resemble the ECM by designing controllable orthogonal peptide environments to influence the NPSCs to differentiate towards a controllable mixed population of neurons and astrocytes.
Lastly, in recent years the state-of-art in immobilizing peptides on biomaterials has demonstrated a shift from 2D surfaces towards 3D surfaces as they present the spatial integrity that the ECM holds. Consequently, this led us to investigate to immobilize the RGD and IKVAV peptides on comparable 2D and 3D surfaces to examine the influence surface chemistry, surface topography and spatial integrity has on the biological response of the NPSCs. Furthermore, these comparable 2D and 3D surfaces would help to take a step closer in establishing the "brain in dish" model that the NPL research group is building in the SLAB system. The presented results in this thesis will be crucial in optimizing the SLAB system with the intention of contributing towards future applications in building artificial neural networks in the fields of tissue engineering and regenerative medicine.

In order to achieve this goal an extensive literature review had to be done on the influence of (i) singular RGD and IKVAV peptide surfaces, (ii) orthogonal chemistry surfaces of RGD and IKVAV, and (iii) RGD and IKVAV conjugation on 3D surfaces on cell response (i.e. adhesion, survival, proliferation, differentiation, and uptake).

The discussed literature provided us with a better insight on how the work done in this thesis will contribute to the state-of-art in immobilizing peptides on 2D and 3D surfaces and their influence on cell response.

2.3.3.1 CELL RESPONSE TO SINGLE PEPTIDE COMPOSITION SURFACES

2.3.3.1.1 RGD FUNCTIONALIZED SURFACES

The RGD peptide sequence is found as part of the cell attachment site in the ECM, blood, and cell surface proteins, hence, the sequence has been extensively immobilized on many natural and synthetic biomaterials. P.M. Yip et al. presented the first set of data that indicated the role of the RGD peptide sequence in the promotion of neurite outgrowth via interaction with the $\alpha_v\beta_3$ integrin on neuronal cells [211]. Many studies have demonstrated that surfaces functionalized with RGD influence cell processes such as cell adhesion, proliferation, migration and differentiation towards different cell fates [97, 212, 213].

In 2007, Jedlicka et al. designed a novel method for producing biologically active peptide ormosils using peptide-modified precursors. Synthesized peptide silanes were conjugated on a thin-film of 3'-(aminopropyl)trimethoxysilane (APTMS), using carbonyldiimadazole (CDI) as a linking molecule. They then seeded embryonic carcinoma stem cell line, P19, on the surfaces and observed more neuron cell fate and longer neurites on the RGD/YIGSR and RGD/YIGSR/NID surfaces compared to tetramethoxysilane (TMOS) controls, Figure 2.2 [214].

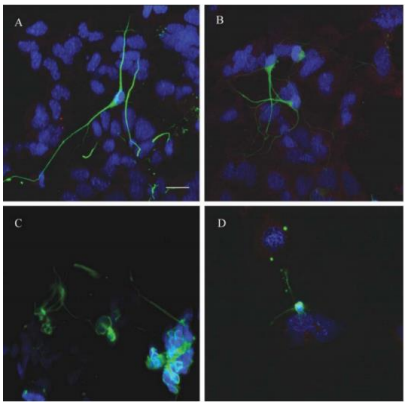


Figure 2.2 Confocal immunofluorescent expression of Tuj1. In situ immunofluorescent analysis was performed to analyze neuronal lineages and observe neurite patterns between materials. (A) RGD/YIG; (B) RGD/YIG/NID; (C) collagen; (D) TMOS derived silica (scale bar = 75 mm). Taken from Jedlicka et al. 2007 [214].

Straley and Heilshorn, published in 2009 their investigation into the effect of changing RGD ligand density on neural cell behavior. They demonstrated that increasing the RGD ligand while maintaining uniform protein surface coverage results in enhanced neurite extension of PC-12 cells; as well as generating tunable, quantifiable, and reproducible surfaces for *in vitro* studies of cell-ligand interactions and for potential application as coatings on neural implants [215].

In 2010, Ananthanarayanan et al. took a different approach and reported on the influence of phospholipid bilayers functionalized with different RGD-containing peptides, GGGNGEPRGDTYRAY ('bsp-RGD(15)') or GRGDSP, on the behavior of adult hippocampal neural stem cells (NSCs). They observed that the NSCs had a lower affinity for the linear GRDSP ligand than the bsp-RGD(15), this was further observed in the proliferation rate with the bsp-RGD(15 and exhibiting phenotype similar to that of the laminin control. Therefore, providing evidence that RGD peptide-functionalized bilayers support NSC adhesion, proliferation, and differentiation into mature neural cells [216].

Progress in the research of neural chips was being made as more work was published in 2010 on the popular tool for monitoring living cell viability under various conditions. Md.A. Kafi et al. fabricated nanopatterned arrays of C(RGD)4, RGD-MAP-C, and PLL deposited on gold (Au) electrodes through nanoporous alumina-masks (i.e. cell chip) to compare their ability to detect electrochemical signals from cells for applications in detecting drug effects or for assessing toxicity electrochemically. The results demonstrated that the peptide coated Au electrodes yielded more stable and stronger redox peaks on the cyclic voltammetry (CV) than that of a bare Au electrode. This was related to the cell adhesion behavior, as patterned peptides on the Au electrodes showed a significant increase of peak current and cell adhesion. Validated by the high cell adhesion on Au/RGD-MAP-C nano-dot array, which produced the highest signal due to arrays highly ordered structures of peptides illustrating the higher affinity for patterned surfaces as they provide better electrochemical signals [217].

In 2011, Diaz-Quijada et al. published their work in progress of developing multisite planar patch-clamp chips capable of recording high resolution electrophysiological function from individual neurons established in culture. They employed the chemical adsorption approach to facilitate the patterning of RGD cyclopeptides on silicon-based surfaces to promote stimulation of important biological process and observe electrophysiological studies, whilst

the pattered RAD cyclopeptide surfaces were the negative control. The results illustrated RGD inducing neuron cell adhesion and the RAD inhibited adhesion, which indicates that one different amino acid can have a major influence on the biological processes of the neuron cells.

As a result, the integrin sites of the neuron cells were in close proximity to the RGD motifs on the surface when they adhered, which meant that the ion channels near the integrin receptors could be used to position the ion channels at or near the orifice in the planar patch-clamp that is being developed. Furthermore, continuing the progress of developing the presented technique would enable the complexity of such synthetic networks to be increased with the design of planar patch-clamp chips that possess an array of micro-orifices with a network of microfluidic channels that are able to independently address each individual orifice, Figure 2.3 [218].

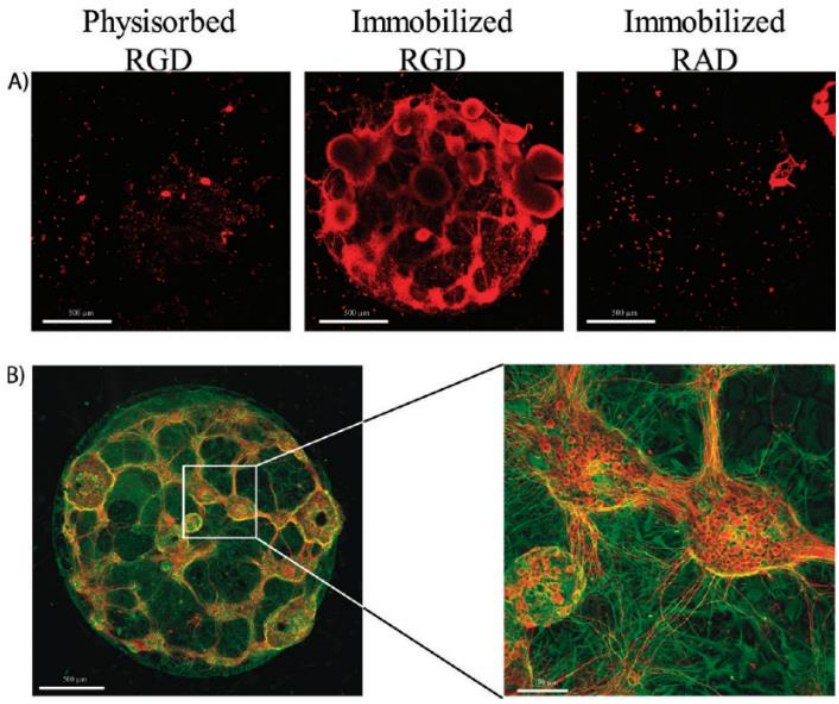


Figure 2.3 (A) Importance of chemical adsorption when using small molecules is illustrated by culturing cryopreserved rat cortical neurons on surfaces that have circular regions of physisorbed and chemisorbed cyclo(RGDFK-PEG). Cells were visualized with a cell membrane dye (RH-237). The negative control experiment with cyclo(RGDFK-PEG) was carried out to corroborate molecular recognition of the RGD motif. (B) Immunofluorescence staining of cells for GFAP (green) and Map2 (red) to corroborate the presence of neurons on the cyclo(RGDFK-PEG) modified surface. Taken from Diaz-Quijada et al.2011 [218].

H. Xie et al. hypothesized in 2013, that conjugating cell binding motifs, such as RGD or IKVAV, to the PHA-binding protein phasin (PhaP) for surface functionalization of PHA materials could better support the growth and differentiation of neural stem cells (NSCs). They observed short-term advantages in promoting the adhesion, proliferation and neural differentiation of rat NSCs on the PhaP-RGD and PhaP-IKVAV coating in comparison to that of the PhaP-coated or uncoated material. Moreover, the presented data strongly suggested that hydrophobic materials coating with PhaP-IKVAV exhibited more NSC adhesion and proliferation, whilst both PhaP-RGD and PhaP-IKVAV had no influence of specific stem cell fate [219]. In 2015, Z. Pellett et al. investigated the incorporation of the CRGDS peptide to promote adhesion, proliferation and differentiation. Minimal concentration of the CRGDC peptide was included in the PEG hydrogel and the results demonstrated that the hydrogel was capable of promoting induced pluripotent stem cells (iPSC)-NSC differentiation into functional neuronal tissues, indicating minimal monolayer complex surfaces can support and sustain iPSC-NSC differentiation [220]. That same year, a paper was published where the RGD peptide sequence was incorporated into a polymer, poly (serinol hexamethylene urea) (PSHU), in a study performed by Yun et al. to determine the effects of PSHU-RGD on human neural stem cells (hNSCs) survival during motor neuron (MN) differentiation. They were able to characterize and validate the design of the controllable polymer, whilst demonstrating that the PSHU-RGD was able to induce adhesion, proliferation and survival during hNSC differentiation to motor neurons (MN). Moreover, the results illustrated a high MN (40%) differentiation in comparison to that of the control surface poly-D-lysine (PDL)-Laminin (< 10%), indicating great implications for PSHY-RGD in future stem cell therapies for SCI treatment [221]. De Luca et al, presented in 2016 the work for developing synthetic polymer conduits as an alternative to autografting in peripheral nerve damage. RGD peptides were conjugated to poly-ε-caprolactone (PCL) films, and seeded with adult adipose-derived stem cells (dASCs) that differentiated to Schwann cells, dissociated dorsal root ganglion (DRG) neurons and a co-culture of dASCs and DRG. The results demonstrated improved adhesion and proliferation of dASCs and DRG on the functionalized surfaces. The DRG neurons grew longer neurite outgrowth in co-culture and in the presence of the RGD. Additionally, the integrin blocking experiment did

not affect the neurite outgrowth suggesting that β1 integrin function can be compensated by other molecules present on the cell membrane [222].

2.3.3.1.2 IKVAV FUNCTIONALIZED SURFACES

J.P. Ranieri et al. published in 1994 and 1995 their work on the immobilization of two laminin sequences, YIGSR and IKVAV (CSRARKQAASIKVAVSADR), on fluorinated ethylene propylene (FEP) films to investigate neuronal cell attachment. They observed exclusive cell attachment of the PC12 cell on the IKVAV patterned FEP films with restricted neurite outgrowth, whilst the NGlOS-15 cells demonstrated selective attachment on the CDPGYIGSR patterned FEP films and differentiated into neurons [223, 224].

In 1996, E. Agius et al. observed in their perturbation experiments (i.e. the modification of neuron-substratum interactions by antibodies and peptide), the antibodies reduced proliferation by 30% and neurite outgrowth by 50%. Moreover, the IKVAV sequence (i.e. in solution) blocked neurite outgrowth on neonatal spinal cord substrata, which was a surprise as IKVAV was a known active sequence in laminin that is responsible for neurite extension. These results demonstrated that the IKVAV peptide could also reduce neurite outgrowth of peripheral neurons on laminin, which might be due to neuronal metabolism altering and reducing the ability of the neuron to deal with the molecular environment or the IKVAV peptide preparation being toxic to the neurons. However, they ruled these hypotheses out as they added IKVAV peptide to the media of the laminin controls and observed not change in the ability of neurons to grow on fibronectin. This enabled them to conclude that IKVAV-containing peptides reduced neurite outgrowth by interfering specifically with the ability of neurons to interact with the tissular substratum. Thus, neuronal cell lines may exhibit a varying sensitivity to the IKVAV sequence [225]. G.A. Silva demonstrated in 2004 that the concentration of the IKVAV peptide on the surface place a role in the differentiation process, higher density concentration lead to significant neuron differentiation and lower concentration inhibit (i.e. molar ratios used of IKVAV:PA were 100:0, 90:10, 50:50, 40:60, 10:90). Also these findings demonstrated that the dimensionality of the IKVAV on the surface was not a key factor [226]. In 2008, Yulin et al. presented their work on the two-dimensional effects of hydrogel functionalized with IKVAV-containing peptide amphiphile have on the growth and differentiation of NSCs. The peptide was synthesized via solid

phase peptide synthesis (SPPS) and functionalized on the hydrogels via physisorption. The NSCs were seeded on the surface layer of self-assembled peptide hydrogel and coverslips for seven days and the surface of the hydrogel induced adhesion, proliferation and differentiation into neurons (i.e. NSCs of neonate rats) and astrocytes (i.e. NSCs of adult rats) [227].

2.3.3.2 CELL RESPONSE TO MIXED PEPTIDE COMPOSITION SURFACES

The research of engineering biomaterials with physical or chemical cues has developed into combining these cues to design materials that present well-defined chemical and physical stimuli that influence major biological cell process. The combination of different physical cues can be achieved by patterning methods (i.e. lithography, direct-writing, 3D), however, combining different chemical cues has been a longstanding challenge until recent progress. Recent publications demonstrated the combination of different biomolecules via 'click chemistry' to design more complex two-dimensional (2D) surfaces in comparison to the commonly single biomolecule conjugated 2D surfaces [228].

L. Aucoin et al., presented work in 2002 where they functionalized poly dimethyl siloxane (PDMS) surfaces by covalent attachment of combinations of cell adhesion and synergistic peptides YIGSR and its synergistic peptide PDSGR from laminin and the fibronectin derived RGDS and PHSRN. They observed that the surface density varied as a linear function of peptide concentration in the reaction solution, and was different for the different peptides examined with GYRGDS the lowest and GYPDSGR the highest density. The surface analysis quantified the differences the wettability and chemical composition of the various surfaces. The results demonstrated that modification with multiple peptides resulted in greater adhesion than modification with single peptides only as a significant difference in adhesion of human corneal epithelial cells was observed. Furthermore, the results showed evidence that the appropriate combinations of the cell adhesion peptides and synergistic peptides may result in improved cell surface interactions [82]. In 2007, L.M. Weber investigated the influence of matrix-derived adhesive peptide sequences on encapsulated β-cell survival and glucose-stimulated insulin release by covalently incorporating synthetic laminin-derived

recognition sequences, IKLLI, IKVAV, LRE, PDSGR, RGD, and YIGSR, and the collagen type I sequence, DGEA on photopolymerized poly(ethylene glycol) (PEG) hydrogels in the peptide combinations IKLLI-IKVAV, IKVAV-YIGSR, and PDSGR-YIGSR to explore synergistic effects. They encapsulated individual MIN6 β-cells into the functionalized hydrogels and observed that the β-cells exhibited preserved viability, reduced apoptosis, and increased insulin secretion. The PDSGR-YIGSR demonstrating to be the best combination, which may be due to the two peptide sequences being in close proximity to each other on the β1 chain of laminin and mimicks the native laminin much better and providing a higher affinity cell-matrix interaction [229]. In that same year, K. Saha et al., presented a systematic engineering approach to designing a combination of bioactive peptides, lam-IKVAV(19) and bsp-RGD(15), of various ratios grafted (i.e. photopolymerization and conjugation) on interpenetrating polymer network (IPN, photoinitiator) surfaces. They observed that the pure lam-IKVAV(19) IPN surfaces neither enhanced proliferation nor differentiation. This was further supported as the differentiation into neuronal and astrocytic lineages progressively decreased as the IKVAV/RGD ratio increased; whilst bsp-RGD(15) was able to functionally substitute for laminin in early differentiation stages of adult NSCs, Figure 2.4. Moreover, the IPN matrices demonstrated precise, tunable microenvironment properties to control the proliferation and differentiation of stem cells, which can be rationally harnessed for basic scientific, bioprocess, and therapeutic purposes [230, 231].

In 2014, Haiqing Li and Justin J. Cooper-White described a facile method by which by which sequential attachment of different adhesion peptides to a nanotopographical, self-assembled block copolymer cell culture surface is made possible through orthogonal click chemistry. They initially tuned non-functionalized polystyrene-b-polyethylene oxide block copolymers (PS-PEO) with an azide and aminooxy functionality to create respectively, PS-PEO-N_3 and PS-PEO-ONH_2 domains, which were then conjugated orthogonally via the azide-alkyne Huisgen cycloaddition reaction and aldehyde-aminooxy oxime ligation reaction with different density concentrations of alkyne-terminated IKVAV or aldehyde-terminated RGD.

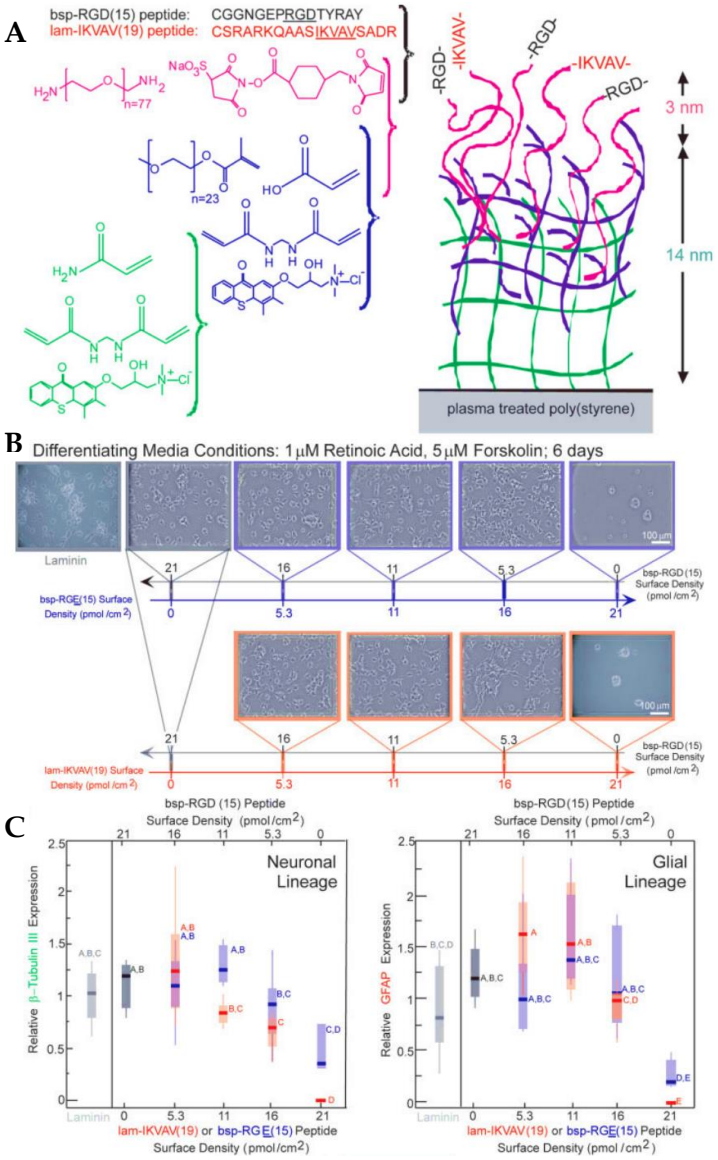


Figure 2.4 Schematic representation of IPN synthesis (not to scale). (A) Sequential polymerization steps create an IPN that is swollen in aqueous media and conjugated with bioactive peptides. (B) In mixed peptide IPNs, bsp-RGD(15) peptide surface density controls phenotype; phase-contrast images of NSCs after 6 days in culture on IPNs with mixed peptide conjugation. Surface density of peptide mixtures correspond to abscissa values directly below for bsp-RGD(15) plus lam-IKVAV(19) or bsp-RGE(15). Gray, black, red, and blue represent laminin, bsp-RGD(15), lam-IKVAV(19), and bspRGE(15), respectively, throughout the figure. (C) Gene expression of early lineage neuronal marker, β-Tubulin III, and glial marker, GFAP, in NSCs grown in differentiation media conditions. Gene expression levels correspond to normalized mRNA abundance as assayed by qRT-PCR after 6 days. The box plots summarize the distribution of points, where the thick line signifies the median and the top and bottom ends of the box delineate the 25th and 75th quartiles. Within each plot, levels not connected by same letter (A, B, C, D) are significantly different ($p < 0.05$; ANOVA between groups with Tukey-Kramer Honestly Significant Difference post hoc test). Taken from Saha et al., 2007 [230, 231].

The human mesenchymal stem cells (hMSCs) exhibited and increase in adhesion and change in morphology, from a rounded shape to a well-spread shape due to cells developing well-organized actin stress fibers, with the increase of the local density of RGD and IKVAV moieties in the domains, Figure 2.5 [232]. Thus, suggesting that the self-assembled block copolymer substrates regulate hMSC adhesion and morphology through modulation of ligand affinity and ligand redundancy, and hence the effectiveness of integrin binding and mechanotransduction signaling, which have been shown to influence the differentiation of hMSC populations.

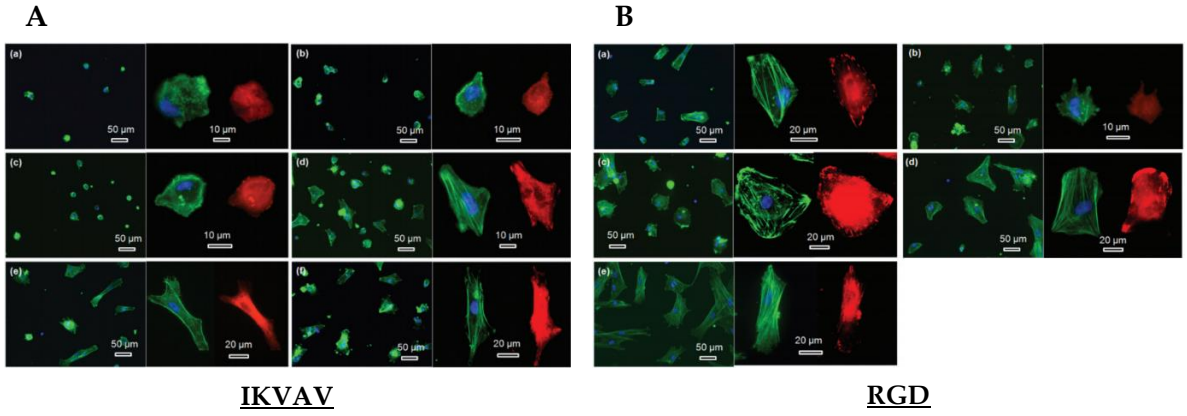


Figure 2.5 Fluorescent microscopy images of hMSCs on different polymer surfaces. (A) PS-PEO-ONH_2 alone (a); RGD conjugated polymer surfaces constructed by co-self-assembly of PS-PEO with 25 wt% (b), 50 wt% (c), and 75 wt% (d) of PS-PEO-ONH_2; RGD conjugated 100% PS-PEO-ONH_2 surface (e). (B) PS-PEO alone (a); PS-PEO-N_3 alone (b); IKVAV conjugated polymer surfaces constructed by co-self-assembly of PS-PEO with 25 wt% (c), 50 wt% (d), and 75 wt% (e) of PS-PEO-N_3; IKVAV conjugated 100% PS-PEO-N_3 surface (f). The green, blue, and red represent actin, nuclei, and vinculin, respectively; average cell area as function of surface content of PS-PEO-ONH_2 in the blended polymer films. Taken from Haiqing Li and Justin J. Cooper-White, 2014 [232].

M.M. Adil et al., published in 2017 the strategy that they developed to enable effective maturation and transplant of human embryonic stem cells (hESCs)-derived midbrain dopaminergic (mDA) neurons. The functionalized three-dimensional (3D) hyaluronic acid (HA)-based hydrogels with RGD and heparin (hep) via 'click chemistry' and tuned the stiffness parameter. The results demonstrated that the mDA neurons exhibited enhanced cell viability by 3.5-fold from the commonly two-dimensional (2D) *in vitro* cell harvest to

encapsulation, increased neurite growth by 2-fold, and presented a robust expression of mature, lineage-specific markers, Figure 2.6 [233]. Thus, indicating that this versatile 3D HA-RGD-hep hydrogel has the promising potential to be encapsulate other classes of neurons at different stages of development, as well as non-neuronal cells, to increase post-transplantation cell survival in regenerative therapies for a range of other conditions.

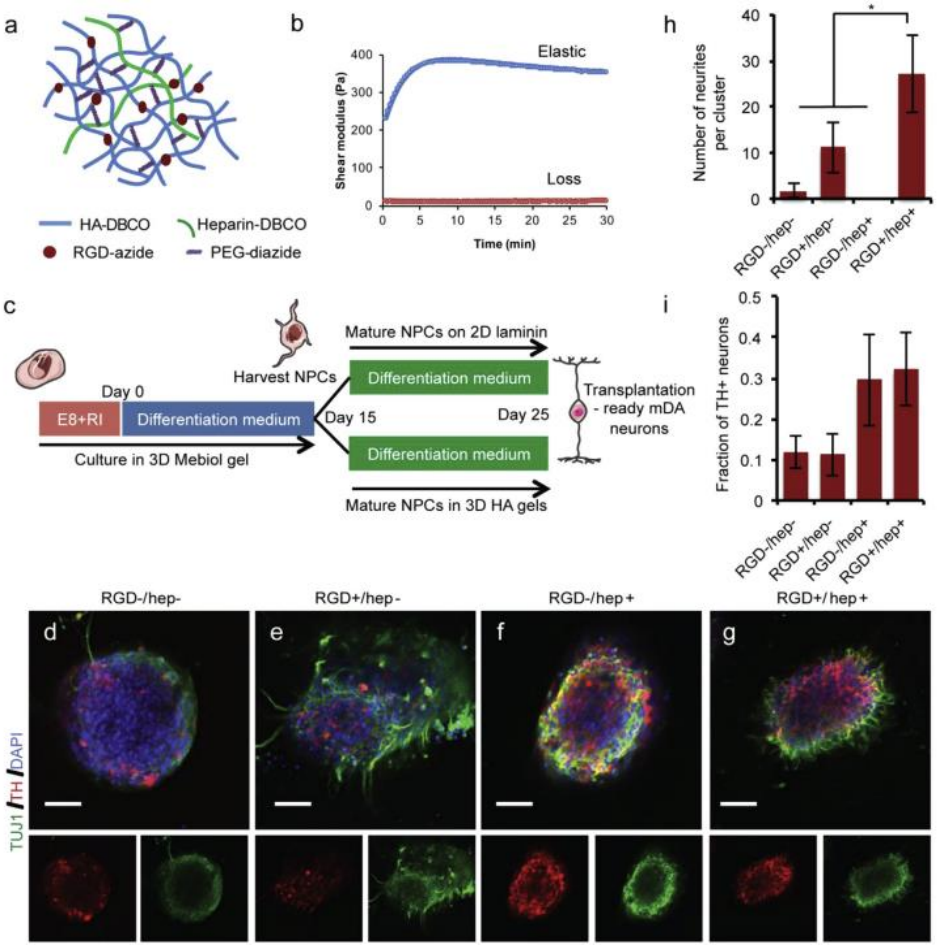


Figure 2.6 Characterization of HA hydrogels and differentiation of mDA neurons. (A) Schematic of the 3D HA-RGD-hep. (B) Gelation kinetics, as determined by time evolution of elastic (blue) and loss (red) moduli of RGD and heparin functionalized HA hydrogels constructed with 3.5% w/v HA. (C) Schematic for generation of mDA neurons from hESCs in 2D vs 3D for implantation on D25; RI - ROCK inhibitor, NPC - neural progenitor cells. d-g) Confocal images showing expression of TH and TUJ1 in mDA neuronal clusters cultured within HA hydrogels (D) without RGD and heparin, (E) functionalized with RGD, (F) functionalized with heparin, and (G) functionalized with RGD and heparin; scale bars are 100 mm. (H) Number of extended neurites per mDA neuronal cluster for mDA neurons cultured within various HA hydrogels. (I) Fraction of cells expressing TH in mDA neurons cultured within various HA hydrogels. Data are presented as mean ± s.e.m for n ¼ 3 independent experiments. *p < 0.05 by Student's unpaired t-test. Taken from M.M. Adil et al., 2017 [233].

2.3.3.3 CELL RESPONSE TO 2D AND 3D SURFACES

Over the last 10 years an increase in the publications transitioning from 2D to 3D surfaces have increased potentially with the technological developments and demand in the medical field and artificial intelligent. Recent publications illustrate the comparison of 2D surfaces to 3D surfaces as a biomimetic surfaces that akin to that of the natural niche of cells in the biological system [234]. Moreover, the physiological events in 2D versus 3D cell cultures has extensively been studied to determine whether a 2D (i.e. sandwich culture, micro-platting, and altering substrate stiffness) or 3D (i.e. spheroid culture, biopolymer scaffolds, prefabricated scaffolds, building block-based scaffold formation, hydrogels, cell sheets, bioreactors with perfusion/dynamic loading/microfluidic actuation, and microfluidics)culture method is the best model and have founded that the answer is not that straight forward [235-245]. Depending on the research question the 2D model microenvironment facilitates feasibility and the results can be meaningful, whilst a 3D model microenvironment could yield more accurate results if successful and done in combination with 2D studies [246, 247].

The high-throughput screening technologies (HTS) investigated in February 2010 the main applications that made use of 3D cell cultures as follows [109];

- Stem cells (64%)
- Primary cells (61%)
- Human cell lines (57%)
- Tissue engineering (38%)
- Transformed or recombinant cell lines (36%),
- Cancer cells (35%)
- Growth factor release (21%)
- Angiogenesis (20%)
- Feeder free embryonic stem cells culture (16%)
- Tumor xenografts and other applications (10%)

The report further highlighted that the trend in the types of primary cells that mostly investigated in 3D cultures are fibroblasts, endothelial cells, mesenchymal stem cells, and hepatocytes respectively. Whilst the most promising 3D scaffolds were respectively the gel/hydrogels, ECM sheet, aggregates/spheroids, and collagen tissue constructs. Furthermore, the 3D cell cultures improved the most the cell (i) viability, (ii) proliferation, (iii) migration, and (iv) signaling in comparison to the 2D cell cultures [109].

Söderstjerna et al., 2013, published their study into the effect that the well-characterized commercially available 20 and 80 nm gold (AuNPs) and silver nanoparticles (AgNPs) have on the growth of the human embryonic neural precursors (HNPCs). They were able to use the HNPCs-based assay to demonstrate that the HNPCs were capable in taking up 20 and 80 nm of AuNPs and AgNPs into the intracellular space. The results further suggested that the AgNPs even at low levels induced a significant stress response in the HNPCs during the growth stage and affected cell proliferation, apoptotic cell death, and in the composition of neural precursors (i.e. increased GFAP levels and reduced DCX expression). In contrast, the AuNPs had only a significant effect on sphere morphology. These results highlight the major implications that certain nanoparticles (NPs) even in low levels can have damaging effect on the developing human neural system [248].

In 2014, Edmondson et al. investigated the cell response to the 2D and 3D model microenvironments and emphasized that the transition from 2D to 3D cell cultures will come with technological development as the industry applications are promising, Table 2.5 [249].

Naghdi et al, published in 2014 their findings of the effect of a combined RGD and tenascin C (i.e. controls neural growth and differentiation) mixture in 3D culture (3D-PEG-RGD-TnC) on the survival, growth and differentiation of bone marrow stem cells (BMSCs) to neural stem cells. The cells were seeded in a three-dimensional (3D) culture scaffold of polyethylene glycol hydrogel (PEG) conjugated with arginyl glycyl aspartic acid (RGD) (PEG-RGD). The survival, proliferation and differentiation of NSCs into the neuronal phenotype in 3D-PEG-RGD-TnC was significantly enhanced than that of the 3D-PEG-RGD, whilst a slight increased difference was observed in the proliferation and migration. Moreover, the results indicated that the 3D-PEG-RGD-TnC induced BMSCs to differentiate

to cell morphology that illustrated neurite outgrowths and increase in the contact between the differentiated cells' extensions [250].

Table 2.5 Key differences in cellular characteristics and processes in two-dimensional and three-dimensional culture systems. Taken and adapted from Rasheena Edmondson et al. 2014 [249].

Cellular Characteristics	Two-dimensional (2D)	Three-dimensional (3D)	Refs.
Morphology	Sheet-like flat and stretched cells in monolayer	Natural shape in spheroid/ aggregate structures	[251-253]
Proliferation	Often proliferate at a faster rate than *in vivo*	May proliferate at a faster/ slower rate compared to 2D-cultured cells depending on cell type and/or type of 3D model system	[254, 255]
Exposure to medium/ drugs	Cells in monolayer are equally exposed to nutrients/ growth factors/ drugs that are distributed in growth medium	Nutrients and growth factors or drugs may not be able to fully penetrate the spheroid, reaching cells near the core	[252, 256]
Stage of cell cycle	More cells are likely to be in the same stage of cell cycle due to being equally exposed to medium	Spheroids contain proliferating, quiescent, hypoxic and necrotic cells	[252, 257, 258]

In 2015, Pickard et al. presented their investigating in magnetic nanoparticles (MNPs) as a non-viral vector alternative in genetically engineering neural stem cells (NSCs). The NSCs were propagated as either neurospheres (i.e. 3D suspension) or as 2D monolayers (i.e. adherent). The results demonstrated that MNPs were able to mediate via 'magnetofection technology' the effective gene transfer to neurospheres, whilst the efficacy for the 2D monolayers was unknown. The transfected NSCs showed high viability, were able to reform as neurospheres, and yielded higher post-transplantation viability versus monolayer cells. The established methodology facilitates the use of MNPs in an oscillating magnetic field in delivering multiple and neurotherapeutic genes, thus, highlighting the future application of

this approach in regenerative neurology (i.e. genetically augmenting the repair capacity of transplant populations) [259].

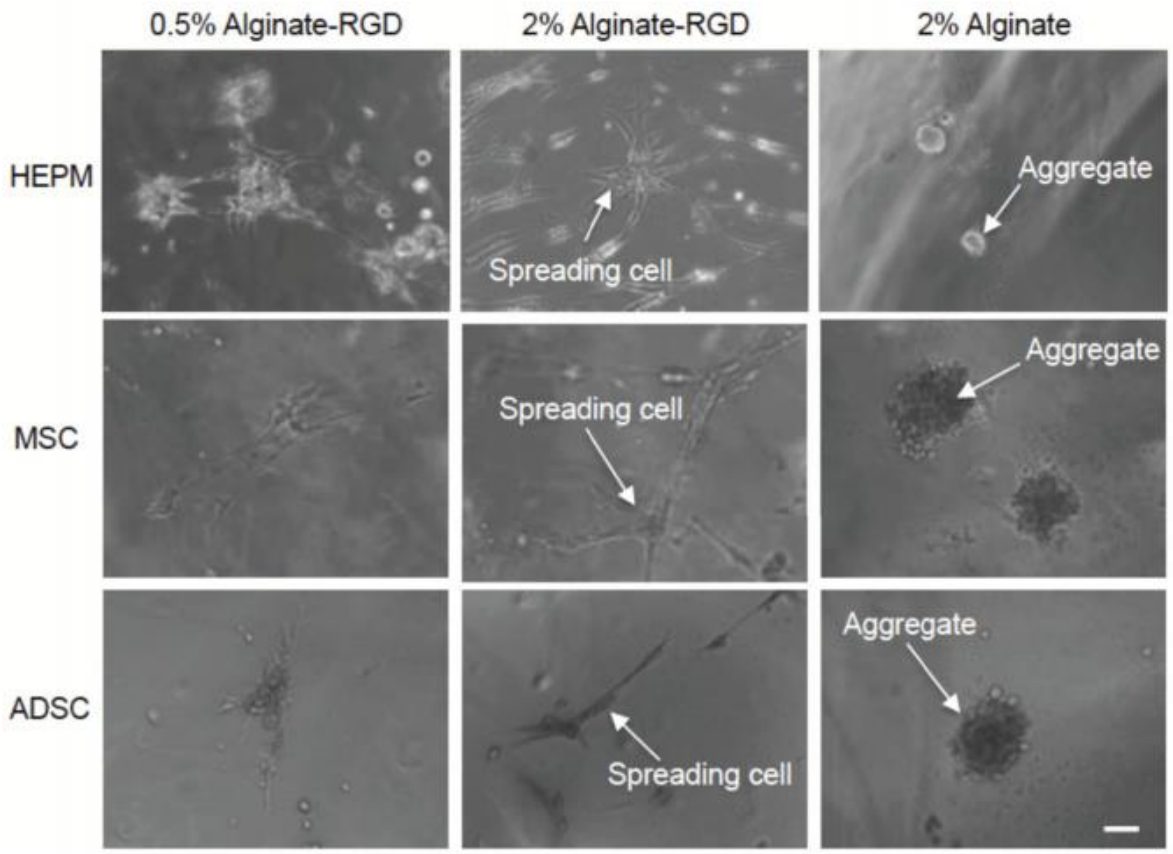


Figure 2.7 Human embryonic palatal mesenchyme (HEPM) cells, mesenchymal stem cells (MSCs), and adipose derived stem cells (ADSCs) cultured on flat hydrogels of 0.5% alginate-RGD, 2% alginate-RGD, and 2% unmodified alginate on day 7. The initial cell density was $5x10^4$ cells per well. Scale bar is 100 μm. Taken from Jenna Dumbleton et al. 2016 [260].

Dumbleton et al., published in 2016 their study if different types of stem cells would demonstrate a difference in the cell response to stiffness effect, or if the RGD effect would take precedence. They cultured human embryonic palatal mesenchyme (HEPM) cells, bone marrow derived mesenchymal stem cells (MSCs), and human adipose derived stem cells (ADSCs) on 2D (i.e. flat hydrogel of different concentrations of alginate-RGD) and miniaturized 3D (i.e. microcapsules with either a 2% alginate or 2% alginate-RGD shell) cultures. The results indicated that on all RGD surfaces (i.e. 2D and 3D) the three stem cell

types attached and spread in all systems in which RGD was present. The three stem cell types preferred a surface that contained a higher concentration of RGD such as indicated in the 2% alginate-RGD shell:0.5% alginate-RGD core versus the 2% alginate shell:0.5% alginate-RGD core, which was further supported by the cell response indicating significant increases in the cell surface area and significant decreases in the circularity ($p < 0.01$). In addition, the presence of RGD outweighed the stiffness effect, Figure 2.7 [260].

In 2016, Zhang et al. performed a neuronal migration study of human-derived neuroprogenitor cells (NPCs) in a soft 3D system (i.e. hydrogel-based assay) that mimics the brain environment and facilitated neural differentiation, maturation and electrophysiologically active neurons by week 3. Furthermore, the assay revealed that a defect in the NPCs due to genotype-specific effect of methyl-CpG-binding protein-2 (MeCP2) dysfunction as the results demonstrated reduced neurite outgrowth and fewer synapses [261].

Fuhrer et al., 2018, presented their studies in using 3D glassy carbon structures with percolated macropores that feature tunable porosity as a scaffold for culturing neural stem cells (NSCs), Figure 2.8 [262]. Magnetic resonance imaging (MRI) was employed to demonstrate the successful 3D location of the NSCs clusters within the glassy carbon surface (i.e. opaque) and enable the visual inspection of the morphological details of individual cell clusters without disturbing them or destroying them. Moreover, preliminary tests were conducted on active cells along with the fixed cells to evaluate the survival of the active cells through the MRI sessions within the carbon scaffold. The results demonstrated that the neurospheres post-MRI could be dissociated, re-cultured and regrown as neurospheres, Figure 2.9 [262].

The MRI-based imaging facilities the possibility to measure NMR spectra of the system to reveal the chemical composition of the sample to monitor major metabolites as a method to assess the health of the culture (i.e. sufficient nutrient supply, excess waste build-up, and stress response). In the long run, this experimental methodology is expected to have a significant impact in how future studies in understanding the mechanism of neurodegenerative disease (ND) development will be conducted [262].

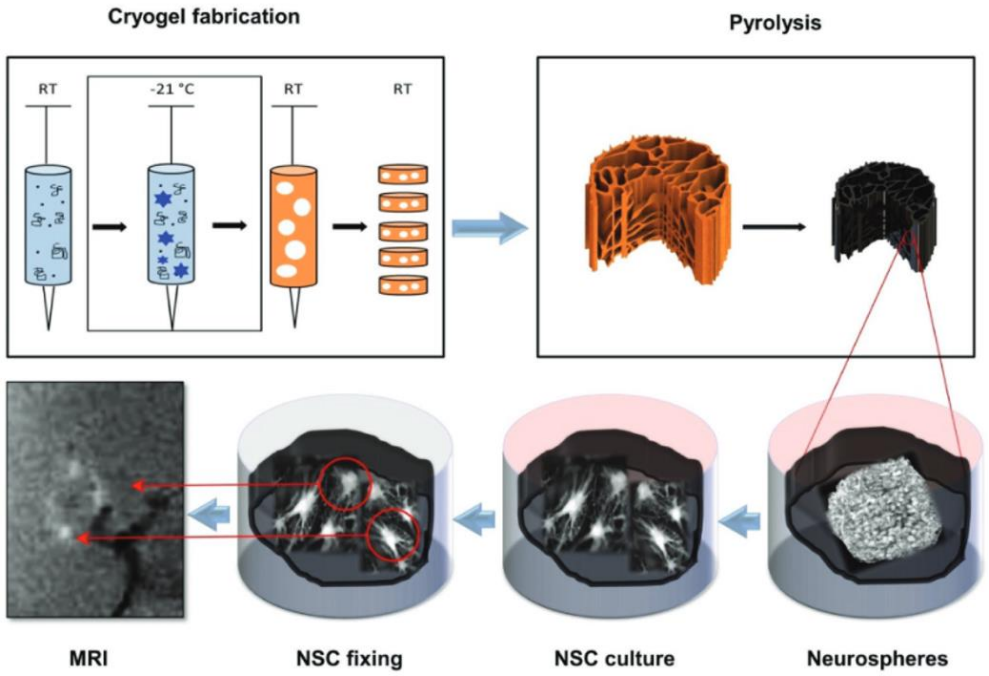


Figure 2.8 Process flow showing cryogel synthesis, pyrolysis, NSCs culture, fixing, and MRI. This protocol could be generalized to any carbonisable precursor polymer and carbon-compatible cell type. Taken from Fuhrer et al., 2018 [262].

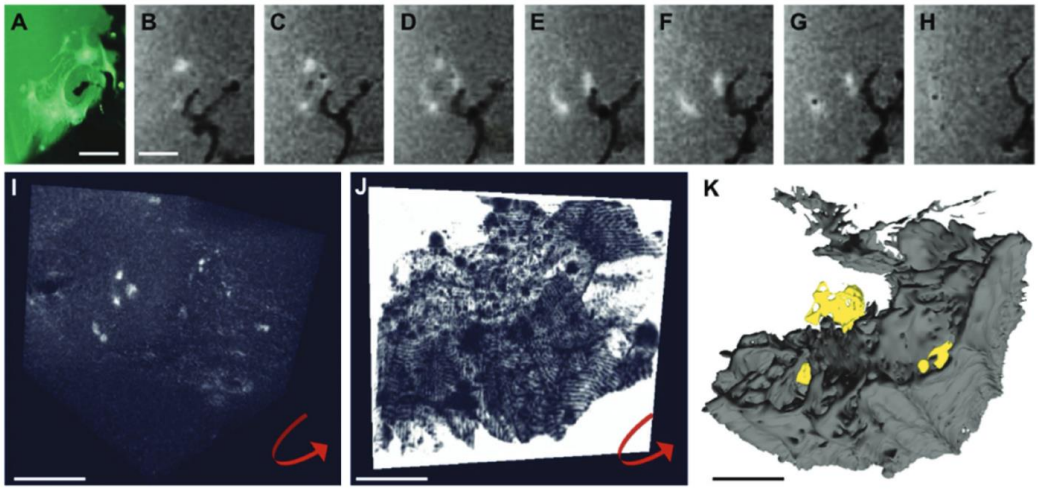


Figure 2.9 MRI of NSCs cultured on a glassy carbon scaffold. (A) An optical image of the NSC cluster; (B-H) corresponding MR images showing NSC clusters in a series of sagittal slices [scale bar: 400 μm, shown in panels (A) and (B)]. 3D extraction of (I) cellular network and (J) carbon scaffold (screenshot; video files in Supporting Information). (K) 3D model of a subsection of scaffold containing NSCs. Yellow regions indicate cell clusters [scale bar: 1 mm in panels (I-K)]. Taken from Fuhrer et al., 2018 [262].

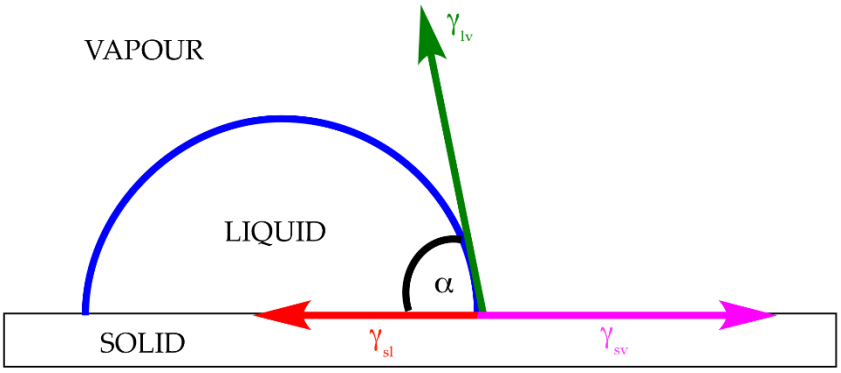
2.4 SURFACE ANALYSIS TECHNIQUES

Engineering the cellular environment with man-made materials has been a long-standing challenge in the biomedical field. The first instance of interface between a medical device and the body is at the surface of the material and the cells. Consequently, prior to *in vivo* trials of the designed medical devices (i.e. implants), the surface properties of the material must be studied to understand the crucial role that surface property of the material plays in achieving the appropriate cellular response. Surface analysis techniques distinguish the surface from the bulk/ interior of a material by characterizing the composition of the surface such as (i) cleanliness (i.e. with respect to contaminant that could cell damage/apoptosis), (ii) elementary and chemical functionality (i.e. with respect to chemical bonding that promote cell adhesion), (iii) roughness (i.e. surface topography) and (iii) quantitative distribution of the elements (i.e. both laterally and with width depth) [263]. Surface analysts utilize several powerful and complementary techniques each with their special advantages. These techniques make use of microscopic chemical and/or physical probes that probe (i) the extreme top layer of atoms, and/or (ii) several microns beneath the sample surface. Listed below are the main surface analytical techniques and cell imaging techniques used to characterize the two-dimensional (2D) and three-dimensional (3D) designed surfaces in this study;

- Sensille Drop Water Contact Angle Measurements (WCA)
- Atomic Force Microscopy (AFM)
- Time of Flight – Secondary Ion Mass Spectroscopy (ToF-SIMS)
- X-ray Photoelectron Spectroscopy (XPS)
- Transmission Electron Microscopy (TEM)
- Optical Microscopy

2.4.1 SENSILLE DROP WATER CONTACT ANGLE (WCA)

Wettability studies determine the solid surface tension as a degree of wetting when a solid and liquid interact. The change in droplet shape is measured as a contact angle and indicates how well the liquid spreads on the surface, thus, contact angles (θ) < 90° spread over a large area of surface; whilst θ > 90° minimize their contact with the surface and form a compact fluid droplet. Whilst the θ = 0 provides a perfect degree of wetting and complete spreading of the liquid on the surface. The interface were solid, liquid, and vapor co-exist is referred to as the 'three-phase contact line', Schematic 2.7.



Schematic 2.7 The water contact angle formed by sessile liquid drops on a smooth homogeneous solid surface.

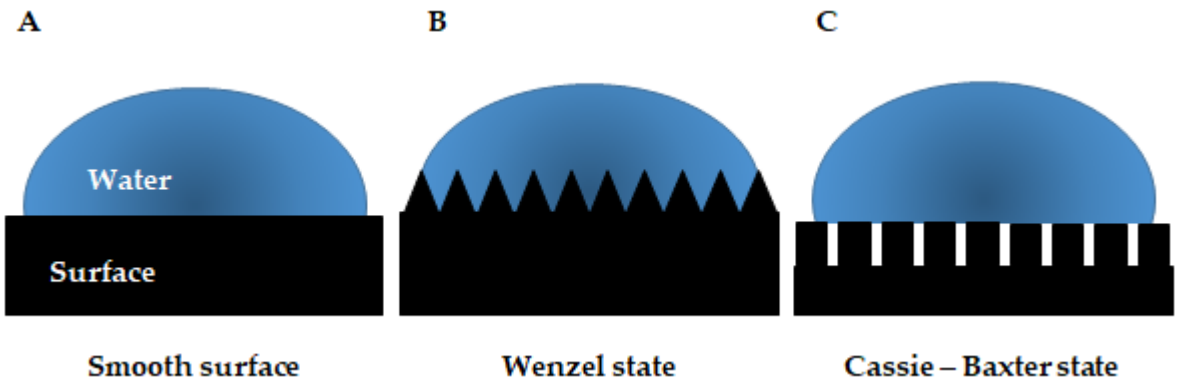
The three interfacial tensions are the intermolecular force responsible for the shape of liquid droplets, as they influence the mechanical equilibrium of the contact angle on an ideal surface; as described in the Young's, Equation 2.1.

$$\gamma_{lv}\cos\theta_y = \gamma_{sv} - \gamma_{sl} \qquad \textbf{Equation 2.1}$$

Where γ_{lv}, γ_{sv} and γ_{sl} represent the liquid-vapor, solid-vapor and solid-liquid interfacial tension, respectively, and θ_y is the Young's contact angle.

Surface roughness influences the contact angle of the droplet on homogenous and heterogeneous surfaces, thus, the Young's model is not applicable to describe the surface

wetting phenomena. Consequently, the thermodynamic equilibrium contact angles on rough and heterogeneous surfaces are called Wenzel and Cassie-Baxter angles, respectively, Schematic 2.8 [264, 265].



Schematic 2.8 The water contact angle of the sensille droplet under (A) Young-Laplace, (B) Wenzel, and (C) Cassie-Baxter conditions [264, 265].

2.4.2 FLUORESCENCE SPECTROSCOPY

Fluorescence spectroscopy is an electromagnetic spectroscopy technique that determines the concentration of a fluorophore or chromophore in solution or on solid surfaces (i.e. non-destructive technique). The sample is exposed to a specific excitation wavelength and the fluorescence emission is detected to determine spectral characteristics in the presence or absence of the fluorophore on the surface (i.e. fluorescence intensity) [266-268].

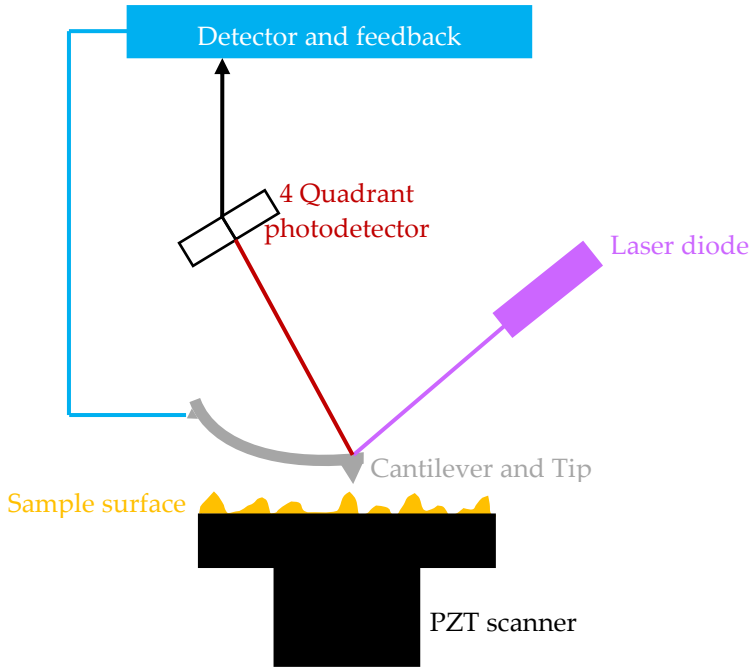
2.4.3 UV/ VISIBLE SPECTROSCOPY

The reflectance spectroscopy in the ultraviolet/visible spectral region is detected as a beam of light is reflected of the sample surface. The radiation region of UV is 10-400 nm and for visible it is 400-800 nm. Metal nanoparticles (i.e. gold) are dielectric and can be validated by detecting the surface plasmon resonance (SPR) phenomena due to their optical properties when they interact with the electromagnetic field. The conducting electrons oscillate collectively and induce a plasmon resonance effect, which couples to the incident

electromagnetic field to propagate across the surface of the particles [269]. The Mie theory provides the theory for the cross-section scattering and absorption for a sphere particle, thus, by applying this theory the metal dielectric constant for the nanoparticle size (i.e. size of particle ≈ wavelength of illuminating light) and the physiochemical environment of the sample as a single nanoparticle or as aggregates can be quantified. Thus, a red shift in the peak is observed on the spectrum due to the dipole resonance with increasing particle size (i.e. weakening of interaction forces) and calculated with the Mie theory equations [270]. Further factors that could cause a shift in the SPR maximum of the sample are physical or chemical interactions on the particle surface, surface charge, and the distance between the particles [271, 272].

2.4.4 ATOMIC FORCE MICROSCOPY (AFM)

AFM uses special probes made of an elastic cantilever with a sharp tip on the end to, (i) image (i.e. 2D), (ii) profile (i.e. 3D), (iii) measure nanoscale surface species, and (iv) measure the interactive force between the tip of the probe and the surface. The AFM display scan of 2D and 3D images both represent height information with the 2D image uses a color scale, whilst the height information is rendered as a pseudo-three-dimensional image in the profile image (i.e. actually see the shape). Surface roughness influences the type of interactive forces present between the surface and the probe contact such as, mechanical contact forces, van der Waals forces, and chemical bonding forces. Schematic 2.9 illustrates the surface sample on the piezoelectronic transduces (PZT) scanner and the motion of the probe across the surface. The contact (i.e. deflection) between the probe and surface is measured by a semiconductor diode laser that is reflected on the cantilever, which is connected to position sensitive 4 quadrant photodiode detector. The measured deflections of the cantilever are processed as a difference in light intensities and converted to a voltage signal. To generate an image in contact mode and tapping mode, the X, Y and Z positions of the piezo scanner are recorded.



Schematic 2.9 The schematic components of the AFM.

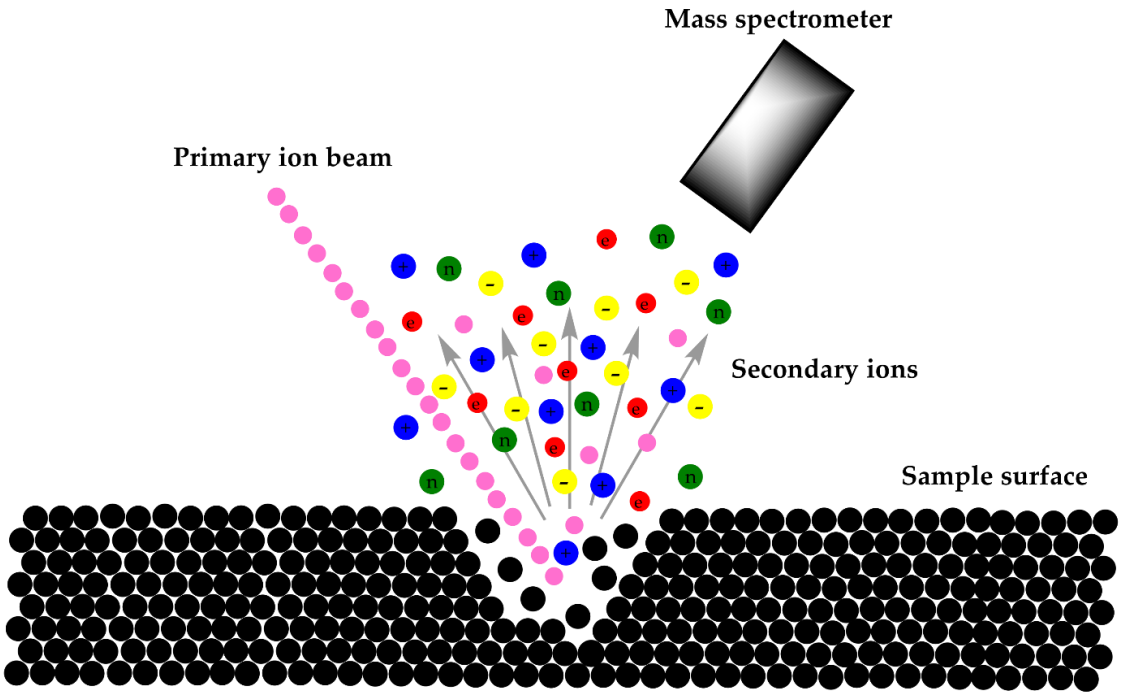
2.4.5 TIME OF FLIGHT – SECONDARY ION MASS SPECTROSCOPY (ToF-SIMS)

ToF-SIMS is a technique that detects the surface chemistry of the surface as a measure of mass resolution in atomic mass units, Schematic 2.10. The ToF-SIMS uses a pulsed ion beam to displace molecules from the outmost atomic mono-layers on the substrate surface, known as secondary ions. These molecules are then transported into a 'flight tube' and their mass is measured by calibrating the time at which they react with the detector. This represents their time of flight and a mass spectrum is produced. There are three modes of operation, (i) surface spectroscopy, (ii) surface imaging, and (iii) depth profiling. The ToF-SIMS measures atomic mass in a range between (i) 0 and 10,000 atomic mass, (ii) positive and negative ions, (iii) molecular compounds and (iv) isotopes. Furthermore, elements in the parts-per-million range can be detected and submicron images can be mapped through rastering the primary beam across the surface. The secondary ions that the ToF-SIMS yields depends directly on the elements ionization probability, which varies from (i) one element or compound to another, (ii) the chemical environment, and (iii) the instrumental setup and parameters. Hence, making it impossible to directly quantify the secondary ion yields in terms of

concentration, so one would need to use a well-known reference to be able to profile under exactly the same experimental conditions (i.e. in shortest time delay possible) to obtain the Relative Sensitivity Factors (RSFs), which the normalized signal of interest. The profile is quantified at each point by selecting a representative signal (i.e. Si^+ in silicon, or Au^- in gold) and normalizing this matrix, which is then computed as an elemental concentration through a linear relationship, Equation 2.2.

$$Concentration_{(element\ of\ interest)} = RSF \cdot \frac{I_{(element\ of\ interest)}}{I_{(matrix\ of\ element)}} \quad \textbf{Equation 2.2}$$

Thus, making the ToF-SIMS a semi-quantitative technique, as it yields quantitative analysis but requires an external calibration method (i.e. reference materials) to yield whole quantification via RSF [273, 274]. A quantitative technique that is used alongside ToF-SIMS is the X-ray photoelectron spectroscopy.



Schematic 2.10 The schematic illustration of generating secondary ions with a primary ion beam.

2.4.6 X-RAY PHOTOELECTRON SPECTROSCOPY

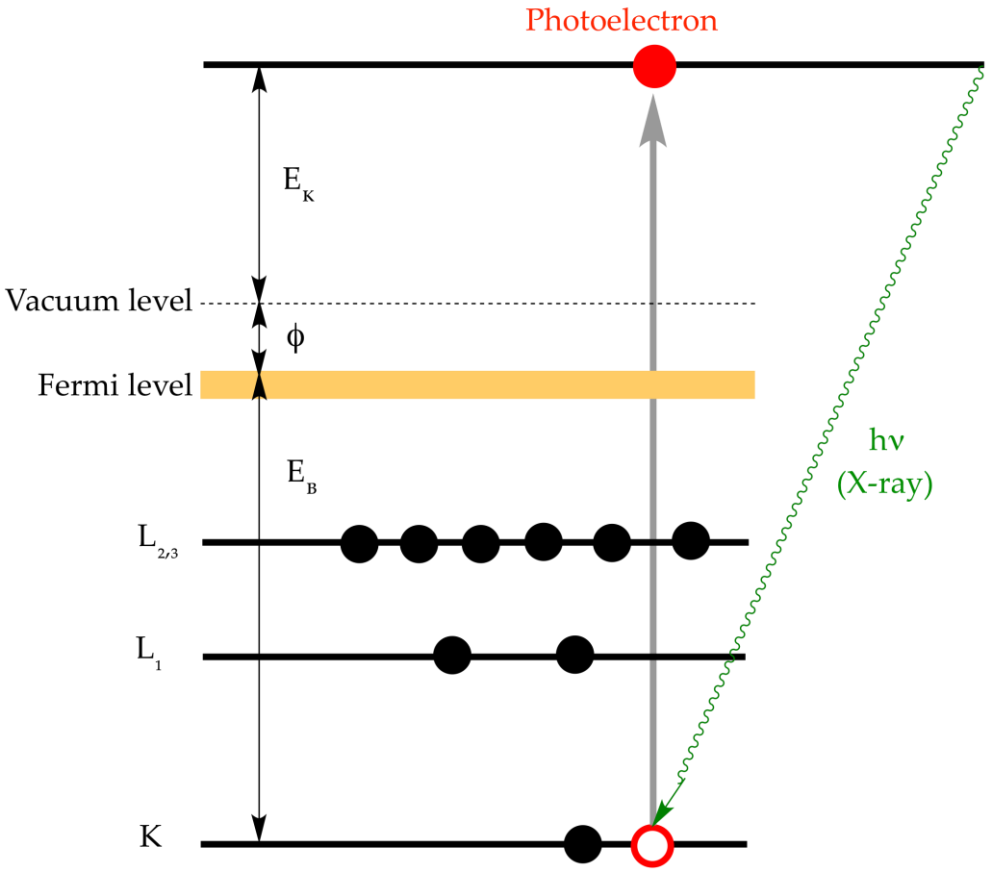
The XPS is a quantitative technique that determines the distribution of chemical species across a substrates surface by relying on the photoelectric effect.

X-rays are used to excite an electron in the core level of the atom and creates a photoelectron (i.e. photoemission) which is transported to the surface of the sample and then escapes (i.e. the extrinsic loss). The parameters required for photoemission to occur are given in Equation 2.3.

$$E_K = h\nu - E_B - W \qquad \textbf{Equation 2.3}$$

The kinetic energy of the emitted photoelectrons is quantified as a measure of the binding energy (EB), which identifies the electron specifically both in terms of parent element and atomic energy level. The instrumental calibration is determined by the work function (W) and the photon energy, hν (h is the Planck's constant, ν is the frequency), of the X-rays. The work function of the spectrometer (i.e. the analyzer) is effectively a chemical binding energy of the photoelectron (i.e. the measured kinetic energy is of the collected electrons that were scattered elastically from the surface), which is calibrated with metallic samples where the binding energies are known (i.e. Cu, Ag, Au) [275, 276]. The photoelectron spectrum records a characteristic XPS fingerprint of the electronic structure of chemical composition and state of the elements on the surface. Moreover, a chemical shift can be observed in the chemical state of the components in the core level positions of the element, due to a change in the oxidative state, chemical and physical environment of the surface. The ionized atom relaxes by emitting an X-ray photon, known as X-ray fluorescence, after the photoelectron has escaped the Fermi level into the vacuum, Schematic 2.11.

XPS spectra contain a substantial background signal due to noise, which at times makes it difficult to distinguish the peak from the background. The Poisson statistics is implemented to estimate the signal to noise ratio for each region on the spectra, which can be computed as the noise is proportional to the square root of the counts per bin for each bin. Thus, normalizing the residual distribution to give a similar count per second (CPS) intensity value irrespective of the background for similarly intense peaks to validate that the observed peak is not due to noise.



Schematic 2.11 X-ray adsorption by an atom in a core level leads to the emission of a photoelectron.

2.4.7 DYNAMIC LIGHT SCATTERING (DLS) AND ζ-POTENTIAL

DLS is a technique that measures particle size distribution down to 1 nm diameter. In practice the DLS measurements range between 1 nm and 1 μm with a lower size limit that depends on certain factors such as (i) optical configuration of the instrument, (ii) laser wavelength/ power, (iii) detector sensitivity, (iv) sample concentration, and (v) excess level of scattering (i.e. the difference between the dispersant used and the particles in the dispersant). The sample is exposed to a laser beam and the random movement (i.e. speed) at which the particles are diffusing due to Brownian motion is measured. Hence, the intensity fluctuations (i.e. scattered light) of the particles are detected at a known scattering angle θ by a fast photon detector [277, 278]. The Brownian motion of large (i.e. slow) and small (i.e. fast)

particles are influenced by the stable temperature (i.e. affects viscosity) of the sample and calculated from the translational diffusion coefficient.

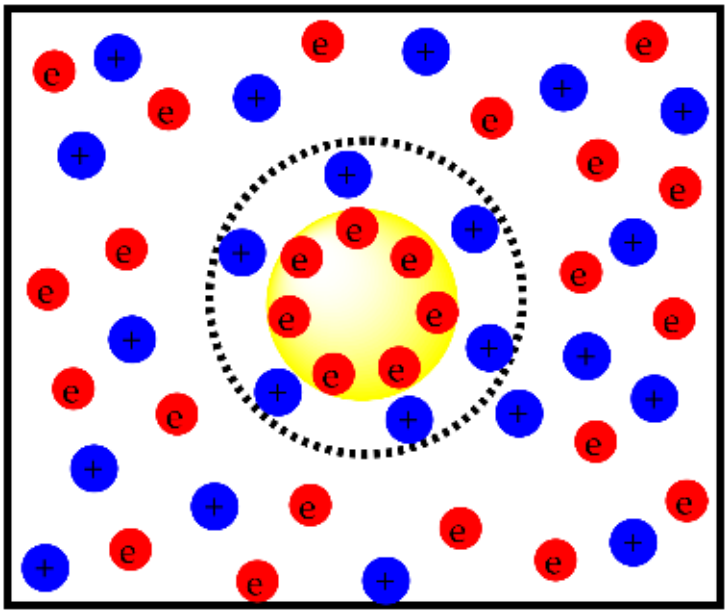
$$d(\mathrm{H}) = \frac{kT}{3\pi\eta D} \qquad \textbf{Equation 2.4}$$

Equation 2.4 is the Stokes-Einstein equation which is used to calculate the hydrodynamic diameter of the particles. Where; $d(\mathrm{H})$ = hydrodynamic diameter, D = translational diffusion coefficient, $k = Boltzmann's\ constant$, T = absolute temperature, η = viscosity. Further factors that can affect the translational diffusion coefficient including particle size are (i) shape, (ii) surface structure (i.e. chemical and physical), and (iii) ionic strength of the medium (i.e. conductivity). Moreover, the later of those factors is measured as the particles are electrically charged and are counterbalanced by the oppositely charged ions in the surrounding solution (i.e. the medium) [279].

ζ-potential is a measure of the velocity (i.e. electrophoretic mobility, μ_{E}) of the particles and determines the electrostatic potential on the surface of the charged particles, Schematic 2.12. Factors that affect the ζ-potential are (i) the pH of the medium, (ii) ionic strength of the medium, (iii) the concentration of any additives, and (v) temperature [280]. The measured values of the ζ-potential indicate the short- and long-term stability of the emulsion, so ζ-potential values that are above ± 25 mV (i.e. electrically stabilized) indicate a stable system due to the electric charge which keeps the system in a disperse state. Whilst aggregates of the particles are observed when the ζ-potential value is between ± 24 mV, which can possibly be related to poor physical stability [281-283]. Consequently, emulsions that have a high negative and positive ζ-potential demonstrate that the repulsive forces exceed the attractive forces, resulting in a relatively stable system [280]. The literature has demonstrated that in *in vitro* experiments (i.e. cell culture medium) have a ζ-potential value of -15 mV to -20 mV is observed regardless of the dispersed particles [284].

In addition, to charge and the size of the particles another measurement that can be made is the polydispersity index of the particle size (PDI), which is a measure of the broadness of the

size distribution in the colloid (i.e. water, PBS, neural basal media). This quantification can be derived from the cumulants analysis of the DLS as a measure of a single Gaussian population with standard deviation σ, and mean size x_{PCS}, $PDI = \frac{\sigma^2}{x_{PCS}}$ is the relative variance of the distribution and measures the quality of the dispersion. Accordingly, PDI values of lower than 0.2 correspond to good quality colloidal suspensions, whereas those closer to a value of 1 are of poor quality samples (i.e. high polydispersity) [285].



Schematic 2.12 Illustration of the distribution of charge around a negatively charged particle, which is counterbalanced by the positively charged ions from the surrounding solution and forms a diffuse layer.

2.4.8 TRANSMISSION ELECTRON MICROSCOPY (TEM)

To overcome the resolution limitations in optical microscopy the TEM was developed in the early 20th century. The TEM instrument is a technique that transmits electrons instead of light through the sample, thus, achieving spatial resolutions down to the scale of several Angstroms (~ 0.19 nm) and allowing for the visualization of even a single column of atoms.

$$d = \frac{\lambda}{2n \sin \alpha} \approx \frac{\lambda}{2\ NA} \qquad \textbf{Equation 2.5}$$

Equation 2.5 is the Rayleigh formula which demonstrates that the main limitation in light microscopy is the resolution due to the inability to reduce the wavelength of the photons of the light source. Where; d = maximum resolution, λ = wavelength of photons, n = index refraction of the medium, α = maximum half-angle of the cone of light, and NA = numerical aperture of the system.

Louis-Victor de Broglie theorized that electrons have the wave and particle properties, thus, relating the kinetic energy of the electrons to the wavelength of the photons in the de Broglie equation and accounting for the electron's velocity approaching the speed of light ($c = 3 \times 10^8$ ms^{-1}) in the TEM.

$$\lambda_e \approx \frac{h}{\sqrt{2m_0E\left(1 + \frac{E}{2m_0c^2}\right)}} \qquad \textbf{Equation 2.6}$$

Equation 2.6 demonstrates the Rayleigh formula corrected for this limitation by using electrons in a de Broglie relationship. Where; λ_e = wavelength of electrons, h = Planck's constant, m_0 = rest mass of an electron, E = energy of the accelerated electron, and c = velocity of the electrons.

Consequently, the more appropriate wave equation for relativistic electrons would be the Dirac equation, Equation 2.7.

$$\left(i\hbar c\gamma^{\mu}\partial_{\mu} - mc^2\right)\Psi = 0 \qquad \textbf{Equation 2.7}$$

Where; $\hbar = Planck's\ constant\ divided\ by\ 2\pi\ (i.e. 1.051\ x\ 10^{-34} m^2 kgs^{-1})$, $i = imaginery\ unit\ \left(i = \sqrt{-1}\right)$, c = speed of light (3 x 10^8 ms^{-1}), $\gamma^{\mu} = Dirac\ matrix$, $\partial_{\mu} = four-gradient\ \left(\frac{1}{c}\frac{\partial}{\partial t}, \nabla\right)$, m = rest mass of the electron (i.e. 0.511 $MeVc^{-2}$), and Ψ = wave function of the system (i.e. quantum state).

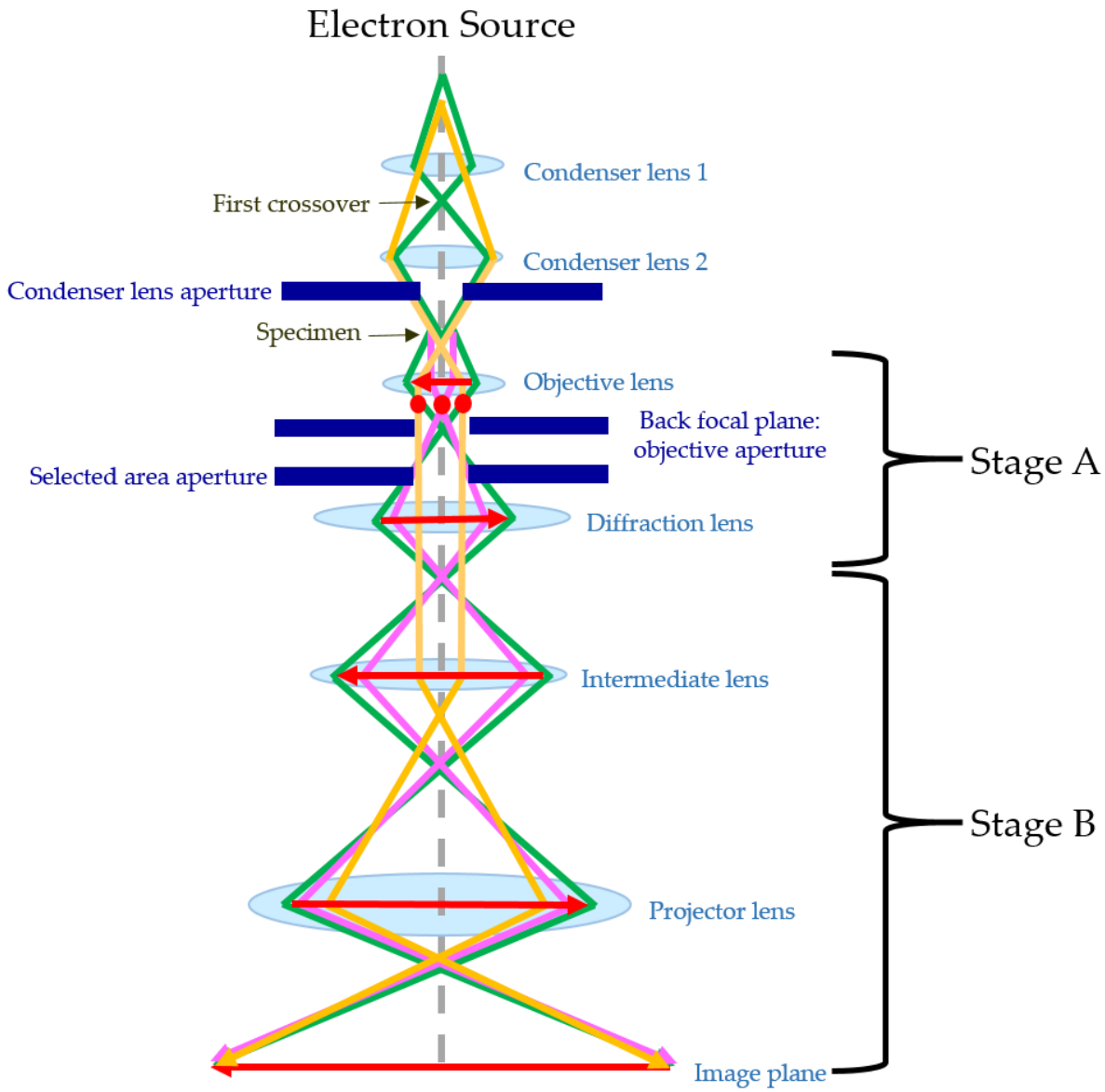
The TEM is capable of providing atomic scale imaging, elemental, chemical and physical characterization of the sample in question by monitoring what has happened to the beam of electrons (i.e. de Broglie wavelength) in transit. Furthermore, the thickness of the samples is important as electrons have the ability to penetrate samples that have a thickness below the value of 500 nm (i.e. able to attain detecting values below 0.1 nm) and this is significant as many of the electrons undergo inelastic scattering processes when they pass through the sample, which result in an energy loss. Ultrathin samples produce elastic forward scattering at angles < 10^o as inelastic scattering is very sensitive to atomic weight at high angles, whereas in thin samples backscattering is observed. Consequently, the inelastic process enables the chemical analysis of materials in the TEM due the emission of the characteristic X-ray quanta (i.e. Augur electrons, light) during the relaxation processes. Hence, characterizing the local chemistry of the sample by detecting (i) emitted X-rays (i.e. Energy Dispersive Spectroscopy, EDS/ EDX) and (ii) energy lost by incident electron (i.e. Electron Energy Loss Spectroscopy, EELS). The TEM images are formed by the electron waves exiting from the sample, which contain the prerequisite information such as electron density and phase. The TEM images are formed in two stages as illustrated in Schematic 2.13;

- Stage 1 – The incident electron beam is scattered by the sample. The objective lens focusses the scattered radiation to form either an image or diffraction pattern of the sample (i.e. according to Bragg's Law or Laue Conditions).
- Stage 2 – The primary image is magnified using the additional lenses to form a highly magnified final image.

The scattered electron wave produces a diffraction pattern (i.e. Fourier transform) at the back focal plane of the object lens and this is the basis in forming high-resolution

transmission electron microscopy (HRTEM). The increased resolution in TEM enables it to be a desired instrument for studying, (i) ultrastructures in organelles in the medical field, and (ii) crystallographic information of particles in the field of material sciences and nanotechnology.

The few difficulties that come with the use of the TEM are (i) laborious sample preparation and the images are black and white, (ii) potential artefacts from sample preparation, (iii) samples must be electron transparent, fit in the vacuum chamber and able to tolerate it. For instance, biological samples must be (i) fixed (i.e. stabilized and not destroyed) as living things cannot survive an electron microscope, (ii) completely dried (i.e. dehydration) thoroughly so that the vacuum does not affect them, (iii) embedded into a resin to support the sample and allow for thin cross-sectional sectioning, stained to increase contrast between different structures (i.e. nucleus, vesicles, mitochondria in the cell), and (iv) and then the sample is mounted on a slide to protect the sample to allow for long term viewing and analysis. Whilst for surface materials the thickness of the sample is crucial (i.e. electrons must be able to pass through the sample) and the contrast of the sample relative to the background (i.e. the sample mount which is a copper grid coated with a thin layer of carbon). Materials that are suitable for TEM surface material characterization are (i) most metals (i.e. gold, silver, copper, aluminum), (ii) most oxides (i.e. silica, aluminum oxide, titanium oxide), and (iii) a selective group of other particles (i.e. polymer nanoparticles, carbon nanotubes, quantum dots, magnetic nanoparticles) [286].



Schematic 2.13 Illustrates the concept of forming TEM images in two stages.

2.4.9 OPTICAL MICROSCOPY

Optical microscopes use visible light (i.e. light microscope) to magnify the image of small samples (i.e. specimen) using one or a series of lenses. The purpose of a microscope is to (1) produce a magnification image of the sample, (2) separate the details of the image, and (3) render the details visible to the human eye or camera. The microscope presents the image in the colors of the visible spectrum with varying degrees of light intensity. Modern optical microscope can be adapted with additional equipment to specialize them for a specific technique for study purposes such as (i) bright field illumination, (ii) phase contrast illumination, (iii) dark field illumination, (iv) differential interference contrast illumination (DIC), and (v) fluorescence illumination.

2.4.9.1 FLUORESCENCE MICROSCOPY

Epifluorescence microscopes can be incorporated with a phase ring to produce high-quality phase contrast images as well as bright fluorescence images. Phase contrast images can be taken of living cells when observing the dynamics in cell adhesion, proliferation and survival days *in vitro*, whilst providing a contrast enhancing effect of the bright field images. In order to observe cell differentiation the sample must be fluorescent, so the sample is fixed and stained with an immunofluorescent (i.e. antibodies). The primary antibody binds to the antigen in the cell and the secondary antibody contains the fluorophore and forms an antibody-antigen complex. Molecules absorb the high energy light from the light source (i.e. mercury or xenon lamp) and jump to a higher energy level and emit radiation once the excited molecules return to ground state. The fluorophore emits light at a characteristic wavelength (i.e. fluorescence) and the antibody-antigen complex is detected, thus, locating and identifying specific protein expression in cells, Table 2.6. The fluorescence microscope is checked for the number of lasers, filters and detectors before selecting the fluorophore as spectral overlap can cause severe compensation. Therefore, determining the correct combination of fluorophores is crucial immunocytochemistry experiments, Figure 2.10.

Table 2.6 Secondary antibody labelling with a fluorophore.

Fluorophore	Absorption (nm)	Emission (nm)
HOECHST ® 3342	343	483
Alexa Fluor 488	494	517
Alexa Fluor 647	649	666

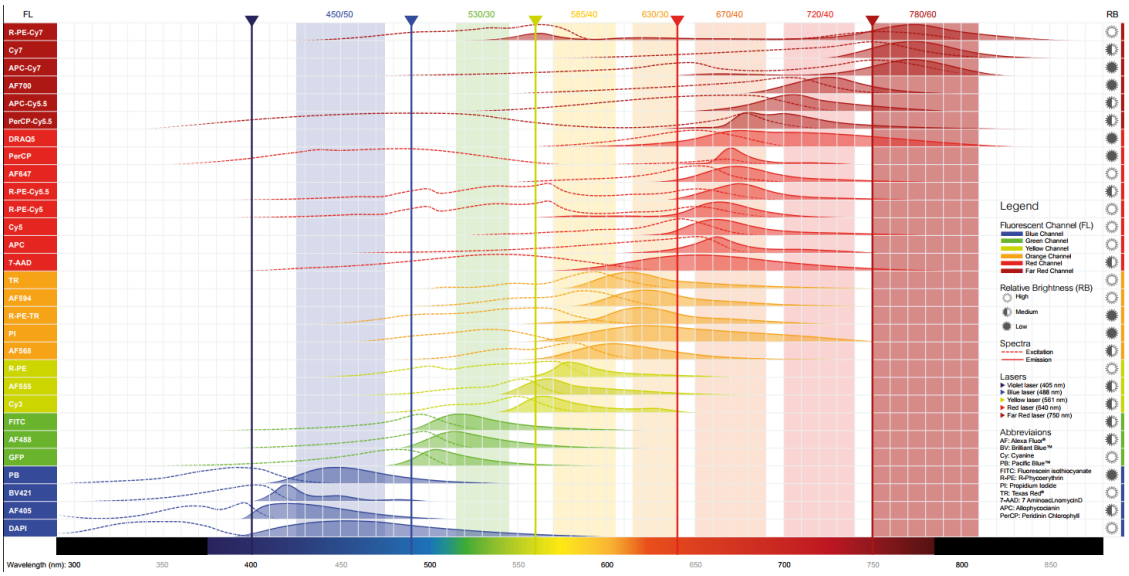
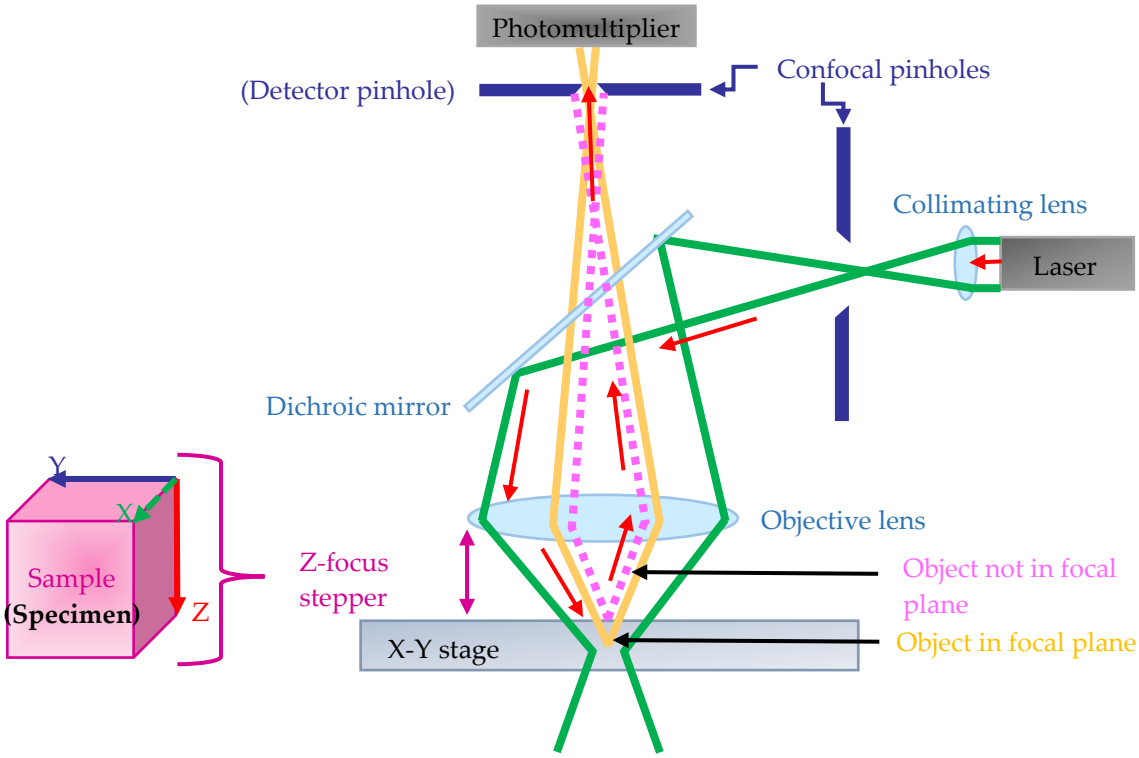


Figure 2.10 Fluorophore chart aligning emission and excitation fluorescence spectra to guide the correct selection of fluorophore.
Retrieved September 9th, 2017, from https://www.abcam.com/secondary-antibodies/fluorochrome-chart-a-complete-guide.

2.4.9.2 CONFOCAL LASER SCANNING MICROSCOPY (CLSM)

The CLSM is a more complicated and powerful design of the epifluorescence microscope that uses optical sectioning of the sample to generate 3D reconstruction and high-resolution images. The laser beam is the light source in the CLSM, which is focused to a point and scanned over the sample (i.e. point by point, line by line) to excite the stained fluorophore, Schematic 2.14. The CLSM has a narrow depth of field (i.e. 0.4 mm) and enables optical sections (i.e. no physical contact) of the sample at different focus levels. CLSM images demonstrate reduced out-of-focus-blur, higher z-resolution (i.e. 0.5 μm, accurate signal discrimination) and the collection of the images is rapid. A maximum intensity projection

image can be constructed on one plane of all the optical sections of the sample to produce a high-resolution image. Furthermore, these optical sections can also be sampled to generate a z-stacking image by defining volume and resolution. Samples can be immersed in glycerol to allow deeper penetration into the sample without severe light loss or distortion.



Schematic 2.14 Illustration of the simplified optical principle in the CLSM. An image is generated when the single point is scanned in an X-Y manner as the laser focus is moved over the sample. The optical sectioning is performed via the Z-focus stepper to view the sample as a 3D image.

2.4.10 OTHER TECHNIQUES

Other surface analysis techniques were considered to characterize the properties of the functionalized surfaces, such as surface plasmon resonance (SPR) and quartz crystal microbalance (QCM) as both techniques provide a quantitative characterization of peptide-surface interactions [287]. However, both techniques have the limitations that they require the functionalization of the peptides on nanoscale thick surfaces on a gold sensor chip (i.e. SPR) or a quartz sensor chip (i.e. QCM). This meant that SPR could be used to analyze the peptide interaction with the gold coated glass coverslip surfaces (i.e. Chapter 6) and not the non-gold coated glass coverslip surfaces (i.e. Chapter 4 and Chapter 5), so we would not be able to collect a complete set of data points for all the functionalized surfaces. Another option was the use of thermogravimetric analysis (TGA), which is a method that measures the physical and chemical properties of materials as a function of (i) increasing temperature and (ii) time. The thermal events of interested in the change observed in the material are (i) deposition, absorption, sublimation, vaporization, oxidation, reduction and decomposition. The thickness and density of the functionalized material can be obtained as a result. However, our experimental setup on the 19 mm glass coverslips would have given us negligible results with the TGA technique [288].

After taking all of this information into consideration we made the final decision to focus on the results collected from the ToF-SIMS and AFM data to provide us an overview of the peptide-surface interactions for all the surface functionalization characterization in this thesis.

3 METHODOLOGY

3.1 SURFACE PREPARATION AND CHARACTERIZATION

3.1.1 CLEANING OF GLASS SURFACES

Round glass coverslips (d = 19 mm and h = 0.2 mm) were racked onto a 12 glass coverslips holder then placed in a beaker and organic solvent cleaned inside an ultrasonic bath. The glass coverslips were cleaned inside an ultrasonic bath for 5 minutes respectively in acetone, methanol, isopropanol and MiliQ-grade water (18.2 MΩ-cm). The glass coverslips were dried under nitrogen stream before immersion in a piranha solution 3:1 (v/v) sulphuric acid/hydrogen peroxide (30%) for 40 minutes at room temperature. The glass coverslips were then rinsed extensively with MilliQ-grade water and dried under nitrogen stream. There are other cleaning methods of glass coverslips (i.e. acid bath, 'decon 90', plasma cleaning), however, the piranha cleaning procedure provided the best results even though it being a more dangerous reaction.

3.1.2 SILANISATION OF GLASS SURFACES

The piranha treated glass coverslips were immersed in (3-glycidyloxypropyl)trimethoxysilane (GOPTS, ≥ 98%) at 37 ^{o}C for 1 hour. The silane glass coverslips were rinsed extensively in acetone and dried under nitrogen stream.

3.1.3 PEG_{18}-DIAMINE COUPLING TO SILANISED GLASS SURFACES

The silanized glass coverslips were functionalized with PEG_{18}-diamine powder by placing it into a vacuum oven at 75 ^{o}C. At 20 minutes a small metal spatula was used to evenly cover the samples with the melted PEG_{18}-diamine and left overnight. The unreacted PEG_{18}-diamine was washed off extensively with MilliQ-grade water and dried under nitrogen stream.

3.1.4 PEPTIDE COUPLING TO PEG_{18}-DIAMINE

3.1.4.1 SURFACES WITH SINGLE PEPTIDE COMPOSITION

Amino acids were covalently coupled to the PEG_{18}-diamine surfaces through their amine terminated functional groups using the standard solid phase peptide synthesis (SPPS) procedures according to the modified literature procedures [289]. Fluorenylmethoxycarbonyl (Fmoc) protected amino acids were dissolved in dry *N'*,*N'*-Dimethylformamide (DMF, 20 mM) together with Ethyl(hydroimino)cyanoacetate (EHICA, > 97% [T]) (40 mM). Typically, 20 mL of this solution was added to a glass petri-dish containing 72 glass cover slips. To this, two equivalents of *N'*,*N'*-Diispropylcarbodiimide (DIC, purum > 98% [GC]) were added and the reaction was allowed to proceed for 2 hrs at room temperature on an orbital shaker. The samples were subsequently washed with DMF, isopropanol, methanol and DMF for 15 minutes on the orbital shaker, and then to be exposed to the same amino acid reaction mixture overnight to ensure high conversion of the amine groups on the surface. The samples were then washed in the previous mentioned solvent sequence. The Fmoc group was removed by immersion of the samples in a solution of 20% piperidine in DMF for 2 hrs, and then washed as mentioned previously ready for the following amino acid to be coupled to the surface. The sequences were build-up from the C to the N terminus using the following protected amino acids: for the RGD peptide surfaces Fmoc-Arg(Pbf)-OH (arginine, R), Fmoc-Gly-OH (glycine, G), Fmoc-Asp(OtBu)-OH (aspartic acid, D) and for the IKVAV peptides surfaces Fmoc-Ile-OH (isoleucine, I), Fmoc-Lys(Z)-OH (lysine, K), Fmoc-Val-OH (valine, V) Fmoc-Ala-OH.H_2O (alanine, A). After completion of the sequence and removal of the Fmoc group the remaining protection groups were removed by immersion in 95% Trifluoacetic acid (TFA) containing 5% MilliQ-grade water for 4 hrs. The samples were washed in MilliQ-grade water, DMF, isopropanol, methanol, rinsed extensively in MilliQ-grade water and dried under nitrogen stream. Illustrated in Schematic 1.2(A) and Schematic 4.4.

3.1.4.2 OPTIMISATION OF SURFACES WITH MIXED PEPTIDE COMPOSITION

3.1.4.2.1 BIOFUNCTIONALITY OF -NH_2 and -OH SURFACES

Surfaces were silanized with GOPTS or APTMS at 37 ^{o}C for 1 hr, washed respectively with acetone, MilliQ-water and dried under nitrogen stream. The APTMS surfaces exhibit the desired terminal amine end, whereas the GOPTS epoxy ring was hydrolyzed with sulphuric acid to give hydroxyl functional groups. The surfaces were then exposed to Fmoc-R + EHICA + DIC or Fmoc-R + DCC + DMAP to facilitate the selective attachment of the amino acid to the NH_2 group followed by the attachment to the -OH group. Therefore, each condition would produce four surfaces respectively, (i) -OH/-NH_2 + EHICA + DIC (control), (ii) -OH/ -NH_2 + DCC + DMAP (control), (iii) -OH -NH_2 + Fmoc-R + EHICA + DIC, and -OH/-NH_2 + Fmoc-R + DCC + DMAP. Illustrated in Schematic 1.2(B) and Schematic 5.4(A).

3.1.4.2.2 BIOFUNCTIONALITY OF -NH_2 and -Cl SURFACES

Surfaces were functionalization with 10% 2-chloroethylamine hydrochloride (CEA.HCl) in MilliQ-water, at 40 ^{o}C for 3 hrs on orbital shaker, washed with MilliQ-water, and dried under nitrogen stream to provide chlorine terminated surfaces, whilst the APTMS surface would provide the different functional group. The surfaces were then exposed to Fmoc-V with the same coupling agents' conditions as above. Furthermore, some of the -Cl terminated surfaces were then immersed in a solution of molar ratio 1:5 cysteine (20 mM), tris(2carboxyethyl)phosphine hydrochloride (TCEP), MES buffer (0.1 M) and left overnight (> 24 hrs) on the orbital shaker at room temperature. The cysteine was immobilized on the chlorine terminated surfaces to compare the WCA measurement of these surfaces with that of the surfaces that were functionalized with Fmoc-V and coupling agents'. Illustrated in Schematic 1.2(B) and Schematic 5.4(B).

3.1.4.2.3 BIOFUNCTIONALITY OF -Fmoc and -OCH_3 SURFACES

Two linkers with different functional groups, Fmoc-GABA-OH and monomethyl glutarate, are conjugated to the PEG_{18}-diamine linker through their amine terminated functional groups using the SPPS procedures [289]. The two linkers are mixed in various ratios (0%, 25%, 50%, 75%, and 100%) in dry DMF (200 mM) together with EHICA (40 mM) and two

equivalents of DIC. The reaction was allowed to proceed at the surface through the coupling step overnight, followed with the washing step, and then the deprotection of the Fmoc protected linker by immersion of the samples in a solution of 20% piperidine in DMF for 2 hrs and washed. The surfaces are functionalized with the available amine ($-NH_2$) groups of the GABA linker and methyl ester ($-OCH_3$) groups from the monomethyl glutarate. The IKVAV peptide sequence is then grafted from the surfaces via the available amine groups in the procedure mentioned before. The final amino acid in the IKVAV is protected with a Boc protecting group which isn't base sensitive, so it will not be removed during the Fmoc deprotection step for the RGD build-up. The samples are immersed in 1N NaOH for 15 minutes on the orbital shaker and washed with MilliQ-grade water. The NaOH is able to hydrolyse the methyl ester group to hydroxyl group (-OH). The available hydroxyl groups are coupled with a linker, 3-(Fmoc-amino)-1-propanol, in dry DMF (20 mM) together with the coupling reagents DCC and DMAP. The reaction is allowed to proceed overnight, washed, Fmoc deprotected and washed as the respectively mentioned in the washing steps. The next peptide sequence is grafted from the surface, washed, Fmoc deprotected and washed; as the surfaces have now available amine groups to graft the RGD peptide sequence from. After completion of the sequences the remaining side protection groups were removed by immersion in 95% TFA containing 5% MilliQ-grade water for 4 hrs. The samples were washed in MilliQ-grade water, DMF, isopropanol, methanol, rinsed extensively in MilliQ-grade water and dried under nitrogen stream. Illustrated in Schematic 1.2(B) and in the optimization orthogonal chemistry in Schematic 5.5.

3.1.5 PEPTIDE COUPLED TO GOLD EVAPORATED ON GLASS SURFACES

3.1.5.1 GOLD EVAPORATED ON GLASS SURFACES

The piranha treated glass coverslips were placed in sample chamber under vacuum, 10^{-5} mbar, and prepared for thermal metal evaporation in a bell jar. A liquid cold trap was used to prevent contamination of the samples by diffusion pump oil vacuum back streaming. The adhesion layer between the glass coverslip and gold (Au) coating was Titanium (Ti) to form stabile oxides with glass and metallic bonds with Au. The evaporated Au condenses on all

surfaces in 'line of sight' of the filament. A uniform thickness of 50 nm was coated onto the cover slips. This was achieved by monitoring the deposition with a quart crystal microbalance from the filament as the cover slips.

The peptide conjugation occurred on Au surfaces that were either functionalized with (i) only 11-amino-1-undecanethiol (AUT) or on Au surfaces that were functionalized with (ii) benzene-1,4-dithiol/ Au nanoparticles (i.e. 15.87 nm ± 4.29)/ AUT. To achieve Au FLAT or Au nanoparticles (AuNPs) functionalized AUT surfaces.

(i) AUT ON Au SURFACES

The Au coated glass coverslips were rinsed in ethanol and then immersed in a solution of AUT in ethanol (1 mM) and left overnight (i.e. > 18 hrs). The samples were respectively rinsed extensively in ethanol, MilliQ-grade water and then dried under nitrogen stream. Illustrated in Schematic 1.3(A) and Schematic 6.9.

(ii) Benzene-1,4-dithiol/ AuNPs/ AUT

The gold coated glass coverslips were rinsed in ethanol and then immersed in a solution of benzene-1,4-dithiol in ethanol (10 mM) and left overnight (i.e. > 18 hrs). The samples are respectively rinsed extensively in ethanol, dried under nitrogen stream and immersed in a solution of AuNPs (i.e. 15.87 nm ± 4.29, see synthesis of AuNPs below) to be left for 2 days. The surfaces were thoroughly washed with MilliQ-grade water and then dried under nitrogen stream. The AUT functionalization occurred overnight (i.e. as above), washed with ethanol, MilliQ-grade water and then respectively dried under nitrogen stream. Illustrated in Schematic 1.3(B) and in Schematic 6.9.

3.1.5.2 PEPTIDE COUPLED TO AUT ON Au SURFACES

The peptide sequences are 'grafted from' via the surfaces through their amine terminated functional groups of the AUT using the SPPS procedure mentioned above. To achieve Au FLAT-RGD or -IKVAV, and Au NPs-RGD or -IKVAV functionalized surfaces. Illustrated in Schematic 1.3(C) and Schematic 6.8.

3.1.6 SYNTHESING PEPTIDE IN REACTION VESSEL

The peptides for the 'grafting to' approach were synthesized to the modified literature procedures [289].

3.1.6.1 RESIN SWELLING

Dry 2-Chlorotrityl chlorine resin is placed in a SPPS reaction vessel and the reactor is filled with dry Dichloromethane (DCM) until all resin beads are immersed. The resin suspension is gently mixed with a PTFE stick and left for 30 minutes. The DCM is removed by filtration under vacuum. Solution of three equivalent Fmoc amino acids and 7.5 equivalent of N,N'-Diisopropylethylamine (DIPEA) in dry DCM (10 mL/g resin). The SPPS reaction vessel is placed on a rotation shaker to stir the mixture for 1 hour at room temperature. The resin is washed with dry DMF three times, followed by adding 10 mL mixture of DCM/ methanol/ DIPEA (80:15:5) to cap any remaining chloride group from the trityl-based resin which was allowed to mix for 15 minutes and then filtered off. The resin is then washed three times with dry DMF and dry DCM. After dying under vacuum, the successful substitution is measured from the Fmoc release. The presence of resin-bound free amines are validated within 10 minutes via the TNBS, which is a solution mixture of 5% DIPEA in DMF: 1% 2,4,6-Trinitrobenzenesulfonic acid (TNBS) in water: 1% DMF (i.e. yellow when free amines are present, and red when the amine group is still bound by a protecting group).

3.1.6.2 STANDARD WASHING PROCEDURE

The SPPS reaction vessel is filled with dry DMF, the mixture is stirred gently for 10 seconds and then the solvent is filtered. The SPPS reaction vessels screw cap and edges are carefully washed with the next solvent to not minimize loss of any product. The washing procedure consists of repetitive solvent washes respectively in DMF, DMF, methanol, DCM and DMF (i.e. all solvents are in the dry state).

3.1.6.3 STANDARD COUPLING PROCEDURE

The resin is successfully swelled and washed once more in DMF. A mixture of 2.9 equivalent HATU, 3 equivalent Fmoc amino acid in DMF and 7.5 equivalent DIPEA are added

respectively and stirred with a PTFE stick to ensure complete dissolution. The SPPS reaction vessel is placed on a rotation shaker to stir the mixture for 1 hour at room temperature. The coupling solution is filtered and the resin is washed properly according to before mentioned procedure. A very small sample of the resin is removed to qualitatively monitor the coupling reaction using the TNBS test.

After the coupling reaction and washing procedure, the resin is washed once in DMF and filtered. The SPPS reaction vessel is filled with 20% piperidine in DMF and left to stir on the rotation shaker for 30 minutes. The Fmoc deprotection solution was filtered of and washed via the washing procedure ready for the next amino acid coupling. Once the complete peptide is grafted from the resin and Fmoc deprotected, the SPPS reaction vessel is filtered of any solution. The resin removed from the vessel and weighed and then placed in a round bottom flask and add 10 mL of cleavage solution of TFA/ Water/ Triisopropylsilane (TIS) (95:2.5:2.5) per 100 mg of resin. The resin left on the rotation shaker for 90 minutes under gentle stirring. The resin is filtered on a glass frit and washed twice with fresh cleavage cocktail. The filtrate is recovered in a round bottom flask and the cleavage cocktail is concentrated in vacuo to approximately a quarter of its original volume. Under vigorous stirring, Methyl tert-butyl ether (MTBE) is added to precipitate the peptide. At least 10 times the initial volume of MTBE should be added to precipitate the unprotected peptide. Filter the precipitate on a 4-porosity glass frit. Triturate and wash by filtrating the precipitated peptide on the frit three times with MTBE. The final peptides synthesized are RGD and RGDC.

3.1.7 CONJUGATING PEPTIDE TO GOLD NANOPARTICLES

3.1.7.1 PREPARATION OF AuNPs

The AuNPs were prepared by the standard Turkevich and Frens method according to the modified literature procedures [290, 291]. Gold hydrochlorate ($HAuCl_4.3H_2O$/ 51 mg, 0.15 mmol) was dissolved in MilliQ-water (300 mL, 0.5 mM) and the gold solution was heated for 20 minutes until bubbles appeared. A solution of sodium citrate dihydrate (342 mg) in MilliQ-water (30 mL) was added immediately and stirred vigorously for 20 minutes. The colorless solution becomes red wine in color which is characteristics of 15-20 nm sized

nanoparticles. The solution is allowed to cool down whilst still being stirred. Consequently, the solution is filtered using a sterile Millipore filter 0.22 μm PES (Fast Flow, Lot MP3256705A).The filtered solution is stored in stock at all times in the fridge (i.e. AuNPs, 15.87 nm ± 4.29).

3.1.7.2 PREPARATION OF GOLD-COATED SiO_2 NANOPARTICLES

3.1.7.2.1 SYNTHESIS OF SiO_2NPs

The SiO_2NPs were prepared according to the modified literature procedures by mixing 250 mL of an ethanolic solution containing Tetraethyl orthosilicate (TEOS) (25.7 mL, 0.20 mol) with 250 mL of an ethanolic solution containing Ammonium hydroxide (NH_4OH) (35 mL, 1.1 mol) and MilliQ-water (128.5 g, 14.3 mol), which were poured into a 1L Erlenmeyer flask and vigorously stirred (i.e. final concentrations of 0.2M TEOS, 1.1M ammonia (NH_3), and 17.0M H_2O) [292]. The mixture will turn turbid to indicate SiO_2NPs formation and the reaction is left overnight (> 24 hrs), after which the solution was centrifuged for 10 minutes (6000 rpm), the supernatant is discarded to leave SiO_2NPs as pellets at the bottom of the centrifuge tubes. The SiO_2NPs were purified by repeated sonication, centrifugation and resuspension in a series of 10mL supernatants in the respective solvents, 100% water, 25% ethanol, 50% ethanol, 75% ethanol (twice), and 100% ethanol by 10 minutes sonication followed by 10 minutes centrifugation between each solvent change/discard. Next the SiO_2NPs were air-dried overnight after the final rinse, transferred to a petri-dish to break any large aggregates with a spatula, and then placed in a furnace programmed to heat the nanoparticles for 4 hrs at 600 ^oC (i.e. heating rate of 20 $^oCmin^{-1}$). Illustrated in Schematic 6.7.

3.1.7.2.2 SiO_2-Core Au-Shell NANOPARTICLES (SiO_2@AuNPs)

SiO_2NPs of 13.3 g are dispersed in 200 mL of dry acetonitrile, 0.40 mL of APTES and vigorously stirred under a nitrogen balloon overnight to aminate the SiO_2NPs [292]. The aminated SiO_2NPs were isolated by repeated centrifugation and resuspension in acetonitrile, THF, xylene, twice in water, and twice in acetonitrile, followed by air-drying overnight. The aminated SiO_2NPs were then immersed in an aqueous solution of AuNPs (i.e. diluted 6 fold from the stock solution prepared in section 3.1.7.1) for 10 hrs with magnetic stirring. A change in the wine red color of the solution is observed as the surface of the aminated

SiO_2NPs are adsorbed by the gold nanoparticles. The faintly pink nanoparticles were washed and collected via sonication in water and centrifugation at least three times prior to air-drying. Afterwards the nanoparticles were ground up and 200 mL of gold-plating solution (0.1% w/w $HAuCl_4$ in 0.40 mM $NH_2OH.HCl$) was added and vigorously stirred for 30 minutes. A deep purple color change of the colloidal solution is observed as gold shells are chemically deposited on the surface of the SiO_2NPs. Next the gold-coated nanoparticles, SiO_2@AuNPs, were collected, centrifuged and rinsed repetitively with deionized water at least five times. The modified nanoparticles were dried under nitrogen to give a purple powder (SiO_2@AuNPs, 250.00 nm ± 89.65). Illustrated in Schematic 6.7.

3.1.7.3 CONJUGATING PEPTIDE TO Au NANOPARTICLES

3.1.7.3.1 GRAFTING PEPTIDES TO NANOPARTICLES

The synthesized peptides from section 3.1.6 are 'grafted to' to the 15.87 nm ± 4.29 AuNPs and the 250.00 nm ± 89.65 SiO_2@AuNPs via the thiol SAM's on the gold surfaces. Add to 10 mM of nanoparticles Tween-20 to achieve a concentration of 0.1% and leave for 10 minutes. Bring the colloidal mixture to 0.2M NaCl and 0.001 phosphate buffer (pH 7.4) and stir for 5 minutes. The thiolated peptides (i.e. RGDC or IKVAVC) were added to the nanoparticle solution (i.e. AuNPs or SiO_2@AuNPs) as 1.7 nmol peptide per 1 mL of nanoparticle. The final mixture was brought to 0.3M NaCl overnight (> 24 hrs) and shaken for additional 24 hrs to complete the functionalization process. The particles were centrifuged (6000 rpm), resuspended twice with 0.1M Na_2CO_3 and twice with (2x) PBS (0.0067 M phosphate buffer, pH 7.4, 0.3 M NaCl), and finally resuspended in (2x) PBS [293]. Illustrated in Schematic 1.4 and in Schematic 6.8.

3.2 CELL CULTURE AND CHARACTERIZATION

3.2.1 ETHICS

All primary neural cells used for experiments were obtained in accordance with guidelines set out in the code of practice for humane killing under Schedule 1 of the UK Home Office Animals (Scientific Procedures) Act 1986, and approved by the University of Nottingham Animal welfare and Ethical Review body.

3.2.2 COATING OF CONTROL SURFACES FOR CELL CULTURE

Glass coverslips are prepared as mentioned as above to the piranha solution cleaning step at which point the surfaces are treated with Poly-L-Ornithine (PLO) solution of 20 μg/mL in cold sterile deionized water. The coverslips are placed in 12 well plates and 1mL of PLO solution is added to immerse the coverslips and are incubated overnight in the incubator (37 ^{c}o. / 5% CO_2/ Humidity > 90%). The PLO solution is removed from the coverslips and rinsed three times with sterile deionized water. Laminin solution of 5 μg/ mL in cold deionized water was prepared, and 1 mL of Laminin solution was added to immerse the coverslips and incubated overnight. The laminin solution is aspirated off the glass coverslips and rinsed three times in water and once in phosphate buffer solution (PBS, no Ca^{2+}/ Mg^{2+}) and allowed to dry at room temperature in the flow laminar under sterile conditions at all times.

3.2.3 ISOLATION OF HIPPOCAMPI FROM E18 BRAIN

3.2.3.1 ANIMAL DISSECTION

This method is modified according to the cell culture laboratory handbook.

The pregnant rat is delivered to the laboratory on the morning of the dissection. The following preparations need to be done before the dissection takes place; (1) take 50 mL of ice cold PBS (Ca^{2+}/Mg^{2+}) in 100 mL Duran bottle on ice, (2) have at hand sterile medical scissors and medical forceps, (3) 70% ethanol, tissue, gloves, and (4) yellow bag for disposal of Biological/ Clinical Laboratory waste. The 18 days embryo (E18) timed pregnant rat is euthanized with carbon dioxide under the Schedule 1 killing method (SK1) and death is confirmed of the pregnant rat before proceeding to dissection, which is performed in the open face dissection hood.

The rat is laid on its back and sprayed up and down the lower underside with 70% ethanol. Using the medical forceps the fur is pinched near the lower abdomen and cut upwards with the scissors through skin and the muscle layer. Cut around both sides of the abdomen posterior to anterior until there is a clear access to the embryos beneath a flap of skin. The fur is peeled back to expose the abdomen wall, which is pinched and cut peeled back to expose the uterus. The medical forceps are used to firmly hold the uterus in a gap between embryos in the middle of the body and then pulled gently upwards. The connective tissue

that holds the uterus is place is cut and the uterus should come out easily in a long string containing usually around 8-14 embryos per rat. The uterus is gently lifted holding it away from the body to prevent contamination, then cut at each end of the uterus and then place the uterus into the sterile ice cold PBS (Ca^{2+}/Mg^{2+}) in the Duran bottle with the lid sealed is placed on ice. The area of dissection is cleaned with the 70% ethanol, the carcass of the rat is placed into the yellow bag which is doubled up with another yellow bag and disposed under the relevant clinical waste and incineration legislation. Further details on the SK1 legislation and conditions can be found here;
https://www.gov.uk/government/uploads/system/uploads/attachment_data/file/548693/0193-archived.pdf

3.2.3.2 HIPPOCAMPAL DISSECTION

The uterus in the Duran bottle is removed from the ice box and sprayed with 70% ethanol and placed in the flow laminar under sterile conditions. The uterus is removed from the Duran bottle and placed in an empty 90 mm petri-dish and the embryos removed by using small scissors to puncture the embryonic sac. The pups usually slide out easily once the embryonic sac is punctured and by holding the head of the pups in place with round tip forceps' and decapitated under the SK1 method. The heads are moved to one of the two 90 mm petri dishes containing Hank's solution (30 mL/petri-dish). The heads are held in place with iris forceps' by skewering through the eyes, using the dissection scissors find the back of the skull and insert one of the scissors into the opening towards the cerebellum. Carefully make small cuts across the middle of the skull towards the nose, whilst carefully not damaging the cortex. At the point where the scissors were inserted use small forceps and pinch the tip of one side of the skull and peal laterally towards the nose, thus, peeling off the skull and skin to real the brain. Carefully push the brain out back of skull and repeat these steps until all the brains have been removed from their heads. Then for each brain, use one pair of small forceps to hold it in place, and separate the hemispheres with another pair of forceps by pinching between the hemispheres. Once all the hemispheres have been separated from all the brains remove the hemispheres to the fresh 90 mm petri-dish containing Hanks Solution (30 mL) and discard the midbrain. For each hemisphere remove the meninges by grasping the base of the hemisphere and then with the other pair gently roll

the hemisphere out of the membrane. The hippocampus is identified and using a small pair of forceps insert into the hemisphere away from the hippocampus and carefully cut it out by using the other forceps to nip the tissue around the hippocampus. Place the hippocampus into a 35 mm petri-dish with Hanks Solution (2 mL) and repeat these steps until all hippocampi have been removed from the hemispheres.

3.2.3.3 NEURAL PROGENITOR STEM CELLS (NPSCs) CULTURE

NPSCs were isolated from E18 rat embryos by dissecting the hippocampal tissue*. The 7-9 hippocampi are transferred within 1 mL of Hanks Solution to an Eppendorf tube from the 35 mm petridish containing all the dissected hippocampi and allow the hippocampi to settle to the bottle and remove the supernatant without disturbing the tissue pellet, wash with PBS (Ca^{2+}/Mg^{2+}) and centrifuge (3 minutes, 200 rcf). Remove the supernatant, triturate and incubate in 1 mL Accumax and 20 μg/mL DNAse for 20 minutes, after which triturate and incubate for a further 10 minutes. The eppendorf is centrifuged, washed in PBS (Ca^{2+}/Mg^{2+}), centrifuged, and replacing the supernatant for NPSCs media**. The cells are counted as number of viable cells by staining 10 μL of the 1 mL stock cell suspension with 10 μL tryphan blue whilst using a hemocytometer.

NOTE:

**** The subgranular zone of the dentate gyrus (DG) of the hippocampus is one of the two main neurogenic zones were the NPSCs exist and they generate excitatory glutamatergic granule neurons in the DG. Enzymatic dissociated NPSCs form and attach as neuroepithelial cells on the surfaces before becoming induced to radial glia form, which have the ability to differentiate into all three neural linages (i.e. neurons, astrocytes, an oligodendrocytes) [294-296]. Without dissociation the cells are aggregated and migrate to form neuroepithelial rosettes which enables them to favor neurogenesis over gliogenesis [296].***

At E18 the hippocampi is homogenously composed of major pyramidal neurons and a few glial cells. The media used is specially designed for the proliferation of NPSCs and dominate over the present neurons. Thus, facilitating the differentiation observed here to be due to the surfaces [296*].

NPSCs media is made up of neuralbasalTM media in a 1:1 with knockout DMEM/F12 media containing N2-supplement (100x), B27-supplement (50x), growth factors EGF and bFGF, penicillin-streptomycin, and HEPES solution.

3.2.3.3.1 NPSCs TWO-DIMENSIONAL CULTURE (2D)

The cells were cultured as $3x10^5$ cells on the PLO/Laminin, RGD, IKVAV and PEG_{18}-diamine surfaces in 6 well plates and placed in the incubator (37 ^oC/ 5% CO_2/ Humidity > 90%) and the media was changed every 2-3 days by removing 800 μL of the media without disturbing the seeded cells on the coverslips and replacing it with 1 mL of fresh NPSCs media (i.e. containing growth factors bFGF and EGF for the initial 7 days and then without growth factors).

3.2.3.3.2 NPSCs THREE-DIMENSIONAL CULTURE (3D)

The cells were cultured as $1.5x10^5$ cells in 12 well plates with 10 μL of peptide functionalized nanoparticles (i.e. gold nanoparticle functionalized with RGDC or IKVAVC/ SiO_2 core-gold shell nanoparticles coated with RGDC and IKVAVC) suspended in the media and placed in the incubator (37 ^oC/ 5% CO_2/ Humidity > 90%) on an orbital shaker. The media was changed every 2-3 days by transferring the cell culture per well individually and centrifuging (600 rcf), removing the supernatant without disturbing the pellet and replacing 800 μL of fresh NPSC's media (i.e. containing growth factors bFGF and EGF for the initial 7 days and then without growth factors) and suspending the pellet in the media to be transferred back to the original well plate***.**

The same approach was taken with RGD and IKVAVC peptides that are soluble in NPSCs media as opposed to the insoluble peptides functionalized on 2D and 3D surfaces.

3.2.3.4 CELL ADHESION AND PROLIFERATION

The cell adhesion, proliferation was observed by cell imaging with the inverted fluorescence microscope on the days that the media was changed (i.e. 2DIV, 5DIV, 7DIV, 9DIV, 12DIV and 14DIV). The cell morphology was observed as a way to identify the way of cell adhesion occurred.

3.2.3.5 CELL DIFFERENTIATION – IMMUNOCYTOCHEMISTRY (ICC)

The cell differentiation was examined by determining cell morphology and cells protein expression through immunocytochemical analysis, imaged on the inverted fluorescence or CLSM microscope.

On 14DIV the media is aspirated from the wells and the coverslips with cells washed carefully with PBS. The cells were fixed on the coverslips with ice-cold methanol for 5 minutes in the fridge. The wells are washed three more times (x3) with PBS, then the cells were permeabilized by adding 0.1% Triton-100 (in PBS) for 10 minutes, and then washed (x3) with PBS. The non-specific binding sites were blocked by incubating with 0.5% BSA in PBS, one hour at room temperature. The primary antibody is diluted in 0.5% BSA in PBS, depending on the data sheet of the antibody, then added to the wells with fixed cells to incubate on a rocker overnight at 4 ^{o}C and then washed (x3) in PBS. The secondary antibody is diluted 1:500 in 0.5% BSA in PBS and left to incubate on the rocker at room temperature for 45 minutes and then washed (x3) in PBS. Hoechst added for 5 minutes as a dilution of 1:10 and then washed (x6) in PBS to remove all background signals. To store the fixed cells the coverslips are mounted with mounting media and kept in a dark storage place to prevent bleaching.

A similar approach to the fixing of the 2D surfaces was taken for the removal of supernatants of 3D cultures (i.e. neurospheres) during the ICC****. The fixing, washing and staining occurs in eppendorfs and centrifuged (600 rcf), and with the final step transferring the neurospheres in PBS to chambered coverslip glass (8 well, #1.5 borosillicate) and stored by covering the samples with aluminum in the fridge.

NOTE:

****NPSCs isolated and exposed to the NPSCs media have the ability to express Nestin in the presence of the growth factors and after the removal of the growth factors at 7DIV to express, βIII-tubulin, and glial fibrillary acidic protein (GFAP) to differentiate into neurons and astrocytes.***

***** No gene-transfer manipulation was performed in this protocol and the only influence should be from the functionalized surfaces in 2D and 3D.***

3.2.3.6 PROCESSING CELLS FOR TRANSMISSION ELECTRON MICROSCOPY (TEM)

The neurospheres in eppendorfs are respectively centrifuged (600 rcf), supernatant removed carefully without disrupting the cell pellet and suspended with EM fixative buffers (3% glutaraldehyde in 0.1M cacodylate buffer) for 30 minutes. Subsequently, centrifuge and remove the fixative to resuspend the cell pellet in 0.1M sodium cacodylate/ phosphate buffer and respectively repeat the centrifuge and wash steps (x3). Remove the supernatant and resuspend in a (1:1) 1% - 2% aqueous osmium tetroxide: 0.2 M buffer stock solution for 30 minutes. Centrifuge and remove the osmium tetroxide and wash (x4) with 0.1M sodium cacodylate/ phosphate buffer, and then wash (x5) 1 minute in MilliQ-water. The cell pellet was dehydrated in a graded ethanol series respectively, (2x) 15 minutes in 50% ethanol, (2x) 15 minutes in 70% ethanol, (2x) 15 minutes in 90% ethanol, (3x) 20 minutes in 100% ethanol, and (2x) 15 minutes in 100% propylene oxide. The samples are then infiltrated with resin [add 25 mL Araldite CY212 resin, 15 mL Agar resin, 55 mL Dodecenylsuccinic anhydride (DDSA), 2 mL Dibutyl phthalate and 1.5 mL 2,4,6-Tris(dimethylaminomethyl)phenol (DMP 30) to make the resin], and left to polymerize for 48 hrs in the embedding oven at 60 ^{o}C. The polymerized resin with cell pellet samples are cut out of the eppendorfs and sectioned ultrathin region of interests with a microtome (Leica EM UC6) and place the slices on TEM grids (i.e. ensure the slices are flat by flattening with chloroform vapor). The slices are stained for 5 minutes with 50% ethanolic urenyle acetate in MilliQ-water and then washed (x2) in MiliQ-water to then be stained with lead acetate (i.e. in the presence of NaOH to mop up and carbon dioxide) for 5 minutes and washed extensively in MilliQ-water to remove the heavy metals as much as possible before left to air-dry.

3.3 ANALYTICAL TECHNIQUES

3.3.1 WATER CONTACT ANGLE (WCA)

Static WCA were measured with MilliQ-grade water on a CAM 200 (KSV Instruments Ltd, Finland) using the sessile drop method. Images of the drops were taken 1 frame every second 20 times after deposition of the drop on the surface, this is done to minimize the change of the contact angle on the surface as a function of time and location (i.e. the WCA is

reduces with time, conditions such as temperature play a role). The complete drop profile at the solid-air interface was evaluated using circular fit. A manual baseline was placed on the image and the contact angle was determined as the tangent of the drop profile at the 3-phase contact point. The contact angle values obtained were the mean of the measurements taken at both sides of each droplet. For each surface, five droplets were placed on each sample (i.e. a total of 10 measurements on 2 samples). The data represents the mean contact angle value obtained over those measurements.

3.3.2 FLUORESCENCE SPECTROPHOTOMETERY

The coverslips were mounted on a microscope slide and fixed to the front surface analyzer intended for the analysis of fixed solid samples (i.e. peptide surfaces). The samples were excited at the wavelength of 290 nm with a Cary Eclipse Fluorescence Spectrophotometer (Varian Inc.) to analyze the emitted fluorescent light from the solid samples.

3.3.3 ATOMIC FORMCE MICROSCOPE (AFM)

Surface functionalized view scans of one micron field were obtained from The Dimesion Icon ® Atomic Force Microscope (Bruker) and the data was analyzed on NanoScope Analysis Software. Scans were conducted in tapping mode with the silicon tip, Tapping Mode Etched Silicon Probes (OTESPA, Veeco Instruments), which are pyramidal in shape that have a front/ back/ side-angles of 25^{o}/ 15^{o}/ 22.5^{o} with a tip height of 10-15 μm and a nominal tip-end radius of 10 nm.

The AFM images were acquired by scanning the sample in air under ambient laboratory conditions. Topography images and surface roughness measurements were obtained using Nanoscope Analysis Software. Root-mean-square (RMS) roughness factor and z-range were measured from several different 1 x 1μm images for each type of sample to obtain quantitative information.

3.3.4 TIME OF FLIGHT – SECONDARY IONISATION MASS SPECTROSCOPY (TOF-SIMS)

Surface functionalized samples were analyzed using ION-TOF ToF-SIMS IV Instrument (Münster, Germany) equipped with a Bi liquid metal ion gun (LMIG) and the primary ions of 25 kV Bi_3^+ (~1.0 pA pulsed target current, angle beam at 45° in relation to the normal) and an analyzer post acceleration voltage of 10 kV was used. A flux of low energy electrons (20 eV) was used to charge compensation. Images were obtained by rastering the primary ion beam over 3 mm x 3 mm and 500 μm x 500 μm sample surface areas at a resolution of 256 pixels x 256 pixels. The displayed spectra were normalized to the total ion intensity. A higher mass resolution was possible due to the recording being under high current bunch mode and spectrums were calibrated with CH_2^+, CH_3^+, $C_3H_2^+$ and $C_4H_3^+$ ions.

3.3.5 X-RAY PHOTOELECTRON SPECTROSCOPY (XPS)

Surface functionalized samples were analyzed using the Kratos AXIS ULTRA with a mono-chromated Al kα X-ray source (hν = 1486.69 eV) operated at 10 mA emission current and 12 kV anode potential.

A wide survey scan over a binding energy range of 0-1200 eV was taken for each sample with pass energy of 80 eV for wide scans and 20 eV for high resolution scans. The dwell time for the wide scan, C 1s, N 1s, and Si $2p_{3/2}$ were respectively; 0.21, 0.52, 1.66, and 0.79.The photoelectron analyzer was set at the take-off angle of 90 ° and all the samples were charge neutralized with a 3x repeat scans. High resolution scans for C 1s, N 1s and Si $2p_{3/2}$ were charge corrected to the main C 1s peak at 284.8 eV. Data analysis was carried out using CASAXPS software with empirically derived Kratos sensitivity factors to determine the atomic concentration percentage from the peak areas. Components were fitted under the core levels to give chemical bonding information. The full width at half maximum (FWHM) values were allowed to vary within constraints (FWHM ranges of 1.1-1.5 eV).

3.3.6 HIGH-PRESSURE LIQUID CHROMATOGRAPHY (HPLC)

The synthesized peptides purity analysis was performed on a LC-20AD, Shimadzu solvent delivery unit. Chromatograms were recorded using a SPD-M20A High Performance Liquid

Chromatography PDA detector, again from Shimadzu. Purifications were performed using a Jupiter C18, 300 Å pore size, 5 μm particle size, 250 X 4.6 mm by Phenomenex.

3.3.7 ELECTROSPRAY IONISATION MASS SPECTROSCOPY (ESI-MS)

The high-throughput LC-MS system, based on a Bruker MicroTOF (Time of Flight) mass spectrometer using ElectroSpray Ionization (ESI) was used to analyze the molecular composition of the synthesized peptides. The instrument has a resolution specification of 10,000 and mass accuracy of 5 ppm (external calibration) or 3 ppm (internal calibration).

3.3.8 NUCLEAR MAGNETIC RESONANCE (NMR)

The structure of the synthesized peptides was characterized out using a Bruker DPX400 UltraShield™ Spectrometer. The spectra produced was analyzed with MestReNova 6.0.2© 2009 Mestrelab Research S.L.

3.3.9 UV/ VISIBLE SPECTROSCOPY

The change in surface plasmon resonance (SPR) was detected by acquired the UV absorption spectra with a Cary 50 UV-Vis Spectrophotometer (Varian Inc.), Cary WinUV software and Hellma quartz 104-OS cuvette with a light path of 10 mm.

3.3.10 ZETASIZER

The measurements for particle size by dynamic light scattering (DLS) and zeta-potential by electrophoresis and laser doppler velocimetry was performed with a NanoZS Zetasizer (Malvern). Disposable folded capillary cells (DTS1070) were used to eliminate the potential contamination issue, as well as providing the accuracy of measurements of a capillary cell.

3.3.11 TRANSMISSION ELECTRON MICROSCOPY (TEM)

The TEM data set were acquired using a JOEL 2100F (point resolution 0.19 nm, accelerating voltage 200 kV) equipped with integrated key features such as Gatan Trickiem Imaging Filter (GIF) for Electron Energy Loss Spectroscopy (EELS) and Energy Dispersive X-Ray

Spectrometer (EDS/ EDX). For ultrathin sections of biological samples, the ultramicrotomy (i.e. section 2.4.8) is performed and then studied at different magnifications in the TEM.

3.3.12 OPTICAL MICROSCOPY

Images were acquired on a Nikon Eclipse T*i* inverted Microscope with a 10x 0.l3N_A dry objective and captured on an ORCA-Flash4.0 (C11440 - Hamamatsu) digital CMOS camera (2048 _ 2048, 6.5 *m*m pixels) with an Epi-fl illuminator unit to freely change between fluorescence filters (i.e. bright field, FITC, CY5 and DAPI) to select wavelength of excitation light. For each surface five non-overlapping images were taken and images were analyzed and processed in ImageJ.

3.3.13 CONFOCAL FLUORESCENCE MICROSCOPY

The confocal fluorescence images were taken on a Zeiss LSM 710 (i.e. laser scanning confocal microscope) with a 40x 1.2 N_A C-Apo water objective to acquire optical sections with contrast and high resolution in x, y and z for the three-dimensional image stitching and z-stack.

3.3.14 STATISTICAL ANALYSIS

All the data was analyzed using Microsoft Excel, Origin and Graph Prism 7 softwares. The statistical significance of normal distributed data containing two groups was either tested by paired t test (i.e. paired groups) whilst the normal distributed datasets containing three or more groups were tested using one-way ANOVA with Sidak's multiple comparisons test , with a single pooled variance and adjusted p values (i.e. 0.1234[ns], 0.0332 [*], 0.0021 [**], 0.0002 [***], <0.0001 [****]).

3.3.15 MILLIQ-GRADE WATER

The Elga PureLab Ultra lab water purification system was used to deionize water to obtain HPLC grade water (18 MΩ-cm). This purified water was used for all the experiments performed in this thesis to minimize contamination.

3.4 CHEMICALS, SOFTWARE AND TECHNIQUES

CHEMICALS		
Name	***Company***	***CAS/ Cat. No.***
Borosilicate Glass Coverslips	neuVitro	[GG-19-1.5]
Acetone (HPLC)	Sigma-Aldrich	[67-64-1]
Methanol (HPLC)	Sigma-Aldrich	[67-56-1]
Isopropanol (HPLC)	Sigma-Aldrich	[67-63-0]
Ethanol (HPLC)	Sigma-Aldrich	[64-17-5]
Sulphuric acid (H_2SO_4)	VWR	[7664-93-9]
Hydrogen peroxide (H_2O_2)	Sigma-Aldrich	[7722-84-1]
Sodium bicarbonate ($NaHCO_3$)	Sigma-Aldrich	[144-55-8]
Sodium hydroxide (NaOH)	VWR	[1310-73-2]
(3-Glycidyloxypropyl)trimethoxysilane (GOPTS)	Sigma-Aldrich	[2530-83-8]
PEG_{18}-diamine	Sigma-Aldrich	[24991-53-5]
N′,N′-Dimethylformamide (DMF)	Sigma-Aldrich	[68-12-2]
Ethyl(hydroimino)cyanoacetate (EHICA)	Sigma-Aldrich	[3849-21-6]
N′,N′-Diispropylcarbodiimide (DIC)	Sigma-Aldrich	[693-13-0]
Piperidine	Sigma-Aldrich	[110-89-4]
Fmoc-Arg(Pbf)- OH	Bachem	[154445-77-9]
Fmoc-Gly-OH (G)	Bachem	[29022-11-5]
Fmoc-Asp(OtBu)- OH (D)	Bachem	[71989-14-5]
Fmoc-Ile-OH (I)	Bachem	[71989-23-6]
Fmoc-Lys(Z)- OH (K)	Bachem	[86060-82-4]
Fmoc-Val-OH (V)	Bachem	[68858-20-8]
Fmoc-Ala-OH.H_2O (A)	Bachem	[35661-39-3]
Trifluoroacetic acid (TFA)	Sigma-Aldrich	[76-05-1]
Fmoc-GABA-OH	Sigma-Aldrich	[116821-47-7]

Monomethyl Glutarate	Sigma-Aldrich	[1501-27-5]
3-(Fmoc-amino)-1-propanol	Sigma-Aldrich	[157887-82-6]
Boc-Ile-OH (Boc-I)	Bachem	[13139-16-7]
4-(Dimethylamino)pyridine (DMAP)	Sigma-Aldrich	[1122-58-3]
N',*N'*-Dicyclohexylcarbodiimide (DCC)	Sigma-Aldrich	[538-75-0]
(3-Aminopropyl)trimethoxysilane (APTMS)	Sigma-Aldrich	[13822-56-5]
2-Chloroethylamine hydrochloride	Sigma-Aldrich	[870-24-6]
MES Solution	Sigma-Aldrich	[MFCD00006181]
Tris (2-carboxyethyl)phosphine hydrochloride	Sigma-Aldrich	[51805-45-9]
L-Cysteine	Sigma-Aldrich	[52-90-4]
11-Amino-1-undecanethiol hydrochloride (AUT)	Sigma-Aldrich	[143339-58-6]
2-Chlorotrityl chlorine resin	Sigma-Aldrich	[42074-68-0]
Dichloromethane (DCM)	Sigma-Aldrich	[75-09-2]
N,N'-Diisopropylethylamine (DIPEA)	Sigma-Aldrich	[7087-68-5]
HATU	Sigma-Aldrich	[148893-10-1]
Triispropylsilane (TIS)	Sigma-Aldrich	[6485-79-6]
Ethyl acetate	Sigma-Aldrich	[141-78-6]
Acetic anhydride	Sigma-Aldrich	[108-24-7]
Methyl tert-butyl ether (MTBE)	Sigma-Aldrich	[1634-04-4]
2,4,6-Trinitrobenzenesulfonic acid solution (TNBS)	Sigma-Aldrich	[2508-19-2]
$HAuCl_4.xH_2O$	Sigma-Aldrich	[27988-77-8]
Sodium citrate dihydrate	Sigma-Aldrich	[6858-44-2]
Benzene-1,4-dithiol	Sigma-Aldrich	[624-39-5]
Tetraethyl orthosilicate (TEOS)	Sigma-Aldrich	[78-10-4]
Ammonia (NH_3)		

Ammonium hydroxide (NH_4OH)	Sigma-Aldrich	[1336-21-6]
(3-aminopropyl)triethoxysilane (APTES)	Sigma-Aldrich	[919-30-2]
Acetonitrile (HPLC)	Sigma-Aldrich	[75-05-8]
Tetrahydrofuran (THF)	Sigma-Aldrich	[109-99-9]
Xylene	Sigma-Aldrich	[106-42-3]
Hydroxylamine hydrochloride ($NH_2OH.HCl$)	Sigma-Aldrich	[5470-11-1]
Chloroform	Sigma-Aldrich	[67-66-3]
CSRARKQAASIKVAVSADR	Designer bioscience Ltd	[2091-2108]
Poly-L-Ornithine (PLO)	Sigma-Aldrich	[27378-49-0]
Laminin	Sigma-Aldrich	[114956-81-9]
Ca^{2+}/Mg^{2+} free - Dulbecco's Phosphate buffer solution (D-PBS)	Sigma-Aldrich	[MFCD00131854]
Phosphate buffer solution (Ca^{2+}/Mg^{2+})	Sigma-Aldrich	[MFCD00131855]
Ca^{2+}/Mg^{2+} free - Hank's balances salt solution	Invitrogen, Paisley, UK	[14175095]
HEPES	Sigma-Aldrich	[H4034]
Accumax solution	Sigma-Aldrich	[MFCD01632904]
DNAse I	Roche, West Sussex, UK	[11284932001]
Neuralbasal ™ Medium	ThermoFisher Scientific	[21103049]
Knockout DMEM/F-12	Invitrogen, Paisley, UK	[DF-041-B]
Penicillin-Streptomycin	Sigma-Aldrich	[P0781]
N2-supplement (100X)	ThermoFisher Scientific	[17502048]
B27-supplement (50X)	Invitrogen, Paisley, UK	[A3582801]
EGF	Gibco	[PHG0314]
bFGF	Gibco	[PHG0024]
Tween-20	Sigma-Aldrich	[9005-64-5]
Sodium carbonate (Na_2CO_3)	Sigma-Aldrich	[144-55-8]
Bovine Serum Albumin solution (BSA)	Sigma-Aldrich	[9048-46-8]

Triton X-100	Sigma-Aldrich	[9002-93-1]
Anti-beta III Yubulin antibody (βIII-Tubulin)	Abcam	[ab18207]
Anti-glial fibrillary acidic protein antibody (GFAP)	Abcam	[ab53554]
HOECHST ® 3342	Tocris	[23491-52-3]
Alexa Fluor 488	Abcam	[ab21206]
Alexa Fluor 647	Abcam	[ab21469]
Sodium cacodylate trihydrate	Sigma-Aldrich	[6131-99-3]
EM Glutaraldehyde solution	Sigma-Aldrich	[111-30-8]
Osmium Tetroxide	Sigma-Aldrich	[20816-12-0]
(R)-(+)-Propylene Oxide	Sigma-Aldrich	[15448-47-2]
Epoxy resin (Araldite CY212) Kit	Agar Scientific	[AGR1030]
Agar 100 Resin Kit	Agar Scientific	[AGR1031]
Dodecenylsuccinic anhydride (DDSA)	Sigma-Aldrich	[26544-38-7]
Dibutyl Phthalate	Sigma-Aldrich	[84-74-2]
2,4,6-Tris(dimethylaminomethyl)phenol	Sigma-Aldrich	[90-72-2]

SOFTWARE		
Name	***Company***	***CAS/ Cat. No.***
Microsoft Excel	Microsoft, Redmond, USA	Microsoft Office 2013 (WINDOWS/ Mac OS X)
Paintbrush	https://paintbrush.sourceforge.io	2.1.2 (Mac OS X)
Graphpad Prism	Graphpad Software, la Jolla, USA	7 (Mac OS X)
ChemBio3D Ultra	PerkinElmer, Seer Green, UK	15.1 (Mac OS X)
CASAXPS	Casa Software Ltd, Teignmouth, UK	2.3.18 (WINDOWS)
Nanoscope	Bruker Nano Inc., Camarillo, USA	9 (WINDOWS)
SurfaceLab – IONTOF	ION-TOF GmbH, Münster, Germany	6 (WINDOWS)
ImageJ (including Micro-Manager)	National Institute of Health, Bethesda, USA	1.51n (Mac OS X)
MestReNova	Mestrelab Research S.L.	6.0.2 (WINDOWS)
Zen Lite	Zeiss International, Oberkochen, Germany	ZEN 2.3 (Mac OS X)

TECHNIQUE			
Name	***Model***	***Company***	***Organizational Unit***
Water Contact Angle (WCA)	CAM 200	KSV	School of Pharmacy, Boots Science Building (BSB)
Fluorescence Spectroscopy	Cary Eclipse	Varian Inc.	School of Pharmacy, Boots Science Building (BSB)
Atomic Force Microscopy (AFM)	Dimension Icon	Bruker	School of Pharmacy, Boots Science Building (BSB)
Time of Flight-Secondary Ion Mass Spectroscopy (ToF-SIMS)	ToF-SIMS IV	ION-TOF	School of Pharmacy, Boots Science Building (BSB)
X-ray Photoelectron Spectroscopy (XPS)	AXIS ULTRA	Kratos	Nanoscale and Microscale Research (NMRC)
UV/ Visible Spectroscopy	Cary 50	Varian Inc.	School of Pharmacy, Boots Science Building (BSB)
Dynamic Light Scattering/ ζ-Potential (DLS/ ζ-Potential)	NanoZS Zetasizer	Malvern	School of Pharmacy, Boots Science Building (BSB)
Transmission Electron Microscopy (TEM)	2100F	JOEL	Nanoscale and Microscale Research (NMRC)
Inverted Fluorescence Microscopy	Eclipse T*i*	Nikon	Faculty of Life Sciences
Confocal Laser Scanning Microscopy (CLSM)	LSM 710	Zeiss	Faculty of Medicine and Health Sciences
Nuclear Magnetic Resonance (NMR)	DPX400 Ultrashield™	Bruker	School of Pharmacy, Centre of Biomedical Sciences (CBS)
Electrospray Ionization Mass Spectroscopy (ESI-MS)	MicroTOF	Bruker	School of Chemistry
High-Pressure Liquid Chromatography (HPLC)	LC-20AD	Shimadzu	School of Pharmacy, Boots Science Building (BSB)
ElgaLabWater (Milli-Q Water)	PURELAB® Ultra	Elga Veolia	School of Pharmacy, Boots Science Building (BSB)

4 IMMOBILIZING PEPTIDES ON GLASS SURFACES

4.1 INTRODUCTION

This chapter focuses on the implementation of biomimetic surfaces that are immobilized with peptides that mimic the *in vivo* ECM composition that interact with neural stem cells and influence stem cell fate. The chapter has been divided into (i) preparation and characterization, and (ii) cell response towards the biomimetic surfaces in the case of RGD and IKVAV surfaces.

4.2 BACKGROUND

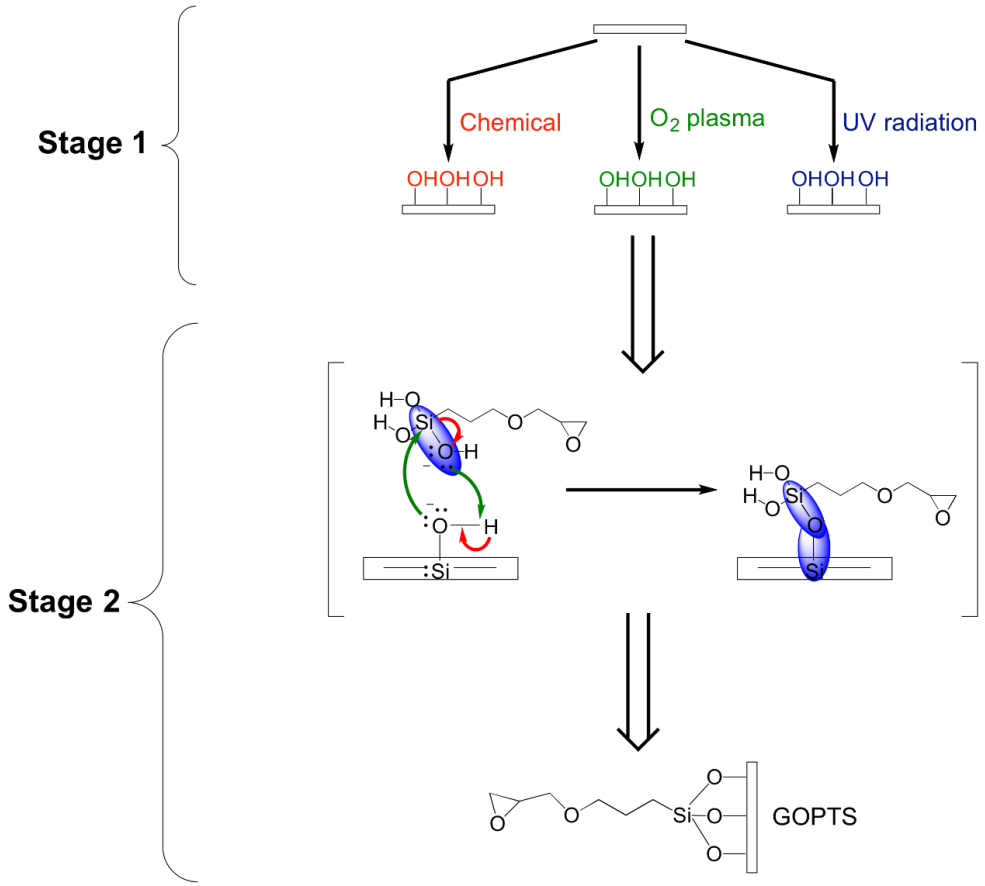
The functionalization of a non-biologically active surface (i.e. borosilicate coverslips) to support neural stem cell differentiation into neurons is presented. The surface modification is accomplished by the salinization of glass coverslips with an epoxy-terminated silane, (3-glycidyloxypropyl)trimethoxysilane (GOPTS); which is then covalently attached with a PEG_{18}-diamine linker to provide a degree of flexibility. The PEG_{18}-diamine linker has an amine terminated functional group that facilitates the tethering (i.e. 'grafting from') of peptides (i.e. RGD and IKVAV) on the surface and enable the interface between surface and the integrins of the cells.

4.2.1 ORGANOSILANES

An organosilane is a silane (i.e. monomeric silicon chemical) that contains at least one carbon-silicon bond (Si-C) and has three characteristic key elements, (i) a non-hydrolysable organic moiety, (ii) an hydrolysable group, and (iii) a spacer. Organosilanes have many applications such as a coupling agent, adhesion promoter, dispersing/ hydrophobic agent, crosslinking agent, blocking agent, silicate stabilizer, and water scavenger [297].

Here we use the GOPTS silane as an adhesion promoter between the glass coverslips and the PEG_{18}-diamine linker to enable immobilization of the peptides on the surface, thus, enabling the maintenance of adhesion even under high temperatures, and acidic/basic conditions. The salinization of a surface occurs in two stages, (i) the activation of the surface

and (ii) functionalization of the surface with the silane. Surfaces of inorganic additives (i.e. silicon oxide and metal oxide) can be activated via the contamination removing processes such as chemical, oxygen plasma, and UV radiation to present hydroxyl groups for silanes to bond with through hydrolysis and condensation reactions, Schematic 4.1. The bonding mechanism is affected by several factors (i.e. pH, thermodynamic compatibility, and activation energy) and the process demonstrates further condensation of the silane after the curing and drying process upon solvent removal of the surface [298-300]. The epoxy functionality in GOPTS makes the silane very reactive (i.e. water, amines, anhydrides, phenols and thiols) and exhibits unique inorganic reactivity, thus, facilitating the immobilization of the amine containing biomolecule of poly(ethyl)glycol (PEG) to be immobilized on the epoxy terminated surface.



Schematic 4.1 Illustrates the chemical adsorption of GOPTS on borosilicate coverslips.

4.2.2 POLY(ETHYLENE)GLYCOL LINKERS

PEG is an inert linear polyether molecule with the synthetic repeating unit of ethylene glycol that is produced in a large range of molecular weight (i.e. linear or branched) and is highly water soluble. PEG is particularly attractive as linkers for conjugation as they improve the surface properties such as solubility, non-toxicity, non-immunogenicity, resistance towards degradation (i.e. *in vivo*), flexibility, cleavable (i.e. enzymatic, pH controlled) and non-cleavable (i.e. peptide and conjugation chemistry) bonds of the surface [301-303]. Moreover, PEG linkers exhibit hydrophilic property due to the -OH terminus groups and the ether oxygen as it forms hydrogen bonding with water, enabling the PEG to reduce the non-specific binding of biomolecules on the surfaces. PEG is an extensively studied polymer for anti-fouling coatings in biomedical devices (i.e. minimizing the adhesion of biofluids such as proteins, cells, pathogens in catheters or implantable devices) or on the hulls of marine vessels (i.e. minimizing coated with marine organisms or their secretions) [304, 305]. Numerous studies have indicated that the properties of PEG such as steric hindrance effect, chain length, grafting density, chain conformation, and hydrophilicity of the grafted polymer play important roles in resisting substance adhesion (i.e. proteins, cells, pathogens, marine organisms) [306, 307]. Furthermore, PEG linker conjugation to a surface or biomolecule will depend on a number of factors such as, chemical structure, molecular weight, steric hindrance, and the reactivity of the biomolecule as well as the polymer, which is governed by the reactive or functional group (i.e. -COOH, -OH, $-NH_2$, and -SH) of the PEG, the surface, and the biomolecule. The conjugation mechanism involves either protection or deprotection of the groups via approaches such as click chemistry, condensation, and self-assembly.

Cruje et al., published in 2014 their research of developing a nanoparticle (NPs) based system to target cancer therapeutics by grafting two PEG chain lengths on gold NPs (GNPs) respectively, (i) longer PEG chain length with high density, (ii) longer PEG chain length with low density, (iii) short PEG chain length with high density, and (iv) short PEG chain length with low density, uptake in cancer cells. Results demonstrated that the higher grafting densities and longer PEG chain lengths showed less protein adsorption and lower GNPs uptake by the cancer cells (i.e. cancer cells in vitro in HeLa, MDA-MB-231 and MCF-7 cells).

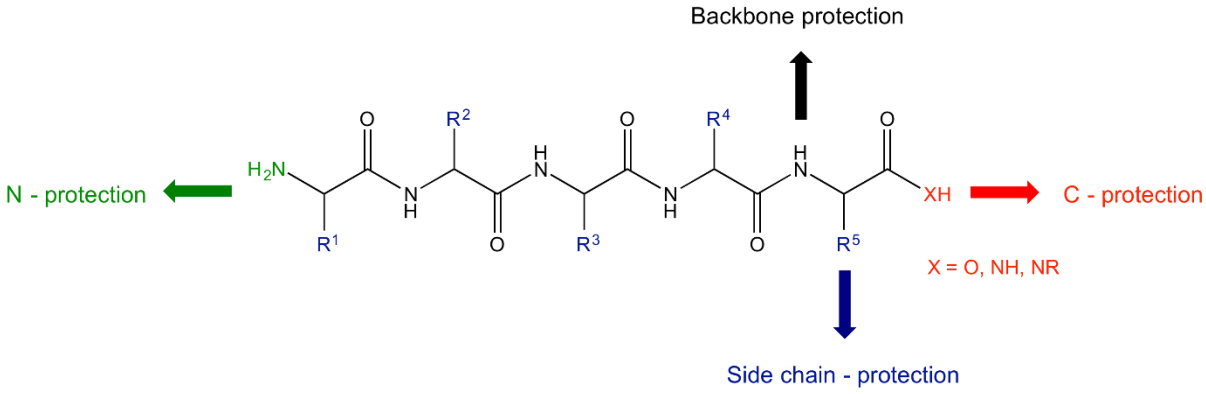
Whilst lower grafting densities and shorter PEG chain lengths indicated higher cellular uptake and greater nonspecific protein adsorption. The most favorable combination was a higher density grafting of shorter PEG chain lengths as the results indicated reduced nonspecific protein adsorption and higher uptake in comparison to the lower density and longer PEG chain length counterparts. Thus, indicating that the PEG chain length and grafting density play crucial role on the behavioral property of the material (i.e. GNPs) in dealing with cellular uptake and clearance from the body [308]. Other literature has demonstrated the use of short and long PEG linkers with repeat units (n) such as (i) n = 4, (ii) n = 8, (iii) n = 18, and n = 24 to mention a few [309-311].

Consequently, we explored the condensation of the amine terminated PEG_{18}-diamine with the epoxy terminated silane functionalized glass coverslips and the amine terminated surface (i.e. PEG-surface) immobilization with peptides [312].

4.2.3 PEPTIDES

Peptides are naturally occurring biomolecules that can also be synthesized and are able to render the surface biocompatible and biodegradable. Hence, the development of peptide-based (i.e. structures of α-helix and β-sheet) biomaterials are for either protein engineering or macromolecular self-assembly applications (i.e. tissue engineering scaffolds, drug delivery matrices, detectors and transducers in biosensors). Moreover, the peptide-based biomaterials are considered "soft" and "wet" in comparison to the "hard" and "dry" surfaces of metals, ceramics and polymers (i.e. expect for the hydrogels) [313]. The immobilization of peptides occurs via two strategies, the 'grafting to' or 'grafting from' the surface [314]. The 'grafting from' is the more straightforward and controlled approach for producing large area films as the peptide is grown from the surface via the amino acid step-by-step build-up versus polymerization (i.e. radical chain polymerization, living cationic polymerization, and ATRP). As polymerization can lead to undesirable side reactions during the peptide synthesis (i.e. uncontrolled synthesis), so side protecting groups are introduced to prevent this (i.e. controlled synthesis). This controlled 'grafting from' follows the ingenious concept of peptide synthesis on a solid support, the solid phase peptide synthesis (SPPS), developed by Robert Bruce Merrified [315]. In this case the solid support is

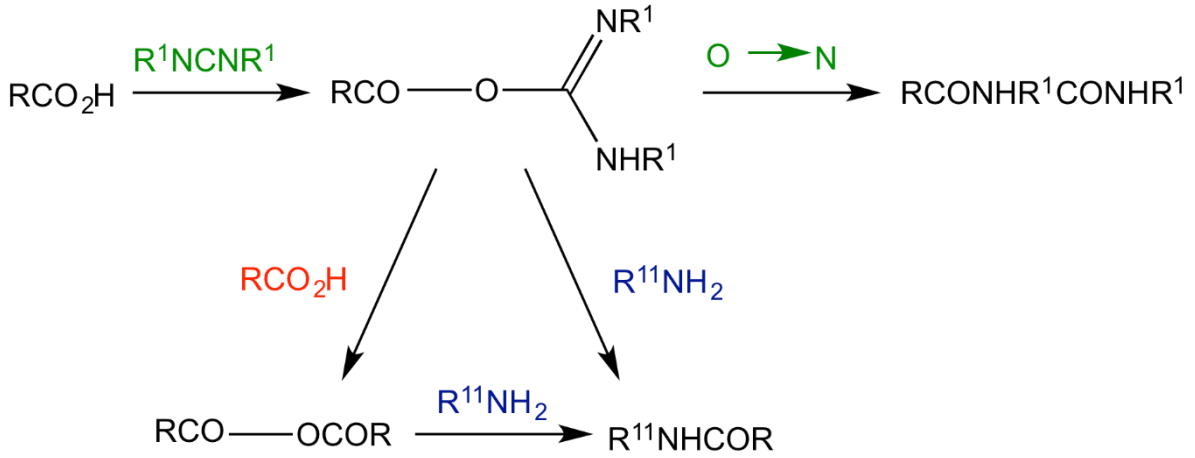
the surface on which the peptide sequence is assembled from the usual manner, starting from the C-terminus and the first amino acid of the peptide to be synthesized is connected via its carboxy group to the amine terminated surface [316]. Moreover, the 'grafting from' strategy has the advantage of not being limited by monomer side chain functionalities (i.e. protecting groups) that are orthogonal with the chain end group used for the conjugation. In contrast, in the 'grafting to' approach the complete peptide sequence is conjugated to the surface, thus, to make the reaction highly efficient an excess of the peptide is required. The major advantage of the 'grafting to' approach lies in that the peptide sequence is initially synthesized, cleaved, purified and characterized via SPPS in a vessel prior to immobilization it on the surface, thus, confirming the correct peptide sequence, Schematic 4.2 [168].



Schematic 4.2 The dissection of a peptide structure whilst taking into consideration potential anchoring sites. Adapted from Fernando Albericio, 2014 [317].

The 'grafting to' and 'grafting from' approaches both adopt the commonly used conjugation mechanism via carbodiimide chemistry. Coupling agents that contain the carbodiimide functionality activate carboxylic acids to form amide and ester formation, thus, making the reaction a very important precursor to the synthesis of peptide links [318]. The carbodiimides such as diisopropylcarbodiimide (DIC), dicyclohexyl carbodiimide (DCC) and 1-ethyl-3-(3-dimethylaminopropyl)carbodiimide (EDC) mediate the conjugation reaction in the presence of an nucleophilic catalyst such 4-Dimethylaminopyridine (DMAP) and Ethyl(hydroimino)cyanoacetate (EHICA) that increase yields and reduce base-induced racemization (i.e. scavenger) [319]. The amino acid coupling reaction (i.e. 'grafting from')

and the peptide coupling reaction (i.e. 'grafting to') involve the carbodiimide reacting with the carboxylic acid groups (i.e. activation) can occur via different ways, (i) intermediate acylating agent is formed, isolated and subjected to aminolysis, (ii) reactive acylating agent is formed from the acid in a separate step(s), followed by immediate treatment with the amine, and (iii) acylating agent generated in situ from the acid in the presence of the amine, by the addition of an activating or coupling agent, Schematic 4.3 [318, 320]. Thus, peptide bond formation occurs, under mild conditions and preferably at room temperature, as a nucleophilic substitution reaction of an amino group (nucleophile) at a carboxy group involving a tetrahedral intermediate.



Schematic 4.3 The mechanism of peptide coupling. The O→N acyl shift is illustrated to give N-acylurea (i.e. tetrahedral intermediate) and racemization, whilst the anhydride and O-acylurea pathways to peptide remain as protagonists. Adapted from Andrew Williams and Ibrahim T. Ibrahim, 1981 [318].

Peptide conjugation to the surfaces can be divided into two categories, (i) growing peptide sequences from primary amino acids linked by native peptide bonds, and (ii) incorporation of other chemical moieties to the peptide sequence to create hybrid materials [321]. Consequently, the initial conjugation approach was implemented for the conjugation of the amino acids on the amine terminated surfaces to generate the RGD and the IKVAV surfaces.

4.3 SURFACE PREPARATION, CHARACTERIZATION AND VALIDATION

4.3.1 SURFACE WETTABILITY AND FLUORESCENCE SURFACES WITH SINGLE PEPTIDE COMPOSITION

The glass coverslips underwent through two cleaning steps to ensure that any remaining volatile organic compounds on the surface have been removed before the surface functionalization procedure. The WCA values were greatly reduced respectively from as-received glass/ organic solvent cleaned glass/ piranha solution cleaned glass ($40.8^{o} \pm 0.4$/ $28.6^{o} \pm 0.8$/ $< 10^{o} \pm 0.6$) to indicate that the glass coverslip surfaces are hydrophilic as illustrated in Figure 4.1. Clean glass coverslips demonstrate surfaces that are very hydrophilic due to the introduced hydroxyl groups introduce by the piranha cleaning solution to present a surface available to react with the chosen silane, GOPTS.

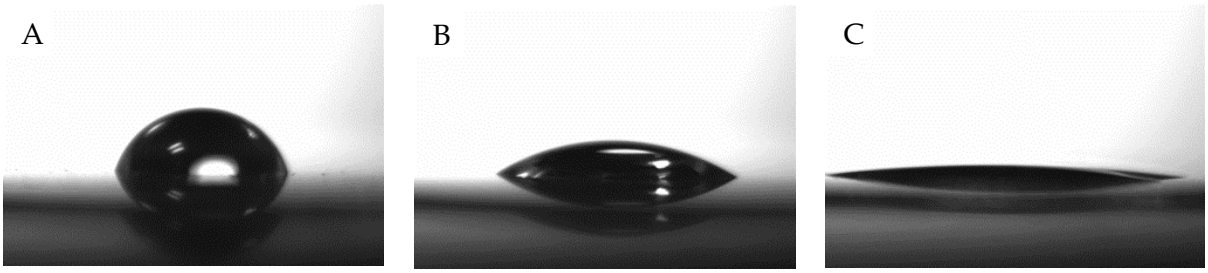
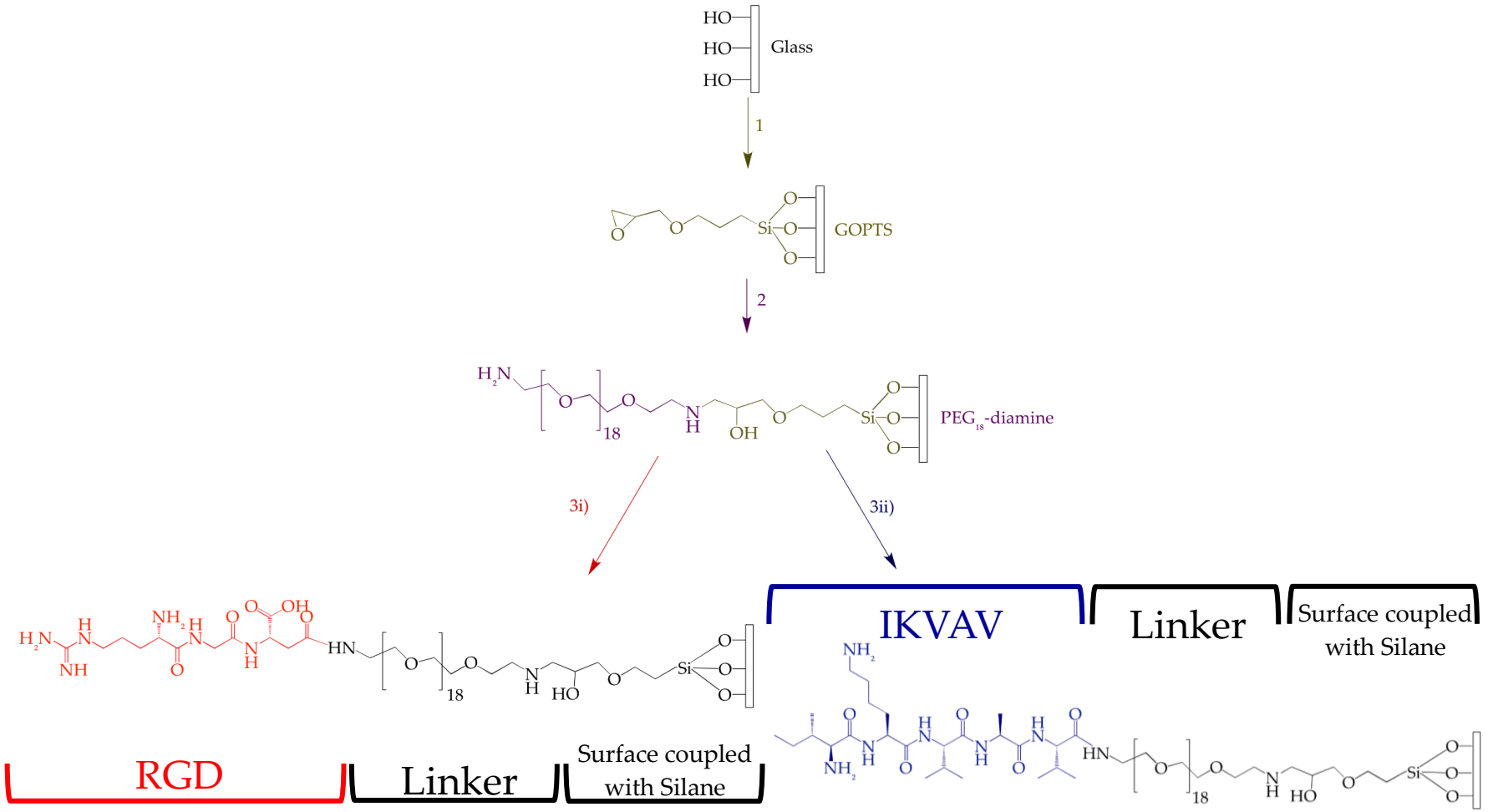


Figure 4.1 The change in the WCA through the cleaning process respectively; (A) as-received, (B) organic solvent cleaned, and (C) piranha cleaned glass coverslips.

Surface wettability is a good indication of the outcome of surface modification as observed with the salinization step where the surface becomes hydrophobic due to the GOPTS hydrocarbon chain and epoxy functional group, $47.6^{o} \pm 0.5$. In addition, the GOPTS provides a functional surface that allows the covalent attachment of the flexible linker chain PEG_{18}-diamine to which the amino acids attach to by 'grafting from' the surface via the solid-phase peptide synthesis (SPPS) approach. A decrease in surface wettability to $37.9^{o} \pm 1.1$ was observed upon functionalization with the PEG_{18}-diamine and the amine terminated functional group of the linker presented on the surface made the glass surfaces more hydrophilic.



Schematic 4.4 The SPPS approach by which the glass coverslips are functionalized to achieve the RGD or IKVAV peptide sequence functionality. Direct preparation of peptide surfaces on glass substrates [322]. (1) GOPTS at 37 °C; (2) PEG_{18}-diamine at 75 °C; (3) Fmoc-amino acid, EHICA, DIC, dry DMF leave for 2 hrs on the orbital shaker; coupling reaction repeated overnight; 20% piperidine in DMF for 2hrs to deprotect; repeat stepwise amino acid build-up until the desired peptide is immobilized on the surface (3i) RGD or (3ii) IKVAV.

The selected peptide, RGD and IKVAV, sequences from the ECM protein laminin will promote cell adhesion, proliferation and differentiate towards neurons (RGD) and astrocytes (IKVAV) [323-325]. The correct build-up of the amino acids in the desired sequence is essential, as the cells will only respond to the correct sequenced peptide, Schematic 4.4. This coupling is a nucleophilic reaction between the amine groups (-NH_2) of the amino acid or peptide and carboxyl group (-COOH) of the next amino acid to be coupled in the peptide sequence, and is commonly catalyzed by the coupling agent EHICA in the presence of an activation agent DIC. The EHICA and/ or DMAP were used to suppress base-induced side reactions (i.e. racemization) by acting as a scavenger in the peptide synthesis of the surfaces functionalized peptides. Other functional groups on the amino acids have side protecting groups to that the amination between the carboxylic acid groups and amino groups will be region-selective specific [326-328]. The measured values of WCA results of the RGD and IKVAV modified surfaces are summarized in Figure 4.2.

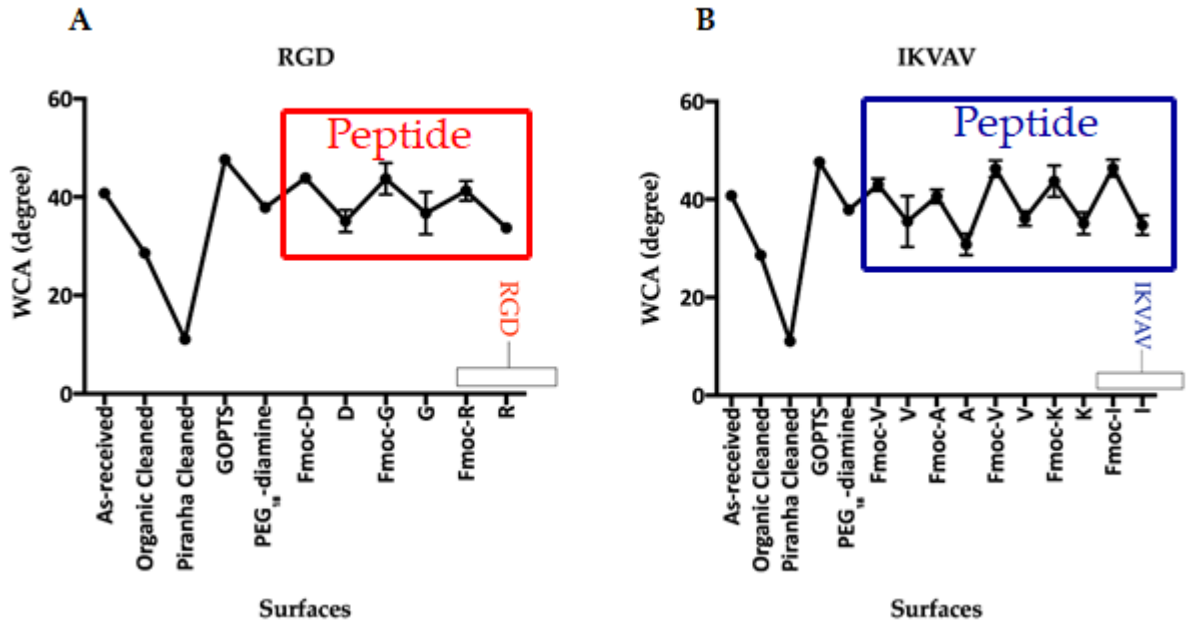


Figure 4.2 Water contact angle measurements through the modification steps to achieve (A) RGD and (B) IKVAV peptide surfaces.

The WCA measurements for RGD and IKVAV respectively, 33.7° ± 1.0 and 34.8° ± 2.0, show a significant increase in hydrophobicity in the presence of the N-terminus protection group of

9-fluorenylmethoxycarbonyl (Fmoc-) coupled amino acids and a decrease in WCA with the removal of the Fmoc-protecting group easily cleaved by 20% Piperidine in DMF base treatment. Fmoc is a hydrophobic and aromatic compound when present in the surface modification promotes hydrophobicity and π-π stacking interactions (i.e. geometry of the aromatic rings) on the surface, whilst the removal of the Fmoc protecting groups causes a decrease in WCA as an amine free terminus is produced on the surface [329-332]. The change in surface wettability indicates the presence or absence of the Fmoc group and provides a trend that can be followed to signify the successful functionalization of RGD and IKVAV via SPPS. Moreover, the Fmoc-protecting group contains a fluorescent fluorenyl ring that is highly UV-active, thus, making it significant in the amino-acid stepwise build-up to follow the self-assemblies of the peptide sequences. Hence, making it a suitable optical property to be explored to validate the functionalization of the amino-acid stepwise build-up. Similar spectral signatures were observed for the emission peak for all the amino acids between 310-330 nm. A practical difference is detected between the Fmoc-protected group present and absent surface. The emission peaks were broad indicating that the intrinsic fluorescence of the Fmoc-protected surface is weaker than it would be in solution due to rapid bleaching, thus, a shorter lifetime as illustrated in Figure 4.3. The spectroscopic recording provided adequate support to the WCA data to say that the surface were functionalized with the self-assembly of amino acids to peptide sequences [333, 334].

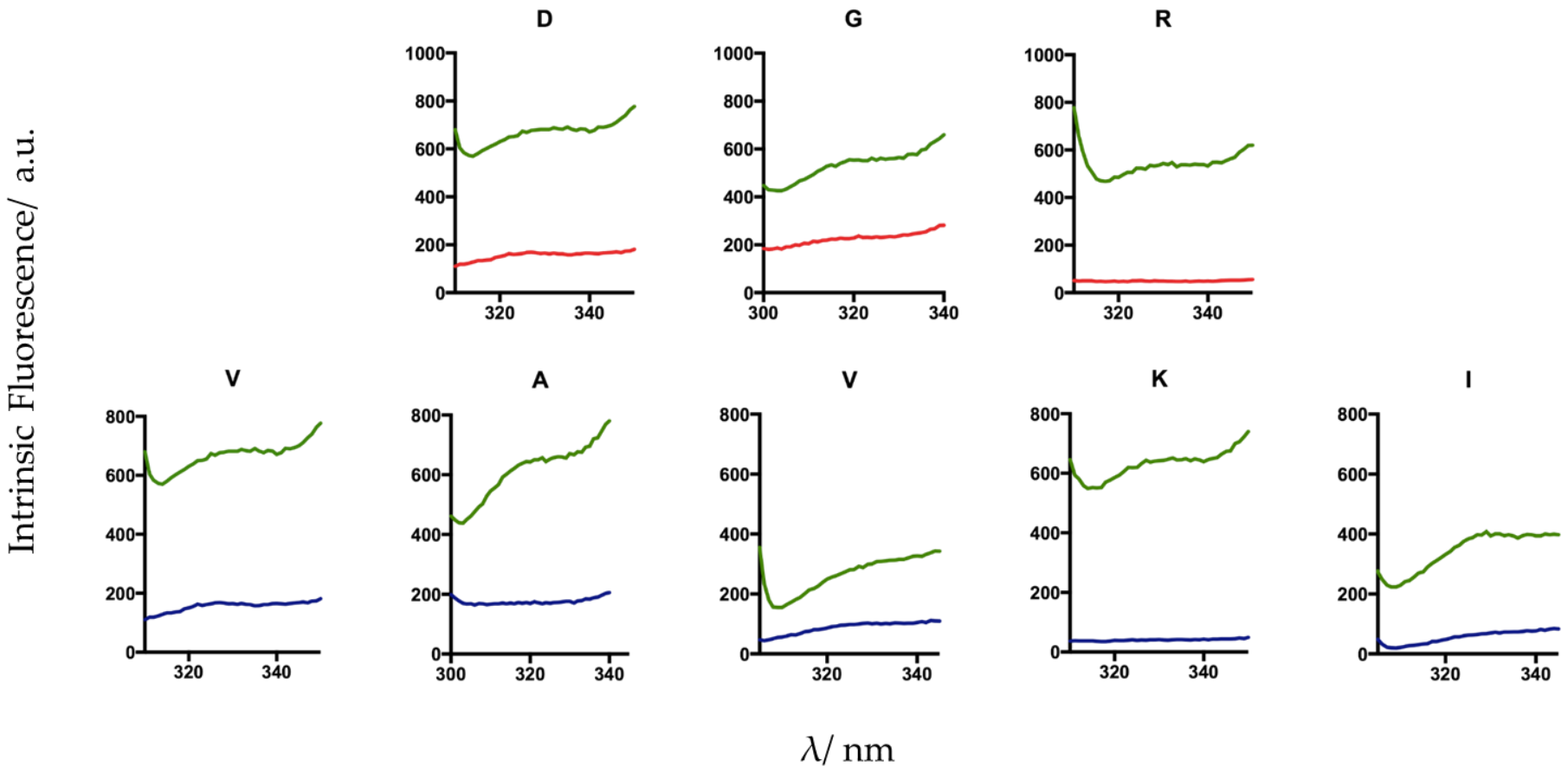


Figure 4.3 Intrinsic fluorescence intensity of the Fmoc-protecting group signal in the present (green) and absence (red and blue) is detected to confirm the build-up of the amino acids to achieve the RGD or IKVAV peptide sequence functionality.

4.3.2 SURFACE TOPOGRAPHY OF SURFACES WITH SINGLE PEPTIDE COMPOSITION

The amino acid build-up of RGD and IKVAV on the surfaces was confirmed by the WCA and next we looked into the surface roughness of the functionalized surfaces. It is desired that the peptides covalently attach to the surfaces by immobilizing in a uniformly assembled monolayer, and therefore providing for reproducible and well-defined surfaces. In 1989, Bennett and Mattson defined the surface roughness as a measure of the topography of a surface and commonly occurs in the form of scratches, digs, pits, dust particles, polishing marks on optical surfaces, machining marks on machined surfaces, granularity or crystallites in films deposited on surfaces [335, 336]. We measured the surface roughness change that occurred through the surface functionalization steps from the as-received glass coverslips to the final peptide functionalized stage (i.e. RGD and IKVAV surfaces) to gain appreciation of the covalent bonding between the amino acids via SPPS and the morphology of the structures on these surfaces by AFM [335]. AFM topography images (i.e. height and phase mode) of 1 μm x 1 μm were taken of eight surfaces at different stages of surface functionalization, as the observed features are in the nanometer range. The average and standard deviation of three different samples of the same functionalized surfaces was used to calculate the root mean square (RMS) and z-range.

Figure 4.4 shows the AFM height images with their profile plot measurements, which were calculated by three selected lines through the AFM height image. The as-received glass coverslip shows a surface that contains nano-pits, different patterns of structures of various heights which can be attributed volatile organic debris observed in the WCA measurements that illustrated low surface wettability. The nano-pits are a characteristic feature of glass coverslips and the observed structures are products associated with the manufacturing stage of the surface of glass coverslips, which we observed in different coverslip types and this is supported by literature [337]. The presence of the nano-pits in the glass coverslips does not deleteriously effect the majority of topographic determination of the surface functionalization. The two cleaning steps reduce the surface roughness from 0.40 nm ± 0.16 to 0.21 nm ± 0.07 with a more steady profile plots across the selected sections in comparison to the as-received surface respectively, 8.47 nm ± 3.37 and 6.35 nm ± 2.30. The salinization

step introduces three-dimensional nano-clusters of various sizes with the nano-pits still very visible on the surface indicating that the GOPTS created a monolayer which can be confirmed by the change in the profile plots as well as the z-range and RMS values of 5.80 nm ± 1.35 and 0.28 nm ± 0.05 are within the relative range of that of the Piranha cleaned surface, 6.35 nm ± 2.30 and 0.21 nm ± 0.07. The PEGylation of the surface with PEG_{18}-diamine presented further nano-clusters on the surface and the profile plot illustrates a specific area on the height image that had a z-range of approximately 4 nm, as well as larger aggregates which were saturated indicating that this z-range is not representative of the full height of the features. The surface roughness increased with the PEGylation from 0.28 nm ± 0.05 to 0.46 nm ± 0.16. Moreover, the saturation would suggest that the reaction conditions of PEG_{18}-diamine might possibly also aggregate more than one molecule on the surface. Hence, creating a surface that is fairly homogenous in morphology and topography with the occasional change in z-range due to the aggregation of PEG_{18}-diamine molecules. The PEG_{18}-diamine surfaces were subjected to vigorous basic and acidic conditions to functionalize the final RGD and IKVAV surface, consequently removing any PEG_{18}-diamine molecules that were not strongly covalently attached to the surface. This is further observed as a decrease in z-range and RMS measurements from the PEG_{18}-diamine surface to the peptide functionalized surfaces illustrated in Table 4.1 and Figure 4.5. The AFM height images showed an interesting difference between the peptide surfaces with the RGD surface having a higher z-range and RMS value in comparison to the IKVAV surface respectively, 5.86 nm ± 1.47 versus 5.46 nm ± 1.25 and 0.34 nm ± 0.06 versus 0.24 nm ± 0.05 which we believe is related back to the PEGylation stage of the surfaces. The z-range and RMS values for RGD and IKVAV indicate that there is no significant difference between the two functionalized surface (i.e. not significant at the 5%). However, such differences in surface roughness (i.e. nanotopography) between the RGD and IKVAV surface could possibly contribute to the cell fate of the NPSCs along with the chemical composition of the surface [338].

These results demonstrate that the surface characterization by AFM validate that the functionalized surfaces are homogenous within an nm scale to another.

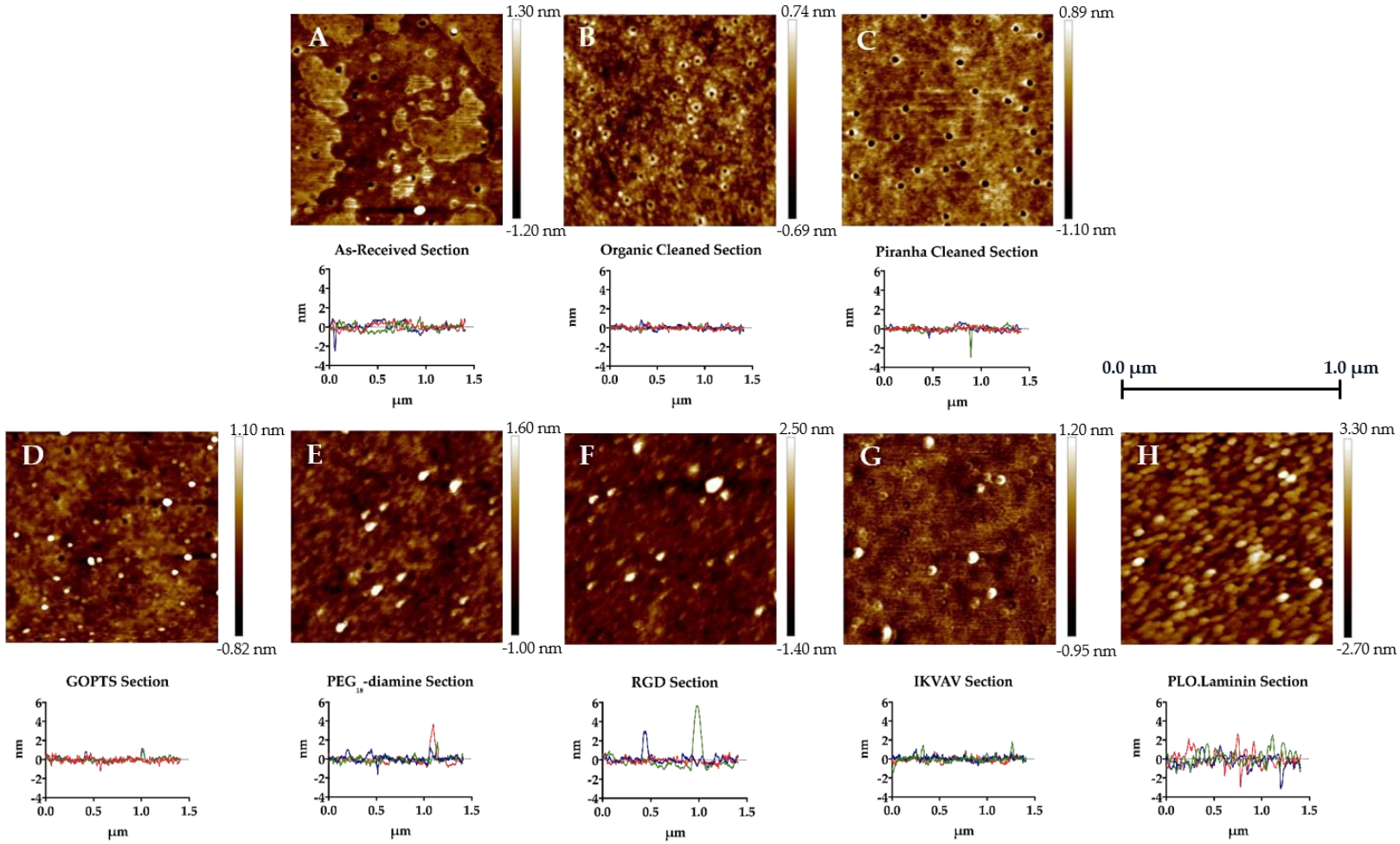


Figure 4.4 The AFM topography images observe the change in surface roughness (nm) through the two-step cleaning process respectively to the peptide functionalized surfaces. (A) As-received, (B) organic solvent cleaned, (C) piranha cleaned, (D) GOPTS, (E) PEG_{18}-diamine, (F) RGD, (G) IKVAV, and (H) PLO.Laminin functionalized glass coverslips. The profile plots illustrate approximately a height between -4 nm and 6 nm, which corresponds to three lines through the AFM topography image.

Table 4.1 Z-range and RMS measurements of the functionalized surfaces obtained from the corresponding AFM Height images, n = 3.

Surfaces	z-range (nm)	± SD (nm)	RMS (nm)	± SD (nm)
As-received	8.47	3.37	0.40	0.16
Organic Solvent Cleaned	3.53	1.81	0.18	0.02
Piranha Cleaned	6.35	2.30	0.21	0.07
GOPTS	5.80	1.35	0.28	0.05
PEG_{18}-diamine	7.23	1.61	0.46	0.16
RGD	5.86	1.47	0.34	0.06
IKVAV	5.46	1.25	0.24	0.05
PLO.Laminin (Control)	9.02	3.10	0.76	0.40

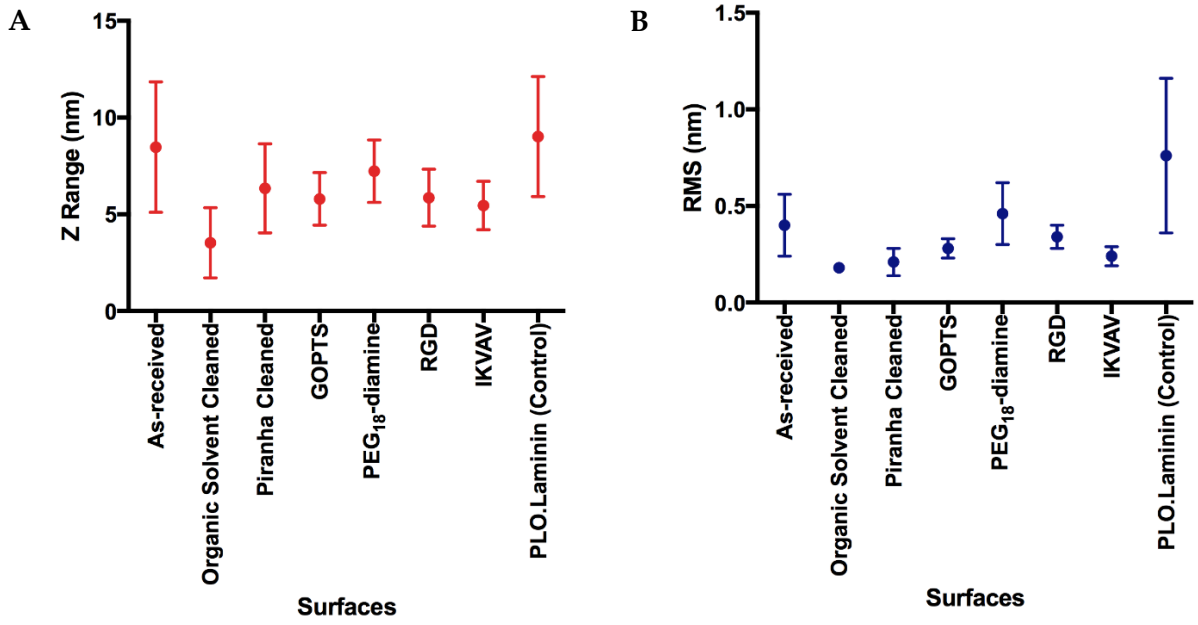


Figure 4.5 (A) Z-range and (B) RMS measurements of the functionalized surfaces obtained from the corresponding AFM Height images, n = 3.

Furthermore, a known positive control surface of PLO.Laminin was chosen on which the NPSC adhere, proliferate and differentiate was also characterized. The PLO.Laminin surface demonstrated in comparison to the peptide surfaces a higher surface wettability of 23.8° ± 1.6 and higher z-range and RMS values of respectively, 9.02 nm ± 3.10 and 0.76 nm ± 0.40.

We also observed in the PLO.Laminin topography image an artifact that could be attributed to AFM tip picking up some of the laminin leaching of the surface of the control sample. As a result we repeated the measurement for the control sample, PLO.Laminin, with a new AFM tip to validate this hypothesis, which the measurements confirmed a similar AFM topography images for the PLO.Laminin as that in Figure 4.4.

4.3.3 TOF-SIMS STUDIES OF MODIFIED GLASS SURFACES

ToF-SIMS analysis was performed to characterize the surface modification of the functionalized surfaces by identifying ion fragments of interest in the positive polarity (i.e. all amino acid fragments of interest are in the positive polarity) on the following surfaces; (i) piranha cleaned, (ii) GOPTS, (iii) PEG_{18}-diamine, (iv) RGD and (v) IKVAV. The outer 10-20 Å surface chemistry and morphology of the surfaces are analyzed by ToF-SIMS to detect the secondary ions generated from the surface and their intensities recorded as a mass spectrum, thus, providing molecular information in the form of marker ion fragments that are distinct to the surface modification. The selected ion fragments were identified in previous publications and were used to determine the surface composition of the five surfaces [339-344]. Accordingly only the major secondary positive ion peaks were labelled in the overlay spectrum in Figure 4.6 and Table 4.2.

The surfaces in the overlay correspond to the labelled ion fragment peaks that are labelled in the piranha cleaned surface. For the data processing the intensity of these ion fragment peaks were normalized to the total ion counts, thus, correcting for differences in total secondary ion yield from spectrum to spectrum, as this can result due to instrumental drift.

The five different surface functionalization stages were analyzed further by considering the change in the intensity of the selected ion fragments to confirm the surface modification at each of those five stages as demonstrated in Figure 4.7. A unique ion fragment was identified for each surface and the presence, absence and/or change in intensity magnitude was observed. Hence, providing an enhanced overview of Figure 4.8 by focusing on those specific differences in the atomic composition of those surfaces. The mass spectra overlay in Figure 4.9 illustrates the absence of the amino acids ion fragments selected on the piranha cleaned surface and the presence of the significant peak at m/z = 28 to represent the silicon

ion fragment attributed to the borosilicate in the piranha cleaned surface. The unique ion fragments for GOPTS and PEG_{18}-diamine, respectively CH_3O^+ and $C_2H_5O^+$, were absent in the piranha cleaned surface and present only after their surface modification step. In accordance with literature values the following secondary ion fragments (i.e. positive) for the amino acids were observed for R (m/z = 70.08), G (m/z = 30.04), D (m/z = 88.09), I (m/z = 86.11), K (m/z = 84.10), V (m/z = 72.09) and A (m/z = 44.06). In the ToF-SIMS spectra for piranha, PEG_{18}-diamine, RGD and IKVAV peaks attributable to PDMS were observed at intensities low enough that any associated effects on the measurement can be considered negligible [345, 346]. The ToF-SIMS data obtained demonstrated a similar trend in the ion fragment presence or absence due to surface modification as shown in previous literature, thus, confirming the successful amino acid stepwise build-up from the PEG_{18}-diamine coated surfaces [329, 330].

The intensity maps of the selected positive ions fragments were reconstruct to obtained raster images of the surface modification stages of the peptide surfaces. Two field of view images were obtained for each surface providing different type of information. Higher resolution of the atomic composition was obtained with the 500 μm x 500 μm images field of view as illustrated in Figure 4.8; whereas the higher magnification field view of 3 mm x 3 mm provided a better overview of the homogeneity of the surfaces after surface modification illustrated in Figure 4.9. The raster images in Figure 4.8 visually reiterates the information provided in Figure 4.7, which validates the peptide functionalization of RGD and IKVAV on the PEGylated surfaces was successful. In addition, Figure 4.9 further confirms the homogeneity of the surface coverage relative to the intensity of secondary ion fragments characteristic to surface and overlay (i.e. surface modification), thus, supporting the high resolution images of the AFM measurements demonstrated in Figure 4.4.

Table 4.2 Positive ion peaks selected for the ToF-SIMS analysis to construct as raster images to illustrate the homogenous surfaces. Normalized ion intensity (x 10^6).

Source	Ion Assignment	Piranha		GOPTS		PEG_{18}-diamine		RGD		IKVAV	
		m/z	Dev.(ppm)	m/z	Dev.(ppm)	m/z	Dev.(ppm)	m/z	Dev.(ppm)	m/z	Dev.(ppm)
Glass	Si^+	27.9758	-20.40	27.9731	-115.30	27.9773	34.00	27.9753	-37.10	27.9760	-13.80
GOPTS	CH_3O^+	31.0186	23.20	31.0191	41.60	31.0209	97.80	31.0211	105.60	31.0212	109.50
PEG_{18}-diamine	$C_2H_5O^+$	45.0347	26.80	45.0561	58.10	45.0376	92.30	45.0383	107.40	45.0380	99.50
Arginine	$C_4H_8N^+$	70.0756	150.10	70.0736	120.90	70.0688	52.50	70.0728	109.60	70.0689	54.40
Glycine	CH_4N^+	30.0368	100.50	30.0387	160.80	30.0379	134.40	30.0369	100.90	30.0368	100.10
Aspartic acid	$C_3H_6NO_2^+$	88.0321	-81.70	88.0431	43.00	88.0545	173.00	88.0531	156.80	88.0547	175.20
Isoleucine	$C_5H_{12}N^+$	86.1006	48.00	86.1030	76.20	86.1013	56.70	86.1001	42.40	86.1029	74.70
Lysine	$C_5H_{10}N^+$	84.0877	82.50	84.0903	113.30	84.0870	74.20	84.0857	58.60	84.0872	76.70
Valine	$C_4H_{10}N^+$	72.0905	135.00	72.0867	82.80	72.0908	139.50	72.0878	97.60	72.0882	103.40
Alanine	$C_2H_6N^+$	44.0546	116.60	44.0561	150.80	44.0509	32.90	44.0518	52.50	44.0506	25.40

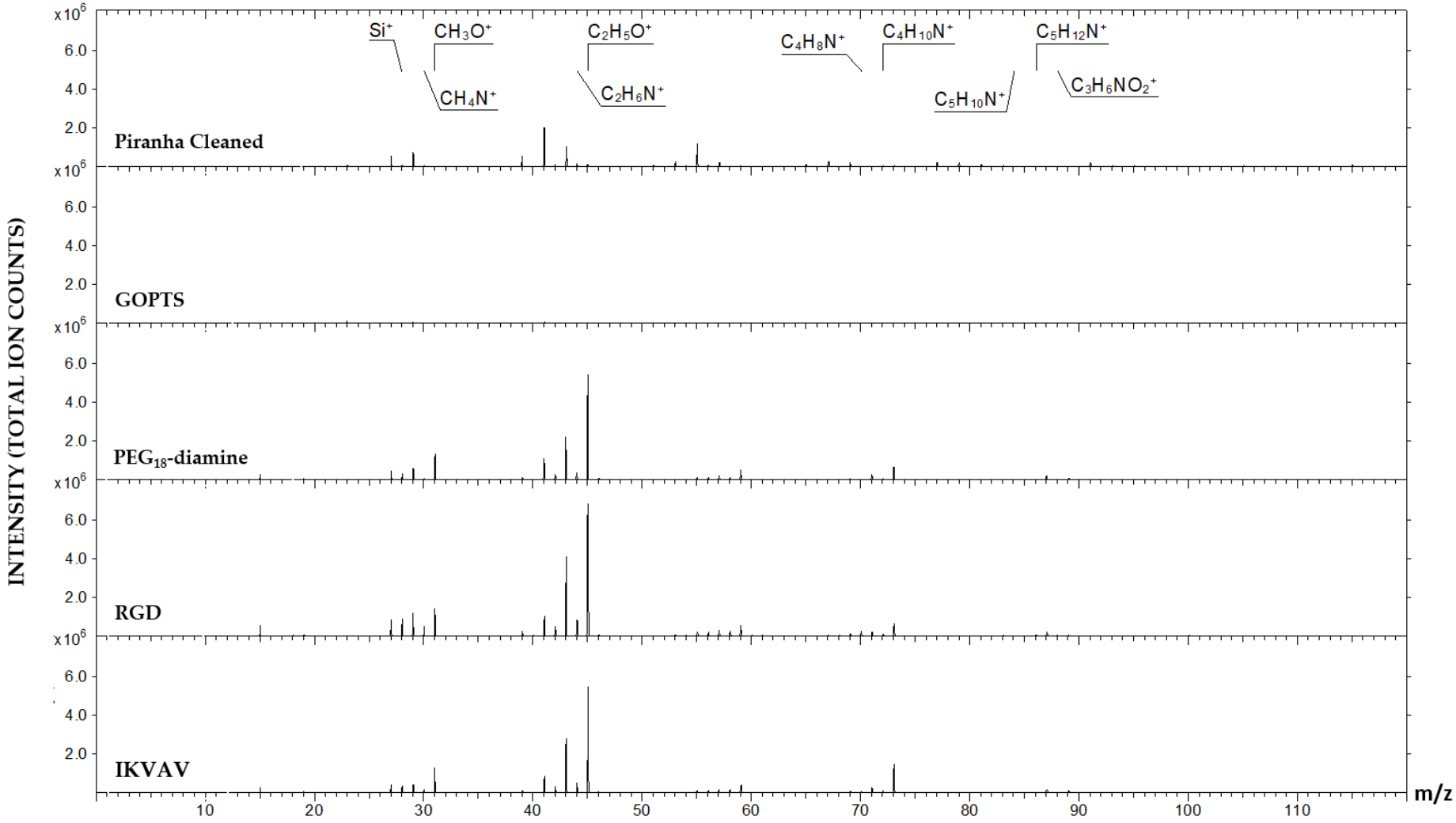


Figure 4.6 ToF-SIMS overall spectrum of the functionalized surfaces annotated with the selected positive ion peaks and normalized to the total ion count.

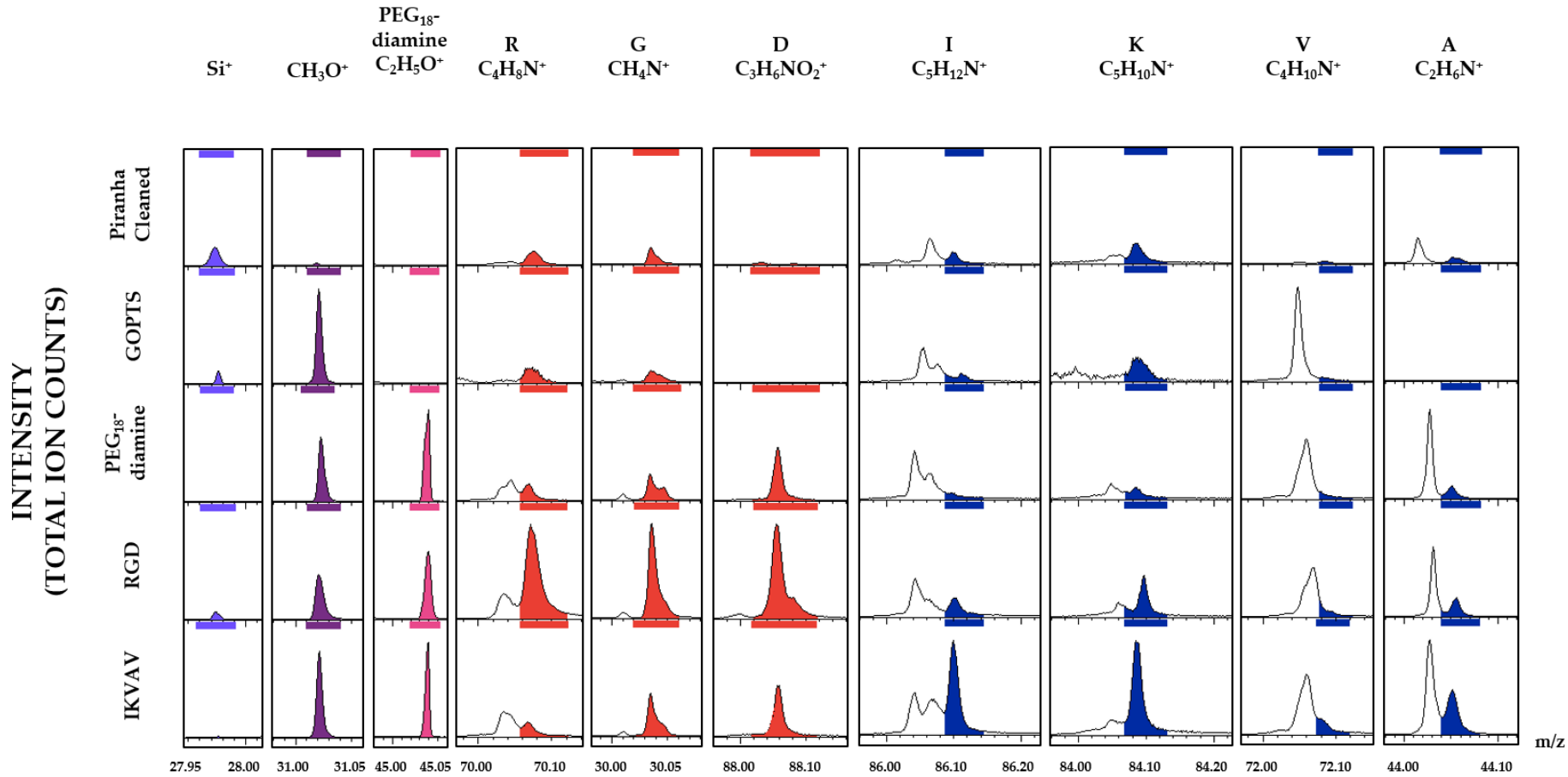


Figure 4.7 ToF-SIMS characterization of marker ion fragments of amino acids distinguishable for surface modification and normalized to the total ion count.

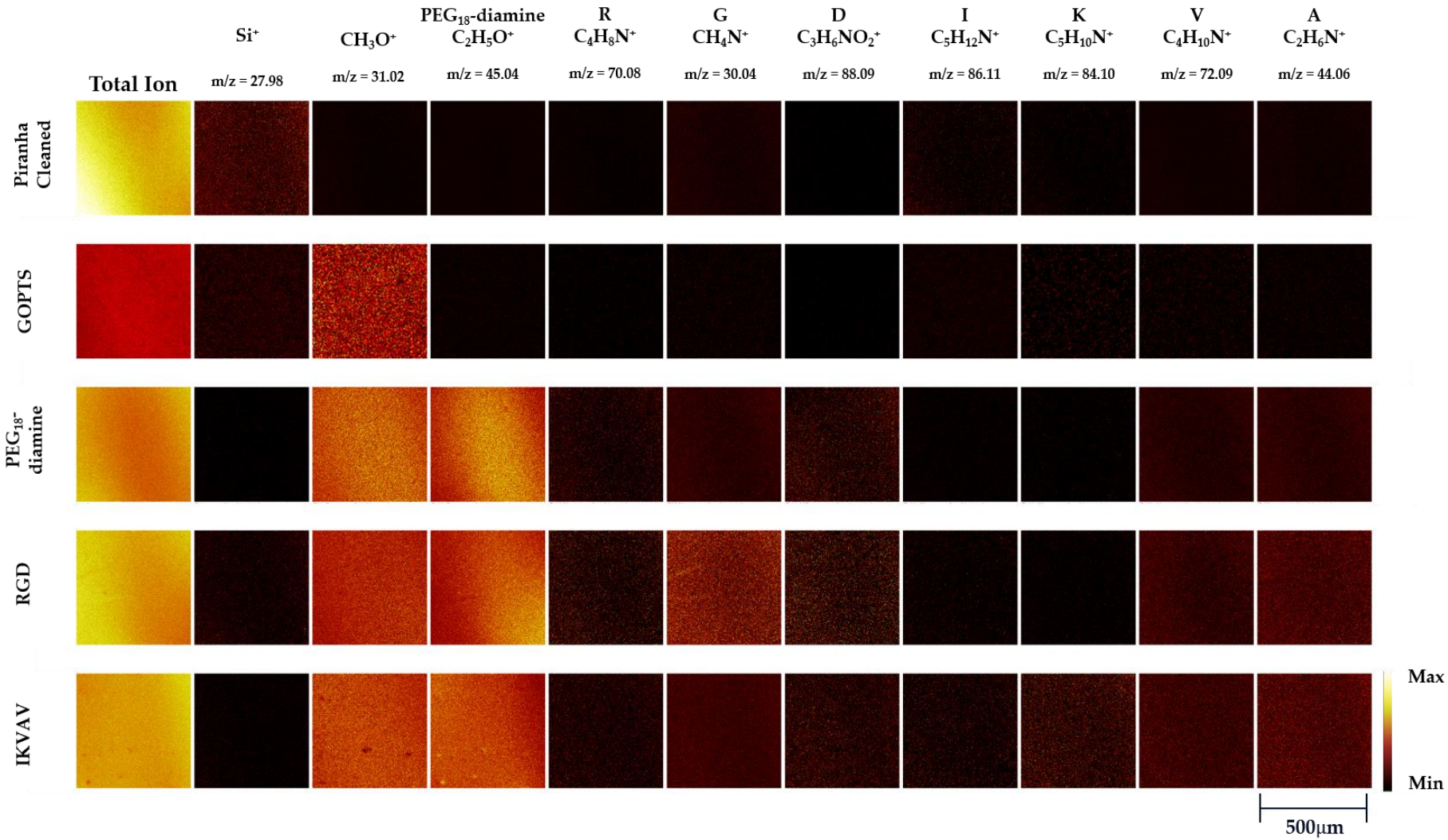


Figure 4.8 ToF-SIMS analysis of the marker ion fragments as raster images to illustrate the homogenous surfaces and normalized to the total ion count, scale is 500 µm x 500 µm.

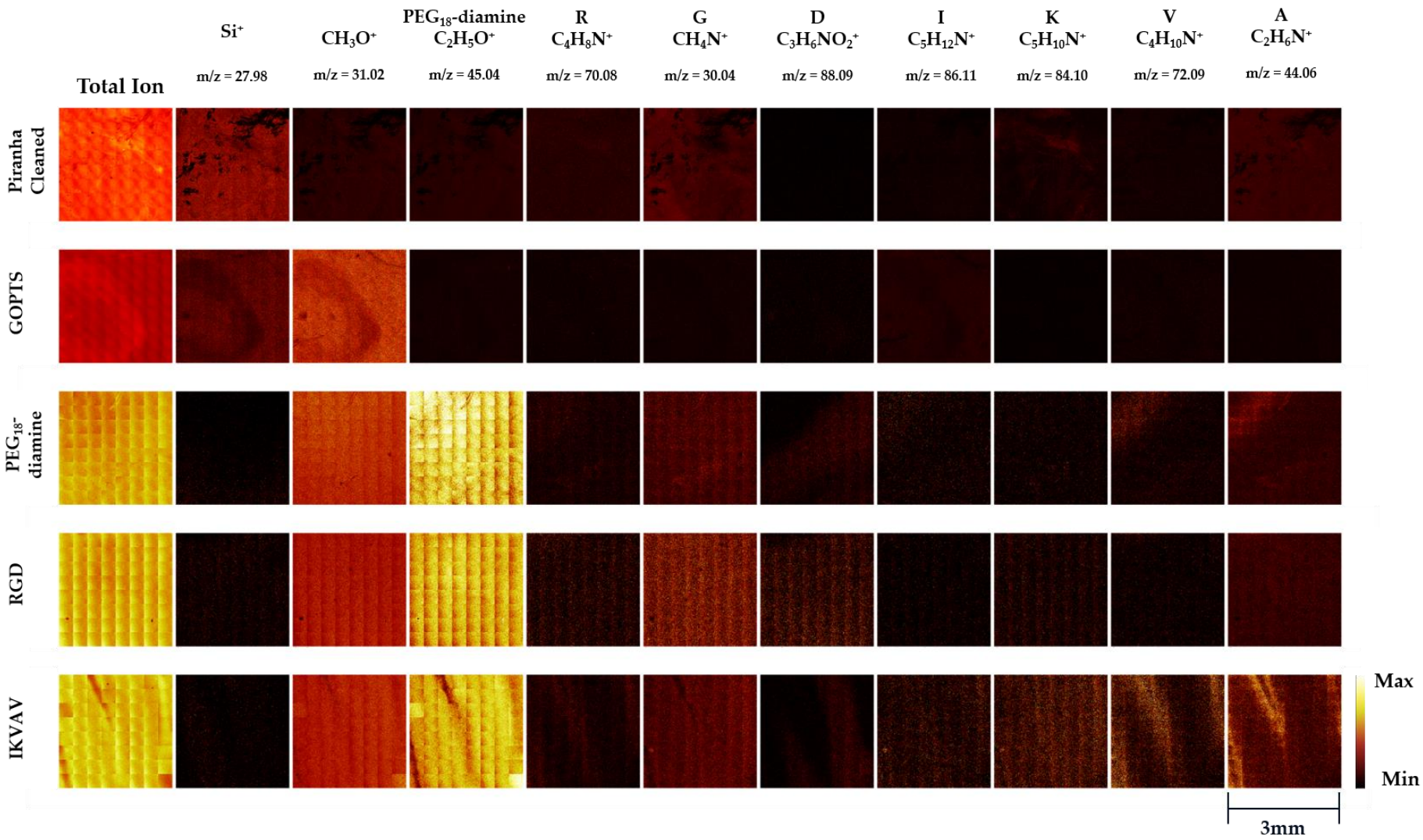


Figure 4.9 ToF-SIMS analysis of the marker ion fragments as raster images to illustrate the homogenous surfaces and normalized to the total ion count, scale is 3 mm x 3 mm.

4.3.4 XPS STUDIES OF MODIFIED GLASS SURFACES

To further elucidate the extent of the peptide grafting surface functionalization to support the semi-quantitative technique of ToF-SIMS an X-ray photoelectron spectroscopy (XPS) study was carried out. XPS is a surface sensitive technique, with probing depths of typical 1-25 nm (5 μm) and area analysis of 10-150 μm for organic materials that provides element-specific chemical state information. XPS chemical shifts vary as function of the chemical state of an element and its local chemical environment, and detailed characterization of amino acids and peptides have been carried out by XPS. Moreover, the XPS provides information of the relative elemental composition at the surface through the peak areas, and is a quantitative technique. The relative elemental atomic concentration of the main elements on the piranha cleaned, GOPTS, PEG_{18}-diamine, RGD and IKVAV modified surfaces were analyzed illustrated in Figure 4.10(A-C) and the chemical shifts due to surface modification observed in Table 4.3 [347-349].

4.3.4.1 WIDE SURVEY O 1s, C 1s, Si $2p_{3/2}$ and N 1s spectra

All the wide survey XPS spectra revealed that O and Si are the predominant species to indicate that the height (i.e. thickness) of the functionalized molecules are a monolayer thick (i.e. ≈ 5-10 nm, relative to the functionalized surface), so the XPS also detects the atomic species of the glass coverslips as the X-ray is able to penetrate. The O and Si species occur at 532 eV and approximately 99 eV, respectively, illustrated in Figure 4.10(B). The piranha cleaned surface demonstrates the major constituents O, Si and presence of the C signal, which is not part of the glass composition and illustrates that even after extensively cleaning the surface is still able to become contaminated by the hydrocarbons in the atmosphere [350]. Amongst the surfaces the piranha cleaned surfaces exhibited the lowest carbon concentration, 14.5% ± 0.4, and the highest oxygen concentration, 51.1% ± 0.2. The C and O signals respectively increased due to the hydrocarbon backbone, and functional epoxy functional group by GOPTS functionalization. Moreover, the expected absence of the N signal was confirmed for the piranha cleaned and GOPTS surfaces. The PEG_{18}-diamine covalent coupling introduced the presence of the nitrogen on the surface, which was detected from its characteristic peak at 399 eV.

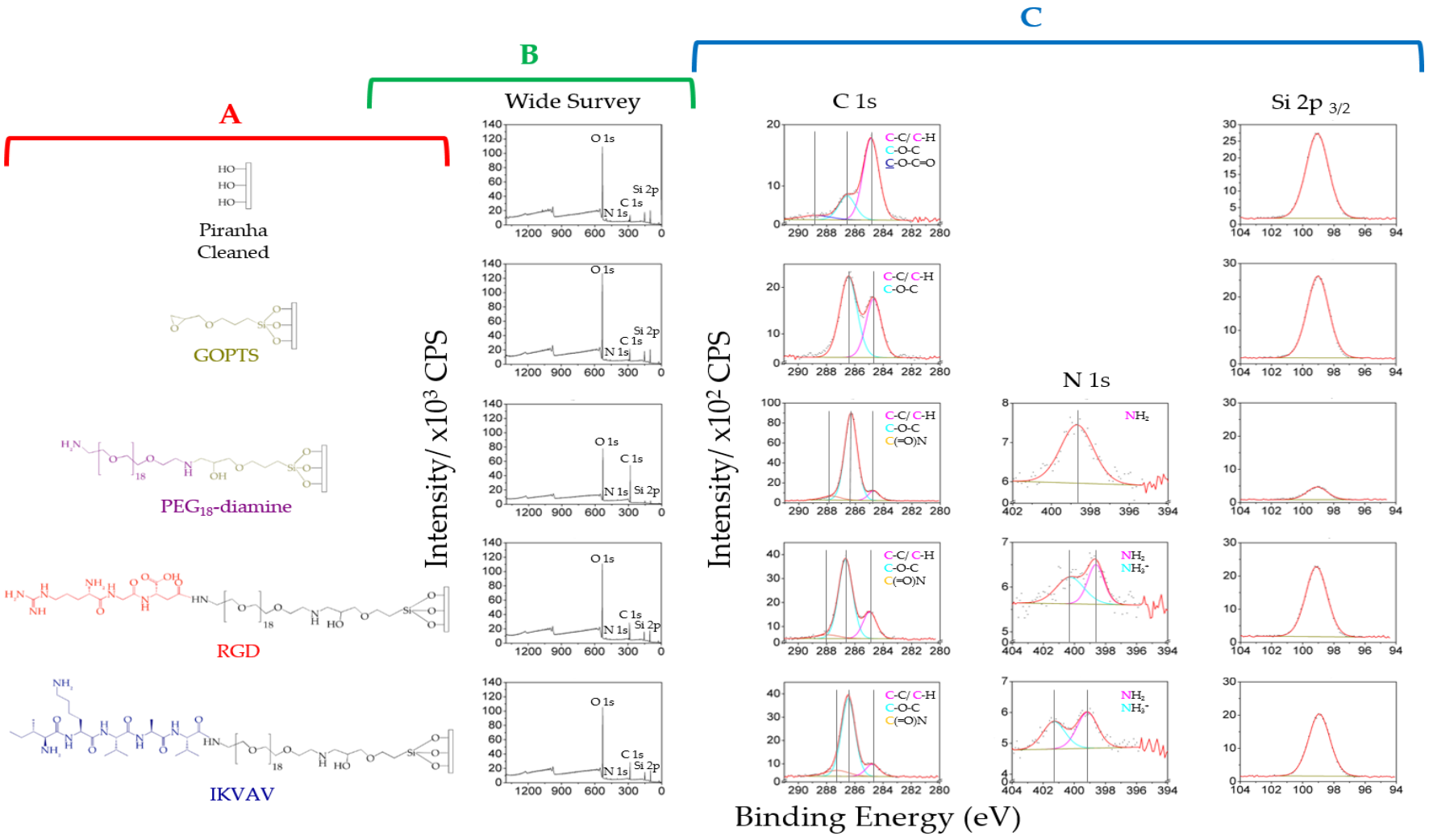


Figure 4.10 XPS anlysis of (A) chemical structures, (B) the wide survey spectra, and (C) high resolution spectra curve fits of the C 1s, N 1s and Si $2p_{3/2}$ core levels of the surfaces. Measured spectrum: black dots, backgorund: green/brown line, and enveope of curve fits: red line.

Table 4.3 XPS chemical shifts (in eV) analysis of the functional groups composition of the surface functionalization.

Species	Surfaces									
	Piranha		GOPTS		PEG_{18}-diamine		RGD		IKVAV	
	eV	±SD (eV)	eV	±SD (eV)	eV	±SD (eV)	eV	±SD (eV)	eV	±SD (eV)
C-C	284.8	0.08	284.86	0.07	284.75	0.05	285.01	0.042	284.79	0.04
C-O	286.47	0.09	286.56	0.05	286.4	0.08	286.687	0.02	286.46	0.01
C(=O)N	/	/	/	/	287.75	0.05	288.34	0.33	287.37	0.18
C(=O)OC	288.62	0.34	/	/	/	/	/	/	/	/
NH_2	/	/	/	/	398.95	0.23	398.64	0.02	399.09	0.06
NH_3^+	/	/	/	/	/	/	400.6	0.3	401.25	0.16

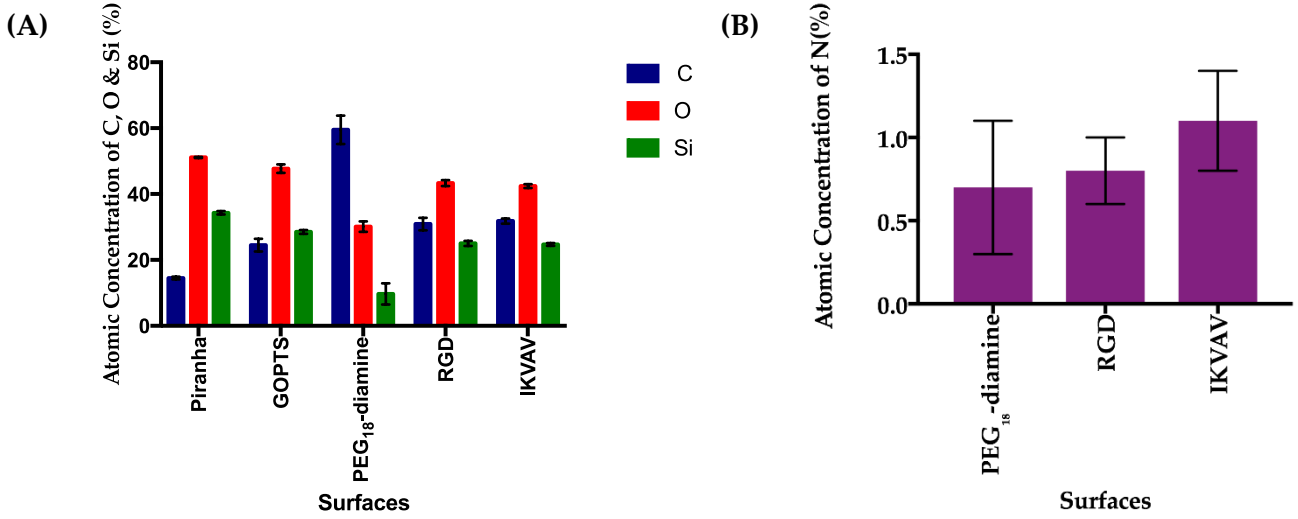


Figure 4.11 The relative atomic concentration (%) of the main elements (A) carbon, oxygen and silicon, and (B) nitrogen on functionalized surface.

A significant reduction in the O signal from 51.1% ± 0.2 to 30.1% ± 1.6, and Si signal from 34.3% ± 0.5 to 9.7% ± 3.2 was observed due to the increase of the hydrocarbon backbone of the flexible linker; whilst also presenting an increase in C signal from 14.5% ± 0.4 to 59.5% ± 4.3 and N signal from no value to 0.7% ± 0.4. The RGD and IKVAV peptide grafting illustrates the previously mentioned suspicion that the strong basic and acidic conditions washed away those unattached PEG_{18}-diamine, as illustrated in Figure 4.11. Consequently, demonstrating RGD and IKVAV surfaces that are reduced in C signal and increased in O, Si and N signals, respectively confirming the chemical surface change. The O, Si element increase corresponds to the removal of any unattached PEG_{18}-diamine, whilst the increase of N element can be attributed to the functionalization by the amine terminated flexible linker and amino acids. Moreover, the percentage of PEG_{18}-diamine that had an available upright amine functional group (i.e. not folded over or in due to the flexible chain) to react with is difficult to calculate, so it is quantified inclusive as the percentage of nitrogen present on the surface due to the PEG_{18}-diamine as the % atomic concentration of N demonstrates a value of 0.7% ± 0.4. Thus, indicating a high significant difference in the available amount of N quantified (i.e. available, left unreacted, reacted) on the surface. The extensive washing, extended duration of 2 hrs functionalization with amino acid/ wash, and overnight functionalization with the same amino acid/ wash (i.e. new amino acid reaction solution) procedure on the PEG_{18}-diamine surfaces was done to increase the chance of the peptide bond forming (i.e. the reaction of the available amine of the PEG_{18}-diamine with the carboxyl group of the amino acid).

4.3.4.2 HIGH-RESOLUTION O 1s, C 1s, Si $2p_{3/2}$ AND N 1s SPECTRA

In order to obtain more XPS information, high-resolution scans of the XPS spectra of C 1s, N 1s and Si $2p_{3/2}$ core levels with their respective deconvolutions were obtained, as shown in Figure 4.10(C).The functional group composition was determined by deconvolution of the C 1s emission spectrum by fitting curves to the C 1s core levels signals. The individual peaks were referenced accordingly to previously published data, therefore using the C-C/C-H component at 284.8 eV to restrict the full width half maximum (FWHM) of all components and fixing the chemical environment positions of the other components corresponding to increasingly electronegative chemical environments [350]. The resulting chemical

modification of the surface was observed by XPS through alteration in the elemental composition, which became evident through additional carbon, oxygen and nitrogen photoemission features.

The chemical environment change from piranha cleaned to GOPTS surface indicates the increase in the C-O environment, 286.47 eV ± 0.09 to 286.56 eV ± 0.05, due to the functionalization of the epoxy group. The adventitious hydrocarbon contamination can be attributed to the C(=O)OC at 288.62 eV ± 0.34 on the piranha cleaned surface is absent in the GOPTS surface. The chemical environment change from piranha cleaned to GOPTS surface indicates the increase in the C-O environment, 286.47 eV ± 0.09 to 286.56 eV ± 0.05, due to the functionalization of the epoxy and ester functional groups. The adventitious hydrocarbon contamination can be attributed to the C(=O)OC at 288.62 eV ± 0.34 on the piranha cleaned surface is absent in the GOPTS surface.

A significant increase in the intensity/x10^2 CPS of the C-O chemical environment is observed with a shift from 286.56 eV ± 0.05 to 286.40 eV ± 0.08, which corresponds to the repeating backbone of the PEG_{18}-diamine that contains an ester group as shown in Figure 4.12. The C-C/C-H chemical environment did not change drastically from the original piranha cleaned surface, GOPTS and then to the PEG_{18}-diamine with a shift respective, from 284.80 eV ± 0.08/ 284.86 eV ± 0.07/ 284.75 eV ± 0.05, across the chemical change of these surfaces. However, the concentration decreased of the C-C/C-H chemical environment in comparison the C-O chemical environment. Furthermore, a chemical shift was observed at 287.75 eV ± 0.05, after the PEG_{18}-diamine functionalization that corresponds to the characteristic peak of the amide group C(=O)N.

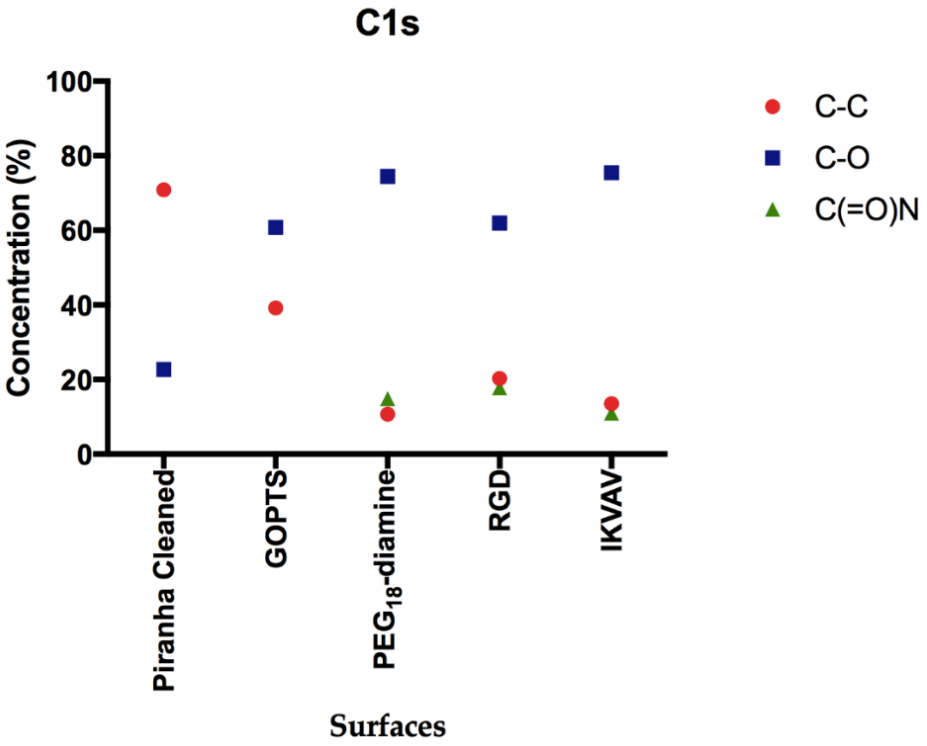


Figure 4.12 The concentration (%) of the chemical environments in C 1s core levels through the surface functionalization.

The immobilization of RGD and IKVAV peptide on the flexible linker caused an increase in the amide group C(=O)N, 287.75 eV ± 0.05/ 288.34 eV ± 0.33/ 287.37 eV ± 0.18, which is due to the peptide bonds between the amino acids during SPPS illustrated in Table 4.3. This further confirms the evolution of the immobilization of the peptides on the piranha clean surfaces.

The N 1s core level spectra demonstrates the evolution of the functionalization with a linker and amino acids leads to further chemical modification of the surface by introducing the N 1s photoemission signal at 399 eV, which is specific of an amide bond. An increase in nitrogen resulted from the covalent coupling of PEG_{18}-diamine, 398.95 eV ± 0.23, introducing amide peptide linkage on the surfaces. It is to be noted that a lower photoemission below 400 eV is distinctive for an amine group (-NH_2), whist an energy level above 400 eV is attributed to a protonation group (-NH_3^+).

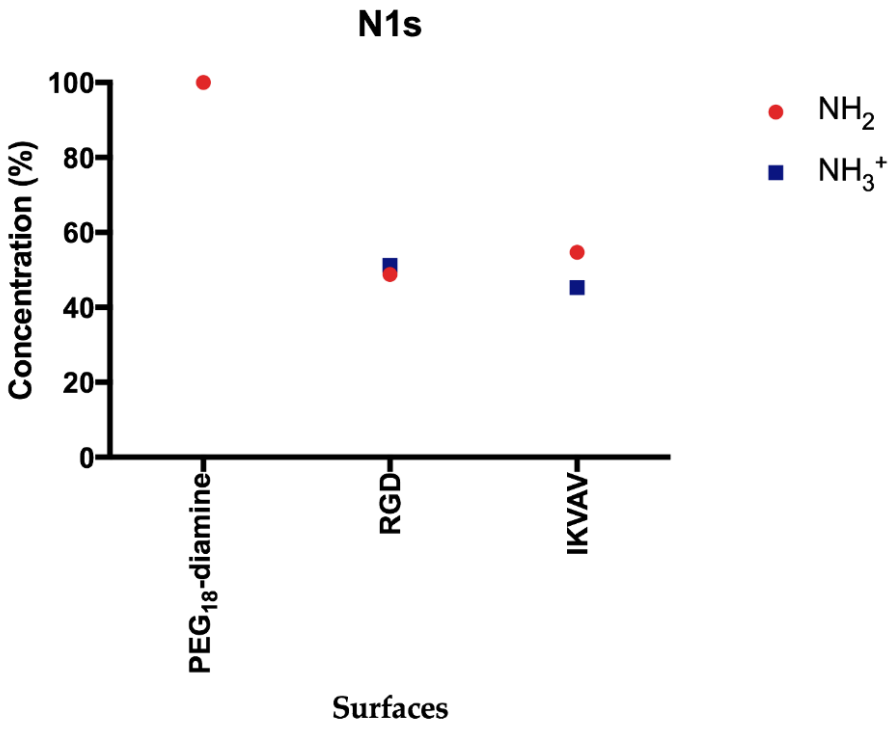


Figure 4.13 The concentration (%) of the chemical environments in N 1s core levels through the surface functionalization.

The immobilization of RGD and IKVAV caused a decrease in the concentration of the NH_2 functional group with a chemical shift respectively at, 398.64 eV ± 0.02 and 399.09 eV ± 0.06 as illustrated in Table 4.3. The presence of the NH_3^+ protonation group on the RGD and IKVAV presented a chemical shift respectively at, 400.60 eV ± 0.30 and 401.25 eV ± 0.16 as shown in Figure 4.13. Consequently, corresponding to the free amines on the side groups of the RGD and IKVAV peptide backbones.

The elemental C/O and N/C concentration change over the evolution of surface functionalization was calculated in Table 4.4. A significant increase in C/O is observed from the piranha cleaned, GOPTS and PEG_{18}-diamine surfaces respectively, 0.28 ± 15.00 to 1.98 ± 1.40, and then reduced on the RGD and IKVAV surfaces. This further confirms our assumption that some unattached PEG_{18}-diamine linkers are still present and only get removed through the washing steps during the immobilization of the RGD and IKVAV surfaces. The N/C ratio also showed an increase from covalently coupling the PEG_{18}-diamine

linker to immobilizing RGD and IKVAV on the surfaces. IKVAV has a higher N/C ratio to RGD, which can be attributed to IKVAV having a longer peptide chain, and therefore more amide linkages on the surafce.

Moreover, the N/C ratio values indicate that the results were not significant in quantifying the chemical composition of the surfaces, which possibly can be related to the thickness of the functionalization to the C/O ratio measured for the glass coverslip. This is something that we took into consideration for any further surface characterization needed to be performed with the XPS technique.

Table 4.4 Ratios of C/O and N/C were recorded to observe the change throughout the surface functionalization.

Surfaces	Ratio of C/O	Ratio of N/C
Piranha Cleaned	0.28 ± 15.00	–
GOPTS	0.51 ± 2.70	–
PEG_{18}-diamine	1.98 ± 1.40	0.0188 ± 8.14
RGD	0.71 ± 3.00	0.0259 ± 4.17
IKVAV	0.75 ± 3.00	0.0346 ± 9.00

4.4 CELL RESPONSE TOWARDS THE IMMOBILIZED PEPTIDE SURFACES

The surface analysis confirmed the immobilization of the RGD and IKVAV peptide sequence on the glass coverslips surfaces, which enabled us to study the effect these peptide surfaces have on the adhesion, proliferation and differentiation of NPSCs

Dissociated NPSCs were seeded at a density of 3 x 10^5 cells/mm^2 on the sample surfaces (diameter = 19 mm) and placed in tissue-culture treated 6 well plates (diameter = 34.8 mm). This was done to increase the chance for the cells to adhere to the surfaces and not the corners of the well plate or underneath the surfaces, which was an issue we observed in the tissue-culture 12 well plates (diameter = 22.1 mm). In addition to the RGD and IKVAV surfaces we had the control surfaces of poly-L-ornithine (PLO).Laminin and PEG_{18}-diamine as comparison parameters to validate against the peptide surfaces. Literature has shown that PLO.Laminin is a surface that supports neuronal stem cell adhesion, proliferation and differentiation into a support system of astrocytes and neural networks [351-353]. The PEG_{18}-diamine was chosen to explore the hypothesis that a surface with just amine terminal groups would not be enough to support NPSCs cultures.

Phase contrast light microscopy images were taken every 2-3 days (i.e. 2DIV, 5DIV, 7DIV, 9DIV, 12DIV, and 14DIV) immediately after changing the media of each well to remove any dead/free floating cells to determine the proliferation and morphology of the cells.

4.4.1 CELL SURVIVAL

The NPSCs were seeded on the RGD, IKVAV, PLO.Laminin and PEG_{18}-diamine surfaces and after the first 6 hrs we found the NPSCs to be round, floating in the media and little to no spreading on the surfaces was observed. Literature has demonstrated that embryonic stem cells must illustrate a rounded cell shape before differentiating into a specific cell lineage [354]. Formation of cell processes (i.e. the formation of axons and dendrites from the cell body of the NPSCs) and adhesion of the cells were observed after 24 hrs only on the PLO.Laminin surfaces, as illustrated in Figure 4.14. This indicates a change from a round cell shape to a flattened morphology, due to the altering of the organization of the cytoskeleton and assembly of the NPSCs.

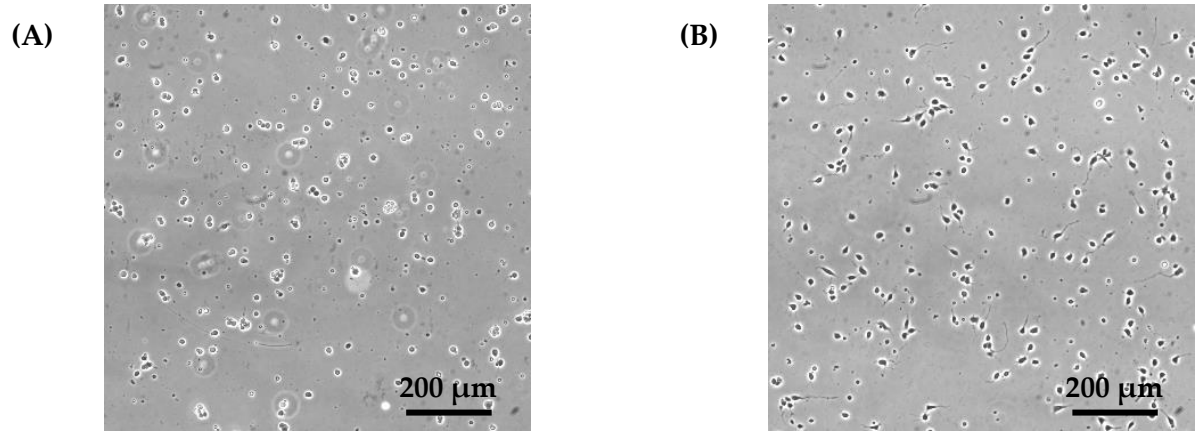


Figure 4.14 Phase contrast images of E18 NPSCs incubated on positive control PLO.Laminin surfaces after (A) 6 hrs and (B) 24 hrs.

The adhesion of the NPSCs on the RGD and IKVAV surfaces took longer than that of the PLO.Laminin surface as some NPSCs adhesion is observed on 2DIV; whilst the PEG_{18}-diamine surfaces demonstrated clusters of cells in the media with very few separate cells (i.e. single cells). The PEG_{18}-diamine surface illustrated the adhesion and lifting off due to the cells being forced to become round, clustering and undergo apoptosis; as demonstrated in Figure 4.15. Thus, clearly indicating that cells require more than just a positively charged primary amine terminal group being present on the surface to have a suitable cell-surface interaction and induce adhesion.

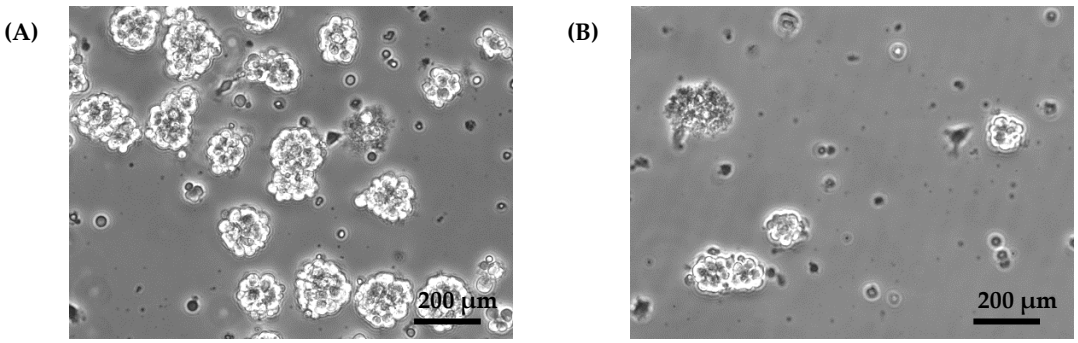


Figure 4.15 Phase contrast images of E18 NPSCs incubated on control PEG_{18}-diamine at (A) 2DIV and (B) 7DIV.

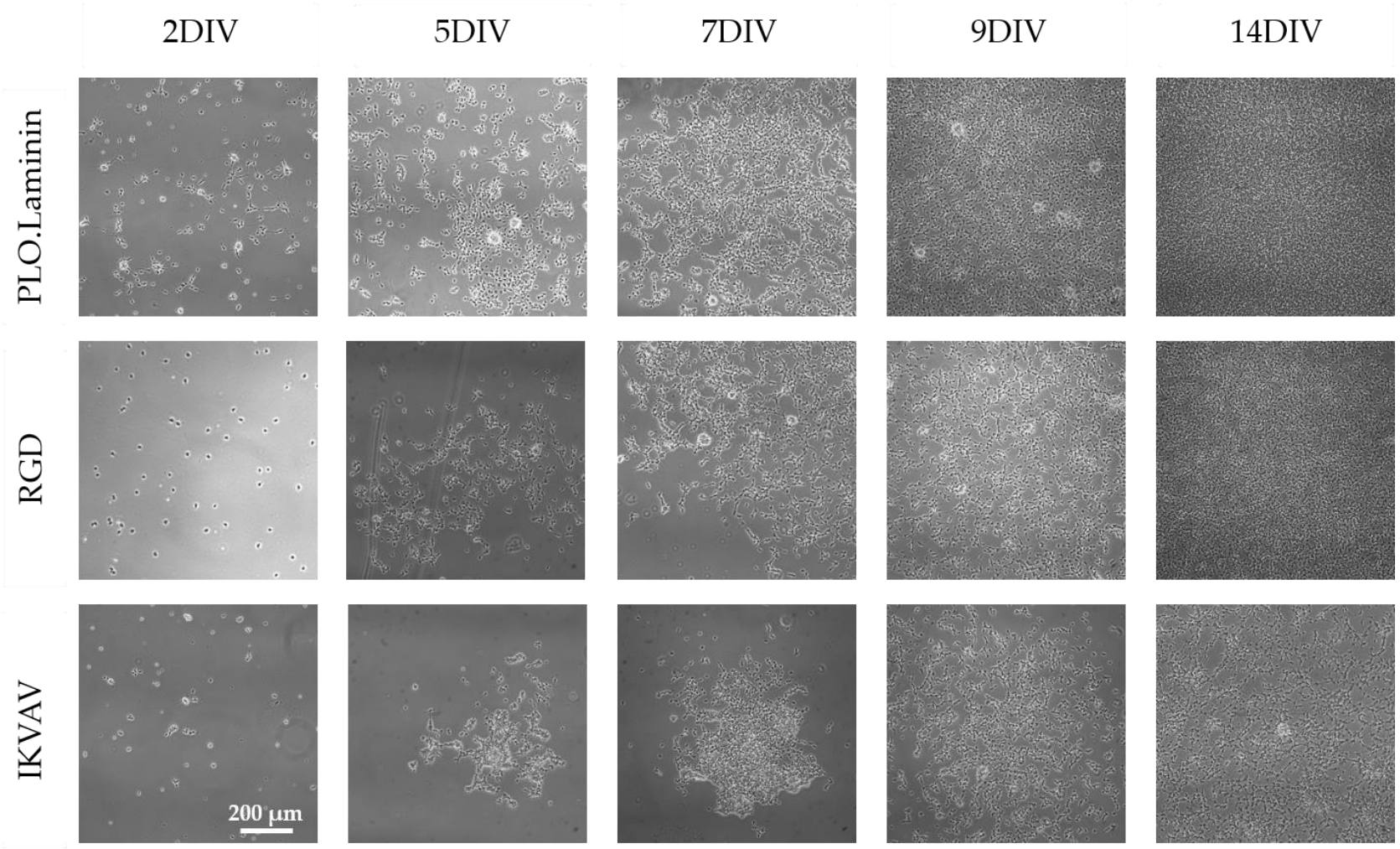


Figure 4.16 Phase contrast images of E18 NPSCs cell cultures on PLO.Laminin, RGD and IKVAV surfaces that are low surface coverage to high surface coverage, n = 3. All the cells were cultured on the surfaces at a density of 3 x 10^5 cell/mm^2 in serum-free media for 14 days *in vitro*.

Liu et al., demonstrated in 2017 their cytotoxicity studies of human cervical cancer cells (HeLa) and a cell line of fibroblasts derived from mice (L929) as model cells on PEG derivatives. The results demonstrated that most of the PEG oligomers such as PEG-400, PEG-1000, and PEG2000 were safe to both types of cells, whilst PEG-based monomers such as poly(ethylene glycol) methyl ether acrylate (mPEGA) and poly(ethylene glycol) methyl ether methacrylate (mPEGMA) showed obvious cytotoxicity in both types of cells [355]. Furthermore, PEG has been demonstrated in literature to be inert, non-immunogenic and non-cell adhesive material, which can be easily modified (i.e. in our case with peptides) to promote cell adhesion, proliferation, and differentiation [150, 356, 357]. The PEG_{18}-diamine surface induced cell apoptosis and with the change of media after 7DIV the clustered cells observed in Figure 4.15 were no longer present. Consequently, the difference in the cell attachment and proliferation observed through phase contrast images over 14DIV was illustrated in Figure 4.16 for the control surface of PLO.Laminin, and the immobilized peptide surfaces of RGD and IKVAV.

The RGD surfaces exhibited a higher number of cell attachment and % area coverage to the IKVAV surfaces, which had a higher number floating clusters of cells in their respective media at 2DIV, 2.86% ± 0.27 and 1.098% ± 0.31, respectively. In comparison to the RGD and IKVAV surfaces the control surface of PLO.Laminin exhibited higher cell % area coverage, which is illustrated in the phase contrast images of the PLO.Laminin surfaces as more developed cell processes and cell surface coverage of 4.708% ± 0.622. We further observed that the cells formed clusters on the IKVAV surfaces and exhibited less surface area coverage and very few cell processes (i.e. the formation of axons and dendrites from the cell body of the NPSCs) at 5DIV and 7DIV with % area coverage of respectively, 8.99% ± 0.78 and 17.48% ± 1.04. Whilst in contrast the RGD surfaces demonstrated higher spread of cell processes formation, higher level of separate cells covering the surface more evenly compared to that of cell clusters, with % area coverages of 8.17% ± 1.14 and 26.04% ± 1.08 respectively. Furthermore, the cells demonstrated to be growing uniformly along the RGD and PLO.Laminin surfaces as predominately separate cells and not cells clusters as observed on the IKVAV surfaces, with some cell clusters still present in the media of the respected surfaces at 7DIV. The RGD and PLO.Laminin surfaces illustrated the development of a more

homogenous network of processes in which cells developed synapses between their axons and dendrites with the increase of surface cell coverage from 7DIV to 9DIV, 35.77% ±1.16 and 82.19% ± 1.85, % area coverage respectively. In contrast, the IKVAV surfaces influenced the cells to initially cluster on the surface from 2DIV (1.098% ± 0.31) to 7DIV (17.477% ± 1.04), whilst at 9DIV (41.41% ± 1.34) we observed the cells to exhibit less cell clusters, more uniform cell coverage of the surface and a more homogenous network (i.e. synapses) between the cells. At 14DIV the cells on the IKVAV surfaces were more widely spread across surface homogenously, versus that of the RGD and PLO.Laminin surfaces which exhibit homogenous surfaces with tightly packed cells with % area coverages of 68.92% ± 1.37, 84.09% ± 1.83, and 93.77% ± 1.64, %, respectively. These three surfaces influenced different populations of cells with the RGD and PLO.laminin surfaces influencing cells to attach and spontaneously spread, whilst the IKVAV influenced the cells to attach and cluster. Moreover, the cell population exhibited a decrease in cell clustering with the increase of cells due to proliferation and influenced homogenous cell spreading as observed from 7DIV to 9DIV and 14DIV. The cell attachment and proliferation rate was the highest on the PLO.Laminin surfaces followed by the RGD surface, and a significant difference was observed in comparison to the IKVAV surfaces. At 2DIV the % area coverage can be attributed to the cell adhesion of the dissociated NPSCs, whereas the increase in cell density after 2DIV is predominately due to the proliferation of the cells on these surfaces; as any dead cells amongst the dissociated NPSCs are removed with the change of media. Thus, we can state that the proliferation of the cells is due to the surfaces they are cultured on, which all demonstrated a positive correlation with incubation time.

The NPSCs adhesion and proliferation on the PLO.Laminin, RGD and IKVAV surfaces was further compared to determine whether these surfaces demonstrated a significant difference, as quantified in Figure 4.17. The PLO.Laminin surface illustrated significantly higher % area coverage ($*p < 0.05$) compared to the RGD and IKVAV surfaces, whilst no significant difference was observed between the RGD and IKVAV surfaces in the % area coverage.

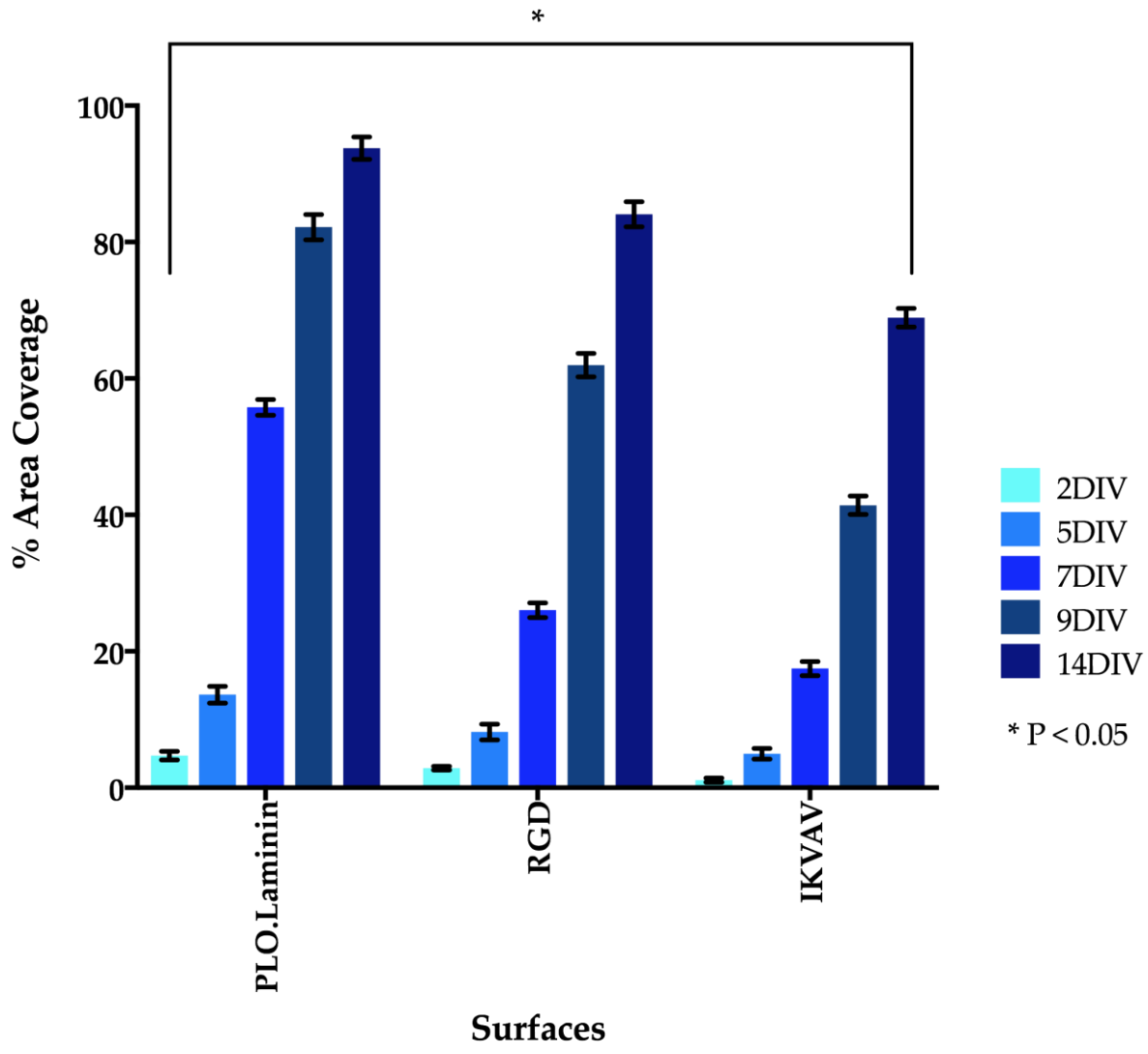


Figure 4.17 % Area coverage of E18 NPSCs on RGD and IKVAV surfaces in comparison to the control PLO.Laminin surface. Error bars represent mean ± SD for n = 3, and significant difference of (*) $p < 0.05$ was observed on the PLO.Laminin surface to the RGD and IKVAV surfaces. All the cells were cultured on the surfaces at a density of 3 x 10^5 cell/mm^2 in serum-free media for 14 days *in vitro*.

4.4.2 CELL DIFFERENTIATION

The prepared peptide surfaces of RGD and IKVAV with the control PLO.Laminin surface provided NPSCs adhesion, spreading and proliferation, whilst PEG_{18}-diamine acted as an inert surface and did not support cell adhesion. We observed that the cells become very confluent on the PLO.Laminin and RGD surfaces after 14DIV and induced the cells to lift off the surfaces, which is observed as a monolayer of cells (i.e. spontaneously) and this is supported by literature [358]. The lifting off occurred after 14DIV, with the cells on the RGD and IKVAV surfaces lifting off at an earlier stage to that of the PLO.Laminin surfaces between 15-18DIV and the later at 21DIV. In addition, we came across further difficulties when we tried fixing the cells for immunocytochemistry which caused some of the cells to lift off whilst others remained adhered to the surfaces, making the data set incomplete and unreliable for comparison. The maturation of NPSCs to neurons and astrocytes in real life would be a time period of 280 days for human gestation and 21 days in rat gestation. However, most NPSCs studies have been designed over relatively short survival times of weeks to a few months *in vitro* and *in vivo* [359]. NPSCs differentiation into different linages occurs before the 14DIV and the neuron processes (i.e. immature) can be observed within 4-7 days and morphologically mature synapses are usually observed after 14DIV (i.e. electrophysiology studies) [360, 361].

Consequently, as the main aim is to determine the influence of these surfaces to guide stem cell differentiation to a specific cell fate and not how long can the cells survive on these surfaces, we fixed the cells at 14DIV and studied the influence of RGD and IKVAV surfaces on the cell fate of the NPSCs into neurons and astrocytes only as we did not stain for other glia cells. The surfaces were stained for the neuron specific βIII-Tubulin protein, astrocyte specific class-II intermediate filament glial fibrillary acidic protein (GFAP), and DNA in the nuclei HOECHST was chosen for the staining of the nuclei as it is a more cell permeable dye in comparison to 4',6-diamidino-2-phenylindole (DAPI) as it contained an additional ethyl group. As mentioned previously we specifically choose laminin as the ECM protein as it both contains the RGD and IKVAV peptide sequence, thus, allowing for a more reliable *in vitro* model to compare to the SPPS 'grafting from' approach we took on the peptide immobilization of RGD and IKVAV on glass coverslips.

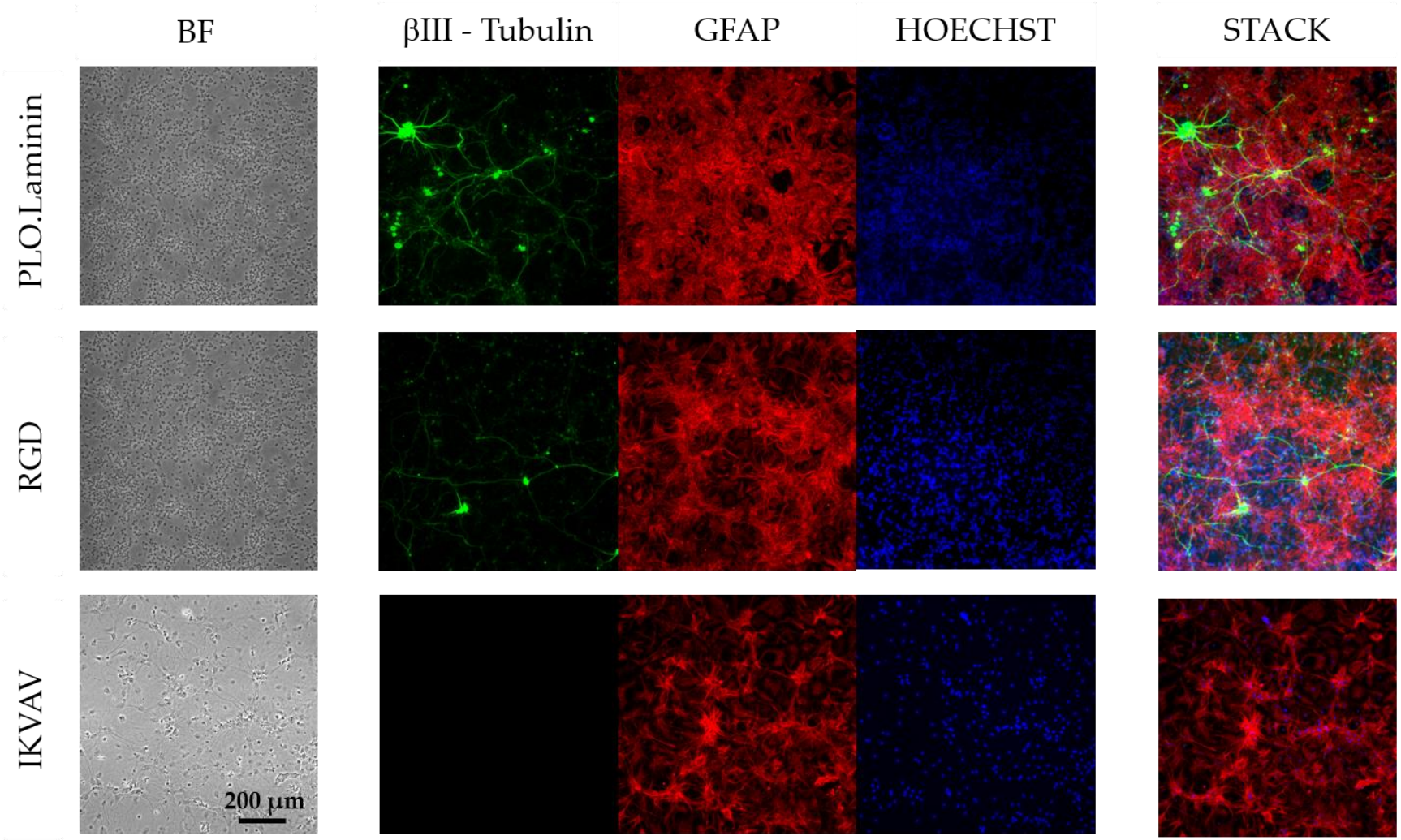


Figure 4.18 Fluorescent microscopy images of differentiated E18 NPSCs on PLO.Laminin, RGD and IKVAV surfaces. The green, red and blue represent respectively βIII-Tubulin in neurons, GFAP in astrocytes, and nuclei. All the cells were cultured on the surfaces at a density of 3 x 10^5 cell/mm^2 in serum-free media for 14 days *in vitro*.

The cells were observed under fluorescence microscopy under filters of phase contrast, FITC (i.e. βIII-Tubulin), CY5 (i.e. GFAP) and UV/DAPI (i.e. DNA) to determine the influence of the peptide immobilized surfaces in comparison to the control surface, as illustrated in Figure 4.18.

The culture media (i.e. neural basal media) used here enabled the NPSCs to proliferate and become dominate over the homogenously composed pyramidal neurons in the dissociated cells and this was checked with the markers Nestin (NPSCs), βIII-Tubulin (neurons), and GFAP (astrocytes) at various days *in vitro* (i.e. 5DIV and 7DIV). We did not observe any neurons on the surfaces at 5DIV and 7DIV, whilst a homogenous dominant NPSCs population was observed. Hence, validating that any influence observed on the NPSCs differentiation to neurons and/ or astrocytes cell fate was due to the surfaces.

The fluorescence images illustrated that the control surface of PLO.Laminin induced the differentiation of NPSCs into neurons and astrocytes as shown in previous literature [362]. The RGD surfaces influenced the cells to differentiate into neurons and astrocytes, with a less establish neural network in comparison to that exhibited on the control surface of PLO.Laminin. On the IKVAV surfaces no neurons were observed as the surface only induced the cells to differentiate into a cell population of astrocytes. Moreover, the later demonstrated astrocytes with a cell morphology that were more spread and looked larger in size, which is clearly illustrated in the phase contrast and HOESCHT images, in comparison to that of the RGD and PLO.Laminin surfaces. As a result, we hypothesized with correlation to literature that single cells/groups as observed on the IKVAV surfaces are larger than the astrocytes observed on the RGD and PLO.Laminin surfaces [363]. The later surfaces exhibited cells that were smaller in size, had a mixed population of neurons and astrocytes and were more tightly packed across the surface to form confluent monolayers of cells.

Next, we quantified the % area coverage of neurons and astrocytes on these surfaces to determine the influence of these surfaces on the differentiation of NPSCs into a specific cell fate as shown in Figure 4.19. The PLO.Laminin illustrated a better established neural networks in comparison to that of the RGD surfaces, with % area coverage of 18.44% ± 10.03 neurons and 16.17% ± 7.48 neurons, respectively. The % area coverage due to astrocytes on the IKVAV, RGD and PLO.Laminin surfaces was respectively, 51.02% ± 12.72 astrocytes,

59.91% ± 9.51 astrocytes, and 69.29% ± 6.35 astrocytes. These results support the literature data that demonstrate that astrocytes have the role as structural cells that support the formation of neural networks, which could be related to the larger % area coverage of astrocytes and neurons on the PLO.Laminin surfaces in comparison to that of the RGD surfaces.

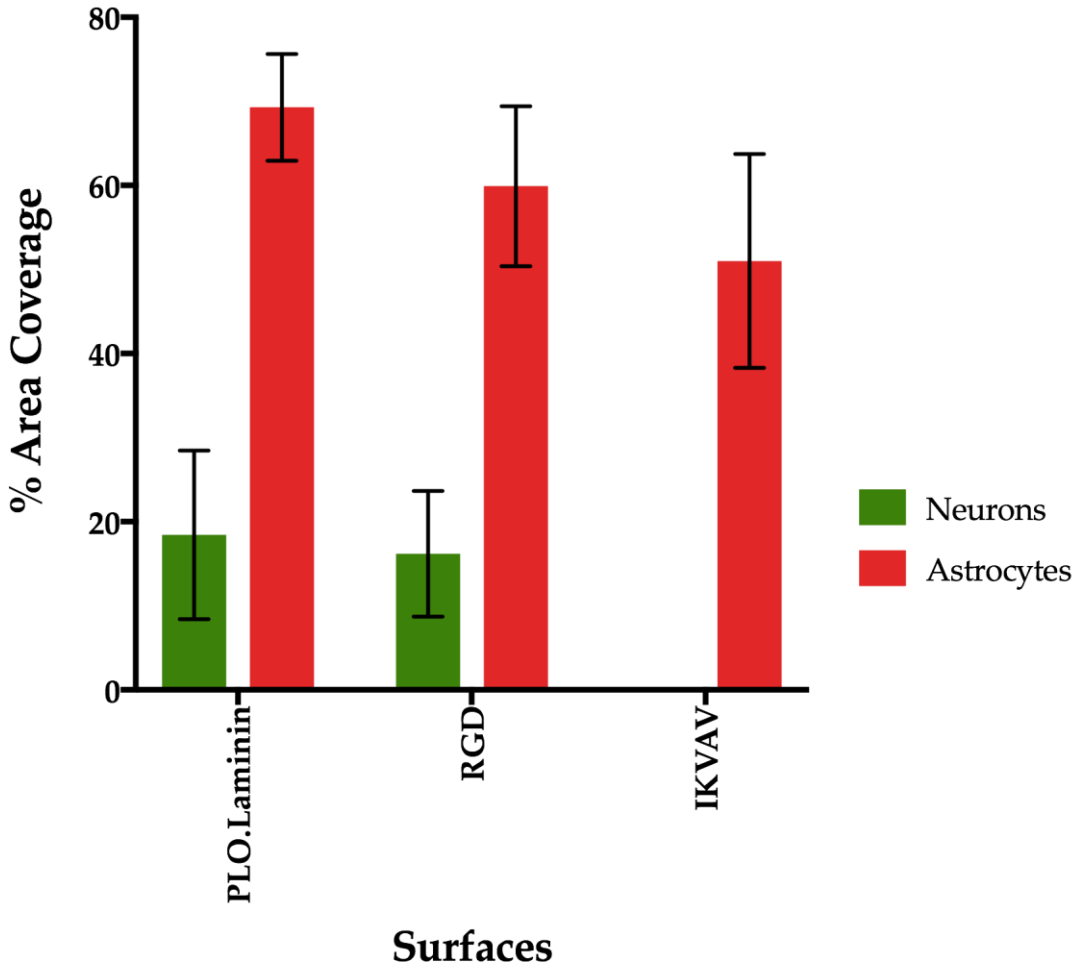


Figure 4.19 Quantification of E18 NPSCs differentiation into neurons (βIII-Tubulin positive, green) and astrocytes (GFAP positive, red) as relative area coverage by each cell type the RGD, IKVAV, and PLO.Laminin surfaces. Error bars represent mean ± SD for n = 3. All the cells were cultured on the surfaces at a density of 3 x 10^5 cell/mm^2 in serum-free media for 14 days *in vitro.*

4.5 SUMMARY

In this chapter we presented the immobilization of peptides on the non-biologically active surface (i.e. borosilicate coverslips) to mimic the *in vivo* ECM composition that interact with neural stem cells and influence stem cell fate. The glass surfaces were subjected to an extensive cleaning process and surface activated through a piranha cleaning step and silanised with the GOPTS adhesion promoter to facilitate the covalent attached with the PEG_{18}-diamine linker. The PEG_{18}-diamine linker (i.e. amine terminal group) permitted for the tethering (i.e. SPPS, 'grafting from') of the Arginine-Glycine-Aspartic acid (RGD) or Isoleucine-Lysine-Valine-Alanine-Valine (IKVAV) peptides surface, which was facilitated through the carbodiimide chemistry. Moreover, the functionalized surfaces were characterized by measuring the relative amounts of peptides on a surface and not the surface concentration or surface density. The peptide surfaces discussed here signify single peptide functionalization such as RGD (i.e. relative amount of 100% RGD) and IKVAV (i.e. relative amount of 100% IKVAV).

Surface characterization was performed by surface sensitive chemical analysis of WCA, fluorescence spectroscopy, AFM, ToF-SIMS, and XPS. The WCA measurements demonstrated a significant decrease in surface wettability in the presence of the Fmoc coupled amino acids and an increase after deprotection of the Fmoc-protecting, thus, facilitating the step-by-step immobilization of RGD or IKVAV on the surface. The fluorescence spectroscopic recording provided adequate support to the WCA data demonstrated that the surface had been functionalized by the self-assembly of amino acids to peptide sequences. A topographical difference was observed between the RGD and IKVAV in comparison to that of the PLO.Laminin control surfaces, with the later showing a higher z-range and RMS values.

The ToF-SIMS measurements provided further support to the AFM results with the acquisition of surface homogeneity, indication that the surfaces were homogenous; whilst the surface chemistry illustrated distinct marker ion fragments for each surface modification to validate the immobilization of RGD or IKVAV surfaces. Subsequently, the chemical compositions of the surfaces was verified by XPS and we observed a decrease in the elemental C/O ratio on the immobilized peptides surfaces and a higher elemental N/C ratio

on the IKVAV surfaces versus the RGD surfaces, due to the presence of more amide linkages on the IKVAV surafces.

Optical phase contrast images of the NPSCs illustrated the cell response to the PLO.Laminin, RGD, IKVAV and PEG_{18}-diamine surfaces. The cell morphology observed in the first few days of *in vitro* of the enzymatic dissociated NPSCs illustrate to attached and spread on the functionalized surfaces, with the characteristic shapes of neuroepithelial cell and then radial glia morphology as illustrated in Schematic 2.2 and Figure 4.18. The initial plating of the NPSCs demonstrate a circular and at times aggregated morphology that float in the NPSCs media. Once plated the neuroepithelial cells developed into radial glia with the cell morphology of long cellular projections which have neurogenic and gliogenic potential *in vitro* (i.e. precursor cells). Hence, indicating that the NPSCs now have the ability to switch from the majority production of neurons to being able to differentiate into all the three neural linages (i.e. neurons, astrocytes and oligodendrocytes) a feature characteristic of NPSCs.

We observed that the NPSCs did not adhere to the PEG_{18}-diamine surfaces and formed clusters in the culture media. The IKVAV surfaces demonstrated a low number of cell adhesion, high level of cell clusters that then slowly spread along the surfaces at 5DIV and after 9DIV we observed a more uniformly cell coverage. The RGD surfaces illustrated a similar trend in cell proliferation and spreading as that of the PLO.Laminin surfaces, but still the difference was significant, (*) $p < 0.05$. Moreover, all three surfaces illustrated suitability for cell adhesion, proliferation and survival. The next analysis was performed to determine whether these surfaces can guide NPSCs differentiation into a specific cell fate, either into neurons or astrocytes. We had postulated that the RGD surfaces would enhance the number of NPSCs differentiating to neurons and that the IKVAV surfaces would influence the cells to differentiate into astrocytes.

Firstly, the results established that the PLO.Laminin and RGD surfaces induced a mixed population of neurons and astrocytes, whilst IKVAV induced a population of astrocytes. Secondly, the prepared peptide surfaces of RGD and IKVAV caused different cell morphology respectively, elongated cells spreading along the surface versus cell clustering into islands. Finally, the RGD surfaces induced the NPSCS towards a not exclusive differentiation in comparison to that of the IKVAV surfaces.

Consequently, our results add on to the published literature by presenting a different approach of immobilizing peptides on glass surfaces as comparable results. The RGD and IKVAV peptide surfaces were successfully prepared, characterized and the influenced the NPSCs to preferentially differentiate towards a neuron and astrocyte cell fate respectively. Furthermore, this outcome permitted us to rationalize that by changing the peptide composition on the surface we will have the ability to control the preferential differentiation of the NPSCs towards a specific cell fate. This hypothesis will be discussed in Chapter 5.

5 IMMOBILIZING CONTROLLED PEPTIDE COMPOSITIONS ON GLASS SURFACES

5.1 INTRODUCTION

The ECM's are composed of many unique compositions that are very diverse, not only are they involved in regulating various processes (i.e. development, physiological and pathological processes), they also participate actively in the establishment, separation and maintenance of differentiated cells. With this in mind this chapter will emphasize on designing a surface that is functionalized by immobilizing peptides in mixed ratios to mimic more closely the akin characteristics of the ECM. Thus, suggesting that by varying the ratios of peptides on the same surface we can control and influence the NPSCs cell fate in producing a microenvironment of neurons and astrocytes that are of various concentration *in vitro*. The chapter has been divided into (i) design, optimization and preparation, (ii) characterization, and (iii) cell response towards the biomimetic surfaces in this case immobilized RGD and IKVAV in various mixed peptide ratios on glass surfaces.

5.2 BACKGROUND

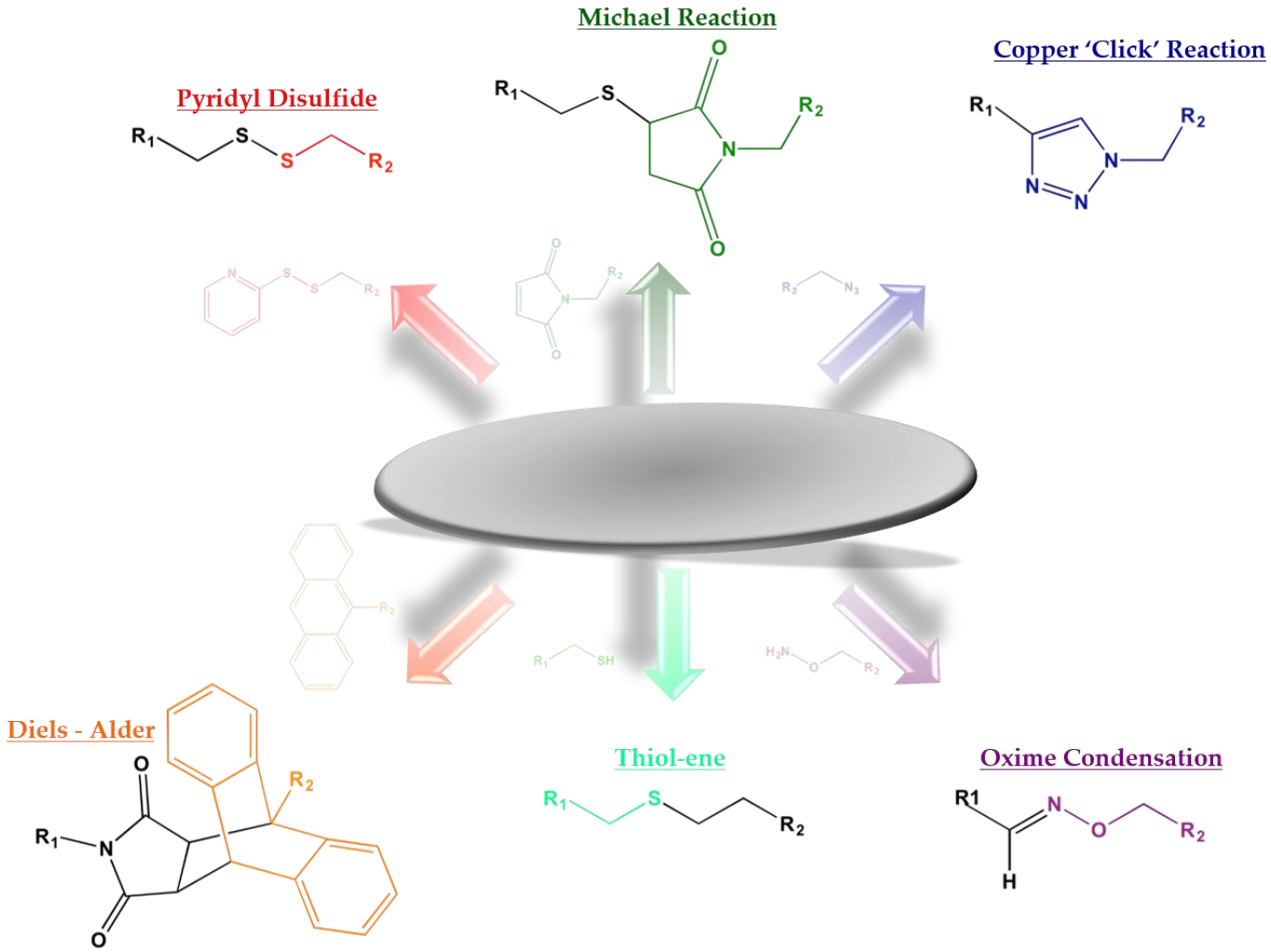
The extracellular microenvironment of cells is most elegant and dynamic, where the proteins, peptides, lipids and nucleic acids are self-assembled in a complex architectural network. Scientist and engineers have been working together to design biomaterials that mimic the ECMs bio-orthogonal properties to provide biological signals to guide cell processes (i.e. adhesion, proliferation, and differentiation). However, the majority of successful biomaterials are composed of only one chemical constituent (i.e. peptide instead of different peptides) of a biological component in the ECM, thus, lacking in bio-functionality (i.e. combining different biological signals) and complexity alike to that of the ECM [321].

Hence, there is need for biomaterials to be more versatile by presenting controllable structural features and construction of various biomolecules on the same platform, thus, enabling the design of a biomaterial that mimics the structural and function of the native

ECM. Synthetic materials have the major advantage over natural materials that they can be tuned to meet specific needs *in vivo*. As a results recent advances in the biomaterials field have focused on engineering "soft" materials that exhibit precise control over architecture, domain size, functionality, polarity, solubility and reactivity [364]. Accordingly, the more effective, easily synthesized and low-cost alternative of peptides (i.e. robust, efficient and present orthogonality) are favored over the challenging large-scale isolation and synthesis of proteins for the bi-functionalization of 2D and 3D biomaterials. Precisely controlled mixed composition of different functional peptides can be immobilized to engineer versatile surfaces for various biomedical applications [321, 365].

5.2.1 PRESENTING ORTHOGONALITY

Bio-orthogonal chemistry refers to the chemical reactions that can occur simultaneously or in sequence in the native cellular environment without interfering with any native biochemical processes, thus, creating the complexity in a living system. With this in mind the interest in engineering controlled bio-functional biomaterials has significantly progressed in recent years. Thus, developing effective bio-orthogonal chemical approaches (i.e. click chemistry) via REO (i.e. robust, efficient, orthogonal) reactions such as the Cu(I)-catalyzed azide/alkyne cycloaddition (CuAAC), thiol-ene, oxime, Diels-Alder, pyridyl disulphide reactions, Michael additions and activated ester couplings [364]. These reactions are highly selective, generate a high yield with little or no by-products under mild conditions to generate bio- and multi-functional biomaterials (i.e. biological systems, 2D and 3D surfaces), Schematic 5.1 [364]. The engineering of orthogonal surfaces relies on the mechanical differences in the deprotection reaction of the selected different protecting groups, temporary and semi-permanent, whilst other protection strategies rely on quantitative rate differences of the deprotection reactions. Orthogonality indicates subsets of protecting conditions, where some protecting groups are deprotected and other protecting groups remain intact facilitated by the chemical cleavage mechanism (i.e. under mild reaction conditions) [366]. Thus, the protecting group orthogonality is a criterion that is especially important for the success of a peptide synthesis.



Schematic 5.1 Highlights the different 'click chemistry' approaches to generate complex biomaterials as two-dimensional, three-dimensional surfaces and biological systems. The types of chemical reactions include those that involve reactive functional groups, which undergo efficient, orthogonal couplings (REO chemistry), selectively and in high yield with limited by-products. Adapted from Craig J. Hawker, 2009 [364].

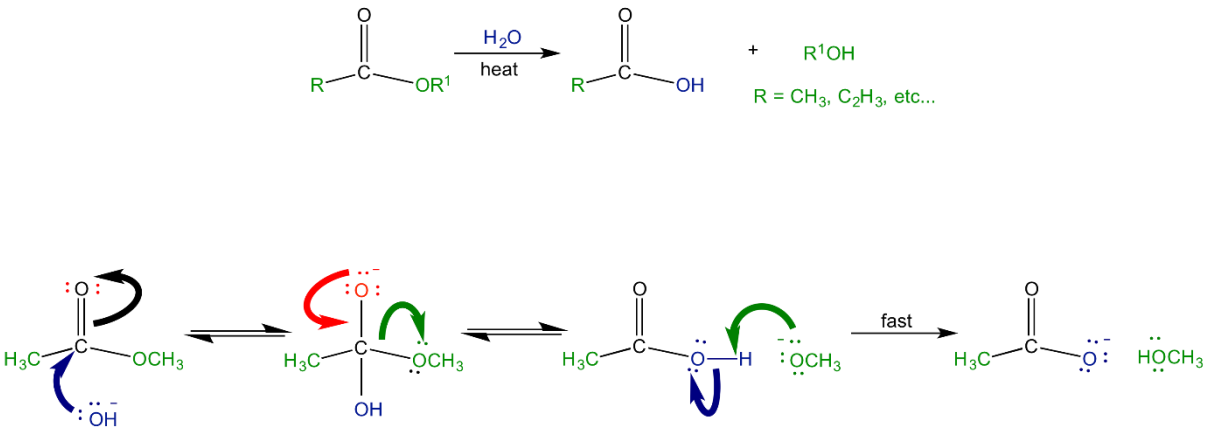
5.2.1.1 Boc AND Fmoc PROTECTING GROUPS

The standard protecting groups of tert-butyloxycarbonyl (Boc) and fluorenyl-9-methyloxycarbonyl (Fmoc) can either be employed as a temporary and/or semi-permanent protecting group. The Boc-protecting tactics (i.e. Merrifield) rely on the selective acidolytic cleavage (i.e. cleaved by TFA) which remains stable under basic conditions; whereas the Fmoc-protecting tactics (i.e. Sheppard) make use of the base lability (i.e. cleaved by piperidine) of the Fmoc group. Hence, the selection of protecting groups rely on the chosen temporary protecting group for the synthesis of particular peptides. When Fmoc is the temporary protecting group, the reactive side groups are protected with tert-butyl (i.e. acid lability) type semi-permanent side-chain protection, which referred to as Fmoc/ tBu tactics. In contrast, a benzyl-type (i.e. base lability) semi-permanent side-chain protection is used in combination when Boc is the temporary protecting group and referred to as the Boc/ Bzl tactics. The stability of the side-chain protecting groups is crucial in the successful synthesis of the desired peptides. Thus, a combination of these two tactics creates a system that enables the cleavage of a particular protecting group to be independent of the other protecting group, thus, enabling orthogonality [366].

5.2.1.2 SAFETY-CATCH LINKER

The safety catch principle was introduced by Kenner in 1971, which describes a special linker moiety that connects the surface to the peptide that is being synthesized [367]. The linker is stable under peptide synthesis conditions and is activated by a separate chemical modification to that of the protecting group deprotection. Safety-catch linkers are categorized as (i) those with hidden orthogonality of the stabile and labile form (i.e. the two forms have different cleavage mechanisms), and (ii) those that rely on different kinetics of the cleavage reaction (i.e. acidic or basic) in both forms. Here, we present a molecule with a monomethyl ester functional group as the safety-catch linker [368]. The monomethyl esters are activated by hydrolysis in a nucleophilic acyl substitution reaction under aqueous NaOH/ heat (i.e. saponification) conditions to hydrolyze to the parent carboxylic ester and an alcohol. The NaOH dissociates into hydroxide nucleophile that attacks the carbon of the C = O to create a tetrahedral intermediate, which collapses to reform the C = O bond and

form a carboxylic acid. Under a rapid equilibrium acid/base reaction the carboxylic acid is deprotonated by the alkoxide (i.e. RO-), which be avoided under an acidic work-up, Schematic 5.2.



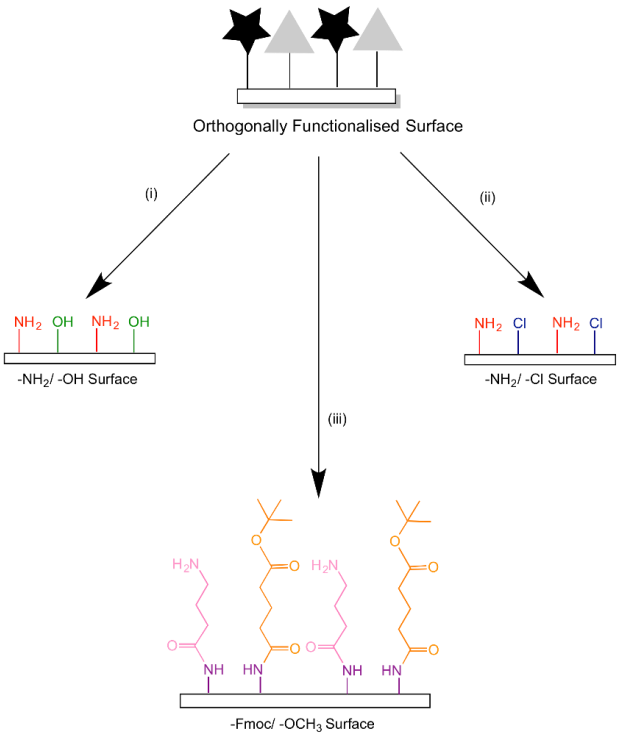
Schematic 5.2 The mechanism of the base hydrolysis of esters.

Consequently, we present here a new approach of conjugating controlled mixed composition of RGD and IKVAV peptide signals on surfaces to influence a mixed population of neurons and astrocytes. The Fmoc was selected as the temporary protecting group, the Boc (i.e. isoleucine) and tBu as the semi-permanent protecting groups on the side-chains, and a safe-catch linker with a monomethyl ester functional group.

5.3 SURFACE PREPARATION, CHARACTERIZATION AND VALIDATION

5.3.1 DESIGN AND OPTIMISING ORTHOGONAL FUNCTIONAL SURFACES

The previous chapter emphasized on selective peptides, either RGD or IKVAV surfaces, and how NPSCs respond to each peptide surface in comparison to each other. Orthogonal surface functionalization provides the ability to functionalize the surfaces with two or more types of functionality based on the simple terminal chemical groups that bind to the surface, thus, allowing for specific selective binding of amino acids or peptides. Consequently, we present here an innovative method of functionalizing RGD and IKVAV peptides in mixed ratios by sequential 'grafting from' glass surfaces these peptides. For the method development we tried the thiol-halogen 'click chemistry' approach with carbodiimide chemistry to immobilize a combination of the peptides on borosilicate coverslips [349].



Schematic 5.3 Concept diagram on designing orthogonally functionalized surfaces of mixed peptide ratios.

To investigate our concept we choose three different orthogonal functionalizing chemistry's to bioconjugate RGD and IKVAV peptides in mixed ratios respectively, (i) amine and hydroxyl groups, (ii) amine and chlorine groups, and (iii) Fmoc-protected amine groups and methyl esters as illustrated in Schematic 5.3. We optimized the orthogonal functional surfaces by functionalizing different functional groups on individual glass surfaces, in order to exploit the difference in reactivity of the functional groups on the surface to test whether we could accomplish selective reactivity or not. Thus, optimizing the surfaces for peptide conjugation with different coupling agents to facilitate orthogonal reactions by coupling to the NH_2 first, followed by coupling to OH groups. The surfaces were immersed with a mixture of Fmoc-protected amino acid (20 mM) and amino acid coupling agents EHICA (40 mM) + DIC (2 equivalent) or DCC (40 mM) + DMAP (2 equivalent) in dry DMF, and then the WCA was measured for all surfaces to observe if a significant difference in surface wettability could be observed after amino acid immobilization.

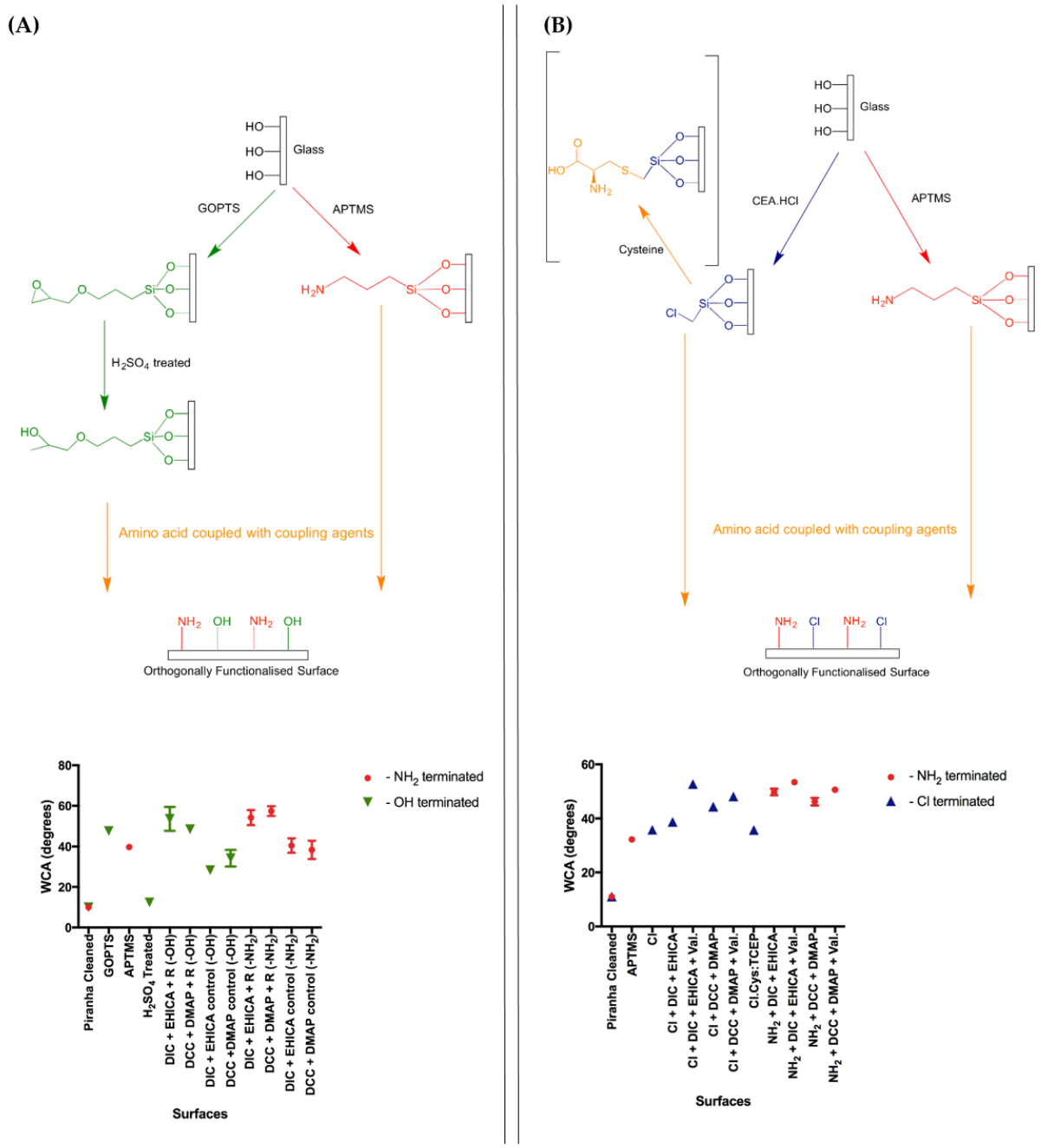
5.3.1.1 OPTIMISING SURFACE WETTABILITY

To determine whether we would be able to design a surface that has the ability to facilitate orthogonal functionality we decided to choose different functional groups to 'graft from'. Here we present the verification in the difference of surface wettability of the chosen functional groups, Schematic 5.4. We initially observed the change in surface wettability with surface modification on each of the selected functional groups individually to determine whether we could observe a distinguishable difference. Therefore, allowing us to select the distinguishable functional groups to then be combined to a surface that displays both functional groups.

5.3.1.1.1 ORTHOGONAL -OH AND -NH_2 SURFACES

Schematic 5.4(A) illustrates the method by which the surface is silanised with GOPTS or APTMS to observe whether it is possible to facilitate the selective attachment of the amino acid to the NH_2 group followed by the attachment to the OH group. The WCA measurements demonstrate that the carbodiimide coupling agents are unlikely to be able to distinguish between the amine and hydroxyl functional groups on the same surface, as the WCA values of the -OH immobilized with Fmoc-R ($53.6^o \pm 5.9$) and the -NH_2 immobilized

with Fmoc-R (54.2° ± 3.7) were not significantly different. Therefore, orthogonal reactions on these surfaces are not feasible as the coupling agents are unable to provide a significant different in surface wettability between the amine and hydroxyl surfaces.



Schematic 5.4 Strategies for the formation of orthogonally functionalized surfaces by carbodiimide chemistry. (A) -NH_2 and -OH surfaces and (B) -NH_2 and -Cl surfaces and their respective WCA measurements. The orthogonally functionalized surfaces illustrate the functional groups that the amino acid 'grafting from' will take place on.

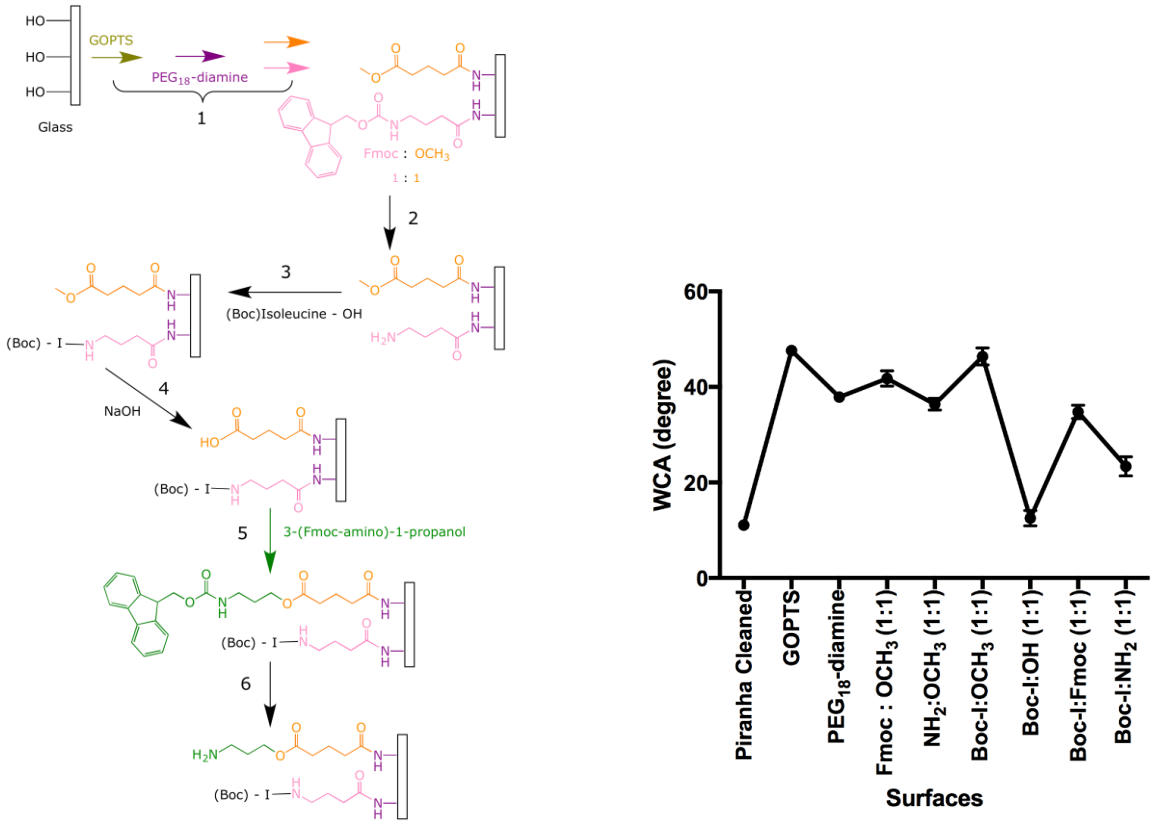
5.3.1.1.2 ORTHOGONAL -Cl AND -NH_2 SURFACES

On the other hand, Schematic 5.4(B) illustrates the surface functionalization with amine and chlorine terminated groups, which demonstrate surface wettability of the same range 32.2° ± 0.3 and 35.8° ± 0.8, respectively, which was similar to the WCA measurements of the cysteine functionalized surfaces, 35.7° ± 0.4. Moreover, the carbodiimide coupling agents did not distinguish between the amine and chlorine functional groups, -Cl exposed to Fmoc-V (48.1° ± 0.5) and the -NH_2 exposed to Fmoc-V (50.6° ± 0.2).

As a result, no significant difference in surface wettability between the chlorine and amine surfaces was observed, indicating that the coupling agents were unable to facilitate orthogonal reactions on any of the above mentioned surfaces (i.e. -OH, -NH_2 and -Cl) if they were to be mixed in order to immobilize peptides in various ratios on the same surface. Hence, another approach had to be found to successful achieve a surface that facilitates mixed peptide ratios functionalization.

5.3.1.1.3 ORTHOGONAL FMOC-GABA-OH AND MONOMETHYL GLUTARATE SURFACES

As a result, we choose to immobilize two distinct functional groups that have a terminal group that is protected or very stable in the functionalization solution on the surface. For the carbodiimide chemistry we selected EHICA with DIC, as their use on surfaces is already well documented strategy in literature for conjugating biomolecules to surfaces. Next, we decided to use the method established in Schematic 4.4 to silanise the surfaces with GOPTS and covalently bond the flexible linker PEG_{18}-diamine to create the initial amine terminated surface. This makes the surfaces available to be functionalized with the chosen linkers in a 1:1 ratio, Fmoc-GABA-OH (-Fmoc(NH_2)) and monomethyl glutarate (-OCH_3), in the presence of the coupling agents EHICA + DIC in dry DMF, Schematic 5.5. This generated surfaces where the linkers' active carboxylic acid covalently conjugate to the amine terminated PEG surfaces via amide bonds. Furthermore, the -Fmoc(NH_2) was deprotected under basic conditions to present the amine groups, making the GABA linker available to be functionalized with an amino acid under carbodiimide reaction as the methyl ester group in monomethyl glutarate is stable under the amino acid coupling and Boc (i.e. protecting group that is acid labile) deprotection conditions but is hydrolyzed with NaOH (1N, ≈ 15 minutes) to provide hydroxyl groups.



Schematic 5.5 Optimizing orthogonally functionalized surfaces by carbodiimide chemistry of two linker functional groups. (A)The surface is functionalized with (1) GOPTS, PEG_{18}-diamine, and with (i) Fmoc-GABA-OH and (ii) monomethyl glutarate mixed in a 1:1 ratio in dry DMF (200 mM) together with EHICA (40 mM) and two equivalents of DIC. (2) The deprotection of the Fmoc protected linker in a solution of 20% piperidine in DMF for 2 hrs and washed. (3) The surfaces are functionalized with the available amine ($-NH_2$) groups of the GABA linker with Boc protected isoleucine (Boc-I) and (4) the methyl ester ($-OCH_3$) groups from the monomethyl glutarate is hydrolyzed to hydroxyl groups (-OH). (5) The available hydroxyl groups are coupled with a linker, 3-(Fmoc-amino)-1-propanol, in dry DMF (20 mM) together with the coupling reagents DCC and DMAP. (6) The Fmoc deprotection of the 3-(Fmoc-amino)-1-propanol presents an available amine ($-NH_2$) groups to graft the next peptide sequence from via the orthogonal chemistry optimization procedure.

In Schematic 5.5 we illustrate this with amino acid Boc-I in the presence of EHICA + DIC, which can be observed in the increase of surface wettability from 36.4° ± 1.2 to 46.4° ± 1.8. The hydrolysis of the methyl ester functional group caused a measurable decrease in the hydrophilicity of the surface to a WCA of 12.5° ± 1.6, confirming the theory that the methyl ester functional group will remain stable under amino acid immobilization steps such as those mentioned in Schematic 4.4. The hydroxyl group was then functionalized with a linker that has an Fmoc-protected amine group and available carboxylic acid end (i.e. 3-(Fmoc-amino)-1-propanol), thus, allowing for an ester bond to be formed between the hydroxyl terminal surface and carboxylic acid end linker. Hence, a significant increase in the WCA measurements to 34.8° ± 1.4 was observed, which decreased to 23.4° ± 2.0 after Fmoc-deprotection. Consequently, the WCA measurements illustrated in Schematic 5.5(B) indicate that the surface has been functionalized with two distinguishable functional groups, -Fmoc(NH_2) and methyl ester, that are able to facilitate the immobilization of different peptides on the same surface.

5.3.1.2 OPTMISING SURFACE HOMGENEITY ON THE ORTHOGONAL Fmoc-GABA-OH AND MONOMETHYL GLUTARATE SURFACES

To support the WCA measurement results, ToF-SIMS analysis was conducted to identify the presence of the two distinguishable functional groups as mixed compositions of Fmoc (NH_2) and OCH_3 (i.e. solution compositions of 0%, 25%, 50%, 75%, and 100%), Schematic 5.5.

Positive ion fragments were identified for the distinguishable functional groups of Fmoc-GABA-OH (Fmoc) and monomethyl glutarate (OCH_3), $C_{13}H_9^+$ and $C_2H_3O_2^+$, respectively. The ion fragments peaks showed a significant increase in $C_{13}H_9^+$ ions and a decrease in $C_2H_3O_2^+$ ions from 0% Fmoc – 100% Fmoc. The Fmoc group was deprotected and functionalized with the Boc ($C_4H_9^+$) protected isoleucine (Boc-I, $C_5H_{12}N^+$) amino acid to further establish that the novel method has the ability to facilitate orthogonal peptide functionalization in mixed composition. An increase in $C_4H_9^+$ ions were illustrated from 0% Fmoc – 100% Fmoc in the presence of Boc protecting group, whilst the change in the $C_5H_{12}N^+$ ion intensity demonstrated the same trend, Figure 5.1. The raster images of the above ion fragments were reconstructed to determine the homogeneity of the surfaces in relation to the mixed composition of Fmoc (NH_2) and OCH_3, Figure 5.2. The images illustrated a clear reduction in

the intensity of $C_2H_3O_2^+$ ions in comparison to the increase in the $C_{13}H_9^+$ from 0% Fmoc – 100% Fmoc functionalized surfaces. Furthermore, the raster images showed homogenous surfaces for the $C_{13}H_9^+$, $C_2H_3O_2^+$, and $C_5H_{12}N^+$ ion fragments. Although, on the Boc-I, 25% Fmoc surface, we did observe a less homogenous surface which can be related to surface preparation.

As a result we were able to design and optimize orthogonal surfaces that have the ability to facilitate mixed composition of functionalized molecules; more specifically for this work controlled mixed compositions RGD and IKVAV. The surface wettability and ToF-SIMS ion signal intensities and distributions validated this claim.

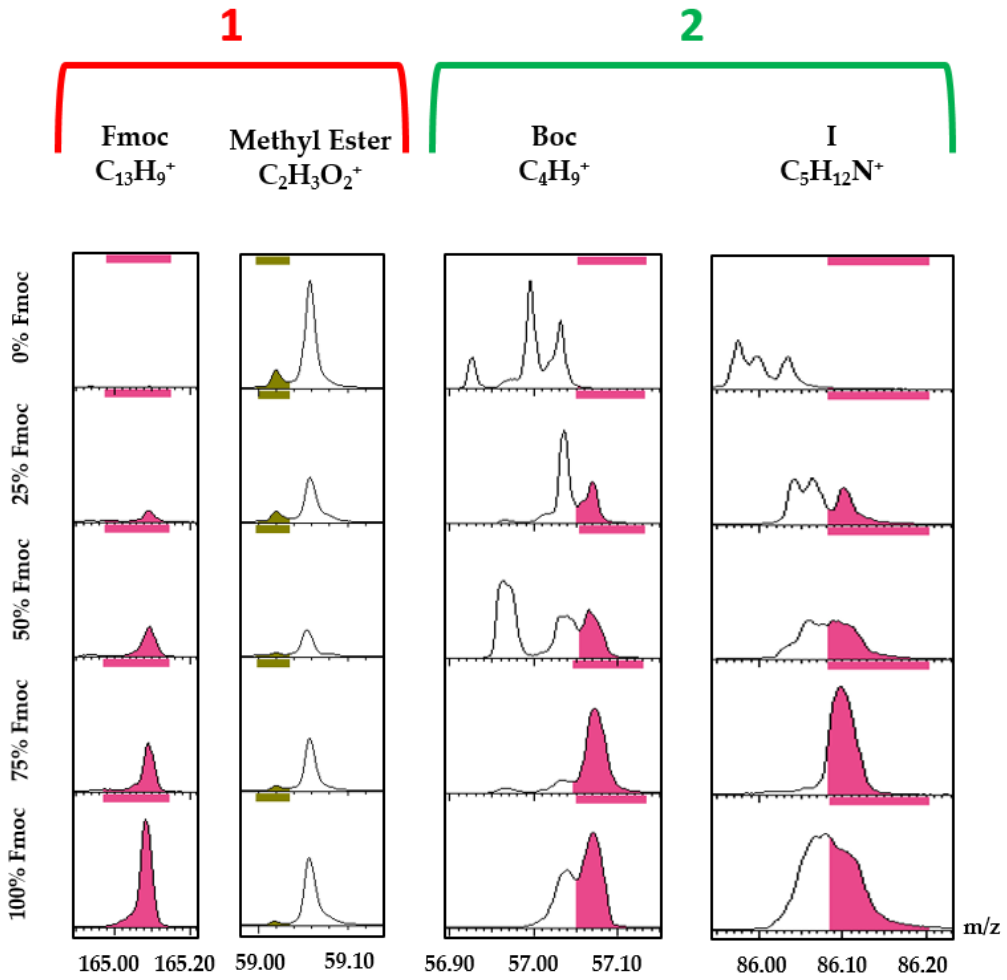


Figure 5.1 ToF-SIMS analysis of the marker ion fragments to illustrate the composition of the surfaces with mixed chemical functionalities. (1) Fmoc and Methyl ester functionalization and (2) Boc-Isoleucine functionalization after Fmoc deprotection on the GABA-OH linker. Normalized to the total ion count.

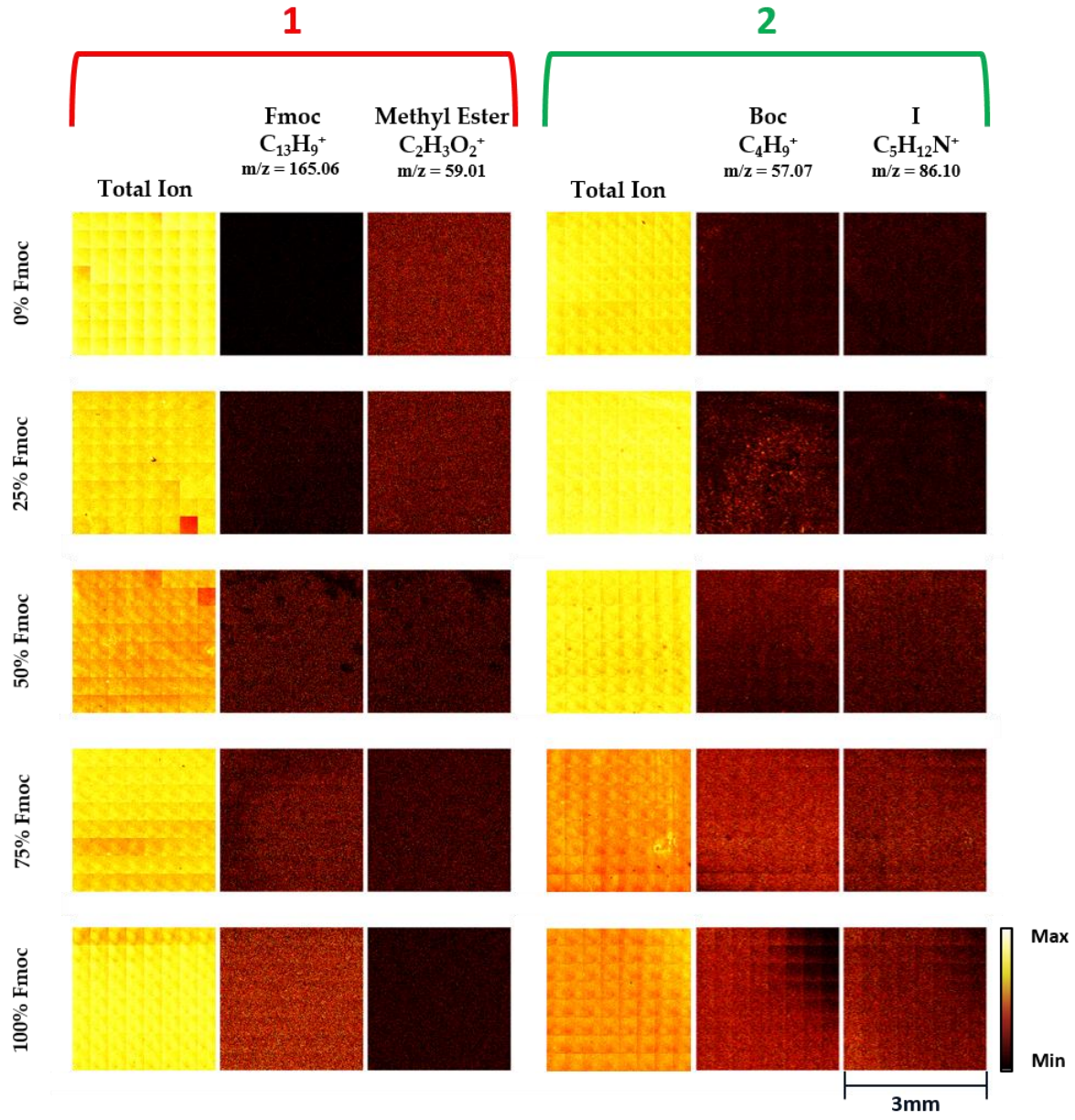
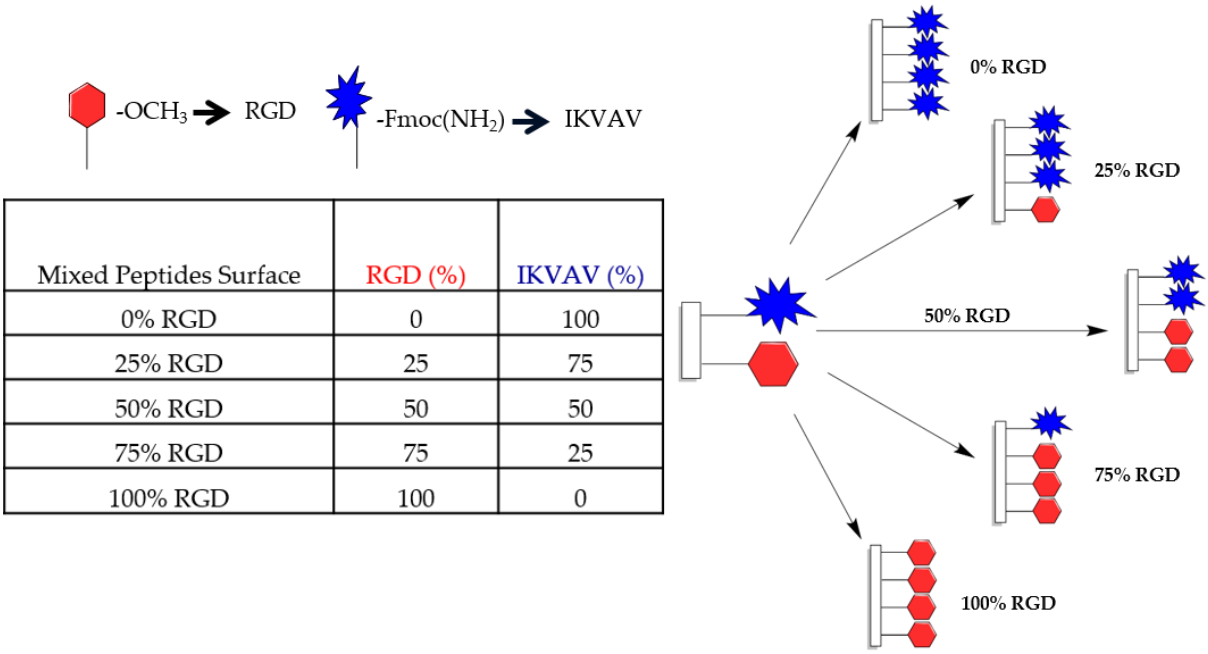


Figure 5.2 ToF-SIMS analysis of the raster images of the marker ion fragments to illustrate the composition and homogeneity of the surfaces with mixed chemical functionalities. (1) Fmoc and Methyl ester functionalization and (2) Boc-Isoleucine functionalization after Fmoc deprotection on the GABA-OH linker. Normalized to the total ion count and scale is 3 mm x 3 mm.

5.3.2 SURFACE WETTABILITY OF SURFACES WITH MIXED PEPTIDE COMPOSITION

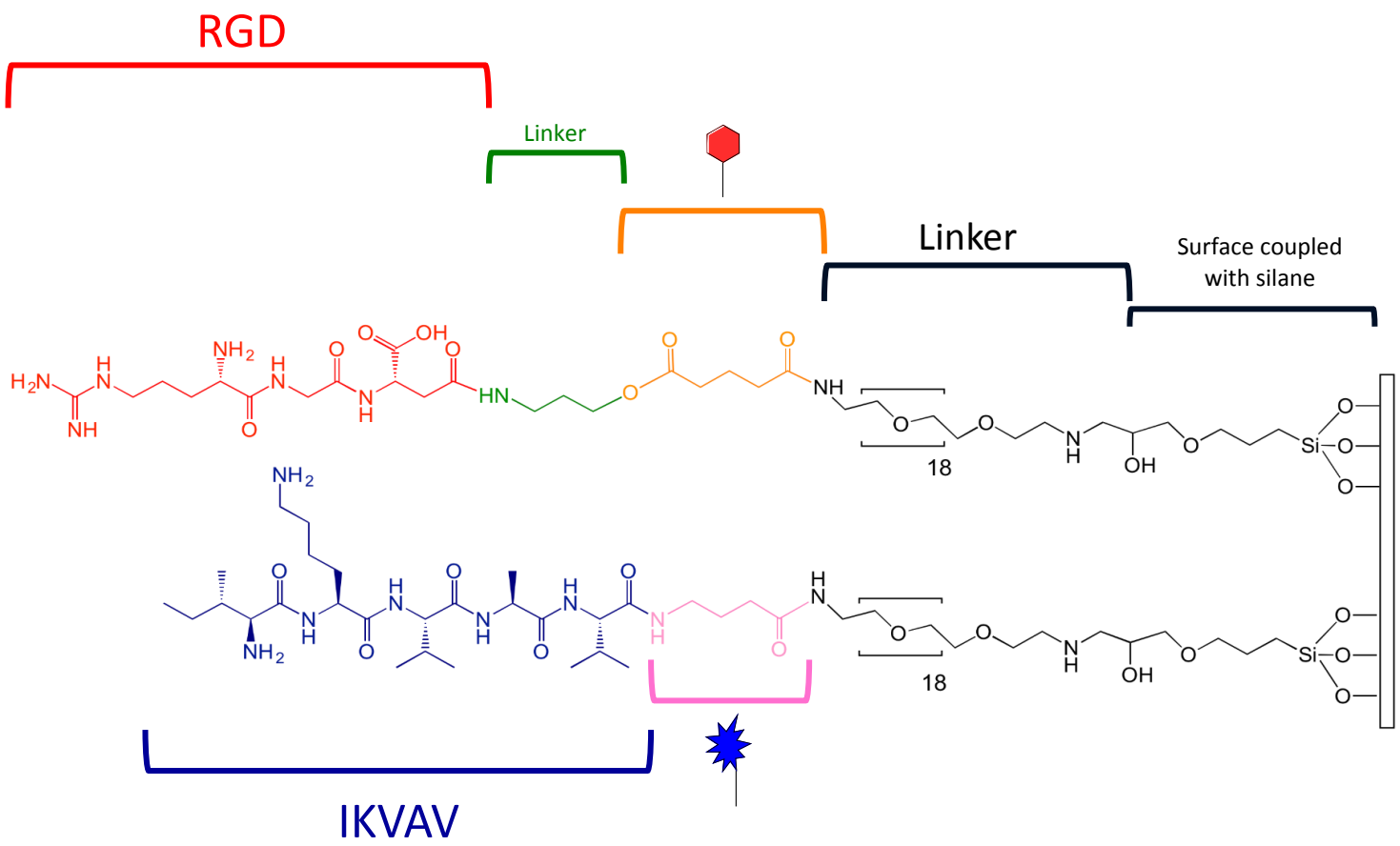
The next step was to change the mixing ratio of these two functional groups and immobilizing RGD and IKVAV peptides to confirm that the above mentioned innovative method is a success. Surfaces were functionalized with five chosen ratios by mixing the linkers -Fmoc(NH_2) and -OCH_3 into five specifically selected ratios as shown in Schematic 5.6.



Mixed Peptides Surface	RGD (%)	IKVAV (%)
0% RGD	0	100
25% RGD	25	75
50% RGD	50	50
75% RGD	75	25
100% RGD	100	0

Schematic 5.6 Concept diagram of the orthogonal surface functionalization of mixed peptide ratios of RGD and IKVAV.

Firstly, the mixed ratios of -Fmoc(NH_2) and -OCH_3 linkers provide a platform for the IKVAV and RGD peptides to be 'grafted from' sequentially. Secondly, specific terminal groups such as the -Boc and -OCH_3 prevent unintended side-reactions and allow chemo-selectivity in the subsequent chemical reaction. Consequently, the IKVAV peptide is 'grafted from' the -Fmoc(NH_2) linker and is Boc-protected, which is an acid labile protecting group. As a result the immobilized IKVAV peptide remains stable under NaOH and basic conditions of the amino acid stepwise build-up approach of the RGD peptide.



Schematic 5.7 The orthogonal innovative method by which the glass coverslips are functionalized with mixed peptide compositions of RGD and IKVAV to achieve peptide functionality. (1) GOPTS at 37 °C; (2) PEG_{18}-diamine at 75 °C; (3) Mixed linker compositions of -Fmoc(NH_2) and -OCH_3 in EHICA, DIC, dry DMF leave for 2 hrs on the orbital shaker; coupling reaction repeated overnight, 20% piperidine in DMF for 2hrs to deprotect; (4) stepwise amino acid build-up(Boc-I)KVAV; (5) treat surface with NaOH (1N) for 15 minutes and covalently attach with linker 3-(Fmoc-amino)-1-propanol, 20% piperidine in DMF for 2hrs to deprotect; (6) stepwise amino acid build-up RGD, and deprotect all acid-labile protecting groups with 95% TFA in 5% water for 4 hrs to finally achieve orthogonal functionalized surfaces of RGD and IKVAV.

Lastly, once both peptides were immobilized on the surface all the protecting groups were deprotected with TFA, Schematic 5.7. The WCA measurements illustrated in Figure 5.3 is the profile of the mixed peptide composition in a 1:1, which is representative for the surface wettability of the other mixed peptide compositions. The surface wettability from the PEG_{18}-diamine surface to the (Boc-I)KVAV:OCH_3 surface presents WCA measurements that are characteristic for the presence of Fmoc-protecting group or amine terminated surface respectively, 37.9° ± 1.1 and 46.4° ± 1.8. A significant reduction in the WCA measurement is observed after the methyl ester functional groups are hydrolyzed, followed with the immobilization of 3-(Fmoc-amino)-1-propanol and amino acid stepwise build-up of RGD that demonstrates a similar trend in surface wettability as the IKVAV functionalization. A further reduction in WCA is observed after the Fmoc-deprotection of the RGD immobilized peptide, which can be attributed to the deprotection of the side-protected functional groups (i.e. Boc-protection on the isoleucine).

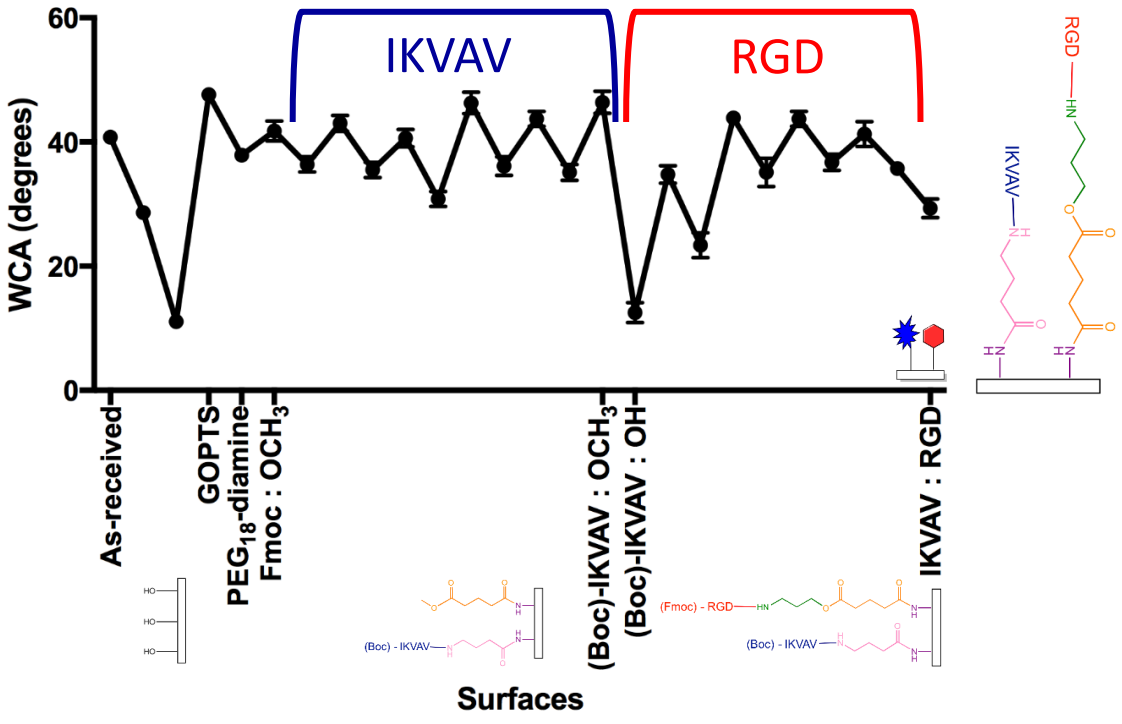


Figure 5.3 Water contact angle measurements through the modification steps to achieve mixed peptide composition in a 1:1 of RGD and IKVAV peptide surfaces. Amino acids were build-up from the C to the N terminus, changes in WCA correspond to the Fmoc protected and Fmoc deprotected of each amino acids in the respective sequence.

The surface wettability reduced from 35.7° ± 1.0 to 29.3° ± 1.5 to signify the successful functionalization of a mixed peptide composited RGD and IKVAV surface in 1:1 ratio. We then functionalized surfaces with the linkers -Fmoc(NH_2) and -OCH_3 into five specifically selected to investigate the change of surface wettability due to mixed linker and peptide composition. Figure 5.4(A) clearly illustrates that the surface wettability is reduced with the increase of -Fmoc(NH_2) functional groups on the surface from 0%, 50% and 100% respectively, 45.2° ± 1.7, 53.9° ± 1.4, and 61.5° ± 1.3. In comparison, Figure 5.4(B) demonstrates that the RGD peptide functionalization makes the surface more hydrophilic, decreasing the WCA from 43.1° ± 1.2, to 29.9° ± 1.5 from the 0% to the 100% RGD surface.

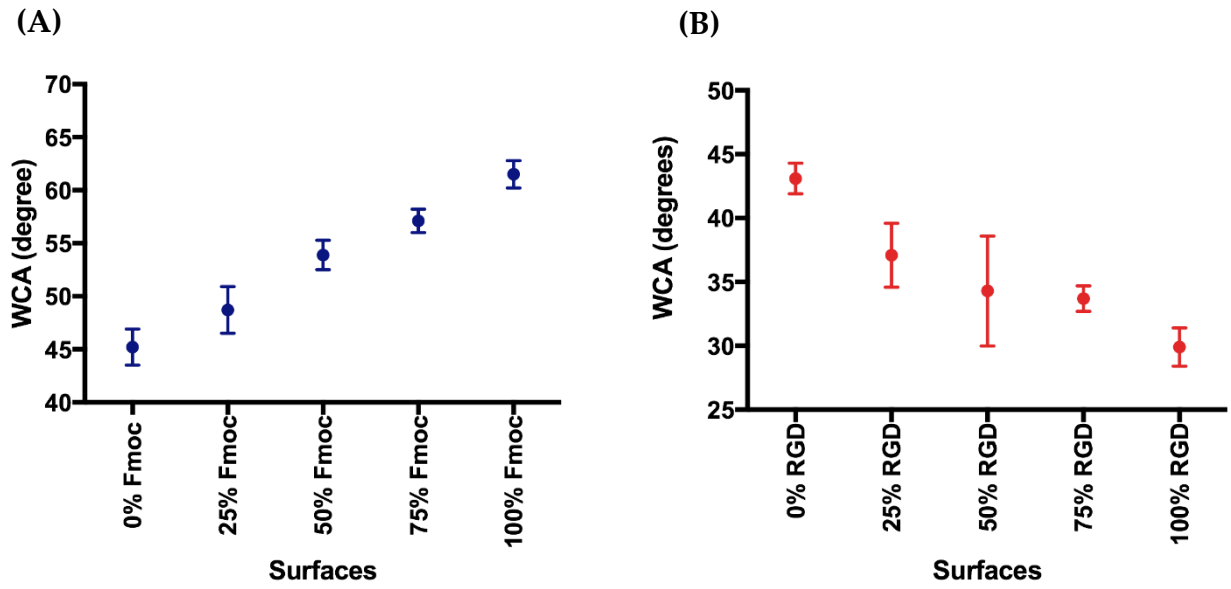


Figure 5.4 WCA measurements for mixed peptide compositions as a percentage of (A) Fmoc(NH_2) functionality and (B) RGD functionality for the final orthogonal functionalized surfaces.

5.3.3 SURFACE TOPOGRAPHY OF SURFACES WITH MIXED PEPTIDE COMPOSITION

The surface roughness of the mixed peptide composition was investigated to characterize the uniformity or/and presence of any structures on the surfaces. The final orthogonal functionalized surfaces are referred to as 0% RGD – 100% RGD, as illustrated in Figure 5.5.

The 0% RGD functionalized surface has the lowest RMS value in comparison to the other surfaces such as 50% and 100% respectively, 0.22 nm ± 0.02, 3.13 nm ± 1.54, and 4.34 nm ± 2.54, as illustrated in Table 5.1 and Figure 5.5. This is due to the increase of RGD peptide immobilization on the surface, which corresponds to the increase in z-range from 0%, 50% and 100% respectively, 7.02 nm ± 1.65, 28.57 nm ± 5.62, and 40.60 nm ± 6.73. Additionally, from the error bars for each surface it is evident that the surfaces become less uniform with the increase of RGD content. This is possibly also related to an increase in the monomethyl glutarate linker that the RGD is tethered to, as we observed that the linker was more viscose than the dry DMF it was dissolved in and with the increase of the linker more aggregated domains were formed on the surface and this clearly illustrated in the AFM topography images in Figure 5.6.

Table 5.1 Z-range and RMS measurements of the functionalized surfaces obtained from the corresponding AFM Height images, n = 3.

Surfaces	Z-range (nm)	± SD (nm)	RMS (nm)	± SD (nm)
0% RGD	7.02	1.65	0.22	0.02
25% RGD	32.37	6.13	3.74	1.54
50% RGD	28.57	5.62	3.13	1.97
75% RGD	32.70	3.03	5.44	0.35
100% RGD	40.60	6.73	4.34	2.54

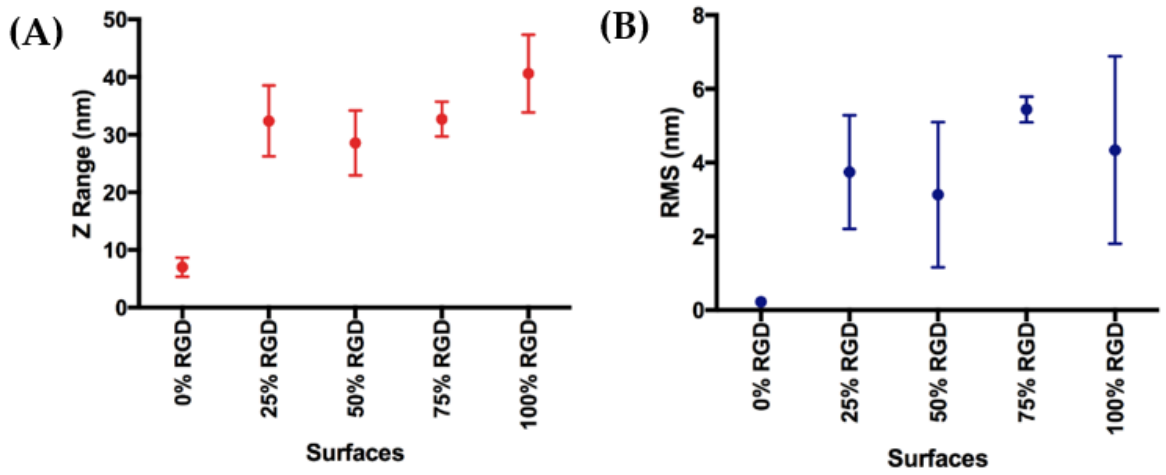


Figure 5.5 (A) Z-range and (B) RMS measurements of the functionalized surfaces obtained from the corresponding AFM Height images, n =3.

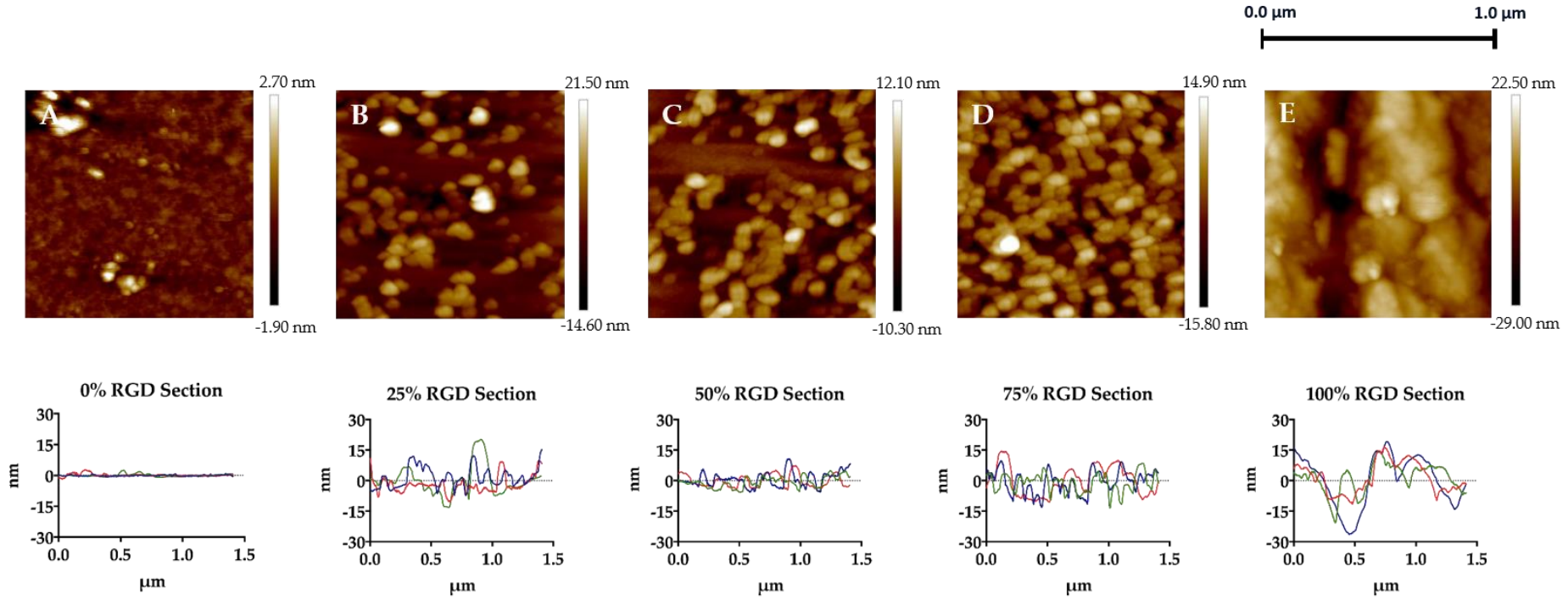


Figure 5.6 The AFM topography images observe the change in surface roughness (nm) through the orthogonal chemistry functionalization to the well controlled composition peptide surfaces. (A) 0% RGD, (B) 25% RGD, (C) 50% RGD, (D) 75% RGD, and (E) 100% RGD orthogonally functionalized glass coverslips. The profile plots illustrate approximately a height between -30 nm and 30 nm, which were measured by calculating as three lines sectioning through the AFM topography image.

5.3.4 SURFACE HOMOGEINITY OF SURFACES WITH MIXED PEPTIDE COMPOSITION

To investigate the surface homogeneity ion fragments of interest in the positive polarity were selected as identified in the previous chapter (Chapter 4). Additionally, for the orthogonal surfaces we also identified ion fragments for the functional groups of Fmoc(NH_2) ($C_{13}H_9^+$) and OCH_3 ($C_2H_3O_2^+$). Accordingly only the major secondary positive ion peaks are labelled in the overlay spectrum in Figure 5.7 and Table 5.2. The surfaces in the overlay correspond to the labelled ion fragment peaks that are labelled in the 0% RGD surface. For the data processing the intensity of these ion fragment peaks were normalized to the total ion counts, thus, correcting for differences in total secondary ion yield from spectrum to spectrum, as this can result due to instrumental drift.

We observed an increase in the R ($C_4H_8N^+$), G (CH_4N^+) and D ($C_3H_6NO_2^+$) ion fragments, whilst in correlation to the ion fragments in the RGD immobilized surfaces we observed a reduction in I ($C_5H_{12}N^+$), K ($C_5H_{10}N^+$), V ($C_4H_{10}N^+$), and A ($C_2H_6N^+$) ion fragments of the IKVAV immobilized surfaces. Thus, indicating the successful surface functionalization of orthogonal controllable compositions of RGD and IKVAV surfaces respectively, 0% RGD – 100% RGD surfaces, Figure 5.8. The intensity maps of the selected positive ions fragments were reconstruct to obtained raster images of the surface modification stages of the peptide surfaces at the higher magnification field view of 3 mm x 3 mm. Thus, providing a better overview of the homogeneity of the surfaces after surface modification and increase of RGD ion fragments in correspondence to the reduction in IKVAV ion fragments.

Figure 5.9 further confirms the homogeneity of the surface coverage relative to the intensity of secondary ion fragments characteristic to surface and overlay (i.e. surface modification). Moreover, the optimization of the orthogonally functionalized Fmoc(NH_2) and OCH_3 surfaces shown in Figure 5.1 and Figure 5.2 support the high resolution images of the AFM measurements demonstrated in Figure 5.6.

Table 5.2 Positive ion peaks selected for the ToF-SIMS analysis to construct as raster images to illustrate the homogenous surfaces. Normalized ion intensity (x 10^6).

Source	Ion assignment	0% RGD		25% RGD		50% RGD		75% RGD		100% RGD	
		m/z	Dev.(ppm)	m/z	Dev.(ppm)	m/z	Dev.(ppm)	m/z	Dev.(ppm)	m/z	Dev.(ppm)
Glass	Si^+	27.9757	-23.60	27.9757	-23.60	27.9760	-12.10	27.9758	-20.10	27.9757	-22.50
GOPTS	CH_3O^+	31.0194	19.40	31.0193	48.20	31.0198	62.80	31.0197	60.40	31.0198	62.30
PEG_{18}-diamine	$C_2H_5O^+$	45.0338	7.30	45.0332	-6.10	45.0345	21.80	45.0341	13.20	45.0342	16.80
Fmoc	$C_{13}H_9^+$	165.0639	-36.10	165.0609	-54.70	165.0639	-35.90	165.0632	-40.30	165.0662	-22.30
Methyl Ester	$C_2H_3O_2^+$	59.0132	6.80	59.0151	39.60	59.0138	18.10	59.0140	20.30	59.0144	28.30
Arginine	$C_4H_8N^+$	70.0738	123.90	70.0697	65.50	70.0727	107.40	70.0722	100.50	70.0714	88.80
Glycine	CH_4N^+	30.0364	84.90	30.0363	81.10	30.0368	99.10	30.0369	102.50	30.3690	100.70
Aspartic acid	$C_3H_6NO_2^+$	88.0776	43.40	88.0774	45.80	88.0789	41.70	88.0784	43.20	88.0801	46.30
Isoleucine	$C_5H_{12}N^+$	86.0972	9.10	86.0958	-7.30	86.0976	13.90	86.0978	15.50	86.099	29.40
Lysine	$C_5H_{10}N^+$	84.0833	29.60	84.0816	9.80	84.0834	31.20	84.0834	31.80	84.0841	39.70
Valine	$C_4H_{10}N^+$	72.0831	32.70	72.0811	4.60	72.0837	40.90	72.0836	39.10	72.0835	37.90
Alanine	$C_2H_6N^+$	44.0521	60.10	44.0517	51.40	44.0522	62.20	44.0527	72.70	44.0519	55.50

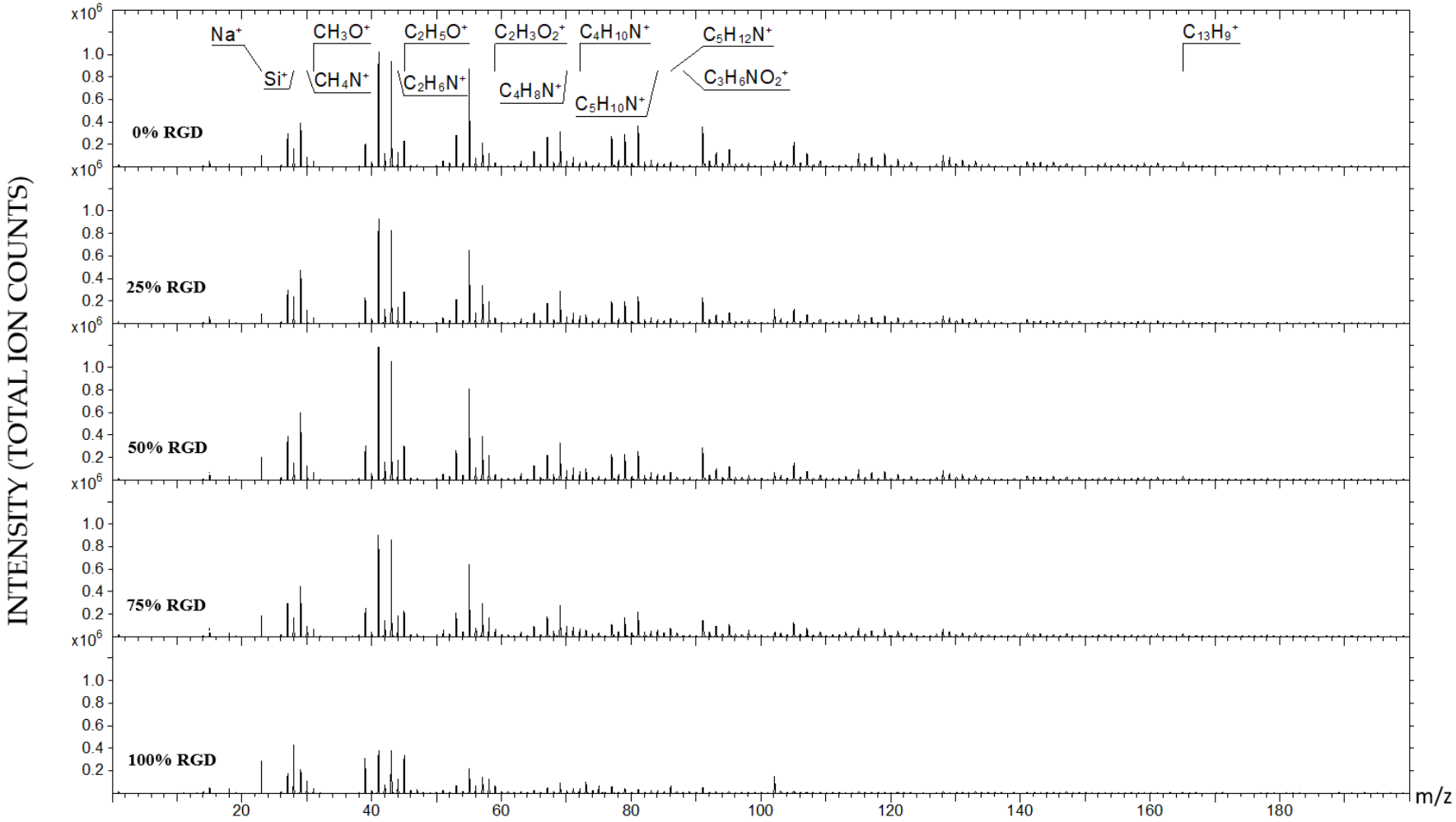


Figure 5.7 ToF-SIMS overall spectrum of the functionalized surfaces annotated with the selected positive ion peaks and normalized to the total ion count.

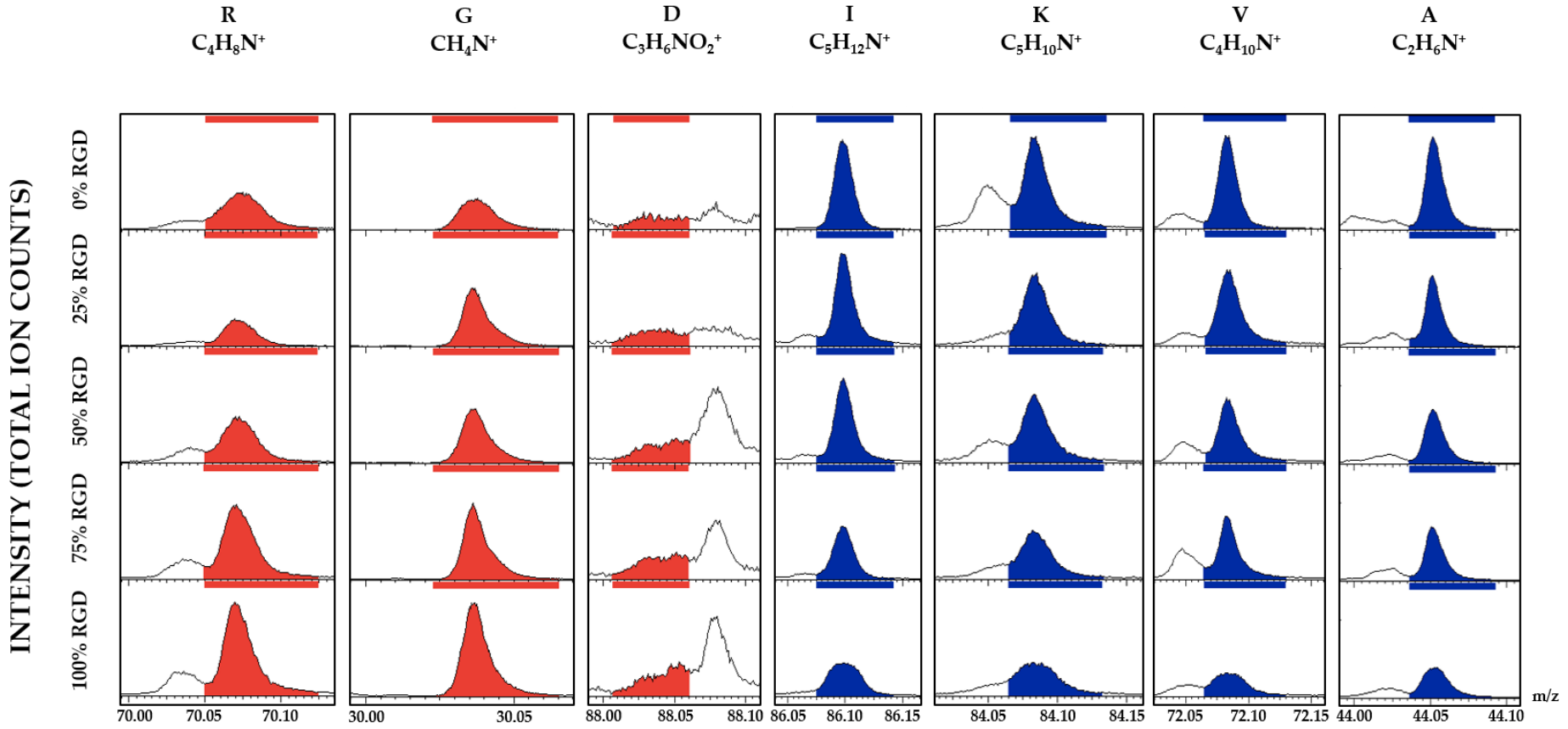


Figure 5.8 ToF-SIMS characterization of marker ion fragments of amino acids distinguishable for surface modification and normalized to the total ion count.

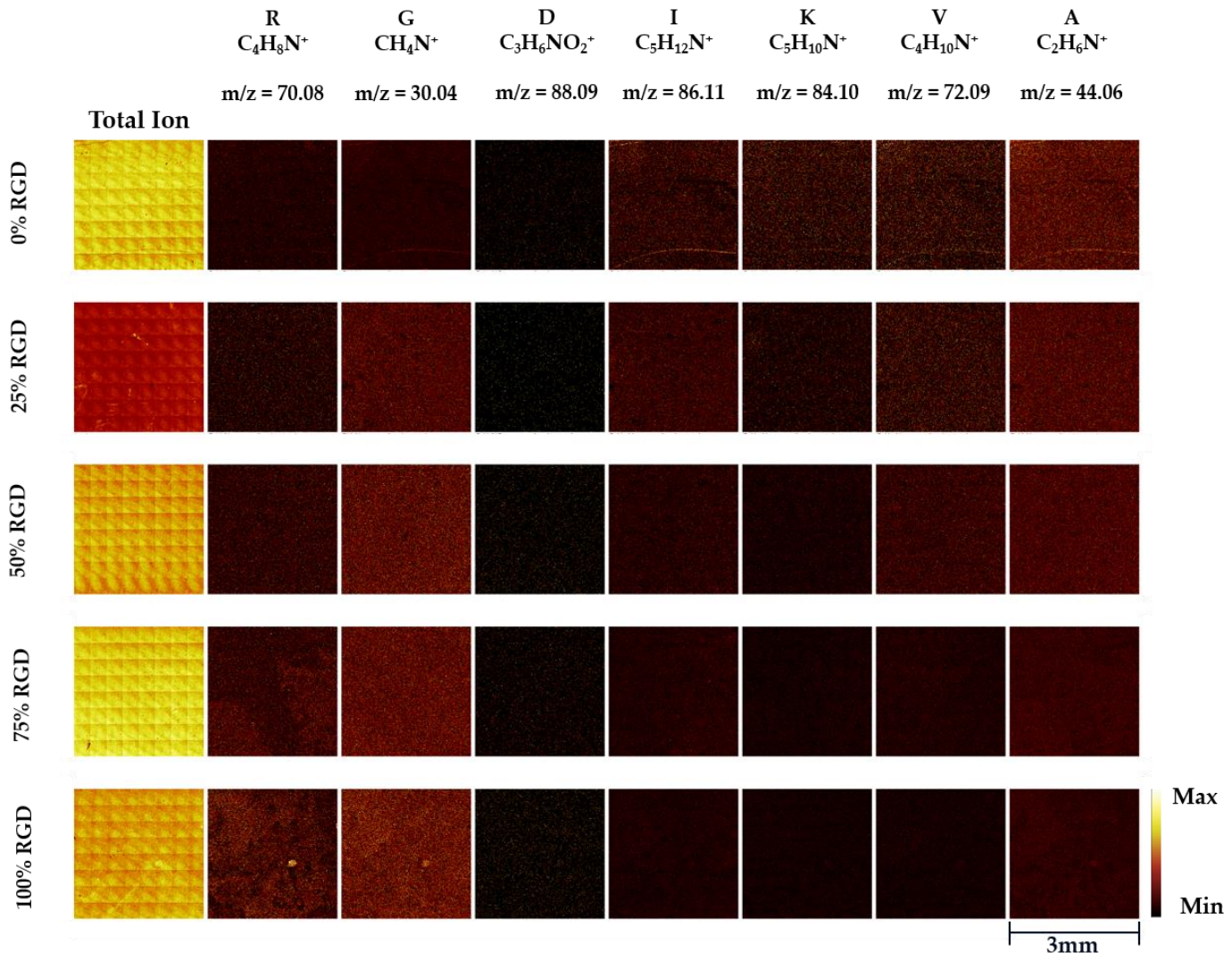


Figure 5.9 ToF-SIMS analysis of the marker ion fragments as raster images to illustrate the homogenous surfaces and normalized to the total ion count.

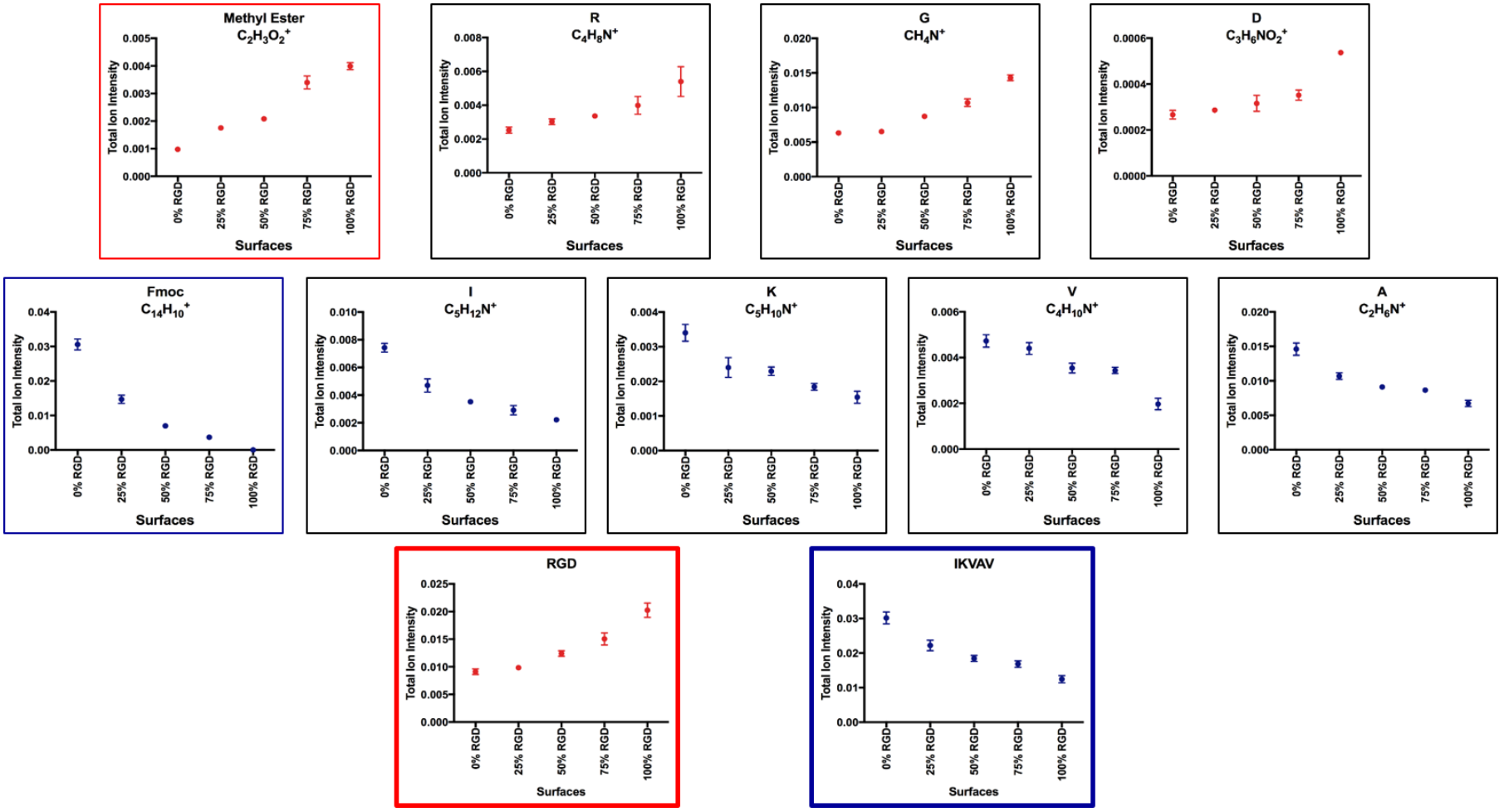


Figure 5.10 The summary of region of interest (ROI) of the of the mixed peptide composition of marker ion fragments of IKVAV in relation to those of RGD on the orthogonal functionalized surfaces. Normalized to the total ion count.

5.3.4.1 REGION OF INTEREST

We further analyzed the higher magnification field view of 3 mm x 3 mm and sectioned each image into four equal regions of interest (ROI), Figure 5.10.

Each region of interest would represent a higher resolution image of the atomic composition of the surfaces and a better understanding of the ion fragment distribution in different areas on of the total raster image, thus, minimizing interpretation ambiguity. The four ROI for each identified fragment for the RGD and IKVAV surface peptides were summed to quantify the change in total ion intensity for each ion fragment across in relation to the surface modification from 0% RGD – 100% RGD surfaces. A positive correlation was observed with the OCH_3 functional group and the immobilized RGD peptide, this is shown in the increase of their identified ion fragments. In comparison, the IKVAV peptide was immobilized on the Fmoc(NH_2) functional group, which illustrated a corresponding decrease in their identified ion fragments. Next, we summed the ion fragments for each peptide, RGD or IKVAV, to exhibit a stronger total ion intensity for each peptide in comparison to the individual ion fragments, Figure 5.11.

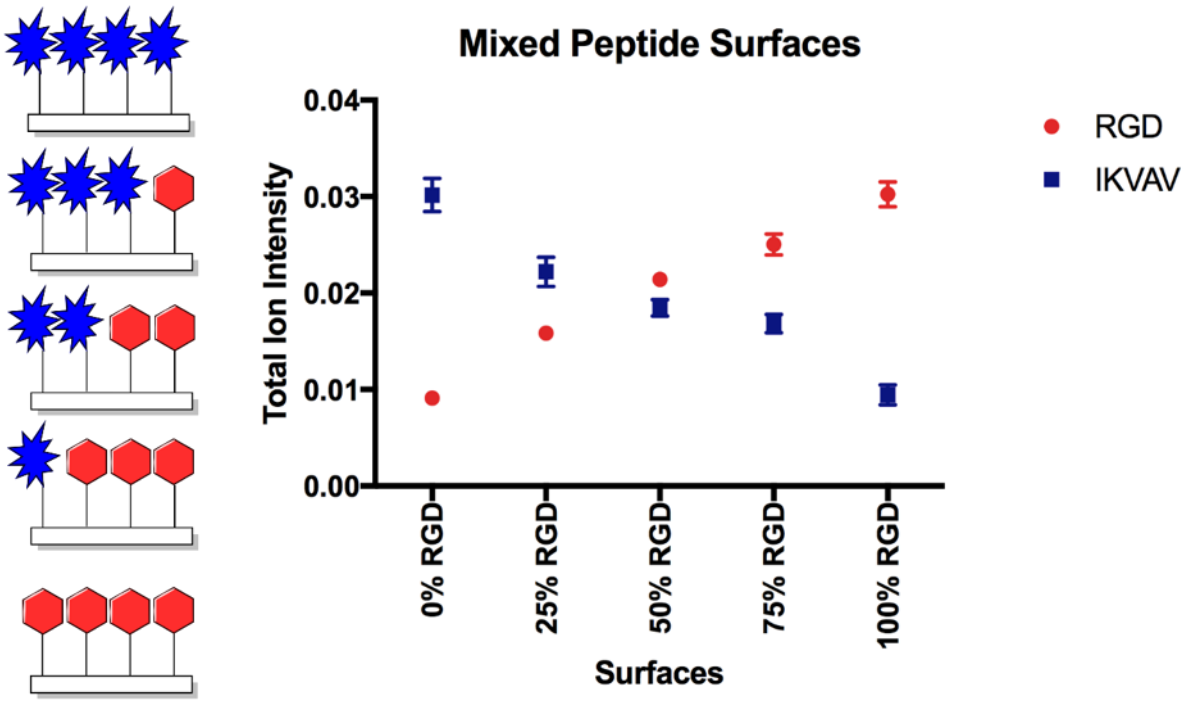


Figure 5.11 The summary of the mixed peptide composition of IKVAV in relation to RGD on the orthogonal functionalized surfaces. Normalized to the total ion count.

5.4 CELL RESPONSE TO CONTROLLABLE COMPOSITION OF PEPTIDES

The surface analysis confirmed the immobilization of RGD and IKVAV peptide sequences as a controlled composition on the glass coverslips surfaces, which enabled us to study the effect these mixed peptide surfaces have on the adhesion, proliferation and differentiation of NPSCs.

This study presents the orthogonal functionalization of controllable composition of peptides via the SPPS surface design approach that differs from the previously discussed literature in that we do not use any hydrogels to create different domains (i.e. patterned or 3D) and exhibit hard and soft material properties that cells respond to [231-233]. In our study we investigated the immobilization of controllable composition peptides on inorganic solid surface (i.e. borosilicate) with linkers and not hydrogels, which in theory exhibits a hard material property. Hence, our work would be more equivalent to the study performed R. Hassert et al. 2012 where they functionalized silicon surfaces with N-terminally biotinylated peptides in TBS buffer, which bound with nM affinity to the surface through a Diels-Alder reaction with inverse electron demand and Copper(I) Catalyzed Azide-Alkyne Cycloaddition reaction (i.e. click chemistry, orthogonal reaction) [369]. Consequently, the literature review demonstrated that there were more studies that incorporate hydrogels in their surface design and that there was a lack of studies that would support our results, so we decided to contextualize our findings from the previous chapter (i.e. Chapter 4) with these literatures.

For the control surfaces we choose PLO.Laminin, RGD and IKVAV surfaces to monitor and compare cell response towards the controllable mixed peptide composition surfaces. We hypothesize that with the increase of IKVAV peptides as a control of mixed peptide composition, the NPSCs will differentiate more into the astrocyte cell fate versus that of the neuron cell fate as we observed on the IKVAV surfaces as verified in the previous chapter (i.e. Chapter 4). Whilst an increase of RGD peptides (i.e. relative to the decrease in IKVAV peptides) would illustrate a more established neural network as well as a mixed population of neurons and astrocytes more similar to that of the RGD and PLO.Laminin (i.e. control)

surfaces (i.e. Chapter 4). Thus, it was crucial in this study to compare the cell response to the single peptide surfaces against the new approach of immobilizing controlled composition of RGD and IKVAV peptide surfaces.

5.4.1 CELL SURVIVAL

The NPSCs were seeded on the RGD, IKVAV, PLO.Laminin control surfaces and the controlled composition of peptide surfaces of 0% RGD, 25% RGD, 50% RGD, 75% RGD and 100% RGD. The difference in the cell attachment and proliferation observed through phase contrast images over 14DIV was illustrated in Figure 5.12, Figure 5.13, and Figure 5.14.

The 0% RGD surfaces (i.e. 100% IKVAV) demonstrated very low surface coverage, clusters of cells in the media and clusters of cell processes (i.e. the formation of axons and dendrites from the cell body of the NPSCs) from 2DIV to 7DIV, which is very similar to that of the IKVAV surfaces in the previous chapter (i.e. Chapter 4). We observed that the higher IKVAV peptide composition surfaces supported clusters of cells that proliferated outwards from the clustered cells, so the 0% RGD and 25% RGD surfaces illustrated islands of clustered cells across the surfaces. The cells present a more circular morphology rather than the desired spreading along the surface morphology. With the increase in the relative amount of RGD on the surface, 25% RGD to 50% RGD, the NPSCs exhibited an increased surface coverage due to cells spreading along the surface rather than remaining clustered in the media.

Moreover, on the 75% RGD and 100% RGD samples it was observed that the cells demonstrated an increase in the number cells (i.e. % area coverage) that adhered and spread along the surface to the surface with better established connections through the cell processes. The change in round cell shape to the elongated cell spread along the surfaces was further evident at 5DIV and 7DIV with the increase of RGD peptides on the surfaces from 0% RGD – 100% RGD surfaces. At 9DIV and 14DIV with the increase of RGD composition on the surface we observed an increase in NPSCs proliferation and a more homogenous surface coverage with a confluent population at 14DIV illustrated as more densely packed areas observed in the phase contrast images of 50% RGD , 75% RGD and 100 RGD surfaces.

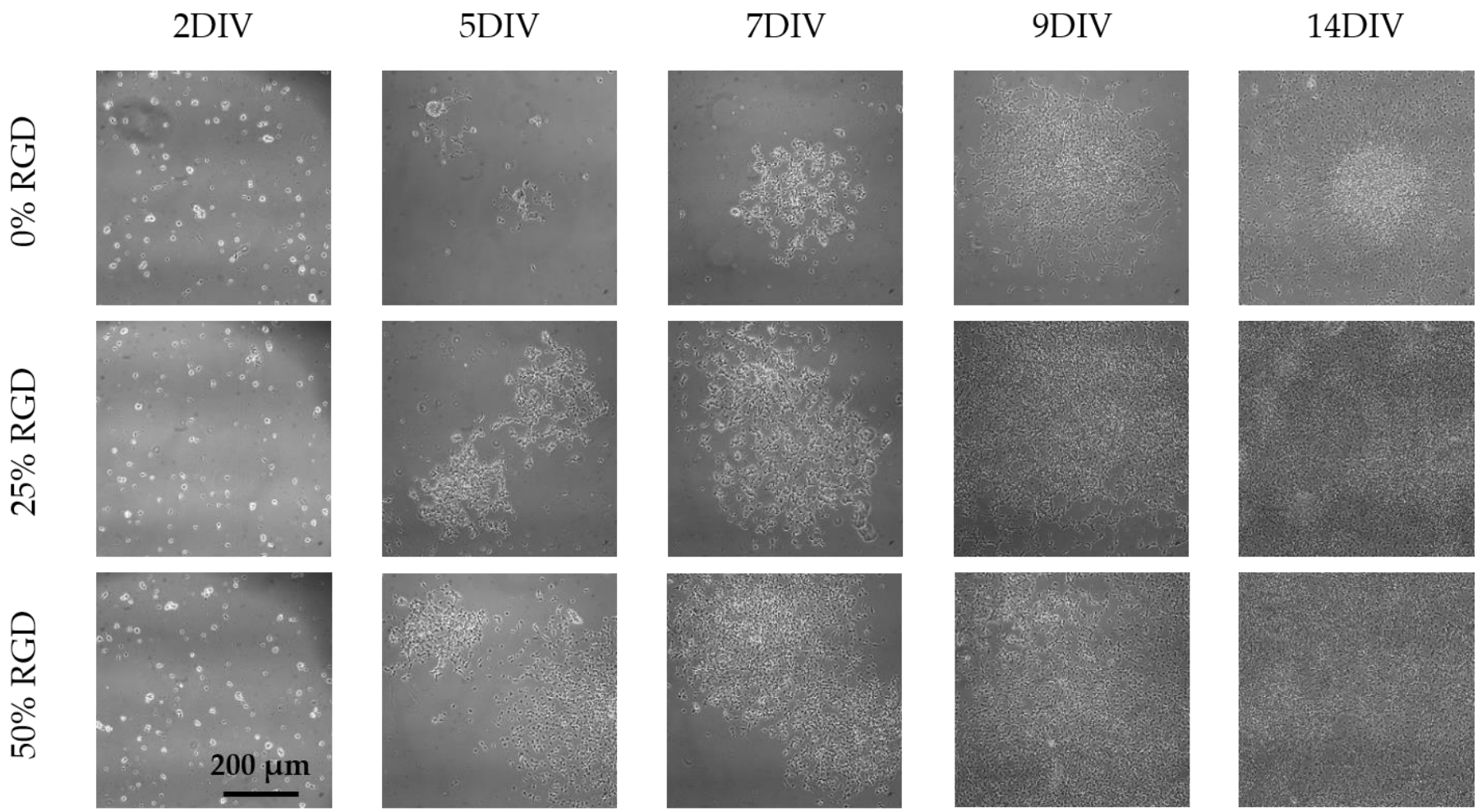


Figure 5.12 Phase contrast images of E18 NPSCs cell cultures on 0% RGD – 50% RGD surfaces that are low surface coverage to high surface coverage, n = 3. All the cells were cultured on the surfaces at a density of 3 x 10^5 cell/mm^2 in serum-free media for 14 days *in vitro*.

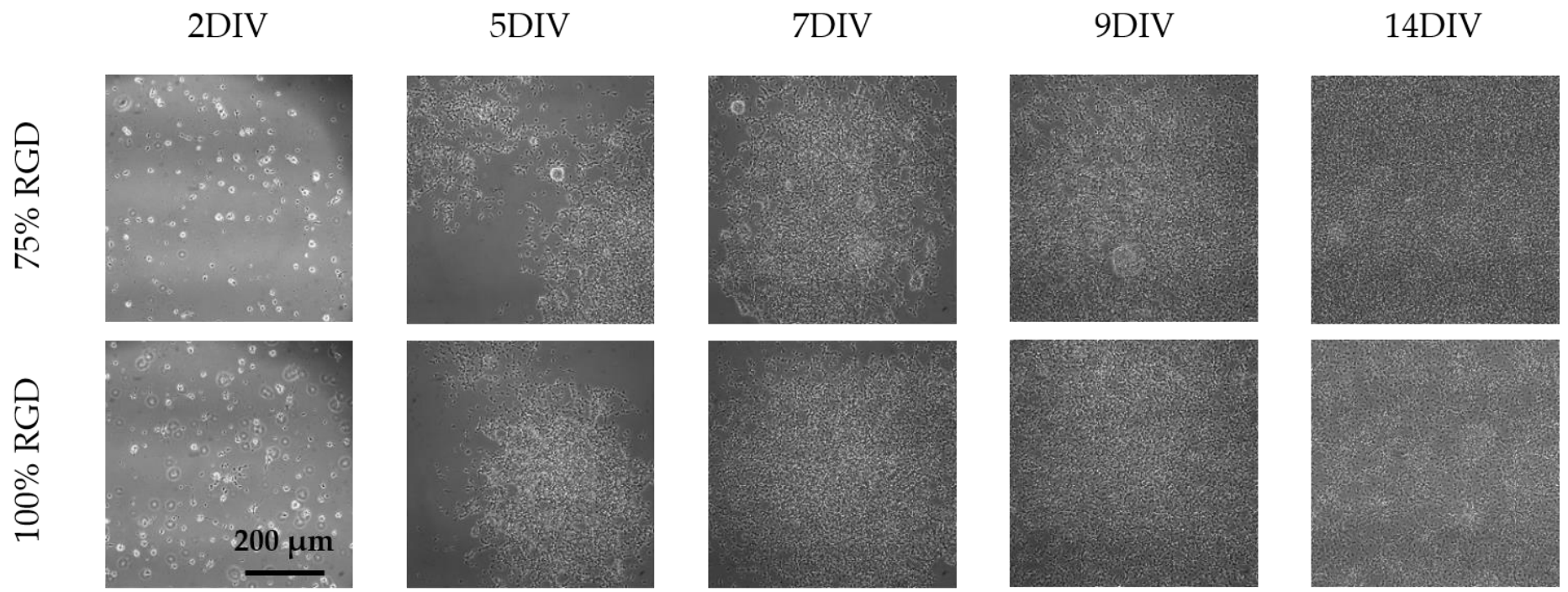


Figure 5.13 Phase contrast images of E18 NPSCs cell cultures on 75% RGD – 100% RGD surfaces that are low surface coverage to high surface coverage, n = 3. All the cells were cultured on the surfaces at a density of 3 x 10^5 cell/mm^2 in serum-free media for 14 days *in vitro*.

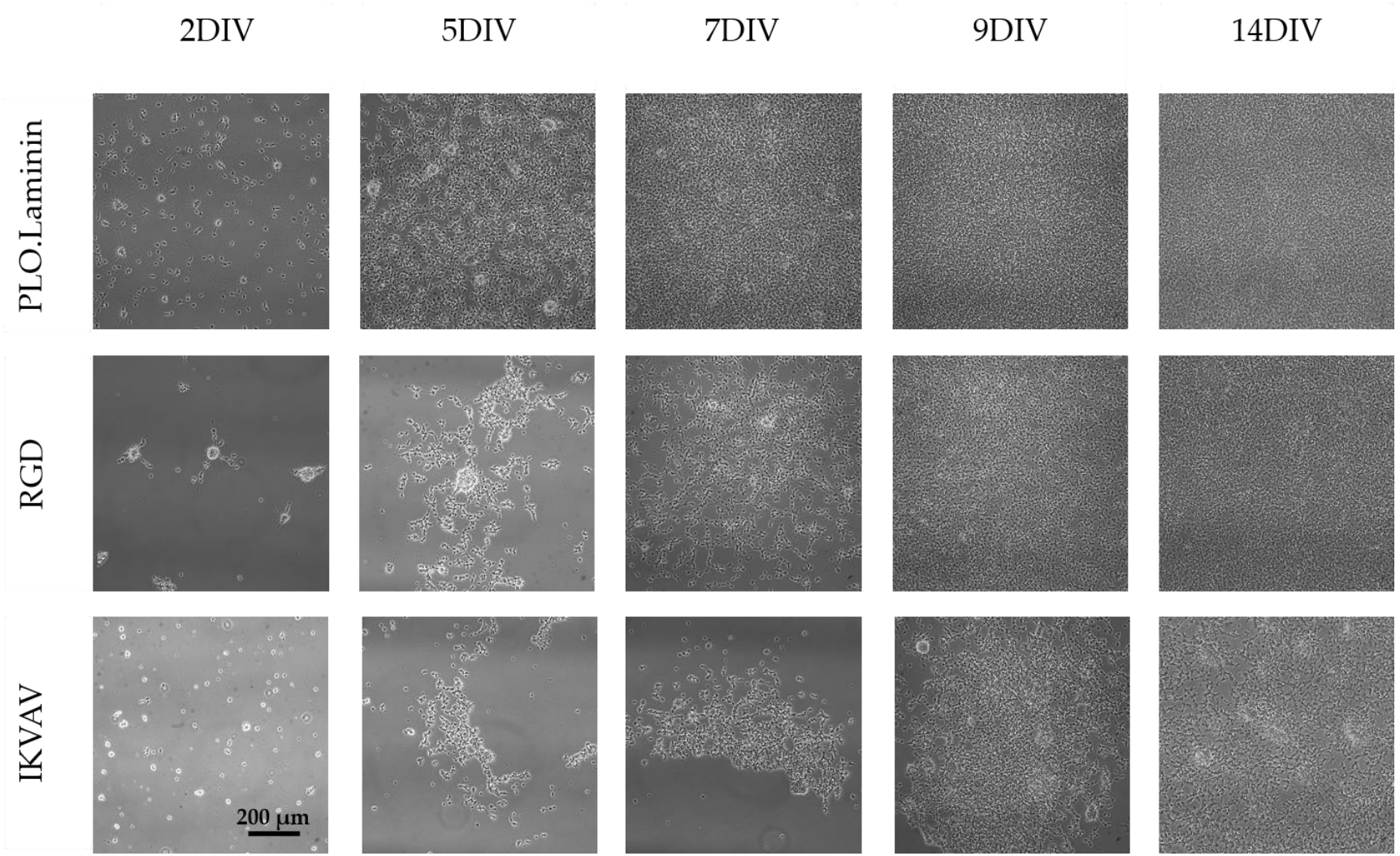


Figure 5.14 Phase contrast images of E18 NPSCs cell cultures on PLO.Laminin, RGD and IKVAV surfaces that are low surface coverage to high surface coverage, n = 3. All the cells were cultured on the surfaces at a density of 3 x 10^5 cell/mm^2 in serum-free media for 14 days *in vitro*.

Consequently, the increase in RGD peptide composition enabled the cells to adhere and proliferate better on the 75% RGD and 100% RGD versus those of the 0% RGD, 25% RGD and 50% RGD in the early days of incubation. By 14DIV the least confluent surface was the 0% RGD (i.e. 100% IKVAV), which can be theorized to be due to the absence of RGD cues on the surface which is adhesion peptide that allows for cells to develop cytoskeletal stress [96, 97]. These results further support previous literature that the absence of RGD peptides on the surfaces induces low cell adhesion, and an increase in RGD peptide composition induces an increase in NPSCs surface coverage due to high cell adhesion whilst exhibiting elongated and spread cell morphology. The control surfaces demonstrated a similar cell response as in the previous chapter with the IKVAV surface results being equivalent to that of the 0% RGD surface, and the RGD and PLO.Laminin surfaces similar to that of the higher concentration of RGD composition surfaces.

Next we quantified the difference in the NPSCs attachment and proliferation observed through phase contrast images to verify the above statement that an increase in RGD composition influence an increase in NPSCs adhesion, see Figure 5.15.
We observed that the % area coverage for the 0%RGD and 25% RGD surfaces were similar to that of the IKVAV control surface respectively, 1.26% ± 1.19, 2.88% ± 1.15, and 1.96% ± 1.33 cells at 2DIV. Moreover, with the increase of RGD peptide composition an increase in cell adhesion was demonstrated on the 50% RGD, 75% RGD, and 100% RGD surfaces with % area coverages of 3.76% ± 1.23, 4.09% ± 1.14 and 4.86% ± 1.08. Additionally, the RGD control surface we observed a similar cell adhesion to that of the 100% RGD surface with a % area coverage 4.24% ± 1.26 at 2DIV. In comparison to the RGD and IKVAV control surfaces and the controllable composition of peptide surfaces the control surface of PLO.Laminin exhibited higher cell attachment and faster cell proliferation, which is illustrated in the phase contrast images of the PLO.Laminin surfaces as more developed cell processes and a % area coverage of 7.08% ± 1.63.

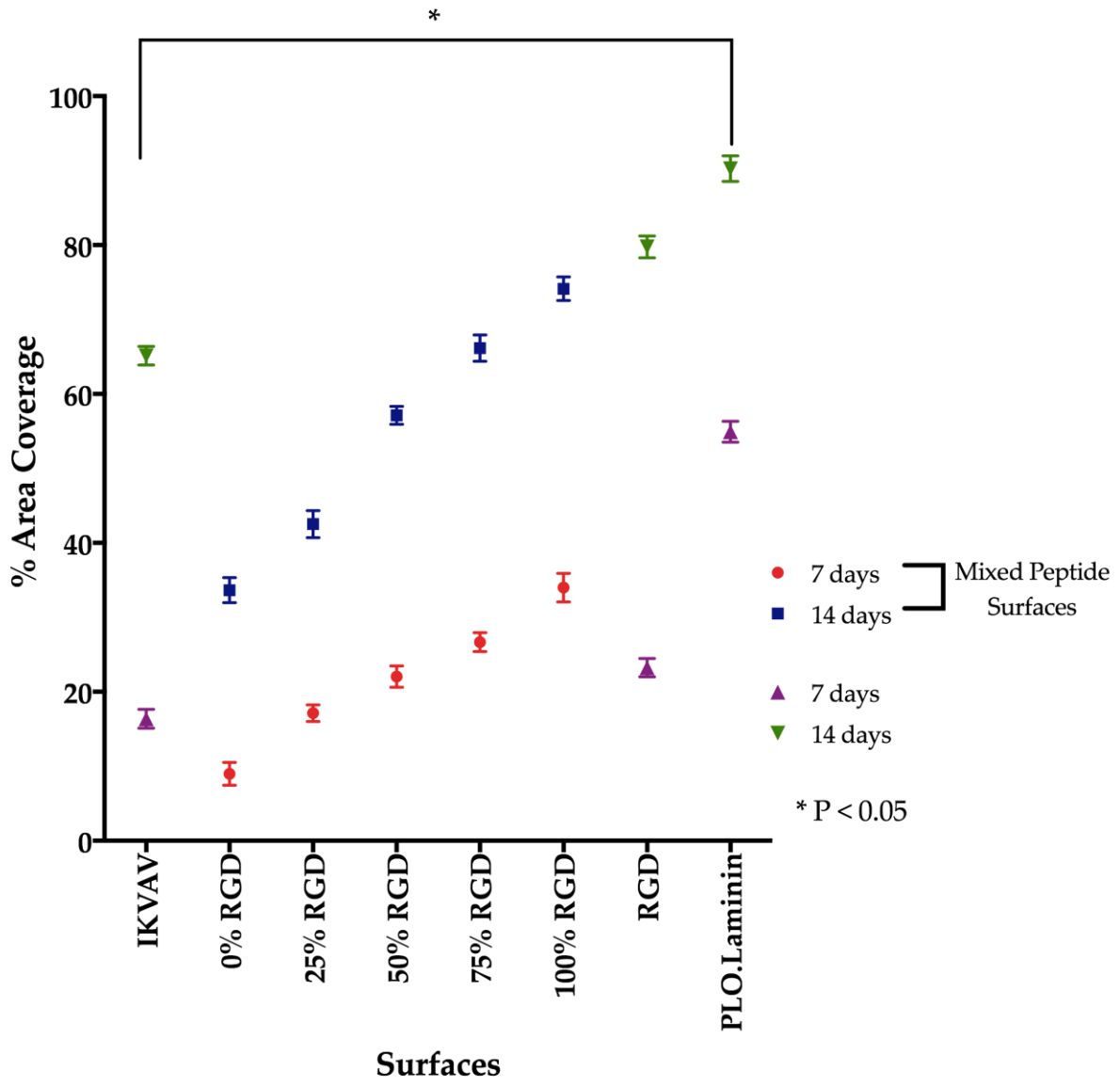


Figure 5.15 % Area coverage of E18 NPSCs on 0% RGD – 100% RGD surfaces with PLO.Laminin, RGD and IKVAV surfaces as controls. Error bars represent mean ± SD for n = 3, and significant difference of (*) $p < 0.05$ was observed on the PLO.Laminin surface to the 0% RGD – 100% RGD surfaces , and the control surfaces of RGD and IKVAV. All the cells were cultured on the surfaces at a density of 3 x 10^5 cell/mm^2 in serum-free media for 14 days *in vitro*.

The 75% RGD and 100% RGD surfaces induced a higher % area coverage in comparison to the lower RGD composition surfaces of 0% RGD, 25% RGD and 50% RGD, as well as inducing cells to proliferate significantly faster on the 75% RGD and 100% RGD after 2DIV. At 7DIV the controllable composition of peptide surfaces inducing more separate cells in cell-surface interaction with uniform cell processes with the increase in RGD composition of

the surface. A significant difference in the number of cells on the surface was observed between the 25% RGD and 0% RGD surfaces respectively, 17.14% ± 1.12 and 8.99% ± 1.53 cells. This further supports the presence of the RGD peptide on the surface enables an increase in cell adhesion with an elongate and spread cell morphology, and cell proliferation on the surface. In contrast, a reduced number of RGD composition (i.e. 100% RGD – 0% RGD) on the surface induced cell clusters and clustered processes due to the increase of IKVAV peptides present on the surfaces.

The proliferation profile of cells cultured on these surfaces all demonstrated a positive correlation with incubation time, which showed an increase in number of cells with the increase of RGD peptides composition as demonstrated on the 50% RGD, 75% RGD and 100% RGD surfaces respectively, 22.04% ± 1.43, 26.68% ± 1.27 and 33.99% ± 1.92.

The controllable peptide composition surfaces were compared to the control surfaces of PLO.Laminin, RGD and IKVAV surfaces at 7DIV and 14DIV where we observed that the IKVAV surfaces showed a higher proliferation against its equivalent surface of 0% RGD (i.e. 100% IKVAV) with % area coverages of 8.99% ± 1.53 and 33.65% ± 1.69. Moreover, the 25% RGD surface demonstrated a % area coverage of 17.14% ± 1.12 at 7DIV, which is similar to that of the IKVAV control surface at also 7DIV. We observed that the 100% RGD surfaces were equivalent to that of the RGD control surfaces, which also illustrated a higher proliferation rate at 7DIV of 33.99% ± 1.29 and 23.24% ± 1.24, and similar at 14 DIV of 74.14% ± 1.58 and 79.76% ± 1.46. This can be related to the RGD surfaces having a more tightly packed cell population; in comparison the 100% RGD surfaces induce a more cell spread morphology with more extended processes along the surfaces, thus, a lower number of adhered cells on the surface. Furthermore, the surface functionalization of two surfaces, (i) the immobilized RGD and IKVAV surfaces (i.e. GOPTS, PEG_{18}-diamine) and (ii) the controllable composition of peptide surfaces (i.e. GOPTS, PEG_{18}-diamine, Fmoc-GABA-OH, Monomethyl Glutarate, and 3-(Fmoc-amino)-1-propanol), were chemically functionalized using slightly different pathways while they display the same peptides of RGD and IKVAV. Whilst the two surfaces are likely comparable they certainly not identical (i.e. surface chemistry), which demonstrated in the biological response of the cells on the two surfaces. The PLO.Laminin control surface presented the highest % area coverage of all the surfaces with 54.93% ± 1.39 and 90.27% ± 1.71 at 7DIV and 14DIV. Consequently, the PLO.Laminin

surface illustrated an enhanced cell proliferation significantly, (*) $p < 0.05$, different to all the controllable peptide composition surfaces, as well as those of the RGD and IKVAV surfaces.

5.4.2 CELL DIFFERENTIATION

The prepared controllable composition peptide surfaces and the control surfaces of RGD, IKVAV and PLO.Laminin provided NPSCs adhesion, spreading and proliferation with the increase of RGD peptide composition on the controllable composition peptide surfaces (i.e. 0% RGD – 100% RGD surfaces). We observed that the cells become very confluent on all of the surfaces with the exception of the 0% RGD surfaces after 14DIV and induced the cells to lift off the surfaces, similar to that observed in Chapter 4 as a monolayer of cells (i.e. spontaneously) [358].

Our results demonstrated the 0% RGD surfaces to induce NPSCs to differentiate into astrocytes and no neurons were observed on these particular surfaces, Figure 5.16. The cells spread along the surfaces in an elongated morphology, so less cells were quantified by HOECHST staining of the nuclei. The increase in RGD composition on the surface from 25% RGD surface to 50% RGD surface demonstrated an increase in the number of cells on the surfaces, which was further evident with the staining of the nuclei.

Moreover, the 0% RGD surfaces induced NPSCs to differentiate only into astrocytes, whilst the increase in RGD composition on the surfaces with a decrease in the size of the astrocyte cell morphology, an increase in surface coverage, and increase in cell confluence on the surfaces. The 25% RGD surfaces induced the differentiation of NPSCs into neurons, but no neural network is observed. Whilst the 50% RGD surfaces demonstrate some of the neurons connecting to another and the further increase in RGD peptides surface of 75% and 100% RGD surfaces illustrate a more established neural network. Consequently, the increase in RGD peptides on the surfaces illustrated an increase in the neuron specific β III-Tubulin proteins on the surfaces, thus, signifying that the presence of RGD peptides induced NPSCs to differentiate into neurons. In the previous chapter (i.e. Chapter 4) we hypothesized with correlation to literature that that single cells/groups as observed on the IKVAV surfaces are larger than the astrocytes observed on the RGD and PLO.Laminin surfaces [363].

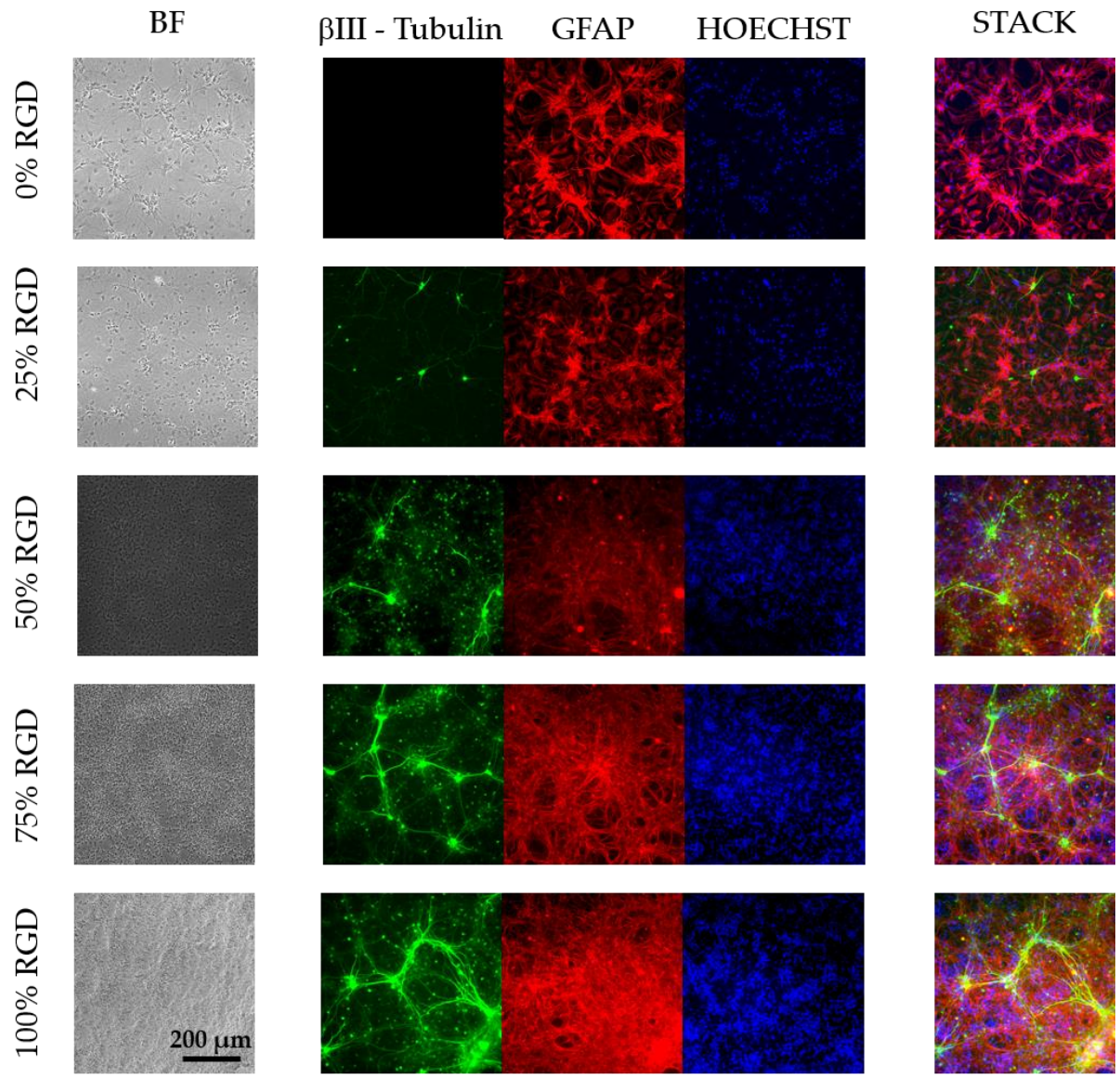


Figure 5.16 Fluorescent microscopy images of differentiated E18 NPSCs on 0% RGD-100% RGD surfaces. The green, red and blue represent respectively βIII-Tubulin in neurons, GFAP in astrocytes, and nuclei. All the cells were cultured on the surfaces at a density of 3 x 10^5 cell/mm^2 in serum-free media for 14 days *in vitro*.

The later surfaces exhibited cells that were smaller in size, had a mixed population of neurons and astrocytes and were more tightly packed across the surface to form confluent monolayers. This is clearly observed in the fluorescence GFAP images between the 0% RGD and 100% RGD surfaces. Consequently, the controllable peptide composition surfaces demonstrate that the change in cell morphology (i.e. cell length, width, total spread area of

cell), cell adhesion and differentiation all are dependent on the composition of RGD versus IKVAV peptides on the surfaces. Additionally, previous evidence has pointed out that neurons require a good network of supporting cells, astrocytes, as their neighboring cells in order to establish a neural network.

Furthermore, we quantified the % area coverage of neurons and astrocytes on these surfaces to determine the influence of controllable composition peptide surfaces versus that of the control surfaces of RGD, IKVAV, and PLO.Laminin on the differentiation of NPSCs into a specific cell fate as shown in Figure 5.17. The 0% RGD surfaces are equivalent to the IKVAV surfaces in their biological response as both surfaces do not induce NPSCs to differentiate into neurons. Whilst in contrast the % area coverage for the astrocytes is lower on the 0% RGD surfaces than the IKVAV surfaces respectively, 25.22% ± 4.36 area coverage and 52.89% ± 3.09 area coverage. This difference between the %RGD surfaces and the IKVAV surfaces was also observed in the WCA measurements respectively, 43.1^{o} ± 1.2 and 34.8^{o} ± 2.0, which can be related to the two surface functionalization procedure (i.e. surface chemistry for IKVAV is GOPTS/PEG/IKVAV and the % RGD is GOPTS/PEG/Fmoc(NH_2)/IKVAV) of the two different surfaces and their cell response. The 25% RGD and 50% RGD surfaces exhibited a correlating increase in the % area coverage for astrocyte from 33.80% ± 3.06 to 48.98% ± 3.02 area coverage and neurons from 7.10% ± 3.20 to 14.78% ± 3.36 area coverage. A significant difference, (**) $p < 0.01$, is observed from the 50% RGD to the 75% RGD surfaces in % area coverage of neurons, 14.78% ± 3.36 to 35.79% ± 3.98 area coverage, and astrocytes, 48.98% ± 3.02 to 88.66% ± 3.56 area coverage, due to the establishment of more advanced neural networks.

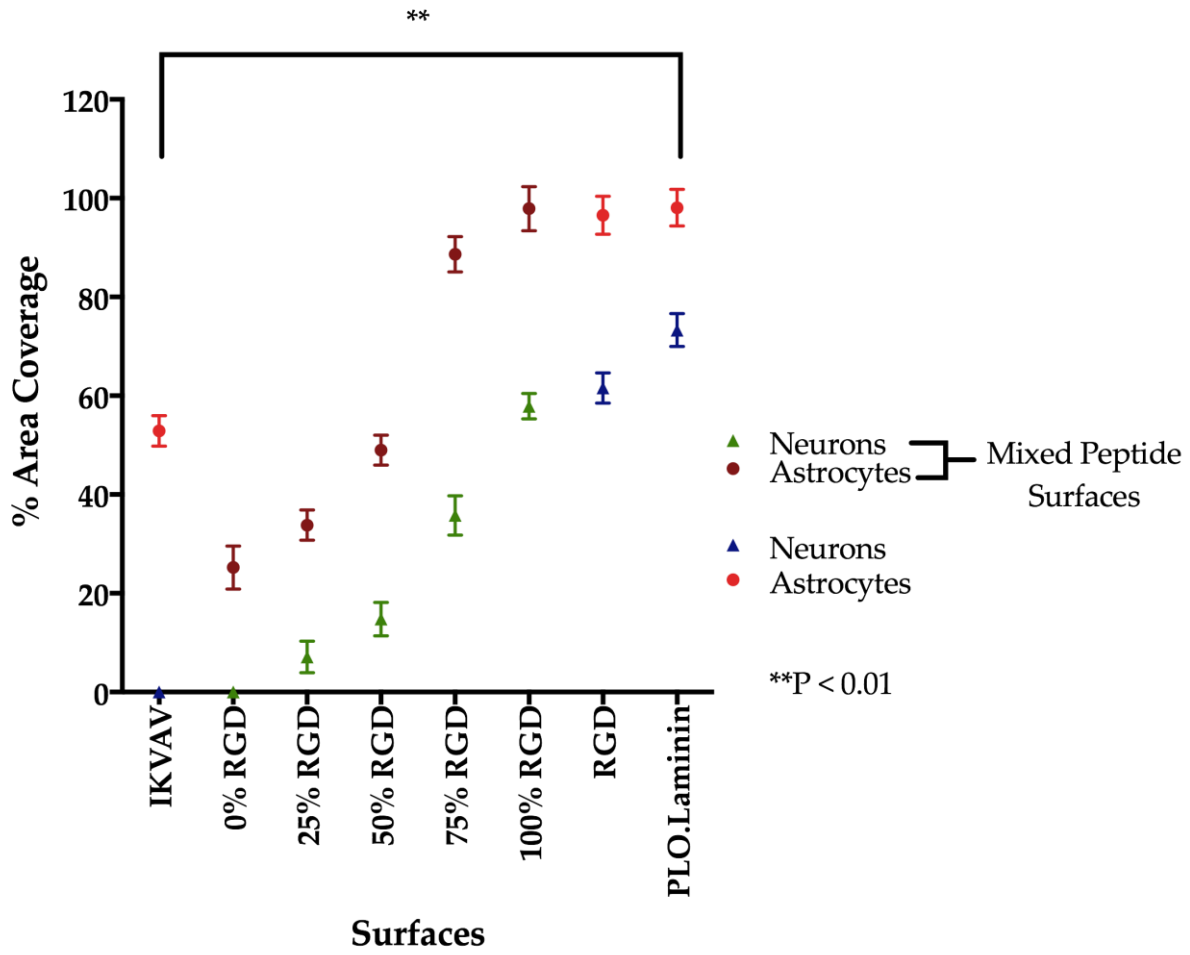


Figure 5.17 Quantification of E18 NPSCs differentiation into neurons (βIII-Tubulin positive) and astrocytes (GFAP positive) as relative area coverage by each cell type on 0% RGD – 100% RGD surfaces and the control surfaces of PLO.Laminin, RGD and IKVAV. Error bars represent mean ± SD for n = 3 and a significant difference of (**) $p < 0.01$ is observed for population of neurons to astrocytes on these functionalized surfaces. All the cells were cultured on the surfaces at a density of 3 x 10^5 cell/mm^2 in serum-free media for 14 days *in vitro.*

The 100 % RGD surfaces present a similar % area coverage to that of the RGD surfaces in their biological response in the number of astrocytes, 97.88% ± 4.45 and 96.52% ± 3.84 area coverage. Whereas the RGD control surfaces induced a slightly higher area coverage of neurons in comparison to the 100% RGD surfaces, 61.57% ± 3.05 and 57.88% ± 2.56 area coverage, respectively. The PLO.Laminin illustrated a better established neural networks in comparison to that of the other surfaces respectively, with a 73.29% ± 3.33 area coverage of neurons and 98.08% ± 3.70 area coverage of astrocytes of which the latter is similar to that of

the RGD control surface and the 100% RGD surfaces. Furthermore, the larger % area coverage of astrocytes and neurons (i.e. better established) on the PLO.Laminin surfaces in comparison to that of the RGD control surface and 100% RGD surfaces can be related to the astrocytes, which have the role as structural cells to support the formation of neural networks. This is further evident in the % area coverage for the astrocytes on these particular surfaces and further supported with positive correspondence on the 100% RGD surfaces. In addition, the 100% RGD surfaces demonstrate a % area coverage for the neurons and astrocytes that is equivalent to that of the control surfaces of RGD and PLO.Laminin surfaces. Next we quantified the relative composition of the cell population by plotting the ratio of % area coverage of neurons to astrocytes on the surfaces as a % area coverage and found a significant difference, (**) $p < 0.01$, for the relation of neurons versus astrocytes on the surfaces, Figure 5.18. We observed an increase in % area coverage of neurons versus astrocytes with the introduction of RGD peptides from 0% RGD to 25% RGD inducing a 20.96% ± 3.98, which increases systematically to 59.13% ± 4.52 for the 100% RGD surfaces.

The IKVAV control surfaces were equivalent to the 0% RGD surfaces and the RGD control surfaces were comparable to the 100% RGD surfaces with % area coverage of, 63.79% ± 2.84 and 59.13% ± 4.52, respectively. Whilst the PLO.Laminin surface demonstrated a higher % area coverage relation for neurons versus astrocytes of 74.73% ± 3.76.

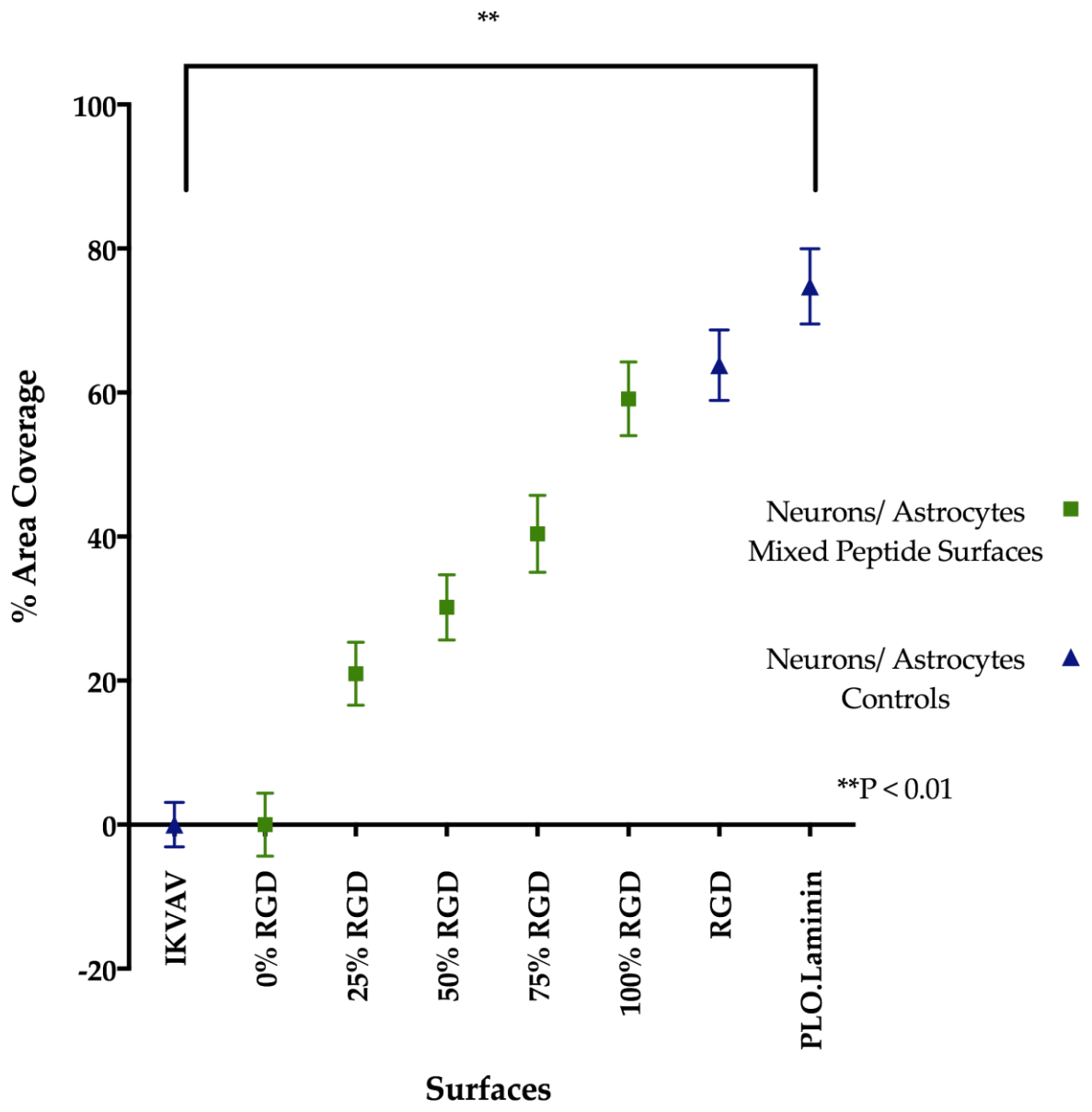


Figure 5.18 Quantification of E18 NPSCs differentiation as a change in the relative composition of the cell population expressed as ratio of % area coverage of neurons (βIII-Tubulin positive) and astrocytes (GFAP positive) on 0% RGD – 100% RGD surfaces and the control surfaces of PLO.Laminin, RGD and IKVAV. Error bars represent mean ± SD for n = 3 and a significant difference of (**) $p < 0.01$ is observed for population of neurons to astrocytes on these functionalized surfaces. All the cells were cultured on the surfaces at a density of 3×10^5 cell/mm^2 in serum-free media for 14 days *in vitro.*

Lastly, we plotted the summed RGD ion fragments quantified in Figure 5.11 against the % area coverage of neurons versus astrocytes to quantify the systematic trend observed in the fluorescence STACK images of the controllable composition peptide surfaces in Figure 5.16 and Figure 5.17. The plotted graph quantifies an increase in RGD peptide composition on the surfaces induced an increase in the neurons on the surfaces in a positive correlation, Figure 5.19. Thus, further supporting and validating our hypothesis that the amount of RGD peptide composition present on the surface influences a biological response in the NPSCS to differentiate into neurons versus no neurons in the absence of the RGD peptides.

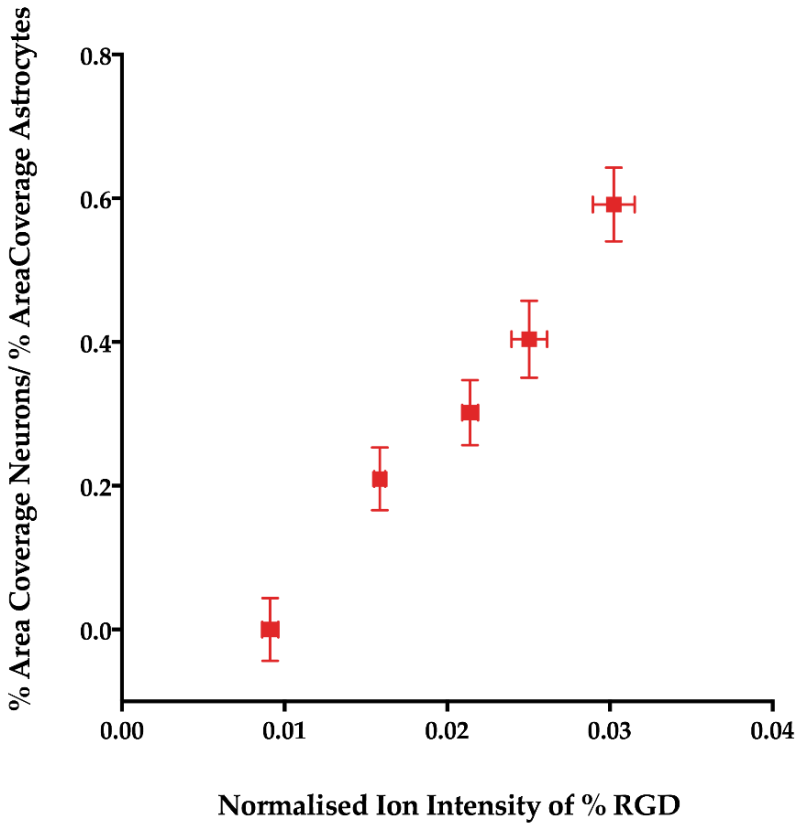


Figure 5.19 The quantification of E18 NPSCs differentiation into neurons (βIII-Tubulin positive) in relation to the increase in % RGD peptides ion fragments on the surfaces. Error bars represent mean ± SD for n = 3, and ion fragments are normalized to total ion intensity.

5.5 SUMMARY

We hypothesized in this chapter that by varying the ratios of peptides on the same surface we would be able to control the preferential differentiation of the NPSCs and influence a controlled microenvironment of neurons and astrocytes to mimic more closely the akin characteristics of the ECM. The functionalized surfaces were characterized by measuring the relative amounts of peptides on a surface and not the surface concentration or surface density. The peptide surfaces discussed here signify a composition of RGD to IKVAV ratios of 0%RGD (0:100), 25%RGD (25:75), 50%RGD (50:50), 75%RGD (75:25), and 100%RGD (100:0) of relative amount of peptide functionalization surfaces.

Surface characterization was performed by the physicochemical surface sensitive analysis using WCA, AFM, and ToF-SIMS. Orthogonal chemistry facilitated us to optimize and present an innovative method of immobilizing controlled composition peptide surfaces by sequential SPPS 'grafting from' two distinct linkers, Fmoc-GABA-OH and Monomethyl glutarate, that allowed us specific and selective binding of the peptides. A significant increase in surface wettability was observed after the hydrolysis of the methyl ester functional group of the monomethyl glutarate linker on the surfaces. Furthermore, the WCA and AFM measurements demonstrated positive correlation in surface hydrophobicity and a decrease in surface topography with the increasing Fmoc composition; whilst in comparison an increase in surface wettability and surface topography was observed with the increase of RGD composition on the surface. An increase in the selected RGD marker ion fragments was observed with the increase of RGD composition on the surfaces from 0% RGD – 100% RGD in relation to the decrease of the IKVAV marker ion fragments on the same surfaces. The ToF-SIMS raster images demonstrated that the controlled composition peptides surfaces were homogenous and ROI measurements validated the successful orthogonal functionalization of controllable composition peptides surfaces, thus, an increase in RGD composition relative to a decrease in the IKVAV composition was observed.

Optical phase contrast images of the NPSCs showed the cell response to the controllable composition peptide surfaces of 0% RGD – 100% RGD. A systematic trend concerning cell adhesion was observed with the increase of RGD composition on the surfaces, which was very evident at 5DIV and 7DIV. The NPSCs adhesion and proliferation on the higher content

RGD peptide surfaces were favored with a significant difference, (**) $p < 0.01$, between the control surface of PLO.Laminin and the controllable peptide composition surfaces.

These results demonstrated that the increase in RGD composition on the surfaces increased the suitability for cell adhesion, proliferation and survival. Next we postulated that the increase in RGD peptides on the 0% RGD – 100% RGD surfaces would control the preferential differentiation of the NPSCs towards the specific cell fate of neurons.

Firstly, we established that in the absence of the RGD peptides the surfaces induced the NPSCs to differentiate towards the astrocyte cell fate and with elongated and spread cell morphology. Secondly, the increase of RGD composition on the surfaces influenced the NPSCs to differentiate into neurons and astrocytes in a positive correlation to the % RGD surfaces. Additionally, a significant difference, (**) $p < 0.01$, in the increase in mature neural network was observed as the RGD composition on the surfaces increased, as well as more tightly packed cell morphology of astrocytes. This outcome was quantified as an increase in % area coverage of neurons versus astrocytes.

Finally, we compared the normalized total ion fragments of RGD to the % area coverage of neurons versus astrocytes to validate our hypothesis, which states that the amount of RGD peptide composition present on the surface would influence the biological response of the NPSCs to differentiate into neurons versus no neurons in the absence of the RGD peptides.

Moreover, our results can be supported by the conclusions made in the publications of Saha et al., 2007 and H.Li and J.J. Cooper-White, 2014, which both demonstrated that the absence of RGD on the functionalized surfaces made for very poor cell adhesion and an increase in cell adhesion was observed in correlation with the increase of RGD [231, 232]. Whilst the increase in the ratio of RGD versus IKVAV revealed that the stem cells favored the differentiation into the neuron linage to that of the glial linage in Saha et al., 2007 [231].

The results presented in this chapter demonstrated the successful preparation, optimization, and characterization of designing bifunctional surfaces via a novel method of orthogonal chemistry. This method provided us with the ability to control the composition of the RGD and IKVAV peptides on the same surface and influence the cultured NPSCs to differentiate to controllable population of neurons and astrocytes. The well-controlled compositions of RGD and IKVAV ratios present a 2D environment that can be reasoned to that akin of the

ECM. Moreover, our novel approach can be used to facilitate the control of orthogonal functionalization of other molecules (i.e. proteins, carbohydrates, lipids, DNA, nanoparticles) to engineer versatile and easy 2D and 3D. In view of that, in recent years we have seen a significant increase of publications demonstrating a shift in 2D surfaces to 3D surfaces, thus, in Chapter 6 we propose the immobilization of peptides on comparable 2D and 3D surfaces in order to examine the biological response of NPSCs to both microenvironment.

6 IMMOBILIZING PEPTIDES TO DESIGN 2D AND 3D MICROENVIRONMENTS

6.1 INTRODUCTION

The wide interest in NPSCs stems lies in the tremendous therapeutic potential that these cells offer in regenerative medicine and tissue engineering applications, such as regenerate, repair and replace of diseased and/or damaged cells. However, current NPSCs cell cultures are greatly simplified in 2D *in vitro* models versus their natural neural *in vivo* complex ventricular zone microenvironment (i.e. 3D) where they reside [370, 371]. Current 2D models lack the environmental cues that are present in a 3D environment, which play a crucial role in cellular maturation and function [246]. In this chapter we present the design of immobilizing peptides on comparable 2D and 3D surfaces to examine the biological response of NPSCs to both microenvironment and add to understanding on how to mimic the akin characteristics of the ECM more closely.

The chapter has been divided into three sections, the first two sections investigate the surface preparation and characterization of 3D surfaces in comparison to the more commonly designed 2D surfaces, and the third section will study the cell response towards the biomimetic surfaces in relation to their 2D and 3D microenvironment.

The most common material used for designing 3D surfaces to support studies in cell proliferation, migration, differentiation, angiogenesis and tumor growth are the Matrigel, hydrogels and cryogels. These materials provide a 3D hydrated network that is comprised of natural polymers (i.e. collagen, hyalluronates, chitosan), synthetic polymers (i.e. polyvinyl caprolactam and polyethylene glycol), or gelatinous proteins (i.e. laminin, collagen IV, and entactin) [262]. Moreover, their chemical and physical properties enable the tuning of their porous structure by varying freezing conditions and concentration of the cross-linker (i.e. cryogels).

Their disadvantages are that they can (i) introduce culture-to-culture variation (i.e. Matrigels are chemically poorly characterized), (ii) extensive process in functionalizing cellular chemical cues (i.e. hydrogels), (iii) drawback in controlling culture conditions (i.e.

temperature, pH, CO_2 and O_2 levels, (iv) possible entrapment of residual chemical within the gel (i.e. toxicity), and (v) long exposure to the media can lead to the degradation of the 3D surfaces (i.e. affecting the mechanical integrity that support the cells) [262].

To overcome these challenges we propose the use of nanoparticles as the 3D surface to support NPSCs adhesion, survival, proliferation, differentiation, and cellular uptake. The dissociated NPSCs are cultured in the media as a suspension, which permits them to form 3D neurospheres with the functionalized nanoparticles to establish a 3D architectural organization that is more closely related to that of the natural niche that support the development of NPSCs.

Furthermore, the nanoparticles were chosen as the 3D surface as it complements the work done so far in the functionalized 2D surfaces in the previous chapters, as well as being a surface that can be easily integrated as a 3D environment (i.e. neurospheres) into the mentioned SLAB system (i.e. microfluidics, MEA, biosensors).

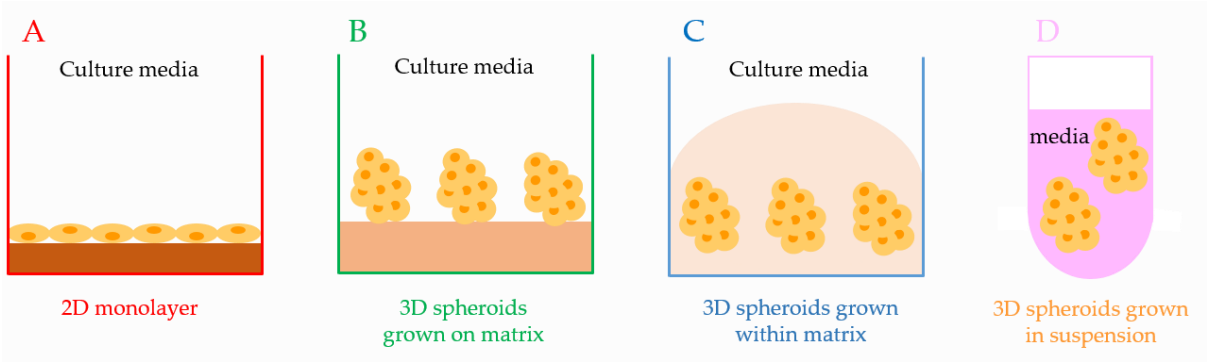
6.2 BACKGROUND

6.2.1 THREE-DIMENSIONAL (3D) MODEL MICROENVIRONMENTS

The extracellular matrix (ECM) is a dynamic and complex 3D microenvironment that cells are surrounded by and is involved in regulating the fundamental processes such as cell adhesion, survival, proliferation, migration, differentiation, apoptosis, and tissue morphogenesis [47-53]. Extensive research has gone into the studying the biological system at different levels (i.e. organismal, tissue, cellular and molecular levels) to gain understanding of their structural, functional and biological interactions within the system.

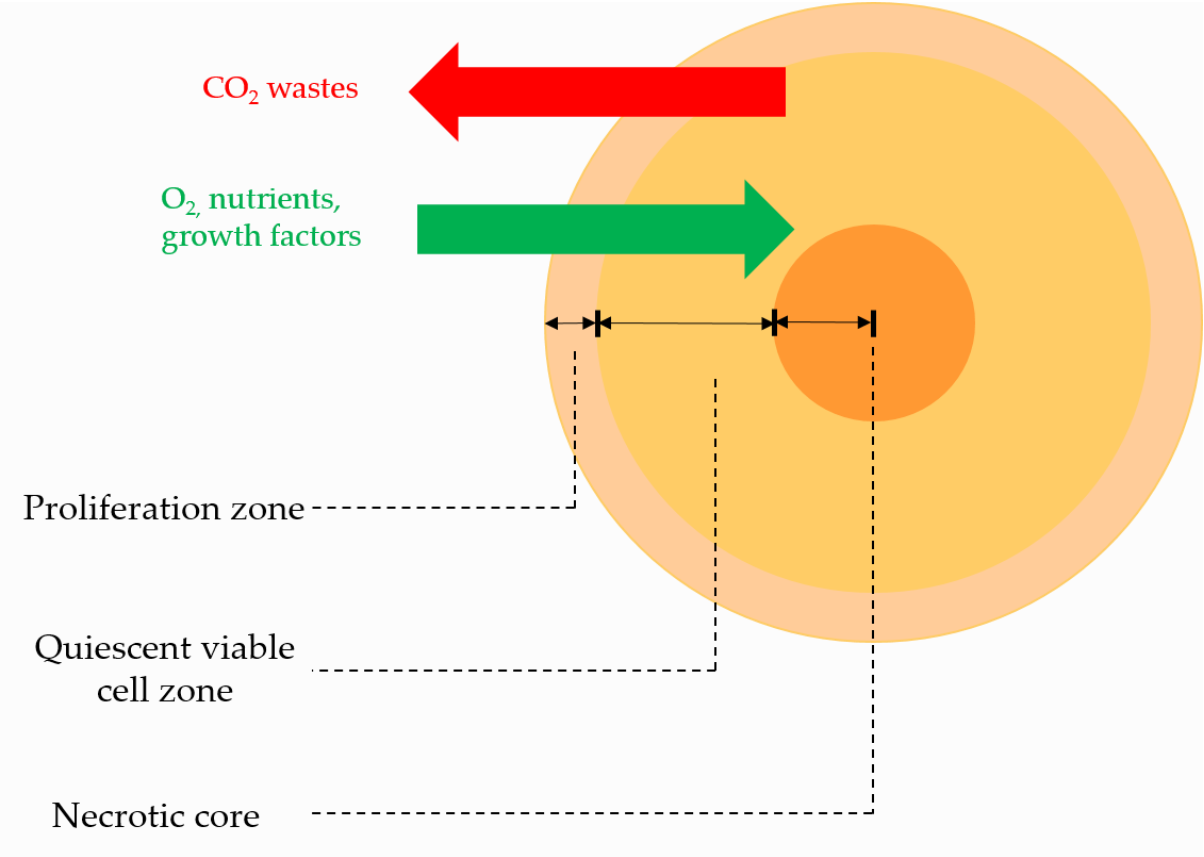
Since the 1900s all *in vitro* studies (i.e. basic, clinical, and pharmaceutical industry) have been facilitated through the conventional and well-established 2D culture environment [372]. Technological developments in the fields of tissue engineering and regenerative medicine has been focusing on designing biomimetic materials that mimic more closely the natural cellular activities akin to that of the ECM, thus, intensive research has gone into the creation of highly tunable and functional 3D model microenvironments (i.e. bone, cartilage, skin, heart, lung, liver, and cornea) [373-379]. Schematic 6.1 illustrates the conventional 2D model microenvironment which usually is a glass or polystyrene tissue

culture surface that the cells are seeded and facilitates (i) homogenous amount of nutrients and growth factors from the culture media, (ii) proliferation versus necrotic (i.e. detach at an early stage), (iii) a cell morphology that is flat and spread on the surface.



Schematic 6.1 Concept diagram of the traditional two-dimensional (2D) monolayer cell culture (A) and three typical three-dimensional (3D) cell culture systems: cell spheroids/aggregates grown on matrix (B), cells embedded within matrix (C), or scaffold-free cell spheroids in suspension (D). Taken and adapted from Rasheena Edmondson et al. 2014 [249].

In comparison the 3D model microenvironment can facilitate the cells to aggregate to form 3D spheroids and grow (i) on a matrix scaffold, (ii) within a matrix scaffold (i.e. solidification or polymerization of cells in liquid matrix), and (iii) in suspension (i.e. nanoparticles) [380, 381]. The 3D spheroids resemble the natural cell morphology that akin to that of the cells in the ECM and present cells at various stages in the cell cycle (i.e. proliferating, quiescent, apoptotic, hypoxic, and necrotic cells) [249, 372]. The cells on the outer layer of the 3D spheroid are proliferating as they are surrounded by the culture media where they exchange their waste and are highly exposed to the nutrients and growth factors. Whilst the core of the 3D spheroid is necrotic due to the lack of oxygen, nutrients and growth factors and are either in the quiescent or hypoxia stage (i.e. as observed in tumors) as illustrated in Schematic 6.2 [249]. Furthermore, 2D and 3D model microenvironments demonstrate different rate of proliferation depending on the cell line and microenvironment (i.e. type of surface functionality, on matrix, within matrix) in question [382, 383].



Schematic 6.2 The typical zones of cell proliferation in a 3D spheroid, with the models of oxygenation, nutrition, and CO2 removal. Taken and adapted from Rasheena Edmondson et al. 2014 [249].

3D model microenvironments demonstrated advantages such as, (i) imaging live phenomena, and (ii) cells exposure to sequential extracellular factors. However, they also have major drawbacks such as difficulties in cell culture preparation and keeping the cells alive for long periods due to inability to supply nutrients to all cells and removing waste. As a result even with the state-of-the-art research developments in 3D model microenvironments the conventional 2D model microenvironments are still indispensable [372, 384]. Consequently, in this chapter we compare the conventional surface functionalization of immobilizing peptides on 2D surfaces (i.e. height and width) to that of 3D (i.e. height, width and depth) surfaces and observing the NPSCs biological response in relation to cell adhesion, proliferation and differentiation.

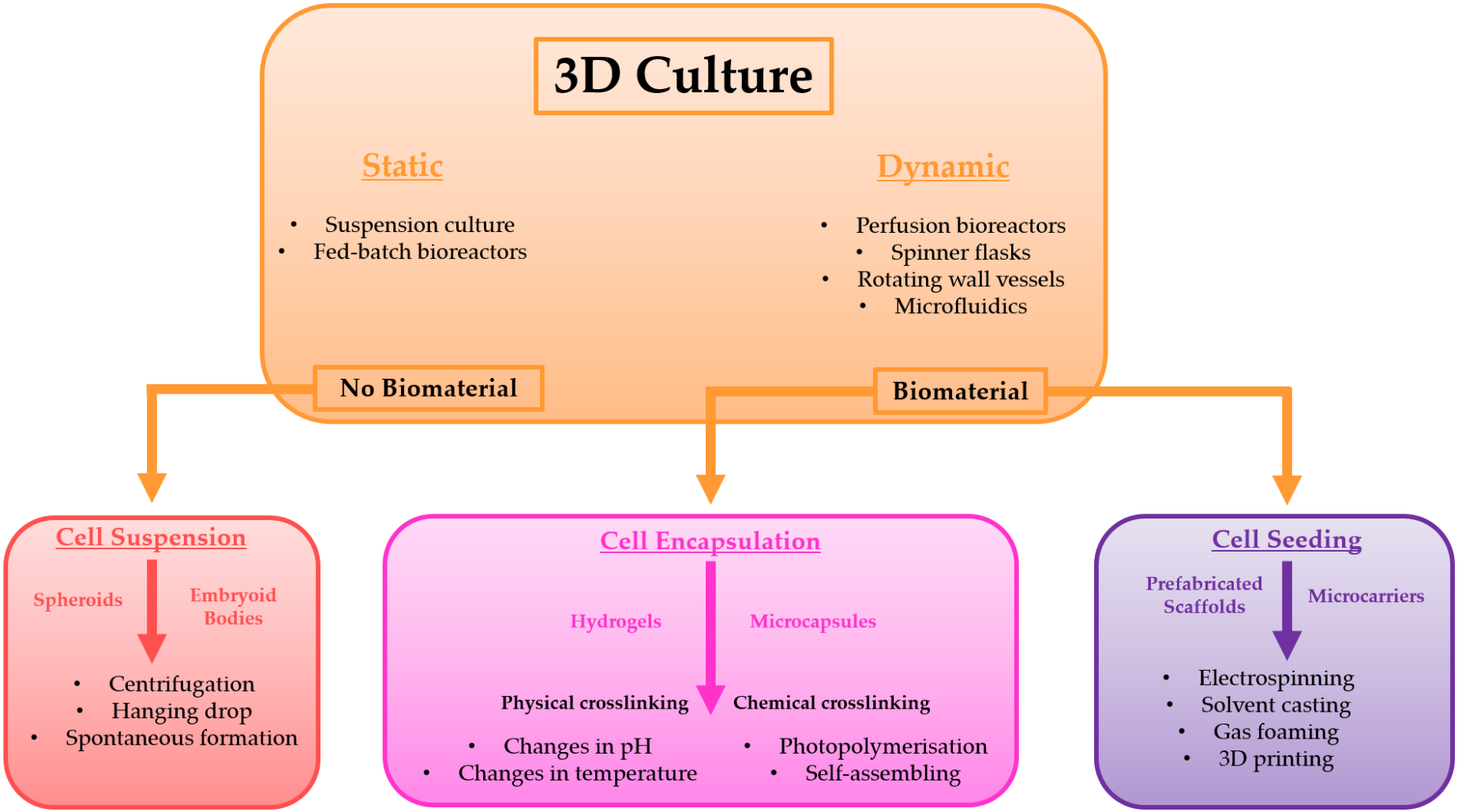
For the 3D microenvironment we propose a neurospheres model to tackle the previously mentioned difficulties by demonstrating that NPSCs in the form of neurospheres (i) are easy to prepare, (ii) are able to be maintained in large numbers, and (iii) their 3D dynamic environment can be changed by adjusting the growth factor(s) and ECM composition present in their culture media. Whilst the 3D surface that we employed in this chapter are nanoparticles that are comparable to the surface chemistry of the 2D surfaces that have been presented in the previous chapters.

6.2.1.1 NEUROSPHERES

The study of the tissue-specific NPSCs that can give rise to all neural populations can be investigated *in vitro* by culturing as a 2D monolayer or as a 3D spheroid as illustrated in Schematic 6.1. These 3D spheroid are referred to as neurospheres in the case of the NPSCs as they are floating structures obtained after the dissociation of embryonic or adult central nervous system (CNS) tissue and exposed to a media containing growth factors, Schematic 6.3 [370*]. The neurospheres are heterogeneous spheroid structures that are useful to evaluate NPSCs multipotentiality (i.e. cell phenotypes after differentiation) and analyze NPSCs self-renewal (i.e. clonal secondary neurosphere assays). Moreover, neurospheres present a complexity that is critical in establishing the 3D organization that is required and is found in the development of NPSCs in their natural niche. This complexity can be attributed to the neurospheres having the ability to produce their own ECM molecules (i.e. laminin, fibronectin), β1 integrins, and growth factor receptors to resemble more closely the *in vivo* conditions.

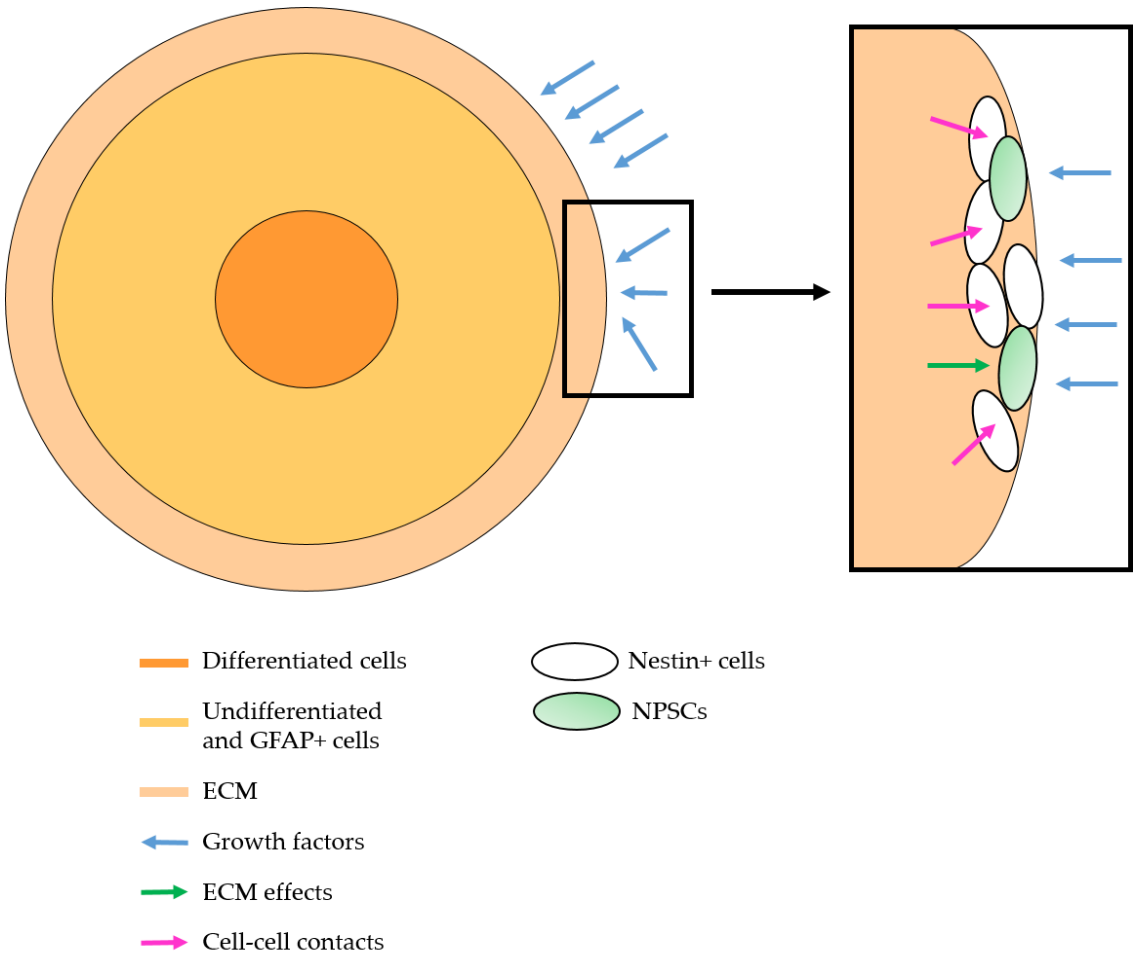
Neurospheres have demonstrated their usefulness in distinguishing between those cells that are in their stem cell maintenance/renewal stage and those in their committed progenitor proliferation stage. Furthermore, studies with the neurospheres can provide for detailed analysis of signaling events in a complex niche where the NPSC remain in contact with supporting cells and can accessibly be manipulated via biochemical or genetic means [370].

The preparation and maintenance of the neurospheres in large numbers for *in vitro* culture is easy and their 3D organization creates a dynamic changing environment, which can be achieved by adjusting the growth factors and ECM composition present in the culture media, Schematic 6.4 [370].



Schematic 6.3 Illustrates the approaches used for the 3D culturing of stem cells. Taken and adapted from McKee and Chaudhry, 2017 [370*].

Published data has suggested that the neurospheres established *in vitro* are useful in the analysis of time-dependent changes in NPSC population as a valid complement to any *in vivo* studies to investigate the influence of cell-cell and cell-ECM adhesion during neural development.

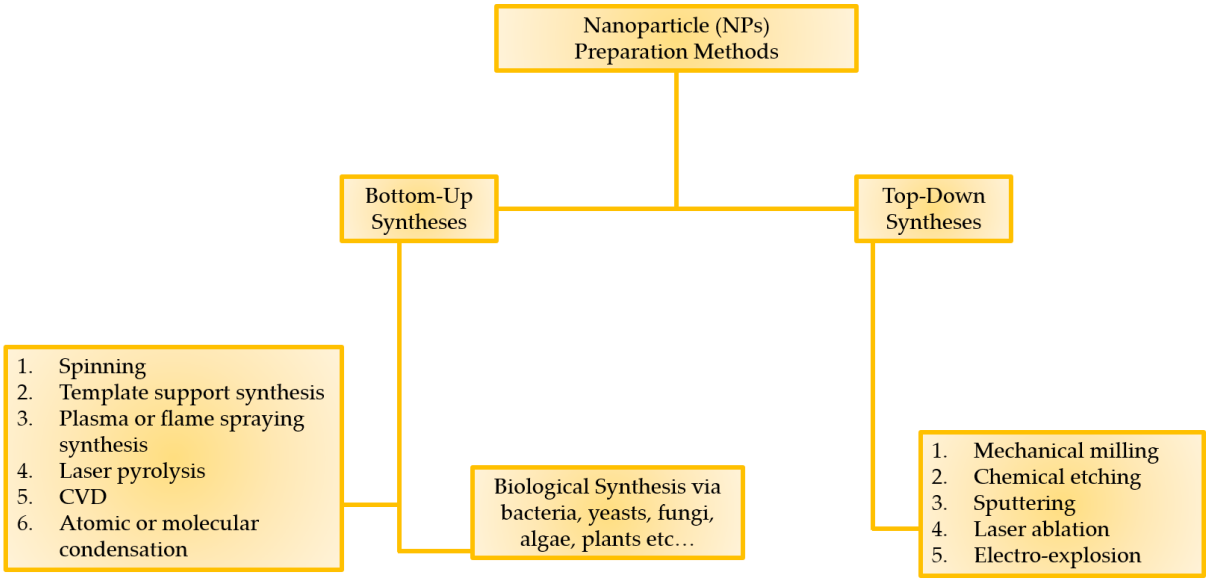


Schematic 6.4 Illustrates the edge of a neurosphere as a niche model. The core of the neurosphere (which contains βIII tubulin+ and GFAP+ cells) is shown in orange and the progenitor Nestin+ rich area in yellow. To simplify the diagram, the ECM molecules present at the edge (peach/light orange) are illustrated outside the orange Nestin+ region, although in reality they overlap. The inset represents the edge of the neurospheres were putative stem cells (green cells) may interact (pink arrows) with the surrounding stem cells (white cells, possibly Nestin+), in an environment enriched in ECM molecules (i.e. laminins, yellow background). This organized structure provides a special environment (i.e. niche) where the effects of growth factors may be modulated by cell-ECM and cell-contacts. Blue arrows indicate the presence of growth factors in the media. Taken and adapted from Lia Scotti Campos, 2004 [370].

6.2.1.2 NANOPARTICLES

Over the last decade nanomaterials have been at the leading edge of the rapidly developing field of nanotechnology. The scientific knowledge and commercial exploration period that nanoparticles have entered in this period have facilitated their development for applications in biology and medicine [385].

Cells are typically 10 μm across and made of many different cell parts (i.e. organelles and cell membrane) that are in sub-micron size domain, such as proteins which are characteristically 5 nm. Commercially nanoparticles have been synthesized that are larger and smaller than the proteins, 400 nm and 3 nm, respectively.



Schematic 6.5 Typical synthetic methods of NPs for the bottom-up and top-down approaches. Taken and adapted from Khan et al., 2017 [386].

These synthesized nanoparticles provide a simple comparison as very small probes (i.e. bio-tagging or -labelling) that facilitate the studies such as the cellular uptake into the cells as a synthetic carrier to influence the cell's signaling pathway, Schematic 6.5 [386]. The nanoparticles are classified depending on their morphology, size, and chemical properties as (i) carbon-based, (ii) metal, (iii) ceramics, (iv) semi-conductors, (v) polymeric, and (vi) lipid-based nanoparticles [385]. Moreover, nanoparticles are composed of three layers (i) the surface layer that may be functionalized with small molecules, metal ion, surfactants and

polymer, (ii) the shell layer that is chemically a different material from the core in all aspects, and (iii) the core which is the central portion and usually refers to nanoparticle itself.

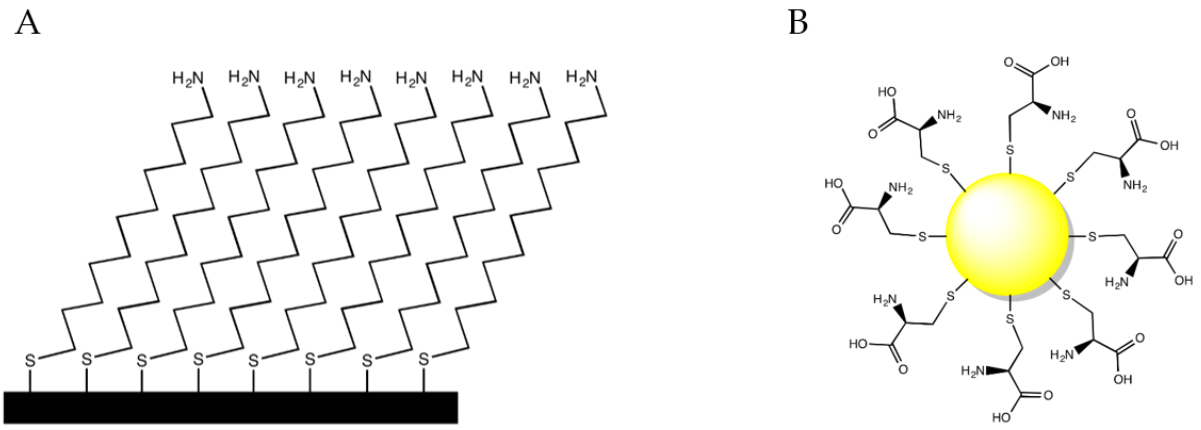
The nanoparticles are made biocompatible by means of functionalizing with a biological or molecular coating (i.e. antibodies, ECM proteins, or monolayers of small molecules) in order for it to interact with the biological target [386]. Thus, enabling the various applications that nanoparticles have in biology and medicine are as (i) fluorescent biological labels, (ii) drug and gene delivery, (iii) detection of proteins, (iv) tissue engineering, (v) MRI contrast enhancement, (vi) tumor destruction via heating (hyperthermia), and (vii) phagokinetic studies to mention a few [385].

Recent development in nanoparticles have presented progress in directing and remotely controlling their function by external signal or by the local environment, such as releasing drug load at tumors after driving magnetic nanoparticles to the target site or heating them in order to destroy the surrounding tissue [385, 387].

6.2.2 SELF-ASSEMBLED MONOLAYERS (SAMs) OF THIOLS

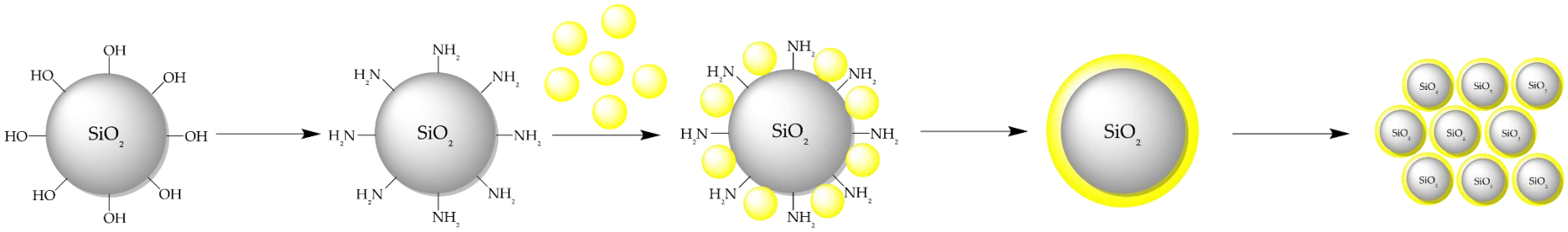
The 2D and 3D surfaces that we present are coated with a gold layer, as gold is an inter metal (i.e. biocompatible), it's not affected by oxidation, resists corrosion from most chemicals, and exhibits plasmonic properties (i.e. sensing applications) [388-390]. Moreover, the surface modification of gold surfaces is easily performed via different fabrication techniques (i.e. physical vapor deposition, electrodeposition or electroless deposition). We choose the physical vapor deposition of the gold on the 2D surfaces with a titanium biocompatible primer to obtain an almost-single-crystal gold-film and allow for the best surface functionalization. The surface functionalization with thiols (i.e. highly reactive with the inert gold), which are organosulfur compounds that contain the functionality of a carbon-bonded sulfhydryl (-C-SH or R-SH) group forming a self-assembled monolayer (SAMs) illustrated in Schematic 6.6. The thiols act as a adhesion promoter through forming thiol-gold SAMs between the gold surface and following functionalization stage on the surface (i.e. immobilizing peptides, DNA, antibodies) whilst facilitating (i) maximum molecule bonding on the surface and (ii) well-orientation of the molecules when in contact with biological media (i.e. *in vitro*, *in vivo*). The thiolation of a surface occurs in two stages, (i)

the activation of the surface via oxygen plasma cleaning and (ii) functionalization of the surface with the thiol via chemical adsorption (i.e. strong bonding). 11-amino-1-undecanthiol (AUT) is an aminoalkanethiols which facilitates the surface modification of gold surfaces to introduce amino groups on it, which allows for the further immobilization of peptides in our work via the SPPS "grafting from" approach established in the previous chapters (i.e. Chapter 4 and Chapter 5).



Schematic 6.6 Illustrates the chemical adsorption of (A) AUT on gold coated borosilicate coverslips and (B) the thiolated amino acid (i.e. cysteine) on nanoparticles.

Furthermore, the alkyl chain length of the AUT allows for a flexible linker, which is advantageous during the formation of the SAMs. Whilst functionalizing molecules with thiol functional group allows for the thiol-chemistry approach without using any short or long alkyl chain aminoalkanethiols such us the amino acid cysteine to facilitates the functionalization of gold surfaces via a one step "grafting to" approach (i.e. 3D surfaces) or multistep "grafting from" approach (i.e. 2D and 3D surfaces).



Schematic 6.7 Illustrates the process by which a gold shell is grafted around silica nanoparticle cores. Silica spheres were prepared to the modified literature procedure, (1) the silica cores were aminated with APTES stirred overnight under nitrogen; (2) the aminated silica spheres were then immersed into a solution of gold nanoparticles prepared according to the literature procedure and left overnight to absorb onto the surface of the spheres; (3) the spheres were then immersed in a solution of gold-plating [0.1% w/w $HAuCl_4$ in 0.4 mM $NH_2OH.HCl$]; and (4) the uniform thickness gold coating to form a complete gold shell around each silica sphere [292, 291].

6.3 SURFACE PREPARATION, CHARACTERIZATION AND VALIDATION

6.3.1 NANOPARTICLE SYNTHESIS AND CHARACTERIZATION

In this chapter we present the preparation and investigation of two differently sized nanoparticles, (i) gold nanoparticles (AuNPs) and (ii) silica spheres (SiO_2NPs) to silica core-gold shell nanoparticles (SiO_2@AuNPs) prepared according to modified literature procedures [292]. Moreover, the biological response of the NPSCs towards the different sizes of nanoparticles will provide us with understanding on whether the cells will uptake the nanoparticles as it's known that nanoparticles below the size of 50 nm are taken up by the cells. Whilst the uptake of larger nanoparticles is highly size-dependent for all cell lines and uptake will therefore be very slow [381, 391].

6.3.1.1 MORPHOLOGY OF NANOPARTICLES

The synthesis of the AuNPs was a one step process, in contrast the synthesis procedure for the SiO_2NPs and SiO_2@AuNPs were an elaborate four steps process illustrated in Schematic 6.7. Both synthesis procedures produced stable nanoparticles at room temperate for short term and storage for long term in the fridge. Qualitative observations showed a change in color from clear to wine red with the formation of AuNPs, indicating stabilization of the nanoparticles in the citrate buffer and the presence of nanoscale sized particles. The SiO_2NPs are white in color and exhibited a lilac/purple color after the grafting of the gold shell around the spheres to form SiO_2@AuNPs, thus, indicating the chemical adsorption of the AuNPs between the amine ligands and the gold-plating solution to form an uniform thickness coating around the silica spheres, Figure 6.1.

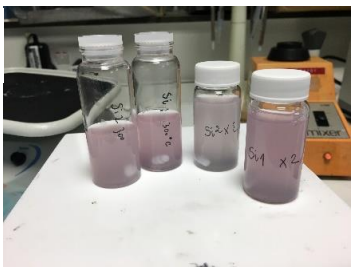
(A)  **(B)** 

Figure 6.1 Colors of nanoparticles. (A) AuNPs is wine colored, (B) SiO_2NPs is white in color and a color change is observed to lilac when the gold is adsorbed on the silica core to form SiO_2@AuNPs.

6.3.1.2 SIZE OF NANOPARTICLES

The synthesized nanoparticles were thoroughly characterized for (i) AuNPs, (ii) SiO_2NPs, and (iii) SiO_2@AuNPs to determine the essential particle properties via dynamic light scattering (DLS), ζ-potential, and transmission electron microscopy (TEM) analysis. The DLS measurements of the nanoparticles were calculated to their effective z-average Stokes-Einstein hydrodynamic radii R_H and the poly dispersity index (PDI) in solution (i.e. PBS). The charge of the nanoparticles determines their electrophoretic mobility, which is calculated as a measure of ζ-potential in the PBS solution; whilst the TEM bright field micrographs presented us with the measurement for the nanoparticles average size distribution, average radius (r_n) and calculated PDI, Equation 6.1.

$$r_{n=}\frac{1}{n}\sum_{i=1}^{n} r_i \qquad \textbf{Equation 6.1}$$

Table 6.1 The nanoparticles average radius (r_n), hydrodynamic radii (R_H), and ζ-potential was characterized via TEM, DLS and electrophoretic mobility measurements.

Nanoparticles (NPs)	r_n [TEM] (nm)	PDI [TEM]	R_H [DLS] (nm)	PDI [DLS]	ζ-potential (mV)
AuNPs	15.87 ± 4.29	0.27	16.85 ± 0.15	0.18	-34.2 ± 7.98
SiO_2NPs	190.18 ± 20.62	0.11	233.80 ± 27.56	0.42	-9.33 ± 3.04
SiO_2@AuNPs	250.00 ± 89.65	0.35	282.60 ± 7.10	0.34	-23.2 ± 3.21

The TEM and DLS measurements for the AuNPs are in good agreement, 15.87 nm ± 4.29 and 16.85 nm ± 0.15, respectively. The TEM measurements indicate a higher PDI in this particular sample in comparison to the DLS, which is due to the inclusion of AuNPs aggregates in the TEM micrographs leading to a broader distribution size measurements illustrated in Table 6.1 and Figure 6.2.

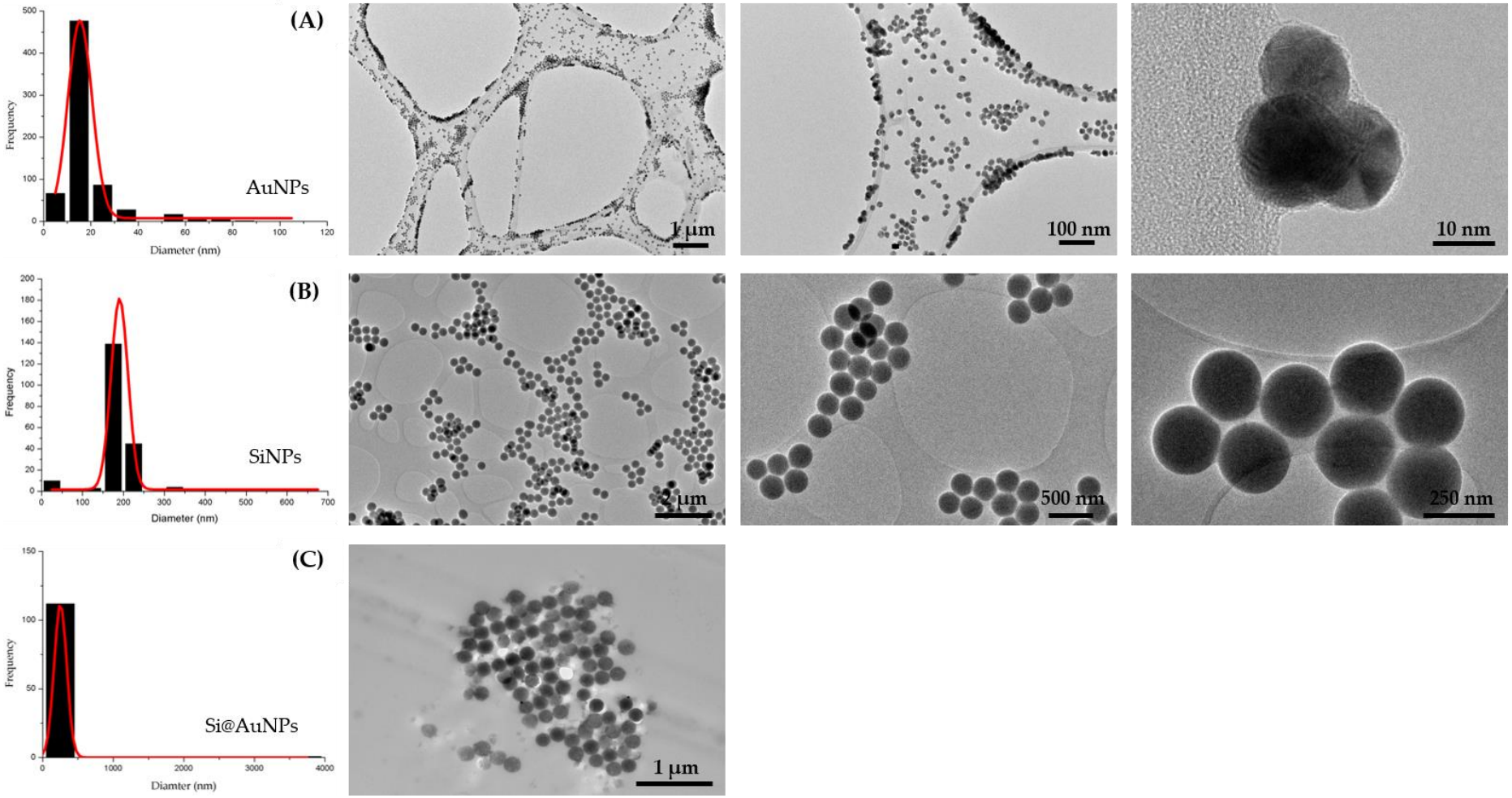


Figure 6.2 TEM micrographs of (A) AuNPs, (B) SiO_2NPs, and (C) SiO_2@AuNPs seeded on copper grips to determine nanoparticles size.

Furthermore, the DLS PDI measurements of 0.18 (i.e. low) indicates the stability of the AuNPs in PBS solution. A difference is observed in the TEM and DLS measurements for the SiO_2NPs and SiO_2@AuNPs measurements respectively, 190.18 nm ± 20.62 and 233.80 nm ± 27.56; 250.00 nm ± 89.65 and 282.60 nm ± 7.10. This difference can be related to the PBS solvent that the nanoparticles are dispersed in, which is predominately water. Water is a solvent that acts as a hydrogen donor and acceptor when in associating with particles in a non-covalent manner, so a hydration shell forms around the particles and contributes to the value of the particle radius. In comparison the TEM preparation of the nanoparticles are dried on copper grids before the analysis as the technique is under vacuum and we cannot use wet samples, so the hydration shell effect on the spheres is not present. Consequently, we observe a higher R_H versus r_n for the SiO_2NPs and SiO_2@AuNPs, whilst the AuNPs were a tenth in size of the silica cores nanoparticles, so the effect of the hydration shell is not significant. As the DLS measurements cannot exclude any presence of minor populations of aggregation, we included the presence of such populations in our TEM results as well, therefore increasing the measured size of the nanoparticles.

6.3.1.3 SURFACE CHARGE OF NANOPARTICLES

The stability of the particles in solution was investigated and the results demonstrated that the surfaces of the nanoparticles exhibited a negative ζ-potential surface charge. The negative surface charge on the AuNPs and SiO_2@AuNPs is due to the sodium citrate capping agent, which stabilizes the gold surface of these two particle types and presents as negative charge (i.e. adsorbed citrate). The stability is a measured as the repulsion between the nanoparticles to prevent aggregation, therefore the ζ-potential needs to be kept above 25 mV (positive or negative). The AuNPs demonstrate a stable system of particles in solution (-34.2 mV ± 7.98), whilst the SiO_2@AuNPs shows a moderate stability with a ζ-potential of -23.2 mV ± 3.21. The SiO_2NPs exhibited a low ζ-potential, -9.33 mV ± 3.04, indicating the aggregation (i.e. 500 nm, 1000 nm, and 2000 nm) of its nanoparticles and corresponds to the PDI value of the DLS measurements of 0.42 as illustrated in Table 6.1 This PDI value is higher than the accepted value (i.e. PDI = 0.2), however, it is important to emphasize that we observed a PDI value of 0.11 in the TEM measurements indicating that the SiO_2NPs are not

aggregated in their dry state in the TEM (i.e. under vacuum) versus the aggregation in the liquid state measured by the DLS, Figure 6.2.

6.3.1.4 SURFACE CHEMISTRY OF NANOPARTICLES

The Energy-Dispersive X-ray spectroscopy (EDX) was employed to confirm the chemical composition of the nanoparticles and we observed an optical absorption band peak at approximately 2.2 keV for the AuNPs, with a shift in this peak due to the silica core in the SiO_2@AuNPs to approximately 1.8 keV illustrated in Figure 6.3.

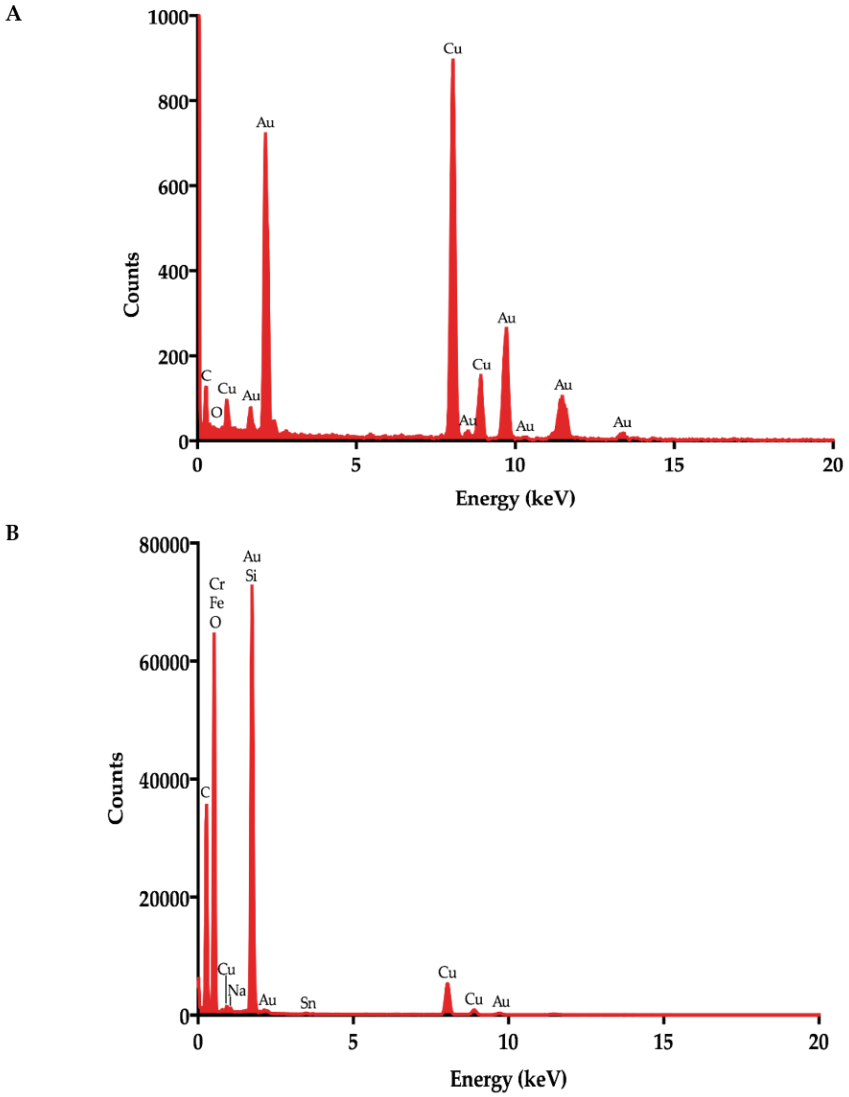


Figure 6.3 EDX spectra to illustrate the elemental mapping of (A) AuNPs and (B) SiO_2@AuNPs in correspondence to the TEM micrograph region of the nanoparticles.

6.3.2 SURFACE FUNCTIONALIZATION OF AuNPs AND SiO_2@AuNPs

The characterized AuNPs and SiO_2@AuNPs were confirmed to be approximately 16 nm and 250 nm in diameter, respectively. The AuNPs and SiO_2@AuNPs were immobilized with the RGD and IKVAV peptide sequences. However, due to the complexity of attempting the SPPS 'grafting from' approach on the nanoparticles as in the previous chapters (i.e. Chapter 4 and Chapter 5) due to many disadvantages such as, (i) time consuming (i.e. many washing steps), (ii) increase the chance of making mistakes (i.e. contamination), and (iii) difficult to characterize at each step of surface modification (i.e. protection and deprotection of the amino acids). We therefore decided to functionalize the AuNPs and SiO_2@AuNPs via a conventional approach of direct conjugation of completely synthesized peptides on the gold surfaces with thiol-gold chemistry. Consequently, we synthesized the peptides on a resin via the SPPS approach and characterized by High-Pressure Liquid Chromatography (HPLC), Electrospray Ionization-Mass Spectroscopy (ESI-MS) and Nuclear Magnetic Resonance (NMR) respectively, (i) to quantify the purity, (ii) to detect the pseudo molecular ion, and (iii) to obtain physical, chemical, electric and structural information of the synthesized peptides.

The peptides that we were interested were (i) RGDC and IKVAVC, and (ii) RGD and IKVAV. We initially consider to use a spacer to conjugate the peptides to the NPs, but decided against it as spacers are bulky, and could present steric hindrance with a higher chance of aggregation. Thus, we decided to use the amino acid cysteine (C) in the peptide sequence (i.e. RGDC and IKVAVC) to enable the conjugation of the peptide sequences to the nanoparticles through thiol-gold chemistry. Whilst the synthesized RGD and IKVAV peptides would provide for the soluble factors in the cell culture as another parameter to be considered in the biological response of the NPSCs.

The synthesis of the peptides was more complicated than expected after attempting the synthesis a few times, the RGD and RGDC peptides were synthesized and successfully characterized as shown in Appendix 1, Appendix 2, Appendix 3, and Appendix 4. The RGDC peptide after cleaving from the resin formed a disulphide bond at the thiol functional group of the cysteine amino acid, which was broken after treating it with excess TCEP [293].

On the other hand, the synthesis of the IKVAV and IKVAVC peptides remained unsuccessful as we were unable to pinpoint exactly what was causing the branching of the IKVAV and IKVAVC peptides as illustrated in Appendix 5. We measured a 60%-70% purification for these peptides, which is attributed to IKVAV and IKVAVC having low solubility in both aqueous and organic solvents. Consequently, we decided to purchase a cysteine containing IKVAV peptide and the only commercially available IKVAV peptide with a cysteine we could find was a long peptide chain that corresponds to a sequence fragment in the ECM protein laminin, Cys-Laminin A Chain (**Cys** – Ser – Arg – Ala – Arg – Lys – Gln – Ala – Ala – Ser – **Ile – Lys – Val – Ala – Val** – Ser – Ala – Asp – Arg, **C**SRARKQAAS**IKVAV**SADR) denoted here as IKVAVC(19).

This far we functionalized surfaces via the amino acid stepwise build-up approach, accordingly after successfully synthesizing the RGDC peptide and purchasing the IKVAVC(19) peptide we needed to confirm the direct peptide conjugation approach. Therefore, the RGDC and IKVAVC peptides were initially tested on 2D gold surfaces before conjugating them to the desired 3D model (i.e. nanoparticles). The gold surfaces 'grafted to' the surface are denoted as Au Peptides surfaces.

6.3.2.1 DIRECT PEPTIDE CONJUGATION APPROACH ON 2D GOLD SURFACES

6.3.2.1.1 SURFACE WETTABILITY OF Au PEPTIDE SURFACES

Firstly, we observed an increase in surface wettability after oxygen plasma etching of the gold surface from 86.04° ± 1.28 to 7.52° ± 1.23. The RGDC functionalized surface demonstrated a surface wettability of 66.66° ± 1.02 and the IKVAVC(19) surface presented a surface wettability of 73.387° ± 1.25. The change in surface wettability indicates the immobilization of the peptides on the gold surfaces, Figure 6.4.

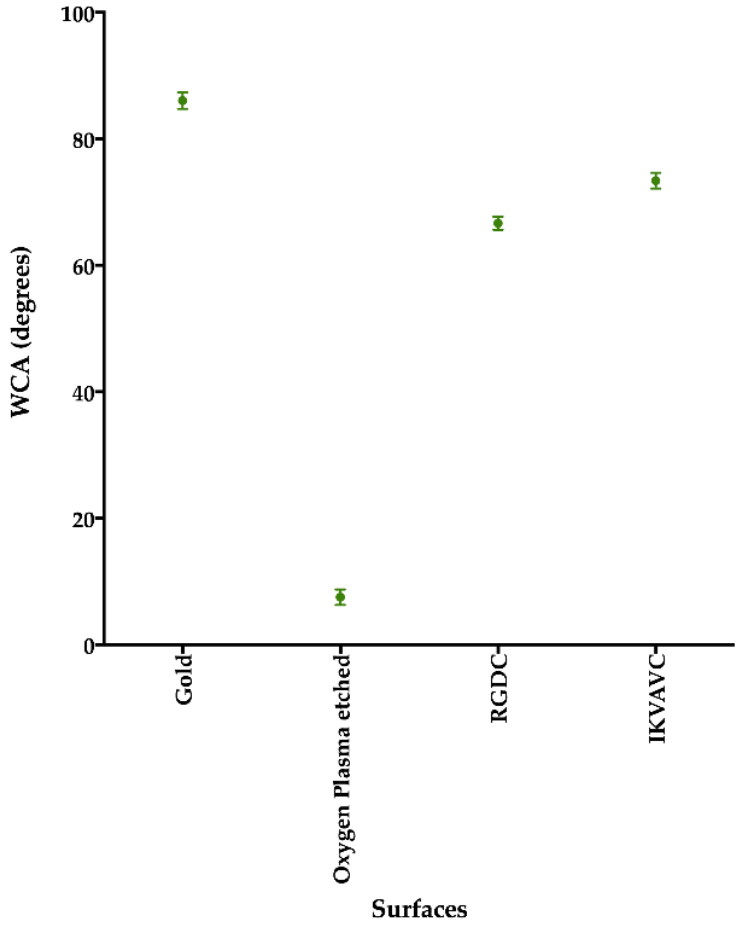


Figure 6.4 WCA measurements following the surface functionalization of XYZ surfaces with RGDC and IKVAVC(19) peptides, n = 3.

6.3.2.1.2 SURFACE TOPOGRAPHY OF Au PEPTIDE SURFACES

The surface topography was analyzed with AFM to observe whether the length difference in the peptide sequence would have a significant effect on the surface roughness of the IKVAVC(19) surface versus that of the RGDC and gold surfaces, Table 6.2 and Figure 6.5. The functionalization with RGDC and IKVAVC(19) peptides increased the difference in z-range from 11.6 nm ± 2.69 to, 44.1 nm ± 5.2 and 35.1 nm ± 4.59, respectively. The length of the IKVAVC(19) peptide provides flexibility as well as being able to fold on itself unlike the RGDC, thus, indicating that the functionalization with a shorter peptide increased the z-range (i.e. roughness) of the surface,

Figure 6.6. The surface functionalization method required the chemical adsorption of the peptides in ethanol, which can be related to the observed increase in roughness of the surface topography and profile plots in the RGDC and IKVAVC(19) sections in comparison to that of the Au (gold) section. Hence, we observed the clustering of the peptides on the surface due to the top-bottom chemical adsorption approach of 'grafting to' the surface. Furthermore, in comparison to the z-range the peptide functionalized surfaces exhibited similar surface roughness, 4.72 nm ± 1.86 and 4.43 nm ± 1.76, respectively.

Table 6.2 Z-range and RMS measurements of the functionalized Au Peptide surfaces obtained from the corresponding AFM Height images, n = 3.

Surfaces	Z-range (nm)	RMS (nm)
Gold	11.6 ± 2.69	1.15 ± 0.56
RGDC	44.1 ± 5.20	4.72 ± 1.86
IKVAVC(19)	35.1 ± 4.59	4.43 ± 1.76

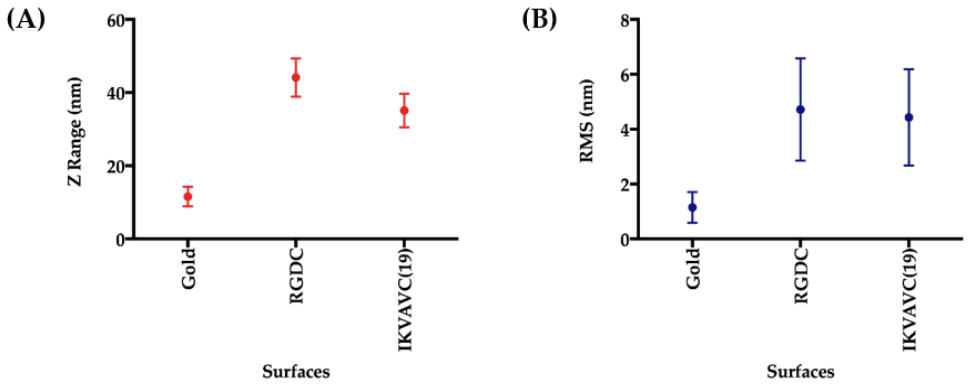


Figure 6.5 (A) Z-range and (B) RMS measurements of the functionalized Au Peptide surfaces obtained from the corresponding AFM Height images, n =3.

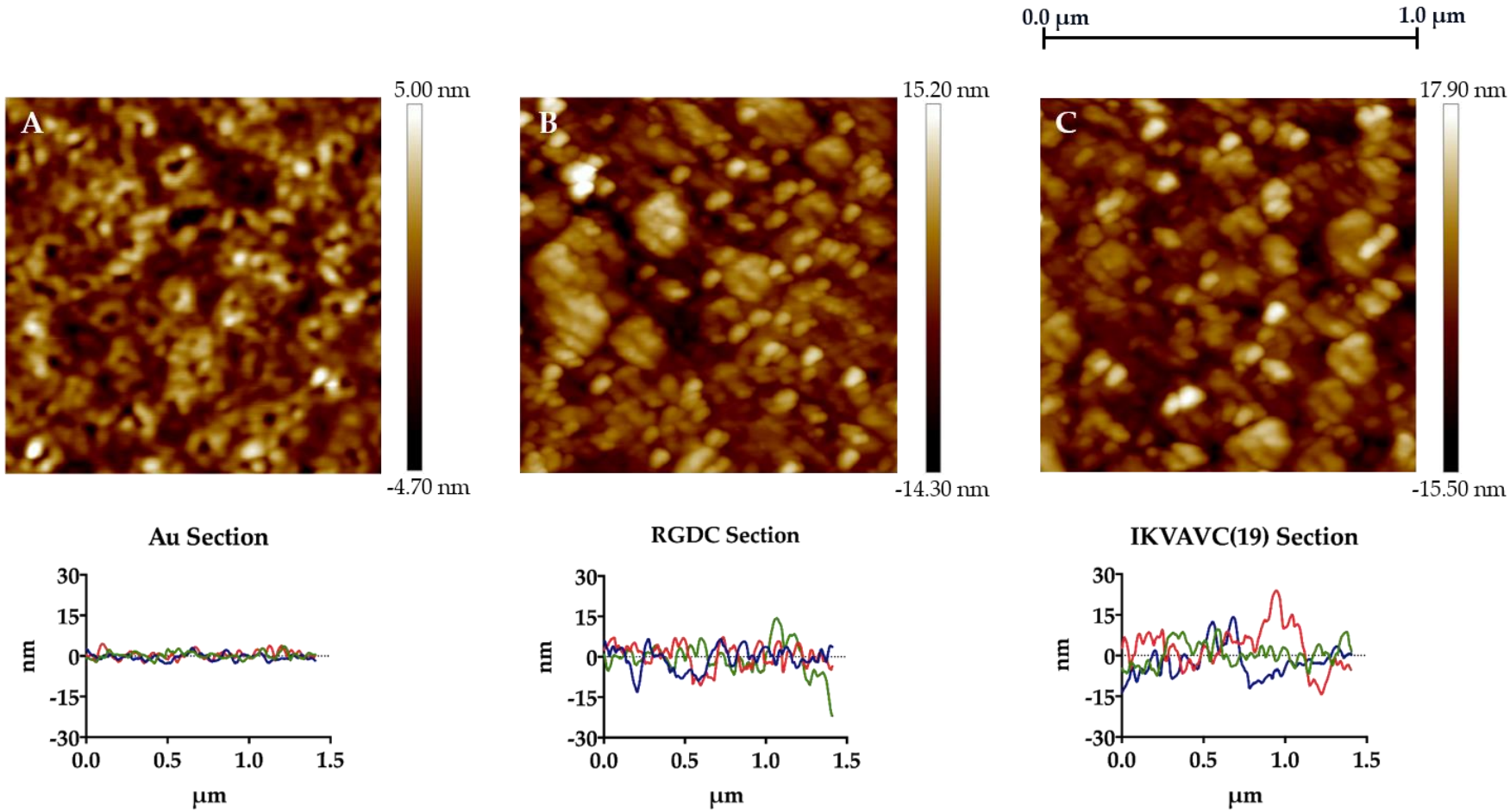


Figure 6.6 The AFM topography images observe the change in surface roughness (nm) through the oxygen plasma activation respectively to the Au Peptide functionalized surfaces. (A) Gold, (B) RGDC, and (C) IKVAVC(19) functionalized glass coverslips. The profile plots illustrate approximately a height between -30 nm and 30 nm, which were measured by calculating as three lines sectioning through the AFM topography image.

6.3.2.1.3 SURFACE HOMOGENEITY OF Au PEPTIDE SURFACES

The ToF-SIMS results for the major secondary ion peaks are labelled in the negative and positive overlay spectrum of the Au Peptides surfaces in Figure 6.7, Figure 6.8, and Table 6.3, respectively. As the peptides contain a cysteine amino acid with a thiol functional group, the RGDC and IKVAVC(19) peptides can be covalently attached via the thiol-gold chemistry though a one step process. An increase in the cysteine, $C_2H_6NS^+$, ion intensity is observed for the RGDC and IKVAVC(19) immobilized surfaces, indicating the presence of the thiol functionality. The RGDC functionalized surface showed an increase in the R ($C_4H_8N^+$), G (CH_4N^+) and D ($C_3H_6NO_2^+$) ion fragments in comparison to the Gold and IKVAVC(19) surface. The IKVAVC(19) functionalized surface presented an increase in the I ($C_5H_{12}N^+$), K ($C_5H_{10}N^+$), V ($C_4H_{10}N^+$), and A ($C_2H_6N^+$) ion fragments. Moreover, the IKVAVC(19) (i.e. **C**SRARKQAAS**IKVAV**SADR) surface also demonstrates an ion intensity for D ($C_3H_6NO_2^+$) and R ($C_4H_8N^+$) comparable to that of the RGDC surface, thus, indicating the RGDC and IKVAVC(19) peptides were immobilized on the gold surfaces via the direct conjugation reaction, Figure 6.9.

The intensity maps of the selected negative and positive ions fragments were reconstructed to obtain raster images of the surface modification stages of the peptide surfaces at the higher magnification field of view of 3 mm x 3 mm. Figure 6.10 confirms the homogeneity of the surface coverage relative to the intensity of secondary ion fragments characteristic to surface and overlay (i.e. surface modification). The surfaces demonstrated homogeneity and the difference in ion intensity was easily monitored, thus, indicating the successful functionalization of RGDC and IKVAVC(19) surfaces.

Table 6.3 Negative and positive ion peaks selected for the ToF-SIMS analysis to construct raster images to illustrate the homogenous Au Peptide surfaces. Normalized ion intensity (x 10^6).

Source	Ion assignment	Gold		RGDC		IKVAVC(19)	
		m/z	Dev.(ppm)	m/z	Dev.(ppm)	m/z	Dev.(ppm)
Negative Polarity							
Gold	Au^-	196.95	-106.40	196.95	-112.90	196.94	-118.90
Positive Polarity							
Cysteine	$C_2H_6NS^+$	76.03	72.80	76.03	63.70	76.03	72.00
Arginine	$C_4H_8N^+$	70.08	144.70	70.08	150.40	70.07	132.00
Glycine	CH_4N^+	30.04	148.00	30.04	102.70	30.04	81.00
Aspartic acid	$C_3H_6NO_2^+$	88.03	-137.10	88.03	-60.00	88.03	-82.30
Isoleucine	$C_5H_{12}N^+$	86.11	155.40	86.10	91.20	86.11	109.00
Lysine	$C_5H_{10}N^+$	84.09	78.70	84.084	38.30	84.09	78.60
Valine	$C_4H_{10}N^+$	72.09	136.40	72.09	87.90	72.09	65.10
Alanine	$C_2H_6N^+$	44.06	165.60	44.05	102.10	44.05	101.70

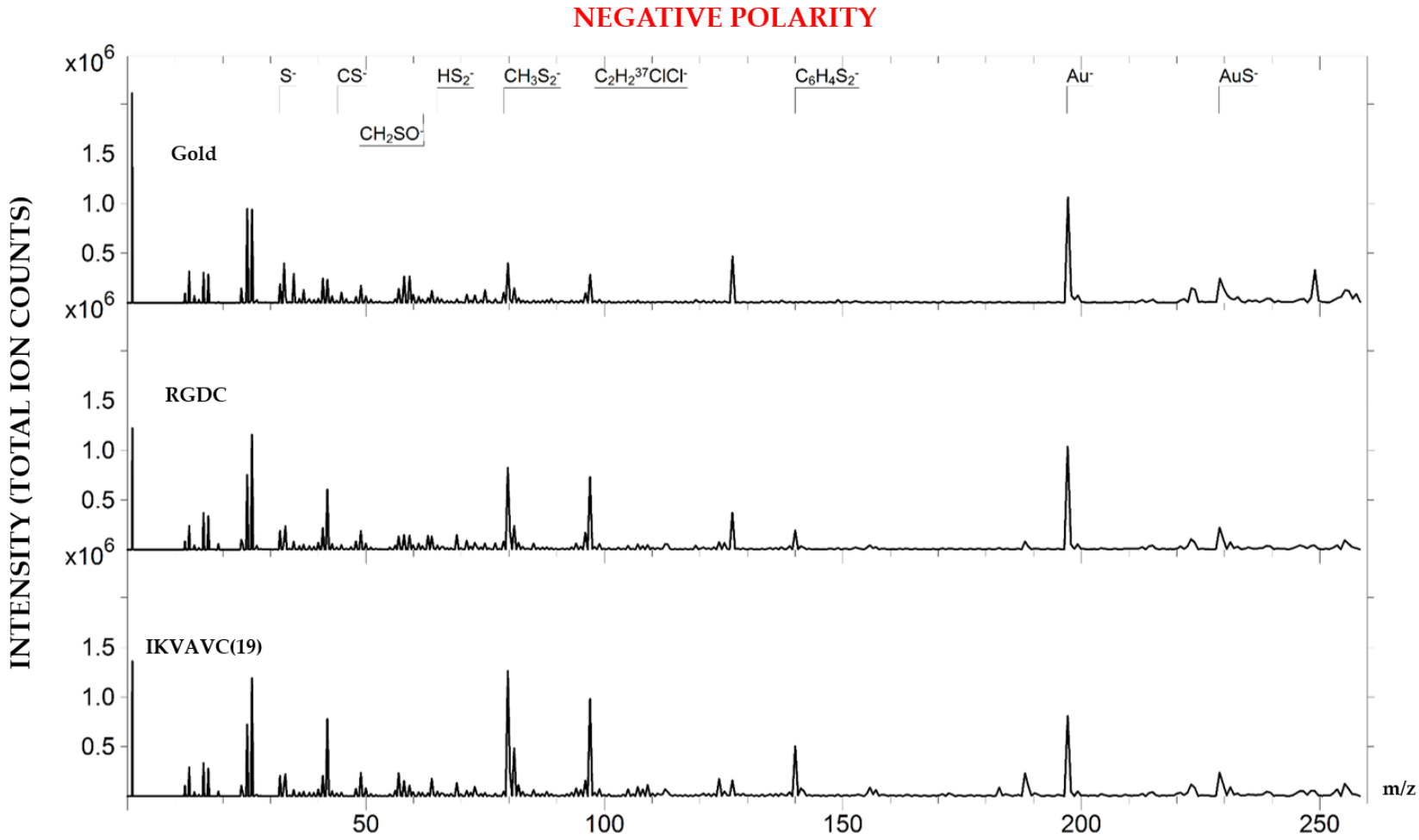


Figure 6.7 ToF-SIMS overall spectrum of the Au Peptide functionalized surfaces annotated with the selected negative ion peaks and normalized to the total ion count.

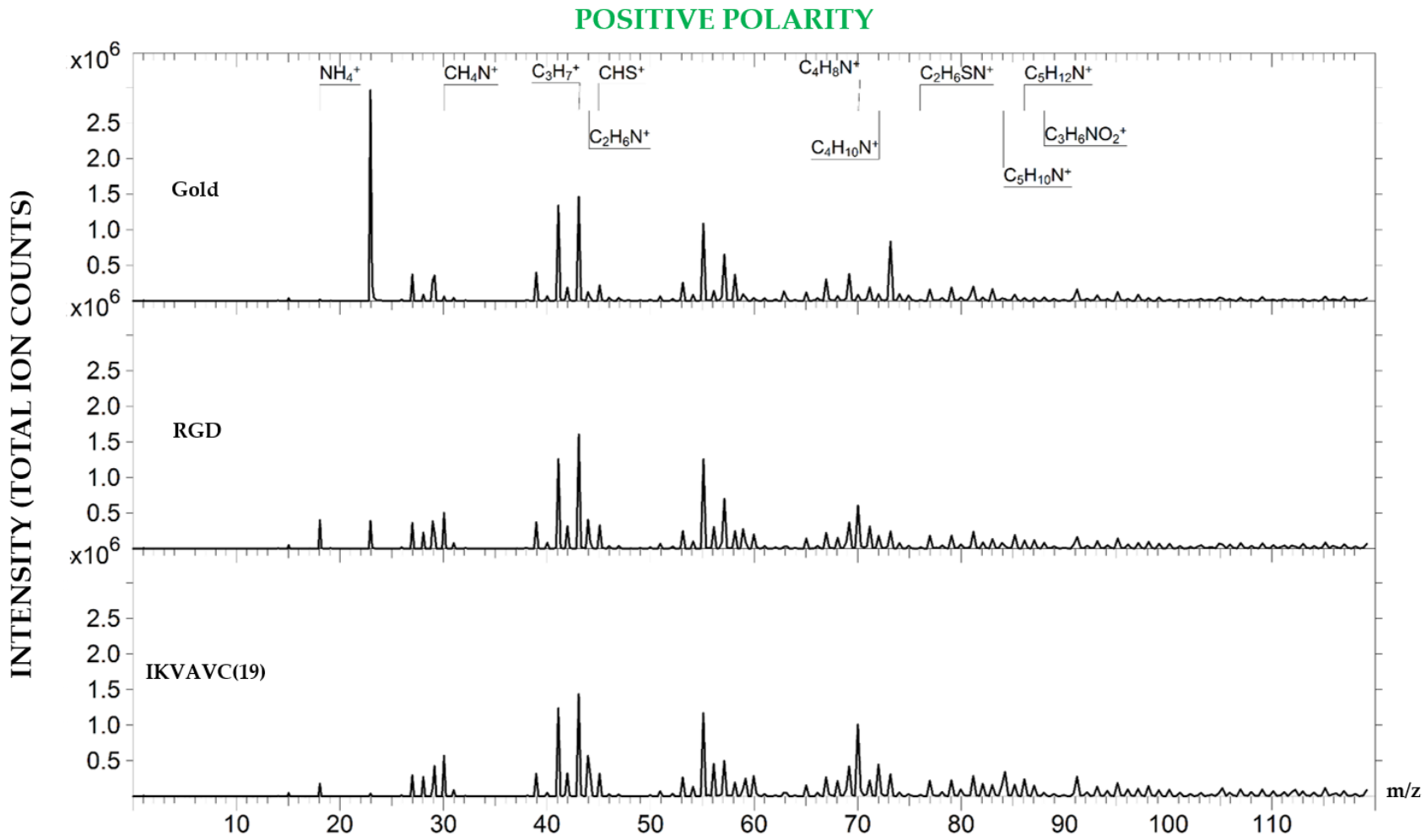


Figure 6.8 ToF-SIMS overall spectrum of the Au Peptide functionalized surfaces annotated with the selected positive ion peaks and normalized to the total ion count.

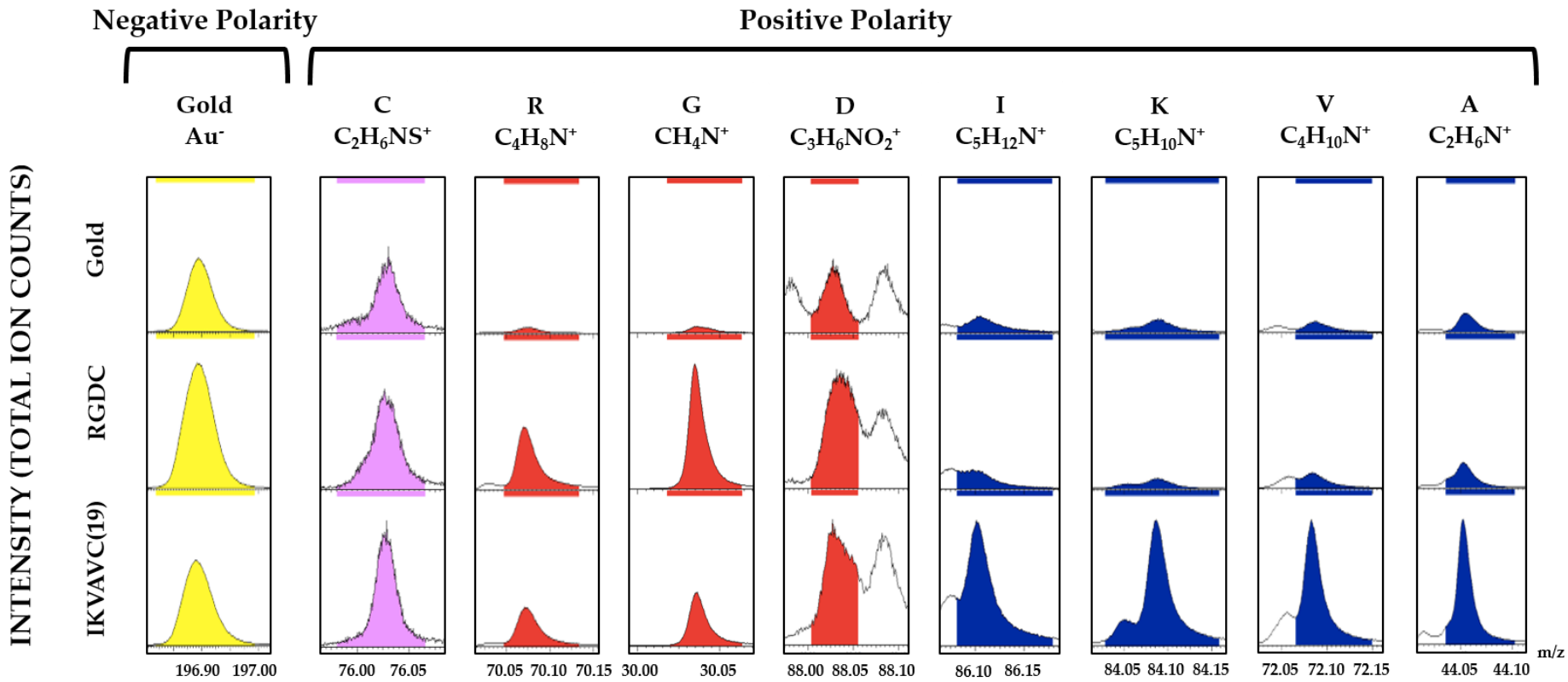


Figure 6.9 ToF-SIMS characterization of marker ion fragments of amino acids distinguishable for Au Peptide surface modification and normalized to the total ion count.

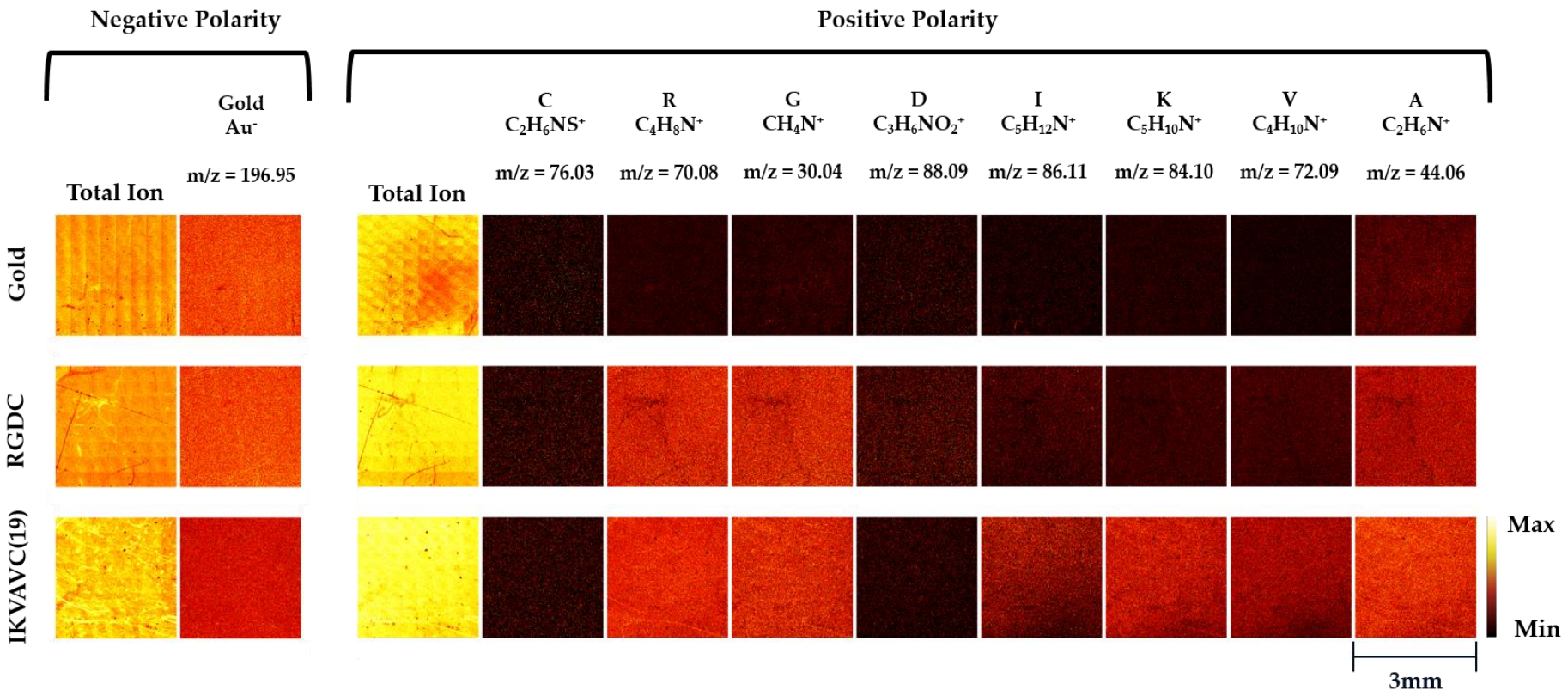
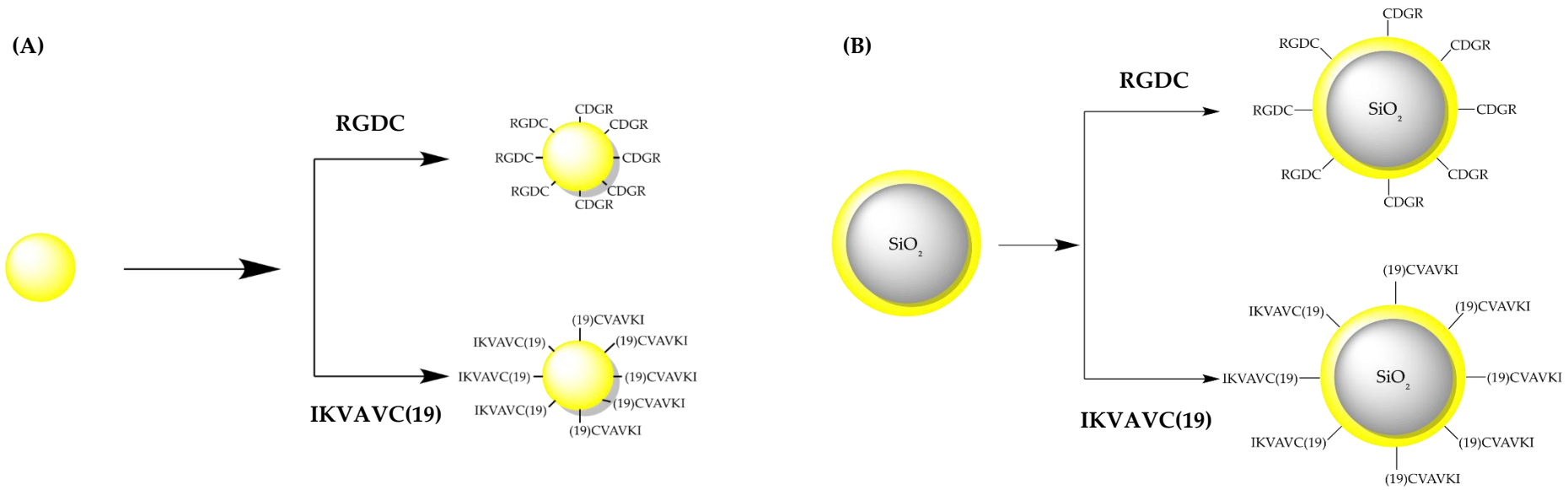


Figure 6.10 ToF-SIMS analysis of the marker ion fragments as raster images to illustrate the Au Peptide homogenous surfaces and normalized to the total ion count, scale is 3 mm x 3 mm.



Schematic 6.8 Illustration of the direct peptide conjugation approach via the thiol-gold chemistry as 1.7 nmol peptide per 1 mL of (A) AuNPs and (B) SiO_2@AuNPs in PBS.

6.3.2.2 DIRECT PEPTIDE CONJUGATION APPROACH ON 3D GOLD SURFACES

With the successful validation of the feasibility of the direct peptide conjugation approach on 2D gold surfaces by WCA, AFM and ToF-SIMS analysis. The 3D gold surfaces, AuNPs and SiO_2@AuNPs, were functionalized with the RGDC and IKVAVC(19) peptides illustrated in Schematic 6.8.

The conjugation of the peptides on the nanoparticles was characterized via UV/visible spectroscopy, as gold nanoparticles (GNPs) exhibit a distinguishable surface plasmon resonance (SPR) signal at 524 nm wavelength as a measure of optical density (OD) in absorbance. Consequently, any conjugation of the peptides on the nanoparticles would be demonstrated as a shift in the wavelength of the gold nanoparticles SPR signal as presented in Figure 6.11.

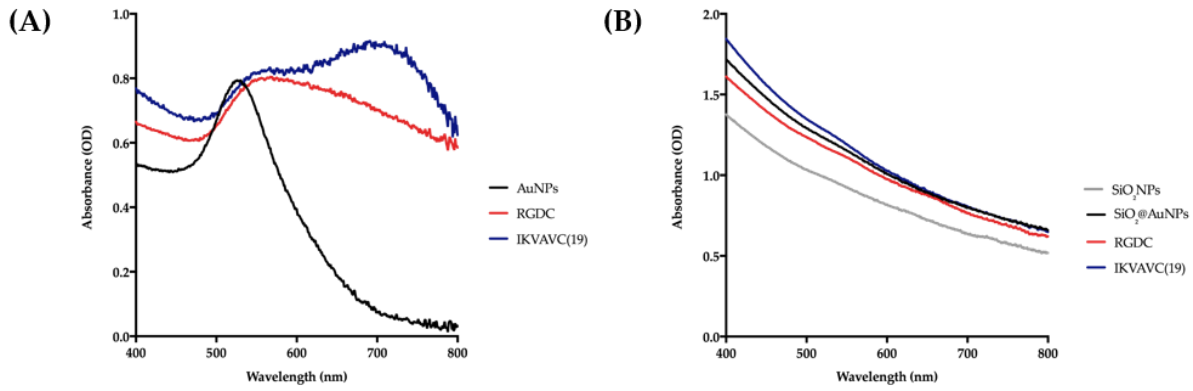


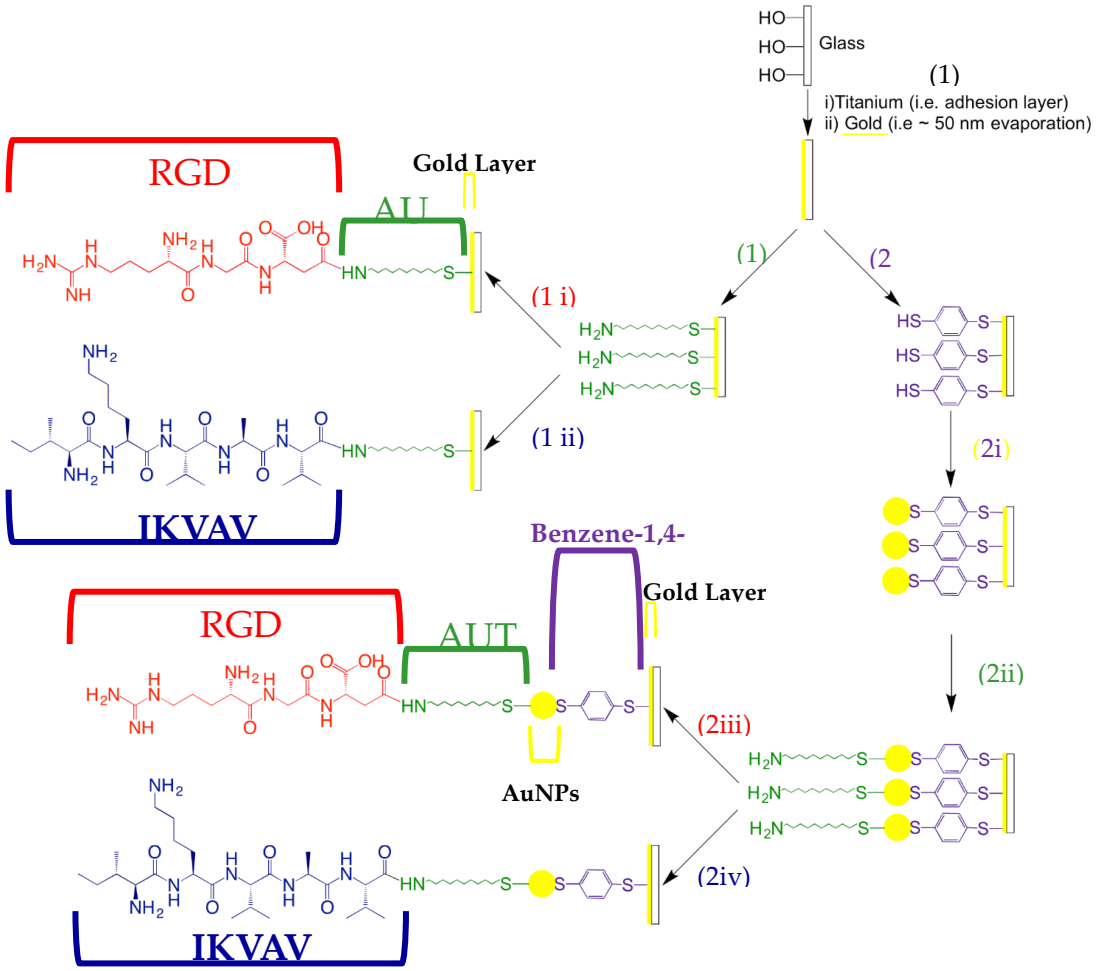
Figure 6.11 UV/visible spectra of (A) AuNPs and (B) SiO_2@AuNPs at 400-800 nm of the peptide conjugation on the gold surfaces.

The AuNPs illustrates a strong SPR signal at 525 nm, with the conjugation of the RGDC and IKVAVC(19) peptides on the AuNPs we observed a red-shift in the SPR peak to the right respectively, 556 nm and 562 nm. The SPR peaks for peptide conjugated AuNPs were broad, particularly the AuNPs-IKVAVC(19) had a second peak at approximately 700 nm indicated that some of the nanoparticles had aggregated in solution.

In contrast, no peak was observed for SiO_2NPs and the SPR peak for the SiO_2@AuNPs was weak and observed at 538 nm, which indicates a red-shift in the SPR peak due to the properties of the silica core and gold shell properties of the nanoparticle. The conjugation with RGDC showed further red-shift in SPR speak to 559 nm, whilst conjugation with IKVAVC(19) demonstrated a SPR peak at 532 nm which is closer to that of GNPs (i.e. 524 nm). The red-shift is related to the conjugation of molecules that attenuate the electric charge of the nanoparticles, so reducing the restoring electric force and the resonance frequency, which is observed for SiO_2@AuNPs and SiO_2@AuNPs-RGDC in comparison to that of GNPs. The conjugation with the IKVAVC(19) peptide had a lesser effect on the electric charge on the SiO_2@AuNPs than that of the RGDC conjugation, which could be due a few factors such as the choice of colloidal solution, surface chemistry, size and shape after peptide conjugation of the nanoparticle. Therefore, we considered the ζ-potential surface charge of the peptide conjugated nanoparticles to observe their stability in PBS illustrated in Table 6.4. The AuNPs and AuNPs-RGDC demonstrated a stable system of particles in PBS at -34.2 mV ± 7.98 and -24.8 mV ± 5.28, respectively. The AuNPs-IKVAVC(19) exhibited a lower ζ-potential, -18.5 mV ± 11.4, indicating the aggregation of its nanoparticles which is supported by the UV/visible spectra in Figure 6.11(A). The gold shell coating around the SiO_2NPs to SiO_2@AuNPs stabilizes the surface charge of the nanoparticles from -9.33 mV ± 3.04 to -23.2 mV ± 3.21, respectively. Furthermore, no aggregation was observed in Figure 6.11(B) as SiO_2NPs does not exhibit a SPR peak. The RGDC and IKVAVC(19) conjugated SiO_2@AuNPs demonstrated a stable ζ-potential of -32.9 mV ± 3.31 and -30.6 mV ± 3.66, which suggests that the observed increase is due to the peptide conjugation successfully and further stabilising the colloidal systems.

Table 6.4 The ζ-potential surface charge of the nanoparticles without and with peptide conjugation in PBS.

Conjugate	AuNPs	SiO_2@AuNPs
	ζ-Potential (mV)	ζ-Potential (mV)
SiO_2NPs	—	-9.33 ± 3.04
AuNPs	-34.2 ± 7.98	-23.2 ± 3.21
RGDC	-24.8 ± 5.28	-32.9 ± 3.31
IKVAVC(19)	-18.5 ± 11.4	-30.6 ± 3.66



Schematic 6.9 The peptide functionalization of Au Flat and Au NPs surfaces via the 'grafting from' approach. Titanium adhesion layer is evaporated on the glass coverslip after which ~ 50 nm of gold is evaporated on the surfaces. The peptide conjugation occurred on gold surfaces that were either functionalized with (1) only AUT at 1 mM overnight or (2) on gold surfaces that were functionalized with benzene-1,4-dithiol at 10 mM overnight , (i) AuNPs (i.e. 16 nm) left for 2 days, and (ii) AUT at 1 mM overnight. To achieve (1i/ 1ii) Au FLAT or (2iii/ 2iv) Au NPs functionalized peptide surfaces via the SPPS stepwise amino acid build-up approach.

6.3.3 SURFACES FUNCTIONALIZATION OF 2D GOLD SURFACES

To further contextualize the surface functionalization and characterization of the nanoparticles (i.e. 3D surfaces) we designed the following 2D surface models of (i) Au Flat and (ii) Au NPs peptide functionalized surfaces by immobilizing the peptides via the 'grafting from' approach employed in the previous chapters (Chapter 4 and Chapter 5). This will provide for a more comparable study as the 2D surfaces will be gold functionalized and enable the immobilization of the peptides via the SPPS thiol-gold chemistry approach. Furthermore, enabling us to study any differences in surface analysis between the SPPS 'grafting to' (i.e. Au Peptides surfaces) and the 'grafting from' (i.e. Au Flat and Au NPs surfaces) approaches directly.

6.3.3.1 SURFACE WETTABILITY OF Au FLAT AND Au NPs SURFACES

In chapters 4 and 5 we used glass coverslips as the model 2D surfaces on which we immobilized the RGD and IKVAV peptides. Here we present gold coated (~50 nm) glass coverslip surfaces that are functionalized (i) with the synthesized AuNPs (~16 nm), and (ii) without AuNPs after which the peptides are immobilized on the surfaces via the AUT linker via 'the grafting from' carbodiimide chemistry amino acid stepwise build-up approach, Schematic 6.9.

The surface wettability of the Au Flat and Au NPs surfaces were measured to follow the surface modification, which could be affected by surface chemistry as well as surface topography as illustrated in Figure 6.12. A significant decrease in contact angle is observed on the Au Flat surface after oxygen plasma etching, $86.04^{o} \pm 1.28$ to $< 10^{o}$, which indicates the removal of adventitious environmental hydrocarbons that had adsorbed to the surface. The covalent attachment of AUT through thiol chemistry at the surface interface and the presence of the amine functional group at the terminal end increase the hydrophobicity of the surface to $52.90^{o} \pm 1.71$. The 'grafting from' approach for the peptides illustrated a noticeable difference in the surface wettability of RGD to IKVAV. The RGD functionalized surfaces presented a water contact angle closer to those in the previous chapters (Chapter 4, Chapter 5), $47.99^{o} \pm 1.10$, versus that of the IKVAV functionalized surfaces which were more hydrophobic than previously documented, $74.15^{o} \pm 1.32$.

The Au NPs surfaces where functionalized with Benzene-1,4-dithiol, which is a benzene molecule that has a thiol functional group at both para positions. Hence, facilitating the covalent bonding to the gold interface at surface and the other to covalently bond to the AuNPs after treated the surfaces with a solution of AuNPs respectively, 67.79° ± 4.03 to 82.85° ± 1.00. The AUT increased the surface wettability, 64.15° ± 6.70, whilst a reduction was observed after the functionalization with RGD or IKVAV respectively, 74.02° ± 1.73 and 78.26° ± 1.22. Additionally, the Au NPs surfaces immobilized with RGD and IKVAV illustrated surface wettability within range of each other as in previous chapters (Chapter 4, Chapter 5). However, the changes observed in surface wettability on the Au Flat and Au NPs surfaces are considerably higher in comparison to those on the peptide functionalized glass surfaces, which will be further explored in how the cells respond to these surfaces.

The Au Flat and Au NPs surfaces functionalized with the RGD peptide demonstrated respectively, a lower surface wettability of 47.99° ± 1.10 and higher surface wettability at 74.02° ± 1.73, in comparison to that of the Au Peptides surface (i.e. 'grafting to' approach) of 66.66° ± 1.02. We further observed that the IKVAVC(19) functionalized Au Peptides surface presented a surface wettability, 73.387° ± 1.25, similar to that of the Au Flat IKVAV and Au NPs IKVAV surfaces respectively, 74.15° ± 1.32 and 78.26° ± 1.22.

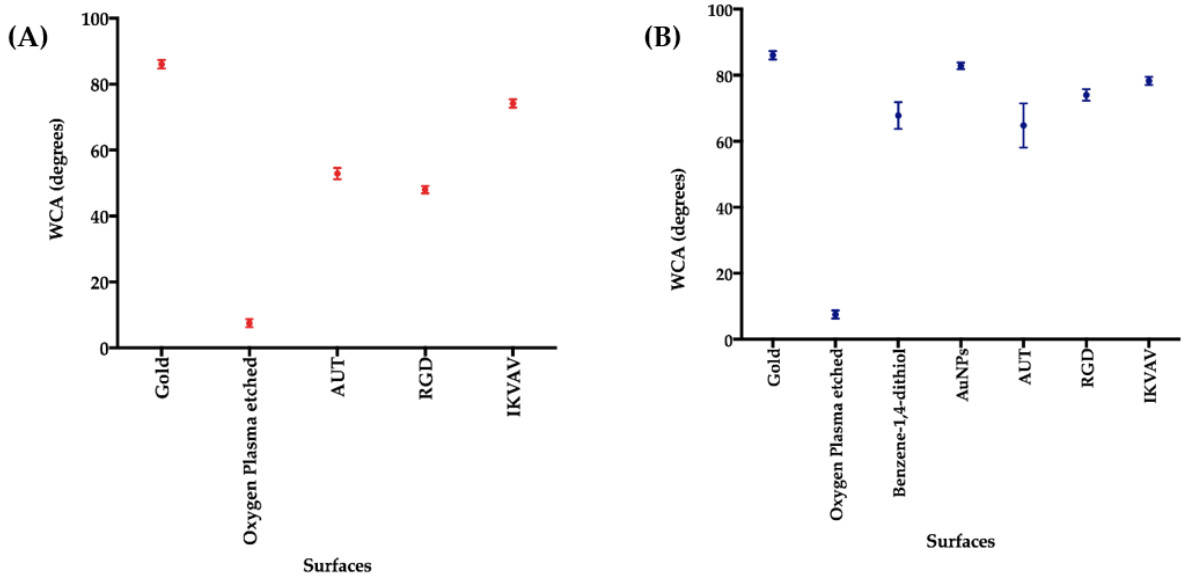


Figure 6.12 WCA measurements following the surface functionalization of RGD and IKVAV peptides on (A) Au Flat and (B) Au NPs surfaces, n = 3.

6.3.3.2 SURFACE TOPOGRAPHY OF Au FLAT AND Au NPs SURFACES

Topographical scans of the gold functionalized surfaces with/without AuNPs were taken to determine surface uniformity and structural differences due to the functionalization with the nanoparticles.

6.3.3.2.1 Au FLAT SURFACES

The oxygen plasma cleaned gold surface consisted of grains, with a maximum z-range higher than that after the AUT functionalization of 11.60 nm ± 2.69 to 7.185 nm ± 1.76, respectively. However, the root mean square (RMS) roughness was lower than that of the Au Flat AUT sample, 1.15 nm ± 0.56 to 1.69 nm ± 1.96, which indicates that the AUT formed a self-assembling monolayer with a broader range in surface roughness, Table 6.5 and Figure 6.13. The Au Flat RGD surface demonstrated some saturated points evenly distributed across the surface indicating features larger than the z-scale, whilst the Au Flat IKVAV surface showed larger clusters of the IKVAV peptide immobilization in certain areas, thus, a larger difference in deviation in the surface roughness is observed respectively, 1.29 nm ± 1.13 and 1.33 nm ± 0.66. Moreover, the profile section of the Au Flat surfaces illustrates the difference in peak-valley distance after each step of modification, Figure 6.14.

Table 6.5 Z-range and RMS measurements of the functionalized Au Flat surfaces obtained from the corresponding AFM Height images, n = 3.

Surfaces	Z-range (nm)	RMS (nm)
Gold	11.60 ± 2.69	1.15 ± 0.56
AUT	7.185 ± 1.76	1.69 ± 1.96
RGD	14.58 ± 3.13	1.33 ± 0.66
IKVAV	14.38 ± 2.31	1.29 ± 1.13

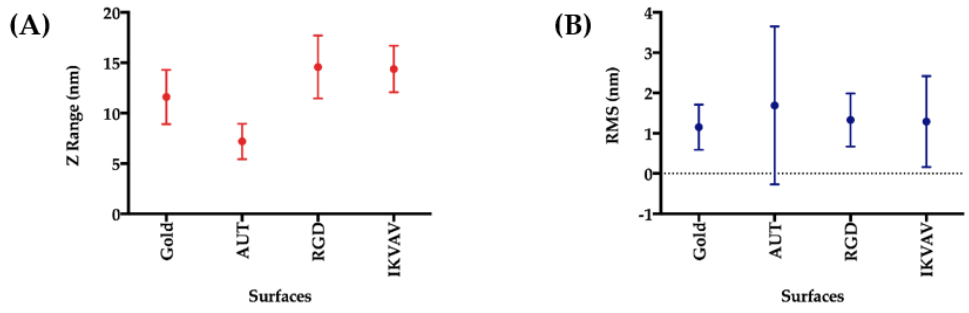


Figure 6.13 (A) Z-range and (B) RMS measurements of the functionalized Au Flat surfaces obtained from the corresponding AFM Height images, n = 3.

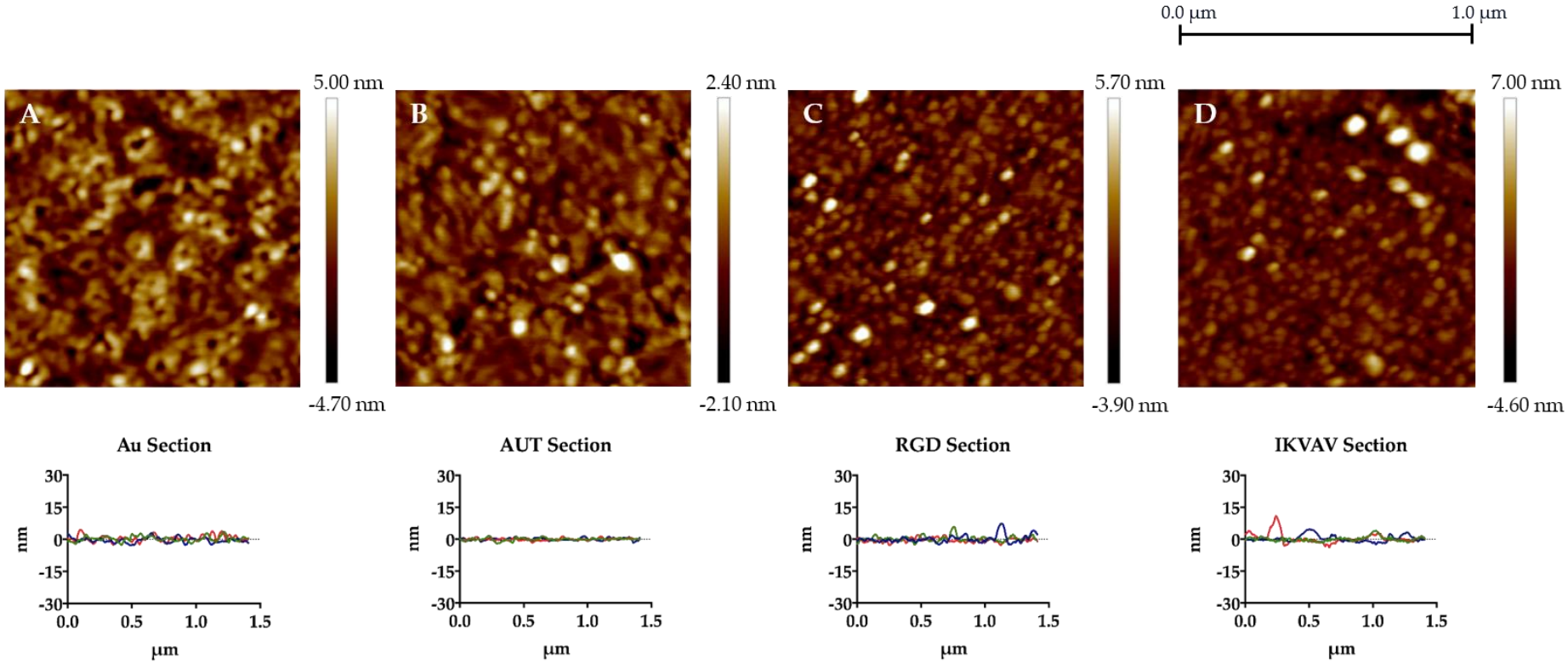


Figure 6.14 The AFM topography images observe the change in surface roughness (nm) through the oxygen plasma activation respectively to the Au Flat peptide functionalized surfaces. (A) Gold, (B) AUT, (C) RGD, and (D) IKVAV functionalized glass coverslips. The profile plots illustrate approximately a height between -30 nm and 30 nm, which were measured by calculating as three lines sectioning through the AFM topography image.

6.3.3.2.2 Au NPs SURFACES

A similar z-range and RMS value was observed for the gold control surface and Benzene-1,4-dithiol functionalized surface which demonstrated respectively, 11.60 nm ± 2.69 and 11.5 nm ± 1.38, and 1.15 nm ± 0.56 and 1.24 ± 0.45, in Table 6.6 and Figure 6.15. A significant difference is observed in z-range with AuNPs and AUT functionalization of 28.10 nm ± 4.67 and 48.45 nm ± 5.35, which indicates that the surface has been modified successfully. With each modification step we observe an increase in surface roughness with RMS values of 2.64 nm ± 0.76 and 4.34 nm ± 2.23, respectively. Furthermore, the AUT surface exhibited structural features that can be attributed to the topographical points collected around the spherical AuNPs functionalized on the surface, and with the functionalization of AUT the peak-valley would for that reason exhibit a higher z-range, Figure 6.16.

Table 6.6 Z-range and RMS measurements of the functionalized Au NPs surfaces obtained from the corresponding AFM Height images, n = 3.

Surfaces	Z-range (nm)	RMS (nm)
Gold	11.60 ± 2.69	1.15 ± 0.56
Benzene-1,4-dithiol	11.50 ± 1.38	1.24 ± 0.45
AuNPs	28.10 ± 4.67	2.64 ± 0.76
AUT	48.45 ± 5.35	4.34 ± 2.23
RGD	29.46 ± 3.77	2.37 ± 1.09
IKVAV	27.68 ± 7.36	3.60 ± 1.91

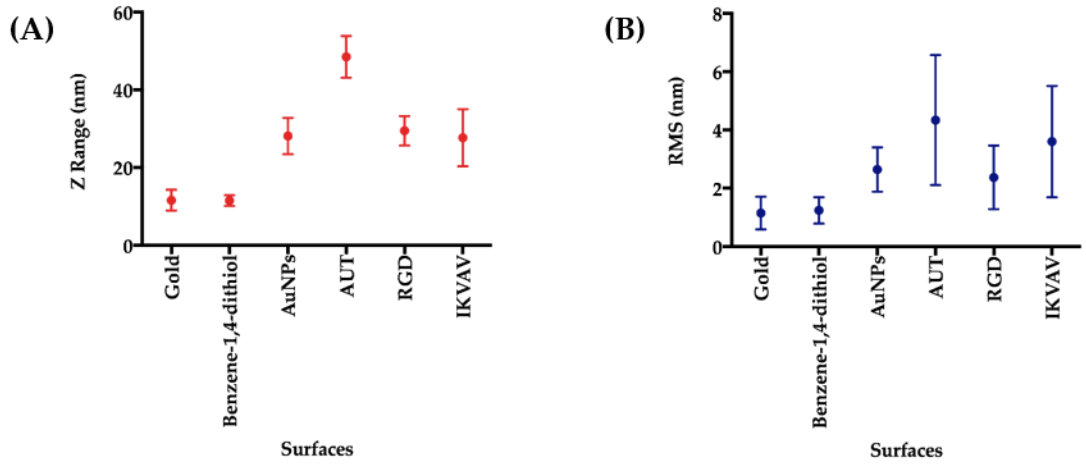


Figure 6.15 (A) Z-range and (B) RMS measurements of the functionalized Au NPs surfaces obtained from the corresponding AFM Height images, n =3.

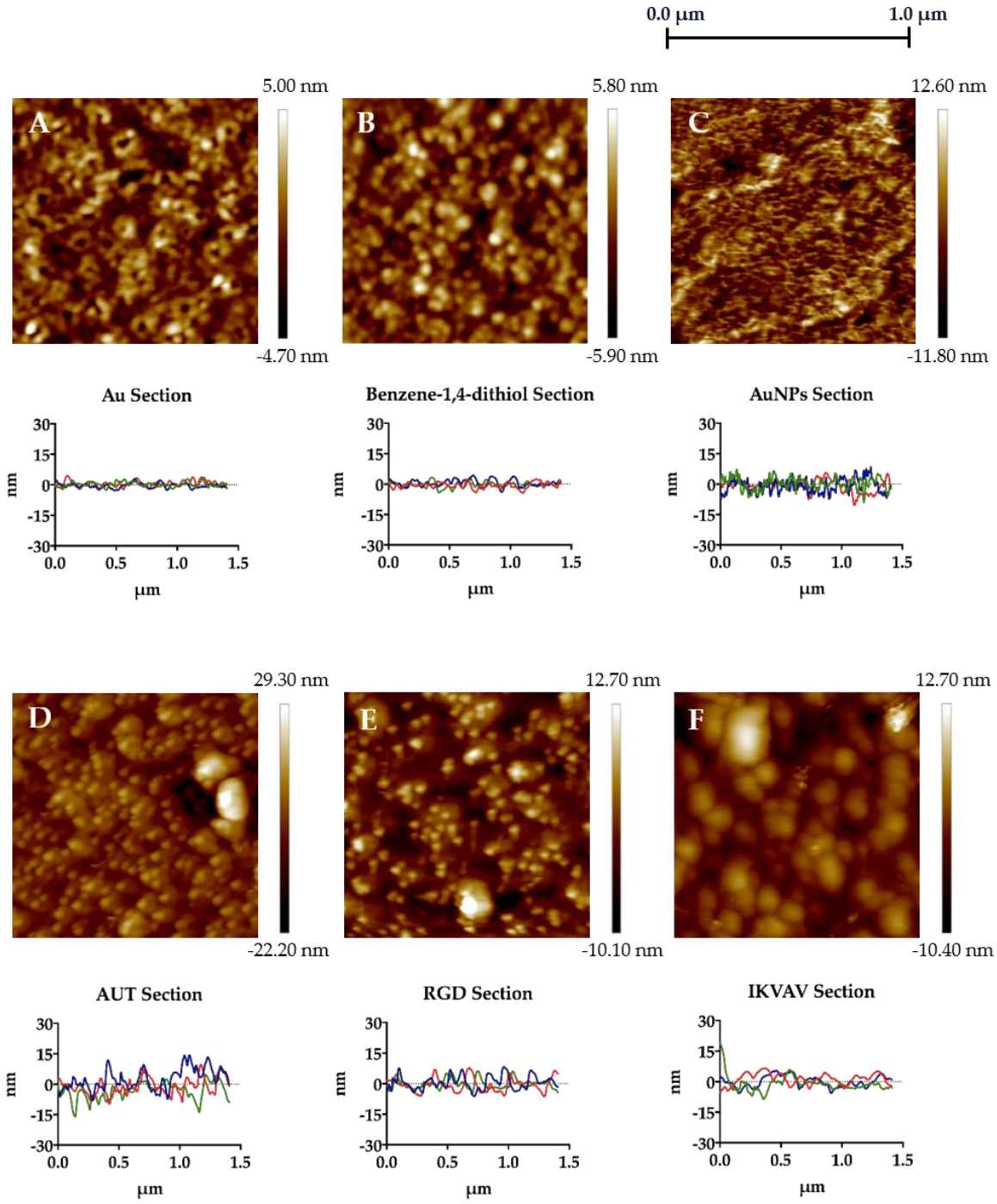


Figure 6.16 The AFM topography images observe the change in surface roughness (nm) through the oxygen plasma activation respectively to the Au NPs peptide functionalized surfaces. (A) Gold, (B) Benzene-1,4-dithiol, (C) AuNPs, (D) AUT, (E) RGD, and (F) IKVAV functionalized glass coverslips. The profile plots illustrate approximately a height between -30 nm and 30 nm, which were measured by calculating as three lines sectioning through the AFM topography image.

The Au NPs RGD and Au NPs IKVAV surfaces demonstrated a similar appearance as the RGD and IKVAV functionalized Au Flat surfaces, thus, indicating smaller clusters of RGD peptides and larger domains of clusters of IKVAV peptides on the surfaces pointing to height features outside the displayed z scale. This difference observed between the Au NPs RGD and Au NPs IKVAV surfaces could be related to the longer chain of the IKVAV peptide on the AUT linker chemically bonded on the AuNPs features on the Au NPs surfaces, which creates more flexibility and looping back and forming more clusters of the peptide on the surface. Whilst the Au Flat IKVAV surface showed larger clusters of the IKVAV peptide immobilization in certain areas, thus, 2.37 nm ± 1.09 and 3.60 nm ± 1.91, respectively.

6.3.3.2.3 COMPARING Au FLAT VS Au NPs VS Au PEPTIDES SURFACES

The Au Flat surfaces of RGD and IKVAV exhibited lower z-range and RMS values of 14.58 nm ± 3.13; 1.33 nm ± 0.66 and 14.38 nm ± 2.31; 1.29 nm ± 1.13 in comparison to that of the Au NPs surfaces functionalized with RGD and IKVAV which were respectively, 29.46 nm ± 3.77; 2.37 nm ± 1.09 and 27.68 nm ± 7.36; 3.60 nm ± 1.91. The Au Peptides surfaces (i.e. 'grafted to') demonstrated a higher z-range and RMS values in comparison to the 'grafting from' approach surfaces (i.e. Au Flat and Au NPs) for RGD and IKVAVC(19) of 44.1 nm ± 5.2; 4.72 nm ± 1.86 and 35.1 nm ± 4.59; 4.43 nm ± 1.76, respectively. This difference in z-range and RMS value indicates the 'grafting to' approach caused for a rougher topography in comparison to that of the 'grafting from' approach, thus, confirming that that method of functionalization can have a topographical effect on the surface.

6.3.3.3 SURFACE HOMOGEINITY OF Au FLAT AND Au NPs SURFACES

ToF-SIMS analysis was conducted to study the surface chemistry and homogeneity of the gold treated and peptide functionalized surfaces. The ToF-SIMS results showed that the ion fragments of interest lie in the positive as well as the negative polarity. The same parameters were set for collecting the spectra and reconstructing the raster images as the previous chapters (Chapter 4 and Chapter 5). However, in this chapter the control sample chosen is the gold coated piranha cleaned glass coverslips, with the ion fragment Au^- (m/z = 196.95) and all the ion fragments are normalized to the total ion count.

6.3.3.3.1 Au FLAT SURFACES

The ToF-SIMS results for the major secondary ion peaks are labelled in the negative and positive overlay spectrum of the Au Flat surfaces in Figure 6.17, Figure 6.18, and Table 6.7, respectively. The surface chemistry of the Au Flat surfaces consist of the immobilization of the AUT linker on the gold surface through the thiol chemistry and the AuS^- ion intensity indicates the thiol functional group had successfully bound to the gold, Figure 6.17.

The NH_4^+ ion intensity presence on the AUT modified surfaces and absent on the control is attributed to the amine functionality of the AUT, whilst the CHS^+ and $C_3H_7^+$ ion intensities are attributed to the thiol and alkyl chain of the AUT, respectively, Figure 6.18. The marker fragment of CS^- for the AUT was not as strong and was not distinguishable between the surfaces, whilst the NH_4^+ ion intensity was very strong on the AUT surface and clearly indicates a surface modification.

The RGD functionalized surface showed an increase in the R ($C_4H_8N^+$), G (CH_4N^+) and D ($C_3H_6NO_2^+$) ion fragments in comparison to the other surfaces. The IKVAV functionalized surface presented an increase in the I ($C_5H_{12}N^+$), K ($C_5H_{10}N^+$), V ($C_4H_{10}N^+$), and A ($C_2H_6N^+$) ion fragments, thus, indicating the successful surface functionalization of AUT, RGD and IKVAV functionalized surfaces, Figure 6.19. Furthermore, we observed the presence of some of these fragments on the other surface modification such as the G ion intensity that is strong on the AUT surface, which is due to the surface chemistry on these surfaces being very similar.

The intensity maps of the selected negative and positive ions fragments were reconstructed to obtain raster images of the surface modification stages of the peptide surfaces at the higher magnification field view of 3 mm x 3 mm. Figure 6.20 further confirms the homogeneity of the surface coverage relative to the intensity of secondary ion fragments characteristic to surface and overlay (i.e. surface modification). Additionally, we did observe some surface marks which could be due to the handling of the samples with the tweezers through the extensive steps of surface functionalization and washing.

Table 6.7 Negative and positive ion peaks selected for the ToF-SIMS analysis to construct as raster images to illustrate the homogenous Au Flat surfaces. Normalized ion intensity (x 10^6).

Source	Ion assignment	Gold		AUT		RGD		IKVAV	
		m/z	Dev.(ppm)	m/z	Dev.(ppm)	m/z	Dev.(ppm)	m/z	Dev.(ppm)
Negative Polarity									
Gold	Au^-	196.95	-106.40	196.95	-108.30	196.93	-193.00	196.95	-102.60
Positive Polarity									
AUT	NH_4^+	18.04	227.60	18.04	167.30	18.04	211.60	18.04	132.40
Arginine	$C_4H_8N^+$	70.078	144.70	70.07	97.80	70.07	135.20	70.07	14.10
Glycine	CH_4N^+	30.034	148.00	30.04	80.60	30.04	99.30	30.03	-11.70
Aspartic acid	$C_3H_6NO_2^+$	88.03	-137.10	88.03	-66.60	88.03	-101.10	88.02	-188.10
Isoleucine	$C_5H_{12}N^+$	86.11	155.40	86.11	101.10	86.11	128.40	86.10	33.60
Lysine	$C_5H_{10}N^+$	84.09	78.70	84.09	65.30	84.09	79.00	84.07	-83.60
Valine	$C_4H_{10}N^+$	72.09	136.40	72.09	74.50	72.09	72.80	72.08	-4.20
Alanine	$C_2H_6N^+$	44.06	166.80	44.06	128.40	44.05	122.70	44.05	34.40

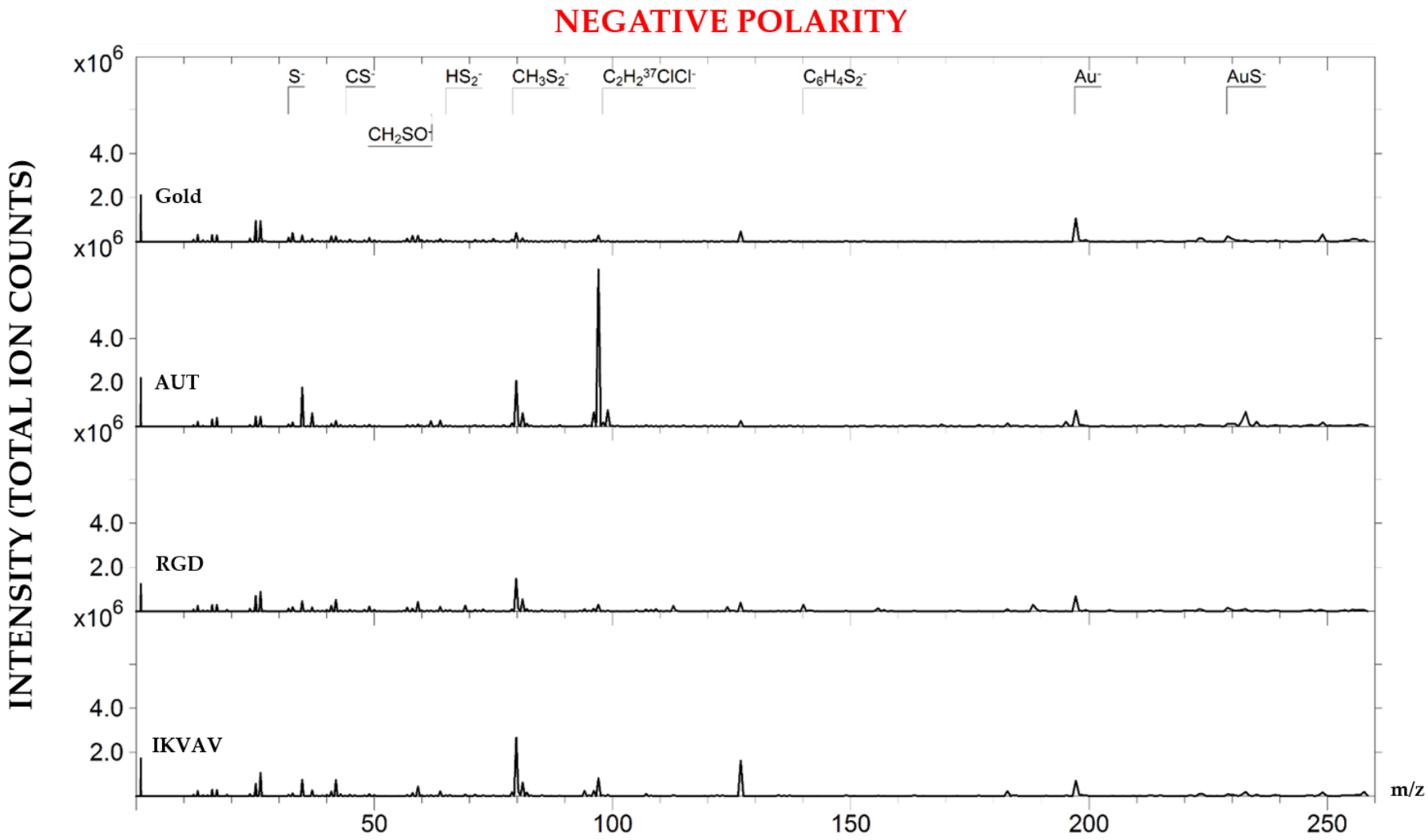


Figure 6.17 ToF-SIMS overall spectrum of the Au Flat functionalized surfaces annotated with the selected negative ion peaks and normalized to the total ion count.

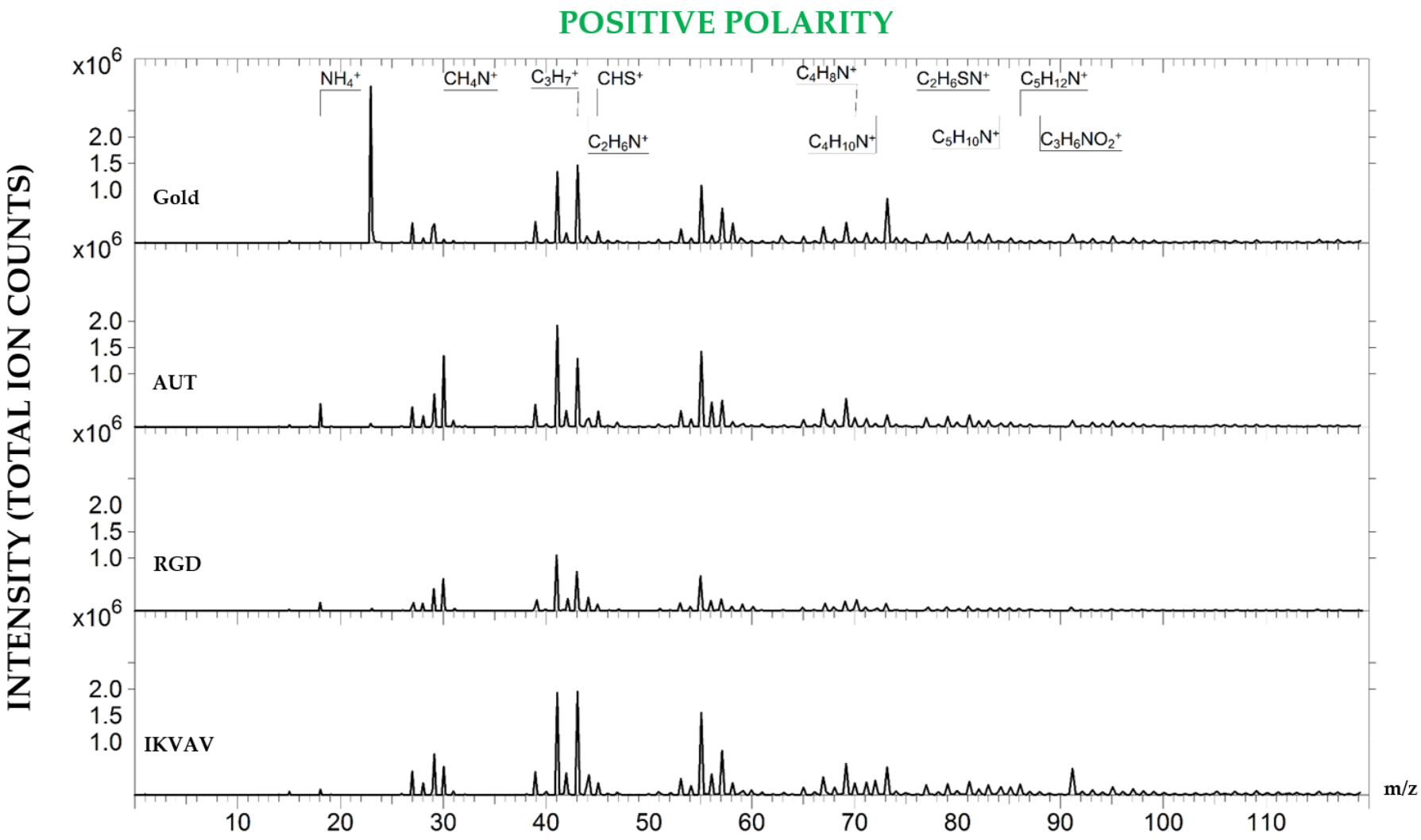


Figure 6.18 ToF-SIMS overall spectrum of the Au Flat functionalized surfaces annotated with the selected positive ion peaks and normalized to the total ion count.

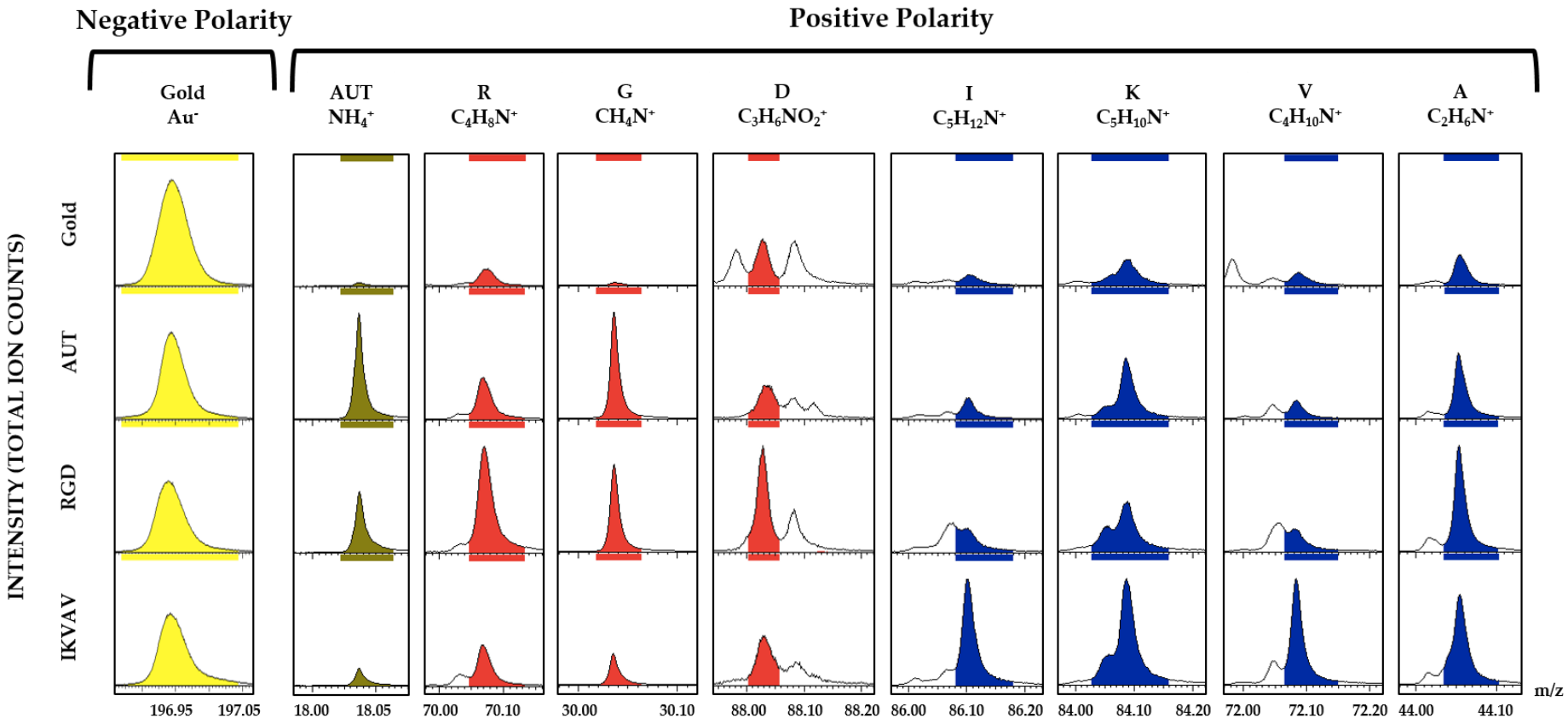


Figure 6.19 ToF-SIMS characterization of marker ion fragments of amino acids distinguishable for Au Flat surface modification and normalized to the total ion count.

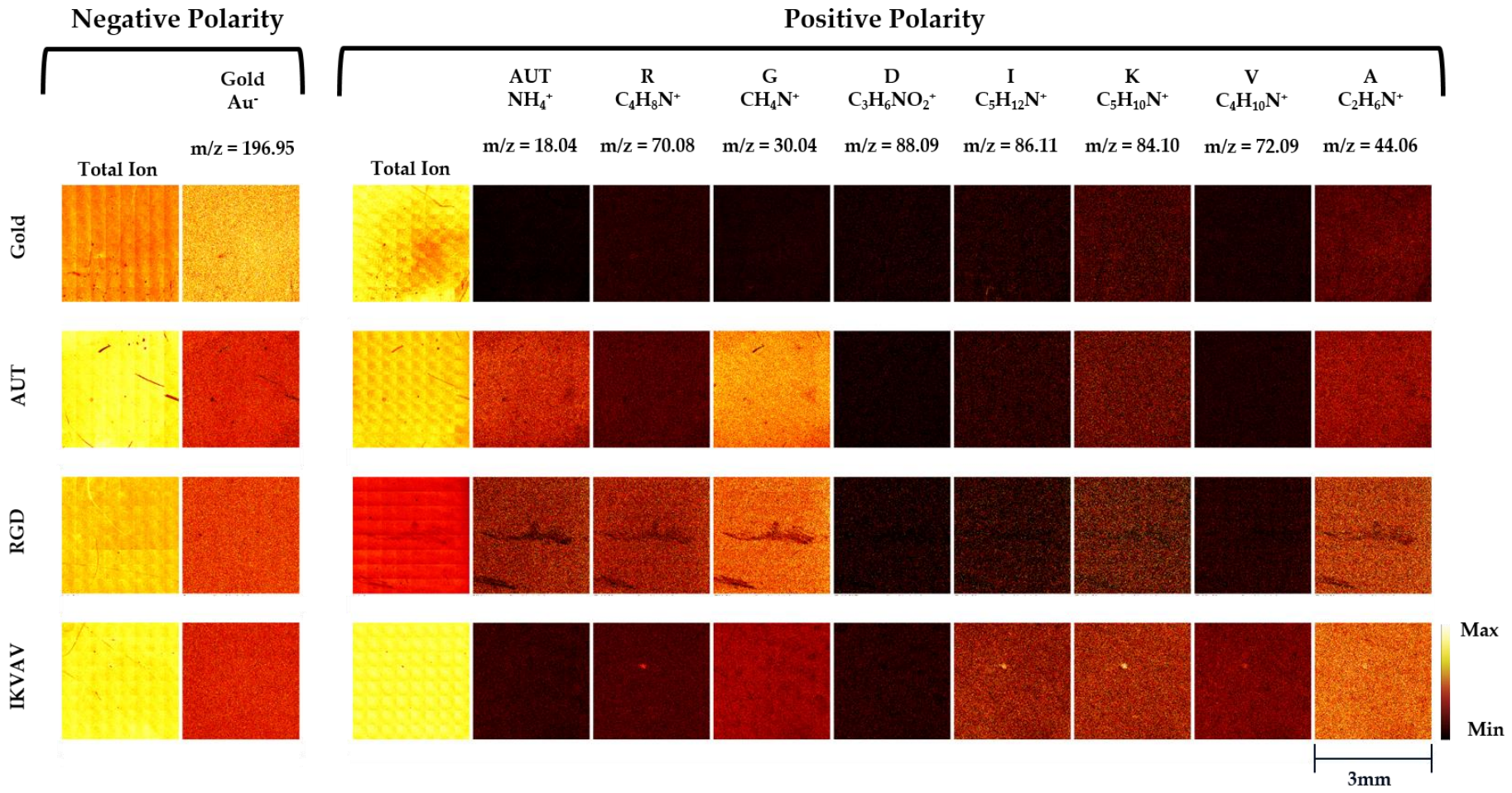


Figure 6.20 ToF-SIMS analysis of the marker ion fragments as raster images to illustrate the Au Flat homogenous surfaces and normalized to the total ion count, scale is 3 mm x 3 mm.

6.3.3.3.2 SURFACE HOMOGEINITY OF Au NPs SURFACES

The ToF-SIMS results for the major secondary ion peaks are labelled in the negative and positive overlay spectrum of the Au NPs surfaces in Figure 6.21, Figure 6.22, and Table 6.8, respectively. The surface chemistry of the Au NPs surfaces consist of the immobilization of the Benzene-1,4-dithiol, a benzene ring linker with a thiol group at the para positions. Thus, making it a suitable linker for the immobilization onto the gold surface and an available thiol group linker for the covalent attachment with the AuNPs for the next surface modification. The Benzene-1,4-dithiol functionalization results in an increase in the $C_6H_4S_2^-$, HS_2^- and AuS^- ion intensities respectively, for the terminal thiol functional group and the thiol functional group bound to the gold, Figure 6.21. The successful functionalization of the surface with AuNPs was observed as an increase in the $CH_3S_2^-$ ion intensity indicating the bound gold nanoparticle on the thiol functional group of the benzene ring. The CS^- ion intensity indicates the presence of the AUT linker of the thiol group bound to the gold surface of the nanoparticle through the thiol-gold chemistry. Moreover, the NH_4^+ ion intensity indicated that this ion fragment was less specific in identifying the functionalization of AUT on the Au NPs surfaces as the NH_4^+ ion fragment was strongly present on the Benzene-1,4-dithiol and AuNPs functionalized surfaces, Figure 6.22. Consequently, for the Au Flat surfaces we used the NH_4^+ as the marker fragment and on the Au NPs surface we used CS^- as the marker fragment. The RGD functionalized surface showed an increase in the R ($C_4H_8N^+$), G (CH_4N^+) and D ($C_3H_6NO_2^+$) ion fragments in comparison to the other surfaces. The IKVAV functionalized surface presented an increase in the I ($C_5H_{12}N^+$), K ($C_5H_{10}N^+$), V ($C_4H_{10}N^+$), and A ($C_2H_6N^+$) ion fragments, thus, indicating the successful surface functionalization of AUT, RGD and IKVAV functionalized surfaces, Figure 6.23.

The intensity maps of the selected negative and positive ions fragments were reconstructed to obtain raster images of the surface modification stages of the peptide surfaces at the higher magnification field view of 3 mm x 3 mm. Figure 6.24 illustrate confirms the homogeneity of the surface coverage relative to the intensity of secondary ion fragments characteristic to surface and overlay (i.e. surface modification). Evenly distributed surface coverage of ion intensity on the RGD and IKVAV surfaces was observed, whilst the Benzene-1,4-dithiol and AuNPs surfaces demonstrated some inhomogeneities. These

patterns could possibly be attributed to the washing of the samples, which indicates a more vigorous washing approach is required as these features are not present on the RGD and IKVAV surfaces. Furthermore, we observed on the AUT surface that the sample had been damaged, which possibly could have been due to the flood gun of the ToF-SIMS as a large circle amount of the ion fragments were not detected.

Table 6.8 Negative and positive ion peaks selected for the ToF-SIMS analysis to construct as raster images to illustrate the homogenous Au NPs surfaces. Normalized ion intensity (x 10^6).

Source	Ion Assignment	Gold		Benzene-1,4-dithiol		AuNPs		AUT		RGD		IKVAV	
		m/z	Dev.(ppm)	m/z	Dev.(ppm)	m/z	Dev.(ppm)	m/z	Dev.(ppm)	m/z	Dev.(ppm)	m/z	Dev.(ppm)
Negative Polarity													
Gold	Au^-	196.95	-106.40	196.94	-129.00	196.95	-102.10	196.89	-384.60	196.94	-127.60	196.94	-123.70
AUT	CS^-	43.97	-60.10	43.97	-73.70	43.97	-58.00	43.97	-84.10	43.97	-67.10	43.97	-59.00
Benzene-1,4-dithiol	HS_2^-	64.95	-23.70	64.95	-42.20	64.95	-16.80	64.95	-15.00	64.95	5.60	64.95	21.80
AuNPs	$CH_3S_2^-$	78.96	-109.90	78.96	-93.20	78.96	-95.20	78.96	-93.90	78.96	-113.20	78.96	-129.20
Positive Polarity													
Arginine	$C_4H_8N^+$	70.08	144.70	70.08	141.90	70.07	98.40	70.07	112.90	70.07	47.50	70.07	77.90
Glycine	CH_4N^+	30.04	148.00	30.04	105.30	30.04	81.50	30.04	88.10	30.03	20.60	30.04	94.20
Aspartic acid	$C_3H_6NO_2^+$	88.03	-137.10	88.03	-106.90	88.03	-118.40	88.03	-94.40	88.03	-82.40	88.03	-75.50
Isoleucine	$C_5H_{12}N^+$	86.11	155.40	86.11	135.30	86.11	112.20	86.11	107.90	86.10	54.80	86.10	77.50
Lysine	$C_5H_{10}N^+$	84.09	78.70	84.09	99.80	84.09	79.90	84.08	35.90	84.08	-46.70	84.08	47.90
Valine	$C_4H_{10}N^+$	72.09	136.40	72.09	95.30	72.09	75.40	72.09	61.60	72.08	20.20	72.08	56.50
Alanine	$C_2H_6N^+$	44.06	166.80	44.06	146.00	44.05	113.80	44.05	116.70	44.05	55.60	44.05	110.80

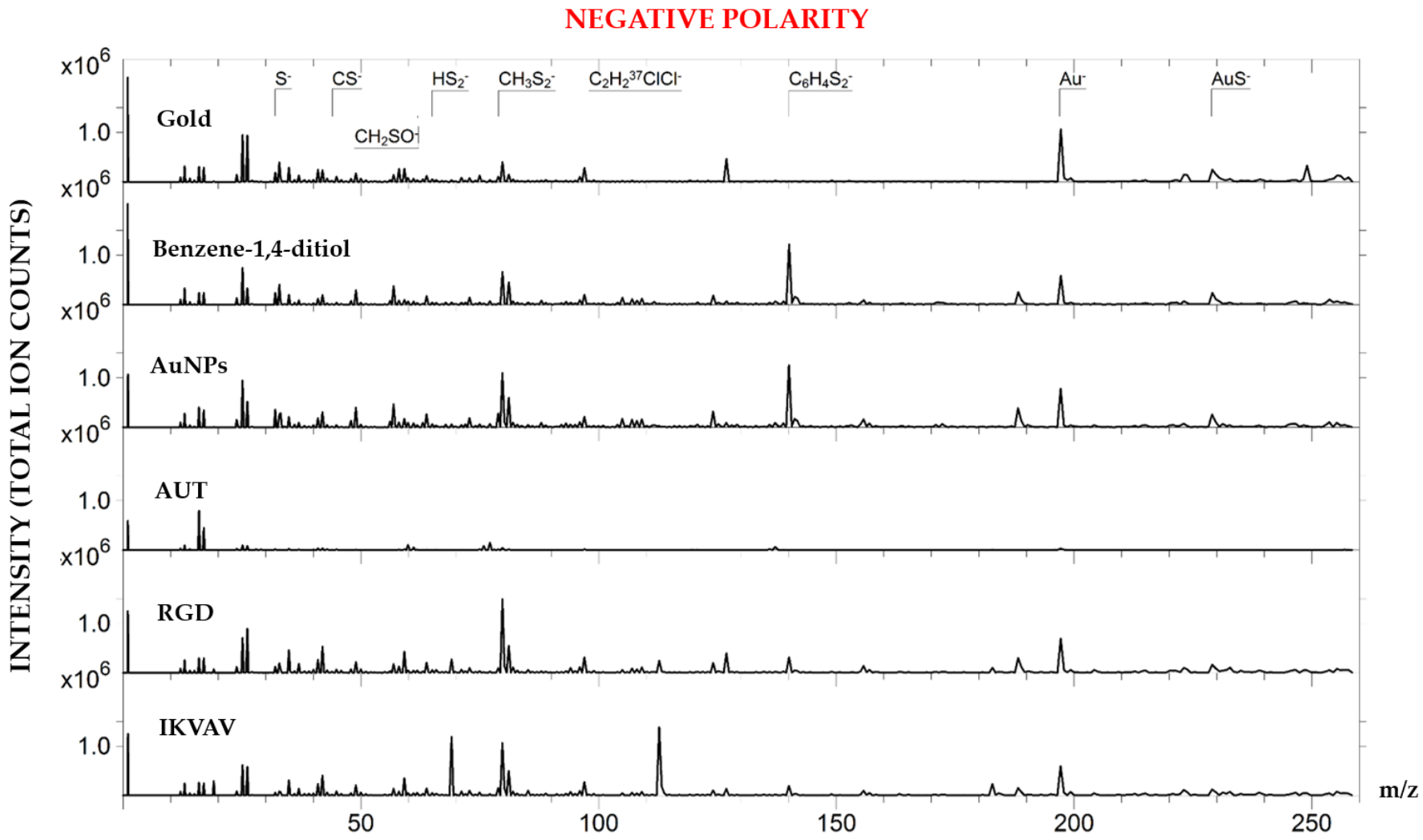


Figure 6.21 ToF-SIMS overall spectrum of the Au NPs functionalized surfaces annotated with the selected negative ion peaks and normalized to the total ion count.

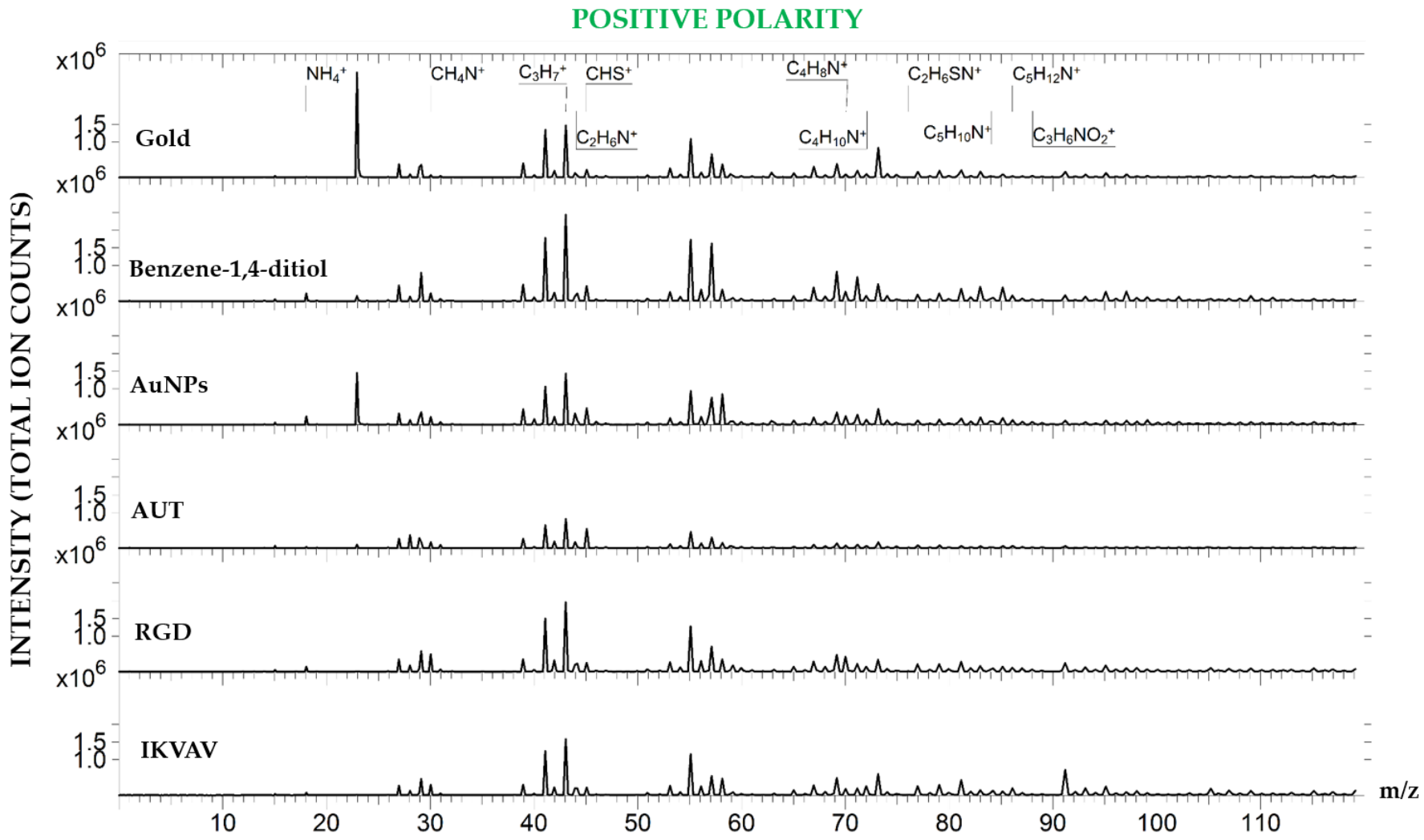


Figure 6.22 ToF-SIMS overall spectrum of the Au NPs functionalized surfaces annotated with the selected positive ion peaks and normalized to the total ion count.

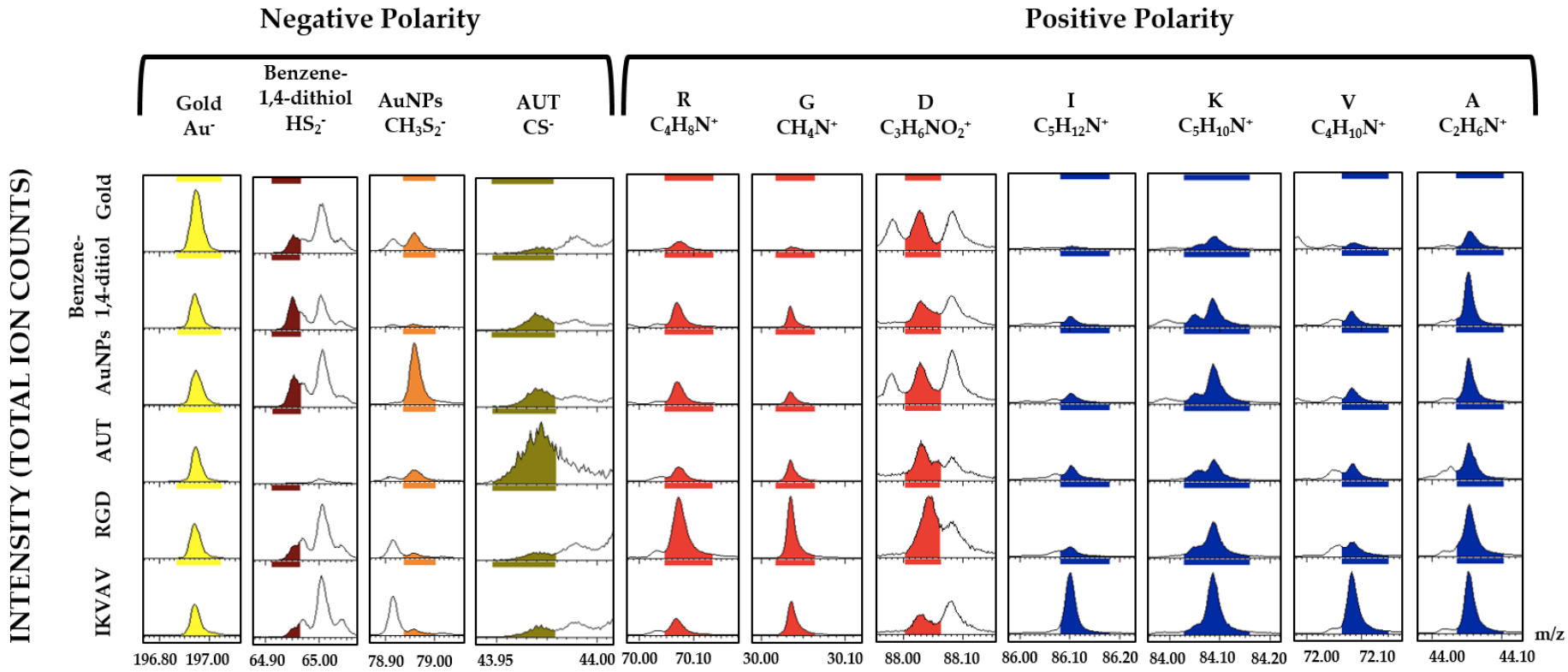


Figure 6.23 ToF-SIMS characterization of marker ion fragments of amino acids distinguishable for Au NPs surface modification and normalized to the total ion count.

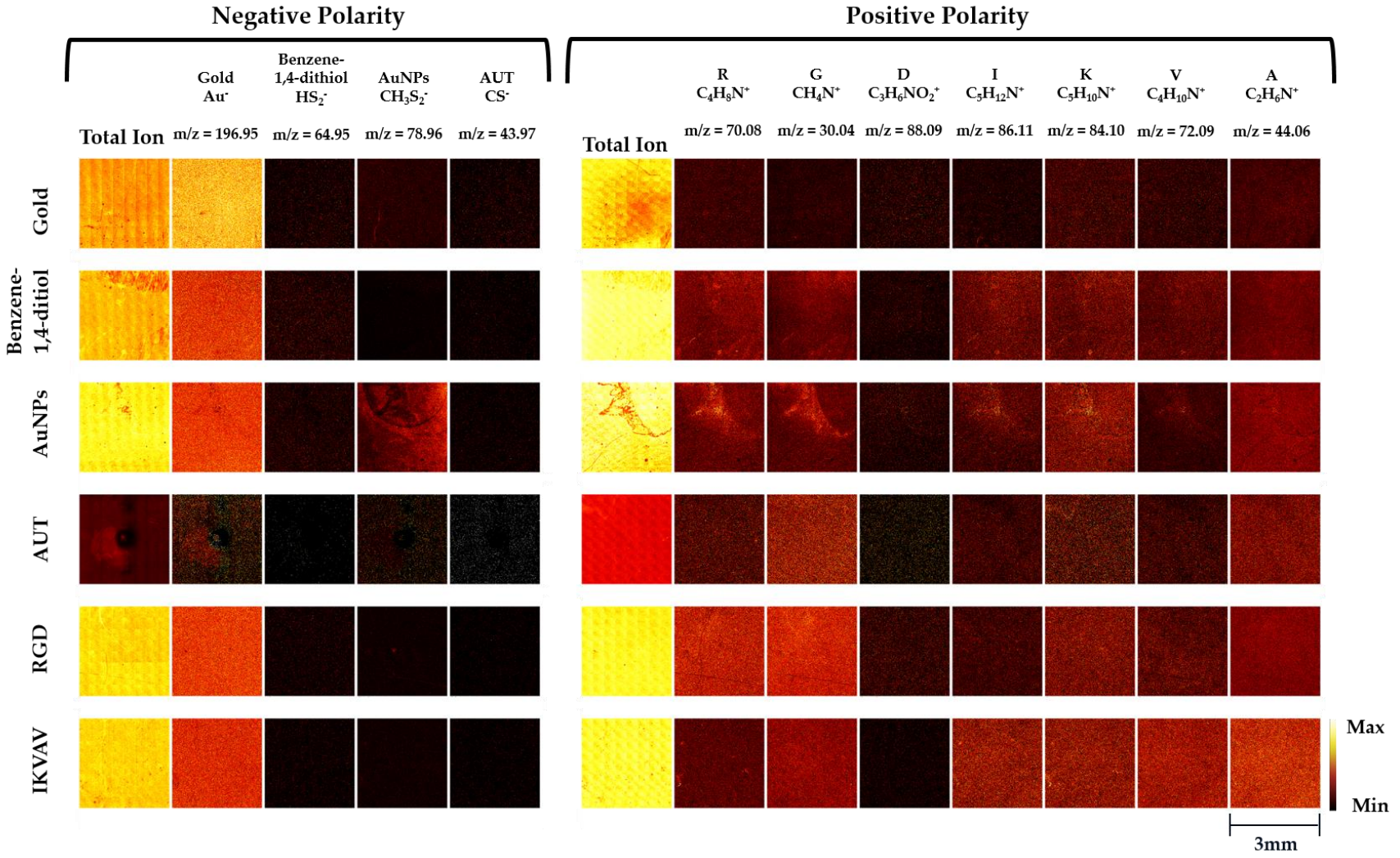


Figure 6.24 ToF-SIMS analysis of the marker ion fragments as raster images to illustrate the Au NPs homogenous surfaces and normalized to the total ion count, scale is 3 mm x 3 mm.

6.4 CELL RESPONSE TO 2D AND 3D SURFACES

The surface analysis confirmed the immobilization of RGD and IKVAV peptide sequences on the Au Flat and Au NPs surfaces, and RGDC and IKVAVC(19) peptide sequences on the Au Peptides, AuNPs and SiO_2@AuNPssurfaces. The surface validation enabled us to study the effect that 2D and 3D surfaces have on the adhesion, proliferation and differentiation of neural progenitor stem cells (NPSCs).

The PLO.Laminin (glass) control used in previous chapters (Chapter 4 and Chapter 5) was used to monitor and compare the cell response to the gold surfaces controls of Au Flat AUT and Au NPs AUT surfaces. The functionalized AuNPs and SiO_2@AuNPs were cultured with dissociated NPSCs, 1.5 x 10^5 cells/mm^2, in serum-free media to study their suitability for cell adhesion, proliferation and differentiation. For the control we choose the non-conjugate AuNPs and SiO_2@AuNPs to monitor and as a comparison to the cell response. Furthermore, we also studied cell response on the Au Peptides surfaces as a comparison to functionalized AuNPs and SiO_2@AuNPs to provide a direct comparison of surface chemistry inducing specific cell fate on 2D (i.e. Au Peptides surfaces) versus 3D (i.e. AuNPs and SiO_2@AuNPs) surfaces.

6.4.1 CELL SURVIVAL ON 2D SURFACES

6.4.1.1 ADHESION AND PROLIFERATION ON Au FLAT AND Au NPs SURFACES

The NPSCs were seeded on the gold functionalized surfaces of Au Flat-RGD, Au Flat-IKVAV, Au NPs-RGD and Au NPs-IKVAV and the control surfaces of Au Flat-AUT, Au NPs-AUT, and PLO.Laminin. The Au NPs surfaces present a different chemistry and conjugation with AuNPs in comparison to the Au Flat surfaces that lack this feature of the nanoparticles, see Schematic 6.9. The difference in the cell attachment and proliferation observed through phase contrast images over 14DIV was illustrated in Figure 6.25, Figure 6.26, and Figure 6.27.

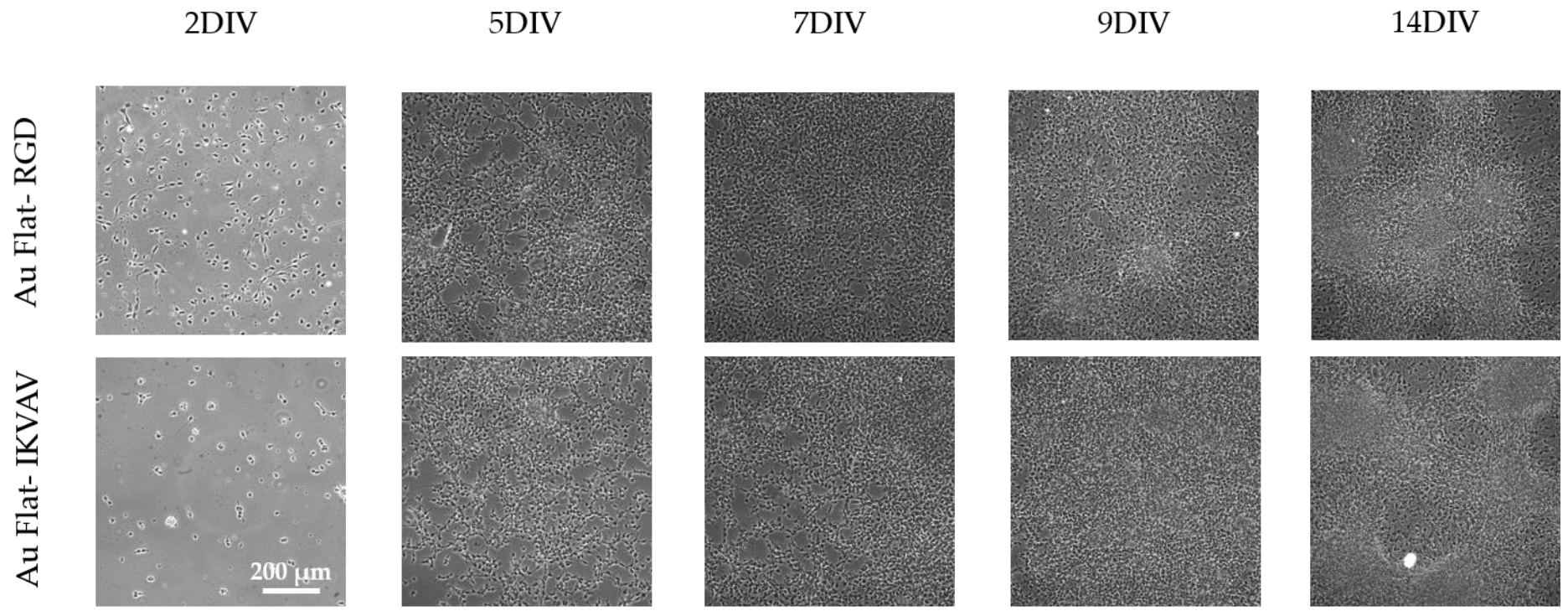


Figure 6.25 Phase contrast images of E18 NPSCs cell cultures on Au Flat surfaces functionalized with RGD or IKVAV surfaces that are low surface coverage to high surface coverage, n = 3. All the cells were cultured on the surfaces at a density of 3 x 10^5 cell/mm^2 in serum-free media for 14 days *in vitro*.

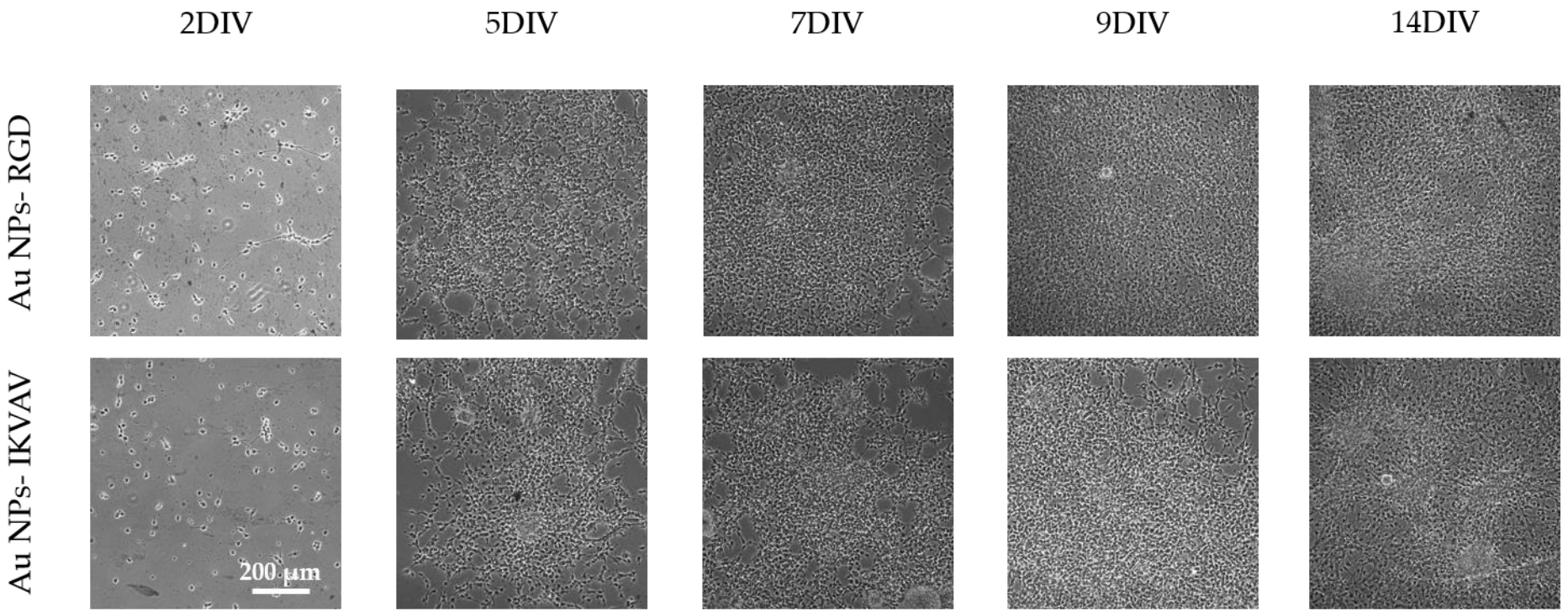


Figure 6.26 Phase contrast images of E18 NPSCs cell cultures on Au NPs surfaces functionalized with RGD or IKVAV surfaces that are low surface coverage to high surface coverage, n = 3. All the cells were cultured on the surfaces at a density of 3 x 10^5 cell/mm^2 in serum-free media for 14 days *in vitro*.

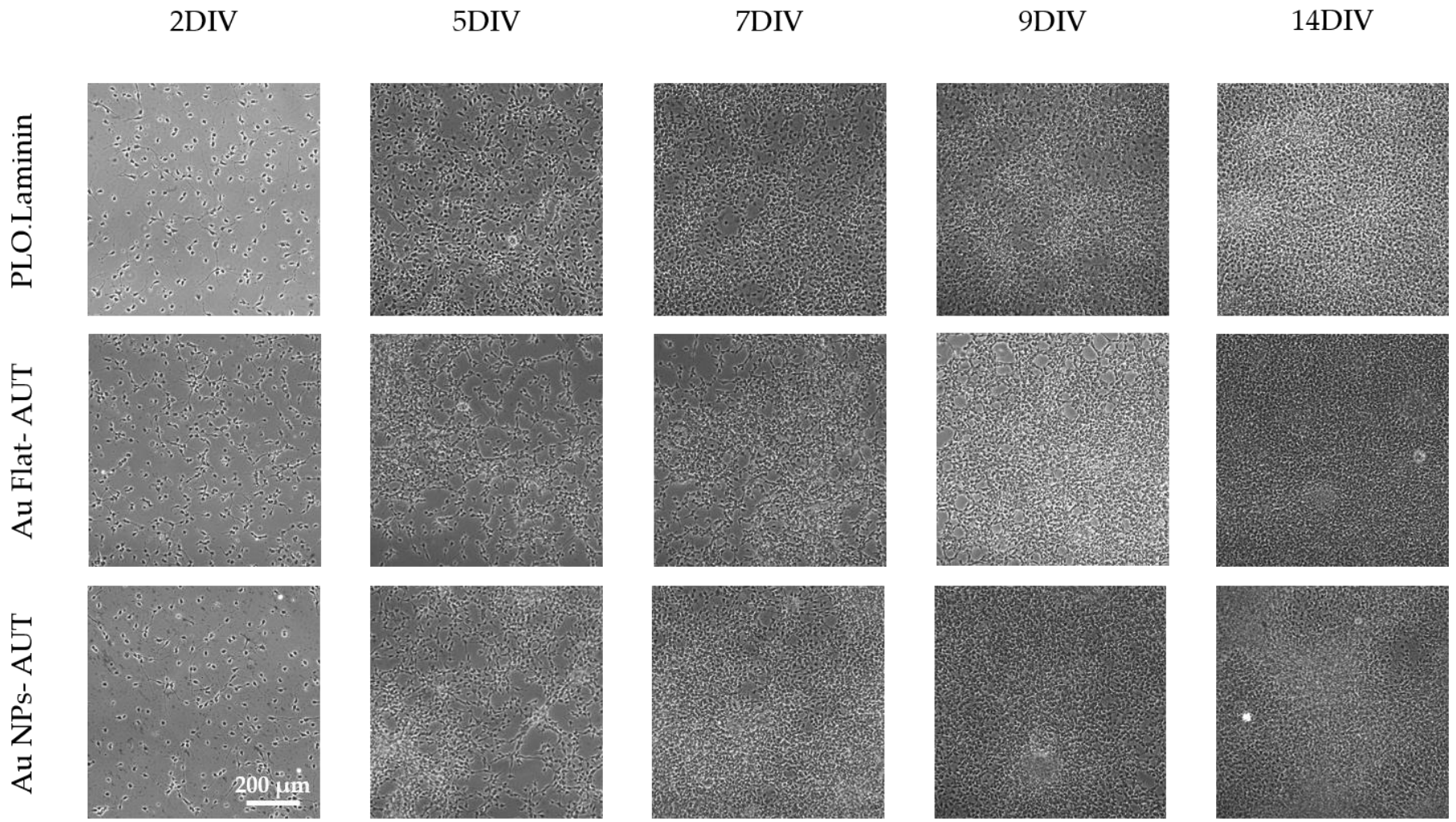


Figure 6.27 Phase contrast images of E18 NPSCs cell cultures on control surfaces respectively, (i) PLO.Laminin (glass), (ii) Au Flat-AUT, and (iii) Au NPs-AUT surfaces that are low surface coverage to high surface coverage, n = 3. All the cells were cultured on the surfaces at a density of 3 x 10^5 cell/mm^2 in serum-free media for 14 days *in vitro*.

6.4.1.1.1 FUNCTIONALIZED Au FLAT SURFACES

The cells adhered well on the Au Flat-RGD surface and reached a high surface coverage by 7DIV. The confluency of the NPSCs on the surfaces led to the clustering of cell processes (i.e. the formation of axons and dendrites from the cell body of the NPSCs), thus, a film thicker than a monolayer was observed by 14DIV. The Au Flat-IKVAV surfaces showed very low surface coverage as cells formed patches of cells with clustered cell processes, which suggests that the cells preferred the cell-cell interaction over the cell-surface interaction at 2DIV and by 5DIV the surface exhibited a higher surface coverage in comparison to the IKVAV functionalized surfaces in the previous chapters (Chapter 4 and Chapter 5).

Furthermore, the morphology of the cells on the Au Flat-RGD surfaces remained consistent and uniform with the proliferation of the cells on the surfaces and cell processes were observed along the surface. In comparison, the Au Flat-IKVAV surfaces illustrated cells forming clustered processes with very tightly packed areas of cells on the surface to areas were the processes between the cells can be observed from 7DIV to 14DIV. The cells were very confluent by 14DIV on the IKVAV functionalized surfaces and a film of cells was observed as that on the Au Flat-RGD surfaces, Figure 6.25.

6.4.1.1.2 FUNCTIONALIZED Au NPs SURFACES

The NPSCs exhibited a lower surface coverage on the functionalized Au NPs surfaces than that of the functionalized Au Flat surfaces. The cells that adhered demonstrated cell processes along the Au NPs-RGD and Au NPs-IKVAV surfaces at 2DIV. Islands of clusters of cells were observed on Au NPs-IKVAV surfaces, whilst the Au NPs-RGD surfaces illustrated uniform surface coverage. Furthermore, the cells on the Au NPs-RGD surfaces exhibited more tightly packed areas of cells and were confluent at 9DIV. The Au NPs-IKVAV surfaces induced initial confluency of the cells in their island clusters at 7DIV to 9DIV on the surfaces before high surface coverage was observed at 14DIV. Moreover, we observed that the cells on the Au NPs-IKVAV surfaces at 14DIV exhibited processes extensions between the islands of cell clusters, which proposes that the cells were able to establish communication and a high surface coverage, Figure 6.26.

6.4.1.1.3 FUNCTIONALIZED CONTROL SURFACES

The Au Flat and Au NPs surfaces were functionalized with AUT, as literature has demonstrated it to be a good control to observe neurite outgrowth on gold surfaces with results presenting a high promotion of cell attachment and neurite outgrowth [392]. We compared the cell response on the AUT functionalized surfaces to that of the previously used control of PLO.Laminin (glass), which exhibited good cell adhesion, proliferation and survival (i.e. Chapter 4 and 5).

The control surfaces of Au Flat-AUT and Au NPs-AUT demonstrated uniform surface coverage of separate cells and cell processes along the surfaces. The Au NPs-AUT surfaces demonstrate cell confluency at 7DIV, whilst Au Flat-AUT reached confluence after 9DIV. At 14DIV, the Au NPs-AUT surfaces were highly confluent and showed clusters of cells and cell processes, whereas the Au Flat-AUT surfaces reached confluence and only started to demonstrate the formation of some cell clustering due to confluence of the cells.

The PLO.Laminin surface induced cell adhesion and long outgrowth of the cells processes along the surface at 2DIV and by 5DIV the cells had proliferated to a high surface coverage. By 9DIV the surface exhibited cell clusters due to high confluence of the cells and by 14DIV we observed a film thicker than that observed on the Au Flat and Au NPs functionalized surfaces, Figure 6.27.

Next we quantified the difference in the NPSCs attachment and proliferation observed through the phase contrast images on the gold functionalized surfaces of Au Flat-RGD, Au Flat-IKVAV, Au NPs-RGD and Au NPs-IKVAV and the control surfaces of Au Flat-AUT, Au NPs-AUT, and PLO.Laminin as a measure of % area coverage illustrated in Figure 6.28.

We observed at 7DIV that the Au Flat-RGD and Au NPs-RGD surfaces induced cells to proliferate faster respectively, 32.15% ± 1.93 area coverage and 40.43% ± 3.50 area coverage, than those of the Au Flat and Au NPs surfaces respectively, 19.57% ± 1.73 area coverage and 22.23% ± 1.43 area coverage. Moreover, we observed a significant difference, (*) $p < 0.05$, on the Au NPs surfaces. The Au Flat-AUT and Au NPs-AUT surfaces demonstrated a lower % area coverage respectively, 25.75% ± 1.84 area coverage and 36.64% ± 1.58 area coverage, at 7 DIV in comparison to that of Au Flat-RGD and functionalized surfaces. Confluency of cells was observed at 14DIV on all the functionalized Au surfaces in the order of highest % area

coverage of AUT, RGD and IKVAV for the Au Flat surfaces, 63.70% ± 1.33, 61.40% ± 1.22, and 55.98% ± 1.26 area coverage. Whereas the AUT and RGD functionalized Au NPs surfaces presented a similar % area coverage respectively, 57.94% ± 2.15 area coverage and 57.05% ± 1.25 area coverage, followed by a lower % area coverage for the Au NPs-IKVAV surfaces of 53.47% ± 3.56 area coverage. The functionalized Au NPs surfaces presented a higher % area coverage in comparison to that of the functionalized Au Flat surfaces at 7DIV, but a lower % area coverage at 14DIV. This can be related to the surface topography of the Au NPs surfaces, which induces a more cell spread morphology in comparison to that of the functionalized Au Flat surfaces. The phase contrast images illustrate this as a more tightly packed cell population with a higher % area coverage. The PLO.Laminin surface illustrated an enhanced cell proliferation significantly, (*) $p < 0.05$, at 7DIV in relation to the functionalized Au Flat and Au NPs surfaces with a 46.87% ± 1.9 area coverage.

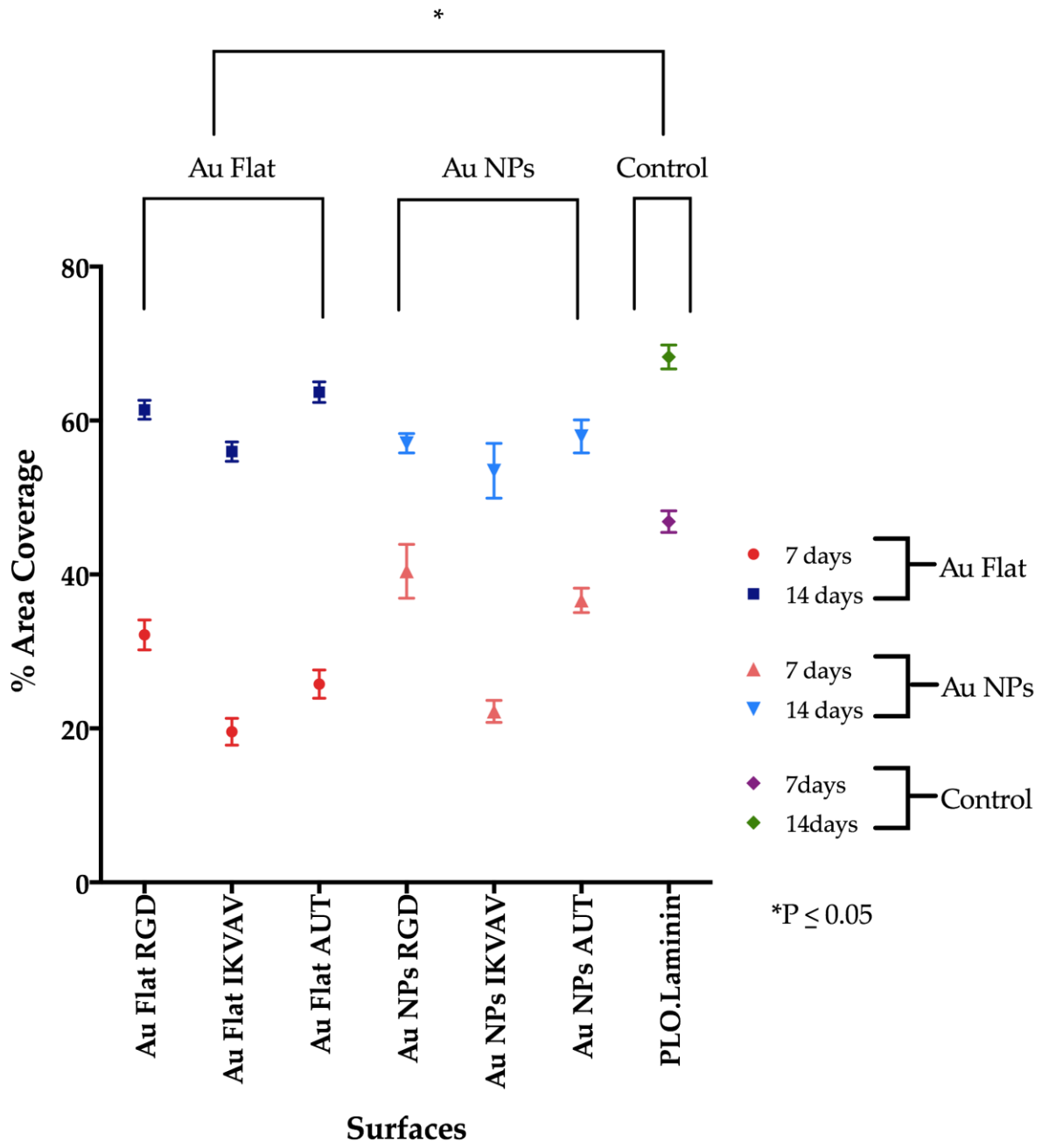


Figure 6.28 % Area coverage of E18 NPSCs on Au Flat, Au NPs surfaces and the PLO.Laminin surface as comparison control surface. Error bars represent mean ± SD for n = 3, and significant difference of (*) $p < 0.05$ was observed on the PLO.Laminin surface to the peptide functionalized Au Flat, Au NPs surfaces. All the cells were cultured on the surfaces at a density of 3 x 10^5 cell/mm^2 in serum-free media for 14 days *in vitro*.

6.4.2 CELL DIFFERENTIATION ON FUNCTIONALIZED 2D SURFACES

The functionalized on the gold functionalized surfaces of Au Flat-RGD, Au Flat-IKVAV, Au NPs-RGD and Au NPs-IKVAV and the control surfaces of Au Flat-AUT, Au NPs-AUT, and PLO.Laminin provided NPSCs attachment, spreading and proliferation. The Au surfaces demonstrated a difference in proliferation rate after certain days *in vitro*, thus, we observed a higher % area coverage for functionalized Au NPs surfaces at 7DIV and at 14DIV functionalized Au Flat surfaces demonstrated a higher % area coverage. We observed that the cells become very confluent on the functionalized Au surfaces after 14DIV and induced the cells to lift off the surfaces, which is observed as a monolayer of cells (i.e. spontaneously) and this is supported by literature [358].

6.4.2.1 FUNCTIONALIZED Au FLAT SURFACES

The Au Flat-RGD surfaces demonstrated a mature and uniform neural network, with high surface coverage and no astrocytes. The Au Flat-IKVAV surfaces presented a cell population of only astrocytes and high surface coverage. Moreover, the cells on the Au Flat-IKVAV surfaces demonstrated a more tightly packed population in comparison to that on the Au Flat-RGD surface, which is due to the cells morphology and extended cell processes (i.e. the formation of axons and dendrites from the cell body of the NPSCs) along the surface. This was further quantified by the HOECHST staining of the nuclei, which demonstrates some cell clustering on the Au Flat-RGD and higher number of single cells on the Au Flat-IKVAV surfaces, Figure 6.29.

6.4.2.2 FUNCTIONALIZED Au NPs SURFACES

On the Au NPs-RGD surfaces we observed a neural network established from connected islands of clustered cells and none of the cells stained for astrocytes. The Au NPs-IKVAV surfaces induced a similar cell morphology on the NPSCs as we observed elongated cells along the surfaces, which all had differentiated into astrocytes. Furthermore, the HOECHST staining of the nuclei indicated that the Au NPs-IKVAV and Au NPs-RGD surfaces induces a uniform cell population and surface coverage. Consequently, the surface coverage and

clustering of the cells can be related to the surface topography and surface chemistry of these functionalized Au NPs surfaces, Figure 6.30.

6.4.2.3 FUNCTIONALIZED CONTROL SURFACES

The AUT functionalized surfaces of Au Flat and Au NPs surfaces induced the NPSCs to differentiate into neurons and no astrocytes were observed on these surfaces, Figure 6.31. We further observed a significant difference in cell morphology and % area coverage on these particular surfaces. The Au Flat-AUT surfaces demonstrated a higher % area coverage, with neurons that were yet to establish a mature neural network. The Au NPs-AUT surfaces illustrated that the cells had formed some establishing neural networks between the clustered populations.

The PLO.Laminin surfaces demonstrated high cell confluence and surface coverage, with a cell population of neurons and astrocytes as demonstrated in the previous chapters (i.e. Chapter 4 and Chapter 5). These results demonstrate that the staining of the cells worked and that the functionalized Au surfaces induced a specific cell fate. The RGD and AUT functionalized Au surfaces favored to differentiate towards a neuron cell fate, whilst the IKVAV functionalized Au surfaces induced astrocyte cell fate. Moreover, the difference in surface topography by changing surface chemistry with the introduction of AuNPs on the Au surfaces to make Au Flat and Au NPs surfaces affected cell morphology (i.e. clustered cells or separate cells) and surface coverage (i.e. high or low % area coverage). Furthermore, the PLO.Laminin surfaces illustrated a comparison on how the surface chemistry on glass differs to that of the same surface chemistry on Au surfaces.

We then quantified the % area coverage of neurons and astrocytes on these gold surfaces of Au Flat-RGD, Au Flat-IKVAV, Au NPs-RGD, and Au NPs-IKVAV with the control surfaces of Au Flat-AUT, Au NPs-AUT, and PLO.Laminin to determine the influence of surface chemistry and topography had on the differentiation of NPSCs into a specific cell fate as shown in Figure 6.32.

The Au Flat-RGD surfaces demonstrated the highest % area coverage of neurons cell fate, 16.16% ± 1.58 in comparison to the Au Flat-AUT, Au NPs-AUT, and Au NPs-RGD respectively, 10.34% ± 1.93, 9.81% ± 3.02, and 7.79% ± 1.65 area coverage. We observed no

astrocyte cell fate on these particular gold surfaces. Whilst the IKVAV functionalized gold surfaces induces the NPSCs to differentiate only into astrocytes with a higher % area coverage on the Au Flat-IKVAV than the Au NPs-IKVAV, 14.17% ± 1.29 and 9.26% ± 1.22, respectively. The control surface of PLO.Laminin induced a % area cover of 22.10% ± 2.07 and 97.06% ± 1.30, was observed for the differentiated cell fates of neurons and astrocytes respectively. Moreover, the PLO.Laminin surface illustrated a mature neural networks in comparison to that of the functionalized Au Flat and Au NPs surfaces and induced the NPSCs to differentiate into a mixed population of neurons and astrocytes with a significant difference of (**) $p < 0.01$ and (*) $p < 0.05$, respectively.

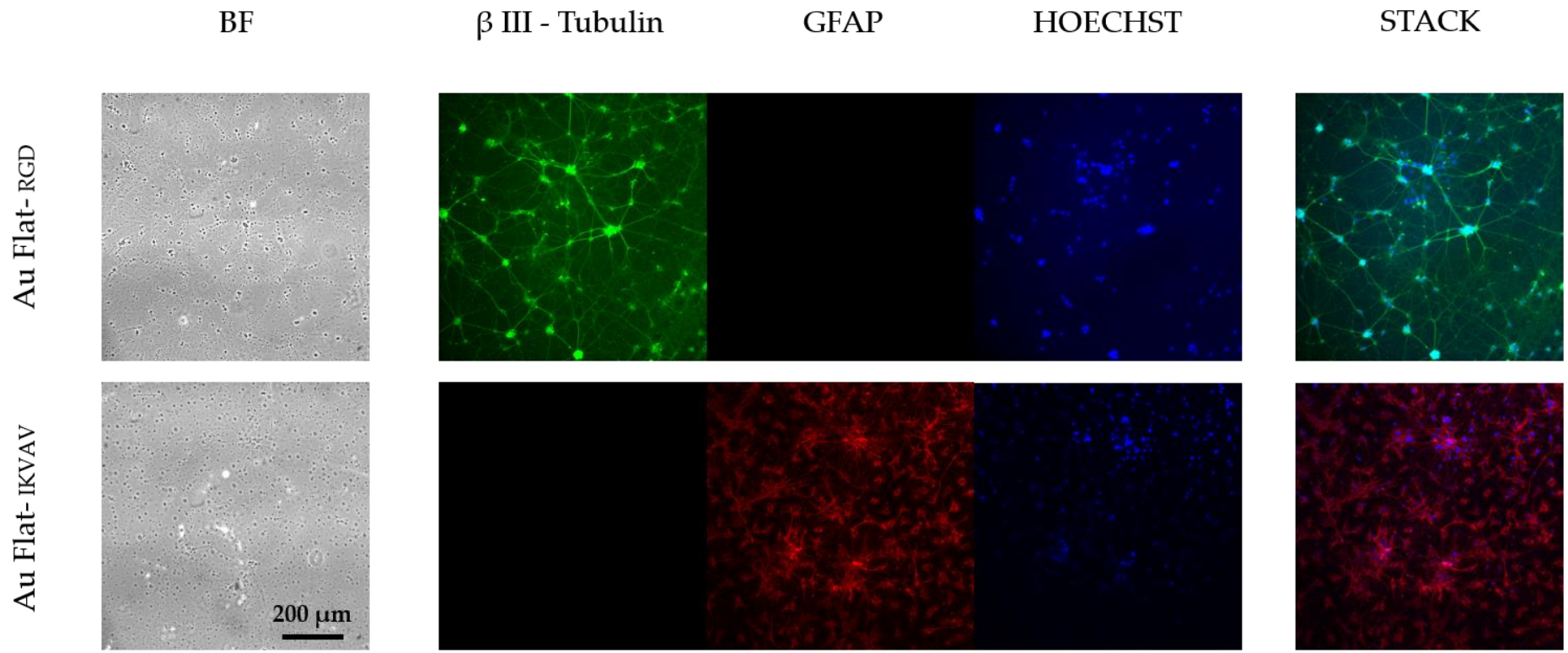


Figure 6.29 Fluorescent microscopy images of differentiated E18 NPSCs on Au Flat surfaces functionalized with RGD and IKVAV. The green, red and blue represent respectively βIII-Tubulin in neurons, GFAP in astrocytes, and nuclei. All the cells were cultured on the surfaces at a density of 3 x 10^5 cell/mm^2 in serum-free media for 14 days *in vitro*.

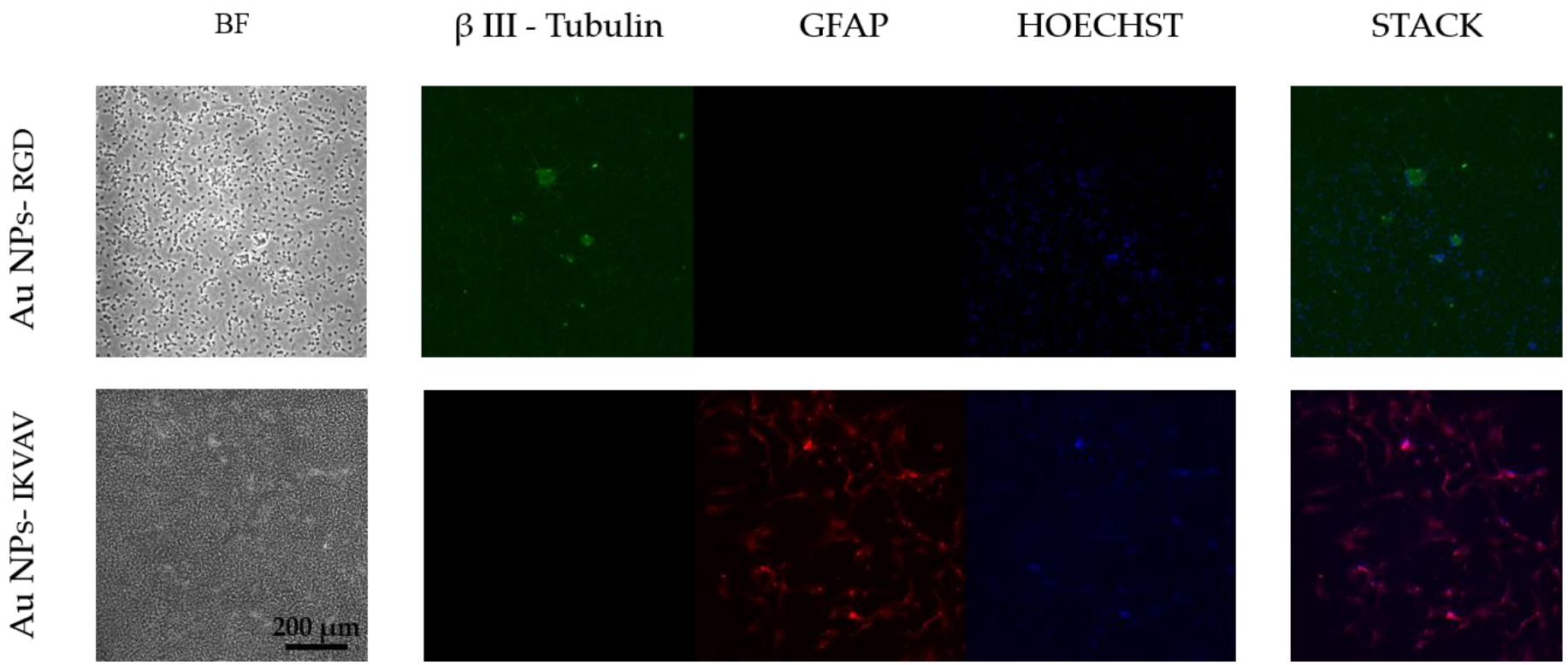


Figure 6.30 Fluorescent microscopy images of differentiated E18 NPSCs on Au NPs surfaces functionalized with RGD and IKVAV. The green, red and blue represent respectively βIII-Tubulin in neurons, GFAP in astrocytes, and nuclei. All the cells were cultured on the surfaces at a density of 3×10^5 cell/mm^2 in serum-free media for 14 days *in vitro*.

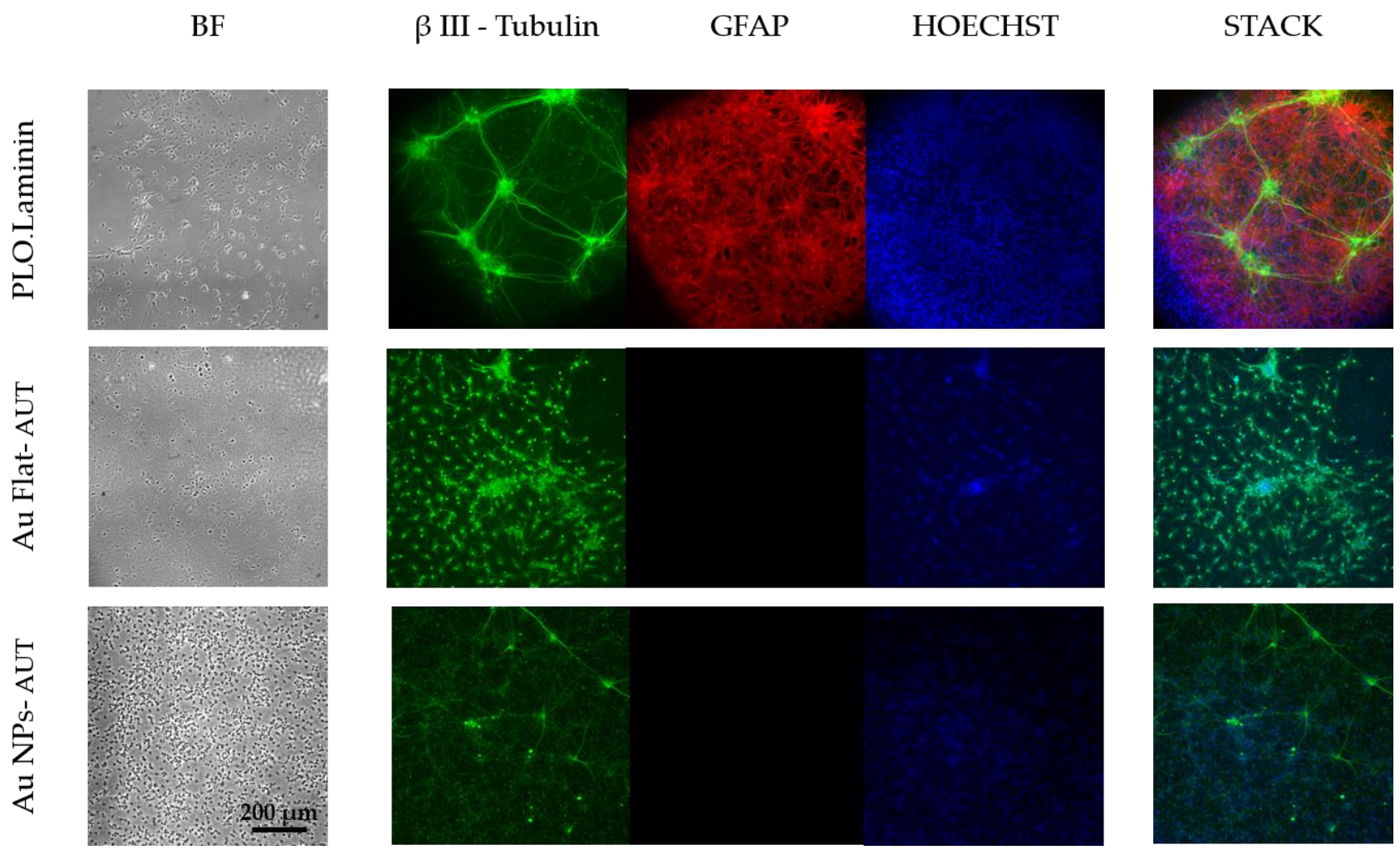


Figure 6.31 Fluorescent microscopy images of differentiated E18 NPSCs on control surfaces respectively, (i) PLO.Laminin (glass), (ii) Au Flat-AUT, and (iii) Au NPs-AUT surfaces functionalized with RGD and IKVAV. The green, red and blue represent respectively βIII-Tubulin in neurons, GFAP in astrocytes, and nuclei. All the cells were cultured on the surfaces at a density of 3 x 10^5 cell/mm^2 in serum-free media for 14 days *in vitro*.

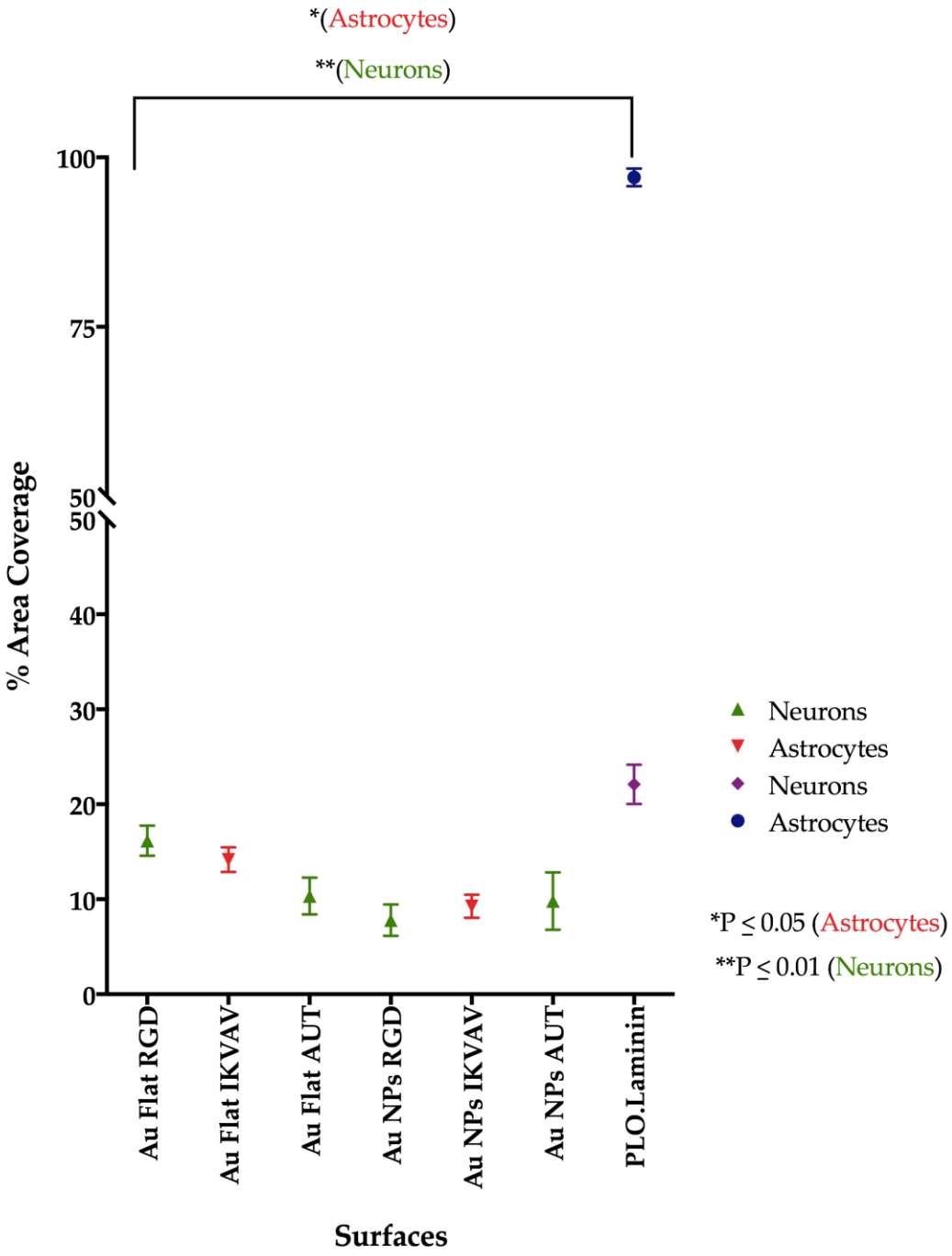


Figure 6.32 Quantification of E18 NPSCs differentiation into neurons (βIII-Tubulin positive) and astrocytes (GFAP positive) as relative area coverage by each cell type on Au Flat, Au NPs surfaces functionalized with RGD, IKVAV and the control surface of PLO.Laminin. Error bars represent mean ± SD for n = 3 and a significant difference of (**) $p < 0.01$ is observed for population of neurons on the RGD and AUT functionalized surfaces and a significant difference of (*) $p < 0.05$ is observed for population of astrocytes on the IKVAV functionalized surfaces All the cells were cultured on the surfaces at a density of 3 x 10^5 cell/mm^2 in serum-free media for 14 days *in vitro.*

6.4.3 CELL SURVIVAL ON 3D SURFACES

6.4.3.1 ADHESION AND PROLIFERATION ON AuNPs AND SiO_2@AuNPs SURFACES

We present the cell response study on the Au Peptides surfaces as a comparison to functionalized AuNPs and SiO_2@AuNPs to provide a direct comparison of surface chemistry (i.e. RGDC and IKVAVC(19)) influencing a specific cell fate on 2D (i.e. Au Peptides surfaces) versus 3D (i.e. AuNPs and SiO_2@AuNPs) surfaces.

6.4.3.1.1 ADHESION AND PROLIFERATION ON FUNCTIONALIZED Au PEPTIDES SURFACES

The Au-RGDC demonstrated medium surface coverage, separate cells (single) and an elongated cell morphology spread along the surface, whilst the Au-IKVAVC(19) surfaces showed clustered cells in media and those on the surface had clustered cell processes (i.e. the formation of axons and dendrites from the cell body of the NPSCs) at 2DIV and 5DIV. The Au-RGDC demonstrated tightly packed cell populations, whereas the Au-IKVAVC(19) showed a higher number of separate cells with spread cell morphology at 7DIV. The Au-IKVAVC(19) surfaces demonstrated to proliferate at a slower rate than the Au-RGDC surfaces illustrated by the medium surface coverage by the cells. Moreover, at 14DIV the cells on the Au-RGDC were highly confluent as we observed cells clustering, whereas the Au-IKVAVC had not reached that level of confluence, Figure 6.33. We then quantified the difference in the NPSCs attachment and proliferation observed through phase contrast images on the gold functionalized surfaces of Au-RGDC, Au-IKVAVC(19) as a measure of % area coverage illustrated in Figure 6.34. A significant difference of (*) $p < 0.05$ was observed between the % area coverage on the Au-RGDC surfaces versus that of the Au-IKVAVC(19) at 7DIV respectively, 26.16% ± 1.34 and 17.69% ± 1.58, and 14DIV respectively, 58.81% ± 1.72 and 39.41% ± 1.40 area coverage. Both surface demonstrated a lower % area coverage in comparison to the control surface of PLO.Laminin at 7DIV and 14DIV, 46.87% ± 1.39 and 68.26% ± 1.55 area coverage. Consequently, the PLO.Laminin surface illustrated an enhanced cell proliferation significantly, (**) $p < 0.01$, at 7DIV in relation to the Au-RGDC and Au-IKVAVC(19) surfaces.

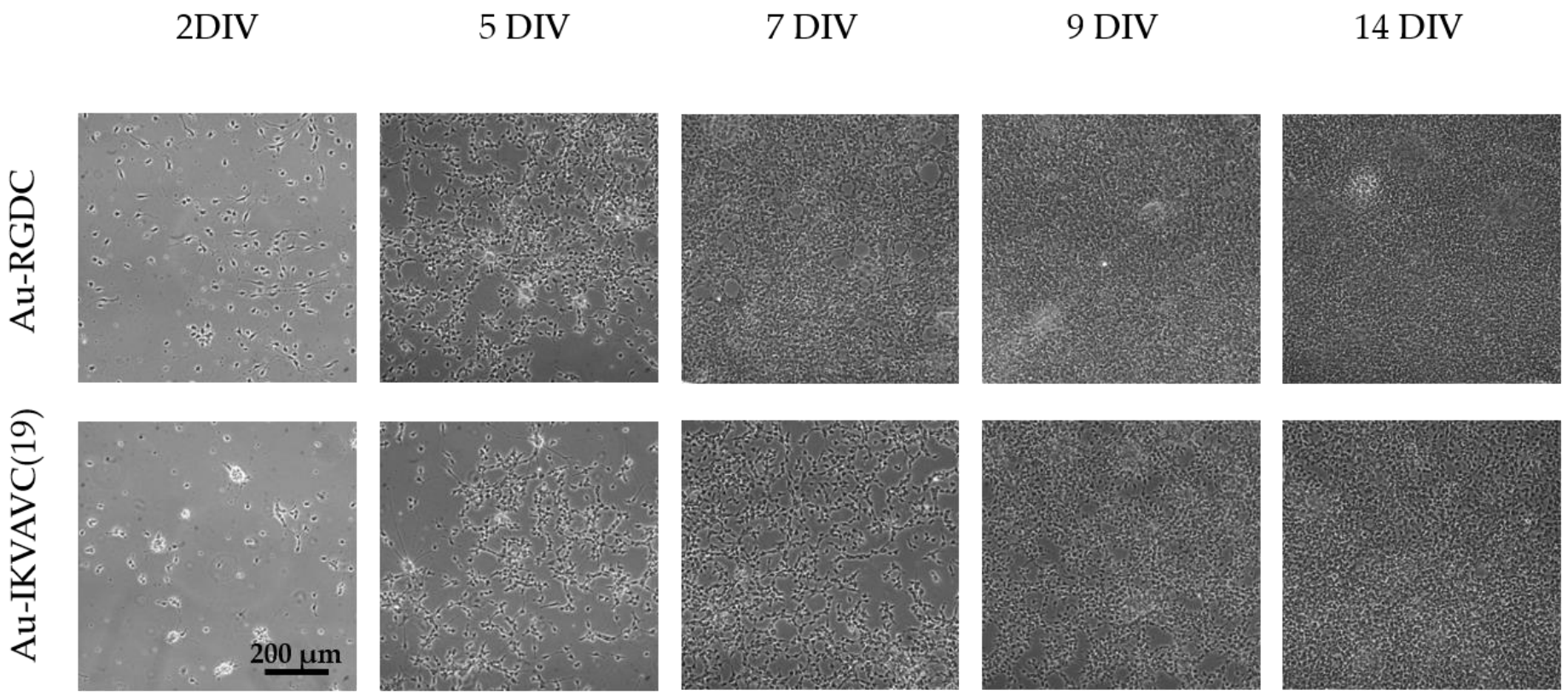


Figure 6.33 Phase contrast images of E18 NPSCs cell cultures on Au-RGDC and Au-IKVAVC(19) surfaces that are low surface coverage to high surface coverage, n = 3. All the cells were cultured on the surfaces at a density of 3 x 10^5 cell/mm^2 in serum-free media for 14 days *in vitro*.

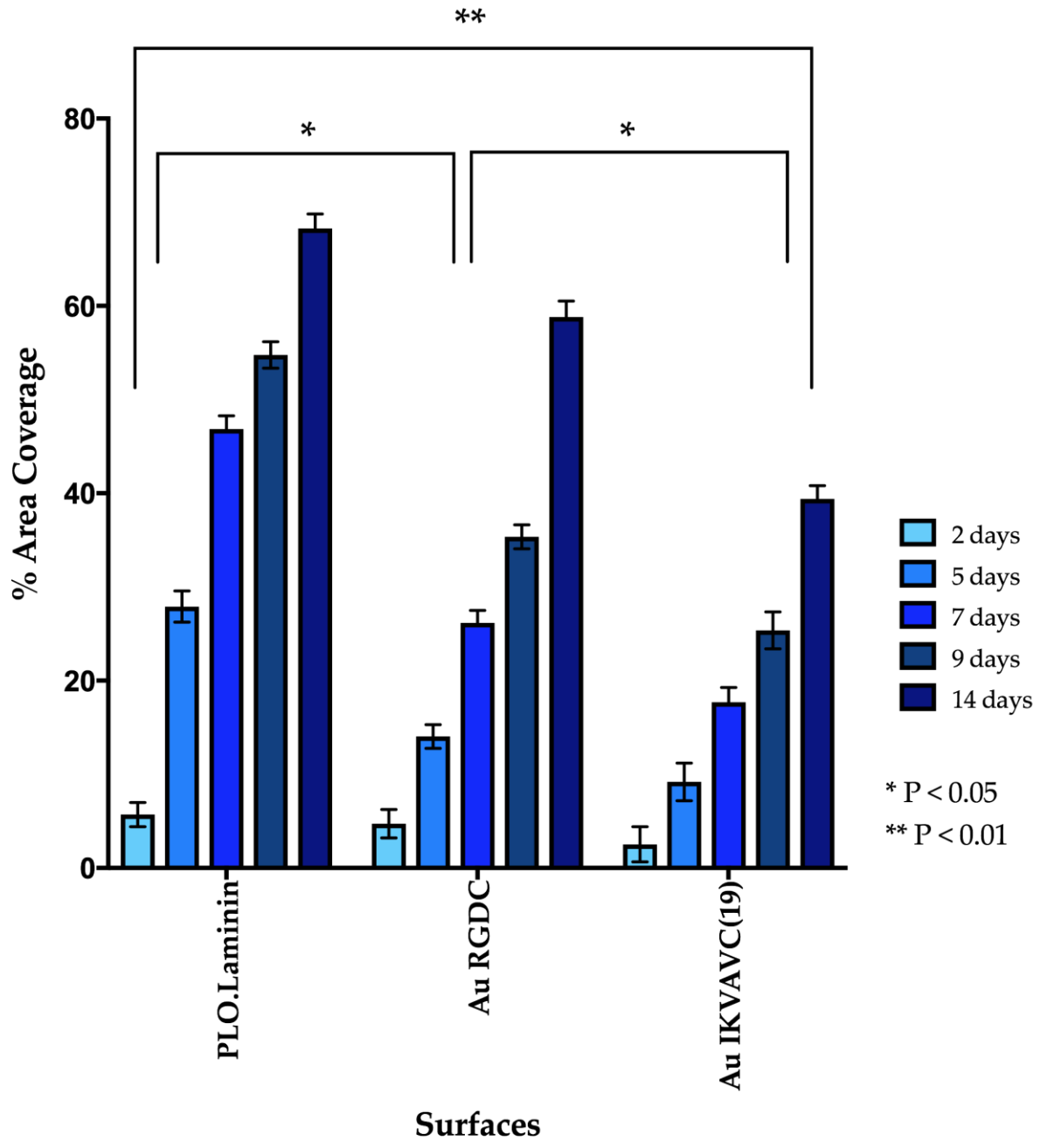


Figure 6.34 Adhesion of NPSCs on functionalized Au Peptides surfaces and the PLO.Laminin surface as comparison control surface. Error bars represent mean ± SD for n = 3, and the significant difference across the surfaces (*) $p < 0.05$ and (**) $p < 0.01$. All the cells were cultured on the surfaces at a density of 3 x 10^5 cell/mm^2 in serum-free media.

6.4.3.1.2 CELL DIFFERENTIATION ON FUNCTIONALIZED Au PEPTIDES SURFACES

The gold functionalized surfaces of Au-RGDC and Au-IKVAV(19) provided NPSCs attachment, spreading and proliferation. We observed that the cells exhibited less of the lifting off effect due to the confluent cells in comparison to that of the Au Flat and Au NPs surfaces functionalized with AUT, RGD and IKVAV.

Our results demonstrated that the cells on the Au-RGDC surfaces had a high surface coverage, induced a cell fate towards neurons that had yet to establish a mature neural network and no astrocytes were observed as illustrated in Figure 6.35. The Au Flat-IKVAVC(19) surfaces presented a cell population of only astrocytes and high surface coverage and no neurons. The cells demonstrated a spread morphology on both surfaces and some clustering cell processes were also observed. Thus, indicating, that the Au-RGDC surfaces induce neurons and the Au-IKVAVC surfaces a population of astrocytes, which further supports the results acquired from the studies of the functionalized Au Flat and Au NPs surfaces.

We then quantified the % area coverage of neurons and astrocytes on these gold surfaces of Au-RGDC and Au-IKVAVC(19) to determine the influence of surface chemistry on the differentiation of NPSCs into a specific cell fate as shown in Figure 6.36. The Au-RGDC surfaces influenced NPSCs to differentiate into neurons with a % area coverage of 11.23% ± 1.54, which is a lower % area coverage than that of the Au Flat-RGD surfaces, 16.16% ± 1.58, but higher than that of the demonstrated on the Au Flat-AUT, Au NPs-AUT, and Au NPs-RGD respectively, 10.34% ± 1.93, 9.81% ± 3.02, and 7.79% ± 1.65 area coverage. We observed no astrocyte cell fate on the Au-RGDC surfaces, whilst the Au-IKVAVC(19) surfaces induced the NPSCs to differentiate only into astrocytes with a % area coverage of 31.55% ± 1.02, which is a higher % area coverage in comparison to that of the Au Flat-IKVAV and the Au NPs-IKVAV surfaces, 14.17% ± 1.29 and 9.26% ± 1.22, respectively. The PLO.Laminin surface induced a higher % area coverage for a neuron and astrocytes cell fate, 22.10% ± 2.07 and 97.06% ± 1.30, respectively was observed for the differentiated cell fates of neurons and astrocytes as illustrated in Figure 6.31.

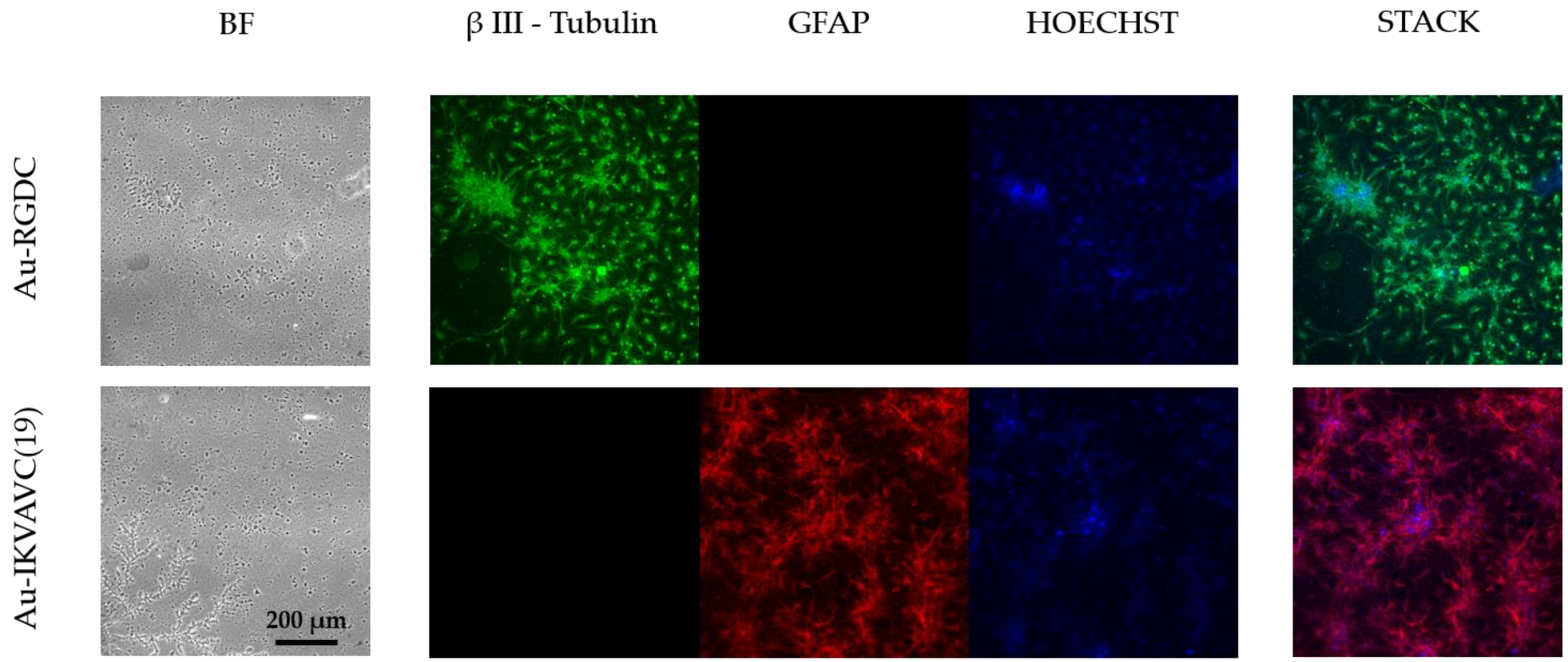


Figure 6.35 Fluorescent microscopy images of differentiated E18 NPSCs on Au Peptides surfaces functionalized with RGDC and IKVAV(19). The green, red and blue represent respectively βIII-Tubulin in neurons, GFAP in astrocytes, and nuclei. All the cells were cultured on the surfaces at a density of 3 x 10^5 cell/mm^2 in serum-free media for 14 days *in vitro*.

Moreover, the PLO.Laminin surface in comparison to that of the functionalized Au Peptides surface illustrated a mature neural networks and induced the NPSCs to differentiate into a mixed population of neurons and astrocytes with a significant difference of (*) $p < 0.05$ and (**) $p < 0.01$.

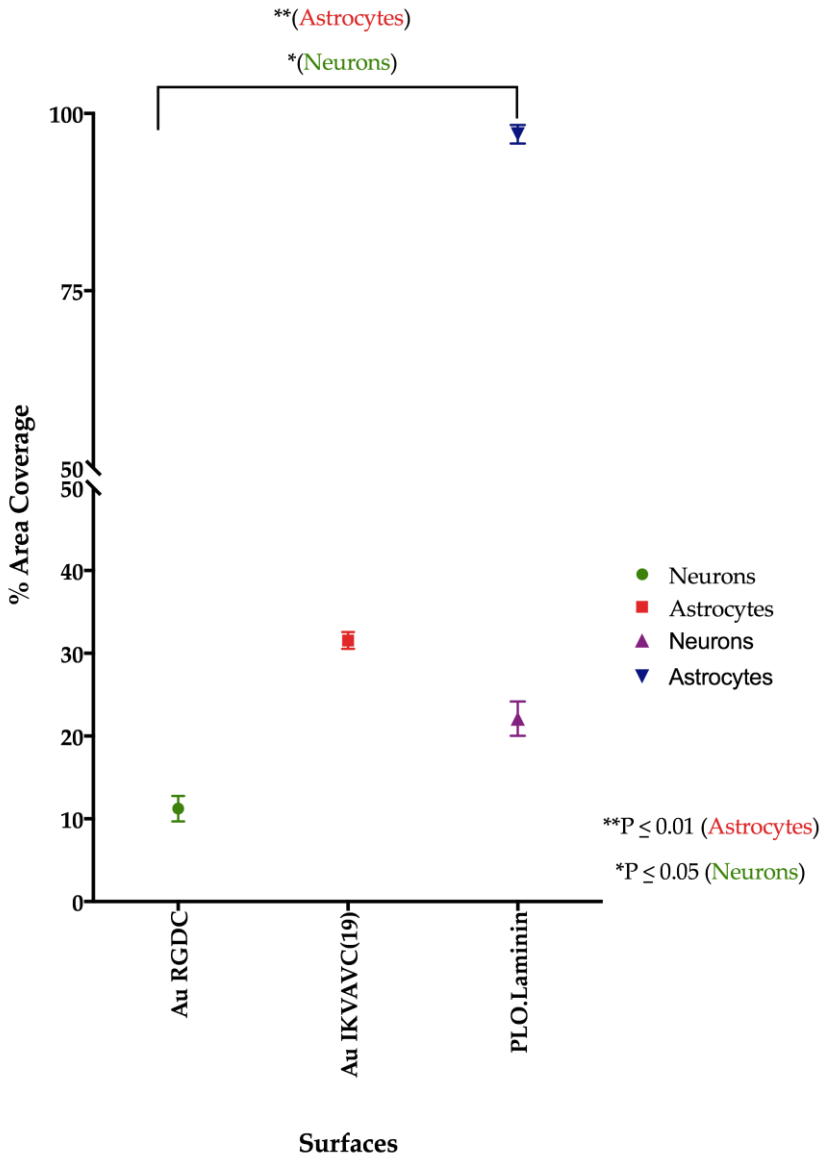


Figure 6.36 Quantification of E18 NPSCs differentiation into neurons (βIII-Tubulin positive) and astrocytes (GFAP positive) as relative area coverage by each cell type on Au Peptides surfaces functionalized with RGDC, IKVAVC(19) and the control surface of PLO.Laminin. Error bars represent mean ± SD for n = 3 and a significant difference of (**) $p < 0.01$ is observed for population of astrocytes on the IKVAVC(19) functionalized surface and a significant difference of (*) $p < 0.05$ is observed for population of neurons on the RGDC functionalized surface. All the cells were cultured on the surfaces at a density of 3 x 10^5 cell/mm^2 in serum-free media for 14 days *in vitro.*

6.4.3.2 CELL ADHESION AND PROLIFERATION ON FUNCTIONALIZED AuNPs AND SiO_2@AuNPs SURFACES

We assessed the cell adhesion and proliferation of the NPSCs on the suspended 3D surfaces, AuNPs and SiO_2@AuNPs as illustrated in Schematic 6.1(D), by phase contrast imaging and evaluated the neurospheres at 2DIV, 7DIV and 14DIV. The AuNPs scatter light very well and we observed them as black particles under the microscope, whilst the SiO_2@AuNPs did not display this property due to its silica core. The neurosphere size was quantified at the different culture time by randomly capturing bright field images (i.e. 5-10 images) at each of the predetermined time points of 2DIV, 7DIV and 14DIV.

6.4.3.2.1 FUNCTIONALIZED AuNPs

The NPSCs clustered in the media and we observed a round cell morphology and a very low number of cells had adhered on the surfaces of AuNPs-Control and AuNPs-IKVAVC(19) at 2DIV. The AuNPs-RGDC demonstrated to interact with the cell and we observed that the cell-surface interaction was as favorable as the cell-cell interaction in the media, Figure 6.37. At 7DIV and 14DIV we observed that the neurospheres size and shape varied due to cell aggregation facilitated by cell adhesion and proliferation. We quantified the neurospheres size at 7DIV and 14DIV by measuring the diameter of the aggregate, Figure 6.39. The AuNPs-IKVAVC(19) and AuNPs-RGDC demonstrated neurospheres similar in size, 17.18 μm ± 1.50 and 16.12 μm ± 9.16, respectively at 7DIV. A significant increase, (**) $p < 0.01$, in neurospheres size was observed at 14DIV for all of the AuNPs surfaces. Moreover, AuNPs-IKVAVC(19) showed a larger diameter of 49.26 μm ± 11.49 in comparison to those of AuNPs-RGDC and AuNPs-Control respectively, 35.37 μm ± 1.39 and 24.75 μm ± 5.53, at 7DIV. Furthermore, we observed a significant difference in the neurospheres morphology with the AuNPs-RGDC demonstrating a circular morphology, whereas the AuNPs-IKVAVC(19) and AuNPs-Control facilitated oval shaped neurospheres. We also observed more AuNPs-RGDC neurospheres than AuNPs-IKVAVC(19) and AuNPs-Control, as all the AuNPs surfaces have been seeded with the same cell density of NPSCs this suggests that a better cell survival and proliferation is observed on the AuNPs-RGDC surfaces.

This is significant as it demonstrates that the NPSCs are responding more favorable towards the nanoparticles conjugated with RGDC peptide cue than the IKVAVC(19) peptide cue, which is a similar cell response that the NPSCs had towards that of the flat surfaces with RGD versus IKVAV, see Chapter 4, Chapter 5 and the 2D surfaces in this Chapter 6.

6.4.3.2.2 FUNCTIONALIZED SiO_2@AuNPs

The SiO_2@AuNPs surfaces demonstrated a similar cell response to that of the AuNPs surfaces at 2DIV, indicated the cell-cell interaction in the media were preferred, Figure 6.38. At 7DIV the SiO_2@AuNPs surfaces showed more neurospheres in comparison to those of the AuNPs surfaces, suggesting that the SiO_2@AuNPs surfaces proved to have stronger cell-surface interactions. Figure 6.39 shows SiO_2@AuNPs-RGDC and SiO_2@AuNPs-IKVAVC(19) neurospheres were of a similar size, 19.07 μm ± 0.95 and 18.03 μm ± 3.50, respectively at 7DIV. A significant increase in neurospheres size was observed for all the SiO_2@AuNPs surfaces, (*) $p < 0.05$, from 7DIV to 14DIV. The SiO_2@AuNPs-RGDC neurospheres were considerably larger in diameter of 46.15 μm ± 13.75 in comparison to those of SiO_2@AuNPs-IKVAVC(19) and SiO_2@AuNPs-Control respectively, 27.81 μm ± 3.24 and 26.63 μm ± 1.98, at 14DIV. Furthermore, the cell morphology of the SiO_2@AuNPs-RGDC neurospheres were circular in shape and an oval shape was observed for the AuNPs-IKVAVC(19) and AuNPs-Control neurospheres. Thus, suggesting that the functionalization with the RGDC peptide induces circular neurospheres and the IKVAVC(19) peptide facilitates neurospheres to take an oval shaped morphology. This can be observed in the phase contrast images at 7DIV on the peptide conjugated AuNPs in Figure 6.38 and at 14DIV on the peptide conjugated SiO_2@AuNPs in Figure 6.39, which could be related to the peptide cue of IKVAVC(19) that has a 19 amino acid sequence chain versus that of the RGDC that is 4 amino acids long.

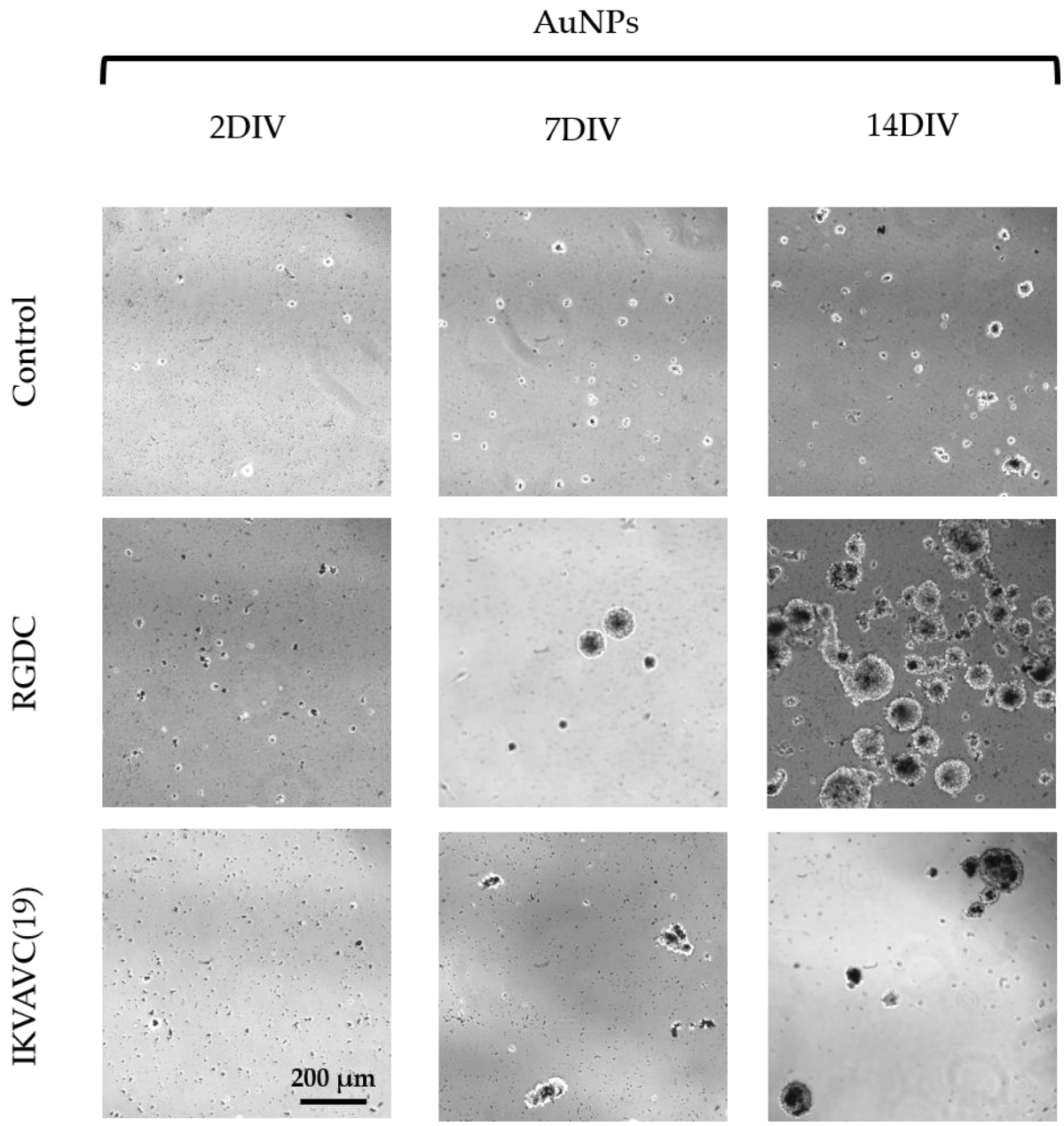


Figure 6.37 Phase contrast images of E18 NPSCs aggregates forming neurospheres with bare AuNPs, AuNPs-RGDC and AuNPs-IKVAVC(19), n = 3. All cells were cultured suspended in the serum-free media with the nanoparticles at a density of 1.5 x 10^5 cell/mm^2 for 14 days *in vitro*.

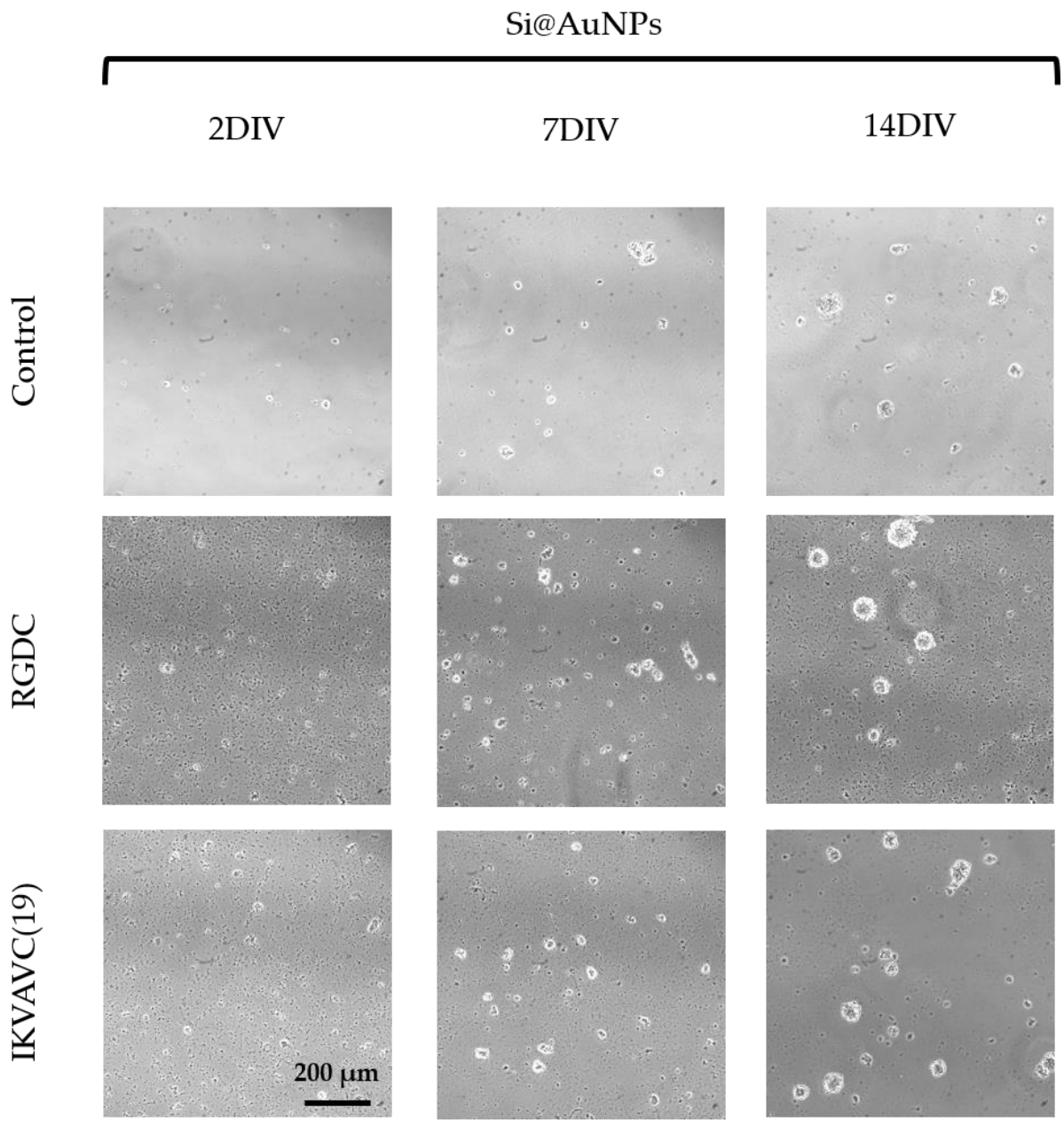


Figure 6.38 Phase contrast images of E18 NPSCs aggregates forming neurospheres with bare SiO_2@AuNPs, SiO_2@AuNPs-RGDC and SiO_2@AuNPs-IKVAVC(19), n = 3. All cells were cultured suspended in the serum-free media with the nanoparticles at a density of 1.5 x 10^5 cell/mm^2 for 14 days *in vitro*.

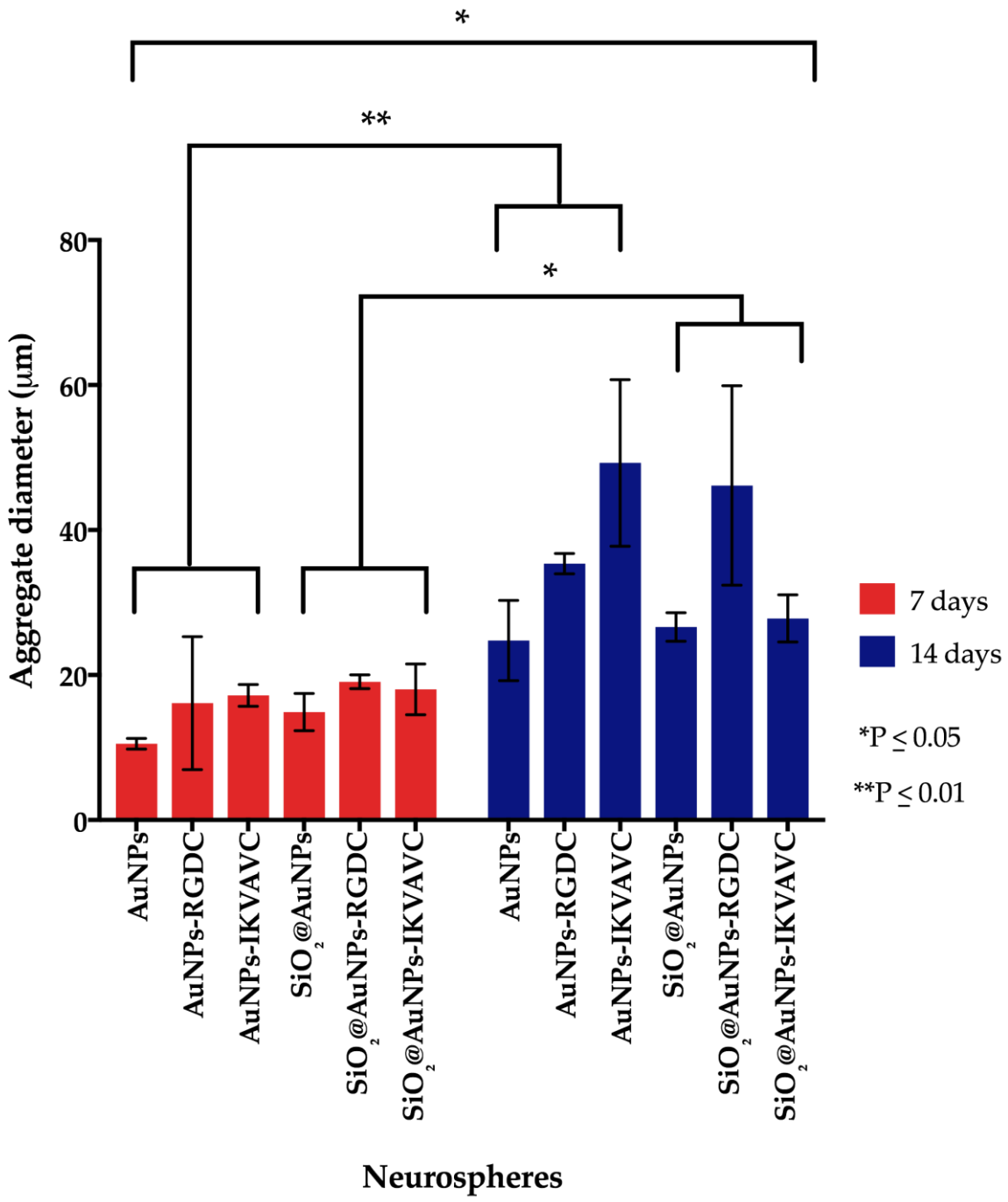


Figure 6.39 Quantification of the neurospheres diameter due to aggregated e18 NPSCs on functionalized AuNPs and SiO_2@AuNPs surfaces and the bare AuNPs and SiO_2@AuNPs surfaces as the comparison control surfaces. Error bars represent mean ± SD for n = 3 and a significant difference of (**) $p < 0.01$ is observed on the neurospheres diameter on the AuNPs bare, RGDC, and IKVAVC(19) functionalized surfaces between 7DIV and 14DIV. Whilst a significant difference of (*) $p < 0.05$ is observed on the SiO_2@AuNPs bare, RGDC, and IKVAVC(19) functionalized surfaces; as well as across the two functionalized surfaces between 7DIV and 14DIV. All the cells were cultured suspended in the serum-free media with the nanoparticles at a density of 1.5×10^5 cell/mm^2 for 14 days *in vitro*.

6.4.3.2.3 PEPTIDES AS A SOLUBLE FACTOR

Additionally, we also considered the effect of peptides in solution versus peptides immobilized on 2D and 3D surfaces, thus, we present here a soluble factor control parameter to determine the effect it would have on the biological response of NPSCs. We cultured dissociated NPSCs, 1.5 x 10^5 cells/mm^2, in 1 mL serum-free media with 20 μL of synthesized RGD and IKVAVC(19) to study their suitability for cell adhesion, proliferation and differentiation as shown in Appendix 1 and Appendix 2. For the control we used the serum-free media and observed the cell culture over 30DIV.

We observed very low cell survival and proliferation in the Control (i.e. no peptides, just cell media), whilst cells cultured in media containing RGD and IKVAVC(19) soluble factors demonstrated a few neurospheres of a smaller diameter in comparison of those on the 3D surfaces of AuNPs and SiO_2@AuNPs illustrated in Figure 6.37 and Figure 6.38. Moreover, very low cell adhesion was observed on the well plates and by 30DIV no cells remained adhered as illustrated in Figure 6.40. This indicates that peptides in solution are unable to sustain the capacity of NPSCs adhesion and proliferation.

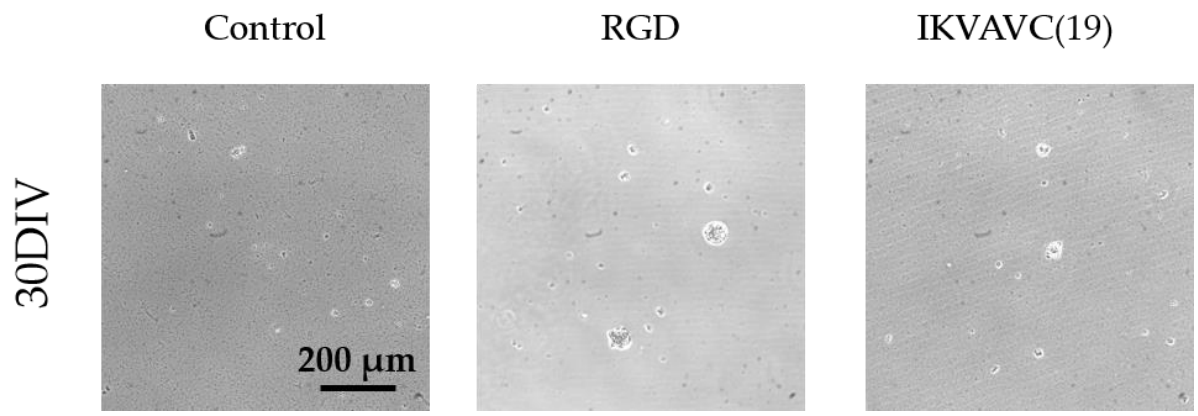


Figure 6.40 Phase contrast images of E18 NPSCs aggregates forming neurospheres in serum-free media with (i) no peptides, (ii) RGD, and (iii) IKVAVC(19) at 30 days of *in vitro*, n = 3.

We then fixed the cells at 30DIV to assess the influence the soluble RGD and IKVAVC(19) had on the cell fate of the NPSCs into neurons and astrocytes.

Figure 6.41 illustrates that the RGD peptides influenced the NPSCs to express only βIII-Tubulin protein, whereas the control and IKVAVC(19) expressed predominately for GFAP with some indication that they induce some expression of βIII-Tubulin protein. Consequently, indicating that the soluble factors of the chosen peptides, RGD and IKVAVC(19), were unable to maintain cell survival and proliferation, and remained relatively unchanged in the observed number of cells from 14DIV to 30DIV.

In comparison the Au Peptides surfaces influenced the NPSCs to adhere to the surface, cell survival, proliferation and differentiation as illustrated in Figure 6.33 and Figure 6.35.

These results suggest that the presence of the same peptides in the media as a soluble factor is not sufficient to enable the NPSCs to proliferate. Thus, indicating that the interaction of the cell to the surface chemistry along with the contact with surface topography in the nm range is required for the NPSCs to survive, proliferate and differentiate.

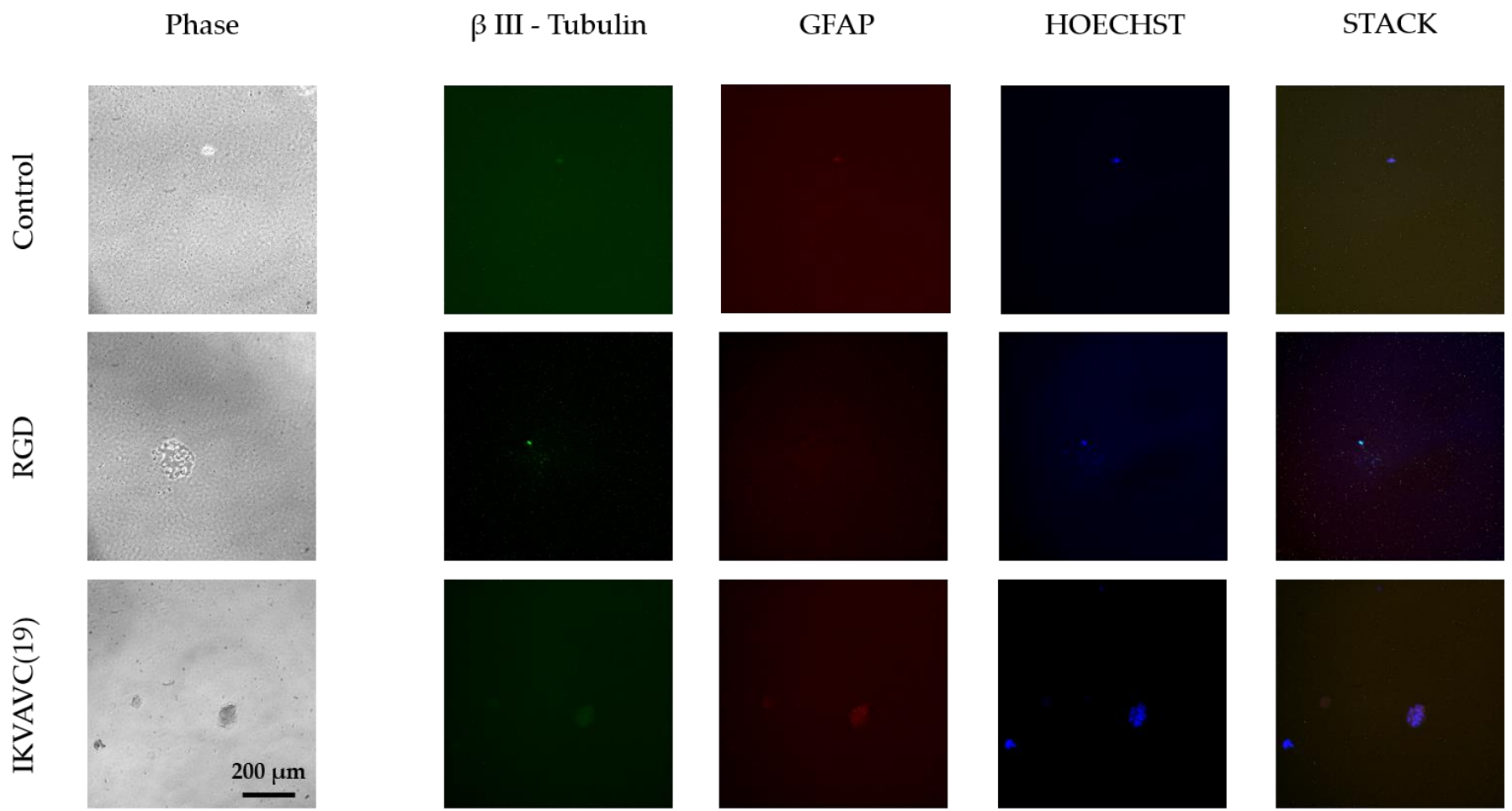


Figure 6.41 Fluorescent microscopy images of differentiated E18 NPSCs aggregates forming neurospheres in serum-free media with (i) no peptides (control), (ii) RGD, and (iii) IKVAVC(19). The green, red and blue represent respectively βIII-Tubulin in neurons, GFAP in astrocytes, and nuclei. All the cells were cultured in serum-free media at a density of 1.5 x 10^5 cell/mm^2 for 30 days *in vitro*.

6.4.4 CELL DIFFERENTIATION ON 3D SURFACES

The functionalized AuNPs and SiO_2@AuNPs surfaces demonstrated a difference in neurospheres diameter and shape. We fixed the cells at 14DIV and examined the influence of functionalized AuNPs and SiO_2@AuNPs has on the cell fate of the NPSCs into neurons and astrocytes. The cell imaging was performed on the confocal microscope and the neurospheres were stained for the neuron specific βIII-Tubulin protein, astrocytes specific class-II intermediate filament glial fibrillary acidic protein (GFAP), and DNA in the nuclei.

6.4.4.1 FUNCTIONALIZED AuNPs

The phase contract images demonstrated the functionalized AuNPs to be localized within the neurospheres indicating cellular uptake, which was further supported by the confocal laser scanning microscopy (CLSM) images of the z-stacks.

The confocal microscopy analysis showed that the AuNPs-Control neurospheres expressed βIII-Tubulin protein and GFAP. The orthogonal projection demonstrating that the cell population of astrocytes formed the core of the neurosphere, whilst the neurons formed a shell around them, Figure 6.42. However, the AuNPs-RGDC neurospheres revealed the contrary as we observed the neurons at the core and the astrocytes encircling them. The 3D reconstruction illustrated the localization of the AuNPs-RGDC was within the neurospheres, Figure 6.43. The AuNPs-IKVAVC(19) neurospheres showed the largest 3D reconstruction of 61 μm in diameter (i.e. z-stack) in comparison to that of AuNPs-RGDC and AuNPs-Control, 36 μm and 28 μm, respectively. Furthermore, the AuNPs-IKVAVC(19) neurospheres also influenced the NPSCs to differentiate to astrocytes cell fate at the core of the neurospheres and the neurons around, Figure 6.44.

The orthogonal projections of the z-stack of the AuNPs-RGDC and AuNPs-IKVAVC(19) neurospheres indicate that that the functionalized AuNPs were concentrated at the center of the neurosphere. Thus, suggesting their uptake into the cells facilitated by the surface chemistry of the AuNPs.

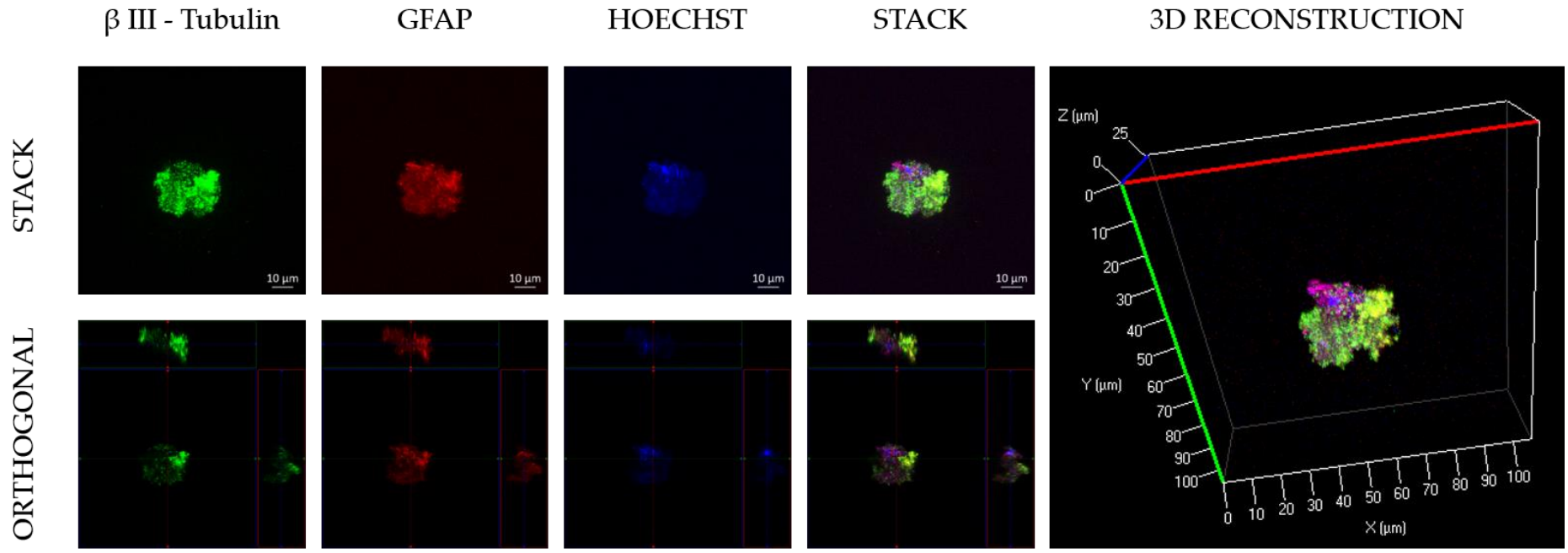


Figure 6.42 Confocal microscopy images of E18 NPSCs aggregates forming AuNPs-Control neurospheres (i) stack of the maximum intensity projection, (ii) orthogonal sectioning in xyz axis, and (iii) 3D reconstruction of the AuNPs-Control neurosphere. The green, red and blue represent respectively βIII-Tubulin in neurons, GFAP in astrocytes, and nuclei. All cells were cultured suspended in the serum-free media with the nanoparticles at a density of 1.5 x 10^5 cell/mm^2 for 14 days *in vitro*.

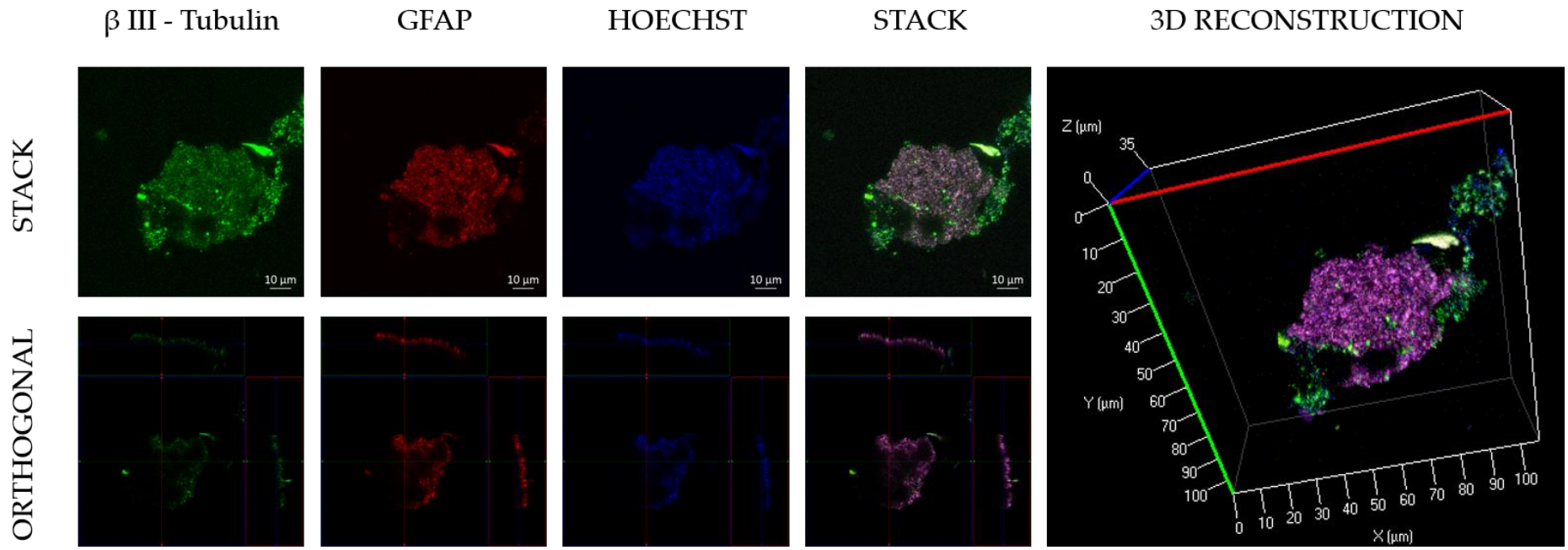


Figure 6.43 Confocal microscopy images of E18 NPSCs aggregates forming AuNPs-RGDC neurospheres (i) stack of the maximum intensity projection, (ii) orthogonal sectioning in xyz axis, and (iii) 3D reconstruction of the AuNPs-RGDC neurosphere. The green, red and blue represent respectively βIII-Tubulin in neurons, GFAP in astrocytes, and nuclei. All cells were cultured suspended in the serum-free media with the nanoparticles at a density of 1.5×10^5 cell/mm^2 for 14 days *in vitro*.

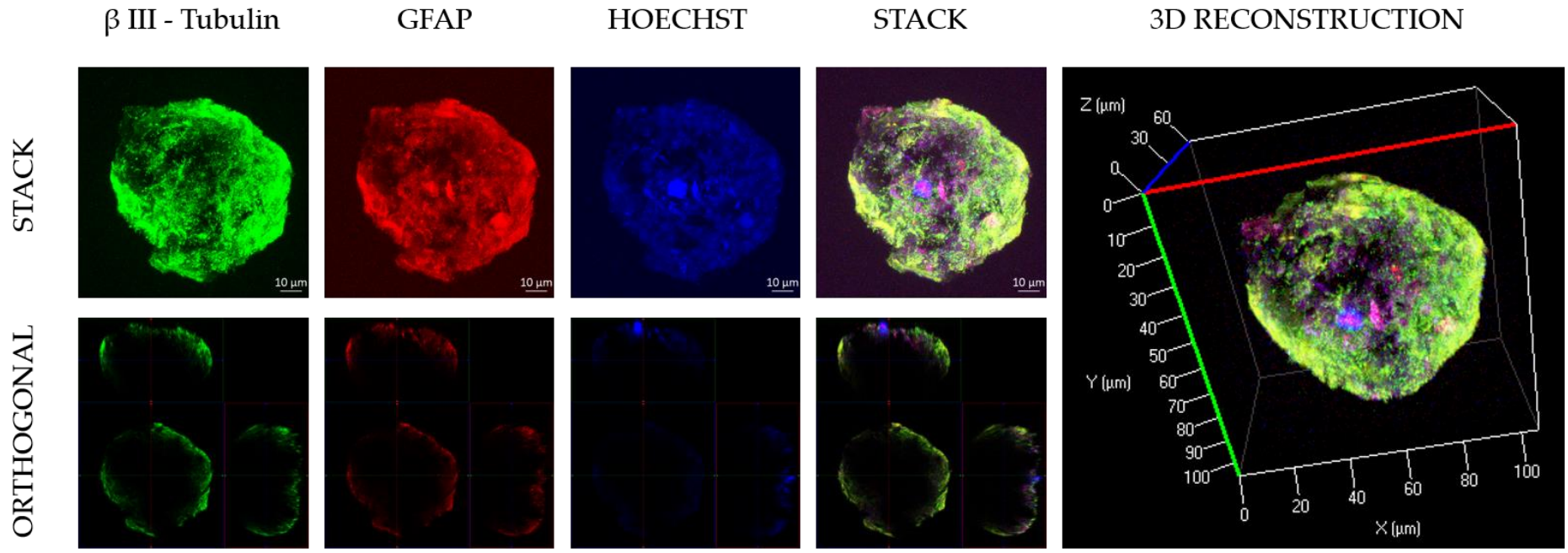


Figure 6.44 Confocal microscopy images of e18 NPSCs aggregates forming AuNPs-IKVAVC(19) neurospheres (i) stack of the maximum intensity projection, (ii) orthogonal sectioning in xyz axis, and (iii) 3D reconstruction of the AuNPs-IKVAVC(19) neurosphere. The green, red and blue represent respectively βIII-Tubulin in neurons, GFAP in astrocytes, and nuclei. All cells were cultured suspended in the serum-free media with the nanoparticles at a density of 1.5 x 10^5 cell/mm^2 for 14 days *in vitro*.

6.4.4.2 FUNCTIONALIZED SiO_2@AuNPs

We were unable to clearly identify whether the functionalized SiO_2@AuNPs had been localized within the neurospheres to form cell-surface interaction or taken-up into the cell. The CLSM images of the SiO_2@AuNPs-Control neurosphere illustrate a homogenous and a sphere morphology stain coverage of the nanoparticle, thus, making it more difficult to observe the NPSCs biological response (i.e. cellular uptake or did the cells grow around the nanoparticles). Moreover, the orthogonal projection showed an even expression for βIII-Tubulin protein, GFAP and nuclei in the SiO_2@AuNPs-Control neurosphere, Figure 6.45.

The CLSM images of the z-stack of the functionalized SiO_2@AuNPs indicated localization within the neurosphere for SiO_2@AuNPs-RGDC, whereas SiO_2@AuNPs-IKVAVC(19) suggested that the NPSCs aggregated around the nanoparticles. The SiO_2@AuNPs-RGDC had a large diameter size of 60 μm in comparison to that of SiO_2@AuNPs-IKVAVC(19) and SiO_2@AuNPs-Control, of 25 μm and of 27 μm, respectively. Thus, indicating that with more days *in vitro* the SiO_2@AuNPs-IKVAVC(19) may have maintained the proliferation and formed all the way around the nanoparticles similar to that of SiO_2@AuNPs-RGDC. The confocal microscopy analysis showed that the SiO_2@AuNPs-RGDC and SiO_2@AuNPs-IKVAVC(19) neurospheres expressed βIII-Tubulin protein and GFAP, Figure 6.46 and Figure 6.47. The orthogonal projection demonstrating that the NPSCs differentiation into a mixed population of neurons and astrocytes, similar to that observed on 2D surfaces. We further observed that SiO_2@AuNPs-RGDC neurospheres expressed higher βIII-Tubulin protein in comparison to that of the SiO_2@AuNPs-IKVAVC(19) and SiO_2@AuNPs-Control, which demonstrated higher expression of GFAP.

Consequently, the CLSM images indicate NPSCs differentiation into a mixed population of neurons and astrocytes, whilst favoring one cell fate more than the other.

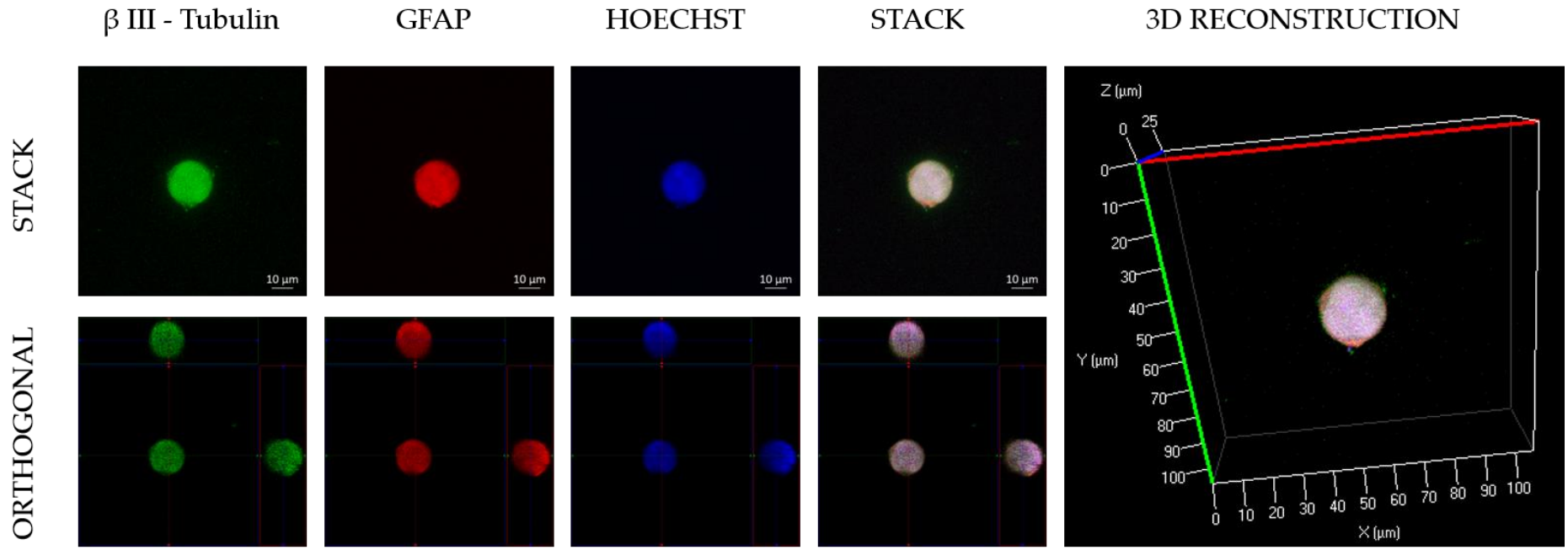


Figure 6.45 Confocal microscopy images of E18 NPSCs aggregates forming SiO_2@AuNPs-Control neurospheres (i) stack of the maximum intensity projection, (ii) orthogonal sectioning in xyz axis, and (iii) 3D reconstruction of the SiO_2@AuNPs-Control neurosphere. The green, red and blue represent respectively βIII-Tubulin in neurons, GFAP in astrocytes, and nuclei. All cells were cultured suspended in the serum-free media with the nanoparticles at a density of 1.5 x 10^5 cell/mm^2 for 14 days *in vitro*.

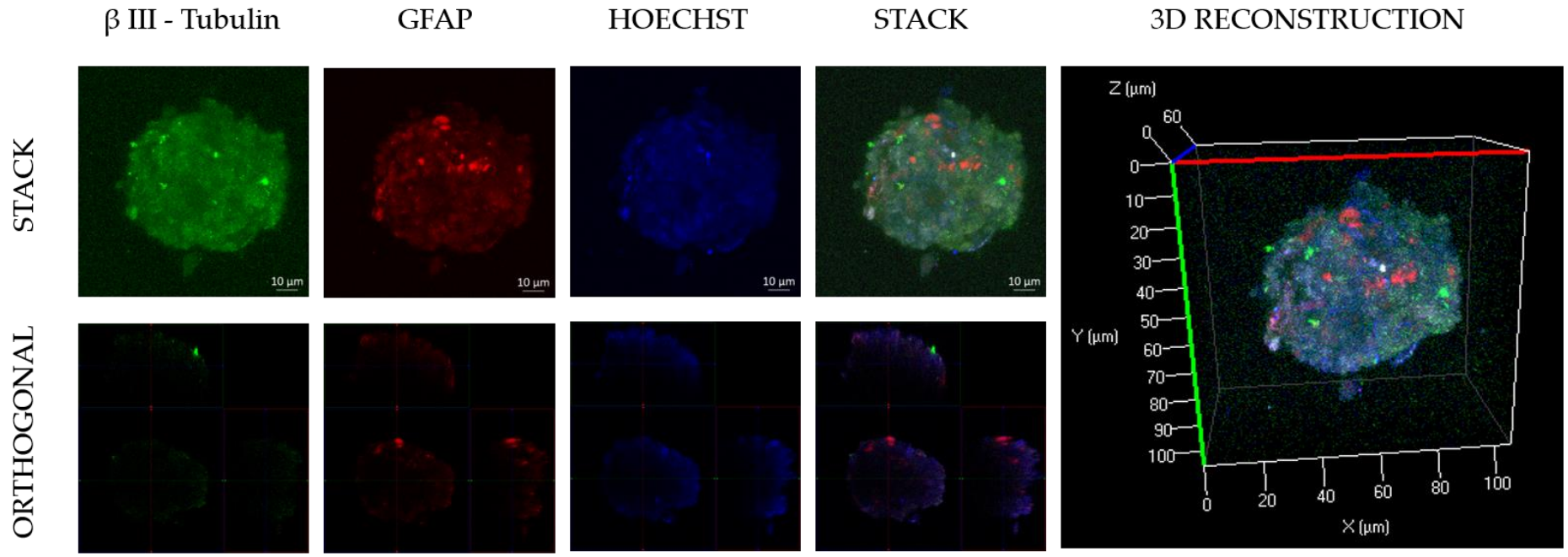


Figure 6.46 Confocal microscopy images of E18 NPSCs aggregates forming SiO_2@AuNPs-RGDC neurospheres (i) stack of the maximum intensity projection, (ii) orthogonal sectioning in xyz axis, and (iii) 3D reconstruction of the SiO_2@AuNPs-RGDC neurosphere. The green, red and blue represent respectively βIII-Tubulin in neurons, GFAP in astrocytes, and nuclei. All cells were cultured suspended in the serum-free media with the nanoparticles at a density of 1.5 x 10^5 cell/mm^2 for 14 days *in vitro*.

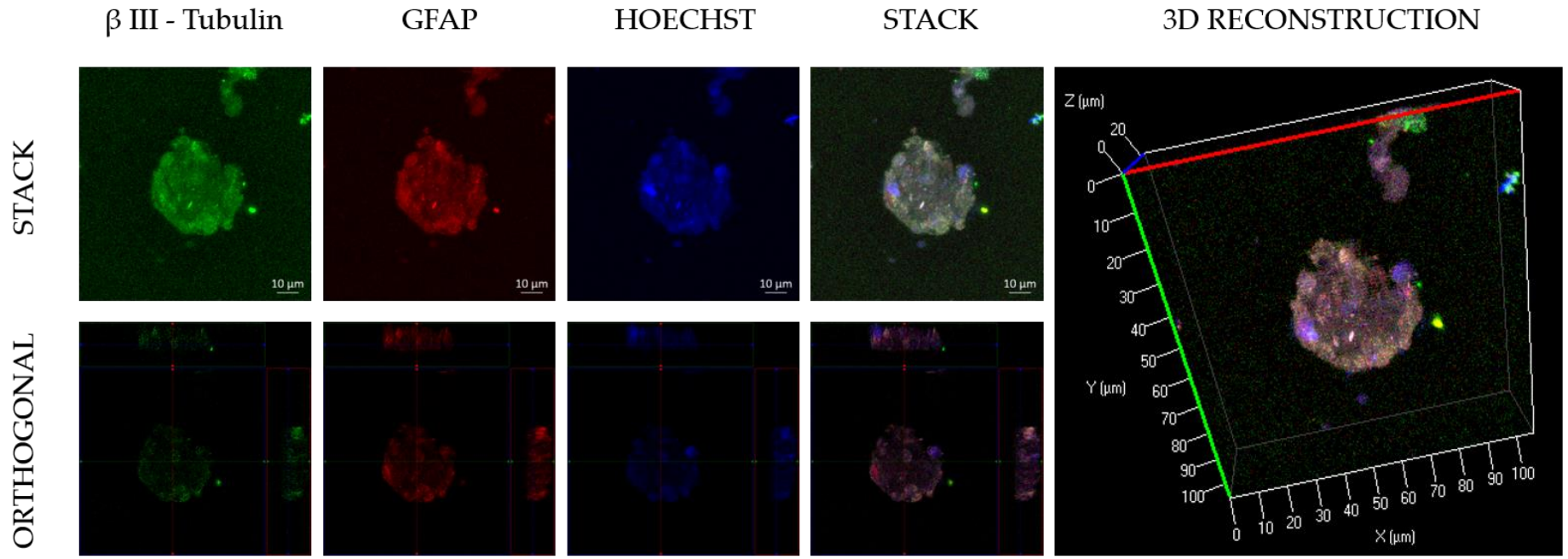


Figure 6.47 Confocal microscopy images of E18 NPSCs aggregates forming SiO_2@AuNPs-IKVAVC(19) neurospheres (i) stack of the maximum intensity projection, (ii) orthogonal sectioning in xyz axis, and (iii) 3D reconstruction of the SiO_2@AuNPs-IKVAVC(19) neurosphere. The green, red and blue represent respectively βIII-Tubulin in neurons, GFAP in astrocytes, and nuclei. All cells were cultured suspended in the serum-free media with the nanoparticles at a density of 1.5 x 10^5 cell/mm^2 for 14 days *in vitro*.

6.4.5 CELLULAR UPTAKE OF 3D SURFACES

Transmission electron microscopy (TEM) analysis was performed to evaluate the uptake (i.e. endocytosis) of the functionalized AuNPs and SiO_2@AuNPs of neurospheres [393]. The process of cellular uptake is performed by endocytosis, which can be categorized as (i) clathrin-mediated endocytosis (i.e. absorb and digest molecules that are ≈ 100 nm in diameter), (ii) caveolae (i.e. absorb and digest molecules that are < 50 nm in diameter), micropinocytosis (i.e. absorb and digest particles that are 0.5-5 nm in diameter), and phagocytosis (i.e. absorb and digest particles that are 0.75 nm in diameter) [394]. The clathrin- and caveole-mediated endocytosis pathways are the important pathways for the internalization of the AuNPs and SiO_2@AuNPs. The TEM micrographs provided an advantageous resolution limit over the CLSM images, thus, we were able to decipher the cell architecture in relation to the detection and localization of the nanoparticles due to the high atomic number of the AuNPs and SiO_2@AuNPs illustrated in Figure 6.48.

The TEM micrographs of the bare and functionalized AuNPs demonstrated their uptake by the NPSCs under expansion conditions, which was observed as dark spots of densely packed agglomerates. The high magnification images illustrated that the AuNPs were localized inside membrane-enclosed structures. Hence, indicating the likely uptake of AuNPs-Control, AuNPs-RGDC and AuNPs-IKVAVC(19) into the cells was via endocytosis, and localizing the AuNPs positioninside the cytoplasmic body of endosome. The AuNPs-Control and AuNPs-RGDC micrographs only demonstrated cellular uptake, whereas on the AuNPs-IKVAVC(19) micrographs also illustrated these nanoparticles interacting with the cell membrane of the neurospheres. Moreover, the AuNPs-IKVAVC(19) micrographs demonstrate what seems to be the initial formation of pseudopod-like projections to interact with the nanoparticles and enclose them inside the endosome. Furthermore, the high resolution micrographs showed different sizes of agglomerates through various cellular regions except for the nucleus, this is supported in literature amongst them is the work published by Söderstjerna et al. 2012 demonstrating that nanoparticles are taken-up and localized into the cytoplasm as compact aggregates [393]. The TEM micrographs of the bare and functionalized SiO_2@AuNPs illustrate the NPSCs adhering and proliferating around the

agglomerates of the nanoparticles. Furthermore, the observed cellular structures in the AuNPs micrographs were difficult to distinguish and appeared to be absent, which suggest that the SiO_2@AuNPs were not taken-up into the cells.

Consequently, this indicates that the difference in the cellular uptake mechanism for the functionalized AuNPs and SiO_2@AuNPs depended majorly on the agglomerates of nanoparticles than the size of the nanoparticles individually.

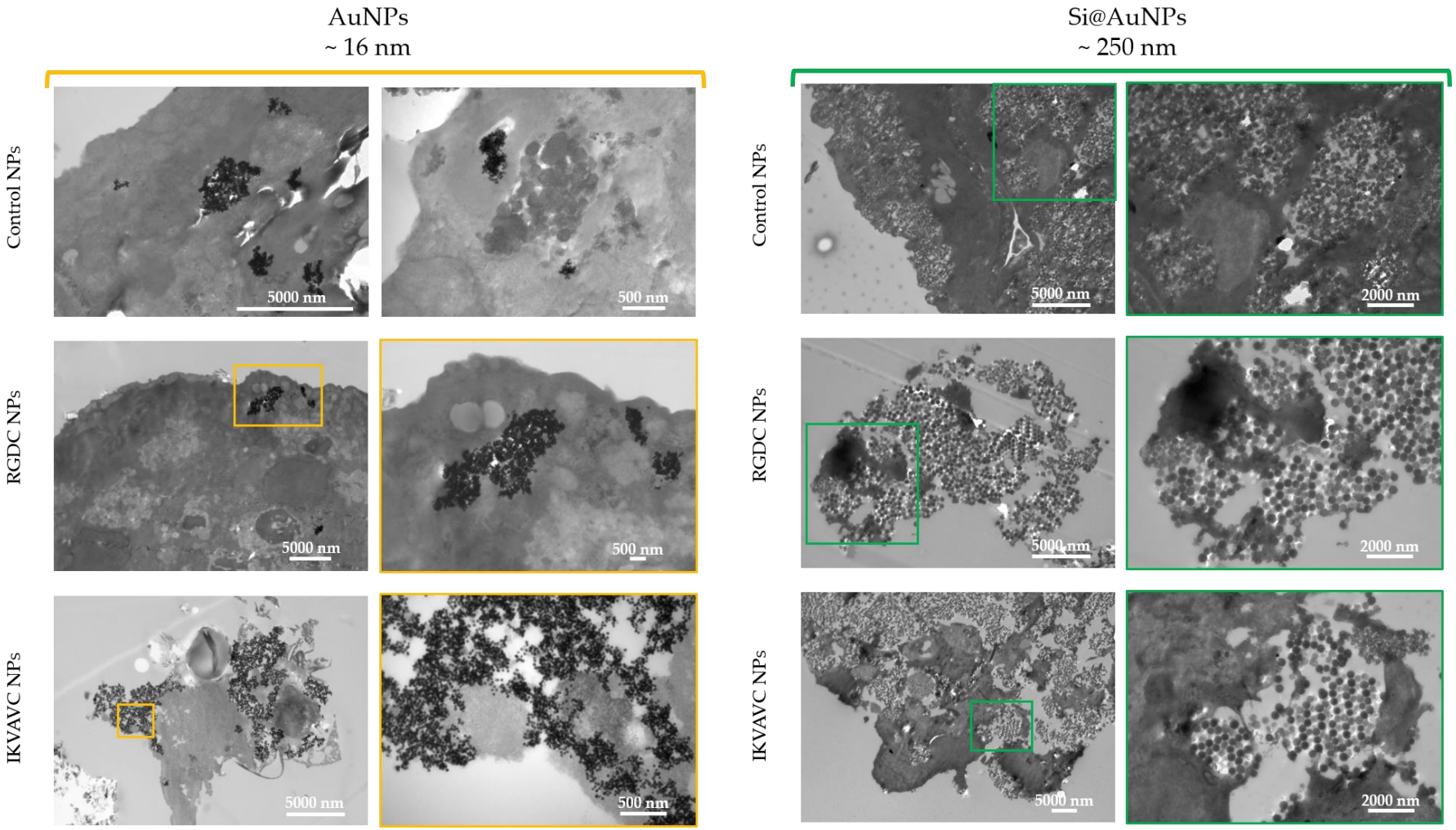


Figure 6.48 Representative TEM micrographs of ultrathin sections of the functionalized AuNPs and SiO_2@AuNPs neurospheres. High magnification images are illustrated in the yellow and green boxed areas. All cells were cultured suspended in the serum-free media with the nanoparticles at a density of 1.5 x 10^5 cell/mm^2 for 14 days *in vitro*.

6.4.6 COMPARING 2D VS 3D SURFACES

The NPSCs demonstrated to adhere, proliferate and differentiate on all of the functionalized Au Flat surfaces, Au NPs surfaces, Au Peptides surfaces, AuNPs surfaces, and SiO_2@AuNPs surfaces. The 2D surfaces enabled us to quantify the cell number and % area coverage for proliferation and differentiation, whilst the 3D surfaces formed aggregates of neurosheres and we were unable to quantify this. However, the functionalized 3D surfaces enabled us to investigate the cellular uptake of different sizes of nanoparticles into the cells. Furthermore, we observed that the RGDC functionalized AuNPs and SiO_2@AuNPs surfaces induced a preferential differentiation towards a neurons cell fate and the IKVAVC(19) functionalized surfaces of AuNPs and SiO_2@AuNPs favored an astrocytes cell. The CLSM images indicate that the astrocytes population were predominately in the core or quiescent zone and the neurons observed in the proliferation zone of the neurosphere.

Consequently, our results further support the literature in stating that depending on the research question the 2D model microenvironment facilitates feasibility and the results can be meaningful; whilst a 3D model microenvironment could yield more accurate results if successful and done in combination with 2D studies [246, 247].

Furthermore, we observed that the 2D gold coated glass surfaces functionalized with RGD or RGDC influenced the NPSCs to differentiate towards a neuron cell fate, whilst the glass surface (i.e. without gold coating) functionalized with RGD induced a mixed population of neurons and astrocytes cell fate in the NPSCs. Whereas on the glass surfaces functionalized with IKVAV and IKVAVC(19) with and without gold coating influenced the NPSCs to preferentially differentiate into astrocytes. Consequently, this suggests that the gold coated surfaces functionalized with RGD and RGDC would be the best surface to investigate for electrophysiology experiments to validate that the synapses in established neural networks are performing action potential (i.e. functioning neurons).

6.5 SUMMARY

The ECM is a dynamic and complex 3D structure that consists of many proteins that regulate cell adhesion, proliferation, migration, differentiation, provide tensile strength, supply oxygen and nutrients, and remove waste products. Recent technological developments demonstrate a shift from 2D model microenvironments to creating highly tunable and functional 3D model microenvironments. Thus, we present here the design of immobilized peptides on comparable 2D and 3D surfaces to examine the biological response of NPSCs to both microenvironment and add to the understanding on how to mimic the akin characteristics of the ECM more closely. We choose a gold surface in order to make the 2D and 3D surface comparable, as it provided us the ability to explore the SPPS "grafting from" and "grafting to" approaches via the thiol-gold chemistry reaction. The 2D microenvironments were categorized as (i) Au Flat, (ii) Au NPs, and (iii) Au Peptides and allowed us to consider (i) surface chemistry and (ii) surface topography. Whilst the 3D surfaces were categorized as (i) AuNPs and (ii) SiO_2@AuNPs as we took into consideration the nanoparticles (i) size, (ii) morphology, (iii) surface charge, and (iv) surface chemistry. Moreover, the functionalized surfaces were characterized by measuring the relative amounts of peptides on a surface (i.e. ToF-SIMS on the 2D surfaces) and not the surface concentration or surface density. The peptide surfaces discussed here signify single peptide functionalization on (i) Au Flat, (ii) Au NPs, and (iii) Au Peptides with peptides such as RGD (i.e. relative amount of 100% RGD), RGDC (i.e. relative amount of 100% RGDC), IKVAV (i.e. relative amount of 100% IKVAV), and IKVAVC(19) (i.e. relative amount of 100% IKVAV(19)).

Surface characterization was performed by surface sensitive physicochemical analysis of WCA, AFM, ToF-SIMS, DLS, ζ-potential, UV/visible spectroscopy, EDX, and TEM. The successful synthesis of AuNPs (i.e. wine colored colloid) and SiO_2@AuNPs (i.e. lilac/ purple colored colloid) led to the formation of approximately 16 nm and 250 nm in diameter, respectively established by the TEM and DLS. We further demonstrated through the ζ-potential results that both nanoparticles were stable in solution and confirmed the successful synthesis of the gold shell coating around the silica core to SiO_2@AuNPs. The SPPS "grafting to" approach of RGDC and IKVAVC(19) peptides was validated by UV/vis spectroscopy as

we observed a red-shift in the spectra after peptide conjugation on the gold surfaces of the nanoparticles in relation to the non-conjugated gold surfaces of AuNPs and SiO_2@AuNPs. The ζ-potential of the SiO_2@AuNPs functionalized surfaces were more stable as a colloid system in comparison to that of the AuNPs functionalized surfaces. Next we considered the "grafting to" approach of the RGDC and IKVAVC(19) peptides on the 2D gold surfaces, Au Peptides surfaces, in comparison to 3D surfaces and 2D gold surfaces of Au Flat and Au NPs surfaces that were peptide immobilized via the SPPS "grafting from" approach. An overall increase of surface wettability was observed respectively on the Au Peptides, Au NPs, and Au Flat immobilized peptide surfaces. The AFM measures of z-range and RMS values demonstrated an increase in topography on the surfaces respectively, Au Flat, Au NPs and Au Peptides. This confirmed that the method of functionalization can introduce a topographical effect on the surface. The ToF-SIMS raster images illustrated homogenous Au Peptides and Au Flat functionalized surfaces. However, the Au NPs functionalized surfaces indicated defects on the sample surface that could possibly be due to the flood gun effect of the ToF-SIMS on the conjugated nanoparticles on the surface. The distinguishable marker ion fragments validated the successful immobilization of the RGD, RGDC, IKVAV, and IKVAVC(19) peptides on their chosen surfaces (i.e. Au Flat, Au NPs, and Au Peptide surfaces).

Optical phase contrast images of the NPSCs showed the cell response to the RGD and IKVAV peptide sequences on the Au Flat and Au NPs surfaces, and RGDC and IKVAVC(19) peptide sequences on the Au Peptides (i.e. 2D), AuNPs and SiO_2@AuNPs (i.e. 3D) surfaces. The 2D surfaces showed an increase in % area coverage at 7DIV on the functionalized surface respectively, Au NPs surface, Au Flat surface, and Au Peptides surfaces; whilst at 14DIV the Au Flat surfaces demonstrated a higher % area coverage of cells in comparison to that of the Au NPs surfaces; whilst the Au Peptides surfaces demonstrated the lowest % area coverage. These results suggest that the nanoparticle features (AuNPs) on the Au NPs surfaces have an influence on the cells % area coverage at 7DIV. The PLO.Laminin surfaces indicated a significant difference, (**) $p < 0.01$, to the functionalized Au Peptides surface and a significant difference, (*) $p < 0.05$, to the functionalized Au Flat and Au NPs surfaces.

Next we postulated that the surface chemistry would have a stronger influence on the preferential differentiation of the NPSCs towards the specific cell fate of neurons than surface topography. Firstly, we established that in the absence of the RGD or RGDC peptides the surfaces induced the NPSCs to differentiate towards the astrocyte cell fate and no neurons; whilst the RGD or RGDC functionalized surfaces induced only a neuron cell fate. Secondly, an increase in % area coverage of neurons and astrocytes was observed on the functionalized surfaces, Au NPs surfaces, Au Peptides surfaces, and Au Flat surfaces, respectively. Thus, validating our hypothesis that surface chemistry would precede over surface topography as illustrated by the nanoparticles (i.e. AuNPs) functionalized on the Au NPs surfaces. Finally, we observed that the PLO.Laminin surface illustrated a mature neural networks in comparison to that of the functionalized Au Flat and Au NPs surfaces and induced the NPSCs to differentiate into a mixed population of neurons and astrocytes respectively, with a significant difference of (**) $p < 0.01$ and (*) $p < 0.05$. On the other hand, the Au Peptides surfaces we observed a significant difference of (*) $p < 0.05$ and (**) $p < 0.01$, respectively for neurons and astrocytes.

For the 3D functionalized surfaces, we observed that at 7DIV the SiO_2@AuNPs surfaces showed the presence of a higher number of neurospheres in comparison to those of AuNPs surfaces, suggesting that the SiO_2@AuNPs surfaces had stronger cell-surface interactions. A significant difference, (*) $p < 0.05$, in neurospheres formation is shown on the SiO_2@AuNPs functionalized surfaces from 7DIV to 14DIV. In comparison the AuNPs functionalized surfaces indicated a significant difference of (**) $p < 0.01$, which can be related to the smaller size of approximately 16 nm facilitating larger neurospheres aggregates to the approximately 250 nm of SiO_2@AuNPs. Next we considered the control parameter of soluble factors as direct comparison to the culture media of the functionalized AuNPs and SiO_2@AuNPs and observed that the chosen peptides, RGD and IKVAVC(19), were unable to maintain cell survival and proliferation.

The NPSCs differentiation on the functionalized 3D surfaces of AuNPs and SiO_2@AuNPs was investigated using CLSM, which indicated the cell differentiation of the NPSCs into a mixed population of neurons and astrocytes. We observed that the RGDC functionalized AuNPs and SiO_2@AuNPs surfaces induced a preferential differentiation towards a neurons cell fate and the IKVAVC(19) functionalized surfaces of AuNPs and SiO_2@AuNPs favored an

astrocytes cell. Moreover, the CLSM images showed that the astrocytes population was predominately in the core or quiescent zone and the neurons were observed in the proliferation zone of the neurospheres. The AuNPs and SiO_2@AuNPs functionalized surfaces both did not demonstrate neuron-like extensions in their neurospheres, which suggests that the neurospheres should be cultured for more than 14DIV to observe such cell morphology. Lastly, we determined whether cellular uptake of the functionalized AuNPs and SiO_2@AuNPs was occurring in the neurospheres. The TEM micrographs illustrated the localization of the functionalized AuNPs were localized inside membrane-enclosed structures, whilst the micrographs of functionalized SiO_2@AuNPs surfaces suggest that they were not taken-up into the cells. Thus, indicating that the difference in the cellular uptake mechanism for the functionalized AuNPs and SiO_2@AuNPs depends majorly on the agglomeration of the nanoparticles than on the size of the nanoparticles individually.

The work established in this chapter demonstrated that 2D and 3D surfaces could be functionalized via the same approach and the cell response towards any surface topographical and surface chemistry changes could be observed in the cell survival, proliferation and differentiation. These surfaces have been successfully validated in their ability to influence NPSCs differentiation to a mixed population of neurons and astrocytes (i.e. AuNPs, SiO2@AuNPs, PLO.Laminin) or two a specific cell fate (i.e. Au Flat, Au NPs, Au Peptides surfaces). The results suggest that the functionalized 2D and 3D surfaces are ready to be integrated into the microfluidics and MEA aspects of the SLAB system.

7 CONCLUSION & OUTLOOK

7.1 CONCLUSION

The overall aim of this thesis was to develop a suitable method to engineer versatile biointerfaces that direct stem cells to preferentially differentiate to a specific composition of neurons and glia to permit for the integration into the fully-controlled and monitored SLAB system as a feedback paradigm that emulates brain activity and interaction with an environment to gain the essential knowledge for producing 3D brain-like models.

The first hypothesis for the thesis was that we could functionalize surfaces with surface chemistry to control neural stem cell differentiation to a specific cell fate for future application in building artificial neural networks. We initially postulated by immobilized single peptides the RGD surfaces would induce an enhanced level of neurons and the IKVAV surfaces would influence the NPSCs to differentiate into astrocytes. The *in vitro* evaluation established that the PLO.Laminin control and RGD surfaces induce a mixed population of neurons and astrocytes, whilst the IKVAV induced a population of astrocytes. The results demonstrated that the RGD surfaces induced not exclusive differentiation in the NPSCs in comparison to that of the IKVAV surfaces. Consequently, this led us to rationalize that by changing the peptide composition on the surface we would be able to control the preferential differentiation of the NPSCs towards a specific cell fate.

This lead to the exploration into bifunctional surfaces, as a result, 0% RGD – 100% RGD surfaces were designed via a novel orthogonal functionalization approach. An increase in the selected RGD marker ion fragments were observed with the increase of RGD composition and a relative linear decrease of the IKVAV marker ion fragments on the same surfaces. The ToF-SIMS raster images demonstrated that the controlled composition peptides surfaces were homogenous and the ROI measurements further validated the successful orthogonal functionalization of controllable composition peptides surfaces. The *in vitro* studies on the controllable peptide composition surfaces revealed that an increase in RGD composition on the surfaces influenced the NPSCs to differentiate into neurons and astrocytes in a positive correlation to the increase in % RGD on the surfaces. Moreover, by comparing the normalized total ion fragments of RGD to the % area coverage of neurons

versus astrocytes we were able to validate our second hypothesis that the amount of RGD peptide composition present on the surface influences a biological response of the NPSCs to differentiate into neurons versus no neurons in the absence of the RGD peptides.

Successfully, we were able to design and optimize a novel approach to control the bi-functionalization (i.e. orthogonal chemistry) of molecules (i.e. peptides, proteins, DNA, nanoparticles) on surfaces to engineer versatile 2D and 3D surfaces.

Next we decided to investigate the immobilization of peptides on comparable 2D and 3D surfaces to examine the biological response of NPSCs to both microenvironment and add to understanding on how to mimic the akin characteristics of the ECM more closely. We choose a gold surface in order to make the 2D and 3D surface comparable, as well as having the ability to explore the SPPS of "grafting from" and "grafting to" approaches via the thiol-gold chemistry reaction. The 2D surfaces were characterized as Au Flat, Au Peptides, and Au NPs surfaces and the later had topographical features (i.e. nanoparticles functionalized on the surface) and the 3D surfaces were of two different sizes respectively, AuNPs (~ 16 nm) and SiO_2@AuNPs (~ 250 nm) surfaces. The surface characterization of the 2D surfaces demonstrated that surface chemistry had a greater influence than that of surface topography (i.e. Au NPs surfaces), whilst the 3D surfaces revealed that the SiO_2@AuNPs surfaces were more stable in solution than those of the AuNPs surfaces. The *in vitro* evaluation indicated that both the RGD or RGDC functionalized surfaces respectively, 2D and 3D surfaces, induced preferential differentiation into a neuron cell fate, whereas in the absence of RGD or RGDC (i.e. presence of IKVAV or IKVAVC(19) the NPSCs favored the differentiation towards the astrocyte cell fate. Moreover, a subtle difference in the biological response of the NPSCs in response to the functionalized 2D and 3D surfaces was observed. The 3D surfaces demonstrated a mixed population of neurons and astrocytes, whilst the 2D surfaces only demonstrated one stem cell fate either neurons or astrocytes. The CLSM images of the functionalized 3D surfaces demonstrated that the astrocytes population predominately were in the core or quiescent zone and the neurons were observed in the proliferation zone of the neurosphere. Additionally, the TEM micrographs suggested a difference in the cellular uptake mechanism for the functionalized SiO_2@AuNPs and AuNPs, where the later demonstrated cellular uptake and were found to be localized in cell membrane enclosed

vesicles inside the cells. The successfully validated 2D and 3D surfaces are now ready to be integrated into the SLAB system.

In conclusion, we developed a suitable method to functionalize controllable peptide compositions on 2D, which can be applied also to 3D surfaces in order to influence NPSCs to preferentially differentiate to a specific composition of neurons and glia. The peptide immobilized 2D and 3D model microenvironments influenced the NPSCs to exhibit cell adhesion and spreading, proliferation, and differentiation. We observed different cell morphologies with distinct patters, (i) separate cells (i.e. single), (ii) cells clustered together in islands, and (iii) cells aggregated into neurospheres. Thus, demonstrating that these surfaces establish anatomical heterogeneity similar to that of the cerebral cortex cellular systems [14]. As a result, this work presents the potential to add on to the state-of-the-art research in designing 3D brain-like models as it facilitates the ability to study comparable 2D and 3D model microenvironments side-by-side in a highly reproducible, consistent and stable long-term experiments that can be adopted from *in vitro* to *in vivo* conditions.

7.2 FUTURE WORK

Due to the limitation time set during the Ph.D thesis we were unable to explore further *in vitro* and *in vivo* evaluations required to complete the set of experiments to evaluate the integration of these functionalized 2D and 3D surfaces into the SLAB system. Unfortunately, some questions will remain unanswered in this Ph.D, however, a brief collection of possible future work is discussed below.

7.2.1 WORK TO BE CONTINUED

The work accomplished in this thesis allows for the 2D and 3D surfaces to be ready for the incorporation into a microfluidic and MEA aspects of the SLAB system. Whilst the novel approach of preparing controllable peptide compositions surfaces presented here opens up the possibility to be explored in other 2D and 3D surfaces (i.e. hydrogels, 3D carbon scaffolds, carbon nanotubes).

In this thesis we already established the preliminary work of having controllable peptide composition 3D surfaces, but were unable to complete the experiments and the results were not included here. The next analysis would be to complete the evaluation of the mixed SiO_2@AuNPs-RGDC with SiO_2@AuNPs-IKVAV(19), and AuNPs-RGDC with AuNPs-IKVAV(19) in the same ratios as demonstrated in Chapter 5 and seeded with NPSCs as demonstrated in Chapter 6. The results obtained so far demonstrated that the mixed composition of functionalized 3D surfaces were able to support cell survival, adhesion, and proliferation of the NPSCs. As a result the cell survival and differentiation would need to be quantified and analyzed before comparing these results to the orthogonal functionalization of the RGDC and IKVAV(19) on the same 3D surfaces of SiO_2@AuNPs and AuNPs, which then would be relatively comparable to that in Chapter 5 (i.e. 2D vs 3D). Furthermore, parameters such as (i) peptide layer thickness, (ii) peptide concentration, (iii) peptide density, and (iv) peptide leaching on the surfaces would need to be quantified (i.e. XPS, AFM, TGA, ninhydrin test) as we only measured relative amounts of peptides on a surface. For the 3D surfaced the size and functionality of these surfaces need to be considered and the influence of mixing different sized nanoparticles has on the NPSCs cell response towards, (i) cell survival and proliferation, (ii) differentiation, and (iii) cell-uptake. These measurements would provide valuable insight into the chemical adsorption of the peptides on the surfaces under different conditions and the particular cell responses we observed on these surfaces due to these parameters (i.e. thickness, concentration, density, focal adhesion, leaching).

An important parameter that requires to be assessed further is how long the surface functionalization last on the 2D and 3D surfaces, as this is crucial if the samples will be stored for long periods of time or experiments performed or analyzed at a different. The synthesized 3D surfaces are stable for over a year (i.e. at 2-8 ^{o}C conditions) due to the citrate cap that was used in the synthesis, and we used these nanoparticles in our experiment within 6 months. The surface functionalization on the 3D surfaces remains to be characterized for how long they last. Whilst for the 2D functionalized surfaces we stored them in a desiccator (i.e. under vacuum) before exposure to the cell culture. The 2D surfaces have been characterized by ToF-SIMS successfully up to 2 months, after which point we always prepared new surfaces.

Furthermore, a time series experiment must be conducted in order to evaluate the conditions and point at which the cells secrete ECM proteins in the media and a western blot with the cell culture supernatants must be made. These ECM proteins have the potential to cover and influence the effect that the functionalized peptide surfaces have on the cell behavior of the NPSCs, as well as degrade the surfaces overtime (i.e. long-period of time in media).

Additionally, a less harsher ICC fixation method needs to be established as we tried to optimize this method to the best of our capabilities, but the cell lifting of the surfaces was still observed on the 2D surfaces and pellets lost in 3D surfaces due to the extensive washing procedure. This is clearly observed in the difference of cell confluency on the 2D surfaces in the phase images of the cell survival images versus the cell differentiation images. The neurosphere require further analysis by determining cell viability by ICC with the incorporation of 5-Bromo-2-deoxyuridine (BrdU) cell proliferation assay to detect the proliferation of the NPSCs in the neurospheres, whilst the MTT assay would assess the cell metabolic activity.

The cellular uptake of the nanoparticles in the NPSCs at predetermined time points needs to be investigated after 14DIV by CLSM and TEM to observe the cellular behavior and architecture. The work accomplished here for the neurospheres is preliminary and more characterization is required in the morphology and arrangement of the neurospheres (i.e. due to the nanoparticles or centrifugation and handling of the pellets) and the endocytosis mechanism by which the neurospheres uptake the nanoparticles (i.e. single or aggregated nanoparticles). The results indicated in the TEM and CLSM images show the uptake of the functionalized AuNPs, whilst the neurospheres suggest to be growing around and adhering to the functionalized SiO_2@AuNPs surfaces. Consequently, further experimental parameters need to be set to answer (i) the time point at which cellular uptake occurs, (ii) does aggregation occur during shaking of the media in the absence of NPSCs, (iii) is the aggregation of nanoparticles due to pH of media or due to the endocytosis mechanism, (iv) quantify the migration distance between the neurospheres and surface in static and dynamic conditions, and (v) the focal adhesion in the neurospheres with the nanoparticles is required to be characterized in order to validate this statement.

7.2.2 OUTLOOK

This work represents the beginning of evaluating the cell-material interaction facilitated by surface chemistry to control stem cell preferential differentiation to a specific cell fate. This work has opened the opportunity to integrate this suitable method of functionalizing controllable peptide composition on surfaces to:

- Evaluating gene expression of the differentiated cell type to determine other cell fates [77, 395, 396].
- Incorporating the established novel approach of immobilized controllable peptide composition into microfluidic devices, multi-electrode arrays (MEAs), hydrogels, and as an *in vitro* model for machine learning experiments [397-403].
- Evaluating the physiological properties of the differentiated cells by electrophysiology to determine action potential (i.e. are the cells functioning as they should?) [404, 405].
- Test for cell communication by evaluating levels of neurotransmissions present in the culture media (i.e. presence or absence of synapsin), focal adhesion, as well as to expand the range of neural phenotypes that can be studied [261, 406].
- Evaluation of the predictive potential of the established models for neurotoxicity testing and in other cell types [407].
- Evaluate the mechanisms of endocytosis and exocytosis by investigating the effects of different sizes, shapes, and surface chemistry on toxicity and gene regulation [394].
- The novel approach of preparing controllable peptide composition surfaces may have future applications various biomaterials field such as, (i) green chemistry (i.e. peptide functionalized nanoparticles as porphyrin catalyst), (ii) physics exploring the free-energy landscape of the peptides, (iii) drug delivery, (iv) antimicrobial, and (v) biosensors [408-414].

7.3 YESTERDAY, TODAY, & TOMORROW

Modern medicine saw the first real progress in organ transplantation as Dr Joseph Murray pioneered the first successful kidney transplantation in 1954, followed by successful isolation and transplantations of other major organs (i.e. pancreas, heart, liver) in the 1960s [415]. Hence, leading to rapid developments in the medical field especially in regenerative medicine and tissue engineering as they offered the potential to solve the problem of organ donor shortage (i.e. increase in population due to baby boomer generation and people living longer) [4, 416]. Current research focusses on materials development to design biocompatible medical devices that can be used to influence cell replacement, repair and regeneration in *in vitro* conditions to be successfully transplanted back into the patient (i.e. engineered from their own stem and precursor cells). Consequently, the research done today is increasing the technological developments to advance the engineering of tissues by becoming more sophisticated by performing animal and small pilot human studies to pave towards the treatment and cure of intractable diseases. This research has enabled, (i) FDA-approved therapies, and (ii) the design and validation of sophisticated surfaces that influence cell manipulation technologies for controlling cell behavior. The future looks bright as clinicians and scientists (i.e. physicist, chemists, biologist, and engineers) direct their collaborative efforts to translate basic scientific findings to solve major challenges such as, (i) constructing validated bioreactors (i.e. in vivo microenvironment) to avoid animal testing, (ii) contracting principles (i.e. pre-clinical and clinical) to make regenerative medicine and tissue engineering a gold standard for treating all diseases, and (iii) enhancing tissue engineering by engineering organs with different cell types and revitalizing worn-out body parts to restore full functionality [3, 417-419].

APPENDICES

RGD PEPTIDE

Appendix 1 ^{1}HNMR spectrum of RGD.

Appendix 2 RGD peptide characterization, (A) COSY 2D NMR spectrum, (B) HPLC, and (C) ESI-MS.

RGDC PEPTIDE

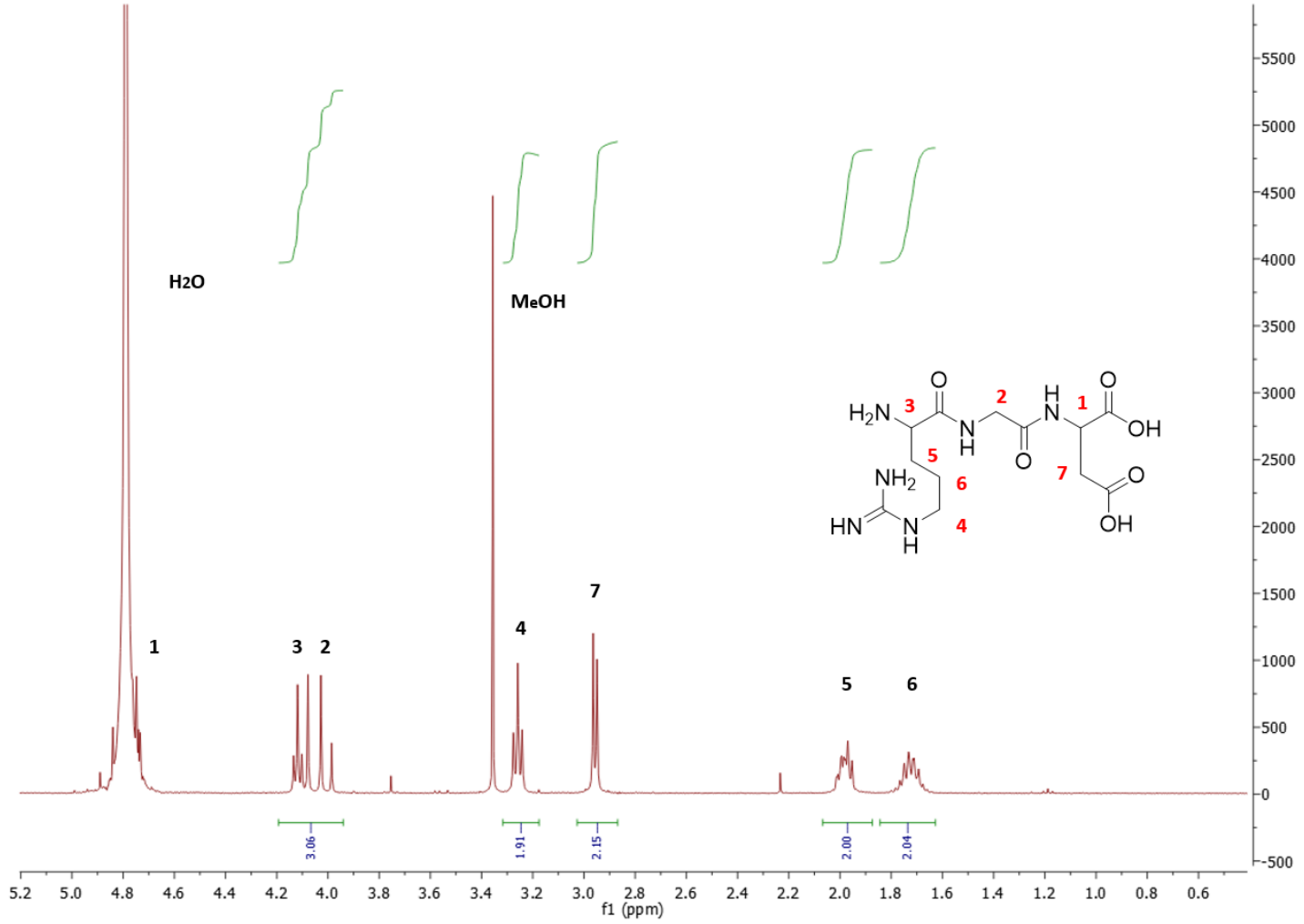
Appendix 3 ^{1}HNMR spectrum of RGDC-CDGR.

Appendix 4 RGDC-CDGR peptide characterization, (A) COSY 2D NMR spectrum, (B) HPLC, and (C) ESI-MS.

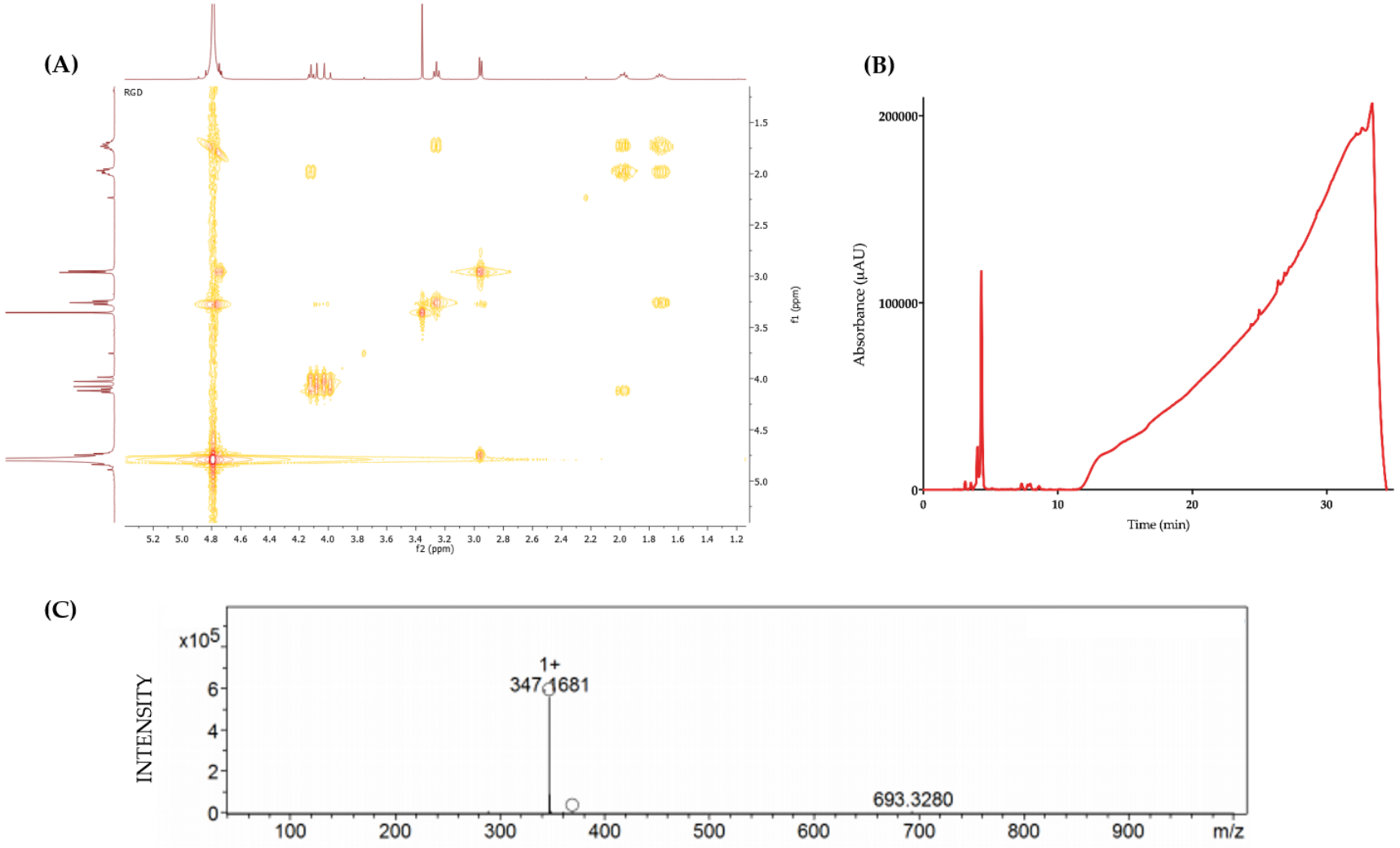
IKVAV PEPTIDE-UNSUCCESFUL

We are only able to purify it to 60% - 70%, contained another molecule.

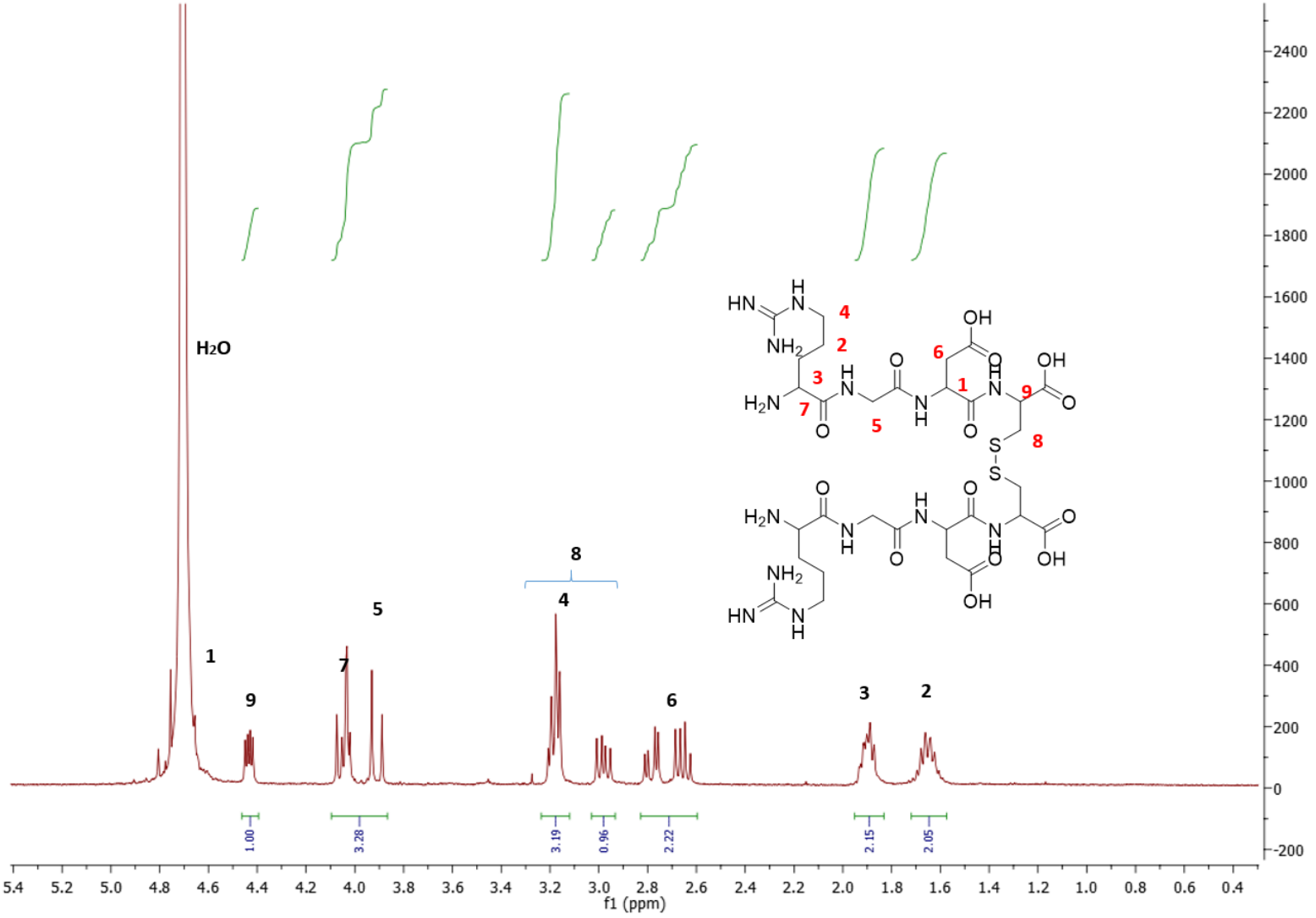
Appendix 5 IKVAV peptide characterization, (A) HPLC and (B) ESI-MS.



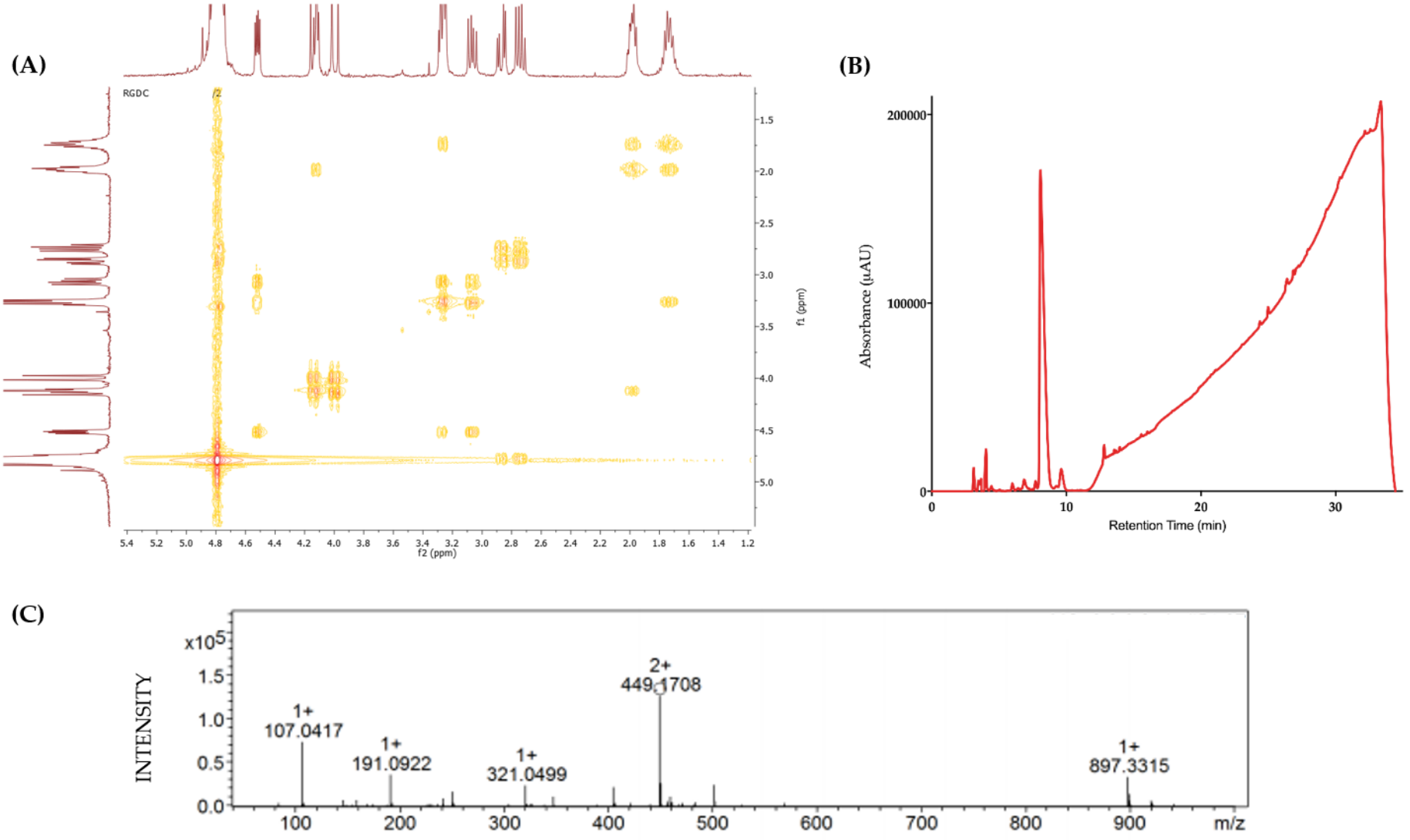
Appendix 1 ^{1}HNMR spectrum of RGD.



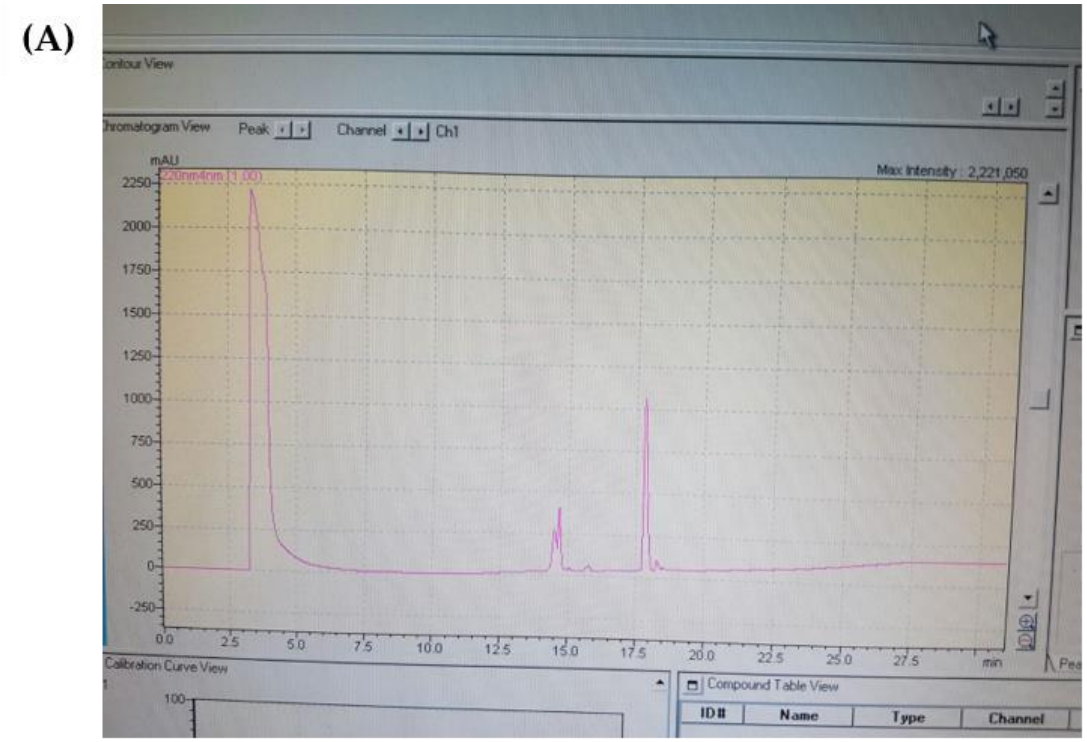
Appendix 2 RGD peptide characterization, (A) COSY 2D NMR spectrum, (B) HPLC, and (C) ESI-MS.

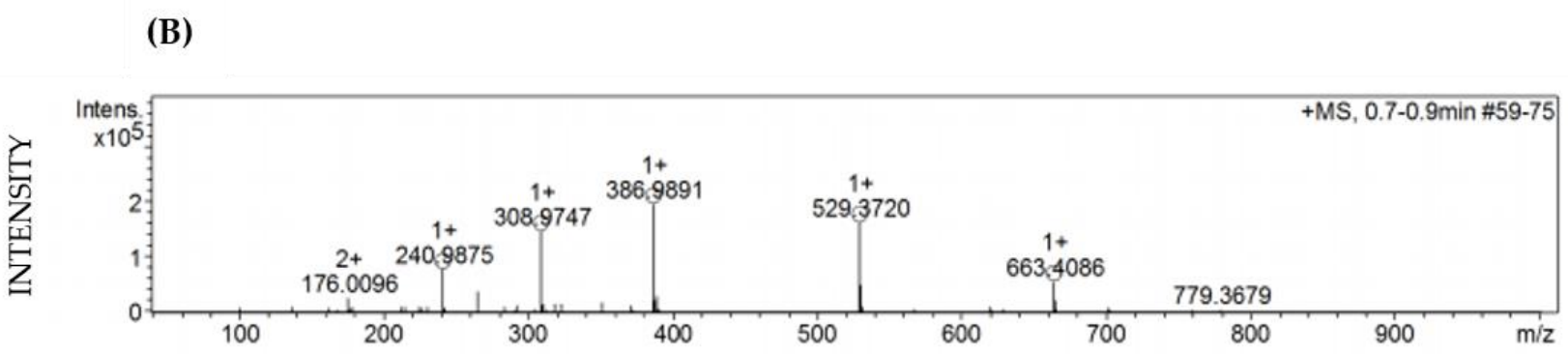


Appendix 3 ^{1}HNMR spectrum of RGDC-CDGR.



Appendix 4 RGDC peptide characterization, (A) COSY 2D NMR spectrum, (B) HPLC, and (C) ESI-MS.





Appendix 5 IKVAV peptide characterization, (A) HPLC and (B) ESI-MS.

BIBLIOGRAPHY

1. Bloom, D. A., Milen, M. T. & Heininger, J. C. Claudius galen: From a 20th century genitourinary perspective. *J. Urol.* **161,** 12–19 (1999).
2. Sampogna, G., Guraya, S. Y. & Forgione, A. Regenerative medicine: Historical roots and potential strategies in modern medicine. *J. Microsc. Ultrastruct.* **3,** 101–107 (2015).
3. Rosenthal, N. & Badylak, S. Regenerative medicine: today's discoveries informing the future of medical practice. *npj Regen. Med.* **1,** 16007 (2016).
4. Heidary Rouchi, A. & Mahdavi-Mazdeh, M. Regenerative medicine in organ and tissue transplantation: Shortly and practically achievable? *International Journal of Organ Transplantation Medicine* **6,** 93–98 (2015).
5. Parveen, S., Krishnakumar, K. & Sahoo, S. New era in health care: tissue engineering. *J. Stem Cells Regen. Med.* **1,** 8–24 (2006).
6. Bonneh-Barkay, D. & Wiley, C. A. Brain extracellular matrix in neurodegeneration. *Brain Pathology* **19,** 573–585 (2009).
7. Webber, M. J., Kessler, J. A. & Stupp, S. I. Emerging peptide nanomedicine to regenerate tissues and organs. in *Journal of Internal Medicine* **267,** 71–88 (2010).
8. Hinderer, S., Layland, S. L. & Schenke-Layland, K. ECM and ECM-like materials - Biomaterials for applications in regenerative medicine and cancer therapy. *Advanced Drug Delivery Reviews* **97,** 260–269 (2016).
9. Bellis, S. Advantages of RGD peptides for directing cell association with biomaterials. *Biomaterials* **32,** 4205–4210 (2011).
10. Ross, A. . M. & Lahann, J. Current Trends and Challenges in Biointerfaces Science and Engineering. *Annu. Rev. Chem. Biomol. Eng.* **6,** 161–186 (2015).
11. Le, X., Poinern, G. E. J., Ali, N., Berry, C. M. & Fawcett, D. Engineering a biocompatible scaffold with either micrometre or nanometre scale surface topography for promoting protein adsorption and cellular response. *International Journal of Biomaterials* **2013,** (2013).
12. Macgregor, M., Williams, R., Downes, J., Bachhuka, A. & Vasilev, K. The role of controlled surface topography and chemistry on mouse embryonic stem cell attachment, growth and self-renewal. *Materials (Basel).* **10,** (2017).

13. Variola, F. *et al.* Nanoscale surface modifications of medically relevant metals: state-of-the art and perspectives. *Nanoscale* **3,** 335–353 (2011).
14. Ren, M., Du, C., Herrero Acero, E., Tang-Schomer, M. D. & Özkucur, N. A biofidelic 3D culture model to study the development of brain cellular systems. *Sci. Rep.* **6,** (2016).
15. Grainger, D. W. The Williams dictionary of biomaterials. *Mater. Today* **2,** 29 (1999).
16. Shi, X. & Garry, D. J. Muscle stem cells in development, regeneration, and disease. *Genes Dev.* **20,** 1692–708 (2006).
17. Conover, J. C. & Notti, R. Q. The neural stem cell niche. *Cell and Tissue Research* **331,** 211–224 (2008).
18. Wang, L. D. & Wagers, A. J. Dynamic niches in the origination and differentiation of haematopoietic stem cells. *Nature Reviews Molecular Cell Biology* **12,** 643–655 (2011).
19. Hsu, Y. C. & Fuchs, E. A family business: Stem cell progeny join the niche to regulate homeostasis. *Nature Reviews Molecular Cell Biology* **13,** 103–114 (2012).
20. Vescovi, A. L., Galli, R. & Reynolds, B. A. Brain tumour stem cells. *Nature Reviews Cancer* **6,** 425–436 (2006).
21. Kleinsmith, L. J. & Pierce, G. B. Multipotentiality of Single Embryonal Carcinoma Cells. *Cancer Res.* **24,** 1544–1551 (1964).
22. Martin, G. R. Isolation of a pluripotent cell line from early mouse embryos cultured in medium conditioned by teratocarcinoma stem cells. *Proc. Natl. Acad. Sci.* **78,** 7634–7638 (1981).
23. Evans, M. Discovering pluripotency: 30 years of mouse embryonic stem cells. *Nature Reviews Molecular Cell Biology* **12,** 680–686 (2011).
24. Nelson, T. J., Behfar, A., Yamada, S., Martinez-Fernandez, A. & Terzic, A. Stem cell platforms for regenerative medicine. *Clinical and Translational Science* **2,** 222–227 (2009).
25. Mahla, R. S. Stem cells applications in regenerative medicine and disease therapeutics. *International Journal of Cell Biology* **2016,** (2016).
26. Dhara, S. K. & Stice, S. L. Neural differentiation of human embryonic stem cells. *Journal of Cellular Biochemistry* **105,** 633–640 (2008).
27. Kuegler, P. B. *et al.* Markers of murine embryonic and neural stem cells, neurons and astrocytes: reference points for developmental neurotoxicity testing. *ALTEX Altern.*

zu Tierexperimenten **27,** 17–42 (2010).

28. MacKay-Sim, A. Stem cells and their niche in the adult olfactory mucosa. *Archives Italiennes de Biologie* (2010). doi:10.4449/AIB.V148I2.1143
29. Chen, S., Lewallen, M. & Xie, T. Adhesion in the stem cell niche: biological roles and regulation. *Development* (2013). doi:10.1242/dev.083139
30. Clark, D. P., Pazdernik, N. J., Clark, D. P. & Pazdernik, N. J. Chapter 18 – Cloning and Stem Cells. in *Biotechnology* (2016). doi:10.1016/B978-0-12-385015-7.00018-1
31. Taylor, D. A. *et al.* Identification of Bone Marrow Cell Subpopulations Associated with Improved Functional Outcomes in Patients with Chronic Left Ventricular Dysfunction: An Embedded Cohort Evaluation of the FOCUS-CCTRN Trial. *Cell Transplant.* (2016). doi:10.3727/096368915X689901
32. Morrison, S. J. & Spradling, A. C. Stem Cells and Niches: Mechanisms That Promote Stem Cell Maintenance throughout Life. *Cell* **132,** 598–611 (2008).
33. Zeng, H. & Sanes, J. R. Neuronal cell-type classification: Challenges, opportunities and the path forward. *Nature Reviews Neuroscience* **18,** 530–546 (2017).
34. Jäkel, S. & Dimou, L. Glial Cells and Their Function in the Adult Brain: A Journey through the History of Their Ablation. *Front. Cell. Neurosci.* **11,** (2017).
35. Zhang, J. & Jiao, J. Molecular Biomarkers for Embryonic and Adult Neural Stem Cell and Neurogenesis. *BioMed Research International* **2015,** (2015).
36. Kimelberg, H. K. & Nedergaard, M. Functions of Astrocytes and their Potential As Therapeutic Targets. *Neurotherapeutics* **7,** 338–353 (2010).
37. Allen, N. J. & Barres, B. A. Neuroscience: Glia - more than just brain glue. *Nature* (2009). doi:10.1038/457675a
38. Dallérac, G., Chever, O. & Rouach, N. How do astrocytes shape synaptic transmission? Insights from electrophysiology. *Front. Cell. Neurosci.* **7,** (2013).
39. Bushong, E. a, Martone, M. E., Jones, Y. Z. & Ellisman, M. H. Protoplasmic astrocytes in CA1 stratum radiatum occupy separate anatomical domains. *J. Neurosci.* (2002). doi:22/1/183 [pii]
40. Wade, J. J., McDaid, L. J., Harkin, J., Crunelli, V. & Kelso, J. A. S. Bidirectional coupling between astrocytes and neurons mediates learning and dynamic coordination in the brain: A multiple modeling approach. *PLoS One* (2011).

doi:10.1371/journal.pone.0029445

41. Halassa, M. M., Fellin, T., Takano, H., Dong, J.-H. & Haydon, P. G. Synaptic Islands Defined by the Territory of a Single Astrocyte. *J. Neurosci.* (2007). doi:10.1523/JNEUROSCI.1419-07.2007
42. Wu, X. M. *et al.* Bi-directionally protective communication between neurons and astrocytes under ischemia. *Redox Biol.* (2017). doi:10.1016/j.redox.2017.05.010
43. Swanson, R., Ying, W. & Kauppinen, T. Astrocyte Influences on Ischemic Neuronal Death. *Curr. Mol. Med.* (2004). doi:10.2174/1566524043479185
44. Araque, A. Astrocytes process synaptic information. *Neuron Glia Biology* **4,** 3–10 (2008).
45. Perea, G., Navarrete, M. & Araque, A. Tripartite synapses: astrocytes process and control synaptic information. *Trends in Neurosciences* **32,** 421–431 (2009).
46. Spradling, A., Drummond-Barbosa, D. & Kai, T. Stem cells find their niche. *Nature* **414,** 98–104 (2001).
47. Ayala, R. *et al.* Engineering the cell-material interface for controlling stem cell adhesion, migration, and differentiation. *Biomaterials* **32,** 3700–3711 (2011).
48. Cavalcanti-Adam, E. A. *et al.* Lateral spacing of integrin ligands influences cell spreading and focal adhesion assembly. *Eur. J. Cell Biol.* **85,** 219–224 (2006).
49. Charras, G. & Sahai, E. Physical influences of the extracellular environment on cell migration. *Nat. Rev. Mol. Cell Biol.* **15,** 813–824 (2014).
50. Reilly, G. C. & Engler, A. J. Intrinsic extracellular matrix properties regulate stem cell differentiation. *J. Biomech.* **43,** 55–62 (2010).
51. Frantz, C., Stewart, K. M. & Weaver, V. M. The extracellular matrix at a glance. *J. Cell Sci.* **123,** 4195–4200 (2010).
52. Hubmacher, D. & Apte, S. S. The biology of the extracellular matrix: Novel insights. *Current Opinion in Rheumatology* **25,** 65–70 (2013).
53. Kim, S. H., Turnbull, J. & Guimond, S. Extracellular matrix and cell signalling: The dynamic cooperation of integrin, proteoglycan and growth factor receptor. *Journal of Endocrinology* **209,** 139–151 (2011).
54. Bonnans, C., Chou, J. & Werb, Z. Remodelling the extracellular matrix in development and disease. *Nature Reviews Molecular Cell Biology* (2014). doi:10.1038/nrm3904

55. Hala S Dhowre, Sunil Rajput, Noah A Russell, and M. Z. Responsive cell-material interfaces. *Nanomedicine* **10,** 849–871 (2015).

56. Frantz, C., Stewart, K. M. & Weaver, V. M. The extracellular matrix at a glance. *J. Cell Sci.* **123,** 4195–200 (2010).

57. Kleinfeld, D., Kahler, K. H. & Hockberger, P. E. Controlled outgrowth of dissociated neurons on patterned substrates. *J. Neurosci.* **8,** 4098–4120 (1988).

58. Nicosia, R. F., Bonanno, E., Smith, M. & Yurchenco, P. Modulation of angiogenesis in vitro by laminin-entactin complex. *Developmental biology* **164,** 197–206 (1994).

59. Ancsin, J. B. & Kisilevsky, R. Laminin interactions important for basement membrane assembly are promoted by zinc and implicate laminin zinc finger-like sequences. *J. Biol. Chem.* **271,** 6845–6851 (1996).

60. Kruegel, J. & Miosge, N. Basement membrane components are key players in specialized extracellular matrices. *Cellular and Molecular Life Sciences* (2010). doi:10.1007/s00018-010-0367-x

61. Guldager Kring Rasmussen, D. & Karsdal, M. A. Laminins. in *Biochemistry of Collagens, Laminins and Elastin: Structure, Function and Biomarkers* (2016). doi:10.1016/B978-0-12-809847-9.00029-5

62. Ma, Y. *et al.* Cross Talk Between Inflammation and Extracellular Matrix Following Myocardial Infarction. in *Inflammation in Heart Failure* (2015). doi:10.1016/B978-0-12-800039-7.00004-9

63. Reichardt, L. Extracellular Matrix Molecules And Their Receptors: Functions In Neural Development. *Annu. Rev. Neurosci.* **14,** 531–570 (1991).

64. Kirkbride, K. C., Ray, B. N. & Blobe, G. C. Cell-surface co-receptors: Emerging roles in signaling and human disease. *Trends in Biochemical Sciences* **30,** 611–621 (2005).

65. Cattaneo, F. *et al.* Cell-surface receptors transactivation mediated by G protein-coupled receptors. *International Journal of Molecular Sciences* **15,** 19700–19728 (2014).

66. Horstkorte, R. & Fuss, B. Chapter 9 – Cell Adhesion Molecules. in *Basic Neurochemistry* (2012). doi:10.1016/B978-0-12-374947-5.00009-2

67. Calderwood, D. A., Shattil, S. J. & Ginsberg, M. H. Integrins and actin filaments: Reciprocal regulation of cell adhesion and signaling. *Journal of Biological Chemistry* **275,** 22607–22610 (2000).

68. Parsons, J. T., Horwitz, A. R. & Schwartz, M. A. Cell adhesion: Integrating cytoskeletal dynamics and cellular tension. *Nature Reviews Molecular Cell Biology* **11,** 633–643 (2010).

69. Hynes, R. O. Integrins: Versatility, modulation, and signaling in cell adhesion. *Cell* **69,** 11–25 (1992).

70. Hynes, R. O. Integrins. *Cell* **110,** 673–687 (2002).

71. Barczyk, M., Carracedo, S. & Gullberg, D. Integrins. *Cell and Tissue Research* **339,** 269–280 (2010).

72. Moura-Neto, V. *et al.* Glioblastomas and the Special Role of Adhesion Molecules in Their Invasion. in *Glioma Cell Biology* (2014). doi:10.1007/978-3-7091-1431-5

73. Campbell, I. D. & Humphries, M. J. Integrin structure, activation, and interactions. *Cold Spring Harbor Perspectives in Biology* **3,** 1–14 (2011).

74. Wegener, K. L. & Campbell, I. D. Transmembrane and cytoplasmic domains in integrin activation and protein-protein interactions (Review). *Molecular Membrane Biology* **25,** 376–387 (2008).

75. Plow, E. F., Haas, T. A., Zhang, L., Loftus, J. & Smith, J. W. Ligand binding to integrins. *Journal of Biological Chemistry* **275,** 21785–21788 (2000).

76. Stefansson, S. *et al.* The contributions of integrin affinity and integrin-cytoskeletal engagement in endothelial and smooth muscle cell adhesion to vitronectin. *J. Biol. Chem.* **282,** 15679–15689 (2007).

77. Shekaran, A. & Garcia, A. J. Nanoscale engineering of extracellular matrix-mimetic bioadhesive surfaces and implants for tissue engineering. *Biochimica et Biophysica Acta - General Subjects* **1810,** 350–360 (2011).

78. Feng, Y. & Mrksich, M. The synergy peptide PHSRN and the adhesion peptide RGD mediate cell adhesion through a common mechanism. *Biochemistry* **43,** 15811–15821 (2004).

79. Wang, W. *et al.* Peptide REDV-modified polysaccharide hydrogel with endothelial cell selectivity for the promotion of angiogenesis. *J. Biomed. Mater. Res. - Part A* **103,** 1703–1712 (2015).

80. Tselepis, V. H., Green, L. J. & Humphries, M. J. An RGD to LDV motif conversion within the disintegrin kistrin generates an integrin antagonist that retains potency but

exhibits altered receptor specificity. Evidence for a functional equivalence of acidic integrin- binding motifs. *J. Biol. Chem.* **272,** 21341–21348 (1997).

81. Boateng, S. Y. RGD and YIGSR synthetic peptides facilitate identical cellular adhesion as laminin and fibronectin but alter the physiology of neonatal cardiac myocytes. *AJP Cell Physiol.* (2004). doi:10.1152/ajpcell.00199.2004

82. Aucoin, L., Griffith, C. M., Pleizier, G., Deslandes, Y. & Sheardown, H. Interactions of corneal epithelial cells and surfaces modified with cell adhesion peptide combinations. *J. Biomater. Sci. Polym. Ed.* **13,** 447–462 (2002).

83. Bachman, H., Nicosia, J., Dysart, M. & Barker, T. H. Utilizing Fibronectin Integrin-Binding Specificity to Control Cellular Responses. *Adv. Wound Care* (2015). doi:10.1089/wound.2014.0621

84. Ventre, M., Causa, F. & Netti, P. A. Determinants of cell-material crosstalk at the interface: towards engineering of cell instructive materials. *J. R. Soc. Interface* **9,** 2017–2032 (2012).

85. Pierschbacher, M. & Ruoslahti, E. Cell attachment activity of fibronectin can be duplicated by small synthetic fragments of the molecule. *Nature* **309,** 30–33 (1984).

86. Aumailley, M. *et al.* A simplified laminin nomenclature. *Matrix Biology* **24,** 326–332 (2005).

87. Colognato, H. & Yurchenco, P. D. Form and function: The laminin family of heterotrimers. *Developmental Dynamics* **218,** 213–234 (2000).

88. Adair-Kirk, T. L. *et al.* A Site on Laminin 5, AQARSAASKVKVSMKF, Induces Inflammatory Cell Production of Matrix Metalloproteinase-9 and Chemotaxis. *J. Immunol.* **171,** 398–406 (2003).

89. Horejs, C.-M. *et al.* Biologically-active laminin-111 fragment that modulates the epithelial-to-mesenchymal transition in embryonic stem cells. *Proc. Natl. Acad. Sci.* **111,** 5908–5913 (2014).

90. Pook, M. *et al.* Changes in laminin expression pattern during early differentiation of human embryonic stem cells. *PLoS One* **10,** (2015).

91. Yamada, K. M. Adhesive recognition sequences. *Journal of Biological Chemistry* **266,** 12809–12812 (1991).

92. Perlin, L., MacNeil, S. & Rimmer, S. Production and performance of biomaterials

containing RGD peptides. *Soft Matter* (2008). doi:10.1039/b801646a

93. Tisi, D., Talts, J. F., Timpl, R. & Hohenester, E. Structure of the C-terminal laminin G-like domain pair of the laminin alpha2 chain harbouring binding sites for alpha-dystroglycan and heparin. *EMBO J.* (2000). doi:10.1093/emboj/19.7.1432
94. Calderwood, D. A., Tuckwell, D. S., Eble, J., Kühn, K. & Humphries, M. J. The integrin α1 A-domain is a ligand binding site for collagens and laminin. *J. Biol. Chem.* (1997). doi:10.1074/jbc.272.19.12311
95. MILES, A. J., SKUBITZ, A. P. N., Furcht, L. T. & Fields, G. B. PROMOTION OF CELL-ADHESION BY SINGLE-STRANDED AND TRIPLE-HELICAL PEPTIDE MODELS OF BASEMENT-MEMBRANE COLLAGEN ALPHA-1(IV)531-543 - EVIDENCE FOR CONFORMATIONALLY DEPENDENT AND CONFORMATIONALLY INDEPENDENT TYPE-IV COLLAGEN CELL-ADHESION SITES. *J. Biol. Chem.* (1994).
96. D'Souza, S. E., Ginsberg, M. H. & Plow, E. F. Arginyl-glycyl-aspartic acid (RGD): a cell adhesion motif. *Trends Biochem. Sci.* **16,** 246–250 (1991).
97. Ruoslahti, E. RGD AND OTHER RECOGNITION SEQUENCES FOR INTEGRINS. *Annu. Rev. Cell Dev. Biol.* **12,** 697–715 (1996).
98. Cardwell, M. C. & Rome, L. H. Evidence that an RGD-dependent receptor mediates the binding of oligodendrocytes to a novel ligand in a glial-derived matrix. *J. Cell Biol.* **107,** 1541–1549 (1988).
99. Lee, T. T. *et al.* Light-triggered in vivo activation of adhesive peptides regulates cell adhesion, inflammation and vascularization of biomaterials. *Nat. Mater.* **14,** 352–360 (2015).
100. Zamuner, A. *et al.* Smart biomaterials: Surfaces functionalized with proteolytically stable osteoblast-adhesive peptides. *Bioact. Mater.* **2,** 121–130 (2017).
101. Dunehoo, A. L. *et al.* Cell adhesion molecules for targeted drug delivery. *Journal of Pharmaceutical Sciences* **95,** 1856–1872 (2006).
102. Eskandari, S., Guerin, T., Toth, I. & Stephenson, R. J. Recent advances in self-assembled peptides: Implications for targeted drug delivery and vaccine engineering. *Advanced Drug Delivery Reviews* **110–111,** 169–187 (2017).
103. Frantz, C., Stewart, K. M. & Weaver, V. M. The extracellular matrix at a glance. *J. Cell Sci.* **123,** 4195–4200 (2010).

104. Wilson, C. J., Clegg, R. E., Leavesley, D. I. & Pearcy, M. J. Mediation of Biomaterial–Cell Interactions by Adsorbed Proteins: A Review. *Tissue Eng.* **11,** 1–18 (2005).

105. García, A. J. Interfaces to control cell-biomaterial adhesive interactions. *Advances in Polymer Science* **203,** 171–190 (2006).

106. Zelzer, M., Albutt, D., Alexander, M. R. & Russell, N. a. The Role of Albumin and Fibronectin in the Adhesion of Fibroblasts to Plasma Polymer Surfaces. *Plasma Process. Polym.* **9,** 149–156 (2012).

107. Roach, P., Farrar, D. & Perry, C. C. Surface tailoring for controlled protein adsorption: Effect of topography at the nanometer scale and chemistry. *J. Am. Chem. Soc.* **128,** 3939–3945 (2006).

108. Bae, H. *et al.* Development of functional biomaterials with micro- and nanoscale technologies for tissue engineering and drug delivery applications. *Journal of Tissue Engineering and Regenerative Medicine* **8,** 1–14 (2014).

109. Anton, D., Burckel, H., Josset, E. & Noel, G. Three-dimensional cell culture: A breakthrough in vivo. *International Journal of Molecular Sciences* (2015). doi:10.3390/ijms16035517

110. Murphy, W. L., McDevitt, T. C. & Engler, A. J. Materials as stem cell regulators. *Nature Materials* **13,** 547–557 (2014).

111. Keselowsky, B. G., Collard, D. M. & García, A. J. Surface chemistry modulates fibronectin conformation and directs integrin binding and specificity to control cell adhesion. *J. Biomed. Mater. Res. Part A* **66A,** 247–259 (2003).

112. Webb, K., Hlady, V. & Tresco, P. A. Relative importance of surface wettability and charged functional groups on NIH 3T3 fibroblast attachment, spreading, and cytoskeletal organization. *J. Biomed. Mater. Res.* **41,** 422–430 (1998).

113. Blau, A. Cell adhesion promotion strategies for signal transduction enhancement in microelectrode array in vitro electrophysiology: An introductory overview and critical discussion. *Current Opinion in Colloid and Interface Science* **18,** 481–492 (2013).

114. Mrksich, M. A surface chemistry approach to studying cell adhesion. *Chem. Soc. Rev.* **29,** 267–273 (2000).

115. Cuvelier, D. *et al.* The Universal Dynamics of Cell Spreading. *Curr. Biol.* **17,** 694–699 (2007).

116. Smith, J. T. *et al.* Measurement of cell migration on surface-bound fibronectin gradients. *Langmuir* **20,** 8279–8286 (2004).

117. Lan, M. A., Gersbach, C. A., Michael, K. E., Keselowsky, B. G. & García, A. J. Myoblast proliferation and differentiation on fibronectin-coated self assembled monolayers presenting different surface chemistries. *Biomaterials* **26,** 4523–4531 (2005).

118. Benoit, D. S. W., Schwartz, M. P., Durney, A. R. & Anseth, K. S. Small functional groups for controlled differentiation of hydrogel-encapsulated human mesenchymal stem cells. *Nat. Mater.* **7,** 816–823 (2008).

119. Keselowsky, B. G., Collard, D. M. & García, A. J. Integrin binding specificity regulates biomaterial surface chemistry effects on cell differentiation. *Proc. Natl. Acad. Sci. U. S. A.* **102,** 5953–5957 (2005).

120. Elul, R. Fixed charge in the cell membrane. *J. Physiol.* **189,** 351–365 (1967).

121. Bacakova, L., Filova, E., Parizek, M., Ruml, T. & Svorcik, V. Modulation of cell adhesion, proliferation and differentiation on materials designed for body implants. *Biotechnology Advances* **29,** 739–767 (2011).

122. Liu, L., Chen, S., Giachelli, C. M., Ratner, B. D. & Jiang, S. Controlling osteopontin orientation on surfaces to modulate endothelial cell adhesion. *J. Biomed. Mater. Res. A* **74,** 23–31 (2005).

123. Hayward, A. S. *et al.* Galactose-functionalized polyHIPE scaffolds for use in routine three dimensional culture of mammalian hepatocytes. *Biomacromolecules* **14,** 4271–4277 (2013).

124. Kourouklis, A. P., Lerum, R. V. & Bermudez, H. Cell adhesion mechanisms on laterally mobile polymer films. *Biomaterials* **35,** 4827–4834 (2014).

125. Johansson, S., Svineng, G., Wennerberg, K., Armulik, A. & Lohikangas, L. Fibronectin-integrin interactions. *Front. Biosci.* (1997). doi:10.2741/A178

126. Mitra, S. K., Hanson, D. A. & Schlaepfer, D. D. Focal adhesion kinase: in command and control of cell motility. *Nat Rev Mol Cell Biol* **6,** 56–68 (2005).

127. Dalby, M. J. *et al.* The control of human mesenchymal cell differentiation using nanoscale symmetry and disorder. *Nat. Mater.* **6,** 407–413 (2007).

128. Stevens, M. M. Exploring and Engineering the Cell Surface Interface. *Science (80-.).* **310,** 1135–1138 (2005).

129. Dalby, M. J., Riehle, M. O., Johnstone, H., Affrossman, S. & Curtis, A. S. G. In vitro reaction of endothelial cells to polymer demixed nanotopography. *Biomaterials* **23,** 2945–2954 (2002).

130. Dalby, M. J. *et al.* Rapid fibroblast adhesion to 27 nm high polymer demixed nano-topography. *Biomaterials* **25,** 77–83 (2004).

131. Dalby, M. J. *et al.* Genomic expression of mesenchymal stem cells to altered nanoscale topographies. *J. R. Soc. Interface* **5,** 1055–1065 (2008).

132. Khang, D., Lu, J., Yao, C., Haberstroh, K. M. & Webster, T. J. The role of nanometer and sub-micron surface features on vascular and bone cell adhesion on titanium. *Biomaterials* (2008). doi:10.1016/j.biomaterials.2007.11.009

133. Papageorgiou, I. *et al.* Interaction of micron and nano-sized particles with cells of the dura mater. *J. Biomed. Mater. Res. - Part B Appl. Biomater.* (2014). doi:10.1002/jbm.b.33129

134. Anderson, H. J., Sahoo, J. K., Ulijn, R. V. & Dalby, M. J. Mesenchymal Stem Cell Fate: Applying Biomaterials for Control of Stem Cell Behavior. *Front. Bioeng. Biotechnol.* (2016). doi:10.3389/fbioe.2016.00038

135. Engler, A. J., Sen, S., Sweeney, H. L. & Discher, D. E. Matrix Elasticity Directs Stem Cell Lineage Specification. *Cell* **126,** 677–689 (2006).

136. Kingshott, P., Andersson, G., McArthur, S. L. & Griesser, H. J. Surface modification and chemical surface analysis of biomaterials. *Current Opinion in Chemical Biology* **15,** 667–676 (2011).

137. Lee, W.-H., Loo, C.-Y. & Rohanizadeh, R. A review of chemical surface modification of bioceramics: Effects on protein adsorption and cellular response. *Colloids Surfaces B Biointerfaces* **122,** 823–834 (2014).

138. Saini, M. Implant biomaterials: A comprehensive review. *World J. Clin. Cases* **3,** 52 (2015).

139. Parida, P., Behera, A. & Mishra, S. C. Classification of Biomaterials used in Medicine. *Int. J. Adv. Appl. Sci.* **1,** 125–129 (2012).

140. Mahyudin, F., Widhiyanto, L. & Hermawan, H. Biomaterials in orthopaedics. in *Advanced Structured Materials* **58,** 161–181 (2016).

141. Sáenz, A., Rivera-muñoz, E., Brostow, W. & Castaño, V. M. Ceramic Biomaterials : an

Introductory Overview. *J. Mater. Educ.* **21,** 297–306 (1999).

142. Maitz, M. F. Applications of synthetic polymers in clinical medicine. *Biosurface and Biotribology* **1,** 161–176 (2015).

143. Teo, A. J. T. *et al.* Polymeric Biomaterials for Medical Implants and Devices. *ACS Biomater. Sci. Eng.* **2,** 454–472 (2016).

144. Katti, D., Vasita, R. & Shanmugam, K. Improved Biomaterials for Tissue Engineering Applications: Surface Modification of Polymers. *Curr. Top. Med. Chem.* **8,** 341–353 (2008).

145. Qiu, Z.-Y., Chen, C., Wang, X.-M. & Lee, I.-S. Advances in the surface modification techniques of bone-related implants for last 10 years. *Regen. Biomater.* **1,** 67–79 (2014).

146. Govindarajan, T. & Shandas, R. A survey of surface modification techniques for next-generation shape memory polymer stent devices. *Polymers* **6,** 2309–2331 (2014).

147. Seidlits, S. K., Lee, J. Y. & Schmidt, C. E. Nanostructured scaffolds for neural applications. *Nanomedicine* **3,** 183–199 (2008).

148. Limongi, T. *et al.* Fabrication and Applications of Micro/Nanostructured Devices for Tissue Engineering. *Nano-Micro Letters* **9,** (2017).

149. Sileo, L., Pisanello, F., Martiradonna, L. & De Vittorio, M. Focused Ion Beam technology as a fabrication and inspection tool in neuron interfacing. in *Nanotechnology and Neuroscience: Nano-Electronic, Photonic and Mechanical Neuronal Interfacing* 183–205 (2014). doi:10.1007/978-1-4899-8038-0_6

150. Yu, L. M. Y., Leipzig, N. D. & Shoichet, M. S. Promoting neuron adhesion and growth. *Materials Today* **11,** 36–43 (2008).

151. Wieringa, P., Tonazzini, I., Micera, S. & Cecchini, M. Nanotopography induced contact guidance of the F11 cell line during neuronal differentiation: A neuronal model cell line for tissue scaffold development. *Nanotechnology* **23,** (2012).

152. Irvine, E. J., Hernandez-Santana, A., Faulds, K. & Graham, D. Fabricating protein immunoassay arrays on nitrocellulose using Dip-pen lithography techniques. *Analyst* **136,** 2925 (2011).

153. Pimpin, A. & Srituravanich, W. Reviews on micro- and nanolithography techniques and their applications. *Engineering Journal* **16,** 37–55 (2012).

154. Tran, K. T. M. & Nguyen, T. D. Lithography-based methods to manufacture

biomaterials at small scales. *J. Sci. Adv. Mater. Devices* **2,** 1–14 (2017).

155. Kim, Y. C., Park, J. H. & Prausnitz, M. R. Microneedles for drug and vaccine delivery. *Advanced Drug Delivery Reviews* **64,** 1547–1568 (2012).
156. Ita, K. Transdermal delivery of drugs with microneedles—potential and challenges. *Pharmaceutics* **7,** 90–105 (2015).
157. Wang, M., Hu, L. & Xu, C. Recent advances in the design of polymeric microneedles for transdermal drug delivery and biosensing. *Lab Chip* **17,** 1373–1387 (2017).
158. Indermun, S. *et al.* Current advances in the fabrication of microneedles for transdermal delivery. *Journal of Controlled Release* **185,** 130–138 (2014).
159. Yuan, L. L. & Herman, P. R. Laser scanning holographic lithography for flexible 3D fabrication of multi-scale integrated nano-structures and optical biosensors. *Sci. Rep.* **6,** (2016).
160. Chen, Y. P. *et al.* Fabrication of dendritic silver nanostructure using an integration of holographic lithography and electrochemical deposition. *Electrochim. Acta* **56,** 9088–9094 (2011).
161. Stankevičius, E., Gedvilas, M., Voisiat, B., Malinauskas, M. & Račiukaitis, G. Fabrication of periodic micro-structures by holographic lithography. *Lith. J. Phys.* **53,** 227–237 (2013).
162. Lee, K. & Jung, H. Drawing lithography for microneedles: A review of fundamentals and biomedical applications. *Biomaterials* **33,** 7309–7326 (2012).
163. Stankevicius, E. *et al.* Holographic lithography for biomedical applications. in *Proceedings of SPIE - The International Society for Optical Engineering* **8433,** (2012).
164. Králik, M. Adsorption, chemisorption, and catalysis. *Chemical Papers* **68,** 1625–1638 (2014).
165. Tallawi, M. *et al.* Strategies for the chemical and biological functionalization of scaffolds for cardiac tissue engineering: a review. *J. R. Soc. Interface* **12,** 20150254 (2015).
166. Lutolf, M. P. *et al.* Synthetic matrix metalloproteinase-sensitive hydrogels for the conduction of tissue regeneration: engineering cell-invasion characteristics. *Proc. Natl. Acad. Sci. U. S. A.* **100,** 5413–8 (2003).
167. Coburn, J. & Pandit, a. Development of naturally-derived biomaterials and optimization of their biomechanical properties. *Top. Tissue Eng.* (2007).

168. Reimhult, E. & H????k, F. Design of surface modifications for nanoscale sensor applications. *Sensors (Basel).* **15,** 1635–1675 (2015).

169. van Vught, R., Pieters, R. J. & Breukink, E. SITE-SPECIFIC FUNCTIONALIZATION OF PROTEINS AND THEIR APPLICATIONS TO THERAPEUTIC ANTIBODIES. *Comput. Struct. Biotechnol. J.* (2014). doi:10.5936/csbj.201402001

170. Yamaguchi, A. *et al.* Incorporation of a Doubly Functionalized Synthetic Amino Acid into Proteins for Creating Chemical and Light-Induced Conjugates. *Bioconjug. Chem.* (2016). doi:10.1021/acs.bioconjchem.5b00602

171. Moby, V., Kadi, A., De Isla, N., Stoltz, J. F. & Menu, P. Polyelectrolyte multilayer films: Effect of the initial anchoring layer on the cell growth. in *Bio-Medical Materials and Engineering* (2008). doi:10.3233/BME-2008-0525

172. Yamanlar, S., Sant, S., Boudou, T., Picart, C. & Khademhosseini, A. Surface functionalization of hyaluronic acid hydrogels by polyelectrolyte multilayer films. *Biomaterials* (2011). doi:10.1016/j.biomaterials.2011.04.030

173. Sevastianov, V. I., Drushlyak, I. V, Eberhart, R. C. & Wan Kim, S. Blood compatible biomaterials: Hydrophilicity vs. hydrophobicity. *Macromol. Symp.* (1996). doi:10.1002/masy.19961030103

174. Falde, E. J., Yohe, S. T., Colson, Y. L. & Grinstaff, M. W. Superhydrophobic materials for biomedical applications. *Biomaterials* (2016). doi:10.1016/j.biomaterials.2016.06.050

175. Poon, K., Castellino, V. & Cheng, Y. L. Polymeric hydrophilic polymers in targeted drug delivery. in *Artificial Cells, Cell Engineering and Therapy* (2007). doi:10.1533/9781845693077.1.42

176. Matinlinna, J. P., Lassila, L. V, Ozcan, M., Yli-Urpo, A. & Vallittu, P. K. An introduction to silanes and their clinical applications in dentistry. *Int. J. Prosthodont.* (2004).

177. Doufnoune, R., Haddaoui, N. & Riahi, F. Effects of coupling agents on the tensile properties of calcium carbonate filled LDPE compatibilized with maleic anhydride-g-LDPE (Part I). *Int. J. Polym. Mater. Polym. Biomater.* (2008). doi:10.1080/00914030701476998

178. Ravi, S., Krishnamurthy, V. R., Caves, J. M., Haller, C. A. & Chaikof, E. L. Maleimide-thiol coupling of a bioactive peptide to an elastin-like protein polymer. *Acta Biomater.*

(2012). doi:10.1016/j.actbio.2011.10.027

179. Shih, H., Liu, H. Y. & Lin, C. C. Improving gelation efficiency and cytocompatibility of visible light polymerized thiol-norbornene hydrogels via addition of soluble tyrosine. *Biomater. Sci.* (2017). doi:10.1039/c6bm00778c

180. Müller, P. *et al.* Calcium phosphate surfaces promote osteogenic differentiation of mesenchymal stem cells. *J. Cell. Mol. Med.* (2008). doi:10.1111/j.1582-4934.2007.00103.x

181. Razafiarison, T. *et al.* Biomaterial surface energy-driven ligand assembly strongly regulates stem cell mechanosensitivity and fate on very soft substrates. *Proc. Natl. Acad. Sci. U. S. A.* (2018). doi:10.1073/pnas.1704543115

182. Spaans, S. *et al.* Supramolecular surface functionalization: Via catechols for the improvement of cell-material interactions. *Biomater. Sci.* (2017). doi:10.1039/c7bm00407a

183. Rapp, M. V. *et al.* Defining the Catechol-Cation Synergy for Enhanced Wet Adhesion to Mineral Surfaces. *J. Am. Chem. Soc.* (2016). doi:10.1021/jacs.6b03453

184. Sun, T. & Qing, G. Biomimetic smart interface materials for biological applications. *Adv. Mater.* **23,** H57-77 (2011).

185. Takahashi, H., Nakayama, M., Yamato, M. & Okano, T. Controlled chain length and graft density of thermoresponsive polymer brushes for optimizing cell sheet harvest. *Biomacromolecules* **11,** 1991–9 (2010).

186. Qing, G., Wang, X., Fuchs, H. & Sun, T. Nucleotide-responsive wettability on a smart polymer surface. *J. Am. Chem. Soc.* **131,** 8370–8371 (2009).

187. Tekin, H., Sanchez, J. & Tsinman, T. Thermoresponsive Platforms for Tissue Engineering and Regenerative Medicine. *AIChE …* **57,** 3249–3258 (2011).

188. Inaba, R., Khademhosseini, A., Suzuki, H. & Fukuda, J. Electrochemical desorption of self-assembled monolayers for engineering cellular tissues. *Biomaterials* **30,** 3573–3579 (2009).

189. Fukuda, J., Kameoka, Y. & Suzuki, H. Spatio-temporal detachment of single cells using microarrayed transparent electrodes. *Biomaterials* **32,** 6663–9 (2011).

190. Yeo, W.-S., Yousaf, M. N. & Mrksich, M. Dynamic interfaces between cells and surfaces: electroactive substrates that sequentially release and attach cells. *J. Am. Chem. Soc.* **125,** 14994–5 (2003).

191. Yeo, W. S. & Mrksich, M. Electroactive self-assembled monolayers that permit orthogonal control over the adhesion of cells to patterned substrates. *Langmuir* **22,** 10816–10820 (2006).

192. van Dongen, S. F. M., Maiuri, P., Marie, E., Tribet, C. & Piel, M. Triggering Cell Adhesion, Migration or Shape Change with a Dynamic Surface Coating. *Adv. Mater.* **25,** 1687–1691 (2013).

193. Yousaf, M. N., Houseman, B. T. & Mrksich, M. Turning on cell migration with electroactive substrates. *Angew. Chemie - Int. Ed.* **40,** 1093–1096 (2001).

194. Pan, G. *et al.* Dynamic introduction of cell adhesive factor via reversible multicovalent phenylboronic acid/cis-diol polymeric complexes. *J. Am. Chem. Soc.* **136,** 6203–6 (2014).

195. Todd, S. J., Scurr, D. J., Gough, J. E., Alexander, M. R. & Ulijn, R. V. Enzyme-activated RGD ligands on functionalized poly(ethylene glycol) monolayers: Surface analysis and cellular response. *Langmuir* **25,** 7533–7539 (2009).

196. Liu, B., Liu, Y., Riesberg, J. J. & Shen, W. Dynamic presentation of immobilized ligands regulated through biomolecular recognition. *J. Am. Chem. Soc.* **132,** 13630–2 (2010).

197. Wang, X., Riesberg, J. J. & Shen, W. Reversible regulation of bioactive ligands presented on immobilized gold nanoparticles. *Soft Matter* **8,** 2812 (2012).

198. Gong, Y. H. *et al.* Photoresponsive 'smart template' via Host-Guest interaction for reversible cell adhesion. *Macromolecules* **44,** 7499–7502 (2011).

199. Gong, Y.-H. *et al.* Photoresponsive smart template for reversible cell micropatterning. *J. Mater. Chem. B* **1,** 2013 (2013).

200. Pranzetti, A. *et al.* An electrically reversible switchable surface to control and study early bacterial adhesion dynamics in real-time. *Adv. Mater.* **25,** 2181–5 (2013).

201. Yeung, C. L. *et al.* Tuning Specific Biomolecular Interactions Using Electro-Switchable Oligopeptide Surfaces. *Adv. Funct. Mater.* **20,** 2657–2663 (2010).

202. Ng, C. C. A. *et al.* Using an electrical potential to reversibly switch surfaces between two states for dynamically controlling cell adhesion. *Angew. Chemie - Int. Ed.* **51,** 7706–7710 (2012).

203. Liu, D., Xie, Y., Shao, H. & Jiang, X. Using azobenzene-embedded self-assembled monolayers to photochemically control cell adhesion reversibly. *Angew. Chemie - Int.*

Ed. **48,** 4406–4408 (2009).

204. Lahann, J. *et al.* A reversibly switching surface. *Science (80-.).* **299,** 371–374 (2003).

205. Lamb, B. M. & Yousaf, M. N. Redox-switchable surface for controlling peptide structure. *J. Am. Chem. Soc.* **133,** 8870–3 (2011).

206. Paul, N. *et al.* Molecularly imprinted conductive polymers for controlled trafficking of neurotransmitters at solid–liquid interfaces. *Soft Matter* **9,** 1364 (2013).

207. Mertz, D. *et al.* Mechanotransductive surfaces for reversible biocatalysis activation. *Nat. Mater.* **8,** 731–735 (2009).

208. O'Brien, F. J. Biomaterials & scaffolds for tissue engineering. *Mater. Today* **14,** 88–95 (2011).

209. Aasland, R. *et al.* Normalization of nomenclature for peptide motifs as ligands of modular protein domains. *FEBS Letters* **513,** 141–144 (2002).

210. Saito, H., Kashida, S., Inoue, T. & Shiba, K. The role of peptide motifs in the evolution of a protein network. *Nucleic Acids Res.* **35,** 6357–6366 (2007).

211. Yip, P. M., Zhao, X., Montgomery, a M. & Siu, C. H. The Arg-Gly-Asp motif in the cell adhesion molecule L1 promotes neurite outgrowth via interaction with the alphavbeta3 integrin. *Mol. Biol. Cell* **9,** 277–290 (1998).

212. Tsou, Y.-H., Khoneisser, J., Huang, P.-C. & Xu, X. Hydrogel as a bioactive material to regulate stem cell fate. *Bioact. Mater.* **1,** 39–55 (2016).

213. Griffin, M. F. Control of stem cell fate by engineering their micro and nanoenvironment. *World J. Stem Cells* **7,** 37 (2015).

214. Jedlicka, S. S., Little, K. M., Nivens, D. E., Zemlyanov, D. & Rickus, J. L. Peptide ormosils as cellular substrates. *J. Mater. Chem.* **17,** 5058 (2007).

215. Cai, L. & Heilshorn, S. Designing ECM-mimetic materials using protein engineering. *Acta Biomater.* **10,** 1751–1760 (2014).

216. Ananthanarayanan, B., Little, L., Schaffer, D. V., Healy, K. E. & Tirrell, M. Neural stem cell adhesion and proliferation on phospholipid bilayers functionalized with RGD peptides. *Biomaterials* **31,** 8706–8715 (2010).

217. Kafi, M. A., Kim, T. H., Yea, C. H., Kim, H. & Choi, J. W. Effects of nanopatterned RGD peptide layer on electrochemical detection of neural cell chip. *Biosens. Bioelectron.* **26,** 1359–1365 (2010).

218. Diaz-Quijada, G. A. *et al.* Surface patterning with chemisorbed chemical cues for advancing neurochip applications. *Ind. Eng. Chem. Res.* **50,** 10029–10035 (2011).

219. Xie, H. *et al.* Enhanced proliferation and differentiation of neural stem cells grown on PHA films coated with recombinant fusion proteins. *Acta Biomater.* **9,** 7845–7854 (2013).

220. Pellett, S. *et al.* Human Induced Pluripotent Stem Cell Derived Neuronal Cells Cultured on Chemically-Defined Hydrogels for Sensitive In Vitro Detection of Botulinum Neurotoxin. *Sci. Rep.* **5,** (2015).

221. Yun, D., Lee, Y. M., Laughter, M. R., Freed, C. R. & Park, D. Substantial Differentiation of Human Neural Stem Cells into Motor Neurons on a Biomimetic Polyurea. *Macromol. Biosci.* **15,** 1206–1211 (2015).

222. de Luca, A. C., Faroni, A., Downes, S. & Terenghi, G. Differentiated adipose-derived stem cells act synergistically with RGD-modified surfaces to improve neurite outgrowth in a co-culture model. *J. Tissue Eng. Regen. Med.* **10,** 647–655 (2016).

223. Ranieri, J. P. *et al.* Spatial control of neuronal cell attachment and differentiation on covalently patterned laminin oligopeptide substrates. *Int. J. Dev. Neurosci.* **12,** 725–735 (1994).

224. Ranieri, J. P. *et al.* Neuronal cell attachment to fluorinated ethylene propylene films with covalently immobilized laminin oligopeptides YIGSR and IKVAV. II. *J. Biomed. Mater. Res.* **29,** 779–785 (1995).

225. Agius, E., Sagot, Y., Duprat, A. M. & Cochard, P. Antibodies directed against the β1-integrin subunit and peptides containing the IKVAV sequence of laminin perturb neurite outgrowth of peripheral neurons on immature spinal cord substrata. *Neuroscience* **71,** 773–786 (1996).

226. Silva, G. A. *et al.* Selective Differentiation of Neural Progenitor Cells by High-Epitope Density Nanofibers. *Science (80-.).* **303,** 1352–1355 (2004).

227. Song, Y., Zheng, Q., Wu, Y. & Guo, X. Two-dimensional effects of hydrogel self-organized from IKVAV-containing peptides on growth and differentiation of NSCs. *J. Wuhan Univ. Technol. Mater. Sci. Ed.* **24,** 186–192 (2009).

228. Gaubert, H. E. & Frey, W. Highly parallel fabrication of nanopatterned surfaces with nanoscale orthogonal biofunctionalization imprint lithography. *Nanotechnology* **18,** (2007).

229. Weber, L. M., Hayda, K. N., Haskins, K. & Anseth, K. S. The effects of cell-matrix interactions on encapsulated β-cell function within hydrogels functionalized with matrix-derived adhesive peptides. *Biomaterials* **28,** 3004–3011 (2007).

230. Harbers, G. M., Gamble, L. J., Irwin, E. F., Castner, D. G. & Healy, K. E. Development and characterization of a high-throughput system for assessing cell-surface receptor-ligand engagement. *Langmuir* **21,** 8374–8384 (2005).

231. Saha, K., Irwin, E. F., Kozhukh, J., Schaffer, D. V. & Healy, K. E. Biomimetic interfacial interpenetrating polymer networks control neural stem cell behavior. *J. Biomed. Mater. Res. - Part A* **81,** 240–249 (2007).

232. Li, H. & Cooper-White, J. J. Changing ligand number and type within nanocylindrical domains through kinetically constrained self-assembly-impacts of ligand 'redundancy' on human mesenchymal stem cell adhesion and morphology. *Biomater. Sci.* **2,** 1693–1705 (2014).

233. Adil, M. M. *et al.* Engineered hydrogels increase the post-transplantation survival of encapsulated hESC-derived midbrain dopaminergic neurons. *Biomaterials* **136,** 1–11 (2017).

234. Yoo, S. J., Kim, J., Lee, C.-S. & Nam, Y. Simple and novel three dimensional neuronal cell culture using a micro mesh scaffold. *Exp. Neurobiol.* **20,** 110–5 (2011).

235. Brewer, G. J. & Cotman, C. W. Survival and growth of hippocampal neurons in defined medium at low density: advantages of a sandwich culture technique or low oxygen. *Brain Res.* **494,** 65–74 (1989).

236. Kolind, K., Leong, K. W., Besenbacher, F. & Foss, M. Guidance of stem cell fate on 2D patterned surfaces. *Biomaterials* **33,** 6626–6633 (2012).

237. Discher, D. E., Janmey, P. & Wang, Y. L. Tissue cells feel and respond to the stiffness of their substrate. *Science* **310,** 1139–1143 (2005).

238. Hsiao, A. Y. *et al.* Micro-ring structures stabilize microdroplets to enable long term spheroid culture in 384 hanging drop array plates. *Biomed. Microdevices* **14,** 313–323 (2012).

239. Cukierman, E., Pankov, R., Stevens, D. R. & Yamada, K. M. Taking cell-matrix adhesions to the third dimension. *Science (80-.).* **294,** 1708–1712 (2001).

240. Kawazoe, N., Inoue, C., Tateishi, T. & Chen, G. A cell leakproof PLGA-collagen

hybrid scaffold for cartilage tissue engineering. *Biotechnol. Prog.* **26,** 819–826 (2010).

241. Han, L.-H. *et al.* Microribbon-based hydrogels accelerate stem cell-based bone regeneration in a mouse critical-size cranial defect model. *J. Biomed. Mater. Res. - Part A* **104,** 1321–1331 (2016).
242. Ikonen, L. *et al.* 2D and 3D self-assembling nanofiber hydrogels for cardiomyocyte culture. *Biomed Res. Int.* **2013,** (2013).
243. Shimizu, T., Yamato, M., Kikuchi, A. & Okano, T. Cell sheet engineering for myocardial tissue reconstruction. *Biomaterials* **24,** 2309–2316 (2003).
244. Cimetta, E., Figallo, E., Cannizzaro, C., Elvassore, N. & Vunjak-Novakovic, G. Micro-bioreactor arrays for controlling cellular environments: Design principles for human embryonic stem cell applications. *Methods* **47,** 81–89 (2009).
245. Gogoi, P. *et al.* Development of an Automated and Sensitive Microfluidic Device for Capturing and Characterizing Circulating Tumor Cells (CTCs) from Clinical Blood Samples. *PLoS One* **11,** e0147400 (2016).
246. Duval, K. *et al.* Modeling Physiological Events in 2D vs. 3D Cell Culture. *Physiology* **32,** 266–277 (2017).
247. Bosi, S. *et al.* From 2D to 3D: Novel nanostructured scaffolds to investigate signalling in reconstructed neuronal networks. *Sci. Rep.* **5,** (2015).
248. Söderstjerna, E., Johansson, F., Klefbohm, B. & Englund Johansson, U. Gold- and Silver Nanoparticles Affect the Growth Characteristics of Human Embryonic Neural Precursor Cells. *PLoS One* (2013). doi:10.1371/journal.pone.0058211
249. Edmondson, R., Broglie, J. J., Adcock, A. F. & Yang, L. Three-Dimensional Cell Culture Systems and Their Applications in Drug Discovery and Cell-Based Biosensors. *Assay Drug Dev. Technol.* **12,** 207–218 (2014).
250. Naghdi, P. *et al.* Survival, proliferation and differentiation enhancement of neural stem cells cultured in three-dimensional polyethylene glycol-RGD hydrogel with tenascin. *J. Tissue Eng. Regen. Med.* **10,** 199–208 (2016).
251. Huang, H., Ding, Y., Sun, X. S. & Nguyen, T. A. Peptide Hydrogelation and Cell Encapsulation for 3D Culture of MCF-7 Breast Cancer Cells. *PLoS One* **8,** (2013).
252. Kim, J. Bin. Three-dimensional tissue culture models in cancer biology. *Semin. Cancer Biol.* **15,** 365–377 (2005).

253. Baker, B. M. & Chen, C. S. Deconstructing the third dimension – how 3D culture microenvironments alter cellular cues. *J. Cell Sci.* **125,** 3015–3024 (2012).

254. Gurski, L. a, Petrelli, N. J., Jia, X. & Farach-carson, M. C. 3D Matrices for Anti-Cancer Drug Testing and Development. *Oncol. Issues* **25,** 20–25 (2010).

255. Xu, X. *et al.* Recreating the tumor microenvironment in a bilayer, hyaluronic acid hydrogel construct for the growth of prostate cancer spheroids. *Biomaterials* **33,** 9049–9060 (2012).

256. Yip, D. & Cho, C. H. A multicellular 3D heterospheroid model of liver tumor and stromal cells in collagen gel for anti-cancer drug testing. *Biochem. Biophys. Res. Commun.* **433,** 327–332 (2013).

257. Tibbitt, M. W. & Anseth, K. S. Hydrogels as extracellular matrix mimics for 3D cell culture. *Biotechnology and Bioengineering* **103,** 655–663 (2009).

258. Trédan, O., Galmarini, C. M., Patel, K. & Tannock, I. F. Drug resistance and the solid tumor microenvironment. *Journal of the National Cancer Institute* **99,** 1441–1454 (2007).

259. Pickard, M. R., Adams, C. F., Barraud, P. & Chari, D. M. Using magnetic nanoparticles for gene transfer to neural stem cells: stem cell propagation method influences outcomes. *J. Funct. Biomater.* (2015). doi:10.3390/jfb6020259

260. Dumbleton, J. *et al.* The Effect of RGD Peptide on 2D and Miniaturized 3D Culture of HEPM Cells, MSCs, and ADSCs with Alginate Hydrogel. *Cell. Mol. Bioeng.* **9,** 277–288 (2016).

261. Zhang, Z.-N. *et al.* Layered hydrogels accelerate iPSC-derived neuronal maturation and reveal migration defects caused by MeCP2 dysfunction. *Proc. Natl. Acad. Sci.* **113,** 3185–3190 (2016).

262. Fuhrer, E. *et al.* 3D Carbon Scaffolds for Neural Stem Cell Culture and Magnetic Resonance Imaging. *Adv. Healthc. Mater.* (2018). doi:10.1002/adhm.201700915

263. Alexander, M. R. & Gilmore, I. S. Analytical techniques: Surface and interfacial characterisation. *Current Opinion in Chemical Biology* **15,** 664–666 (2011).

264. Whyman, G., Bormashenko, E. & Stein, T. The rigorous derivation of Young, Cassie-Baxter and Wenzel equations and the analysis of the contact angle hysteresis phenomenon. *Chem. Phys. Lett.* **450,** 355–359 (2008).

265. Bormashenko, E. Young, Boruvka-Neumann, Wenzel and Cassie-Baxter equations as

the transversality conditions for the variational problem of wetting. *Colloids Surfaces A Physicochem. Eng. Asp.* **345,** 163–165 (2009).

266. Moreira, A. B., Dias, I. L. T., Neto, G. O., Zagatto, E. A. G. & Kubota, L. T. Solid-phase fluorescence spectroscopy for the determination of acetylsalicylic acid in powdered pharmaceutical samples. *Anal. Chim. Acta* **523,** 49–52 (2004).
267. Gooijer, C. Introduction to Fluorescence Spectroscopy. *Anal. Chim. Acta* **419,** 116–117 (2000).
268. Lakowicz, J. R. *Principles of fluorescence spectroscopy*. *Principles of Fluorescence Spectroscopy* (2006). doi:10.1007/978-0-387-46312-4
269. Farjami Shayesteh, S. & Saie, M. The effect of surface plasmon resonance on optical response in dielectric (core)–metal (shell) nanoparticles. *PRAMANA c Indian Acad. Sci.* (2015). doi:10.1007/s12043-015-0950
270. Fan, X., Zheng, W. & Singh, D. J. Light scattering and surface plasmons on small spherical particles. *Light Sci. Appl.* (2014). doi:10.1038/lsa.2014.60
271. Haiss, W., Thanh, N. T. K., Aveyard, J. & Fernig, D. G. Determination of size and concentration of gold nanoparticles from UV-Vis spectra. *Anal. Chem.* **79,** 4215–4221 (2007).
272. Amendola, V. & Meneghetti, M. Size evaluation of gold nanoparticles by UV-vis spectroscopy. *J. Phys. Chem. C* **113,** 4277–4285 (2009).
273. Bersani, M. *et al.* D-SIMS and ToF-SIMS quantitative depth profiles comparison on ultra thin oxynitrides. in *Applied Surface Science* (2003). doi:10.1016/S0169-4332(02)00654-2
274. Trouiller, C. *et al.* ToF-SIMS applications in microelectronics: Quantification of organic surface contamination. in *AIP Conference Proceedings* (2005). doi:10.1063/1.2063022
275. Seah, M. P., Gilmore, I. S. & Spencer, S. J. XPS: Binding energy calibration of electron spectrometers 4 - Assessment of effects for different x-ray sources, analyser resolutions, angles of emission and overall uncertainties. *Surf. Interface Anal.* (1998). doi:10.1002/(SICI)1096-9918(199808)26:9<617::AID-SIA407>3.0.CO;2-V
276. Schlaf, R. Calibration of Photoemission Spectra and Work Function Determination. *J. Electron Spectros. Relat. Phenomena* (2001). doi:10.1016/S0368-2048(01)00310-3
277. Chu, B. Dynamic Light Scattering. in *Soft Matter Characterization* 335–372 (2008).

doi:10.1007/978-1-4020-4465-6_7

278. Malvern & Instruments, M. Dynamic Light Scattering : An Introduction in 30 Minutes. *Tech. Note MRK656-01* 1–8 (2011). doi:10.1017/CBO9781107415324.004

279. Tutorials, E. The Zeta Potential. *Building* 1–4 (1999).

280. Lu, G. W. & Gao, P. Emulsions and Microemulsions for Topical and Transdermal Drug Delivery. in *Handbook of Non-Invasive Drug Delivery Systems* (2010). doi:10.1016/B978-0-8155-2025-2.10003-4

281. Nanocomposix. Zeta Potential Analysis of Nanoparticles. *Nanocomposix Publ.* 1–6 (2012).

282. Instruments, M. Zeta potential: An Introduction in 30 minutes. *Zetasizer Nano Serles Tech. Note. MRK654-01* **2,** 1–6 (2011).

283. Bhattacharjee, S. DLS and zeta potential - What they are and what they are not? *Journal of Controlled Release* **235,** 337–351 (2016).

284. Horie, M. & Fujita, K. Toxicity of Metal Oxides Nanoparticles. *Adv. Mol. Toxicol.* (2011). doi:10.1016/B978-0-444-53864-2.00004-9

285. Anton, N. *et al.* A new microfluidic setup for precise control of the polymer nanoprecipitation process and lipophilic drug encapsulation. *Soft Matter* (2012). doi:10.1039/c2sm25357g

286. Wang, Z. *Transmission electron microscopy and spectroscopy of nanoparticles*. *Characterization of Nanophase Materials* (2000). doi:10.1002/3527600094

287. Thyparambil, A. A., Wei, Y. & Latour, R. A. Determination of peptide - Surface adsorption free energy for material surfaces not conducive to SPR or QCM using AFM. *Langmuir* (2012). doi:10.1021/la300315r

288. Prime, R. B., Bair, H. E., Vyazovkin, S., Gallagher, P. K. & Riga, A. Thermogravimetric Analysis (TGA). in *Thermal Analysis of Polymers: Fundamentals and Applications* (2008). doi:10.1002/9780470423837.ch3

289. Zelzer, M. *et al.* Phosphatase responsive peptide surfaces. *Journal of Materials Chemistry* **22,** 12229 (2012).

290. J. Turkevich; P.C. Stevenson; J. Hiller. Synthesis of Gold Nanoparticles Turkevich method. *Discuss. Faraday Soc.* **11,** 55–75 (1951).

291. Kimling, J. *et al.* Turkevich method for gold nanoparticle synthesis revisited. *J. Phys.*

Chem. B **110,** 15700–15707 (2006).

292. Ignacio-De Leon, P. A. A. & Zharov, I. SiO2@Au core-shell nanospheres self-assemble to form colloidal crystals that can be sintered and surface modified to produce pH-controlled membranes. *Langmuir* **29,** 3749–3756 (2013).

293. Patel, P. C., Giljohann, D. a, Seferos, D. S. & Mirkin, C. a. Peptide antisense nanoparticles. *Proc. Natl. Acad. Sci. U. S. A.* **105,** 17222–6 (2008).

294. Guo, W., Patzlaff, N. E., Jobe, E. M. & Zhao, X. Isolation of multipotent neural stem or progenitor cells from both the dentate gyrus and subventricular zone of a single adult mouse. *Nat. Protoc.* (2012). doi:10.1038/nprot.2012.123

295. Daadi, M. M. & Steinberg, G. K. Manufacturing neurons from human embryonic stem cells: Biological and regulatory aspects to develop a safe cellular product for stroke cell therapy. *Regenerative Medicine* (2009). doi:10.2217/17460751.4.2.251

296. Abranches, E. *et al.* Neural differentiation of embryonic stem cells in vitro: A road map to neurogenesis in the embryo. *PLoS One* (2009). doi:10.1371/journal.pone.0006286

296*. Kaneko, A. & Sankai, Y. Long-term culture of rat hippocampal neurons at low density in serum-free medium: Combination of the sandwich culture technique with the three-dimensional nanofibrous hydrogel PuraMatrix. PLoS One (2014). doi:10.1371/journal.pone.0102703

297. Materne, T., de Buyl, F. & Witucki, G. L. Organosilane Technology in Coating Applications : Review and Perspectives. *Dow Corning* 1–16 (2012).

298. Sever, K., Seki, Y., Tavman, I. H., Erkan, G. & Cecen, V. The Structure of γ-Glycidoxypropyltrimethoxysilane on Glass Fiber Surfaces: Characterization by FTIR, SEM, and Contact Angle Measurements. *Polym. Compos.* **30,** 550–558 (2009).

299. Osterholtz, F. D. & Pohl, E. R. Kinetics of the Hydrolysis and Condensation of Organofunctional Alkoxysilanes: A Review. *J. Adhes. Sci. Technol.* **6,** 127–149 (1992).

300. Sonawane, M. D. & Nimse, S. B. Surface Modification Chemistries of Materials Used in Diagnostic Platforms with Biomolecules. *Journal of Chemistry* **2016,** (2016).

301. Jo, S. & Park, K. Surface modification using silanated poly(ethylene glycol)s. *Biomaterials* **21,** 605–616 (2000).

302. Turecek, P. L., Bossard, M. J., Schoetens, F. & Ivens, I. A. PEGylation of

Biopharmaceuticals: A Review of Chemistry and Nonclinical Safety Information of Approved Drugs. *J. Pharm. Sci.* **105,** 460–475 (2016).

303. Trzcinska, R. *et al.* Relevance of the poly(ethylene glycol) linkers in peptide surfaces for proteases assays. *Langmuir* **30,** 5015–5025 (2014).
304. Dalsin, J. L. & Messersmith, P. B. Bioinspired antifouling polymers. *Materials Today* **8,** 38–46 (2005).
305. Zhang, H. & Chiao, M. Anti-fouling coatings of poly(dimethylsiloxane) devices for biological and biomedical applications. *Journal of Medical and Biological Engineering* **35,** 143–155 (2015).
306. Hamming, L. M. & Phillip, B. Fouling Resistant Biomimetic Poly(Ethylene Glycol) Based Grafted Polymer Coatings. *Mater. Matters* (2008).
307. Kobayashi, M. *et al.* Wettability and antifouling behavior on the surfaces of superhydrophilic polymer brushes. *Langmuir* (2012). doi:10.1021/la301033h
308. Chithrani, D. B. Polyethylene Glycol Density and Length Affects Nanoparticle Uptake by Cancer Cells. *J. Nanomedicine Res.* (2014). doi:10.15406/jnmr.2014.01.00006
309. Zhu, J. Bioactive modification of poly(ethylene glycol) hydrogels for tissue engineering. *Biomaterials* (2010). doi:10.1016/j.biomaterials.2010.02.044
310. Banoriya, D., Purohit, R. & Dwivedi, R. K. Advanced Application of Polymer based Biomaterials. in *Materials Today: Proceedings* (2017). doi:10.1016/j.matpr.2017.02.244
311. Hutanu, D. Recent Applications of Polyethylene Glycols (PEGs) and PEG Derivatives. *Mod. Chem. Appl.* (2014). doi:10.4172/2329-6798.1000132
312. Banerjee, S. S., Aher, N., Patil, R. & Khandare, J. Poly(ethylene glycol)-Prodrug Conjugates: Concept, Design, and Applications. *J. Drug Deliv.* **2012,** 1–17 (2012).
313. Chow, D., Nunalee, M. L., Lim, D. W., Simnick, A. J. & Chilkoti, A. Peptide-based biopolymers in biomedicine and biotechnology. *Materials Science and Engineering R: Reports* **62,** 125–155 (2008).
314. Larnaudie, S. C., Brendel, J. C., Jolliffe, K. A. & Perrier, S. Cyclic peptide-polymer conjugates: Grafting-to vs grafting-from. *J. Polym. Sci. Part A Polym. Chem.* **54,** 1003–1011 (2016).
315. Mitchell, A. R. Bruce Merrifield and solid-phase peptide synthesis: A historical assessment. *Biopolymers - Peptide Science Section* **90,** 175–184 (2008).

316. Sahoo, J. K. *et al.* Analysis of enzyme-responsive peptide surfaces by Raman spectroscopy. *Chem. Commun.* **52,** 4698–4701 (2016).
317. Cherkupally, P. *et al.* Immobilized coupling reagents: Synthesis of amides/peptides. *ACS Combinatorial Science* **16,** 579–601 (2014).
318. Williams, A. & Ibrahim, I. T. Carbodiimide Chemistry: Recent Advances. *Chem. Rev.* **81,** 589–636 (1981).
319. Anderson, G. W., Zimmerman, J. E. & Callahan, F. M. The Use of Esters of N-Hydroxysuccinimide in Peptide Synthesis. *J. Am. Chem. Soc.* **86,** 1839–1842 (1964).
320. Montalbetti, C. A. G. N. & Falque, V. Amide bond formation and peptide coupling. *Tetrahedron* **61,** 10827–10852 (2005).
321. Stephanopoulos, N., Ortony, J. H. & Stupp, S. I. Self-assembly for the synthesis of functional biomaterials. *Acta Mater.* **61,** 912–930 (2013).
322. Zelzer, M., Scurr, D. J., Alexander, M. R. & Ulijn, R. V. Development and validation of a fluorescence method to follow the build-up of short peptide sequences on solid 2D surfaces. *ACS Appl. Mater. Interfaces* **4,** 53–58 (2012).
323. Nomizu, M. *et al.* Structure-activity study of a laminin ??1 chain active peptide segment Ile-Lys-Val-Ala-Val (IKVAV). *FEBS Lett.* **365,** 227–231 (1995).
324. Zhang, Z. *et al.* Neurite outgrowth on well-characterized surfaces: Preparation and characterization of chemically and spatially controlled fibronectin and RGD substrates with good bioactivity. *Biomaterials* **26,** 47–61 (2005).
325. Du, J. *et al.* Integrin activation and internalization on soft ECM as a mechanism of induction of stem cell differentiation by ECM elasticity. *Proc. Natl. Acad. Sci. U. S. A.* **108,** 9466–9471 (2011).
326. Zelzer, M., Alexander, M. R. & Russell, N. A. Hippocampal cell response to substrates with surface chemistry gradients. *Acta Biomater.* **7,** 4120–4130 (2011).
327. Zelzer, M. *et al.* Investigation of cell-surface interactions using chemical gradients formed from plasma polymers. *Biomaterials* **29,** 172–84 (2008).
328. Arima, Y. & Iwata, H. Effects of surface functional groups on protein adsorption and subsequent cell adhesion using self-assembled monolayers. *Journal of Materials Chemistry* **17,** 4079 (2007).
329. Todd, S. J., Scurr, D. J., Gough, J. E., Alexander, M. R. & Ulijn, R. V. Enzyme-activated

RGD ligands on functionalized poly(ethylene glycol) monolayers: Surface analysis and cellular response. *Langmuir* **25,** 7533–7539 (2009).

330. Zelzer, M., Todd, S. & Hirst, A. Enzyme responsive materials: design strategies and future developments. *Biomater. Sci.* **1,** 11–39 (2013).
331. Carpino, L. A. & Han, G. Y. The 9-Fluorenylmethoxycarbonyl Amino-Protecting Group. *J. Org. Chem.* **44,** 3739 (1979).
332. Profit, A. A., Felsen, V., Chinwong, J., Mojica, E. R. E. & Desamero, R. Z. B. Evidence of π-stacking interactions in the self-assembly of hIAPP22-29. *Proteins Struct. Funct. Bioinforma.* **81,** 690–703 (2013).
333. Pinotsi, D., Buell, A. K., Dobson, C. M., Kaminski Schierle, G. S. & Kaminski, C. F. A Label-Free, Quantitative Assay of Amyloid Fibril Growth Based on Intrinsic Fluorescence. *ChemBioChem* **14,** 846–850 (2013).
334. Katritzky, A. R. & Narindoshvili, T. Fluorescent amino acids: advances in protein-extrinsic fluorophores. *Org. Biomol. Chem.* **7,** 627–634 (2009).
335. Henke, L., Nagy, N. & Krull, U. J. An AFM determination of the effects on surface roughness caused by cleaning of fused silica and glass substrates in the process of optical biosensor preparation. *Biosens. Bioelectron.* **17,** 547–555 (2002).
336. Bennett, J. M. & Takacs, P. Z. Surface roughness and scattering: papers from the first topical meeting. *Appl. Opt.* **32,** 3333–3334 (1993).
337. Chada, N. *et al.* Glass is a Viable Substrate for Precision Force Microscopy of Membrane Proteins. *Sci. Rep.* (2015). doi:10.1038/srep12550
338. Mosse, W. K. J. *et al.* Peptides Grafted from Solids for the Control of Interfacial Properties. *Langmuir* **25,** 1488–1494 (2009).
339. Wagner, M. S. & Castner, D. G. Characterization of Adsorbed Protein Films by Time-of-Flight Secondary Ion Mass Spectrometry with Principal Component Analysis. *Langmuir* **17,** 4649–4660 (2001).
340. Wagner, M. S., Shen, M., Horbett, T. A. & Castner, D. G. Quantitative analysis of binary adsorbed protein films by time of flight secondary ion mass spectrometry. *J. Biomed. Mater. Res. Part A* **64A,** 1–11 (2002).
341. Wagner, M. S., McArthur, S. L., Shen, M., Horbett, T. A. & Castner, D. G. Limits of detection for time of flight secondary ion mass spectrometry (ToF-SIMS) and X-ray

photoelectron spectroscopy (XPS): Detection of low amounts of adsorbed protein. *J. Biomater. Sci. Polym. Ed.* **13,** 407–428 (2002).

342. Wagner, M. S. & Castner, D. G. Characterization of adsorbed protein films by time-of-flight secondary ion mass spectrometry with principal component analysis. *Langmuir* **17,** 4649–4660 (2001).
343. Mantus, D. S., Ratner, B. D., Carlson, B. A. & Moulder, J. F. Static Secondary-Ion Mass-Spectrometry of Adsorbed Proteins. *Anal. Chem.* **65,** 1431–1438 (1993).
344. Bouchonnet, S., Denhez, J. P., Hoppilliard, Y. & Mauriac, C. Is Plasma Desorption Mass Spectrometry Useful for Small-Molecule Analysis? Fragmentations of the Natural α-Amino Acids. *Anal. Chem.* **64,** 743–754 (1992).
345. Tyler, B. J., Bruening, C., Rangaranjan, S. & Arlinghaus, H. F. TOF-SIMS imaging of adsorbed proteins on topographically complex surfaces with Bi(3) (+) primary ions. *Biointerphases* **6,** 135 (2011).
346. Petershans, A. *et al.* TOF-SIMS analysis of structured surfaces biofunctionalized by a one-step coupling of a spacer-linked GRGDS peptide. *J. Colloid Interface Sci.* **341,** 30–37 (2010).
347. Barazzouk, S. & Daneault, C. Amino Acid and Peptide Immobilization on Oxidized Nanocellulose: Spectroscopic Characterization. *Nanomaterials* **2,** 187–205 (2012).
348. De Luca, A. C. *et al.* Immobilization of cell-binding peptides on poly-e-caprolactone film surface to biomimic the peripheral nervous system. *J. Biomed. Mater. Res. - Part A* **101 A,** 491–501 (2013).
349. Stevens, J. S., De Luca, A. C., Downes, S., Terenghi, G. & Schroeder, S. L. M. Immobilisation of cell-binding peptides on poly-??-caprolactone (PCL) films: A comparative XPS study of two chemical surface functionalisation methods. *Surf. Interface Anal.* **46,** 673–678 (2014).
350. Stevens, J. S. & Schroeder, S. L. M. Quantitative analysis of saccharides by X-ray photoelectron spectroscopy. *Surf. Interface Anal.* **41,** 453–462 (2009).
351. Shanbhag, M. S. *et al.* Neural progenitor cells grown on hydrogel surfaces respond to the product of the transgene of encapsulated genetically engineered fibroblasts. *Biomacromolecules* **11,** 2936–2943 (2010).
352. Cheung, H. H. *et al.* Telomerase protects Werner syndrome lineage-specific stem cells

from premature aging. *Stem Cell Reports* **2,** 534–546 (2014).

353. Gunhanlar, N. *et al.* A simplified protocol for differentiation of electrophysiologically mature neuronal networks from human induced pluripotent stem cells. *Mol. Psychiatry* 1–9 (2017). doi:10.1038/mp.2017.56

354. Clause, K. C., Liu, L. J. & Tobita, K. Directed stem cell differentiation: The role of physical forces. *Cell Communication and Adhesion* **17,** 48–54 (2010).

355. Liu, G. *et al.* Cytotoxicity study of polyethylene glycol derivatives. *RSC Adv.* (2017). doi:10.1039/c7ra00861a

356. Masters, K. S., Shah, D. N., Walker, G., Leinwand, L. A. & Anseth, K. S. Designing scaffolds for valvular interstitial cells: Cell adhesion and function on naturally derived materials. *J. Biomed. Mater. Res. - Part A* **71,** 172–180 (2004).

357. Van Almen, G. C. *et al.* Development of Non-Cell Adhesive Vascular Grafts Using Supramolecular Building Blocks. *Macromol. Biosci.* **16,** 350–362 (2016).

358. Patel, N. G. & Zhang, G. Responsive systems for cell sheet detachment. 93–100 (2013).

359. Lu, P. *et al.* Prolonged human neural stem cell maturation supports recovery in injured rodent CNS. *J. Clin. Invest.* (2017). doi:10.1172/JCI92955

360. Liebau, S., Vaida, B., Storch, A. & Boeckers, T. M. Maturation of Synaptic Contacts in Differentiating Neural Stem Cells. *Stem Cells* (2007). doi:10.1634/stemcells.2006-0823

361. Tennstaedt, A. *et al.* Human neural stem cell intracerebral grafts show spontaneous early neuronal differentiation after several weeks. *Biomaterials* (2015). doi:10.1016/j.biomaterials.2014.12.038

362. Topol, A., Tran, N. N. & Brennand, K. J. A Guide to Generating and Using hiPSC Derived NPCs for the Study of Neurological Diseases. *J. Vis. Exp.* (2015). doi:10.3791/52495

363. Stroka, K. M. & Aranda-Espinoza, H. Effects of morphology vs. cell-cell interactions on endothelial cell stiffness. *Cell. Mol. Bioeng.* **4,** 9–27 (2011).

364. Iha, R. K. *et al.* Applications of orthogonal 'Click' Chemistries in the synthesis of functional soft materials. *Chem. Rev.* **109,** 5620–5686 (2009).

365. Cui, H., Webber, M. J. & Stupp, S. I. Self-assembly of peptide amphiphiles: from molecules to nanostructures to biomaterials. *Biopolymers* **94,** 1–18 (2010).

366. Albericio, F. Editorial: Current perspectives in peptide chemistry. II. Supports.

Biopolymers - Peptide Science Section **55,** 187 (2000).

367. Heidler, P. & Link, A. N-Acyl-N-alkyl-sulfonamide anchors derived from Kenner's safety-catch linker: Powerful tools in bioorganic and medicinal chemistry. *Bioorganic and Medicinal Chemistry* **13,** 585–599 (2005).

368. Panke, G. & Frank, R. Improved preparation of a safety-catch linker for the solid phase synthesis of peptide acids finally released into aqueous buffers. *Tetrahedron Lett.* **39,** 17–18 (1998).

369. Hassert, R. *et al.* Biocompatible silicon surfaces through orthogonal click chemistries and a high affinity silicon oxide binding peptide. *Bioconjug. Chem.* **23,** 2129–2137 (2012).

370*. McKee, C. & Chaudhry, G. R. Advances and challenges in stem cell culture. *Colloids and Surfaces B: Biointerfaces (2017).* doi:10.1016/j.colsurfb.2017.07.051

370. Campos, L. S. Neurospheres: Insights into neural stem cell biology. *Journal of Neuroscience Research* **78,** 761–769 (2004).

371. Ribeiro, A. S., Powell, E. M. & Leach, J. B. Neural Stem Cell Differentiation in 2D and 3D Microenvironments. *26th South. Biomed. Eng. Conf. Sbec 2010* **32,** 422–425 (2010).

372. Bardsley, K., Deegan, A. J., El Haj, A. & Yang, Y. Current state-of-the-art 3D tissue models and their compatibility with live cell imaging. in *Advances in Experimental Medicine and Biology* **1035,** 3–18 (2017).

373. Kwakwa, K. A., Vanderburgh, J. P., Guelcher, S. A. & Sterling, J. A. Engineering 3D Models of Tumors and Bone to Understand Tumor-Induced Bone Disease and Improve Treatments. *Current Osteoporosis Reports* **15,** 247–254 (2017).

374. Foster, N. C., Henstock, J. R., Reinwald, Y. & El Haj, A. J. Dynamic 3D culture: Models of chondrogenesis and endochondral ossification. *Birth Defects Res. Part C - Embryo Today Rev.* **105,** 19–33 (2015).

375. Hewitt, N. J. *et al.* Use of Human In Vitro Skin Models for Accurate and Ethical Risk Assessment: Metabolic Considerations. *Toxicol. Sci.* **133,** 209–217 (2013).

376. Valverde, I. Three-dimensional Printed Cardiac Models: Applications in the Field of Medical Education, Cardiovascular Surgery, and Structural Heart Interventions. *Rev. Española Cardiol. (English Ed.* **70,** 282–291 (2017).

377. Mishra, D. K. *et al.* Human Lung Cancer Cells Grown in an Ex Vivo 3D Lung Model

Produce Matrix Metalloproteinases Not Produced in 2D Culture. *PLoS One* **7,** (2012).

378. Yoon No, D., Lee, K.-H., Lee, J. & Lee, S.-H. 3D liver models on a microplatform: well-defined culture, engineering of liver tissue and liver-on-a-chip. *Lab Chip* **15,** 3822–3837 (2015).
379. Gibney, R., Matthyssen, S., Patterson, J., Ferraris, E. & Zakaria, N. The Human Cornea as a Model Tissue for Additive Biomanufacturing: A Review. in *Procedia CIRP* **65,** 56–63 (2017).
380. Chandrasekaran, A. *et al.* Comparison of 2D and 3D neural induction methods for the generation of neural progenitor cells from human induced pluripotent stem cells. *Stem Cell Res.* **25,** (2017).
381. Shang, L., Nienhaus, K. & Nienhaus, G. U. Engineered nanoparticles interacting with cells: Size matters. *Journal of Nanobiotechnology* **12,** (2014).
382. Riedl, A. *et al.* Comparison of cancer cells in 2D vs 3D culture reveals differences in AKT–mTOR–S6K signaling and drug responses. *J. Cell Sci.* **130,** 203–218 (2017).
383. Sung, K. E. *et al.* Understanding the Impact of 2D and 3D Fibroblast Cultures on In Vitro Breast Cancer Models. *PLoS One* **8,** (2013).
384. Hess, M. W. *et al. 3D versus 2D cell culture. Implications for electron microscopy*. *Methods in Cell Biology* **96,** (2010).
385. Salata, O. *et al.* Applications of nanoparticles in biology and medicine. *J. Nanobiotechnology* (2004). doi:10.1186/1477-3155-2-3
386. Khan, I., Saeed, K. & Khan, I. Nanoparticles: Properties, applications and toxicities. *Arabian Journal of Chemistry* (2017). doi:10.1016/j.arabjc.2017.05.011
387. Hervault, A. & Thanh, N. T. K. Magnetic nanoparticle-based therapeutic agents for thermo-chemotherapy treatment of cancer. *Nanoscale* (2014). doi:10.1039/c4nr03482a
388. Oliverio, M., Perotto, S., Messina, G. C., Lovato, L. & De Angelis, F. Chemical Functionalization of Plasmonic Surface Biosensors: A Tutorial Review on Issues, Strategies, and Costs. *ACS Appl. Mater. Interfaces* **9,** 29394–29411 (2017).
389. Pensa, E. *et al.* The chemistry of the sulfur-gold interface: In search of a unified model. *Acc. Chem. Res.* **45,** 1183–1192 (2012).
390. Li, G. *et al.* A gold nanoparticles enhanced surface plasmon resonance immunosensor for highly sensitive detection of ischemia-modified albumin. *Sensors (Basel).* **13,** 12794–

803 (2013).

391. Messerschmidt, C. *et al.* On the pathway of cellular uptake: New insight into the interaction between the cell membrane and very small nanoparticles. *Beilstein J. Nanotechnol.* **7,** 1296–1311 (2016).

392. Naka, Y., Eda, A., Takei, H. & Shimizu, N. Neurite outgrowths of neurons on patterned self-assembled monolayers. *J. Biosci. Bioeng.* **94,** 434–439 (2002).

393. Yameen, B. *et al.* Insight into nanoparticle cellular uptake and intracellular targeting. *J. Control. Release* **190,** 485–499 (2014).

394. Oh, N. & Park, J. H. Endocytosis and exocytosis of nanoparticles in mammalian cells. *International Journal of Nanomedicine* (2014). doi:10.2147/IJN.S26592

395. Sobers, C. J., Wood, S. E. & Mrksich, M. A gene expression-based comparison of cell adhesion to extracellular matrix and RGD-terminated monolayers. *Biomaterials* **52,** 385–394 (2015).

396. Hazenbiller, O., Duncan, N. A. & Krawetz, R. J. Reduction of pluripotent gene expression in murine embryonic stem cells exposed to mechanical loading or Cyclo RGD peptide. *BMC Cell Biol.* **18,** (2017).

397. Tien, J., Li, L., Ozsun, O. & Ekinci, K. L. Dynamics of Interstitial Fluid Pressure in Extracellular Matrix Hydrogels in Microfluidic Devices. *J. Biomech. Eng.* **137,** 091009 (2015).

398. Vu, T. Q., de Castro, R. M. B. & Qin, L. Bridging the gap: microfluidic devices for short and long distance cell–cell communication. *Lab Chip* **17,** 1009–1023 (2017).

399. Li, N., Tourovskaia, A. & Folch, A. Biology on a chip: microfabrication for studying the behavior of cultured cells. *Crit. Rev. Biomed. Eng.* **31,** 423–488 (2003).

400. Kolaja, K. Stem cells and stem cell-derived tissues and their use in safety assessment. *J. Biol. Chem.* **289,** 4555–61 (2014).

401. Sala, L., Bellin, M. & Mummery, C. L. Integrating cardiomyocytes from human pluripotent stem cells in safety pharmacology: Has the time come? *Br. J. Pharmacol.* 1–17 (2016). doi:10.1111/bph.13577

402. Epa, V. C. *et al.* Modelling human embryoid body cell adhesion to a combinatorial library of polymer surfaces. *J. Mater. Chem.* **22,** 20902 (2012).

403. Fan, K. *et al.* A Machine Learning Assisted, Label-free, Non-invasive Approach for

Somatic Reprogramming in Induced Pluripotent Stem Cell Colony Formation Detection and Prediction. *Sci. Rep.* **7,** (2017).

404. Risner-Janiczek, J. R., Ungless, M. A. & Li, M. Electrophysiological properties of embryonic stem cell-derived neurons. *PLoS One* **6,** (2011).
405. Needham, K., Hyakumura, T., Gunewardene, N., Dottori, M. & Nayagam, B. A. Electrophysiological properties of neurosensory progenitors derived from human embryonic stem cells. *Stem Cell Res.* **12,** 241–249 (2014).
406. Tatman, P. D. *et al.* Self-assembling peptides for stem cell and tissue engineering. *Biomater. Sci.* **4,** 543–554 (2016).
407. Mucke, L. & Selkoe, D. J. Neurotoxicity of amyloid β-protein: Synaptic and network dysfunction. *Cold Spring Harb. Perspect. Med.* **2,** (2012).
408. Li, F., Zhao, Y., Mao, C., Kong, Y. & Ming, X. RGD-Modified Albumin Nanoconjugates for Targeted Delivery of a Porphyrin Photosensitizer. *Mol. Pharm.* **14,** 2793–2804 (2017).
409. Zhang, B., Zheng, W., Papoian, G. A. & Wolynes, P. G. Exploring the Free Energy Landscape of Nucleosomes. *J. Am. Chem. Soc.* **138,** 8126–8133 (2016).
410. Sun, Y. *et al.* RGD Peptide-Based Target Drug Delivery of Doxorubicin Nanomedicine. *Drug Dev. Res.* **78,** 283–291 (2017).
411. Ruan, H. *et al.* Stapled RGD Peptide Enables Glioma-Targeted Drug Delivery by Overcoming Multiple Barriers. *ACS Appl. Mater. Interfaces* **9,** 17745–17756 (2017).
412. Townsend, L. *et al.* Antimicrobial peptide coatings for hydroxyapatite: electrostatic and covalent attachment of antimicrobial peptides to surfaces. *J. R. Soc. Interface* **14,** (2017).
413. Liu, Q., Wang, J. & Boyd, B. J. Peptide-based biosensors. *Talanta* **136,** 114–127 (2015).
414. Liu, X., Marrakchi, M., Xu, D., Dong, H. & Andreescu, S. Biosensors based on modularly designed synthetic peptides for recognition, detection and live/dead differentiation of pathogenic bacteria. *Biosens. Bioelectron.* **80,** 9–16 (2016).
415. Starzl, T. E. History of clinical transplantation. in *Surgery: Basic Science and Clinical Evidence: Second Edition* 1681–1704 (2008). doi:10.1007/978-0-387-68113-9_80
416. Atala, A. Extending life using tissue and organ replacement. *Curr.Aging Sci.* **1,** 73–83 (2008).

417. Salgado, A. J. *et al.* Tissue engineering and regenerative medicine: Past, present, and future. *Int. Rev. Neurobiol.* **108,** 1–33 (2013).

418. Mao, A. S. & Mooney, D. J. Regenerative medicine: Current therapies and future directions. *Proc. Natl. Acad. Sci. U. S. A.* **112,** 14452–9 (2015).

419. Federica Colomboa, Gianluca Sampognaa, G. C. & Salman Yousuf Gurayab, Antonello Forgionea, ∗. Regenerative medicine: Clinical applications and future perspectives. *J. Microsc. Ultrastruct.* **5,** 1–8 (2016).